



## Durham E-Theses

---

### *Seismic imaging of crustal structure at mid-ocean ridges: a three-dimensional approach*

Day, Anthony J.

#### How to cite:

---

Day, Anthony J. (2001) *Seismic imaging of crustal structure at mid-ocean ridges: a three-dimensional approach*, Durham theses, Durham University. Available at Durham E-Theses Online:  
<http://etheses.dur.ac.uk/4274/>

#### Use policy

---

The full-text may be used and/or reproduced, and given to third parties in any format or medium, without prior permission or charge, for personal research or study, educational, or not-for-profit purposes provided that:

- a full bibliographic reference is made to the original source
- a [link](#) is made to the metadata record in Durham E-Theses
- the full-text is not changed in any way

The full-text must not be sold in any format or medium without the formal permission of the copyright holders.

Please consult the [full Durham E-Theses policy](#) for further details.

---

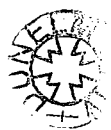
Academic Support Office, Durham University, University Office, Old Elvet, Durham DH1 3HP  
e-mail: [e-theses.admin@dur.ac.uk](mailto:e-theses.admin@dur.ac.uk) Tel: +44 0191 334 6107  
<http://etheses.dur.ac.uk>

# **Seismic imaging of crustal structure at mid-ocean ridges: a three-dimensional approach**

**Anthony James Day**

**The copyright of this thesis rests with the author. No quotation from it should be published in any form, including Electronic and the Internet, without the author's prior written consent. All information derived from this thesis must be acknowledged appropriately.**

**A thesis submitted for the degree of Doctor of Philosophy at the  
University of Durham**



**Department of Geological Sciences  
February 2001**

**17 SEP 2001**

# Declaration

This dissertation describes my own work, except where acknowledgement is made in the text, and is not substantially the same as any work that has been, or is being, submitted to any other university for any degree, diploma or other qualification.

Anthony J. Day

February 2001



# Seismic imaging of crustal structure at mid-ocean ridges: a three-dimensional approach

Anthony J. Day

## Abstract

Over recent years geological, geochemical and geophysical surveys of mid-ocean ridges have revealed a significant degree of along-axis variability not only in seabed morphology, but also in crustal structure, particularly so the magma plumbing system. Numerous geophysical surveys of the Valu Fa Ridge, southwest Pacific, have mapped the extent of an axial mid-crustal reflector. This reflector has been interpreted as representing the top of a sill-like melt lens, comprising a high percentage of partial melt, lying at the top of a crustal magma chamber.

In 1995, a controlled-source, wide-angle seismic dataset was acquired at the Valu Fa Ridge during *R/V Maurice Ewing* cruise EW9512, to investigate the mid-deep crustal structure at this ridge, and particularly the crustal magma chamber associated with the melt lens beneath the ridge axis. The EW9512 acquisition geometry was primarily two-dimensional in design, and modelling of these 2-D profiles revealed the presence of an axial low velocity zone beneath the melt lens. This low velocity zone is thought to represent a region of crystal mush comprising a much lower percentage of partial melt than is present in the overlying melt lens. Similar structures have been modelled beneath a number of other mid-ocean ridges. The primary aim of this study was to build on this 2-D interpretation by taking advantage of three-dimensional ray coverage in the axial region in order to assess the along-axis continuity of the magmatic system, correlate this to any ridge segmentation apparent in the seabed morphology, and determine if ridge segmentation is related to the magma supply.

The 3-D data were analysed using a tomographic inversion technique. The inversion results suggest that the axial low velocity zone may be segmented on a scale of 5–10 km, which correlates with the morphological segmentation of the ridge crest and is believed to reflect episodic magma supply with different ridge segments at different stages of a cycle of magmatic and amagmatic extension. However, three-dimensional ray coverage is not ideal owing to the dominantly 2-D acquisition geometry. Therefore a detailed assessment of data uncertainty and resolution was undertaken to enable a meaningful interpretation of the inversion results in terms of which features have a geological origin and which are artefacts of the inversion process.

*P-S* mode converted arrivals arising from mid-crustal interfaces were also modelled in order to obtain improved geological constraints on the crustal structure than is possible from *P*-wave studies alone. This modelling indicates that the uppermost crust is pervaded by thin cracks. In addition, techniques were developed for modelling the polarisation of *S*-wave arrivals with low signal strength. Application of these methods suggests that the thin cracks have a preferred orientation parallel to the ridge crest on-axis, and oblique to the ridge crest off-axis which is thought to reflect the pattern of southward propagation of the ridge system inferred from regional tectonic and bathymetric studies. Modelling of *P-S* mode converted arrivals arising from conversion at the top of the melt lens provided additional constraints on the properties of the melt lens. In conjunction with the 3-D tomographic results, this work suggests that the southernmost ridge segment in the study area has recently become magmatically active following a period of amagmatic extension suggested by its morphology, thus providing evidence for episodic melt supply at this ridge.

As part of the suggestions for further work, a theoretical investigation of survey resolution was undertaken to test commonly adopted acquisition geometries with a view to optimising the design and cost-effectiveness of future 3-D controlled-source tomographic experiments.

# Acknowledgements

First and foremost, I would like to acknowledge the considerable assistance I have received from my supervisor, Christine Peirce. Over the course of three and a bit years, Chris has offered invaluable advice on how to proceed on many occasions, conjured up the necessary computer hardware to allow this project to be conducted efficiently, provided the funds and the excuse for two trips to the USA, and given me first-hand experience of collecting marine seismic data. In addition, her sterling efforts at ploughing through earlier drafts of this dissertation have undoubtedly made it more readable and informative. For all these things, I am most grateful.

The code used to perform the inversions was written by Colin Zelt, and I am grateful to him for taking the time to personally explain how to use it. Various sections of this dissertation have benefited from suggestions and discussions with Ian Turner, Neil Goulty, Martin Sinha, Lucy MacGregor, Andrew Barclay and Rob Dunn. Ian in particular greatly assisted me during the first two years of this project, his in-depth knowledge of the dataset and helpful suggestions saving me from running down many blind alleys.

I would like to thank the officers and crew of the *R/V Maurice Ewing* and members of the EW9512 Scientific Party, without whose efforts the dataset on which this project is based would not exist. This research cruise was NERC funded, and I have also been financially supported by NERC throughout my Ph.D.

Numerous cavers from the Durham and Cambridge University clubs deserve credit for helping to keep me the right side of sanity. I have yet to find anything quite like dangling over a 45 m drop on a 10 mm thick piece of rope for concentrating the mind and making the previous week's failure to extend the body of geophysical knowledge one iota seem utterly inconsequential. My working environment has been made much livelier by the presence of the various people with whom I have shared an office over the course of three years. I also wish to acknowledge the encouragement and support offered by my family throughout my education, without which I doubt I would have ended up studying for a Ph.D at all.

Finally, thanks to Julia for love and support when it mattered most.

# Contents

<b>1 Introduction.....</b>	<b>1</b>
1.1 Oceanic crust and mid-ocean ridges.....	2
1.2 Segmentation of mid-ocean ridges.....	6
1.2.1 Segmentation of the Mid-Atlantic Ridge.....	6
1.2.2 Segmentation of the East Pacific Rise.....	8
1.3 Seismic studies at mid-ocean ridges.....	9
1.3.1 Seismic studies of axial magma chambers.....	10
1.3.2 Relationship between magmatic budget and crustal structure.....	15
1.3.3 Three-dimensional tomographic studies.....	17
1.3.4 <i>S</i> -wave studies.....	19
1.4 The Valu Fa Ridge.....	23
1.4.1 Geological setting.....	23
1.4.2 Previous geophysical studies.....	26
1.5 <i>R/V Maurice Ewing</i> cruise EW9512 – the Valu Fa Ridge .....	28
1.5.1 Experimental configuration.....	28
1.5.2 Data acquisition.....	30
1.5.3 Data processing.....	32
1.5.4 Modelling results.....	33
1.6 Aims of this study.....	35
1.7 Summary and structure of this dissertation.....	36
<b>2 Three-dimensional tomographic inversion.....</b>	<b>38</b>
2.1 Introduction.....	38
2.2 Method.....	38
2.2.1 Seismic refraction tomography.....	39
2.2.2 Forward modelling step.....	40
2.2.3 Inverse step.....	43
2.3 Data.....	46
2.3.1 First arrival travel time picks.....	47
2.3.2 Shot locations.....	49
2.3.3 Receiver locations.....	50
2.4 Travel time observation uncertainties.....	59
2.4.1 Method.....	59
2.4.2 Results.....	63
2.4.3 Application to the real data.....	71
2.5 Predicted travel time uncertainties.....	72
2.6 Travel time residual uncertainties.....	77
2.7 Forward modelling grid.....	78
2.8 Initial model.....	82
2.9 Inversion parameters.....	88
2.10 Resolution analysis.....	88
2.10.1 Method.....	89
2.10.2 Results.....	93
2.11 Summary.....	97

### **3 Seismic tomographic inversion at the Valu Fa Ridge.....98**

3.1 Introduction.....	98
3.2 Inversion travel time dataset.....	98
3.3 Inversion cell size.....	100
3.4 Preferred initial model.....	106
3.4.1 1-D initial models.....	107
3.4.2 2-D initial model.....	111
3.4.3 Unbiased 2-D initial model.....	115
3.5 Effect of the melt lens.....	118
3.6 Effect of a rough seafloor.....	123
3.7 Effect of reduced ray coverage.....	127
3.8 Discussion.....	132
3.8.1 Statistical significance of the inversion results.....	132
3.8.2 Layer 3.....	134
3.8.3 Layer 2B/C.....	137
3.8.4 Layer 2A.....	140
3.8.5 Evidence for anisotropy.....	142
3.9 Summary.....	145

### **4 Behaviour of *P*-*S* mode converted arrivals.....148**

4.1 Introduction.....	148
4.2 Phase identification.....	149
4.3 Horizontal geophone orientation.....	159
4.4 Travel time modelling.....	164
4.5 Determination of first motion azimuth.....	171
4.5.1 Method.....	173
4.5.2 In-line shots.....	175
4.5.3 Off-line shots.....	185
4.6 Discussion.....	188
4.6.1 Poisson's ratio structure of layer 2A.....	188
4.6.2 Melt lens mode converted arrivals.....	189
4.6.3 <i>S</i> -wave anisotropy.....	191
4.7 Summary.....	194

### **5 Discussion and suggestions for further work.....196**

5.1 Introduction.....	196
5.2 Crustal structure at the Valu Fa Ridge.....	196
5.2.1 Axial low velocity zone.....	197
5.2.2 Properties of the axial melt lens.....	202
5.2.3 Axial velocity anomalies in layer 2B/C.....	206
5.2.4 Geological interpretation of layer 2.....	210
5.3 Segmentation of the Valu Fa Ridge.....	213
5.4 Summary of results.....	216
5.5 Suggestions for further work.....	219
5.5.1 Existing datasets.....	219
5.5.2 Acquisition geometry.....	222
5.5.3 Suggested modifications to the inversion method.....	233
5.5.4 Future experiments.....	236
5.6 Conclusions.....	239

<b>References.....</b>	<b>241</b>
<b>Appendix A.....</b>	<b>252</b>
<b>Appendix B.....</b>	<b>256</b>
<b>Appendix C.....</b>	<b>284</b>
<b>Appendix D.....</b>	<b>289</b>

# List of Figures

<b>Figure 1.1:</b> Compilation of <i>P</i> -wave velocity–depth profiles for the Pacific and Atlantic Oceans. ....	3
<b>Figure 1.2:</b> Comparison of the structural sequence observed for a typical ophiolite with the seismic structure of oceanic crust. ....	4
<b>Figure 1.3:</b> LVZs at a number of mid–ocean ridge locations. ....	11
<b>Figure 1.4:</b> Comparison of petrological and geophysical magma chamber models. ....	14
<b>Figure 1.5:</b> The effect of cracks of different aspect ratio on <i>P</i> - and <i>S</i> -wave velocity, and Poisson's ratio. ....	21
<b>Figure 1.6:</b> Tectonic setting of the Lau–Havre–Taupo back–arc system. ....	24
<b>Figure 1.7:</b> Summary of previous geological and geophysical studies at the VFR. These studies include morphological segmentation, positions and composition of dredge samples and the extent of the axial MCR. ....	27
<b>Figure 1.8:</b> Configuration of the seismic experiment conducted during cruise EW9512. ....	29
<b>Figure 1.9:</b> Construction of the EW9512 airgun array relative to the stern of the ship and the GPS antenna position. ....	30
<b>Figure 1.10:</b> Final 2–D across–axis velocity–depth models of Turner (1998). ....	34
<b>Figure 2.1:</b> Geometry of stencils used to calculate first arrival travel times during the forward modelling step. ....	41
<b>Figure 2.2:</b> Illustration of the vertical and horizontal smoothness constraints applied to each inversion cell during the inverse step. ....	44
<b>Figure 2.3:</b> Example seismic traces, before and after band–pass filtering. ....	48
<b>Figure 2.4:</b> The subset of ship tracks and receivers used for 3–D tomographic analysis. ....	50
<b>Figure 2.5:</b> Direct water–wave arrivals used to relocate SDOBS3. ....	52
<b>Figure 2.6:</b> Water column velocity structure. ....	53
<b>Figure 2.7:</b> The difference between the calculated and observed direct water–wave arrival times for the shots used to relocate each OBS. ....	54
<b>Figure 2.8:</b> Ray paths for the direct water–wave arrival and the first sea surface multiple. ....	56
<b>Figure 2.9:</b> Application of the horizontal geophone data to determine the off–line location of NDOBS1. ....	58
<b>Figure 2.10:</b> Illustration of the various stages involved in determining pick position uncertainty versus SNR relationships. ....	61
<b>Figure 2.11:</b> Pick position uncertainty versus SNR curves for several reference traces formed by stacking traces recorded by NDOBS1. ....	64
<b>Figure 2.12:</b> Detail of traces recorded by the NDOBS1 vertical geophone which were stacked to create one of the reference traces used in Fig. 2.11. ....	64

<b>Figure 2.13:</b> Final set of pick position uncertainty versus SNR curves selected for NDOBS1. ....	64
<b>Figure 2.14:</b> Background noise frequency spectra for blank traces acquired by each OBS. ....	66
<b>Figure 2.15:</b> Pick position uncertainty versus SNR curves for a single reference trace using a variety of background noise frequency spectra. ....	67
<b>Figure 2.16:</b> Pick position uncertainty versus SNR relationships for all OBS positions. ....	68
<b>Figure 2.17:</b> Pick position uncertainty versus SNR curves for several reference traces before and after band-pass filtering. ....	70
<b>Figure 2.18:</b> Pick position uncertainty versus SNR relationships for all OBS positions after band-pass filtering. ....	70
<b>Figure 2.19:</b> Pick position uncertainty versus SNR curves for SDOBS5 hydrophone data. ....	71
<b>Figure 2.20:</b> Water column temperature–depth profiles measured using XBTs. ....	75
<b>Figure 2.21:</b> The difference between the first arrival travel time predicted by the 3–D finite difference method and the theoretical first arrival travel time for a number of 1–D velocity models and a fixed forward grid spacing. ....	80
<b>Figure 2.22:</b> The difference between the first arrival travel time predicted by the 3–D finite difference method and the theoretical first arrival travel time for a fixed 1–D velocity model and a number of forward grid spacings. ....	81
<b>Figure 2.23:</b> 1–D velocity profiles derived by averaging the 2–D models shown in Fig. 1.10. ....	83
<b>Figure 2.24:</b> Raw and smoothed bathymetry within the 3–D study area. ....	86
<b>Figure 2.25:</b> Cross–section through the initial model showing the principal layer boundaries and the positions of the 3.0, 5.0 and 6.2 kms <sup>-1</sup> constant velocity planes, which are used to display sections through 3–D velocity and resolution models in later figures. ....	87
<b>Figure 2.26:</b> Cumulative ray path length sampling each inversion cell in the initial model. ....	89
<b>Figure 2.27:</b> Checkerboard models used to assess lateral resolution. ....	91
<b>Figure 2.28:</b> Examples of the eight variations on the basic checkerboard model used to assess lateral resolution. ....	93
<b>Figure 2.29:</b> Example of a checkerboard model, the model recovered by inversion of synthetic data generated from that model, and the semblance between the synthetic and recovered models, for several checkerboard sizes. ....	94
<b>Figure 2.30:</b> Mean semblance derived from the eight checkerboard patterns for several checkerboard sizes. ....	96
<b>Figure 2.31:</b> Model resolution obtained by determining the minimum checkerboard size for which the semblance exceeds thresholds of 0.7 and 0.9. ....	96
<b>Figure 3.1:</b> Crustal part of the predicted ray paths traced through the <i>basic 1–D initial model</i> for all the shot–receiver pairs used in the inversions. ....	99
<b>Figure 3.2:</b> Velocity anomalies recovered by inversion using the <i>basic 1–D initial model</i> and several inversion cell sizes. ....	101

<b>Figure 3.3:</b> Cumulative ray path length per inversion cell for the <i>basic 1-D initial model</i> and several inversion cell sizes. ....	103
<b>Figure 3.4:</b> Plots of normalised residual against shot–receiver offset for each shot–receiver pair used in the inversion for the <i>basic 1-D initial model</i> and the models recovered by inversion using this initial model for several inversion cell sizes. ....	104
<b>Figure 3.5:</b> 1-D velocity–depth profiles used to create the <i>fast</i> and <i>slow 1-D initial models</i> . ....	108
<b>Figure 3.6:</b> Velocity anomalies relative to the initial model recovered by inversion using the <i>fast</i> and <i>slow 1-D initial models</i> . ....	109
<b>Figure 3.7:</b> Plots of normalised residual against shot–receiver offset for the <i>fast</i> and <i>slow 1-D initial models</i> , and the models recovered by inversion using each of these initial models. ....	109
<b>Figure 3.8:</b> Velocity anomalies recovered by inversion using the <i>2-D initial model</i> . ....	112
<b>Figure 3.9:</b> Plots of normalised residual against shot–receiver offset for each shot–receiver pair used in the inversion for the <i>2-D initial model</i> and the model recovered by inversion using this initial model. ....	112
<b>Figure 3.10:</b> Crustal part of the predicted ray paths traced through the <i>basic 1-D initial model</i> for a subset of shot–receiver pairs for which all shots within 2.5 km of $y = 12$ km and $y = -17$ km have been removed. ....	114
<b>Figure 3.11:</b> Plots of normalised residual against shot–receiver offset for the subset of shot–receiver pairs shown in Fig. 3.10 for the <i>basic 1-D</i> and <i>2-D initial models</i> . ....	114
<b>Figure 3.12:</b> Average of the anomaly distribution shown in Fig. 3.8 plotted against depth beneath the seafloor for the northern and southern halves of the model. ....	116
<b>Figure 3.13:</b> Velocity anomalies recovered by inversion using the <i>unbiased 2-D initial model</i> . ....	117
<b>Figure 3.14:</b> Plots of normalised residual against shot–receiver offset for each shot–receiver pair used in the inversion for the <i>unbiased 2-D initial model</i> and the model recovered by inversion using this initial model. ....	117
<b>Figure 3.15:</b> Example traces recorded by the NDOBS5 vertical geophone showing first arrival travel time picks. ....	119
<b>Figure 3.16:</b> Melt lens extent within the 3-D study area. ....	120
<b>Figure 3.17:</b> Cross-sections through the anomaly field recovered by inversion using the <i>unbiased 2-D initial model</i> with the melt lens explicitly included. ....	121
<b>Figure 3.18:</b> Velocity anomalies recovered by inversion using the <i>unbiased 2-D initial model</i> with the melt lens explicitly included for the forward modelling step only. ....	122
<b>Figure 3.19:</b> Plots of normalised residual against shot–receiver offset for each shot–receiver pair used in the inversion for the <i>unbiased 2-D initial model</i> with the melt lens explicitly included, and the model recovered by inversion using this initial model with the melt lens included at the forward modelling stage only. ....	122
<b>Figure 3.20:</b> Seafloor roughness on the scale of the bathymetric gridding interval of 0.2 km. ....	125
<b>Figure 3.21:</b> Plot of unbiased normalised residual for the model obtained by inversion using the <i>melt lens unbiased 2-D initial model</i> against seafloor roughness at the ray entry point. ....	126



<b>Figure 3.22:</b> Crustal part of the predicted ray paths traced through the <i>unbiased 2-D initial model</i> for all the shot-receiver pairs in the reduced dataset created by preferentially selecting the best (smallest uncertainty) data with a minimum shot spacing of 1.0 km. ....	128
<b>Figure 3.23:</b> Ray coverage and lateral anomaly resolution for the reduced set of shot-receiver pairs. ....	129
<b>Figure 3.24:</b> Velocity anomalies recovered by inversion using the <i>no melt lens unbiased 2-D initial model</i> and the reduced set of shot-receiver pairs. ....	131
<b>Figure 3.25:</b> Plots of normalised residual against shot-receiver offset for each shot-receiver pair in the reduced dataset for the <i>no melt lens unbiased 2-D initial model</i> and the model recovered by inversion using this initial model and the reduced dataset. ....	131
<b>Figure 3.26:</b> Synthetic inversion to establish the degree of continuity in the axial negative anomaly in layer 3. Velocity anomalies relative to the <i>no melt lens unbiased 2-D initial model</i> are shown for a synthetic model based on a 2-D average of the layer 3 structure obtained by inversion using the <i>no melt lens unbiased 2-D initial model</i> and the model recovered by inverting synthetic data created by tracing rays through this synthetic model. ....	136
<b>Figure 3.27:</b> Crustal part of the predicted ray paths traced through the <i>no melt lens unbiased 2-D initial model</i> for a subset of the shot-receiver pairs which travel in layer 2 and the water column only. ....	139
<b>Figure 3.28:</b> Velocity anomalies recovered by inversion using the <i>no melt lens unbiased 2-D initial model</i> and the set of shot-receiver pairs shown in Fig. 3.27. ....	139
<b>Figure 3.29:</b> Plots of normalised residual against shot-receiver azimuth for each shot-receiver pair used in the inversion, and the azimuthal distribution which would be observed for an idealised scenario of an isotropic velocity model which perfectly represents the lateral velocity heterogeneities, but does not account for azimuthal anisotropy arising from vertical cracks. ....	144
<b>Figure 4.1:</b> Detail of traces recorded by SDOBS2 with the vertical and horizontal geophones. ....	150
<b>Figure 4.2:</b> Transmitted and reflected <i>P</i> - and <i>S</i> -waves generated by a <i>P</i> -wave incident on the layer 2A-2B/C boundary from below. ....	154
<b>Figure 4.3:</b> <i>P</i> - and <i>S</i> -wave transmission coefficients calculated for a <i>P</i> -wave incident on the layer 2A-2B/C boundary from below. ....	155
<b>Figure 4.4:</b> Possible ray paths for generation of <i>P-S</i> mode converted arrivals. ....	157
<b>Figure 4.5:</b> Determination of horizontal geophone orientation using direct water-wave arrivals. ....	160
<b>Figure 4.6:</b> Demonstration of the algorithm for determining the horizontal geophone orientation from the direct water-wave arrivals recorded by the <i>x'</i> - and <i>y'</i> -component geophones. ....	160
<b>Figure 4.7:</b> Horizontal geophone orientations for each OBS location based on analysis of direct water-wave arrivals. ....	162
<b>Figure 4.8:</b> 2-D ray trace modelling of the <i>P-S</i> mode converted arrivals, based on the 2-D <i>P</i> -wave velocity models of Turner (1998). ....	166
<b>Figure 4.9:</b> Detail of <i>x</i> -component traces for shots recorded by SDOBS4 with an approximate shot-receiver azimuth of 180° showing <i>P-S</i> mode converted arrivals which are believed to originate from the top of the melt lens. ....	168
<b>Figure 4.10:</b> <i>P</i> - and <i>S</i> -wave transmission coefficients calculated for a <i>P</i> -wave incident on the top of the melt lens from below. ....	169

<b>Figure 4.11:</b> 2-D ray trace modelling of the melt lens $P$ - $S$ mode converted arrivals, based on the 2-D $P$ -wave velocity models of Turner (1998). .....	170
<b>Figure 4.12:</b> Detail of $x$ - and $y$ -component traces for shots recorded by SDOBS2 with an approximate shot-receiver azimuth of $000^\circ$ showing $P$ - $S$ mode converted arrivals with a strong transverse component of particle motion. ....	172
<b>Figure 4.13:</b> Illustration of the phenomenon of $S$ -wave splitting. ....	173
<b>Figure 4.14:</b> Schematic diagram showing a plan view of the $P$ -wave first arrival ray path in the presence of a large off-line seamount. ....	176
<b>Figure 4.15:</b> Histograms of first motion azimuth for $P$ -wave first arrivals and $P$ - $S$ mode converted arrivals for groups of shots with approximately constant shot-receiver azimuth for the <i>Seismic South</i> deployment. ....	178
<b>Figure 4.16:</b> Histograms of first motion azimuth for $P$ -wave first arrivals and $P$ - $S$ mode converted arrivals for groups of shots with approximately constant shot-receiver azimuth for the <i>Seismic North</i> deployment. ....	179
<b>Figure 4.17:</b> Mean first motion azimuths at each OBS location for $P$ -wave first arrivals and $P$ - $S$ mode converted arrivals. ....	184
<b>Figure 4.18:</b> $P$ - $S$ mode converted arrivals recorded at SDOBS3 from off-line shots showing dominantly transverse particle motion. ....	186
<b>Figure 4.19:</b> First motion azimuth plotted against shot-receiver azimuth for direct water-wave arrivals, $P$ -wave first arrivals and $P$ - $S$ mode converted arrivals for off-line shots recorded at SDOBS3. ....	187
<b>Figure 5.1:</b> Summary 3-D perspective view of the axial velocity anomaly beneath the CVFR. ....	198
<b>Figure 5.2:</b> Velocity anomaly at the top of layer 3 recovered using the <i>melt lens unbiased 2-D initial model</i> overlain by the extent of the melt lens and fourth-order ridge segmentation. ....	200
<b>Figure 5.3:</b> $S$ -wave transmission coefficients calculated for a $P$ -wave incident on the roof of the melt lens from below for a number of different melt lens properties. ....	204
<b>Figure 5.4:</b> Acquisition geometries for which resolution tests were performed. ....	225
<b>Figure 5.5:</b> Cross-section through the <i>basic 1-D initial model</i> used in the synthetic resolution tests showing the principal layer boundaries (solid green lines) and the positions of the constant velocity planes used to display sections through 3-D synthetic resolution models in later figures. ....	226
<b>Figure 5.6:</b> Resolution for the <i>EW9512</i> geometry shown in Fig. 5.4. ....	228
<b>Figure 5.7:</b> Resolution for the <i>Small grid</i> geometry shown in Fig. 5.4. ....	228
<b>Figure 5.8:</b> Resolution for the <i>Large grid</i> geometry shown in Fig. 5.4. ....	230
<b>Figure 5.9:</b> Resolution for the <i>Star</i> geometry shown in Fig. 5.4. ....	230
<b>Figure 5.10:</b> Resolution for the <i>Combined star and grid</i> geometry shown in Fig. 5.4. ....	232
<b>Figure 5.11:</b> Cross-section through the <i>basic 1-D initial model</i> with a velocity discontinuity at the Moho included. Predicted first arrival ray paths are shown. ....	233
<b>Figure 5.12:</b> Bathymetry of the SVFR and CVFR overlain with the proposed experimental configuration for a new 3-D seismic tomographic experiment at these ridge segments. ....	237

<b>Figure B.1:</b> Vertical geophone traces recorded at SDOBS3 for all shots within the 3–D study area. ...	257
<b>Figure B.2:</b> Detail of selected traces shown in Fig. B.1. ....	260
<b>Figure B.3:</b> Flow diagram summarising the principal processing steps. ....	275

## List of Tables

<b>Table 2.1:</b> Final RMS misfit for the direct water–wave arrivals used to locate each OBS used in the inversion. ....	55
<b>Table 2.2:</b> Predicted travel time uncertainty for each OBS location used in the inversion arising from instrument location uncertainty. ....	73
<b>Table 2.3:</b> Mean water column velocities and travel times to 1.9 km depth derived from the SV dip meter and XBTs. ....	75
<b>Table 2.4:</b> Summary of contributions to travel time residual uncertainty. ....	77
<b>Table 3.1:</b> Lateral roughness for models generated by inversion using a variety of inversion cell sizes. ....	105
<b>Table 4.1:</b> Summary of each OBS’s horizontal geophone orientation determined using the relative phase amplitude recorded by the orthogonal horizontal geophones for direct water–wave arrivals. ....	163
<b>Table 4.2:</b> Summary of apparent Poisson’s ratio in layer 2A at each OBS location, derived using groups of in–line shots with approximately constant shot–receiver azimuth and the 2–D <i>P</i> –wave velocity models of Turner (1998). ....	167
<b>Table 4.3:</b> Mean first motion azimuths for <i>P</i> –wave first arrivals and <i>P</i> – <i>S</i> mode converted arrivals for the <i>Seismic South</i> deployment. ....	181
<b>Table 4.4:</b> Mean first motion azimuths for <i>P</i> –wave first arrivals and <i>P</i> – <i>S</i> mode converted arrivals for the <i>Seismic North</i> deployment. ....	182
<b>Table 5.1:</b> Summary of the number of OBSs and shots necessary for each synthetic experimental geometry. ....	226

# Glossary of Terms and Abbreviations

The following terms and abbreviations are used throughout this dissertation:

AVR	Axial Volcanic Ridge
CLSC	Central Lau Spreading Centre
CVFR	Central Valu Fa Ridge
deval	deviation in axial linearity
ELSC	Eastern Lau Spreading Centre
EPR	East Pacific Rise
FAST	First Arrival Seismic Tomography
FFT	Fast Fourier Transform
GPS	Global Positioning System
GMT	Generic Mapping Tools
JDFR	Juan de Fuca Ridge
LVZ	Low Velocity Zone
MAR	Mid-Atlantic Ridge
MCR	Mid-Crustal Reflector
MORB	Mid-Ocean Ridge Basalt
NVFR	Northern Valu Fa Ridge
NTO	Non-Transform Offset
OBS	Ocean Bottom Seismograph
OSC	Overlapping Spreading Centre
PDAS	Portable Data Acquisition System
R/V	Research Vessel
RMS	Root Mean Square
SNOO	Small Non-Overlapping Offset
SNR	Signal-to-Noise Ratio
SV dip	Sound-Velocity-Dip
SVFR	Southern Valu Fa Ridge
VFR	Valu Fa Ridge
XBT	Expendable Bathymetric Thermograph

# Chapter 1

## Introduction

Over the last two decades numerous geophysical, geochemical and geological surveys of the Earth's mid-ocean ridge system have shown that crustal accretion is a three-dimensional process no matter the spreading rate. These three-dimensional processes primarily manifest themselves in the seafloor morphology, with ridges subdivided into segments of varying length scales. However, along-axis variation in intra-crustal structure and properties also result from these processes. Thus recent controlled-source seismic experiments undertaken at mid-ocean ridges have adopted a three-dimensional approach to acquisition, with shots fired at a wide range of azimuths into evenly distributed ocean bottom instruments.

During a number of two-dimensional seismic experiments at the Valu Fa Ridge, a back-arc spreading centre in the southwest Pacific, mid-crustal reflections have been imaged beneath the axis, which have been interpreted as originating at the top of an axial magma chamber. The along-axis pattern of these reflections corresponds to the predominant axial segmentation pattern and hence implies three-dimensional accretion. In 1995, a further wide-angle seismic experiment adopted a 2-D and 3-D approach to data acquisition to investigate along-axis variation in crustal structure and properties resulting from this implied pattern of accretion. In this dissertation the results of modelling and interpretation of the 3-D dataset are considered, primarily with respect to resolution of along-axis magma chamber structure in relation to spreading and off-axis crustal structure associated with the development of the Lau Basin over time.

In order to first put the Valu Fa Ridge in its global context this chapter contains a summary of our knowledge of the oceanic crust, how mid-ocean ridges are segmented and how seismic studies of these ridges can further our understanding of ridge accretionary processes. Following a discussion of the geological setting specifically related to the Valu Fa Ridge, aspects of the experiment and its corresponding acquisition geometry are described.



## 1.1 Oceanic crust and mid-ocean ridges

The global mid-ocean ridge system is a 65 000 km long topographic high rising ~1–2 km above the surrounding seafloor, and is widely recognised as the site of oceanic crustal accretion. Oceanic crust comprises more than two-thirds of the surface of the Earth with mid-ocean ridges accounting for 80% of all global volcanism and the majority of heat flow from the interior to the surface environment. Therefore an understanding of the accretionary processes operating at mid-ocean ridges is of major significance to the study of whole Earth processes. However, since mid-ocean ridges lie beneath 3 km of water on average, they are difficult to study directly. Hence indirect geophysical methods have played a dominant role in developing our understanding of the structure of mid-ocean ridges and oceanic crust as a whole. In this section the gross structure of oceanic crust is outlined and the primary methods adopted to investigate finer-scale features, discussed in more detail in later sections, are introduced.

The morphology of mid-ocean ridges is variable depending on the spreading rate (Macdonald 1982), with the fast- and slow-spreading end members generally characterised by axial highs and axial valleys (median valleys) respectively. Ridges are generally defined as fast-spreading for full-spreading rates greater than 90 mm yr<sup>-1</sup>, intermediate-spreading for full-spreading rates of 50–90 mm yr<sup>-1</sup>, and slow-spreading for full-spreading rates less than 50 mm yr<sup>-1</sup>. However seismic studies indicate that the velocity structure of oceanic crust created at these ridges is remarkably uniform world-wide no matter the spreading rate. Analysis of data from early seismic experiments suggested that the oceanic crust comprised a series of layers each of constant velocity (e.g. Raitt 1963), which were interpreted as reflecting the sedimentary succession, igneous material extruded onto the seafloor and igneous material intruded into existing crust as it spreads off-axis. These layers were termed layer 1, layer 2 and layer 3 respectively. Subsequent studies have resulted in the subdivision of some of these layers and a re-evaluation of their geological significance (e.g. Houtz & Ewing 1976; Spudich & Orcutt 1980a; Bratt & Purdy 1984). As a result of these studies, the oceanic crust is now thought to be better represented seismically by a continuous increase in velocity with depth, with layer boundaries defined by changes in vertical velocity gradient rather than velocity discontinuities. A compilation of existing models of the seismic structure of the oceanic crust for a variety of spreading rates by White *et al.* (1992) (Fig. 1.1)

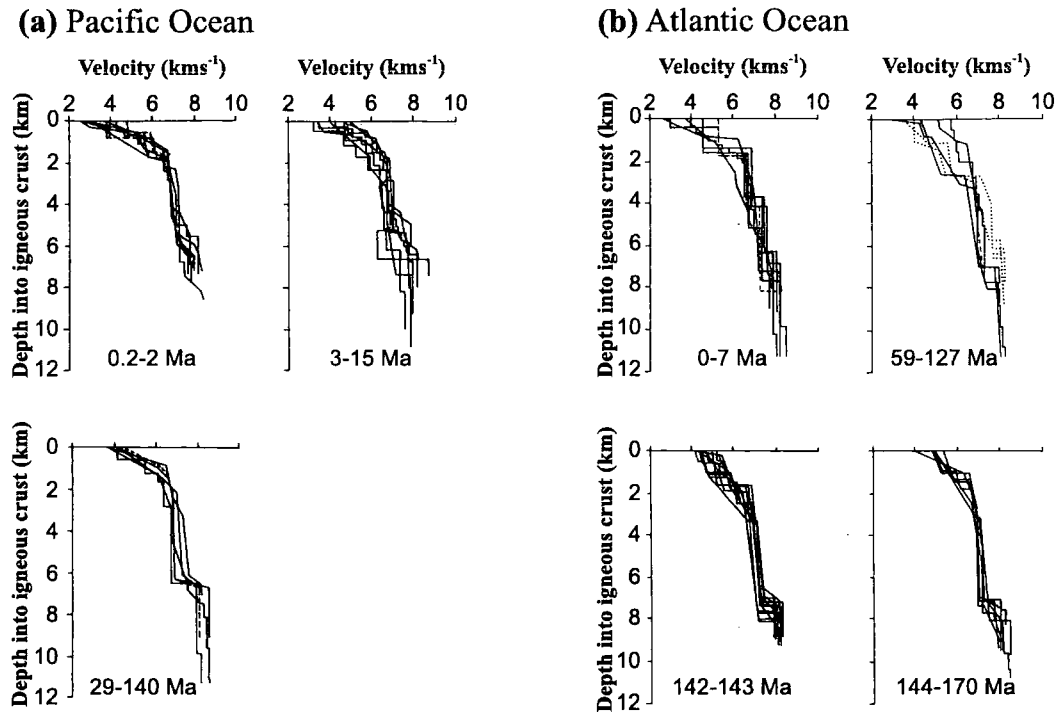


**Figure 1.1:** *P*-wave velocity–depth profiles for the a) Pacific and b) Atlantic Oceans compiled by White *et al.* (1992). Note the remarkable similarity in profiles of a given age in each ocean and the similarity between zero-age crust in the two oceans despite the large difference in spreading rate at the mid-ocean ridges where this crust was generated. This observation suggests that accretionary processes at these mid-ocean ridges and subsequent crustal evolution are spreading rate independent.

illustrates this continuous velocity structure and the similarity in the structure for crusts of similar ages. These observations imply that the accretionary processes operating at mid-ocean ridges are similar at all spreading rates.

Interpretation of the seismic structure of the oceanic crust in terms of its geological equivalence relies primarily on comparison with ophiolite sequences, which are believed to represent ancient oceanic crust. Although geochemical evidence suggests that many ophiolites were formed in a supra-subduction zone setting rather than at typical mid-ocean ridges (e.g. Pearce *et al.* 1984), they remain the best available on-land analogue to oceanic crustal structure. Moreover, the limited in-situ evidence for the true geological nature of the crust obtained from drilling and dredging of crustal sections exposed at large submarine transform faults (e.g. Karson *et al.* 1992), suggests that the ophiolite model represents a suitable and realistic reference. Fig. 1.2 illustrates how the seismically-derived layered structure is generally interpreted in geological terms. A number of petrological models have been proposed (e.g. Cann 1974) to explain

		typical ophiolite		oceanic crust		
		thickness (km)	velocity (km s <sup>-1</sup> )	thickness (km)	velocity (km s <sup>-1</sup> )	velocity gradient (s <sup>-1</sup> )
deep sea sediments		~0.3	-	0.5	~2.0	-
highly fractured pillow lavas		0.3-0.7	3.3	0.5	2.5-4.5	5
less porous extrusives with interfingering dykes				0.5	4.5	0
sheeted dykes		1.0-1.5	4.1	1.0	4.5-6.5	1
gabbro	layer 3A	2.0-5.0	5.1	1.0	6.5-6.8	0.1
	layer 3B			2.0	6.8-7.0	
seismic Moho layered peridotite petrological Moho peridotite, dunite etc. unlayered	layer 4		2.5-4.2		8.0+	0.03

**Figure 1.2:** Comparison of the structural sequence observed for a typical ophiolite with the seismic structure of oceanic crust (after Brown & Musset 1981; Bratt & Purdy 1984; Navin 1996). Note the broad similarity between the vertical velocity structure of ophiolites and oceanic crust, particularly the general decrease in velocity gradient with depth.

how this structure arises. Such models usually incorporate a large, steady-state, vigorously convecting magma chamber beneath the ridge axis to account for the isotropic gabbro layer, and the layered mafic and ultramafic sequences at its base which exhibit cumulate textures and are interpreted as arising from crystal settling at the base of this chamber.

Over the last two decades, and as technology advances, ever more detailed mapping surveys of the seafloor at, and adjacent to, mid-ocean ridges has revealed along-axis variations in morphology on a variety of length scales. Therefore although the gross vertical structure of the oceanic crust is similar everywhere, along-axis ridge crest morphological variation implies that crustal structure may also vary in this dimension. This along-axis variation in seafloor features, or so-called ridge segmentation, is believed to broadly reflect along-axis variation in melt supply from the mantle and its lateral redistribution within the crust (e.g. Macdonald *et al.* 1988; Sempéré *et al.* 1990). This theory and its implications are discussed further in section 1.2. However, laboratory measurements of the *P*- and *S*-wave velocities of



oceanic crustal rocks show that they are sensitive to temperature and melt fraction (e.g. Murase & McBirney 1973). Therefore seismic techniques are well suited to the investigation of melt distribution within the crust and, in particular, the crustal magma chambers in which it nominally accumulates. To this end a number of seismic investigations have been conducted at mid-ocean ridges which have revealed low velocity zones (LVZs) interpreted as representing these chambers. The results and implications of these studies are discussed in detail in section 1.3.1.

Whilst the gross seismic structure of oceanic crust, including the axial LVZs, appears to be similar at all spreading rates, more detailed seismic experiments have begun to reveal finer-scale variations in the crustal layering and how it develops off-axis. These studies have also allowed along-axis variations in crustal structure and magma chamber properties to be identified and interpreted in terms of morphological segmentation. The picture that is emerging from these studies is that crustal structure at mid-ocean ridges is generally three-dimensional, i.e. along- and across-axis variations are superimposed on the gross vertical layering shown in Figs. 1.1 and 1.2. In order to thoroughly investigate this structure a three-dimensional approach to seismic data acquisition is therefore now desirable. The results of a number of such 3-D seismic experiments which have been conducted to date are discussed in section 1.3.3.

As more and higher-resolution seismic data is becoming available, the simple interpretation of the nature of crustal layering in terms of the ophiolite model is increasingly being called into question. To date most seismic studies are based on the the acquisition and interpretation of the *P*-wavefield. However, there is considerable grounds for ambiguity in this interpretation in geological terms and, in the absence of widespread borehole data, other approaches must be adopted to constrain the finer-scale geological features corresponding to the seismic structure. One such technique is to model the *S*-wave velocity structure which, in combination with the *P*-wave velocity structure, can potentially constrain both the porosity and geometry of porosity within layers thus providing insight into their geological nature. This technique is discussed further in section 1.3.4.

One such investigation of oceanic crustal structure which aims to correlate geophysical measurement with geological reality was conducted at the Valu Fa Ridge (VFR), an intermediate-spreading ridge located in a back-arc setting (see section 1.4). This dissertation concerns analysis and interpretation of the seismic part of a multidisciplinary geophysical dataset acquired at this ridge (see section 1.5), with the

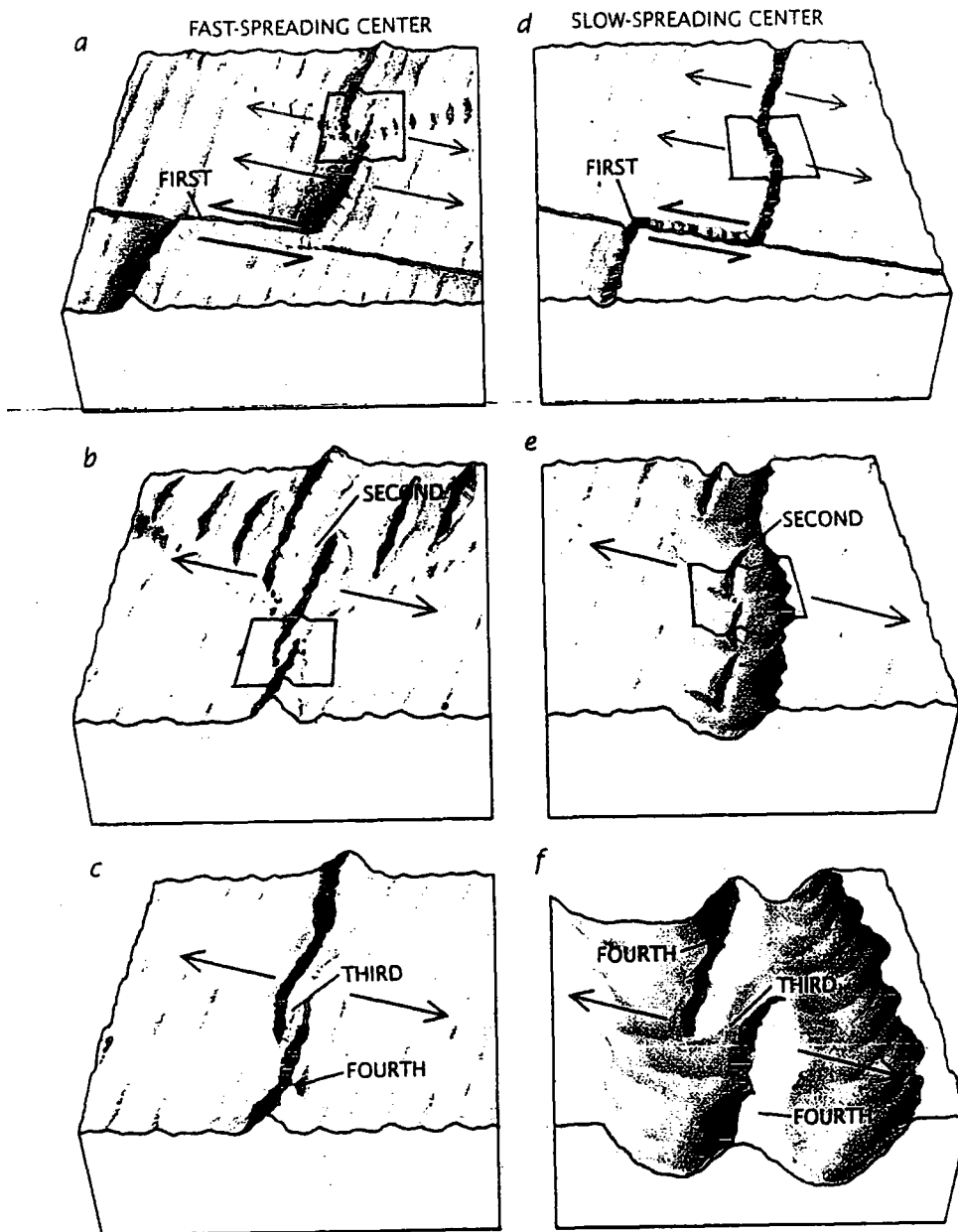


**Figure 1.2A:** Mid-ocean ridge discontinuities can be classified according to shape, size and longevity. For a fast-spreading centre, such as the East Pacific Rise, a first-order discontinuity a) is a transform fault which offsets the ridge by at least 50 km. A second order discontinuity b) is usually a large overlapping spreading centre that offsets the ridge by at least 2 km. A third-order discontinuity c) is a small overlapping spreading centre that offsets the ridge by 0.5–2.0 km. A fourth-order discontinuity c) is characterised by slight deviations in axial linearity. For a slow-spreading centre, such as the Mid-Atlantic Ridge, a first-order discontinuity is also typically a transform fault, but it represents a break in a rift valley rather than a ridge crest. Second- and third-order discontinuities are represented by NTOs<sup>1</sup> whereas a fourth-order discontinuity is a small gap within a chain of volcanoes. First- and second-order structures are usually flanked by distorted crust that formed as the discontinuity evolved. They are known to persist longer than third- and fourth-order discontinuities because the oceanic crust near the higher-order structures does not show evidence of distortion. (After Macdonald & Fox 1990).

<sup>1</sup> The term NTO refers to ridge axis discontinuities which are not associated with transform faults.

aim of resolving variation in crustal structure along-axis associated with segmentation. Previous geophysical surveys of the VFR have revealed the presence of an axial magma chamber. A three-dimensional approach to data analysis was, therefore, adopted in order to constrain the three-dimensional structure of the crust and magma chamber, supplemented by analysis of *S*-wave arrivals targeted towards obtaining better geological constraints on the structure than is possible from the *P*-wave velocity structure alone. These aims are described in more detail in section 1.6.

## 1.2 Segmentation of mid-ocean ridges

Lateral variation in crustal structure at mid-ocean ridges of all spreading rates is most readily observed as along-axis morphological segmentation on a variety of length scales, although the nature of discontinuities between segments varies with spreading rate. In this section the causes of this segmentation are discussed by comparing the morphology of the slow-spreading Mid-Atlantic Ridge (MAR) with that of the the fast-spreading East Pacific Rise (EPR).

### 1.2.1 Segmentation of the Mid-Atlantic Ridge

Four scales of morphological segmentation have been identified at the MAR (Sempéré *et al.* 1990 and 1993). On the largest scale, large transform faults separate sections of ridge hundreds of kilometres long (first-order segments). Second- and third-order segments tens of kilometres long are defined by smaller, non-transform offsets (NTOs).<sup>1</sup> The distinction between second- and third-order is made on the basis of the characteristics of the off-axis bathymetry, with second-order segmentation being related to long-lived NTOs. Minor offsets in the neovolcanic zone in the centre of the median valley with a spatial separation of ~4 km or less, which do not disrupt the continuity of the rift valley, define fourth-order segmentation. Bathymetric variation is associated with segmentation of all scales, with shallower bathymetry found at segment centres than at segment ends (Sempéré *et al.* 1990) (see Fig. 1.2A).

Gravity studies (e.g. Kuo & Forsyth 1988; Lin *et al.* 1990; Detrick *et al.* 1995) have shown negative "bull's eye" mantle Bouguer anomalies associated with many first- and second-order segment centres suggesting significantly thicker crust here than at segment ends. Coincident wide-angle seismic studies have confirmed this inferred crustal thickness variation (Tolstoy *et al.* 1993; Hooft *et al.* 2000). As crustal thickness is fundamentally related to magma supply, these observations suggest that mantle upwelling is focussed beneath segment centres. This conclusion is further supported by

other geophysical, geochemical and morphological evidence. Near 32° S segment ends have been found to be associated with magnetisation highs which have been interpreted as arising from the eruption of highly fractionated lavas at the extremities of crustal magma chambers (Carbotte *et al.* 1991). The along-axis variations in major element chemistry observed in dredge samples collected near 26° S also suggest a higher melt fraction near the segment centre than at the segment end (Niu & Batiza 1994). Segments which have large negative mantle Bouguer anomalies are often found to exhibit pronounced along-axis morphological variation dominated by volcanic construction at the segment centre and tectonic extension at the segment end (Fox *et al.* 1991). All these segment characteristics are consistent with a concentration of melt injection near their centres.

However, not all segments exhibit clear along-axis variation in their geophysical, geochemical and morphological properties as described above. Some segments do not exhibit pronounced gravity anomalies, and their morphology is dominated by tectonic structures (Sempéré *et al.* 1990 and 1993). This observation leads to the suggestion that melt supply at the MAR is cyclic such that periods of active volcanism are succeeded by periods of amagmatic extension prior to the next injection of melt. According to this theory the differences in morphology and gravity signature between segments arise simply because they are at different stages of this cycle. Further evidence for cyclic magma supply comes from identification of off-axis changes in mantle Bouguer anomaly associated with second-order segments, interpreted as representing crustal thickness variations associated with periodic melt injections on a time scale of 2–7 Ma (Tucholke *et al.* 1997; Maia & Gente 1998). A similar explanation has been invoked to explain the variation in morphology of axial volcanic ridges (AVRs) in the neovolcanic zone of the oblique-spreading Reykjanes Ridge, part of the MAR southwest of Iceland. These AVRs are analogous to fourth-order segments elsewhere on the MAR. Some AVRs are unsedimented and show signs of recent volcanic construction, whilst others have a degree of sediment cover and show significant faulting and fracturing suggesting there has been no recent volcanic activity and that the AVR has been disrupted by tectonism subsequent to the end of the magmatic phase (Murton & Parson 1993; Parson *et al.* 1993). Therefore, at the slow-spreading MAR, there is strong evidence that ridge morphology and segmentation reflects spatial and temporal variations in melt supply on a variety of length-scales.

### 1.2.2 Segmentation of the East Pacific Rise

The fast-spreading EPR also exhibits segmentation on a variety of scales (Macdonald *et al.* 1991). First-order segmentation is defined by large transform faults similar to the MAR. Second- and third-order segments are separated by overlapping spreading centres (OSCs) with the distinction between second- and third-order segment boundaries made on the basis of whether or not the OSC has an off-axis bathymetric trace, again similar to the MAR. Fourth-order segmentation is defined by small non-overlapping offsets (SNOOs) and deviations in axial linearity (devals). Macdonald *et al.* (1988) showed that the seismic properties of axial magma chambers at the EPR together with lava geochemistry correlate with morphological segmentation at the EPR, suggesting that enhanced melt supply is associated with segment centres as at the MAR. Subsequent gravity studies (e.g. Wang & Cochran 1993; Cormier *et al.* 1995; Weiland & Macdonald 1996; Scheirer *et al.* 1998) have revealed the presence of negative mantle Bouguer anomalies associated with segment centres. Although the along-axis variations in the gravity field are much smaller than those observed at the MAR, these observations lead to the conclusion that there is also a link between morphological segmentation and melt supply at fast- as well as slow-spreading ridges.

There are a number of places on the EPR where the simple relationship between morphological segmentation and melt supply described above appears to break down. Indicators of enhanced melt supply include: a thicker crust; a thicker extrusive layer; a shallower bathymetric depth to the ridge crest; hydrothermal activity; and the presence of a robust axial magmatic system. Hooft *et al.* (1997) studied an 800 km section of the southern EPR, and found that whilst axial depth and mantle Bouguer gravity anomaly generally show the predicted strong correlation with ridge segmentation, the axial magma chamber characteristics and hydrothermal activity along-axis were found to be highly variable and exhibit no such strong correlation. Hooft *et al.* (1997) concluded that the mantle Bouguer anomaly and axial depth reflect along-axis variation in crustal thickness related to spatial variations in melt supply stable on a time scale of ~100 000 years, whilst other melt supply indicators reflect more ephemeral changes in the magmatic system. However, there are a number of seismic studies which indicate anomalous crustal thickness with respect to the Macdonald *et al.* (1988) model. Under this model the crust at segment ends should be thinner than crust at segment centres. Near the Clipperton transform at 10° 10' N normal thickness crust has been seismically imaged (Begnaud *et al.* 1997; Van Avendonk *et al.* 1998). This transform is a first-order segment boundary, and

would therefore be expected to be relatively magma starved. A seismic study at a ridge segment centred on  $9^{\circ} 50' N$  by Barth & Mutter (1996) indicated thin crust near the segment centre and thick crust near the segment ends, in direct conflict with the model of Macdonald *et al.* (1988). A subsequent detailed seismic reflection study at the OSC at the southern end of this segment has found evidence for a robust melt supply beneath the OSC at the present time (Kent *et al.* 2000). However, a gravity study of this segment indicated a gravity low near the segment centre after the effect of this variable crustal thickness had been removed (Wang *et al.* 1996). This observation suggests that, on the longest time scale, the underlying melt supply from the mantle is mostly concentrated in a zone beneath the segment centre, and that this melt supply is redistributed when it reaches the crustal magma system.

The observations described above demonstrate that the relationship between morphological segmentation and melt supply at the EPR is less clear-cut than at the MAR. Segmentation at the MAR reflects episodic melt injection whereas it has been suggested that the higher spreading rate at the EPR induces a greater degree of passive upwelling which inhibits temporal and along-axis variations in melt supply (Lin & Phipps-Morgan 1992). Additionally the higher magmatic budget at the EPR, and consequent lower magma viscosity, allows more efficient along-axis transport of melt away from the centre of upwelling in contrast to the MAR where the colder, more rigid crust will inhibit lateral melt transport. Hence it is likely that along-axis variations in the underlying pattern of melt supply from the mantle are much less pronounced at the EPR relative to the MAR. This pattern may further be masked by variations in crustal structure which are related to local variations in magma plumbing, making correlation between morphological segmentation and melt supply hard to identify. However, it appears that morphological segmentation at the EPR is broadly related to spatial variations in melt supply on the largest scale, and it is therefore reasonable to assume that the same conclusion applies at ridges of all spreading rates.

### **1.3 Seismic studies at mid-ocean ridges**

In this section, the contribution that seismic studies have made to the study of axial magma chambers and accretionary processes at mid-ocean ridges is outlined by describing the results of a number of specific studies. These example studies demonstrate the strengths and limitations of the various seismic methods considered and their applicability to the study of the structure of the crust at mid-ocean ridges.


### 1.3.1 Seismic studies of axial magma chambers

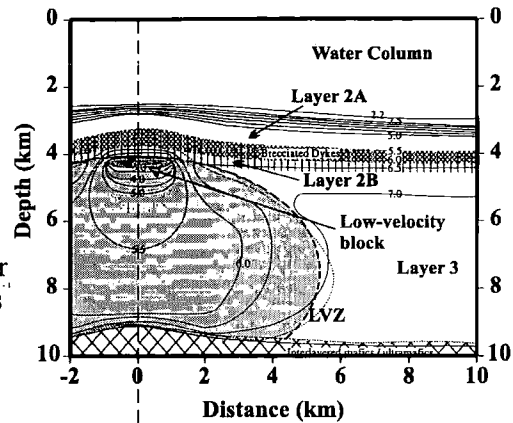
Petrological models for the formation of oceanic crust suggest the existence of large, steady-state, vigorously convecting magma chambers at mid-ocean ridges (e.g. Cann 1974). Such bodies should be detectable using seismic methods since laboratory measurements indicate that the velocity contrast between molten basalt ( $P$ -wave velocity of  $\sim 3.0 \text{ km s}^{-1}$ ) and an uncracked sample of solid basalt ( $P$ -wave velocity of  $\sim 6.0 \text{ km s}^{-1}$ ) (Murase & McBirney 1973) is sufficiently high to generate a large amplitude reflection from their tops. These laboratory measurements suggest an abrupt reduction in velocity occurs when the melt fraction increases to the point at which the melt phase becomes continuously connected (Murase & McBirney 1973). A vigorously convecting magma chamber would be expected to comprise a high melt fraction, in which case a  $P$ -wave velocity anomaly of the order of  $-3.0 \text{ km s}^{-1}$  would thus be expected relative to crust external to the magma chamber at that depth.

Wide-angle seismic experiments are well suited to imaging magma chambers as they provide a measure of the gross velocity structure of the Earth and allow gradual vertical and lateral velocity changes to be identified. Many such experiments have been conducted at mid-ocean ridges, and a number of axial LVZs have been imaged. The fast-spreading EPR near  $9^\circ \text{ N}$  has been the target for a number of such experiments after Orcutt *et al.* (1975) first imaged an axial LVZ at a depth interpreted as corresponding to a crustal magma chamber. A subsequent wide-angle study by Vera *et al.* (1990) constrained the LVZ to be approximately 10–12 km wide, as defined by a velocity anomaly of  $-0.2 \text{ km s}^{-1}$  relative to off-axis crust. Similar LVZs have also been imaged on the EPR near  $13^\circ \text{ N}$  (Harding *et al.* 1989; Caress *et al.* 1992). It is hypothesised that magma chambers are more ephemeral features, and hence less widespread, at lower spreading rates due to the greater temporal variation in melt supply implied by the morphological segmentation described in section 1.2. However, LVZs have also been imaged at the intermediate-spreading VFR (Turner 1998; Turner *et al.* 1999) and Juan de Fuca Ridge (JDFR) (Christeson *et al.* 1993), and the slow-spreading Reykjanes Ridge (Navin 1996; Navin *et al.* 1998). Some examples of LVZs modelled at mid-ocean ridges are shown in Fig. 1.3.

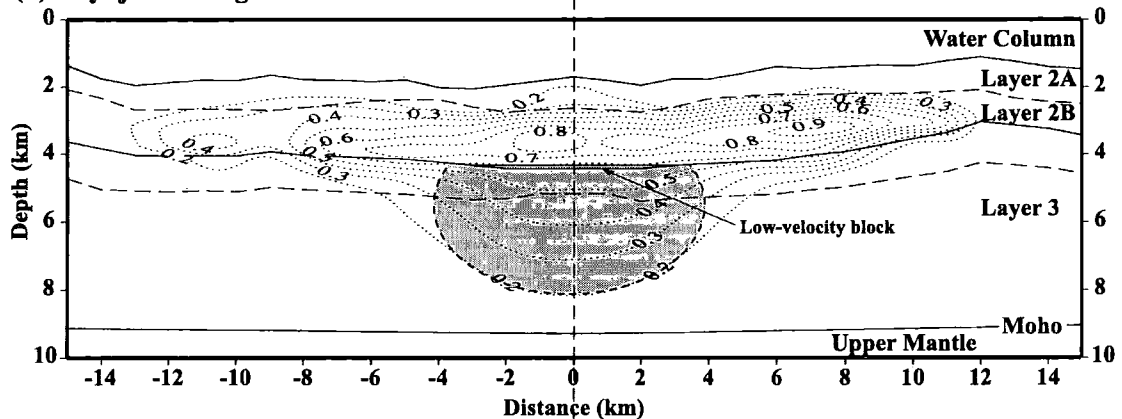
## (a) East Pacific Rise

Layer 2A: Extrusives  
 Layer 2B: Sheeted dykes  
 Layer 3: Isotropic material  
 & layered series

 postulated magma chamber delineated by the  $-0.2 \text{ km s}^{-1}$  velocity anomaly contour



## (b) Reykjanes Ridge



## (c) Valu Fa Ridge

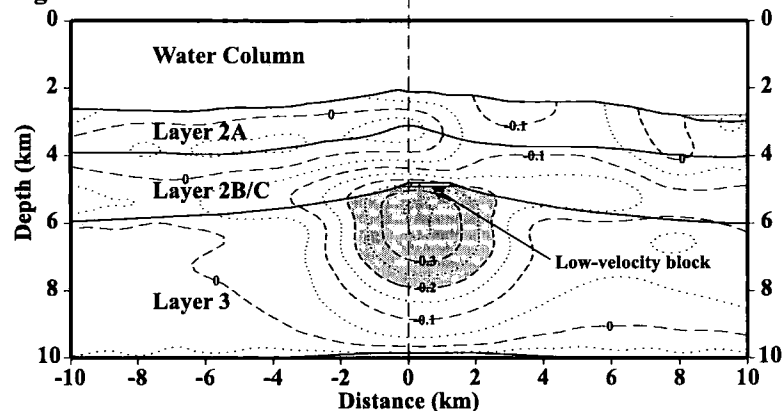


**Figure 1.3:** LVZs at a number of mid-ocean ridge locations (after Turner 1998). a)  $9^\circ \text{ N}$  on the EPR (after Vera *et al.* 1990), b)  $57^\circ 45' \text{ N}$  at the Reykjanes Ridge (after Navin 1996) and c)  $22^\circ 26' \text{ S}$  at the Valu Fa Ridge (after Turner 1998). The shaded region marks the extent of the LVZ as defined by the  $-0.2 \text{ km s}^{-1}$  velocity anomaly contour in each case. The low-velocity blocks at the top of each LVZ will be discussed later in this section. Note the general similarity in anomaly magnitude and dimensions despite the different spreading rates and experimental geometries employed.

Estimates of the amplitude of the velocity anomaly in the LVZs, described above and shown in Fig. 1.3, relative to off-axis crust typically lie in the range  $0.5\text{--}1.0 \text{ km s}^{-1}$ . The precise melt fraction that these velocity anomalies represent is ambiguous. Laboratory experiments on simple binary systems (e.g. Spetzler & Anderson 1968; Stocker & Gordon 1975) have shown that the relationship between



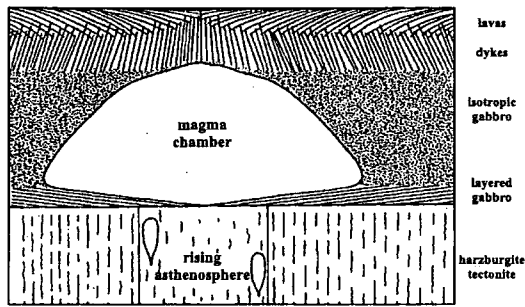
seismic velocity and melt fraction is dependant on the internal, or dihedral, angle at the boundary between solid and fluid, and Sato *et al.* (1989) showed that for a peridotite melt, the observed velocity reduction is consistent with a dihedral angle of  $60^\circ$  up to a melt fraction of 15%. This result was used by Caress *et al.* (1992) to interpret a LVZ beneath the EPR near  $12^\circ 50' \text{ N}$  on the basis that the elastic properties of mafic and ultramafic rocks are similar at high temperatures. The velocity reduction of  $0.7 \text{ kms}^{-1}$  (less than 10% of the off-axis velocity at the same depth) identified by Caress *et al.* (1992) corresponds to a melt fraction of 3–5% on this basis. Wilcock *et al.* (1995) studied the crustal attenuation structure at  $9^\circ 30' \text{ N}$  on the EPR and modelled a high attenuation region on-axis corresponding to the LVZ identified by Vera *et al.* (1990). This feature was found to be of similar magnitude to laboratory measurements of the attenuation of seismic energy in basalt near its solidus temperature. This result similarly implies a very small percentage of partial melt. However, at  $57^\circ 45' \text{ N}$  on the Reykjanes Ridge, modelling of controlled-source electromagnetic data indicates a melt fraction of at least 20% in the axial magma chamber (MacGregor *et al.* 1998). The LVZ imaged at this site by Navin *et al.* (1998) is of similar magnitude to those at the EPR, yet the electromagnetic data suggests a much higher melt fraction.

It is unclear whether the LVZs at the EPR and Reykjanes Ridge comprise different melt fractions or the methods used to determine melt fraction are sensitive to different crustal properties. The electromagnetic method is particularly sensitive to connected melt, and whilst the connectivity of the melt phase also influences the elastic properties of the rock, and hence the seismic velocity, this effect is much smaller on the velocity than on electrical properties. However, the estimate of 20% melt at the Reykjanes Ridge represents a lower limit on the melt fraction determined by MacGregor *et al.* (1998). Therefore it is probable that the discrepancy between the estimates of melt fraction obtained at the Reykjanes Ridge and EPR cannot be explained entirely by the relative sensitivity of seismic and electromagnetic methods to melt connectivity alone. More importantly, all the estimates of melt fraction described above are significantly less than those implied by petrological models of mid-ocean ridge magmatic systems incorporating a vigorously convecting magma chamber (e.g. Cann 1974) and are more consistent with a crystal mush zone comprising a relatively small percentage of partial melt. These observations suggest that the petrological magma chamber model is in need of substantial revision.

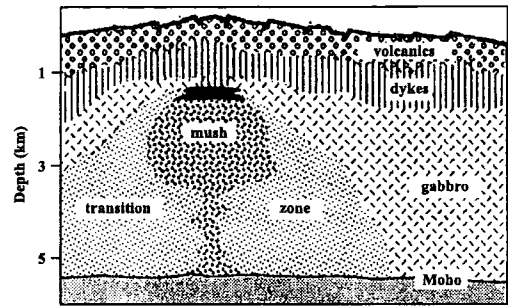
Further evidence for the nature of axial magma chambers has come from seismic reflection studies. The oceanic crust is relatively unreflective due to the generally continuous vertical velocity structure. However, prominent mid-crustal reflectors (MCRs) have been observed at mid-ocean ridges. Herron *et al.* (1980) identified a MCR at the EPR at a depth similar to the top of the LVZ identified by Orcutt *et al.* (1975). A subsequent, more extensive experiment identified a MCR beneath much of the EPR from 8° 50' N to 13° 30' N (Detrick *et al.* 1987). This reflector was found to have negative polarity, implying a velocity inversion, and was therefore interpreted as representing the top of a region of partial melt. Similar MCRs have also been identified at 16° N on the EPR (Carbotte *et al.* 1998), the ultra-fast-spreading southern EPR (Detrick *et al.* 1993; Mutter *et al.* 1995), the intermediate-spreading VFR (Morton & Sleep 1985; Collier 1990; Collier & Sinha 1990 and 1992a) and JDFR (Rohr *et al.* 1988), and the slow-spreading Reykjanes Ridge (Navin 1996; Sinha *et al.* 1998; Navin *et al.* 1998).

The observations of high amplitude reflection events suggest a large velocity contrast, which in turn implies a high percentage of partial melt. These findings contrast with those of the wide-angle seismic experiments described above, which suggest a much lower percentage of partial melt in the LVZs. The low velocity regions these reflectors represent are believed to be very thin (tens or hundreds of metres) on the basis of wide-angle seismic modelling. Such modelling at the EPR (Harding *et al.* 1989; Vera *et al.* 1990), VFR (Turner *et al.* 1999) and Reykjanes Ridge (Navin *et al.* 1998) suggests that the velocity must rise significantly (increases in excess of 2.0 kms<sup>-1</sup>) within a few hundred metres below the MCR in each case. Forward modelling of the MCR identified by Detrick *et al.* (1987) found no evidence for a reflection from the base of the low velocity region, leading to the suggestion that either the region is very thin such that the reflections from its top and base interfere with each other or that its base is merely a gradient zone (Kent *et al.* 1990). Subsequent waveform inversion studies suggest that the region is indeed generally very thin and that it has a relatively sharp base (Collier & Singh 1997; Singh *et al.* 1998).

Seismic observations of LVZs and MCRs have led to revised models of magma chamber structure and accretionary processes at mid-ocean ridges. One such model has been proposed by Sinton & Detrick (1992) and is summarised in Fig. 1.4. This magma chamber comprises a crystal mush zone consistent with the observation of LVZs,

**Petrological model**

Cann (1974)

**Geophysical model**

Sinton and Detrick (1992)

**Figure 1.4:** Comparison of the petrological magma chamber model proposed by Cann (1974) with the model of Sinton & Detrick (1992) which is based on geophysical observations of present day magma chambers. Note that large molten magma chambers required by the model of Cann (1974) have not been observed using geophysical methods. The broad crystal mush zone proposed by Sinton & Detrick (1992) is more consistent with geophysical observations.

overlain by a thin sill of partially molten material consistent with the observation of MCRs. A critical difference between this model and the petrological model of Cann (1974), which is also shown in Fig. 1.4 for comparison, is that convection will be greatly inhibited by the relatively low melt fraction in the mush zone, whereas the large molten body proposed on petrological grounds will convect vigorously. The Sinton & Detrick (1992) model predicts that magma chambers will be widespread at fast-spreading ridges, but will be relatively rare and short-lived at slower-spreading ridges owing to the more episodic melt supply.

The seismic studies described in this section demonstrate that petrological models for the formation of oceanic crust based on ancient ophiolites are inconsistent with geophysical measurements of the properties of present-day magma chambers beneath mid-ocean ridges. It is suggested that these magma chambers incorporate a broad crystal mush zone comprising a relatively small percentage of partial melt overlain by a thin sill comprising a higher melt fraction. Similar structures have been seismically imaged at ridges with a variety of spreading rates suggesting that magma chamber structure is similar at all spreading rates, but at slow-spreading ridges the lower overall magmatic budget is predicted to result in more short-lived magma chambers such that, at any one time, the spatial separation between active magma chambers will be greater than at fast-spreading ridges. The implications for the relationship between magma supply and crustal structure is considered in the next section.

### 1.3.2 Relationship between magmatic budget and crustal structure

The relationship between melt supply and crustal accretionary processes may be analysed on the largest scale by comparing the crustal structure at fast- and slow-spreading ridges. On a smaller scale it may be analysed by examining the relationship between morphological segmentation, which is believed to be broadly related to melt supply as described in section 1.2, and crustal structure. The contribution made by seismic studies to this analysis is discussed in this section.

Wide-angle seismic studies have been used to constrain details of the fine structure of the crust. At the EPR near 9° N layer 2A has been modelled with a very low vertical velocity gradient underlain by a high velocity gradient region at the transition into layer 2B. At this ridge, the layer 2A–2B boundary is believed to represent a lithological transition from extrusive lava to intrusive dykes (Harding *et al.* 1993). Wide-angle arrivals have been observed arising from rays turning in the high velocity gradient transition zone. Modelling of these arrivals, which have been recorded using a variety of experimental geometries and modelling techniques, has allowed mapping of the thickness of layer 2A along- and off-axis (e.g. Vera *et al.* 1990; Christeson *et al.* 1992; Harding *et al.* 1993; Vera & Diebold 1994; Christeson *et al.* 1996). These models have revealed a layer 2A thickness of ~0.10–0.15 km on-axis, which doubles within 2–4 km of the axis and remains constant further off-axis. The amount of off-axis thickening of layer 2A generally appears to correlate with ridge crest morphology and segmentation. The off-axis thickening of layer 2A is less pronounced at 13° N on the EPR where the ridge crest morphology implies a less robust magma supply (Harding *et al.* 1993), and a similar reduction in off-axis thickening was modelled near a deval at 9° 35' N which is similarly regarded as representing a relatively magmatically starved part of the ridge (Christeson *et al.* 1996). Therefore, at this section of the EPR, off-axis extrusive layer thickness appears to be a reliable indicator of long-lived spatial variations in melt supply.

A similar layer 2 structure has been modelled at the JDFR, with a low velocity layer 2A underlain by a high velocity gradient zone at the layer 2A–2B transition (Cudrak & Clowes 1993; McDonald *et al.* 1994). However, at the VFR and Reykjanes Ridge the layer 2A–2B boundary has been modelled without a high velocity gradient zone (Navin *et al.* 1998; Turner *et al.* 1999) suggesting that this feature is not ubiquitous. In general, these slower-spreading ridges have a thicker layer 2A than the EPR and do not exhibit off-axis thickening. This structure is consistent with the relationship between melt supply and the development of layer 2A structure inferred

from along-axis variations at the EPR (Harding *et al.* 1993; Christeson *et al.* 1996). It is suggested that the pronounced off-axis thickening of layer 2A modelled at the magmatically robust sections of the EPR occurs due to burial of earlier lava flows by subsequent eruptions (Harding *et al.* 1993; Hooft *et al.* 1996) and that this process does not apply at ridges with lower spreading rates because the more viscous magmas do not flow as far off-axis. In this case the entire extrusive layer is emplaced within the neovolcanic zone (Macdonald 1982). Therefore there appears to be a relationship between magma supply and the thickness and structure of layer 2A. These examples illustrate how wide-angle seismic studies can provide an insight into accretionary processes at mid-ocean ridges and how those processes relate to differences in magma supply and spreading rate.

The relationship between MCR properties and morphological segmentation has also been investigated, particularly at the EPR which is the most extensively studied of the ridges at which a MCR has been observed. Hooft *et al.* (1997) found that, in general, there was no strong correlation between MCR properties and ridge segmentation at the southern EPR. However, at some locations the width and characteristics of the MCR have been found to correlate with small-scale ridge segmentation, believed to reflect local magma transport within the crust rather than large-scale mantle upwelling (e.g. Macdonald *et al.* 1988; Mutter *et al.* 1995; Babcock *et al.* 1998). A detailed study of the properties of the low velocity region associated with the MCR was conducted by Singh *et al.* (1998) using a waveform inversion technique over a 60 km long section of the southern EPR. They interpreted the *P*- and *S*-wave velocity structure of the low velocity region as predominantly comprising an uneruptable crystal mush, within which are a few regions of high melt fraction each about 2–4 km long and separated by ~15–20 km along-axis. A partial melt body of this size would be expected to crystallise to a mush within a few tens of years which suggests that melt sills, such as those included in the model of Sinton & Detrick (1992), are likely to be very short-lived features relative to the time frame of mantle upwelling at the southern EPR. Since the southern EPR is one of the fastest spreading ridges on Earth, it seems likely that this observation would also apply at other, slower-spreading ridges. Therefore, low velocity region properties need not correlate with ridge segmentation which has developed over a much longer time period.

The example studies described in this section demonstrate the constraints which seismic studies have provided on the crustal structure at mid-ocean ridges and how this structure relates to melt supply on a variety of length and time scales. The differences in crustal structure between ridges of different spreading rates provide insight into the spreading rate dependence of accretionary processes, and along-axis structural changes may be attributed to smaller local variations in melt supply. These variations suggest that in general, crustal structure at mid-ocean ridges is three-dimensional, yet all the studies described so far have adopted a two-dimensional approach to data acquisition and analysis. Three-dimensional modelling of mid-ocean ridges is discussed in the following section.

### **1.3.3 Three-dimensional tomographic studies**

Three-dimensional variations in crustal structure, outlined in the previous section, have been inferred by comparing the results of 2-D experiments often at widely separated locations. In order to fully investigate the 3-D structure of mid-ocean ridges, it is necessary to adopt a three-dimensional approach to data acquisition. Analysis of 3-D datasets is most efficiently performed using a tomographic method. From an initial estimate of the velocity structure, these methods numerically determine a velocity perturbation field which satisfies all the travel time data within appropriate tolerances. A more complete description of the general seismic tomographic method will be given in section 2.2.1.

Seismic tomographic experiments may be performed using active (e.g. airgun array or explosives) or passive sources (earthquakes). The advantage of using an active, or controlled, source is that the source positions and firing times are known and thus the acquisition geometry can be designed to allow optimum data coverage for the geological target of interest. By contrast, earthquake source positions and times are generally unknown and must be determined using arrival travel time data. In addition the temporal and spatial distribution of earthquakes is also uncontrollable. The advantages of earthquake sources are that they occur at a range of depths within the crust, thus potentially providing good ray coverage at depth, and are of greater magnitude than active sources. Therefore for tomographic studies of the deep mantle, passive sources are the only viable option. For studies of the crust and uppermost mantle, to which this discussion is confined, active source experiments dominate.

To date, only a few 3-D tomographic experiments have been conducted at mid-ocean ridges. The EPR at 9° N was the target for a tomographic experiment designed to investigate the 3-D structure of the crust and uppermost mantle. Toomey *et al.* (1990) imaged the 3-D structure of the LVZ at this location and found that the magnitude of the negative velocity anomaly corresponding to the LVZ correlates with ridge segmentation, being maximum at the segment centre which is assumed to be the site of upwelling according to the segmentation model of Macdonald *et al.* (1988). Anomalies have also been modelled in layer 2 by Toomey *et al.* (1994). They modelled a negative velocity anomaly in layer 2B, approximately correlating with the LVZ in layer 3, which they interpreted as arising from a high temperature anomaly. In the mantle Dunn & Toomey (1997) imaged a low velocity anomaly whose amplitude correlates with ridge segmentation in a similar manner to the observed crustal velocity anomalies. Therefore these tomographic analyses have provided direct evidence for 3-D mantle upwelling and have clearly demonstrated that the structure of the overlying magma chamber and crust at this ridge is directly related to deeper mantle processes. Whilst these structures have been hypothesised based on 1-D and 2-D seismic studies, it is only by adopting a 3-D approach that they have been conclusively identified.

The azimuthal coverage required for an effective 3-D tomographic analysis also allows azimuthal anisotropy, or the variation in velocity with ray azimuth, to be investigated directly. Azimuthal anisotropy has commonly been inferred in the uppermost oceanic crust based on 1-D and 2-D experiments (e.g. White & Whitmarsh 1984; Shearer & Orcutt 1985; Caress *et al.* 1992; McDonald *et al.* 1994). The widespread observation of azimuthal anisotropy is usually attributed to the presence of preferentially aligned near-vertical cracks, often perpendicular to the spreading direction (i.e. parallel to the ridge crest in general). For very thin, water saturated cracks (aspect ratios  $<0.001$ ), theory predicts a  $4\theta$  azimuthal dependence on  $P$ -wave velocity with maxima for ray azimuths parallel and perpendicular to the preferred crack orientation (Crampin 1984; Shearer 1988). For larger crack aspect ratios ( $>0.02$ ), a  $2\theta$  dependence is predicted such that the velocity parallel to the preferred crack alignment direction is faster than the velocity perpendicular to this direction. In practice, the latter form of anisotropy is commonly observed.

Although azimuthal anisotropy of the type described above has been invoked as the most likely explanation for azimuthal velocity variations observed in 1-D and 2-D seismic experiments, fully 3-D acquisition geometry is required for unambiguous identification of such structure as two-dimensional modelling of an essentially 3-D structure may give rise to apparent azimuthal velocity variations due to the inadequacy of the 2-D approximation rather than intrinsic anisotropy. The effects of lateral velocity heterogeneity and out-of-plane ray paths which may result from this heterogeneity can only be modelled effectively if the acquisition geometry is three-dimensional. Once these effects have been accounted for any remaining apparent azimuthal variation in velocity may then be ascribed to anisotropy with greater confidence than is possible for 1-D and 2-D experiments. Azimuthal anisotropy in layer 2 has been modelled in 3-D tomographic experiments conducted at the JDFR (Sohn *et al.* 1997) and MAR (Barclay *et al.* 1998). In the uppermost mantle at the EPR, Dunn & Toomey (1997) identified azimuthal anisotropy which is consistent with olivine alignment due to 2-D divergent flow away from the axis.

These example studies demonstrate that a much more detailed model of the velocity structure at mid-ocean ridges can be obtained using a 3-D approach than is possible using 1-D and 2-D modelling methods because 3-D velocity heterogeneity and anisotropy may be identified and modelled more rigorously. The 3-D velocity heterogeneity allows the spatial variation in properties of the magmatic system and the way they relate to mantle structure and ridge morphology to be assessed in detail, and azimuthal anisotropy can also provide insights into the magmatic and tectonic processes at work.

#### 1.3.4 S-wave studies

All of the seismic experiments described in the preceding sections have been targeted towards resolving the *P*-wave velocity structure of the oceanic crust, and specifically young oceanic crust at mid-ocean ridges. Whilst these methods provide constraints on the gross structure of crustal layering, the intra-layer properties and true nature of layer boundaries remain ambiguous. For example, the layer 2A–2B boundary is commonly interpreted as representing a lithological transition from extrusive lava to intrusive dykes (see Fig. 1.2). However, at some locations, it has been suggested that this boundary represents a porosity boundary rather than a lithological transition (e.g. Wilkens *et al.* 1991; Cudrak & Clowes 1993). Similarly the layer 2–3 boundary is widely believed to represent the boundary between dykes and isotropic gabbro even



though seismic studies near a borehole on 5.9 Ma old Pacific crust have indicated that, in the vicinity of this site, this seismically determined boundary lies well within the dyke section (Detrick *et al.* 1994 and 1998). Therefore, whilst the layered nature of oceanic crustal structure appears to be ubiquitous, the geological nature of this layering may not be identical in all locations.

The widespread observation of low  $P$ -wave velocity in layer 2A (typically 2–3  $\text{kms}^{-1}$  compared to  $\sim 6 \text{ kms}^{-1}$  for uncracked basalt) is commonly attributed to high porosity<sup>1</sup> in this extrusive layer. However, it is not possible to precisely quantify this porosity on the basis of  $P$ -wave velocity alone. Theoretical studies have shown that the geometry of cracks within igneous rocks strongly influences their seismic properties (e.g. Kuster & Toksöz 1974; Berge *et al.* 1992) and the range of possible porosities corresponding to any given  $P$ -wave velocity is too great to allow a meaningful interpretation of the  $P$ -wave velocity structure in terms of the porosity-specific structure.

Knowledge of the  $S$ -wave velocity structure in addition to the  $P$ -wave velocity structure can go some way towards resolving this ambiguity. Shearer (1988) showed that thin and thick cracks affect  $P$ - and  $S$ -wave velocity to different degrees. Fig. 1.5 shows the effect of porosity and crack aspect ratio on the seismic velocity of a basalt calculated using several cracking theories. The effect of cracks with different aspect ratios may be expressed in terms of Poisson's ratio,  $\sigma$ , which is related to  $P$ - and  $S$ -wave velocity ( $V_p$  and  $V_s$  respectively) by the formula

$$\sigma = \frac{2 - (V_p/V_s)^2}{2 \left( 1 - (V_p/V_s)^2 \right)}. \quad (1.1)$$

The relationship between  $\sigma$  and crack aspect ratios is also shown in Fig. 1.5.

Poisson's ratio estimates in the oceanic crust are relatively rare due to the difficulty in recording  $S$ -wave arrivals in the marine environment. For active-source experiments no primary  $S$ -waves are generated since the source is in a fluid (the water column) which has no shear strength. Any  $S$ -wave arrivals must, therefore, arise from  $P$ - $S$  mode conversion at intra-crustal interfaces and, hence, they will be of much lower amplitude than  $P$ -wave first arrivals. Although numerous experiments have been conducted using three-component receivers designed to detect horizontally polarised

---

<sup>1</sup> Throughout this dissertation, "porosity" refers to absolute porosity, or total volume of void space within the rock.

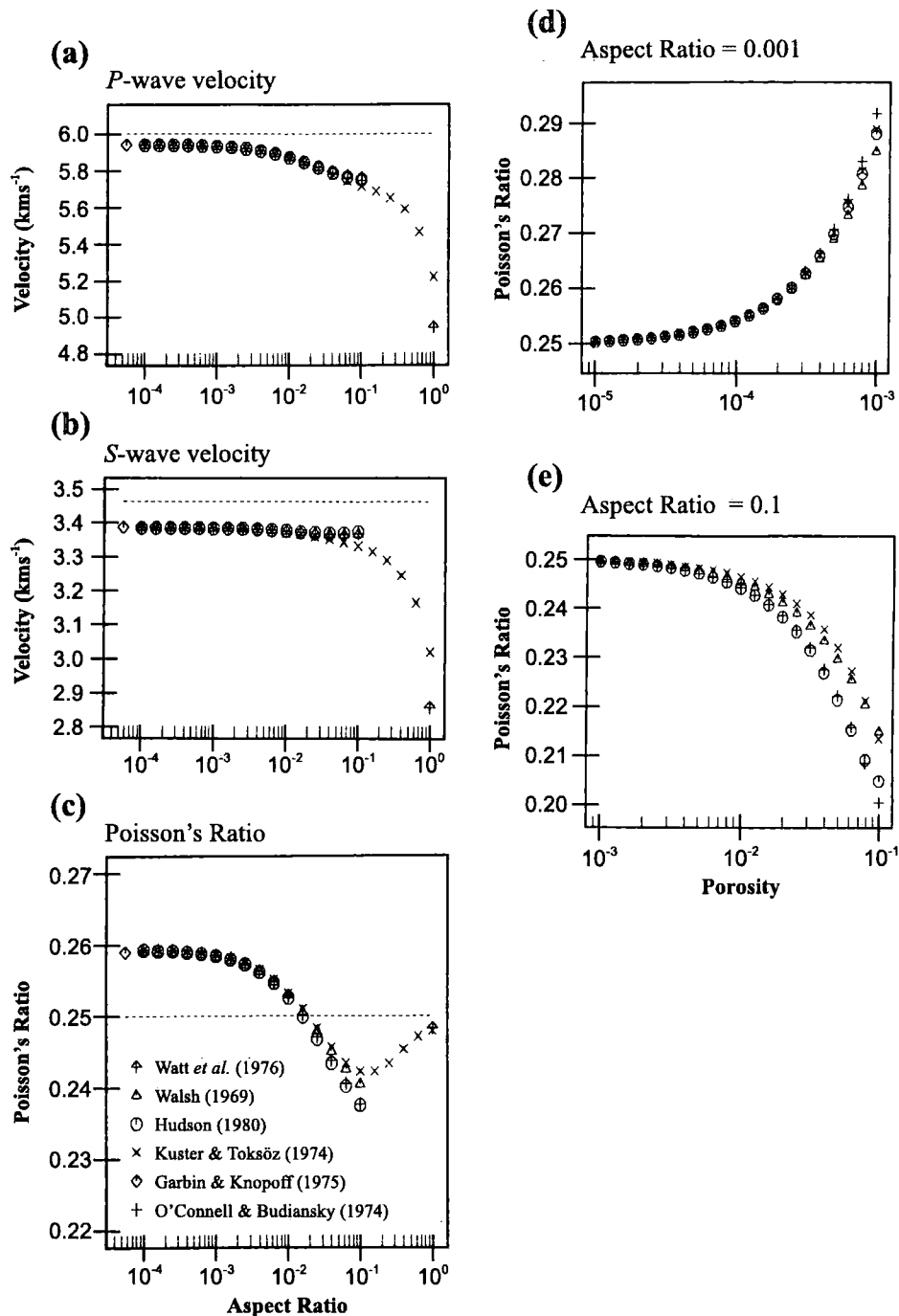


**Figure 1.5:** The effect of cracks of different aspect ratio on  $P$ - and  $S$ -wave velocity, and Poisson's ratio (after Shearer 1988). The theoretical relationship between a)  $P$ -wave velocity, b)  $S$ -wave velocity, c) Poisson's ratio and crack aspect ratio are shown for a constant crack density (number of cracks per unit volume) using a variety of cracking theories (shown by the key in part c) which applies to all other figures). The host rock in this example has properties typical of an uncracked basalt, with a  $P$ -wave velocity of 6.00 kms<sup>-1</sup>, an  $S$ -wave velocity of 3.46 kms<sup>-1</sup> and a Poisson's ratio of 0.25, shown by the dashed lines in parts a), b) and c) respectively. Note that in general, crack aspect ratio affects  $P$ - and  $S$ -wave velocity to different degrees, and this is reflected by the variable Poisson's ratio shown in c). The relationship between Poisson's ratio and porosity is shown in d) for a crack aspect ratio of 0.001 and in e) for a crack aspect ratio of 0.1, representing "thin" and "thick" cracks respectively. Note that the addition of porosity in the form of thin cracks leads to an increase in Poisson's ratio relative to that of the host rock, whilst thick cracks can lead to a reduction in Poisson's ratio. Therefore  $P$ - and  $S$ -wave velocities are dependent on both bulk porosity and the geometry of that porosity, and a measurement of both quantities (and hence Poisson's ratio) can help to constrain this geometry.

$S$ -wave arrivals, they have only been observed and modelled in a few places. Based on synthetic waveform inversions, White & Stephen (1980) demonstrated that  $P$ - $S$  mode conversion is most efficient where there is a large change in velocity over small depth intervals of the order of half a wavelength of both  $P$ - and  $S$ -waves. In the oceanic environment, this criterion is most often satisfied at the sediment-basement interface and most observed  $P$ - $S$  mode converted arrivals have been identified on this basis with conversion occurring on either the up-going or down-going part of the ray path (e.g. Spudich & Orcutt 1980b; Au & Clowes 1984; Bratt & Solomon 1984; Shearer & Orcutt 1986). However, recent studies at the EPR have obtained  $P$ - $S$  mode converted arrivals in young, unconsolidated crust arising from mode conversion at the layer 2A-2B boundary transition zone (Christeson *et al.* 1997; Collier & Singh 1998).

The difficulty in recording detectable  $P$ - $S$  mode converted arrivals in the marine environment normally means that analysis of the Poisson's ratio structure of the crust is limited to the uppermost layers. Nevertheless, these analyses can provide important extra constraints on the properties of layer 2 that are not available from  $P$ -wave studies alone. Laboratory measurements of Poisson's ratio for uncracked basalt lie in the range 0.28-0.31 (Hyndman 1979). Estimates of layer 2A Poisson's ratio from seismic studies are often considerably higher than this, and typically lie in the range 0.30-0.48 (e.g. Spudich & Orcutt 1980b; Bratt & Solomon 1984; Vera *et al.* 1990; Christeson *et al.* 1997; Collier & Singh 1998). The widespread occurrence of high Poisson's ratios in the uppermost crust is attributed to the presence of low aspect ratio cracks based on the theoretical models of Shearer (1988) shown in Fig. 1.5. Some of these Poisson's ratio observations are very much higher than those modelled by Shearer (1988), which may arise in part because the cracking theories used as the basis of this study are not strictly applicable at the high porosities commonly observed in the uppermost crust. However, subsequent theoretical work by Berge *et al.* (1992) has shown that the general results of the cracking theories used by Shearer (1988) are extendable to much higher porosities.

By contrast, Poisson's ratio in the lower part of layer 2 and layer 3 has generally been found to lie in the range 0.25-0.32 (e.g. Spudich & Orcutt 1980b; Au & Clowes 1984; Bratt & Solomon 1984; Christeson *et al.* 1997; Collier & Singh 1998) which is much closer to laboratory measurements for uncracked basalt. These observations have led to models for the evolution of the velocity structure of oceanic crust over time in which the observed changes can be modelled by preferential closure

of low aspect ratio cracks with depth and age due to mineral precipitation during hydrothermal circulation and overburden pressure (e.g. Wilkens *et al.* 1991; Shaw 1994).

These examples demonstrate how the *S*-wave velocity structure in conjunction with the *P*-wave velocity structure can potentially provide much more constraint on porosity and geometry of porosity than is obtainable from the *P*-wave velocity structure alone. Such models may be used to indicate the geological nature of seismic layering or the tectonic processes at work. A knowledge of the porosity and geometry of porosity may also help to constrain models derived from other geophysical datasets, particularly gravity and electromagnetic data. Therefore in order to use seismic data to its fullest potential it is advantageous to design seismic experiments such that *S*-wave arrivals may be recorded, identified and interpreted.

## 1.4 The Valu Fa Ridge

This dissertation concerns the interpretation of a seismic dataset acquired as part of a wide-angle seismic experiment at the VFR in the Lau Basin, southwest Pacific which, like many of the experiments described above, aimed to investigate the 3-D structure at this intermediate-spreading ridge. In this section the tectonic setting of the VFR is described, together with a summary of the results of geological and geophysical investigations undertaken at the VFR to date. A more comprehensive discussion of the geological background is given by Turner (1998).

### 1.4.1 Geological setting

The VFR is situated in the Lau-Havre-Taupo back-arc basin behind the Tonga-Kermadec trench. The regional tectonic structure is shown in Fig. 1.6. The amount of extension in this basin increases from south to north reflecting the position of the Euler pole which describes the motion of the Australian plate with respect to the Pacific plate at 62° S, and consequent northward increase in convergence rate between these two plates (Parson & Wright 1996). In the Lau Basin, located at the far north of the back-arc system, extension has been sufficient to initiate seafloor spreading along the Central and Eastern Lau Spreading Centres (CLSC and ELSC). The northward increase in extension means that these spreading centres are gradually propagating southwards over time. The more northerly CLSC is propagating south at the expense of the older ELSC, and is thought to have developed in response to changes in the regional stress field (Parson *et al.* 1990). However, spreading is still occurring on the ELSC.

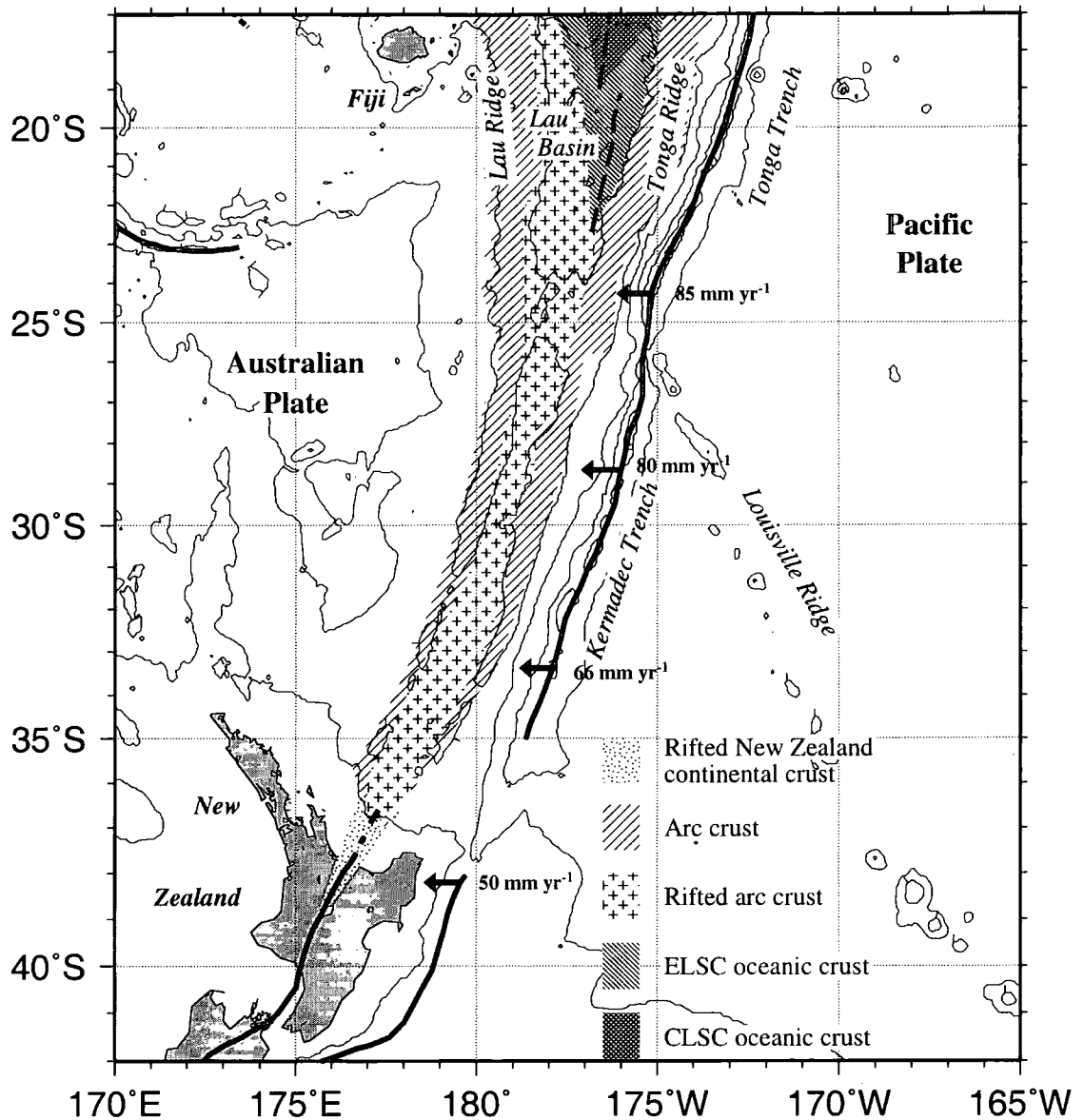


**Figure 1.6:** Tectonic setting of the Lau–Havre–Taupo back–arc system (after Parson & Wright 1996). Bathymetric contours are plotted at 2 km intervals. Plate boundaries are identified as thick solid lines and major ridges, basins and trenches are labelled. Convergence rates of the Pacific plate relative to the Australian plate are also annotated. Note the northward increase in convergence rate, and the related northward increase in the degree of extension in the back–arc basin. In the Lau Basin in the most northerly part of the back–arc system, extension has been sufficient to initiate seafloor spreading along the Central and Eastern Lau spreading centres (CLSC and ELSC respectively). The positions of these spreading ridges are marked by dashed lines. The VFR, with which this study is concerned, forms the southern part of the ELSC.

The southernmost part of the ELSC is referred to as the Valu Fa Ridge, the southern end of which marks the southern extremity of seafloor spreading in the Lau Basin.

On average, the full–spreading rate at the VFR, based on magnetic anomaly identification, is  $70 \text{ mm yr}^{-1}$ . Detailed mapping of anomaly patterns shows a general northward increase in spreading rate consistent with the northward regional increase in

extension (Taylor *et al.* 1996). This average spreading rate classifies the VFR as an intermediate-spreading ridge, although a recent geodetic study suggests a much higher spreading rate ( $\sim 90 \text{ mm yr}^{-1}$  at  $21^\circ \text{ S}$ ) implying that there has been a recent increase (Bevis *et al.* 1995). Accordingly the ridge crest morphology is intermediate between the fast- and slow-spreading end members, being mostly similar to that of the faster-spreading ridges. The VFR is characterised by an axial high and is subdivided into three segments, known as the Northern, Central and Southern Valu Fa Ridges (NVFR, CVFR and SVFR respectively), separated by OSCs (von Stackelberg *et al.* 1988; Wiedicke & Collier 1993) analogous to third-order segmentation at the EPR (Macdonald *et al.* 1991). However, the finer-scale segmentation shows characteristics similar to slow-spreading ridges. The CVFR, with which this study is primarily concerned, may be subdivided on morphological grounds into three higher-order segments (Wiedicke & Collier 1993), each separated by SNOOs or devals and analogous to fourth-order segmentation at the EPR (Macdonald *et al.* 1991). Collier & Sinha (1992b) observed a deepening and widening of the ridge crest from the northernmost to the southernmost fourth-order segment which they attribute to an increase in faulting. They interpreted this morphology in terms of episodic melt supply such that the northernmost segment has been undergoing magmatic accretion while the southernmost segment has been undergoing a period of amagmatic extension. These structures are consistent with cycles of magmatic and tectonic activity inferred to give rise to the variable morphology of AVRs at the slow-spreading Reykjanes Ridge (Murton & Parson 1993) and the temporal variation in magma supply at slow-spreading ridges in general.

The ridge crest morphology also reflects systematic variation in lava composition. Dredging at the CVFR has revealed along-axis changes in composition with the most evolved andesites and dacites found near  $22^\circ 14' \text{ S}$  corresponding to the centre of the northernmost fourth-order segment, and less evolved basalts and basaltic andesites found to the north and south (Frenzel *et al.* 1990). The steep ridge crest morphology at the northern segment is therefore likely to be due in part to the more silicic, and hence more viscous, magma erupting there (Collier & Sinha 1992b). These compositional variations are consistent with southward propagation of the ridge system such that the magmatic system at the north of the CVFR is longer established than that in the south and thus erupts more evolved magmas. Further north at the CLSC, the compositional and geochemical characteristics of the lavas more closely resemble normal mid-ocean ridge basalt (MORB), which is consistent with the widespread

observation that lavas erupted at back-arc basins become more MORB like as the basin widens (Vallier *et al.* 1991; Hilton *et al.* 1993). Hence the more evolved and variable composition of the lavas at the CVFR probably reflects the influence of the nearby subduction zone at a young back-arc spreading centre. This conclusion is supported by the geochemistry of lava samples dredged from the CVFR, which indicates that they are derived from a depleted mantle source with both MORB and island arc affinities (Jenner *et al.* 1987; Vallier *et al.* 1991).

#### 1.4.2 Previous geophysical studies

Regional geophysical studies based upon earthquake observations have revealed details of the structure of the mantle beneath the Lau Basin. Using a waveform inversion technique Xu & Wiens (1997) imaged very low *S*-wave velocities at 30–90 km depth in the mantle beneath the Lau Basin, indicating the presence of partial melt beneath the actively spreading ridges at a similar depth to that at other mid-ocean ridges. The results of a deep mantle tomography experiment reported by Zhao *et al.* (1997) also indicated low velocity anomalies to ~100 km depth beneath the ELSC and CLSC, and a separate low velocity anomaly beneath the island arc, representing the source zone for the island arc magmas. At depths greater than 100 km, a broad low velocity anomaly of substantially lower magnitude was observed extending beneath both the spreading ridge and the island arc to a depth of ~400 km. These results suggest that magmas erupted at the ELSC and CLSC are primarily derived from decompression melting in the uppermost 100 km of the mantle, and therefore the processes at work are directly comparable with other mid-ocean ridges rather than having a strong subduction zone influence. However, there may be a limited degree of magma mixing between the mid-ocean ridge and island arc mantle sources at depth, which would account for the island arc geochemical affinities of VFR lavas.

A MCR was first identified at the VFR by the US Geological Survey in 1982 (Morton & Sleep 1985). Subsequently a cruise aboard the *RRS Charles Darwin* in 1988 (cruise CD34/88) acquired a grid of multichannel seismic profiles encompassing the full length of the CVFR and the OSC at its northern end. Processing of these profiles revealed a MCR along the full length of the CVFR, which was interpreted as representing the top of a robust crustal magma chamber continuous beneath the entire ridge and the OSC (Collier 1990; Collier & Sinha 1990 and 1992a). The along-axis extent and lateral dimensions of the magma chamber inferred from this modelling are shown in Fig. 1.7, together with the fourth-order segments and the location and

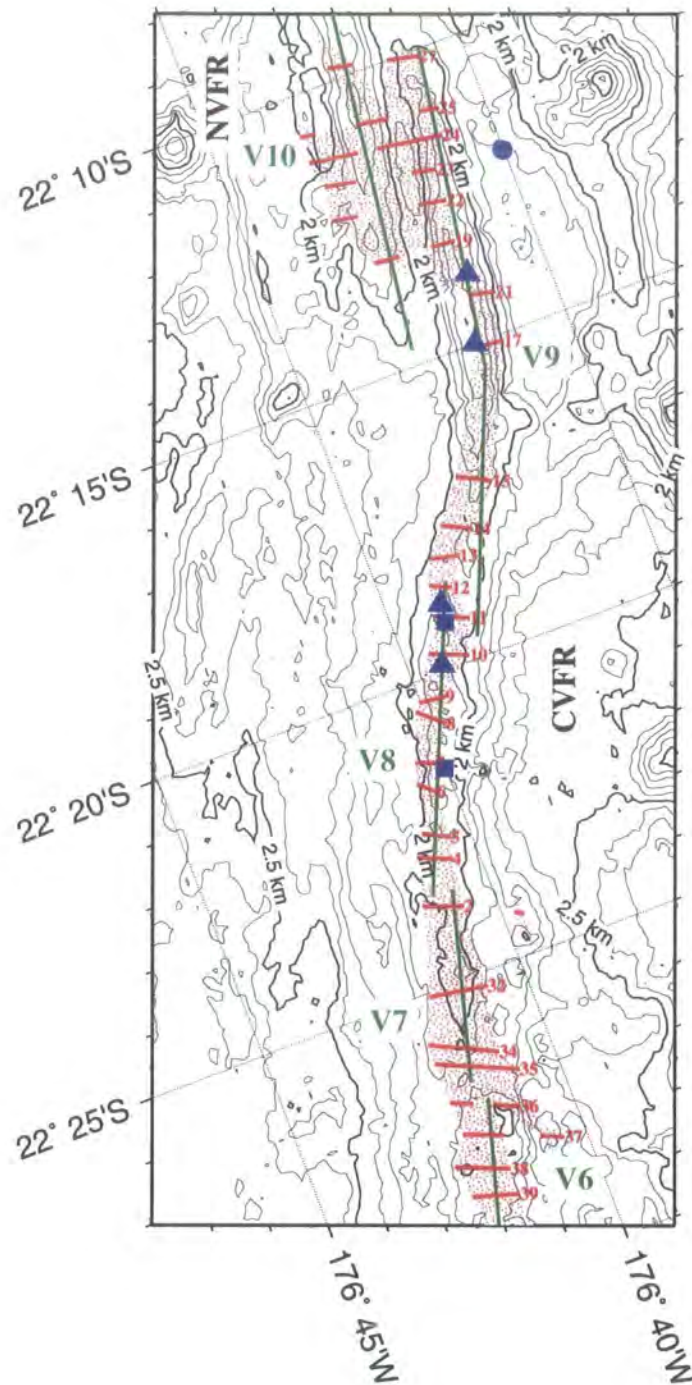


**Figure 1.7:** Summary of previous geological and geophysical studies at the VFR. The area shown encompasses the CVFR and its overlap with the NVFR. The fourth-order segments identified by Wiedicke & Collier (1993) are shown by solid green lines, and labelled V6–V10 according to their nomenclature. The positions of dredge samples are shown by blue symbols. Squares denote basaltic andesite, triangles andesite and dacite, and circles tholeiitic basalt (after Collier 1990; von Stackelberg *et al.* 1988; Vallier *et al.* 1991). Note that the most evolved samples were collected near 22° 14' S in the centre of the V9 segment with less evolved samples recovered north and south of here. The extent of the axial MCR beneath the CVFR and its OSC with the NVFR, as identified from migrated across-axis seismic reflection profiles and forward modelling of unmigrated data, is shown by solid red lines numbered according to the nomenclature of Collier (1990). Stippled shading shows the inferred geometry of the reflector between profiles (Collier 1990). A clear reflector was imaged on most of the across-axis lines, implying along-axis continuity of the MCR. The seafloor bathymetry data, contoured at 0.1 km intervals, which is shown for reference was acquired during a subsequent cruise in 1995 during which the seismic data presented in this dissertation was also obtained (see section 1.5 and Peirce *et al.* 1996).



petrological type of dredge samples. Although apparently continuous along-axis, the width and character of the MCR was found to be variable. These variations correlate with fourth-order ridge segmentation (labelled V6 to V10 in Fig. 1.7, and may reflect segmentation of the axial magma chamber itself as implied by compositional and geochemical variations between segments (Wiedicke & Collier 1993). Modelling of coincident gravity data suggests a northward increase in crustal thickness towards the OSC (Sinha 1995), a result which contradicts standard models of ridge segmentation. These models suggest that ridge axis discontinuities are usually relatively magmatically starved and hence have thinner crust than segment centres (Macdonald *et al.* 1988).

As described above, the VFR has many enigmatic features and was thus chosen as the target for a further multidisciplinary geophysical experiment undertaken in 1995. Analysis of the seismic component of this experiment forms the basis of this study, and a description of the experiment is given in the following section. Precise details of study aims immediately follow in section 1.6.

## **1.5 *R/V Maurice Ewing* cruise EW9512 – the Valu Fa Ridge**

In November–December 1995 a multidisciplinary geophysical experiment was conducted on the *R/V Maurice Ewing* (cruise EW9512) at the VFR. The Central and Northern VFRs were chosen as the target for this cruise on the basis of the results of previous multichannel reflection seismic experiments, described in the previous section, which identified a robust MCR beneath the full length of the CVFR and its overlap with the NVFR (see Fig. 1.7). Detailed descriptions of all the datasets acquired can be found in Peirce *et al.* (1996) and Turner (1998). The wide-angle seismic dataset, which forms the basis of the data analysis and modelling described in chapters 2, 3 and 4, is outlined in this section together with the other subsidiary datasets used in its interpretation. Other modelling which has been undertaken thus far on the data acquired during this cruise is also described.

### **1.5.1 Experimental configuration**

The VFR seismic experimental configuration is summarised in Fig. 1.8. Six coincident wide-angle and normal-incidence seismic profiles were acquired, of which four were oriented parallel and two perpendicular to the general trend of the ridge crest. Data coverage encompasses the full length of the CVFR including its overlap with the NVFR, a 20 km long section of the NVFR, and extends east as far as the active Tonga arc and west into pre-rift crust. Fig. 1.8 also shows the position of the pseudofault

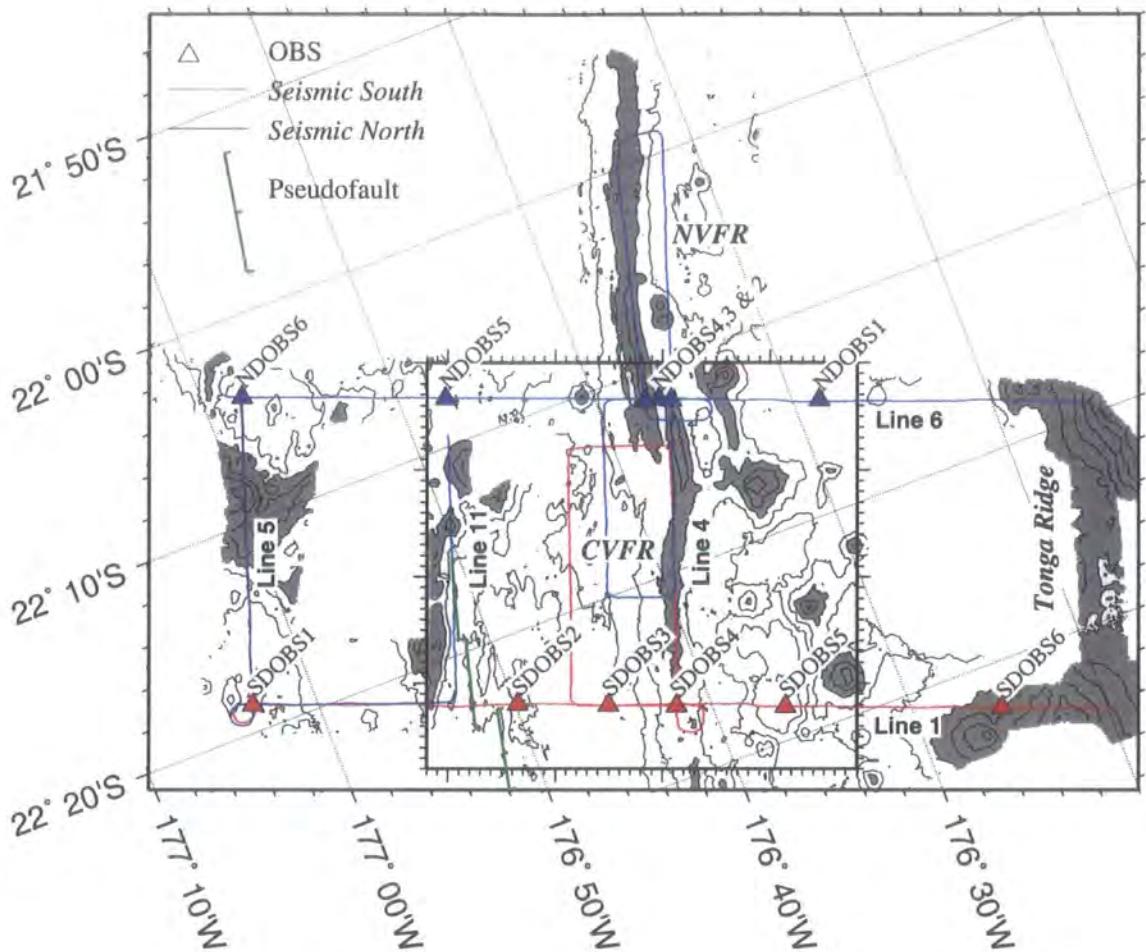


**Figure 1.8:** Ship tracks, OBS locations and bathymetry for the seismic experiment conducted during cruise EW9512. Ship tracks and OBS locations are coloured red for the *Seismic South* deployment and blue for the *Seismic North* deployment. The position of the pseudofault identified by Wiedicke & Collier (1993), which is believed to represent the boundary between pre- and post-rift crust, is marked in green. Bathymetric contours at 0.25 km intervals have been plotted and bathymetry shallower than 2 km has been grey shaded to highlight the ridge axis and large off-axis seamounts. The thick black box indicates the area modelled using a 3-D tomographic approach in this study. The principal 2-D lines modelled by Turner (1998) are labelled Line 1, 4, 5, 6 and 11 (after Peirce *et al.* 1996).

identified by Wiedicke & Collier (1993) which is believed to mark the transition between pre- and post-rift crust. The aim of the EW9512 wide-angle seismic experiment was to resolve the lower-crustal structure including thickness variations, the magma chamber beneath the MCR, and compare the pre- and post-rift crust in order to gain insight into the underlying accretionary processes. The wide-angle seismic data were acquired using a set of six ocean bottom seismographs (OBSs) which were deployed twice. The OBSs were first deployed in positions labelled SDOBS1–6 (*Seismic South*) in Fig. 1.8, which also shows the ship tracks along which shots were fired. The process was then repeated for positions NDOBS1–6 (*Seismic North*). The seismic source and instrumentation are described in section 1.5.2.

Although the experimental configuration is predominantly 2-D, by considering off-line shot-receiver combinations, there is good 3-D ray coverage over the CVFR as shown by the boxed area in Fig. 1.8. Thus by adopting a 3-D approach to modelling this subset of the data the crustal structure in between the 2-D profiles may be imaged, and the 3-D variation in crustal structure evaluated. Neither of these aims are achievable by modelling the widely spaced 2-D profiles alone. The 3-D modelling process adopted will be described in chapters 2 and 3. Data from NDOBS4 was not included because the instrument encountered problems (see below). NDOBS2 was omitted because its close proximity to NDOBS3 means it provides little additional constraint on the crustal structure at the primary target depth, and the quality of data recorded at NDOBS3 was slightly superior.

### 1.5.2 Data acquisition

The seismic profiles shown in Fig. 1.8 were shot using the 8510 in<sup>3</sup> airgun array illustrated in Fig. 1.9. This array was designed to produce a large amplitude source signature with a dominant frequency of ~8 Hz (Turner 1998). The large amplitude and relatively low frequency was necessary in order to generate detectable arrivals at the large shot-receiver offsets required to sample the lower crust. The shot interval of 40 s, resulted in a shot spacing of ~0.1 km. This shot interval was used to provide closely spaced traces for single-channel normal-incidence data acquired contemporaneously

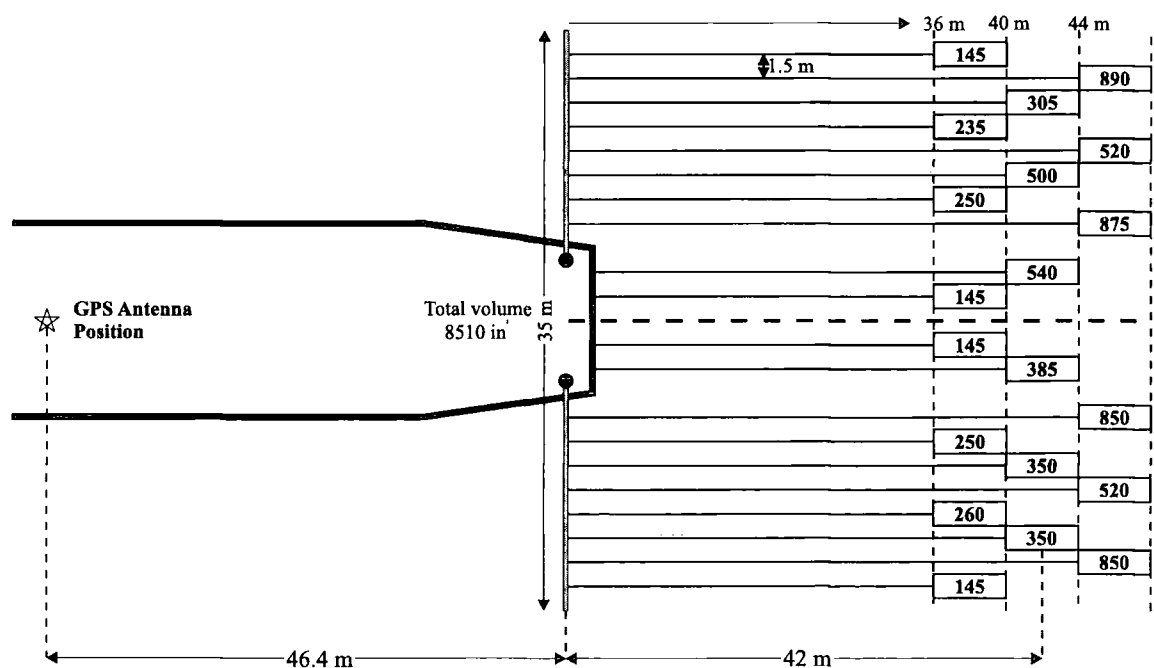


**Figure 1.9:** Construction of the EW9512 airgun array relative to the stern of the ship and the GPS antenna position. Relative gun locations and capacities in in<sup>3</sup> are shown.

with the wide-angle data. Such a small trace spacing is unnecessary for wide-angle data acquisition, so only a subset of these shots was recorded by each OBS as outlined below. Each OBS was equipped with an internal, gimballed, three-component geophone package, an externally mounted hydrophone and a Teledyne Geotech PDAS-100 (Portable Data Acquisition System) datalogger. Full details of the OBS instrumentation are given in chapter 2 (pp. 37-41) of Navin (1996). The dataloggers were programmed to record four-channel data over a 19 s window with a sample interval of 5 ms. Windows were repeated every 80 s and timed to coincide with alternate shots. This recording strategy resulted in a trace spacing of  $\sim 0.2$  km for the wide-angle experiment. On recovery, it was found that NDOBS4 had only recorded a few shots, and the first 520 shots of the *Seismic South* experiment were not recorded by the SDOBS5 vertical geophone. However, all other channels on SDOBS5 successfully recorded all the data. All other OBSs recorded data for each shot on all four channels. Contemporaneously shots were recorded using disposable sonobuoys in an attempt to provide detailed upper-crustal velocity structure control and also with a single-channel streamer to obtain normal-incidence data particularly aimed at mapping the MCR along-axis as a means of providing some control on its continuity (Turner 1998). These latter datasets were analysed as part of Turner (1998)'s 2-D modelling.

A number of other datasets were also collected, and those which were incorporated in this study are described here. Swath bathymetry data, collected using a Krupp Atlas Hydrosweep system, were used in the construction of initial velocity models for the 3-D inversion which will be described in section 2.8. A sound-velocity-dip (SV dip) meter was deployed at  $22^{\circ} 26' S$ ,  $176^{\circ} 36' W$  (Peirce *et al.* 1996), which measured seismic velocity as a function depth in the water column down to 2.7 km. These data were used to model the water column velocity structure, necessary to accurately locate the instruments (section 2.3.3), and water column travel times and ray paths during the inversion process (section 2.8). In addition, twelve expendable bathymetric thermographs (XBTs) were deployed, which measured the temperature and conductivity of the water column. These data were used to assess the variability of the water column velocity structure within the survey area using the method described in section 2.5.

In addition, gravity and magnetic data were acquired during cruise EW9512 (Peirce *et al.* 1996). Modelling and interpretation of these data have been described by Calvert (1996), Turner (1998) and Peirce *et al.* (2001). Controlled-source electromagnetic data were acquired at the southern end of the CVFR and have been modelled by MacGregor *et al.* (2001). These datasets were not used in this study.

### 1.5.3 Data processing

The processing applied to each OBS's raw dataset to create record sections for interpretation are essentially the same as those described in detail in chapter 2 (pp. 53–70) of Navin (1996). A brief overview is provided here.

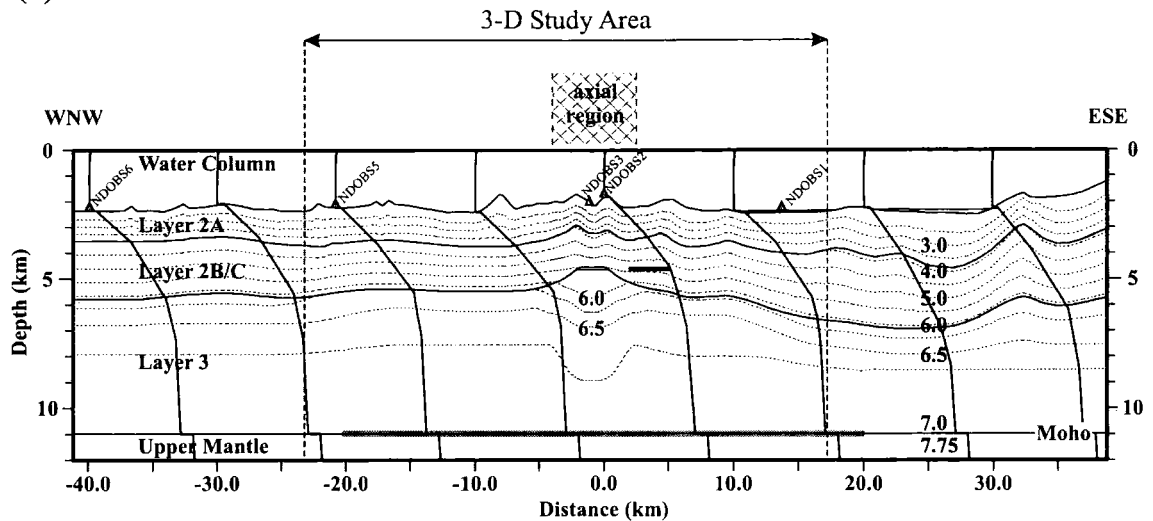
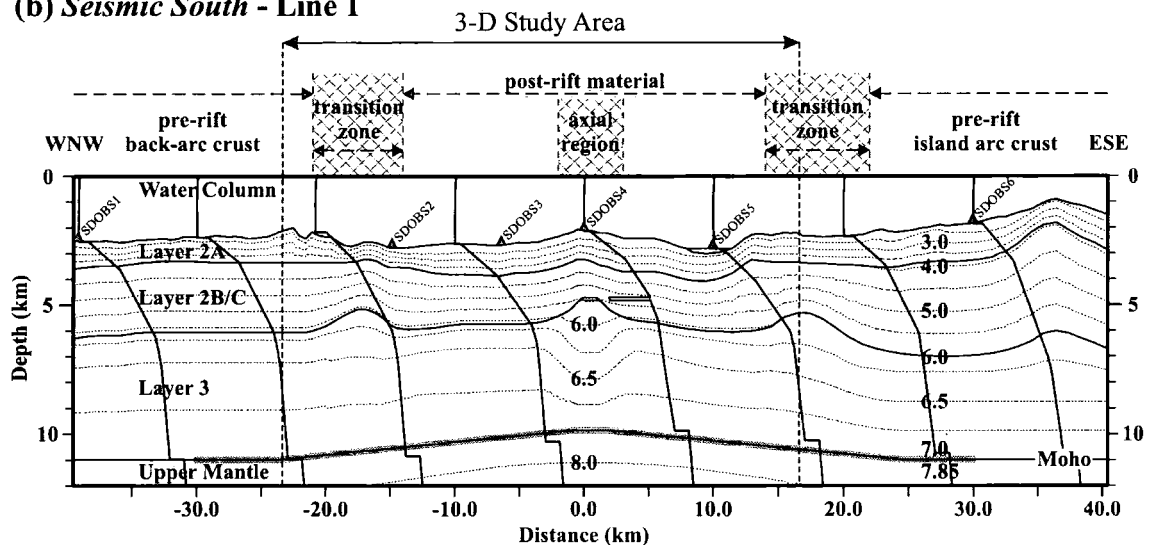
The raw data files were replayed from magnetic back-up tape using *syplus*, degain-ranged and converted to SEG-Y<sub>i</sub> format as described by Navin (1996). This format is a variation on the standard SEG-Y format (Barry *et al.* 1975) for seismic data storage and is described in full by Peirce (1990) and Matthews (1993). The PDAS clocks were synchronised to the *R/V Maurice Ewing's* TrueTime master clock prior to deployment, such that the start of each recorded trace was synchronised with the nominal shot instant. However, shot firing was undertaken in a semi-random manner in which a varying time delay was added to each nominal shot instant in an attempt to reduce constructive water column ringing between adjacent shot instants. These "randomised" shot instants relative to the master clock were recorded and used to extract seismic traces corresponding to each shot from the associated recording window. The PDAS clocks were checked for drift with respect to the ship's clock on recovery, and any necessary corrections were applied during the travel time picking stage described in section 2.3.1.

Interpretation of record sections was performed using *zplot*, a plotting program for seismic data written by Colin Zelt of Rice University, Houston, Texas. This program incorporates an interactive picking tool which was extensively used throughout travel time picking. Hence the data were converted from SEG-Y<sub>i</sub> format to *zplot* format using *sgyi2z*. A full description of the *zplot* file format is given in appendix A. Example record sections and a description of the picking method will be presented in section 2.3.1.

### 1.5.4 Modelling results

In this section, results of modelling and interpretation of EW9512 datasets undertaken thus far are outlined. The gravity data indicates a similar northward thickening of the crust to that modelled using the CD34/88 data (Peirce *et al.* 2001) whilst the electromagnetic data has primarily constrained the conductivity structure of the upper crust (MacGregor *et al.* 2001). Since this study is concerned with the wide-angle seismic dataset, this section is focussed primarily on the results of the two-dimensional modelling of this data which has been undertaken to date.

Two-dimensional modelling and interpretation of the wide-angle seismic profiles shown in Fig. 1.8 has been described by Offer (1996), Rushforth (1996), Turner (1998) and Turner *et al.* (1999). The wide-angle seismic experiment was designed to constrain the structure of the lower crust and the axial magma chamber, the latter of which was believed to be present based on the observation of a MCR. Turner (1998)'s two final across-axis models for Line 1 and Line 6 are shown in Fig. 1.10. Line 1 (*Seismic South*) crosses the southern end of the CVFR and approximately corresponds to Line 35 from cruise CD34/88, while Line 6 (*Seismic North*) crosses the OSC and approximately corresponds to Line 24 (*cf.* Fig. 1.7). Both these profiles exhibit an axial LVZ similar to those observed at other mid-ocean ridges (*cf.* Fig. 1.3), which are generally interpreted as representing a crystal mush zone. The imaging of a LVZ on Line 6 confirms the existence of a robust magmatic system beneath the OSC, implied by the presence of a strong MCR (Collier 1990; Collier & Sinha 1992a). These results are also consistent with the thicker crust modelled at the OSC from the gravity data (Sinha 1995; Peirce *et al.* 2001) which suggests that the OSC has been the site of more vigorous magmatism than elsewhere along the CVFR in the recent past. These observations directly contradict widely accepted models for the relationship between morphological segmentation and melt supply whereby ridge axis discontinuities are expected to be relatively magma starved (e.g. Macdonald *et al.* 1988). Other significant features of Turner (1998)'s models are: 1) approximately constant thickness of the upper crust in the axial region, unlike that at the EPR where significant thickening of layer 2A has been observed immediately off-axis; and 2) the thinning of layer 2 ~20 km off-axis on Line 1. The relative locations of these regions of thinning approximately correspond to the pseudofaults identified by Wiedicke & Collier (1993) and are thus believed to represent the boundary between pre- and post-rift crust. This thinning is analogous to that which is widely observed at passive continental margins and believed to arise from accretion of young oceanic crust onto old, cold continental crust at the

(a) *Seismic North - Line 6*(b) *Seismic South - Line 1*

**Figure 1.10:** Final 2-D, across-axis, velocity-depth models of Turner (1998) for a) Line 6 and b) Line 1 (*cf.* Fig. 1.8). Solid lines indicate the location and geometry of the seafloor, any sediment, the layer 2A–2B/C boundary, the layer 2B/C–3 boundary, the low velocity block and the seismic Moho, the latter of which is constrained at offsets shown by the thicker solid line. Dotted lines represent isovelocity contours at 2.5, 3.0, 3.5, 4.0 (layer 2A–2B/C boundary), 4.5, 5.0, 5.5, 6.0, 6.25, 6.5, 6.75, 7.0 (Moho) and 8.0  $\text{km s}^{-1}$ . OBS locations are shown by triangles. Sections of the models which lie within the 3-D data volume interpreted in this dissertation are indicated by the solid arrows. Velocity-depth profiles are shown at 10 km intervals. Note the low velocities beneath the axial region on both profiles and the thinning of layer 2 at ~20 km offset from the axis on the *Seismic South* profile, which is interpreted as representing the boundary between pre- and post-rift crust.

onset of rifting. In this case, the thinning is associated with the accretion of young oceanic crust onto older, more rigid, pre-rift island arc crust, and such a feature has not previously been observed elsewhere.

The primary aims of this study are to extend the work of Turner (1998) into the third dimension and to consider secondary  $P$ - $S$  mode converted arrivals in order to better constrain the finer-scale structure of geological models of the crustal structure at the VFR. These aims are expanded upon in the following section.

## 1.6 Aims of this study

Although the wide-angle seismic experiment conducted at the VFR during cruise EW9512 was primarily two-dimensional in design, the acquisition geometry provides three-dimensional coverage in the axial region. Additionally, three-component geophone packages comprising one vertical and two mutually orthogonal geophones were used to acquire the seismic data allowing  $P$ - $S$  mode converted arrivals to be recorded and identified. The studies described in sections 1.3.3 and 1.3.4 demonstrate that a 3-D approach to seismic data acquisition and modelling  $P$ - $S$  mode converted arrivals can potentially provide much more information about the 3-D crustal structure and its geological nature than 1-D and 2-D  $P$ -wave studies alone. By taking advantage of the 3-D acquisition geometry in the axial region and the ability to model  $P$ - $S$  mode converted arrivals the purpose of this study is to refine and extend the 2-D modelling of Turner (1998) into three dimensions in the following manner.

- By adopting a fully 3-D approach to modelling data in the axial region, the along-axis continuity of the axial magmatic system and its relationship to morphological segmentation may be assessed. This aim is unachievable using isolated 2-D profiles.
- The 3-D acquisition geometry also allows the 3-D structure of layer 2 to be studied, and its relationship with ridge crest morphology and the underlying magmatic system determined. 3-D interpretation uses rays with a wide range of azimuths, analysis of which allows any anisotropy in crustal structure to be identified. Heterogeneity and anisotropy in layer 2 may be interpreted in terms of the contributions of magmatic and tectonic processes to crustal accretion at the VFR, and the way these processes vary along-axis can be assessed.
- $P$ - $S$  mode converted arrivals have been observed in the VFR dataset, and are believed to arise from mode conversion at the layer 2A-2B/C boundary (Turner 1998). Modelling of these arrivals will provide better geological constraint on the nature of layer 2A and the layer 2A-2B/C boundary (e.g. lithological versus porosity boundary).



- The tomographic approach to modelling the 3-D dataset obtains a best-fitting model using a numerical method and is therefore not biased by any geological preconception. Therefore an independent assessment of model resolution may be conducted in order to establish which features of the models obtained in this study, and those of Turner (1998), are required by the data and which are artefacts of the modelling methods used.

## 1.7 Summary and structure of this dissertation

In this chapter, the contribution of seismic studies to our knowledge of the structure of oceanic crust has been outlined. It has long been recognised that the oceanic crust has a layered structure, though the precise nature of this layering remains ambiguous. The vertical seismic structure of both mature and young oceanic crust is remarkably uniform world-wide yet, as the results of more and more detailed studies become available, it is becoming apparent that along- and across-axis variations are superimposed on the simple layered model. This three-dimensional structure reflects the three-dimensional nature of the accretionary processes at work on a variety of length and time scales. It is therefore more appropriate to employ a three-dimensional acquisition geometry when conducting seismic experiments at mid-ocean ridges in order to image this structure most effectively. It is also desirable to design experiments which allow *S*-wave arrivals to be recorded since these can provide a far superior constraint on the true geological nature of the layering identified. However, the difficulty in generating, recording and interpreting *S*-wave arrivals in the marine environment means they have hitherto only been modelled in a few cases.

Given that the majority of seismic studies at mid-ocean ridges have been conducted at the fast-spreading EPR, there is an ever-increasing need to perform similar experiments at ridges with lower spreading rates in order to ultimately obtain a general model of accretionary processes operating at mid-ocean ridges. This dissertation describes the analysis of a wide-angle seismic dataset acquired at the intermediate-spreading VFR where previous geophysical experiments have identified the presence of a robust magma chamber. The geological setting and previous geophysical experiments conducted at this ridge have been described in section 1.4, and details of the experimental geometry and instrumentation were given in section 1.5.

This study builds on a two-dimensional interpretation of a subset of the wide-angle seismic dataset by Turner (1998) and adopts a seismic tomographic approach in order to extend the study into three dimensions in the axial region. Secondary  $P$ - $S$  mode converted arrivals are also analysed in order to provide geological constraints on the nature of crustal layering at the VFR which have hitherto been unavailable.

The structure of this dissertation is as follows:

- In chapter 2 the three-dimensional tomographic method employed in this study is described together with detailed descriptions of the approaches adopted to determine data uncertainties and model resolution.
- In chapter 3 the results of the tomographic inversion are presented. Tests to determine which features of the models are required by the travel time data and which are artefacts of the modelling method are also described.
- In chapter 4, modelling and interpretation of  $P$ - $S$  mode converted arrivals is described. This analysis was conducted in order to establish the geological nature of layer 2 and also to investigate possible velocity anisotropy in the upper crust.
- In chapter 5 a geological interpretation of the crustal structure at the VFR, based on the analysis described in previous chapters, is presented together with suggested improvements to the experimental design and tomographic inversion method. The proposed improvements would allow more complete and rigorous analysis of future seismic datasets collected at any mid-ocean ridge.

# Chapter 2

## Three-dimensional tomographic inversion

### 2.1 Introduction

In this chapter, details of the seismic tomographic method used to analyse the VFR dataset are described. In section 2.2 the basic principles of the seismic tomographic approach to data analysis are introduced followed by mathematical details particular to the implementation adopted in this study. This method requires that the shot and receiver positions, the first arrival travel time for each shot–receiver pair included in the inversion and the associated travel time uncertainties be known. Additionally, an estimate of the velocity structure is required. Choice of inversion parameters, initial model and data uncertainties for a particular experiment are inevitably interrelated.

Details of the basic raw data required for the inversion are outlined first in section 2.3. Methods for determining data uncertainties follow in sections 2.4 and 2.5 and are summarised in section 2.6. The effect of forward modelling grid node spacing on the accuracy of the forward modelling step, which therefore influences the data uncertainties discussed in previous sections, is considered in section 2.7 and the most appropriate size for the VFR experiment selected. Construction of the initial velocity model using this node spacing is described in section 2.8. The values for the inversion parameters described in section 2.2 are considered in section 2.9. Finally, in section 2.10 a method for assessing the lateral resolution of the models produced by the inversion is described. The methods outlined in this chapter were applied to the VFR dataset, and the results of this modelling will be discussed in chapter 3.

### 2.2 Method

Tomographic inversions were performed using the *FAST* (First Arrival Seismic Tomography) package written by Colin Zelt of Rice University, Houston, Texas. This package performs both regularised inversion and backprojection, and is described in full by Zelt & Barton (1998). Regularised inversion is generally regarded as the superior method, and has been used in this study. In this section, the general seismic tomographic method is first introduced, and its implementation within the *FAST* package described.

### 2.2.1 Seismic refraction tomography

The fundamental problem in 3-D seismic refraction tomography is to resolve the velocity structure within a data volume given a set of first arrival travel times between shots and receivers of known location within that data volume. The problem is most conveniently expressed in terms of the reciprocal of the velocity, or *slowness*. For a single shot–receiver pair, the first arrival travel time,  $t_i$ , may be expressed as

$$t_i = \int_{S_i} u(x,y,z) ds, \quad (2.1)$$

where  $S_i$  is the first arrival ray path between shot and receiver and  $ds$  is a small length element tangential to the ray path (Nolet 1987). The problem of finding the slowness field  $u(x,y,z)$ , given  $n$  travel time observations  $t_{1-n}$ , is highly non-linear since the ray paths  $S_{1-n}$  are dependant on this field. The solution is also non-unique.

Inverse methods assume that an estimate of the slowness structure is available, in which case the problem may be linearised by expressing the slowness field as the sum of an initial estimate of the structure,  $u_0$ , and a perturbation field,  $\delta u$ . A further simplification is made based upon Fermat's principle, whereby first arrival travel times are assumed to be stationary for small shifts in ray location (Nolet 1987). A corollary is that for small perturbations of the slowness field, the first arrival ray path for the initial structure is a close approximation to the first arrival ray path for the perturbed structure. Applying this approximation, equation 2.1 may be rewritten as

$$t_i = \int_{S_i^0} (u_0 + \delta u) ds = \int_{S_i^0} u_0 ds + \int_{S_i^0} \delta u ds, \quad (2.2)$$

where  $S_i^0$  is the first arrival ray path for the initial model,  $u_0$ . Equation 2.2 may be rewritten in terms of the travel time residual,  $\delta t_i$ , which is defined as the difference between the observed and predicted travel times. The latter is given by  $\int_{S_i^0} u_0 ds$  (*cf.* equation 2.1) so the travel time residual may be expressed as

$$\delta t_i = t_i - \int_{S_i^0} u_0 ds = \int_{S_i^0} \delta u ds. \quad (2.3)$$

The inversion process comprises two steps: a forward modelling step and an inverse step. The inverse step aims to find the perturbation field,  $\delta u(x,y,z)$ , which best satisfies all observed travel time residuals (section 2.2.3). The inverse step requires that the predicted first arrival travel times and ray paths for the corresponding shot–receiver pairs must first be calculated for the initial model – this is the forward modelling step.

### 2.2.2 Forward modelling step

The forward modelling step is performed using a modified form of the finite difference algorithm of Vidale (1990). Velocity models are parameterised on a regular node-based grid, converted to slowness, and the first arrival times for rays travelling from a source to every node in the model are calculated. Travel times are calculated progressively away from the source. For nodes lying within a  $5 \times 5 \times 5$  point cube centred on the node nearest the source, travel times are calculated using a straight ray approximation. Travel times to the remaining nodes are calculated on the faces of an expanding cube (i.e. the  $7 \times 7 \times 7$  point cube is treated next, followed by the  $9 \times 9 \times 9$  point cube, and so on) using the finite difference method outlined below.

The method of Vidale (1990) seeks a finite difference solution to the eikonal equation of ray tracing

$$\left(\frac{\partial T}{\partial x}\right)^2 + \left(\frac{\partial T}{\partial y}\right)^2 + \left(\frac{\partial T}{\partial z}\right)^2 = u_0^2(x,y,z), \quad (2.4)$$

where  $T$  is the first arrival travel time from the source position to a given node in the model, and  $u_0$  is the slowness field. Fig. 2.1 shows the three stencils used for calculating nodal travel times. In each case, the largest numbered circle represents the node for which the travel time is calculated using the travel times to nodes represented by the smaller numbered circles. Typically travel times to more than 90% of nodes may be calculated using the stencil shown Fig. 2.1a, which is the most accurate. More than 90% of the rest are calculated using the stencil in Fig. 2.1b, and the remainder are calculated using the stencil in Fig. 2.1c (see Vidale (1990) for a full discussion). The finite difference solutions to equation 2.4 for the three stencils are

$$T_7 = T_0 + \frac{1}{\sqrt{2}} \sqrt{6h^2 U^2 - (T_1 - T_2)^2 - (T_2 - T_4)^2 - (T_4 - T_1)^2 - (T_3 - T_5)^2 - (T_5 - T_6)^2 - (T_6 - T_3)^2} \quad (2.5a)$$

$$T_5 = T_1 + \sqrt{2h^2 U^2 - \frac{1}{2}(T_0 - T_3)^2 - (T_2 - T_4)^2} \quad (2.5b)$$

$$T_5 = T_2 + \sqrt{h^2 U^2 - \frac{1}{4}((T_1 - T_3)^2 - (T_0 - T_4)^2)} \quad (2.5c)$$

where  $T_{\langle \text{num} \rangle}$  is the travel time to the specified node,  $h$  is the node spacing, and  $U$  is the average slowness within the volume occupied by the relevant template shown in Fig. 2.1 (after Vidale 1990).

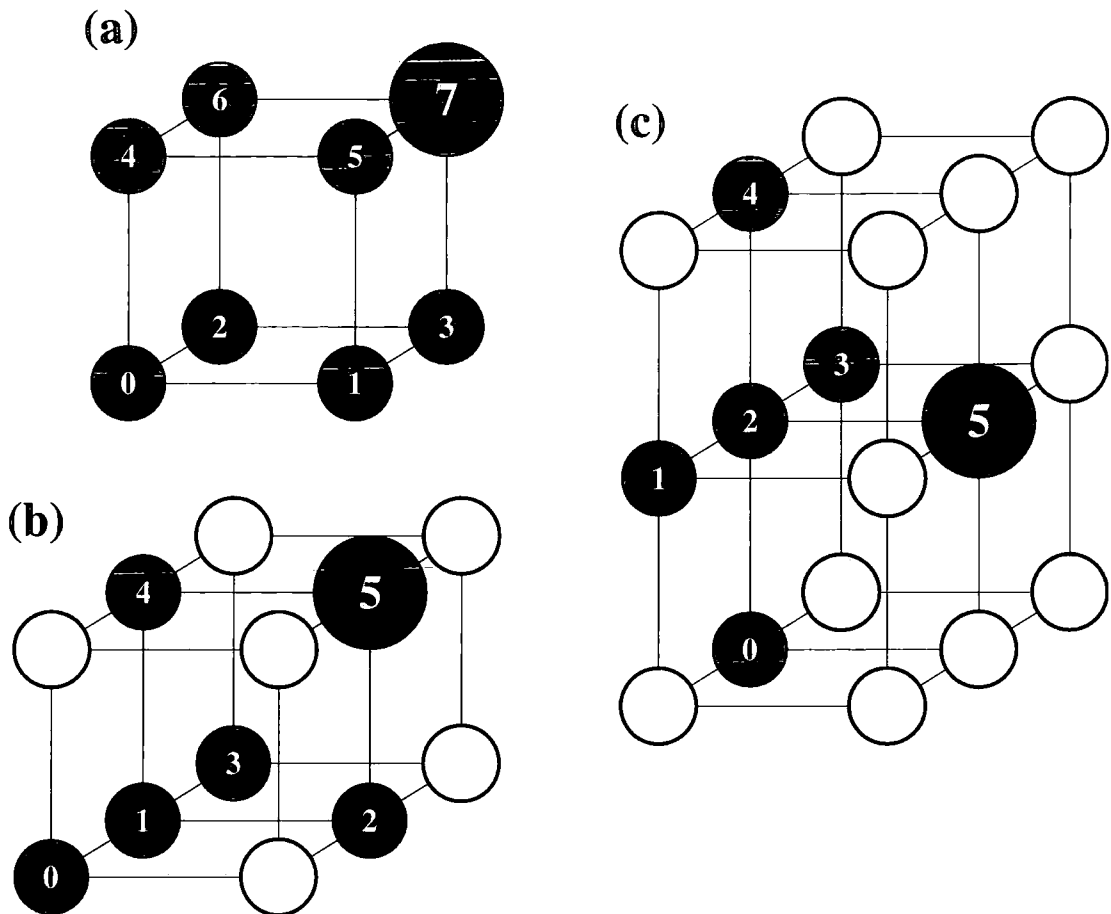


**Figure 2.1:** Geometry of stencils used to calculate first arrival travel times using equations 2.5a–c respectively (after Vidale 1990). Each circle represents a model node. In each case, the first arrival travel time to the node marked with the largest circle is calculated based on the first arrival travel times to each of the nodes marked by smaller numbered circles which have been calculated during previous iterations. Open circles represent nodes which are not used in the calculation.

Hole & Zelt (1995) state that the method of Vidale (1990) breaks down in the presence of first-order velocity boundaries, defined as boundaries across which there is a distinct step in velocity. This problem arises because the method of Vidale (1990) assumes that the expanding cube approximately represents the wavefront, which is not true in the presence of first-order velocity discontinuities where there is an increase in velocity. In this case the first arrival changes abruptly from an arrival which has travelled solely above the velocity discontinuity to a head wave which has undergone critical refraction at the velocity discontinuity. The method of Vidale (1990) cannot simulate these head waves. Failure of the method is indicated by either a causality violation, whereby the calculated travel time is less than the travel times from which it is derived, or a negative value beneath the square roots in equations 2.5a–c. For these nodes, Hole & Zelt (1995) first use 2-D and 1-D head wave operators to calculate

travel times. A reverse propagation is then performed through the model from the bottom using the calculated travel time field as a starting point. Those nodes whose travel times were determined using head wave operators are replaced with the travel time calculated by the reverse propagation only if the latter is smaller (by Fermat's principle). These modifications have been incorporated into the *FAST* package, together with a few minor modifications to improve the algorithm's computational performance which are detailed by Zelt & Barton (1998).

For the VFR experiment, in common with most marine seismic refraction experiments, the number of shots greatly exceeds the number of receivers. In practice it is therefore computationally more efficient to calculate travel times in the reverse direction. Thus, travel times were calculated from each receiver position to every node in the model. Since the receivers were located on the seafloor (a first-order velocity discontinuity), for those travel times calculated using a straight ray approximation (i.e. travel times to nodes within the  $5 \times 5 \times 5$  cube centred on the node nearest the receiver) the velocity at the receiver depends on the location of the node to which the travel time is being calculated. For nodes above the receiver, a velocity of  $1.494 \text{ kms}^{-1}$  (the average water column velocity) was used whilst for timing nodes below the receiver a velocity of  $1.910 \text{ kms}^{-1}$  (the velocity at the top of the crust) was assumed.

Shots are generally not located on model nodes. The predicted first arrival travel time for each shot is therefore determined by linear interpolation between the travel times to the eight nearest nodes which define a cube enclosing the shot. The ray path corresponding to the first arrival ( $S_i^0$  in equation 2.3) is determined by finding the steepest gradient in the first arrival travel time field between receiver and shot (Vidale 1988). The predicted first arrival travel time is subtracted from the corresponding observed first arrival travel time to give the travel time residual ( $\delta t_i$  in equation 2.3). Hence, for the  $n$  first arrival travel time observations, the forward modelling step determines the values of the travel time residuals,  $\delta t_{1-n}$ , and the corresponding ray paths,  $S_{1-n}^0$ , for the initial model. These results are used to perform the inverse step.

### 2.2.3 Inverse step

In order to perform the inverse step, the data volume is divided into cells which are usually of a larger size than the node spacing for the forward modelling step. For a model comprising  $m$  cells, equation 2.3 becomes

$$\delta t_i = \sum_{j=1}^m l_{ij} \delta u_j, \quad (2.6)$$

where  $\delta u_j$  is the slowness perturbation in the  $j$ th cell and  $l_{ij}$  is the ray path length in the  $j$ th cell for the  $i$ th ray which is calculated by the forward modelling step. The purpose of the inverse step is to determine the  $m$  slowness perturbations  $\delta u_{1-m}$  which best satisfy the  $n$  travel time residuals  $\delta t_{1-n}$ . The set of simultaneous equations for all  $n$  observed travel time residuals may be expressed as the matrix equation

$$\delta \mathbf{t} = \mathbf{L} \delta \mathbf{u}, \quad (2.7)$$

where  $\delta \mathbf{t}$  is an  $n$  length vector of travel time residuals,  $\delta \mathbf{u}$  is an  $m$  length vector of slowness perturbations, and  $\mathbf{L}$  is an  $n \times m$  matrix whose elements are  $l_{ij}$  as defined above. A further refinement is that this set of simultaneous equations is weighted according to the uncertainty in each travel time residual observation such that the most reliable data is fit preferentially. This weighting is achieved by pre-multiplying equation 2.6 by  $1/\sigma_i$ , where  $\sigma_i$  is the uncertainty associated with the  $i$ th travel time residual. The resulting set of simultaneous equations may be expressed in matrix form as

$$\mathbf{E}^{-1} \delta \mathbf{t} = \mathbf{E}^{-1} \mathbf{L} \delta \mathbf{u}, \quad (2.8)$$

where  $\mathbf{E}$  is a diagonal matrix with elements  $E_{ii} = \sigma_i$ .

In general, the number of model parameters  $m$  greatly exceeds the number of data observations  $n$ , so the set of equations represented by 2.8 is underdetermined. To address the underdetermined parts of the solution, the inversion is regularised by adding additional constraints. The method of Zelt & Barton (1998) seeks to minimise total model roughness, as defined by the second derivative operator

$$\frac{\partial^2 u_j}{\partial x^2} + \frac{\partial^2 u_j}{\partial y^2} + \frac{\partial^2 u_j}{\partial z^2} = 0, \quad (2.9)$$



where  $u_j$  is the average slowness in the  $j$ th cell. The horizontal and vertical smoothness constraints are treated separately since the inversion cell size may be different in the horizontal and vertical directions. Additionally in many cases the majority of the vertical structure is input in the initial model so the inversion is primarily directed towards determining lateral variations in the structure. Defining  $\mathbf{u}$  as an  $m$  length vector whose elements are  $u_{1-m}$ , the vertical and horizontal smoothness constraints may be expressed in terms of the 1-D and 2-D finite difference operators respectively:

$$\frac{\partial^2 u_j}{\partial z^2} = \frac{u_{j+\gamma} + u_{j-\gamma} - 2u_j}{\Delta v} = 0 \quad (\text{vertical smoothness}) \quad (2.10a)$$

$$\frac{\partial^2 u_j}{\partial x^2} + \frac{\partial^2 u_j}{\partial y^2} = \frac{u_{j+\alpha} + u_{j-\alpha} + u_{j+\beta} + u_{j-\beta} - 4u_j}{\Delta h} = 0 \quad (\text{horizontal smoothness}), \quad (2.10b)$$

These expressions are illustrated in Fig. 2.2.  $\Delta v$  and  $\Delta h$  are the vertical and horizontal cell sizes respectively, and  $\alpha$ ,  $\beta$  and  $\gamma$  are the offsets between elements of the vector  $\mathbf{u}$  representing adjacent cells in the  $x$ ,  $y$  and  $z$  directions respectively.

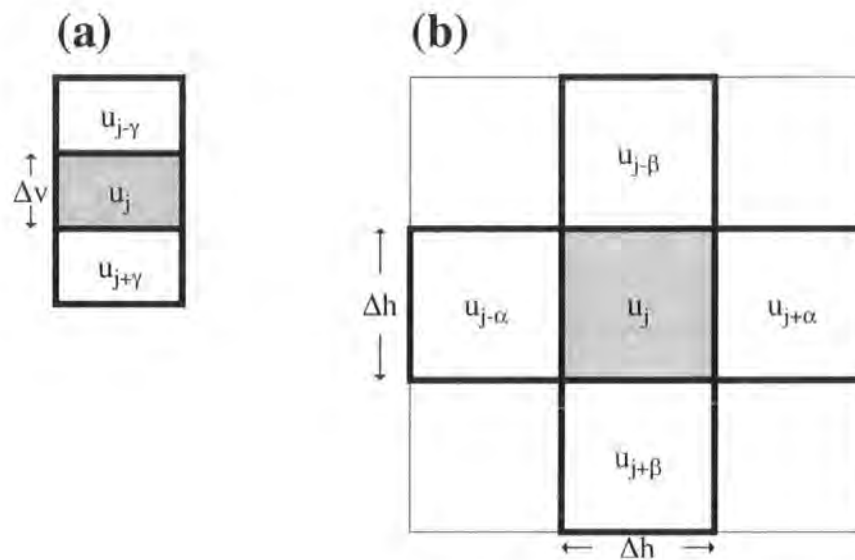


**Figure 2.2:** Illustration of the a) vertical and b) horizontal smoothness constraints applied to the  $j$ th inversion cell (shaded) using equations 2.10a and 2.10b respectively. Each rectangle in a) and square in b) represents an inversion cell, and  $u_k$  is the element of the  $m$  length slowness vector  $\mathbf{u}$  corresponding to the total model slowness in the  $k$ th inversion cell.  $\Delta v$  and  $\Delta h$  are the vertical and horizontal inversion cell dimensions respectively.  $\alpha$ ,  $\beta$  and  $\gamma$  are the offsets between elements of  $\mathbf{u}$  which represent adjacent cells in the  $x$ ,  $y$  and  $z$  directions respectively.

The regularisation is expressed as the matrix equation

$$\begin{bmatrix} \mathbf{H} \\ s_z \mathbf{V} \end{bmatrix} \mathbf{u} = 0. \quad (2.11)$$

Each row in  $\mathbf{V}$  and  $\mathbf{H}$  corresponds to an equation of the form shown in equations 2.10a and 2.10b respectively. The  $s_z$  parameter controls the relative importance of maintaining horizontal versus vertical smoothness. In order to avoid introducing bias towards greater model roughness in high velocity regions, each row in  $\mathbf{V}$  and  $\mathbf{H}$  is normalised by dividing by  $u_j$  (Zelt & Barton 1998). In addition the vertical and horizontal cell dimensions ( $\Delta v$  and  $\Delta h$  in equations 2.10a and 2.10b) are not used to normalise the regularisation equations. Therefore, considering all of the above, for the  $j$ th row in  $\mathbf{V}$ , the only non-zero terms are  $V_{j+\gamma j}$  and  $V_{j-\gamma j}$  which are set to  $1/u_j$  and  $V_{jj}$  which is set to  $-2/u_j$ . Similarly, for the  $j$ th row in  $\mathbf{H}$ , the only non-zero terms are  $H_{j+\alpha j}$ ,  $H_{j-\alpha j}$ ,  $H_{j+\beta j}$  and  $H_{j-\beta j}$  which are set to  $1/u_j$  and  $H_{jj}$  which is set to  $-4/u_j$ . Since this regularisation effectively assumes that the vertical and horizontal cell dimensions are identical, the relative size of  $\Delta v$  and  $\Delta h$  also exerts control over the importance of maintaining horizontal versus vertical smoothness in addition to the  $s_z$  parameter. In order to apply equal weight to horizontal and vertical smoothing,  $s_z$  should be set to  $\Delta v/\Delta h$ .

Substituting  $\mathbf{u} = \mathbf{u}_0 + \delta \mathbf{u}$ , where  $\mathbf{u}_0$  is an  $m$  length vector whose elements represent the average initial model slowness in each cell, and combining with the set of equations in 2.8 gives the set of equations which is solved by the inverse step,

$$\begin{bmatrix} \mathbf{E}^{-1} \mathbf{L} \\ \lambda \mathbf{H} \\ s_z \lambda \mathbf{V} \end{bmatrix} \delta \mathbf{u} = \begin{bmatrix} \mathbf{E}^{-1} \delta \mathbf{t} \\ -\lambda \mathbf{H} \mathbf{u}_0 \\ -s_z \lambda \mathbf{V} \mathbf{u}_0 \end{bmatrix} \quad (\text{after Zelt \& Barton 1998}). \quad (2.12)$$

$\lambda$  is the trade-off parameter between minimising model roughness and minimising data misfit. This set of equations is overdetermined and is solved in a least squares sense using the LSQR variant of the Conjugate Gradient algorithm (Paige & Saunders 1982; Nolet 1987). This algorithm will find the exact least squares solution for  $\delta \mathbf{u}$  if enough iterations are applied. However, since the matrices in equation 2.12 are very sparse the solution converges rapidly. Also since the linearisation assumption is an approximation only 50 iterations of LSQR are applied to yield an approximate solution of sufficient accuracy (Zelt & Barton 1998).

The slowness perturbation field derived by the method described above is converted to a node-based grid by averaging the perturbation in the eight cells which share a common corner. This gives a smoothly varying perturbation field which is added to the initial slowness model (which is usually parameterised on a grid with smaller node spacing) by linear interpolation, and results in a smooth final model which is desirable for stable ray tracing. The forward modelling and inverse steps are then repeated iteratively until a model with a normalised ( $\chi^2$ ) misfit, defined by

$$\chi^2 = \frac{1}{n} \sum_{i=1}^n \frac{\delta t_i^2}{\sigma_i^2}, \quad (2.13)$$

of 1.0 is achieved. This value of misfit indicates that the travel time residuals have been satisfied within their uncertainties.

The matrix equation, 2.12, shows that there are two free parameters,  $\lambda$  and  $s_z$ . However, a further feature of the *FAST* package is that for each iteration, several progressively smaller values of  $\lambda$  are tested until a minimum in  $\chi^2$  is found. The resulting model and value of  $\lambda$  are carried forward to the next iteration. Large values of  $\lambda$  imply a high degree of smoothing, so the longest wavelength perturbations are defined by the earliest iterations. The model is refined by the addition of shorter wavelength perturbations during later iterations as the value of  $\lambda$  becomes smaller. Hence an initial value of  $\lambda$  must be supplied for the first iteration. The only remaining free parameter  $s_z$ , the parameter which controls the relative importance of maintaining horizontal versus vertical smoothness, is provided by the user. The choice of these initial parameters are discussed in section 2.9.

## 2.3 Data

The inversion method described in the previous section requires that the following information be known: the observed first arrival travel time for each shot-receiver pair; the uncertainty associated with each travel time residual; the position of all shots and receivers; and an initial estimate of the velocity structure. A step-by-step description of the detailed method employed to obtain this information, including the software that was used, is provided in appendix B. The inversion method assumes that the shot and receiver locations are precisely known. In practice this is not the case, and it is therefore important that the shot and receiver locations are determined as accurately as possible and a measure of the uncertainty in their locations obtained. These uncertainties may

then be incorporated in the overall travel time residual uncertainties which are used to weight the inversion and establish convergence as described in the previous section.

Data uncertainties and the initial velocity model are considered in sections 2.4 to 2.6 and section 2.8. This section describes how the first arrival travel times, together with the shot and receiver locations were determined for the VFR experiment.

### 2.3.1 First arrival travel time picks

The first stage of first arrival travel time picking involved the creation of data sections in *zplot* format to enable use of the automated travel time picker in-built into this package in addition to manual picking. The processing sequence was outlined in section 1.5.3. The majority of first arrival travel time picks were made from the vertical geophone section since this channel generally showed highest signal-to-noise ratio (SNR) for the crustal first arrivals. In order to pick arrivals in an automated fashion, the user must first define the arrival to be picked on two bracketing seismic traces. The picking tool then applies a cross-correlation process to the traces in between as follows. Firstly each trace is cross-correlated with a reference trace, calculated as an average of the two bracketing traces and weighted by the separation of the trace from each of the bracketing traces. A cross-correlation window of 300 ms (60 samples) was used. Cross-correlation was performed for time shifts of up to  $\pm 100$  ms from a linearly interpolated arrival time between the two bracketing traces with the maximum in cross-correlation defining the pick position. The autopicker worked reliably in areas of high SNR with a typical bracketing trace separation of 2–10 traces, and greatly speeded up the picking of all 2124 arrivals included in the inversion. All arrivals picked using the autopicker were scrutinised and spurious picks corrected by manual picking.

Fig. 2.3a shows example vertical geophone traces for SDOBS2 and the corresponding positions of the first arrival travel time picks. Traces 548–554 exhibit high frequency noise which partially obscures the first arrival pick position. These noise bands occur at regular intervals throughout each section as data is repeatedly transferred from dynamic memory to hard disk storage and is most pronounced on the hydrophone sections. For these areas, a Butterworth band-pass filter was applied with a 3 dB attenuation point at 40 Hz to facilitate picking and improve the performance of the automatic picking tool. Fig. 2.3b shows the same traces as Fig. 2.3a with this low-pass filter applied. The 3 dB attenuation point of 40 Hz is well outside the frequency range of the signal (<20 Hz) and hence application of this filter should not remove any useful

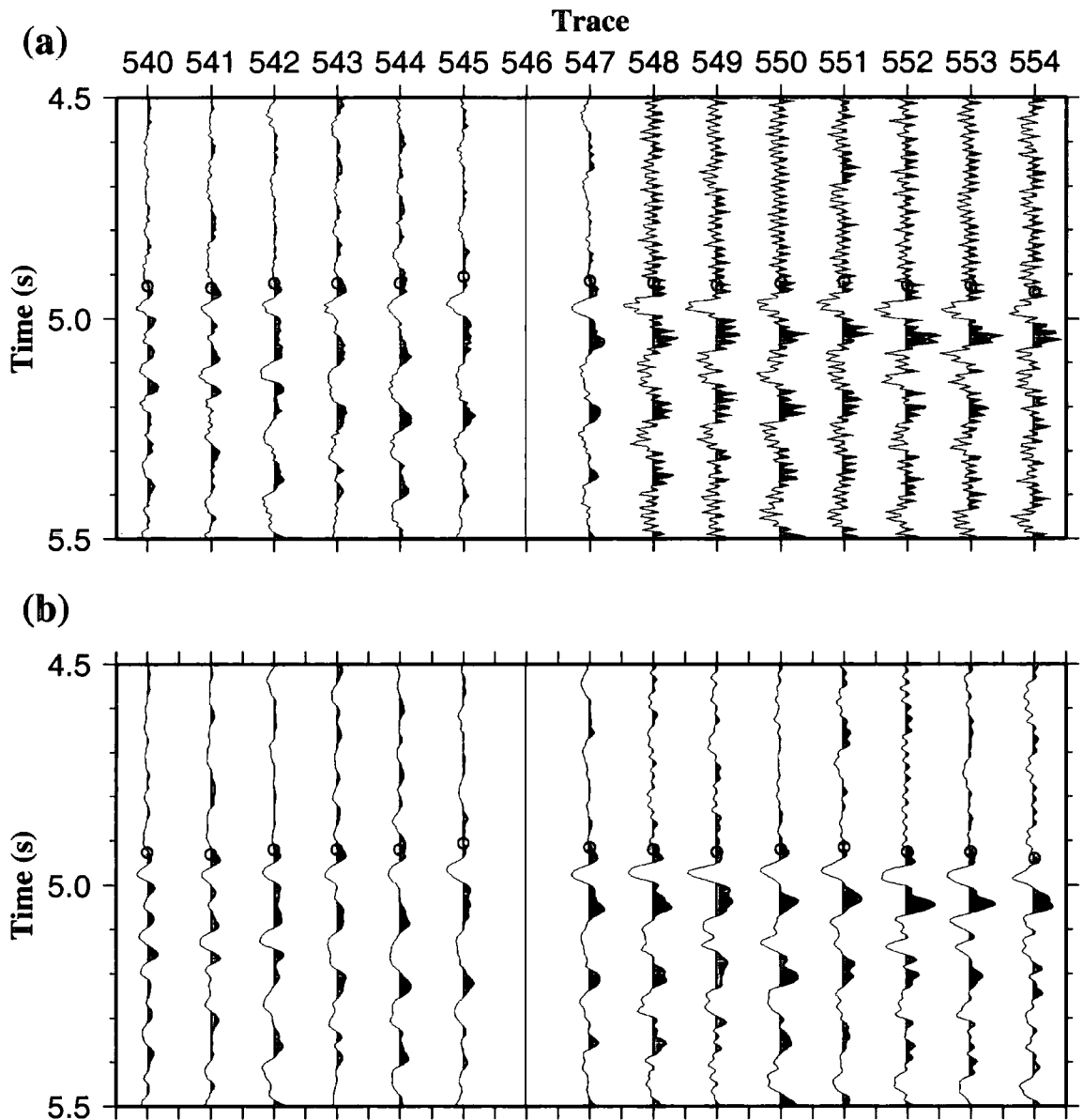


**Figure 2.3:** Example seismic traces. a) Detail of vertical geophone traces recorded by SDOBS2. The centre of each red dot marks the first arrival travel time pick position. Trace 546 was a failed shot and traces 548–554 exhibit high frequency disk spin noise. b) The same seismograms as a) after a Butterworth band-pass filter with 3 dB roll off at 40 Hz has been applied. The first arrival travel time pick positions are much easier to discern for these traces than in a) and comparison of the pick position pre- and post-filtering for traces unaffected by noise (540–545) shows that this filtering does not affect the picking accuracy.

data. Comparison of Figs. 2.3a and 2.3b for those traces which are not affected by high frequency noise shows that the apparent position of the first arrival is unchanged. Hence, those picks made with the low-pass filter applied are considered reliable.

For instrument SDOBS5, the vertical geophone did not record any data for the first 520 shots, so for these shots the first arrivals were picked from the hydrophone section. The hydrophone traces contain additional high frequency noise because hydrophones are broader band sensors than geophones and respond to hard disk

vibration at a lower frequency than the geophones. Therefore a Butterworth band-pass filter was applied to all hydrophone traces with a 3 dB attenuation point of 20 Hz in these areas, and 40 Hz elsewhere.

Picked arrivals were then corrected for clock drift by comparing the discrepancy between the OBS internal clock and the ship's master clock when the instruments were recovered, and assuming that the drift was linear throughout the deployment period. Clock drifts were in the range ~5–75 ms during the *Seismic South* deployment of approximately 46 hours, and ~4–80 ms during the *Seismic North* deployment of approximately 54 hours. The sample interval was 5 ms, so individual instrument clock drifts near the upper ends of these ranges are significant and must be corrected for.

### 2.3.2 Shot locations

The subset of ship tracks and receivers used in the 3-D tomographic inversion are shown in Fig. 2.4. A recording window interval of 80 s results in a shot spacing of approximately 0.2 km at a survey speed of ~5 knots. All shot positions were GPS navigated. The inversion method described in section 2.2 is parameterised on a linear grid, so shot positions were transformed into an x-y co-ordinate system using an oblique transverse Mercator projection centred at 22° 20' S, 176° 40' W with an equator azimuth of 111°. This projection was chosen such that the y-axis approximately parallels the ridge crest. The GMT routine *mapproject* (Generic Mapping Tools – Wessel & Smith 1995) was used for this transformation. The positive x direction is along a bearing of 111° and the positive y direction is along a bearing of 201°.

The centre of the airgun array was located 88.4 m behind the ship's GPS receiver (see Fig. 1.9), and the shot positions were corrected accordingly. The ship's direction of travel was determined by considering the change in both x and y position between the previous shot and the current shot, and between the current shot and the next shot. For each co-ordinate an average of the two offsets weighted for the distance between shots was calculated. This procedure was necessary to determine the direction of travel when the shot spacing was irregular, such as turns where the ship speed was often variable, or where shots misfired leading to a much larger than normal distance between successive shots.

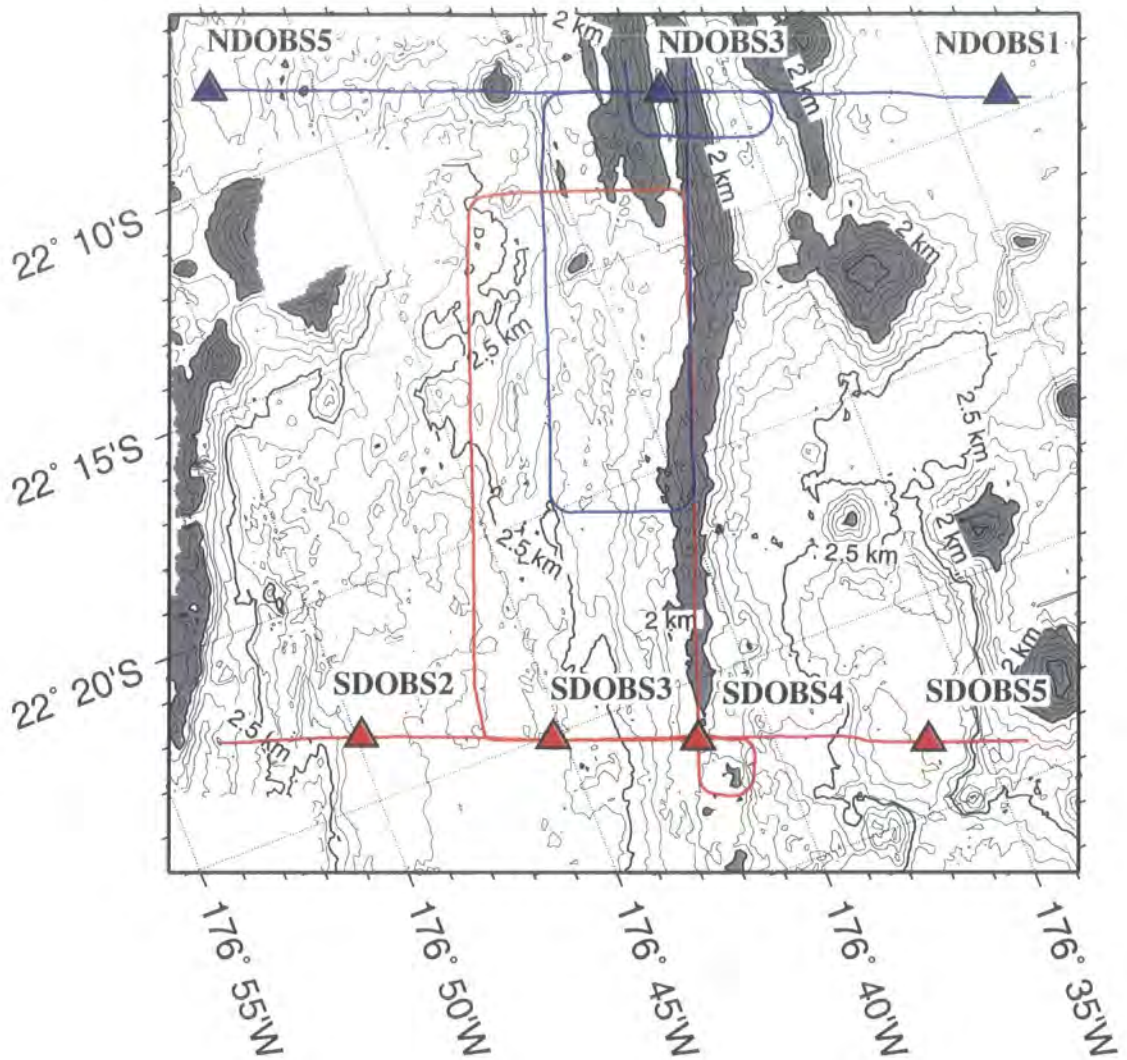


**Figure 2.4:** The subset of ship tracks and receivers used for 3-D tomographic analysis. Ship tracks and OBS locations are coloured red for the *Seismic South* deployment and blue for the *Seismic North* deployment. Bathymetric contours at 0.1 km intervals have been plotted and bathymetry shallower than 2 km has been grey shaded to highlight the ridge axis and large off-axis seamounts.

### 2.3.3 Receiver locations

The ship's position at the time of deployment of each OBS is known, and the water depth at that position can be determined from the swath bathymetry data. However, an OBS may drift laterally as it falls through the water column due to currents, so its precise position on the seafloor is unknown. Therefore each OBS location must be checked, and it repositioned if necessary, using the direct water-wave arrivals as follows.

As described in section 1.5.2, each OBS was equipped with a gimbaled three-component geophone package and an external hydrophone. Signals travelling directly between shot and receiver through the water column, hereafter referred to as the direct water-wave arrivals, are clearest in the hydrophone data and thus were picked from these sections. As an example Fig. 2.5 shows the direct water-wave arrivals used for repositioning SDOBS3, the locations of the source shots and the OBS deployment position. For each OBS the shot-receiver range for each direct water-wave arrival was determined. For ease of interpretation, shots with a more positive  $x$  position than the OBS were assigned a positive range, and those with a more negative  $x$  position a negative range. Ray tracing of the direct water-wave arrivals through the water column was then performed using *RAYINV* (Zelt & Smith 1992), a 2-D ray tracing package. Shots nearest the OBS are most useful for determining its position and also provide the most reliable direct water-wave arrival times due to high SNR. Therefore only shot-receiver ranges up to  $\pm 10$  km were required to accurately locate each OBS. For NDOBS4, located in the overlap basin, preliminary ray tracing indicated that direct water-wave arrivals were only predicted for shot-receiver offsets of less than  $\sim 4$  km due to the steep sides of the overlap basin. For larger shot-receiver offsets the apparent direct water-wave arrivals may have travelled through the crust near the flanks of the overlap basin. Hence, for NDOBS4, repositioning was performed using direct water-wave arrivals with shot-receiver ranges of up to  $\pm 4$  km only for which the assumption that the signal has travelled solely through the water column is most likely to be valid. For water column ray tracing a 1-D model of its velocity structure was derived from the SV dip meter deployed at  $22^{\circ} 26' S$ ,  $176^{\circ} 36' W$  (Peirce *et al.* 1996). The water column was modelled with four constant velocity gradient layers as shown in Fig. 2.6. The receiver position was assigned zero offset and a depth corresponding to the water depth at the OBS deployment position. Shots were placed at 8 m depth (the nominal airgun array depth) at offsets as defined above. Ray tracing was performed in the reverse direction (i.e. from the receiver to the shots) for computational efficiency since there were many shots but only one receiver. The predicted and observed travel times were then compared, and the  $x$  and  $y$  position of the OBS manually adjusted to obtain a better fit.



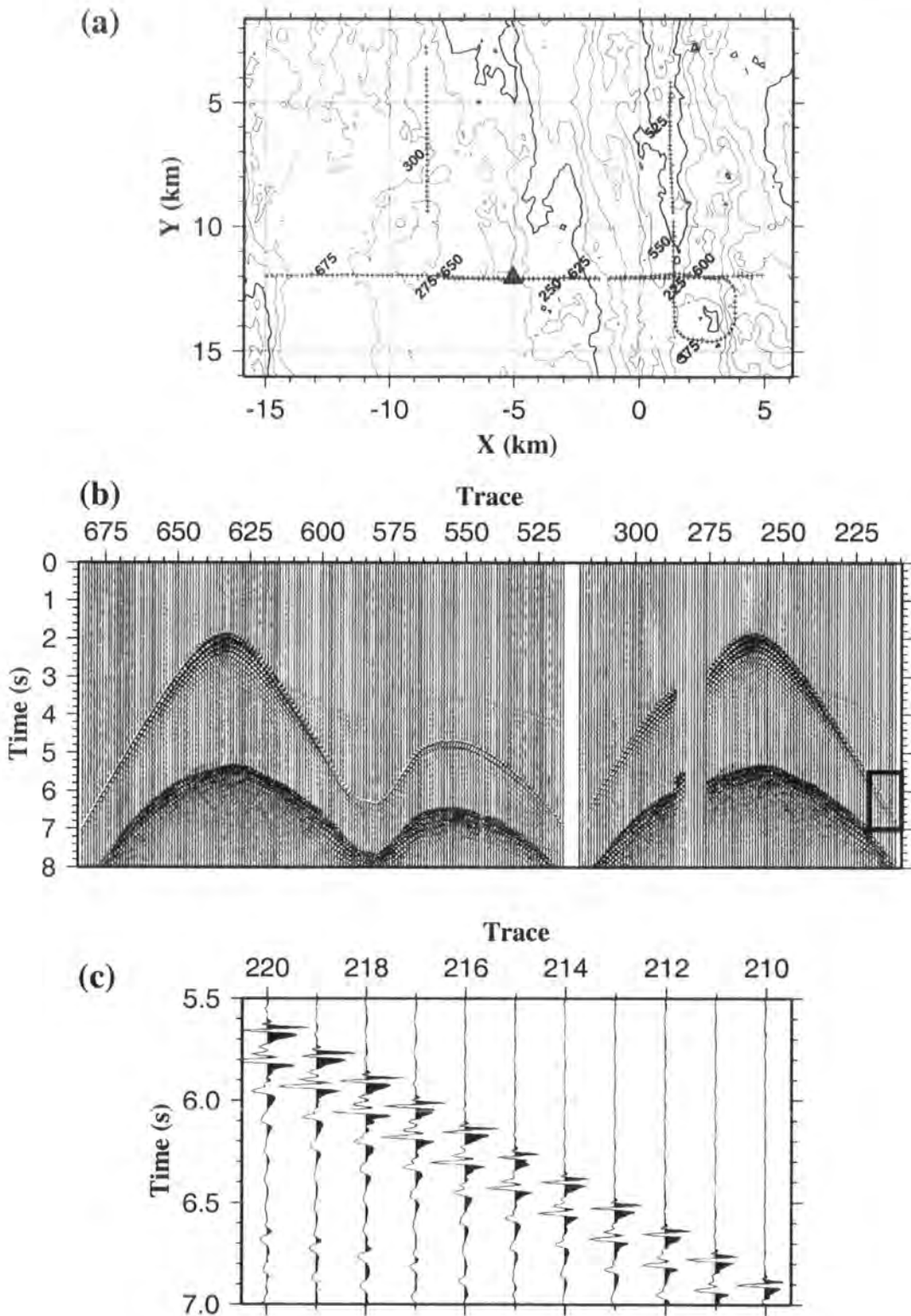


**Figure 2.5:** Direct water-wave arrivals used to relocate SDOBS3. a) Extract from the experimental configuration map (Fig. 2.4), with the transformation described in section 2.3.2 applied, showing the position of SDOBS3 (red triangle) and the shots used to relocate it (crosses). Every tenth cross is coloured green and numbered according to the trace annotation in b) and c). b) Detail of the SDOBS3 hydrophone section corresponding to those shots used to relocate this OBS. The centres of the yellow dots mark the positions of the direct water-wave arrival travel time picks corresponding to the shots shown in a). Shots 276–284 were failed shots and shots 320–517 have been omitted because none of the direct water-wave arrivals recorded for those shots were used to relocate this OBS. c) Detail of the first few traces corresponding to the boxed area marked in b) showing actual picks and data quality.

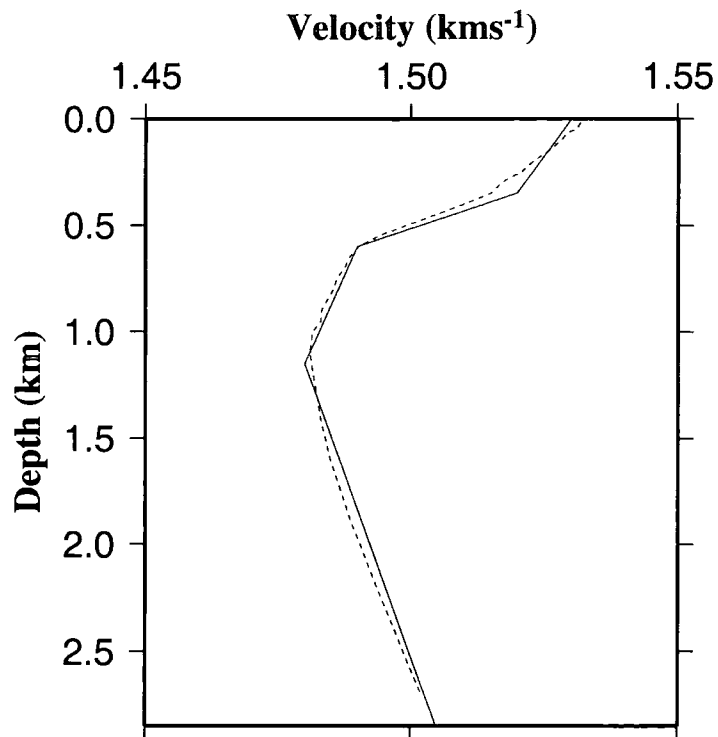


**Figure 2.6:** Water column velocity structure. The dashed line shows the profile determined using the SV dip meter (after Peirce *et al.* 1996), and the solid line is the four layer approximation to this profile. This velocity structure was used to model direct water-wave arrivals used to relocate OBSs.

Generally, since all OBSs were deployed along one of the across-axis 2-D lines, the  $x$  position can be determined accurately from the near-offset in-line shots. The  $y$  position is more uncertain as it is mostly determined from off-line shots located further away. Hence, the  $x$  position was determined first, and the RMS misfit between calculated and observed direct water-wave arrival times used as a guide when adjusting the  $y$  position. The OBS depth at the new position was determined from the swath bathymetry data, and minor adjustments made (up to 35 m, or 0.035 km) to further improve the fit. The improvement in fit for each instrument obtained by using this method for each instrument is illustrated in Fig. 2.7. For all instrument positions, the final RMS misfit was 14 ms or less, i.e. less than three samples. RMS misfits for all OBS locations are shown in Table 2.1. Possible causes of this misfit are discussed in section 2.5.

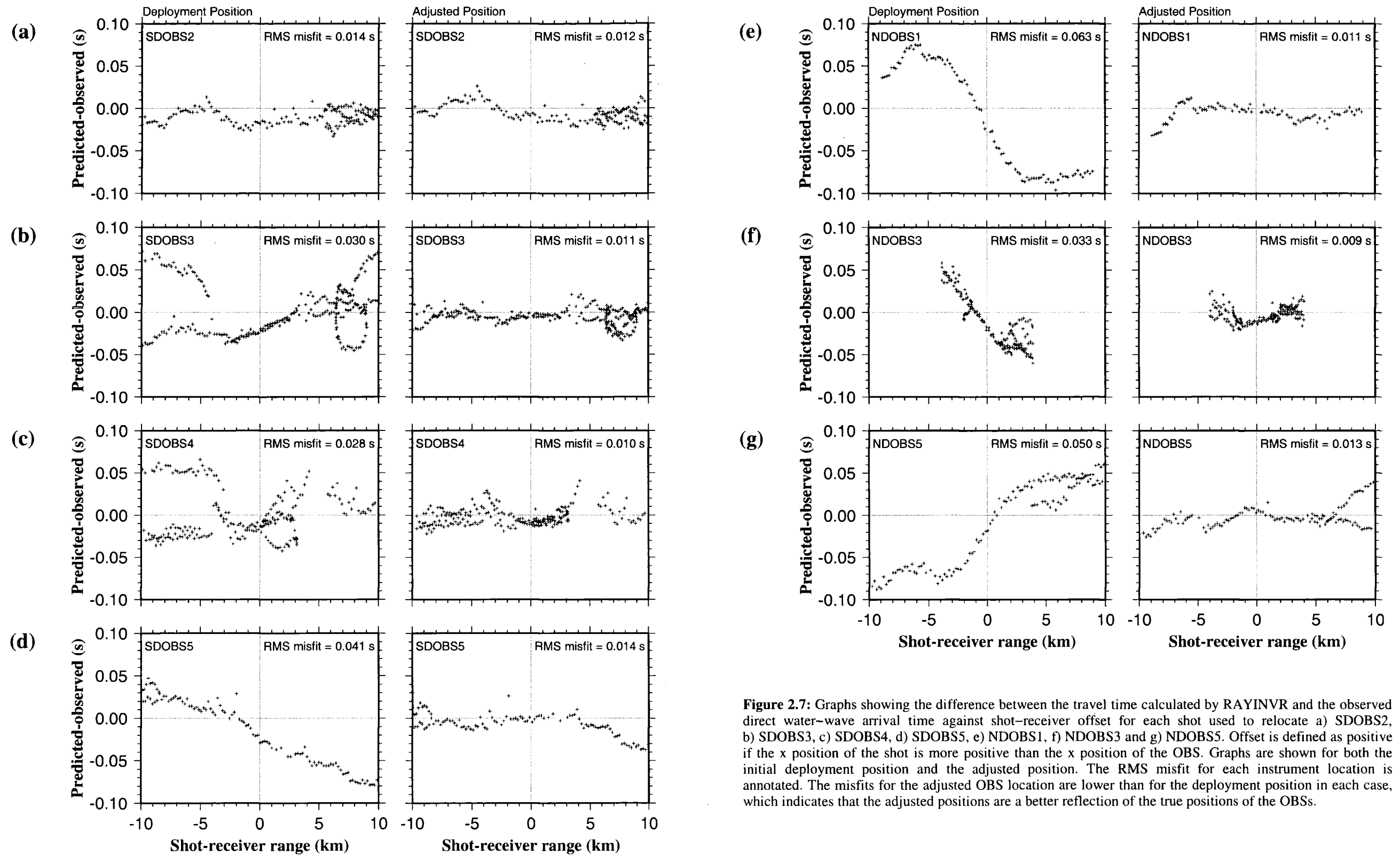


**Figure 2.7:** Graphs showing the difference between the travel time calculated by RAYINVR and the observed direct water-wave arrival time against shot-receiver offset for each shot used to relocate a) SDOBS2, b) SDOBS3, c) SDOBS4, d) SDOBS5, e) NDOBS1, f) NDOBS3 and g) NDOBS5. Offset is defined as positive if the x position of the shot is more positive than the x position of the OBS. Graphs are shown for both the initial deployment position and the adjusted position. The RMS misfit for each instrument location is annotated. The misfits for the adjusted OBS location are lower than for the deployment position in each case, which indicates that the adjusted positions are a better reflection of the true positions of the OBSs.

OBS Position	Final RMS misfit (ms)
SDOBS2	12
SDOBS3	11
SDOBS4	10
SDOBS5	14
NDOBS1	11
NDOBS3	9
NDOBS5	13
Mean misfit	11

**Table 2.1:** Final RMS misfit for the direct water-wave arrivals used to locate each OBS used in the inversion.

For instrument NDOBS1, there is effectively no control on the y position of the instrument as there were very few shots within a 10 km radius of the instrument which did not lie on the across-axis Line 6 (Fig. 1.8). Modelling of the direct water-wave arrival times as outlined above suggests that this OBS cannot lie on Line 6. A better fit was obtained by moving the OBS off-line by 0.35 km. However, the fit could also be improved by increasing the OBS depth which would imply an error in the swath bathymetry data.

In order to investigate further, the relative arrival times of the direct water-wave arrival and its first sea surface multiple were considered. Fig. 2.8 shows ray paths for the direct water-wave arrival and its first multiple for a shot at the sea surface recorded at a sea bottom instrument at horizontal offset  $s$  and depth  $z$ , and assuming a flat seafloor. Inspection of Fig. 2.4 suggests that this assumption is a good approximation in the vicinity of NDOBS1. For this geometry, and assuming a constant water column velocity  $v$ , the travel time for the direct arrival,  $t_d$ , is

$$t_d = \frac{\sqrt{s^2 + z^2}}{v}, \quad (2.14)$$

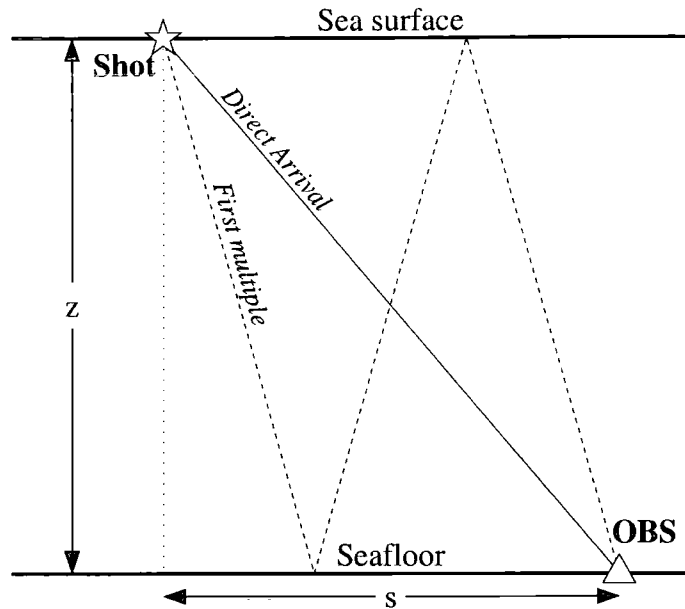


**Figure 2.8:** Ray paths for the direct water-wave arrival (solid) and the first sea surface multiple (dashed) for a shot at the sea surface and a seafloor receiver offset by a horizontal distance  $s$  in a water column of depth  $z$ , assuming a horizontal planar seafloor.

and the travel time for the first multiple,  $t_m$ , is

$$t_m = \frac{3\sqrt{(s/3)^2 + z^2}}{v} = \frac{\sqrt{s^2 + 9z^2}}{v}. \quad (2.15)$$

Dividing equation 2.15 by equation 2.14 eliminates  $v$  and rearranging gives an expression for  $s$  in terms of  $z$ ,  $t_d$  and  $t_m$ :

$$s = z \sqrt{\frac{9t_d^2 - t_m^2}{t_m^2 - t_d^2}}. \quad (2.16)$$

By applying equation 2.16 to a number of shots, the minimum value of  $s$  gives an indication of the distance off-line by which the OBS is offset. A further complication is that, in reality, the source is 8 m (or 0.008 km) below the surface, so the geometry depicted in Fig. 2.8 is inaccurate. In order to correct for this, 0.01 s was subtracted from the observed values of  $t_m$ . This correction corresponds to the approximate travel time through 0.016 km of water at  $1.533 \text{ km s}^{-1}$ , which is the surface water velocity obtained from the SV dip meter. Given the very approximate nature of these calculations and the small incident angles involved, this treatment of the extra travel time for the multiple was felt to be appropriate. With this correction applied, the minimum horizontal offset

calculated for NDOBS1 was found to be  $\sim 0.4$  km. This agrees well with the value of 0.35 km obtained previously, which suggests that the travel time mismatches observed arise from an off-line OBS location rather than an error in the swath bathymetry.

However, it is not possible to determine whether the OBS is offset to the north or south of Line 6 using this method. In order to resolve this ambiguity, the horizontal geophone sections were considered as they provide an indication of the direction to the source. The orientation of the horizontal geophones was unknown, but may be determined by considering the direct water-wave arrivals using a method which will be discussed fully in section 4.3 in relation to modelling  $P$ - $S$  mode converted arrivals. For NDOBS1 the horizontal geophones were found to be rotated by  $344^\circ$  clockwise with respect to the  $x$ - and  $y$ -axes, denoted by the  $x'$  and  $y'$  directions in Fig. 2.9. Since the OBS is known to be offset from the line of shot points, the position of the  $y'$  null point (the point at which the  $y'$  geophone records no signal, i.e. the point at which the shot-receiver azimuth is perpendicular to the orientation of the  $y'$  geophone), will be different depending on whether the OBS is north or south of the line of shots as illustrated in Fig. 2.9a. The position of the null point for the  $x'$  geophone will also be different, but Fig. 2.9a shows that the effect is greater and hence easier to resolve for the  $y'$  geophone in this example. The null point may be identified as the offset at which the polarity of direct arrivals at the  $y'$  geophone change sign. By inspection of the traces in Fig. 2.9c, the null point for the  $y'$  geophone is west of the closest shot to the instrument (indicated by the earliest direct water-wave arrival time). Therefore by comparison with Fig. 2.9a, the OBS must lie to the north of the line of shots. Hence, NDOBS6 was relocated by 0.35 km in the negative  $y$  direction.

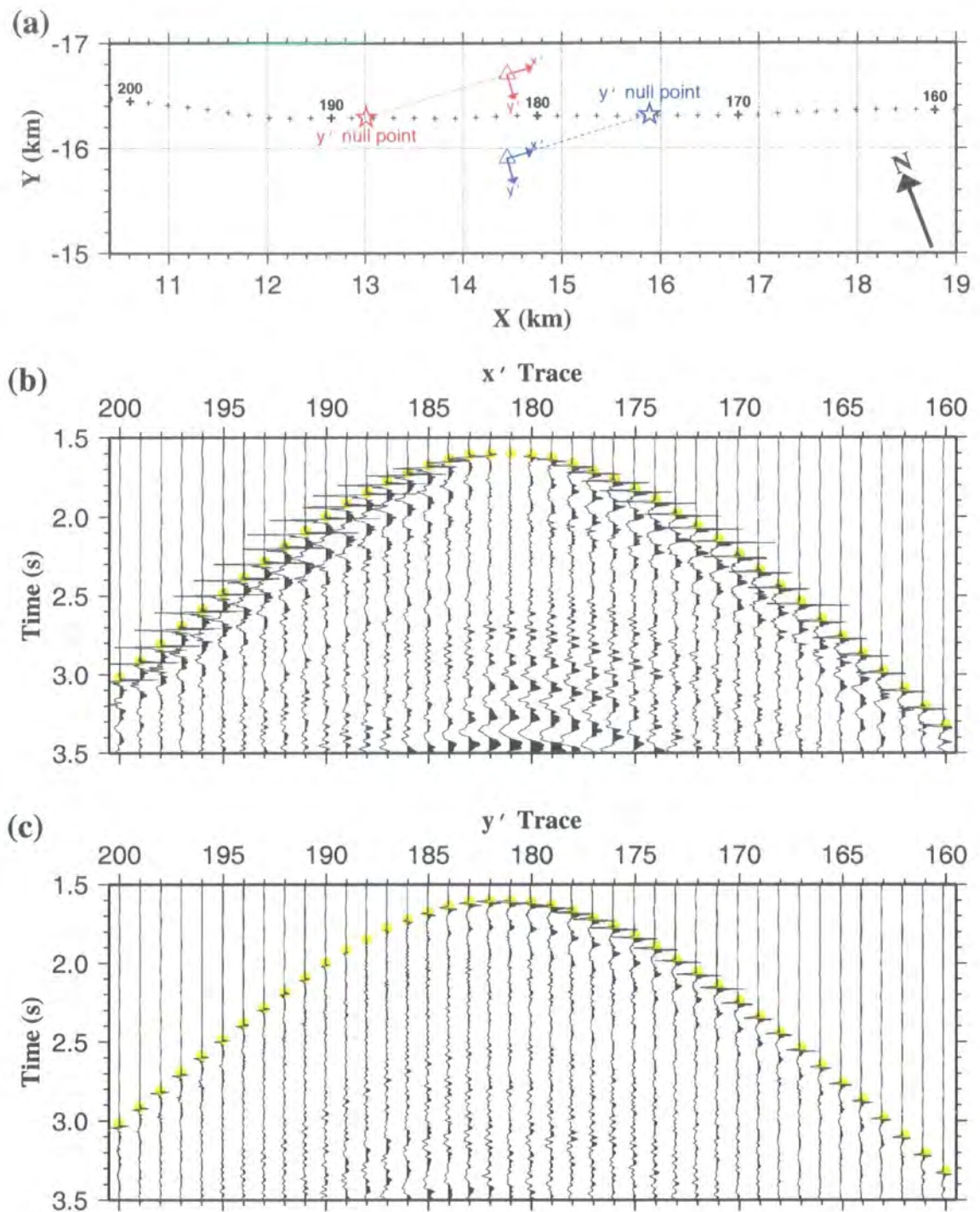


**Figure 2.9:** Application of the horizontal geophone data to determine the off-line position of NDOBS1. a) Shot positions (crosses), the two possible off-line locations for NDOBS1 (red and blue triangles) and horizontal geophone orientations (positive  $x'$  and  $y'$  directions indicated by orthogonal arrows). Shot numbers correspond to traces shown in b) and c). The position of the  $y'$  null point, which is the point at which the  $y'$  geophone would record no signal, is shown by a star for each of the possible locations of NDOBS1. b) and c) Detail of traces recorded by the  $x'$  and  $y'$  horizontal geophones respectively for the shots shown in a). The centre of each yellow dot marks the direct water-wave arrival travel time pick position. The  $y'$  null point is identifiable by a change in polarity of first motion from positive to negative, and is approximately at trace 188. Therefore, NDOBS1 is located in the position marked by the red triangle in a).

## 2.4 Travel time observation uncertainties

The inversion method described in section 2.2 requires that the uncertainty associated with each travel time residual be known. These values are used to weight the inversion such that the most reliable data is fit preferentially (equation 2.8) and the criterion by which the inversion is deemed to have converged is an average of the travel time residuals weighted for their uncertainties – the normalised  $\chi^2$  test (equation 2.13). Hence it is important that reliable estimates of the travel time residual uncertainties are known. These uncertainties comprise two principal elements: uncertainty in the first arrival travel time observations and uncertainty in the predicted first arrival travel times which are subtracted from the observed travel times to obtain the travel time residuals. The method used to determine the uncertainty in first arrival travel time observations and the results of its application to the VFR dataset are discussed in this section. Contributions to the uncertainty in predicted first arrival travel times are discussed in section 2.5, and the combined travel time residual uncertainties summarised in section 2.6.

### 2.4.1 Method

Travel time observation uncertainty arises from uncertainty in the precise position of the first arrival travel time pick on any given seismic trace. Zelt & Forsyth (1994) and Zelt & Barton (1998) assigned pick position uncertainties using an empirical relationship between pick uncertainty and SNR. It is intuitive that picks having low SNR should be less reliable than those with higher SNR. In order to obtain an objective measure of this relationship, a series of synthetic tests were undertaken to test the performance of the automatic picking tool. Although this tool was not used to make all of the travel time picks, it was used to make the vast majority, and so the uncertainties for those pick positions determined by the automatic picking tool are believed to be representative of the pick position uncertainties for the dataset as a whole.



The step-by-step procedure for determining the performance of the automatic picking tool is given in appendix C. The basic method is outlined below and shown in Fig. 2.10.

1. Seven adjacent traces for which a pick had been made, corrected in time to align the picks with the first trace's pick, were stacked to create a reference trace (Fig. 2.10a).
2. A synthetic section was then created comprising 1000 identical reference traces, each one offset in time by a random amount within the range  $\pm 50$  ms. The true pick positions were recorded, and a subset of travel time picks comprising the true position of every seventh pick was generated (Fig. 2.10b). This spacing is typical of the bracketing trace spacing used when picking travel times for the real dataset with the automatic picking tool.
3. White noise was then added to the section, with a frequency spectrum typical of the background noise (Fig. 2.10c and see below). For each trace the SNR was calculated by dividing the RMS value of the trace in a specified time window after the true pick position by the RMS value of the trace in the same time window before the true pick position. Time windows of 100, 200 and 300 ms were considered (discussed fully in section 2.4.2) and the mean SNR for the whole section was determined using each of these time windows.
4. The automatic picking tool was then applied to the incomplete set of picks generated in step 2 to determine the pick position for the remaining traces (Fig. 2.10d). For these tests, the pick position determined by the automatic picking tool was constrained to lie within  $\pm 100$  ms of the linearly interpolated time between the bracketing picks. A cross-correlation window of 300 ms was used. For a dominant source frequency of 8 Hz, this window represents  $\sim 2\frac{1}{2}$  periods. Longer cross-correlation windows were tested, but did not produce significantly different results.
5. The difference between the calculated true pick position was then calculated for the 852 picks determined by the automatic picking tool, and the standard deviation of this sample calculated. This standard deviation was taken as the pick position uncertainty for the particular reference trace and noise level under consideration.
6. Steps 3–5 were then repeated for different levels of noise. In this way, a pick position uncertainty versus SNR relationship was determined.

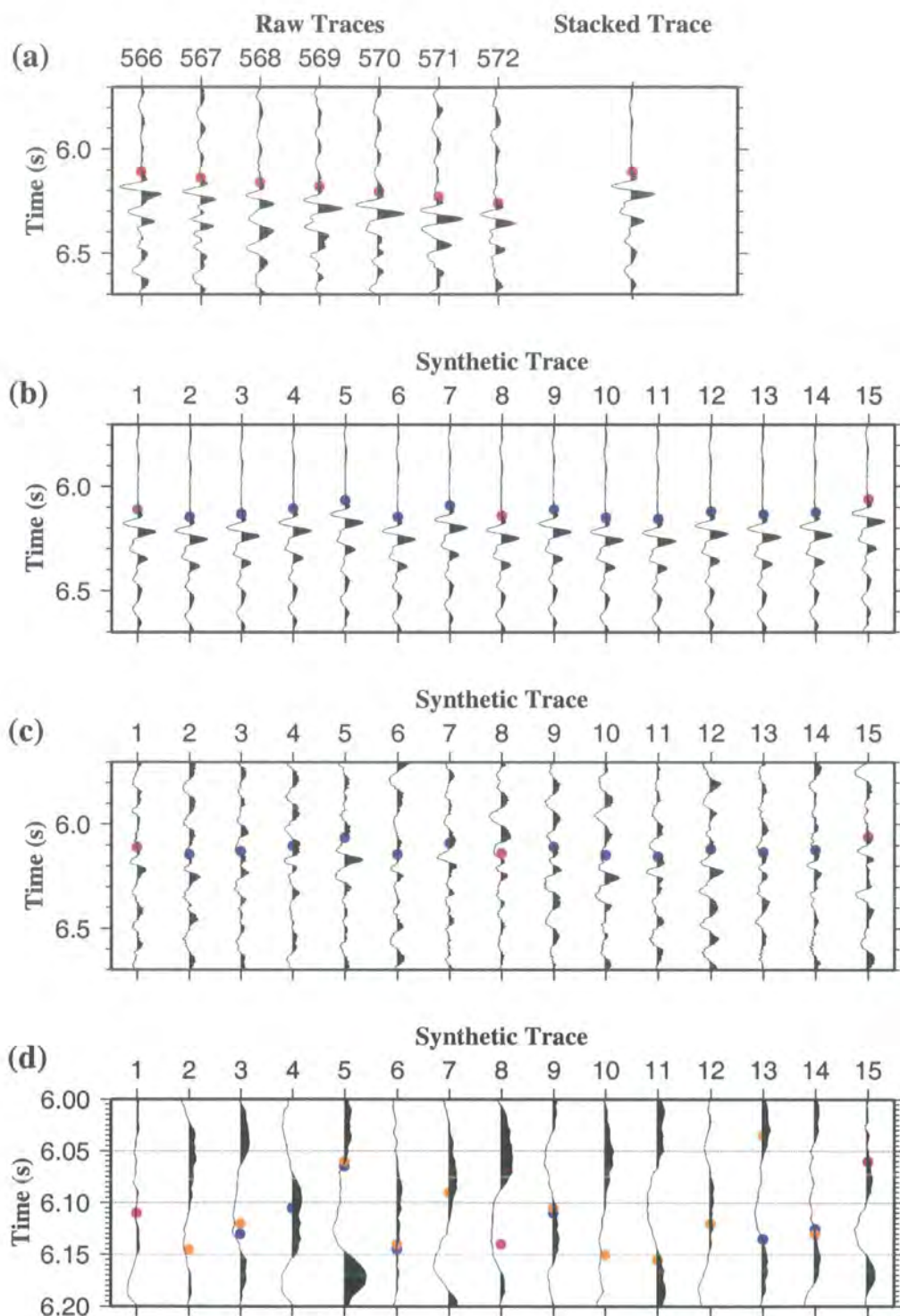


**Figure 2.10:** Illustration of the various stages involved in determining pick position uncertainty versus SNR relationships. a) Detail of traces 566–572 recorded by the NDOBS1 vertical geophone. Red dots mark the first arrival pick positions. These traces were shifted in time to align all picks with the pick for trace 566 and stacked to form the right-hand trace. The pink dot marks the pick position for the stacked trace. b) Part of a synthetic section comprising a number of traces identical to the stacked trace in a) offset randomly in time by up to  $\pm 50$  ms. Blue and pink dots denote the true pick positions; pink dots are on the bracketing traces subsequently used by the automatic picking tool. c) The same traces as b) with white noise added. d) Detail of the traces in c) after the automatic picking tool has been run. Blue dots denote the true pick position, pink dots denote the bracketing picks and orange dots the pick positions determined by the automatic picking tool. Where the blue dot is not visible, this is because the orange dot is in exactly the same place. Note that the position of the arrival determined using the automatic picking tool is generally similar, but not identical, to the true position.

The process described above was performed using a number of different reference traces. However, problems were encountered when the reference trace was created by stacking traces with low SNR. Stacking under these SNR conditions resulted in a reference trace which itself had a low SNR. When pick position uncertainty versus SNR relationships were derived from low SNR reference traces, much smaller pick position uncertainties were observed for a given SNR relative to similar relationships derived using high SNR reference traces. For low SNR reference traces, relatively little additional noise was required to give a total SNR which corresponds to a significant pick position uncertainty, given that the sample interval was 5 ms. Hence there will be a much greater degree of cross-correlation between traces than for synthetic traces of equivalent total SNR derived from a high SNR reference trace, for which a much greater proportion of random noise must be added to achieve the same total SNR. This phenomenon illustrates that using the automatic picking tool, and this method of determining pick position uncertainty, may not be valid in the presence of significant coherent noise. For these synthetic tests, the reference trace SNRs were enhanced by multiplying all samples in the reference trace prior to the pick position by 0.1, thus increasing the SNR whilst leaving the frequency spectrum of both signal and background noise unchanged. By this method the reference trace SNR was guaranteed to be much greater than the SNR typically associated with a pick position uncertainty of 5 ms (the sample interval) thus eliminating the coherent noise problem. This method also allows reference traces formed by stacking arrivals with large shot-receiver offsets, which will therefore have an inherently low SNR, to be meaningfully compared with higher SNR reference traces from smaller offsets.

The white noise added in step 3 above was derived from a 15 s trace with no arrivals present, this being representative of the real background noise. A Fourier transform was performed on the 15 s trace to obtain its amplitude and phase spectra in the frequency domain. The phase spectrum was randomised whilst maintaining an antisymmetric form, and an inverse Fourier transform performed to create a white noise trace with the same frequency spectrum as the original 15 s trace. A multiplier according to the level of noise required was then applied, and the white noise trace added to the reference trace. The whole process was repeated for each of the 1000 traces in the synthetic section.

The basic method for determining the relationship between pick position uncertainty and SNR was applied to a number of reference traces for each OBS location using a number of different background noise frequency spectra. The aim was to derive relationships which could be used to assign pick position uncertainties to first arrival travel time picks, and the way this was ultimately achieved for the entire dataset is discussed in the following section.

#### 2.4.2 Results

Fig. 2.11 shows a typical series of pick position uncertainty versus SNR curves for different reference traces, created from traces recorded at a single OBS location (NDOBS1) using a single white noise frequency spectrum. The curves derived using SNR calculation windows of 100, 200 and 300 ms are shown. Each reference trace and SNR calculation window combination give similar results, although a few do not fit the general pattern. Zelt and Forsyth (1994) used a 300 ms time window for calculating the SNR, which represents  $\sim 2\frac{1}{2}$  periods at the dominant source frequency of the VFR experiment ( $\sim 8$  Hz). This time window was generally preferred because the estimates of signal and noise strength are averaged over the greatest number of samples, and are therefore most reliable, whilst only measuring the strongest part of the signal.

However, for some reference traces, the 300 ms time window gives an anomalous curve whilst one of the shorter time windows gives a curve which is more consistent with the majority. Fig. 2.12 shows a blow-up of traces 244–250 which were stacked to form one of the anomalous reference traces in Fig. 2.11. A strong secondary arrival is clearly visible  $\sim 150$  ms after the first arrival travel time pick. Hence, the SNR calculated using a 100 ms window is markedly smaller than that calculated using a 300 ms window due to inclusion of the strong secondary in the latter time window, and provides a more appropriate estimate of SNR for the first arrival than the 300 ms window in this case. The majority of anomalous curves can be attributed to this cause; others may be attributed to reference traces with very low SNR as described above. By selecting shorter time windows for SNR calculation where appropriate and discarding any remaining anomalous curves, a consistent set of pick uncertainty versus SNR curves was produced. Fig. 2.13 shows the set of curves selected for NDOBS1 plus the median curve, which has been sampled at 5 ms intervals equivalent to the sample interval of the



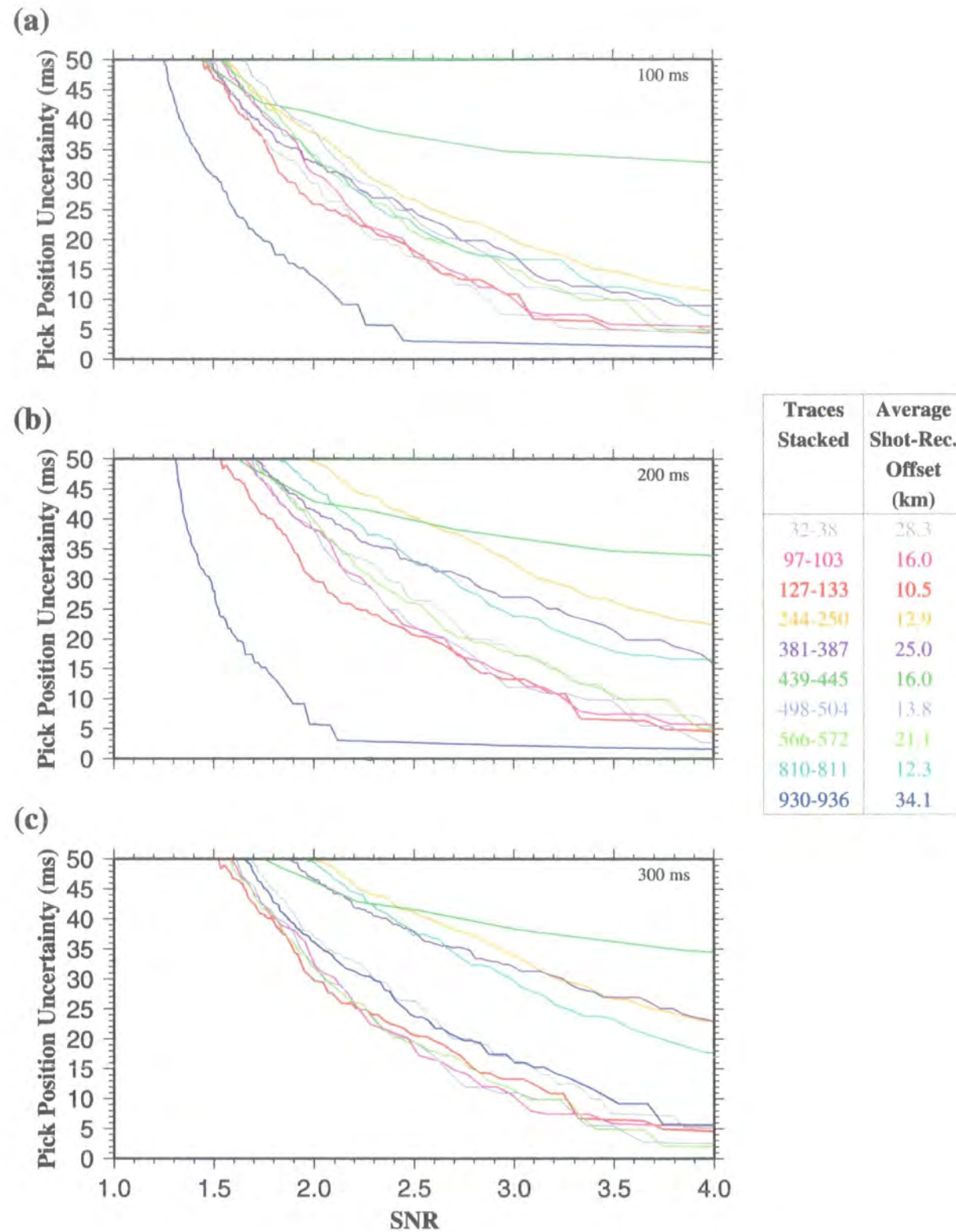


**Figure 2.11:** Pick position uncertainty versus SNR curves for several reference traces formed by stacking traces recorded by NDOBS1. The traces stacked to form each reference trace are indicated in the accompanying side panel. The time window used to calculate SNR was a) 100 ms, b) 200 ms and c) 300 ms. Note that the relationships derived using each calculation window are consistent for some reference traces, and show wide variation for others.

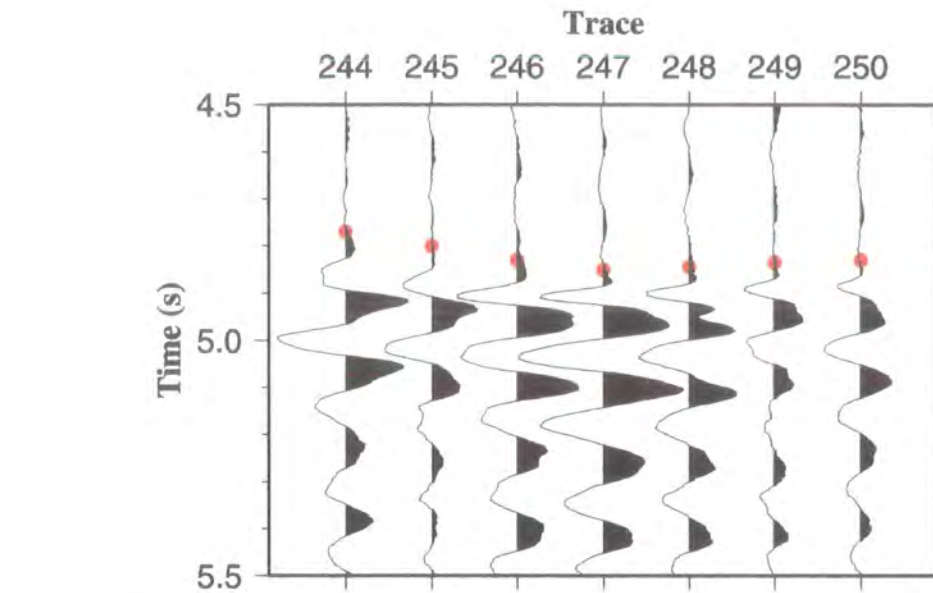
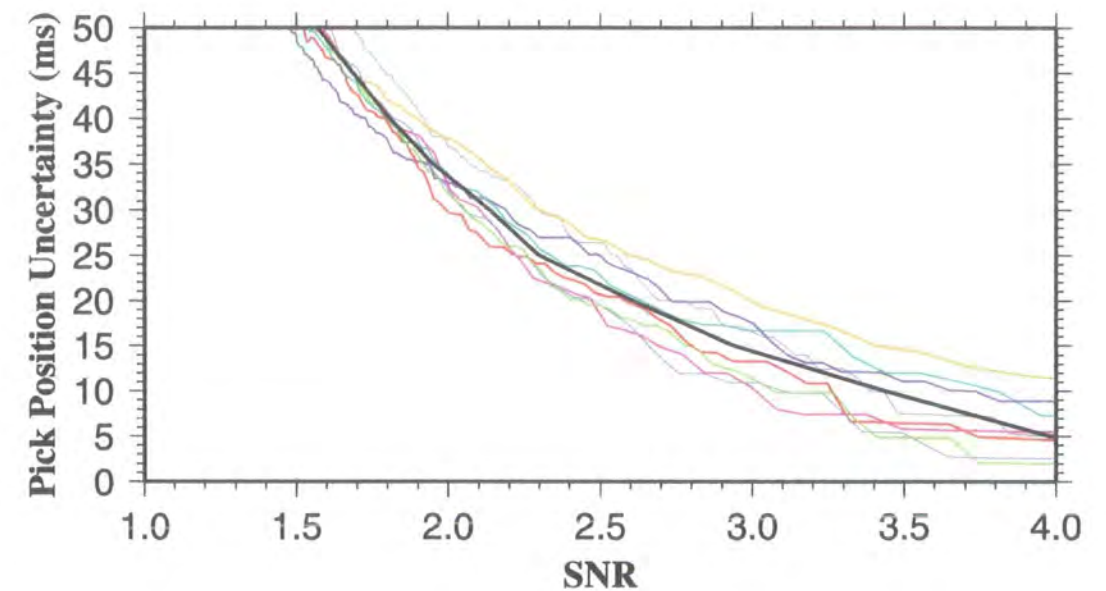


**Figure 2.12:** Detail of traces recorded by the NDOBS1 vertical geophone stacked to create one of the reference traces used in Fig. 2.11. The red dots mark the positions of the first arrival travel time picks. A strong secondary arrival is visible ~150 ms after the first arrival travel time picks.



Traces Stacked	Offset (km)	Window (ms)	Traces Stacked	Offset (km)	Window (ms)
32-38	28.3	300	381-387	25.0	100
97-103	16.0	300	498-504	13.8	300
127-133	10.5	300	566-572	21.1	300
244-250	12.9	100	810-811	12.3	100

**Figure 2.13:** Final set of pick position uncertainty versus SNR curves selected for NDOBS1. The accompanying table shows the traces which were stacked to form each reference trace, the average shot- receiver offset for those traces, and the time window used to calculate the SNR. The thick black line is the median pick position uncertainty versus SNR curve for NDOBS1.

data. The shot-receiver offset of traces stacked to create the reference traces does not appear to have any systematic effect on the shape of the curves (they all follow the same general trend), so the median curve may be used to determine pick position uncertainty at all offsets. The median was preferred as the measure of central tendency over the mean as it is less susceptible to outliers.

However, the frequency spectrum of the white noise was found to affect the shape of the pick position uncertainty versus SNR curve. Fig. 2.14 shows three frequency spectra for each OBS location, which were derived from data traces which showed no arrivals of any kind. These frequency spectra show that for most locations, the dominant frequency of the background noise is  $\sim 8$  Hz, the same as the dominant frequency of the airgun source, implying that the bulk of the background noise is derived from reverberations in the water column from earlier shots. However, a secondary peak of variable strength is often visible with a typical frequency of  $\sim 12$ – $16$  Hz, and for NDOBS3 (Fig. 2.14f) this peak is of similar or greater strength than the 8 Hz peak. A similar phenomenon was observed by Navin (1996) at the Reykjanes Ridge, and was attributed to scattering of seismic energy at the rough seafloor in the vicinity of the OBSs. Comparison of the instrument locations shown in Fig. 2.4 with Fig. 2.14 suggests that the hypothesis of Navin (1996) may be correct for this experiment also as secondary peak strength can also be correlated to seafloor roughness at the VFR: NDOBS1 and NDOBS5 are situated on flat seafloor and exhibit weak or non-existent secondary peaks; NDOBS3 which shows a very strong peak at  $\sim 12$  Hz is situated in the steep-sided overlap basin, i.e. a very rough part of the seafloor which would be expected to show high degrees of scattering; the other instruments are intermediate cases. The exception is SDOBS5 which is situated on a flat area of seafloor but exhibits two dominant peaks at  $\sim 10$  Hz and  $\sim 8$  Hz (Fig. 2.14d). SDOBS5 is unique amongst the instrument locations under consideration in that it is located in a small basin which is believed to be filled with a poorly consolidated layer of ash. This basin could complicate the background noise frequency spectrum, and one possible explanation for the dual peaked background noise frequency spectrum is that the ash basin acts as a notch filter due to peg-leg constructive interference removing frequencies between the two peaks.

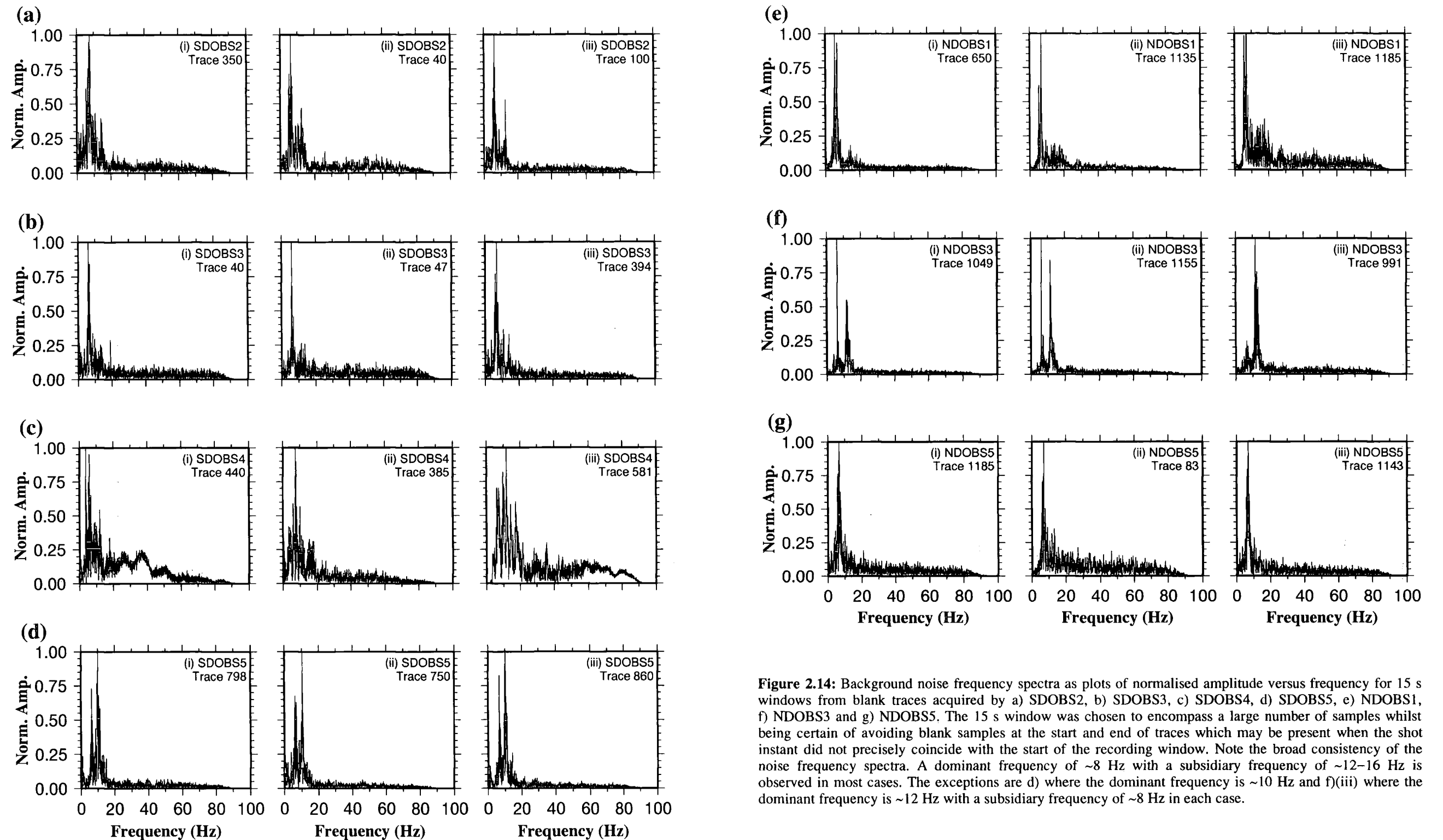
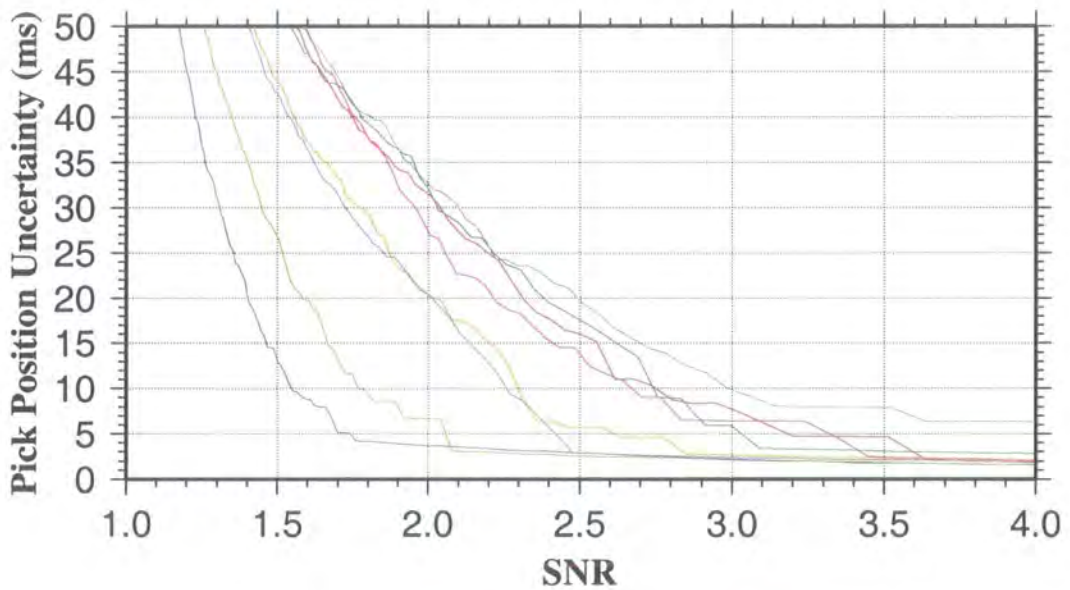


**Figure 2.14:** Background noise frequency spectra as plots of normalised amplitude versus frequency for 15 s windows from blank traces acquired by a) SDOBS2, b) SDOBS3, c) SDOBS4, d) SDOBS5, e) NDOBS1, f) NDOBS3 and g) NDOBS5. The 15 s window was chosen to encompass a large number of samples whilst being certain of avoiding blank samples at the start and end of traces which may be present when the shot instant did not precisely coincide with the start of the recording window. Note the broad consistency of the noise frequency spectra. A dominant frequency of  $\sim 8$  Hz with a subsidiary frequency of  $\sim 12$ – $16$  Hz is observed in most cases. The exceptions are d) where the dominant frequency is  $\sim 10$  Hz and f)(iii) where the dominant frequency is  $\sim 12$  Hz with a subsidiary frequency of  $\sim 8$  Hz in each case.



In order to assess the effect of noise frequency spectrum on the shape of the pick position uncertainty versus SNR curve, a set of curves were produced for one of the reference traces and SNR time windows selected for NDOBS1 using several different frequency spectra. The results, shown in Fig. 2.15, show that different background noise frequency spectra may give rise to very different pick position uncertainty versus SNR curves.



OBS	Trace	OBS	Trace
SDOBS2	350	NDOBS1	650
SDOBS3	40	NDOBS3	991
SDOBS4	440	NDOBS3	1155
SDOBS5	798	NDOBS5	1185

**Figure 2.15:** Pick position uncertainty versus SNR curves for a reference trace formed by stacking traces 566–572 for NDOBS1 using a variety of background noise frequency spectra and an SNR calculation window of 300 ms. The traces from which these frequency spectra were derived are indicated. Note the variation in the shapes of the curves indicating that the frequency spectrum of the background noise influences the shape of the curves.

Fig. 2.14 suggests that the frequency spectrum is approximately constant for a single instrument position, which implies that conditions near the receiver position are predominantly responsible for the observed variations. Therefore a typical noise frequency spectrum was selected for each OBS location and used to derive pick position uncertainty versus SNR curves for several reference traces derived from data recorded at that OBS location. The noise frequency spectra labelled (i) in each of Figs. 2.14a–e and 2.14g were chosen for their respective OBS locations, whilst all three spectra shown



in Fig. 2.14f were used for NDOBS3 because of the unusual variability in noise frequency spectrum observed at that location. The results are shown in Fig. 2.16a, and the corresponding median curves for each OBS location are shown in Fig. 2.16b.

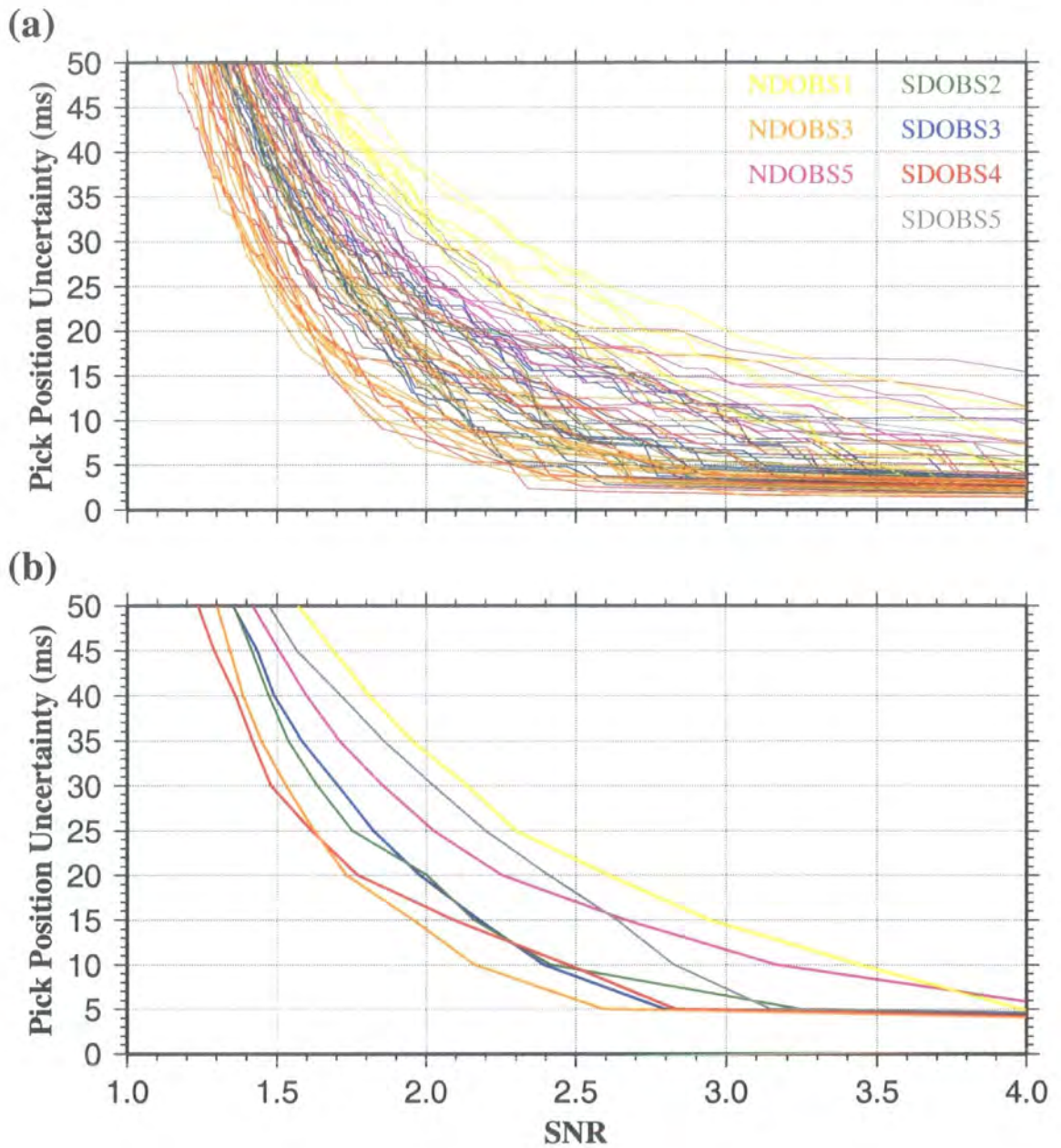
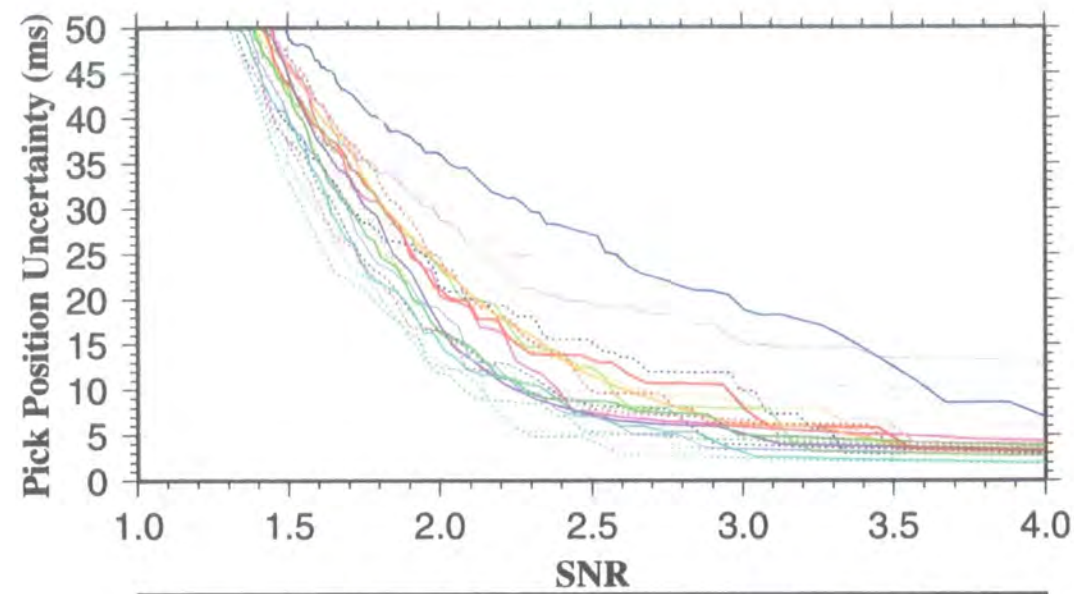


**Figure 2.16:** Pick position uncertainty versus SNR relationships for all instrument positions. a) Final set of pick position uncertainty versus SNR curves for all instruments. Note the wide variation in the curves, but that curves derived for one instrument location tend to cluster in one region of the graph. b) Median curves for each instrument derived from those curves shown in a). These curves were used to assign pick position uncertainties for the real data for each instrument.

This figure shows that for a given SNR, the pick position uncertainty is largest for NDOBS1. This phenomenon is believed to occur because, for this OBS location, the background noise frequency spectrum closely resembles the signal frequency spectrum. It is therefore harder to distinguish signal from noise at a given SNR than at locations where the noise frequency spectrum is very different from the signal frequency spectrum (e.g. NDOBS3 and SDOBS4).

As described in section 2.3.1, a low-pass filter was applied when picking arrivals partially obscured by hard disk spin noise. Fig. 2.17 shows pick position uncertainty versus SNR curves for the reference traces derived from SDOBS3 and plotted in Fig. 2.16. When creating the curves shown as solid lines in Fig. 2.17 the low-pass filter was applied to both the reference trace and the trace used to derive the noise frequency spectrum. The equivalent unfiltered curves are plotted as dashed lines for reference. Fig. 2.17 indicates that application of the band-pass filter has a small but systematic effect on the shape of the curves: for a given SNR, the pick position uncertainty is usually greater with the low-pass filter applied. This finding is consistent with the observation that the proportion of high frequencies in the background noise frequency spectrum influences the shape of the curves, which was discussed previously in the context of the effect of variable seafloor roughness. Application of the low-pass filter thus leads to a reduction in the proportion of high frequencies in the spectrum and the effect on the shape of the curve is similar to that illustrated in Fig. 2.15 for different noise frequency spectra. Hence, for each OBS location, a further set of curves was generated with reference traces derived from stacking traces in areas affected by disk spin, and with the 40 Hz low-pass filter applied. The results are shown in Fig. 2.18 with the unfiltered median curves shown for comparison.





Traces Stacked	Offset (km)	Window (ms)	Traces Stacked	Offset (km)	Window (ms)
104-110	30.6	300	598-604	6.8	300
152-159	20.7	300	702-708	14.2	300
221-227	7.2	300	740-746	22.0	300
325-331	11.7	300	802-808	34.5	200
504-510	11.7	300	850-856	13.9	200
550-556	6.5	300	962-968	11.1	300

**Figure 2.17:** Pick position uncertainty versus SNR curves for several reference traces formed by stacking the traces indicated in the accompanying table recorded by SDOBS3 (dashed lines), the SNR calculation windows indicated in this table, and also with a 40 Hz low- pass filter applied to both reference trace and noise trace (solid lines). Note that application of the low- pass filter appears to have a systematic effect on the position of the curve: for a given SNR, the pick position uncertainty is larger with the low- pass filter applied than without.

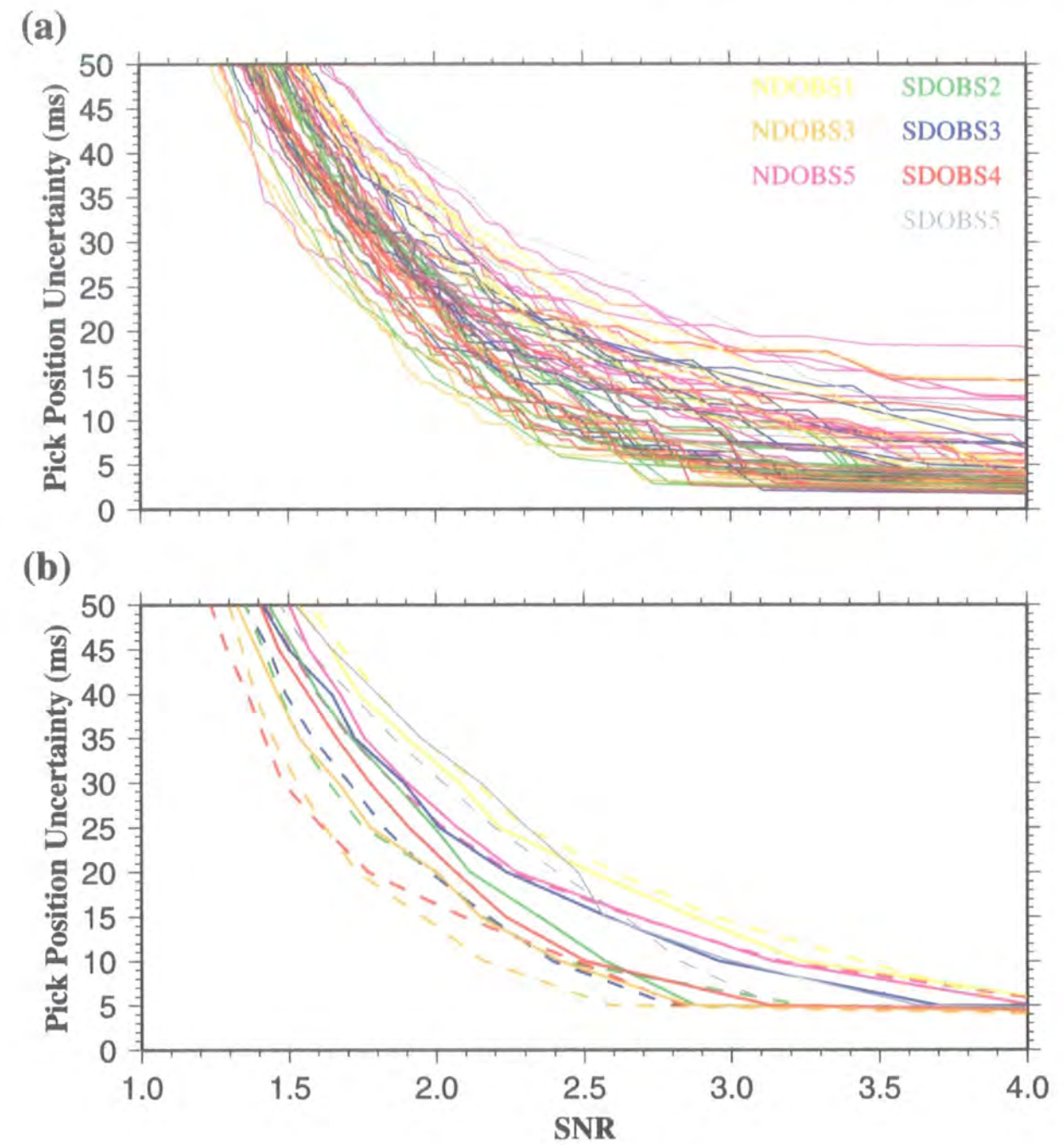


**Figure 2.18:** Pick position uncertainty versus SNR relationships for all instrument positions with a 40 Hz low-pass filter applied. a) Final set of pick position uncertainty versus SNR curves for all instrument positions for reference traces derived from stacking traces which include disk spin noise. A 40 Hz low- pass filter was applied to both the reference traces and the blank trace from which the white noise was obtained. Note that, as in Fig. 2.16, curves derived from reference traces from the same instrument position tend to cluster in one region of the graph. b) Median curves (solid lines) for each instrument derived from those curves shown in a). Equivalent median curves derived from areas with no disk spin noise from Fig. 2.16b are shown for comparison (dashed lines). The solid curves were thus used to assign pick position uncertainties for real data traces which were picked from record sections with a 40 Hz low- pass filter applied in order to aid identification of the travel time pick position.

Finally, as described in section 2.3.1, the hydrophone section was used for picking some of the arrivals at SDOBS5. Pick position uncertainty versus SNR curves were thus also constructed for the hydrophone data for this instrument using the two band-pass filters described in section 2.3.1, and the results are shown in Fig. 2.19.

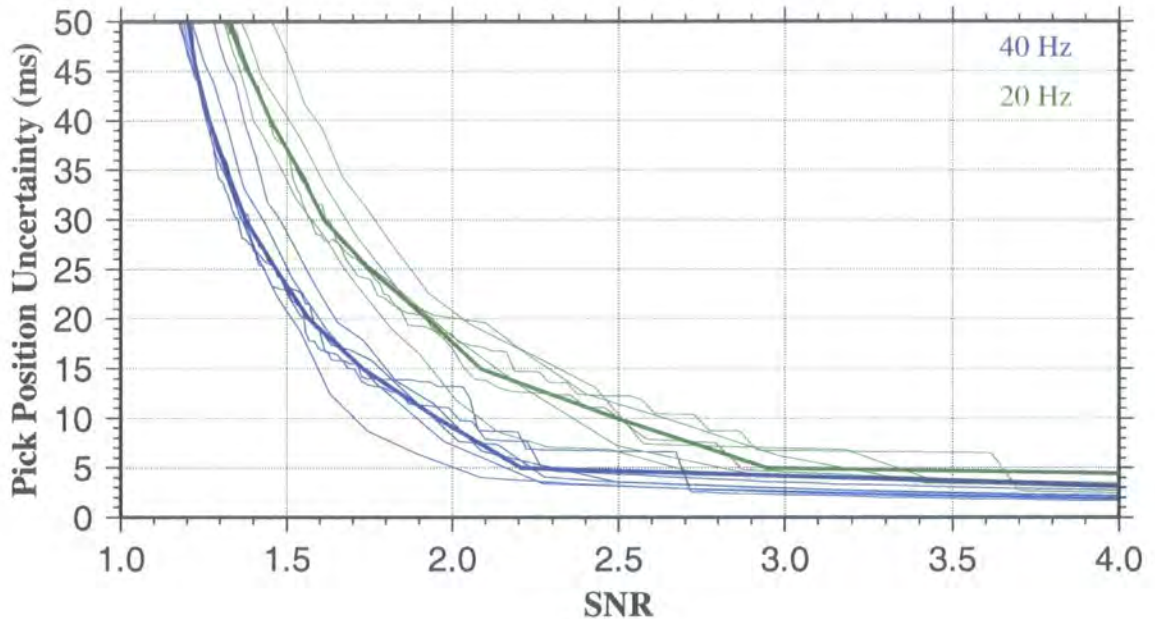


**Figure 2.19:** Final set of pick position uncertainty versus SNR curves for the SDOBS5 hydrophone data, with two different low-pass filters applied. The first 520 shots of the *Seismic South* experiment were not recorded by the SDOBS5 vertical geophone, so first arrivals were picked from the hydrophone section for these shots. A 20 Hz low-pass filter was applied to aid picking in regions affected by disk spin noise, and a 40 Hz low-pass filter was used elsewhere. Thick lines denote the median curves used to assign pick position uncertainties for the real data.

### 2.4.3 Application to the real data

The methods described in sections 2.4.1 and 2.4.2 above were used to create median pick position uncertainty versus SNR relationships for unfiltered and band-pass filtered vertical geophone traces for each OBS location. Additional relationships were derived for SDOBS5 hydrophone data. For each first arrival travel time pick, the factors summarised below were thus established.

- Should the travel time pick be made from the vertical geophone or hydrophone trace?
- Does the trace contain high frequency noise associated with disk spin. If so, the low-pass filter described in section 2.3.1 was applied before calculating the SNR.
- What is the appropriate time window for calculating the SNR? The default value of 300 ms was used except where there was evidence of a strong secondary arrival



within that time window which might give rise to an artificially high SNR. If strong secondary arrivals within the 300 ms window were observed, a shorter time window of 100 or 200 ms was chosen as appropriate.

Using these criteria, the appropriate median curve was selected and the appropriate value of SNR calculated. This value was used to determine the first arrival time observation uncertainty to a precision of 5 ms, equivalent to the sampling interval. The relationships derived are useful in the uncertainty range 0–50 ms. A 50 ms uncertainty implies a two standard deviation uncertainty of 100 ms, i.e. 95% of predicted pick positions lie within  $\pm 100$  ms of the true position. Since the automatic picking tool is forced to place the pick within  $\pm 100$  ms of the linearly interpolated position (point 4 in section 2.4.1), a 100 ms two standard deviation uncertainty suggests that the automatic picking tool is unable to constrain the pick position. Hence, any picks whose SNR was less than the lower limit for the 50 ms band (typically an SNR of  $<1.2$ ) were discarded.

## 2.5 Predicted travel time uncertainties

In this section, contributions to travel time residual uncertainties arising from uncertainties in the first arrival travel times predicted by the forward modelling step are discussed. The possible contributors considered are: uncertainty in shot and OBS location; uncertainty in the water column velocity structure; uncertainties introduced by the rough seafloor bathymetry; and uncertainty due to the inaccuracy of the finite difference travel time calculator used in the forward modelling step. These will now be considered in turn.

The inversion method described in section 2.2 assumes that the shot and receiver positions are known. In practice, the OBS relocation method described in section 2.3.3 indicates that there is significant uncertainty in the true position of an OBS on the seafloor. Table 2.1 summarises the final RMS travel time error for direct water-wave arrivals used to relocate each OBS. This misfit may arise from a combination of uncertainty in the position and depth of the shots used to relocate the OBS, uncertainty in the water column velocity structure, ray tracing errors and uncertainty in the picked positions of the direct water-wave arrivals. The timing errors in Table 2.1 were determined for signals which had travelled solely in the water column. Since the first arrivals approach the OBS from below, the RMS misfit for direct water-wave arrivals

was multiplied by the ratio of the crustal velocity in the immediate vicinity of the OBS (approximately  $1.91 \text{ kms}^{-1}$ ) to the average water column velocity ( $1.49 \text{ kms}^{-1}$ ) to obtain the timing uncertainty due to the OBS locational uncertainty for crustal arrivals. The results are summarised in Table 2.2.

OBS Position	Timing uncertainty (ms)
SDOBS2	9
SDOBS3	9
SDOBS4	8
SDOBS5	11
NDOBS1	9
NDOBS3	7
NDOBS5	10
Mean uncertainty	9

**Table 2.2:** Predicted travel time uncertainty for each OBS location used in the inversion due to instrument location uncertainty.

Shot positions were GPS navigated, but there is no independent measure of the GPS accuracy for the *R/V Maurice Ewing's* system available. The mean RMS travel time error of 11 ms for the direct water-wave arrivals used in relocating the OBSs was used to represent the timing error due to uncertainty in shot location and depth. Using this value implies the assumption that shot location and depth errors are the dominant contributors to the misfit. Of the potential sources of OBS locational uncertainty outlined above, lateral variations in water column velocity structure are likely to be minimal when considering a single instrument position, and the water column velocity structure is smooth and simple so ray tracing errors are also likely to be very small. Given that the SNR for direct water-wave arrivals is very high, the analysis described in section 2.4 suggests that their travel time pick position uncertainties are likely to be very small indeed. Hence, the assumption that the shot position uncertainty is the dominant contributor to the observed misfit is believed to be valid.

Throughout the inversion process, the water column velocity structure was kept constant, so any travel time residual uncertainty which arises from this assumption being invalid should be considered. The water column velocity structure was measured at  $22^{\circ} 26' S$ ,  $176^{\circ} 36' W$  using an SV dip meter (see Fig. 2.6). This water column velocity structure was used for OBS relocation and to define the water column velocity structure everywhere in the initial model (discussed fully in section 2.8). However, it is possible that there are lateral variations in the water column velocity structure, arising from changes in water temperature, density or salinity. There is known to be high temperature hydrothermal activity associated with the axial region (Fouquet *et al.* 1991 and 1993) which might influence the water column properties in the basin. The temperature profile of the water column was measured to a depth of a little less than 2.0 km at eight other locations given by Peirce *et al.* (1996) using XBTs as shown in Fig. 2.20. These temperature profiles may be converted to water velocity profiles using the equation

$$v = 1449.2 + 4.623T - 0.0546T^2 + 0.1605P + 1.391(S - 35), \quad (2.17)$$

where  $v$  is the velocity in  $\text{ms}^{-1}$ ,  $T$  is the temperature in  $^{\circ}\text{C}$ ,  $P$  is the pressure in  $\text{kg cm}^{-2}$ , and  $S$  is the salinity in  $\text{‰}$  (after Shiobara *et al.* 1997). An XBT was deployed at  $22^{\circ} 25.86' S$ ,  $176^{\circ} 36.01' W$ , close to the SV dip meter deployment site. A salinity profile could thus be calculated using equation 2.17 from this XBT profile, the velocity profile measured by the SV dip meter, and a sea water density of  $1031.3 \text{ kgm}^{-3}$  (Shiobara *et al.* 1997). The variations in salinity from the normal value of  $35\text{‰}$  were found to be very small indeed. Assuming this density and salinity profile, the average water column velocity and travel time to a depth of 1.90 km, the maximum depth to which both XBT and SV dip meter measurements were recorded, was calculated at the other eight XBT sites using equation 2.17 and compared with the value calculated from the SV dip meter profile. The results of this analysis and the locations of the XBT deployment sites are summarised in Table 2.3. The standard deviation in the calculated travel times is very small ( $\sim 0.4 \text{ ms}$ ). Since salinity and density variations are likely to have an even smaller effect on velocity, their effect on the timing uncertainty is assumed to be tiny. Thus an overall timing uncertainty due to variations in the water column velocity structure of  $0.5 \text{ ms}$  was assumed.

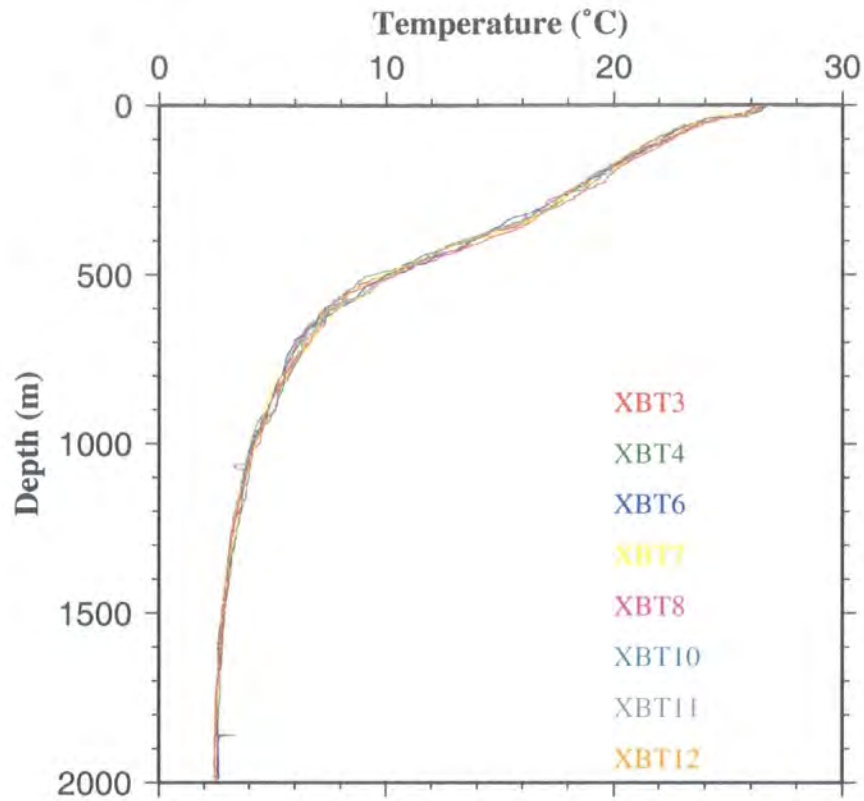


**Figure 2.20:** Water column temperature profiles measured using expendable bathymetric thermographs (XBTs) deployed at locations indicated in Table 2.3. These profiles were used in the calculation of water column velocity structure uncertainty.

XBT or SV dip	Location	Mean velocity (kms <sup>-1</sup> )	Travel time (s)
SV dip	22° 25.90' S, 176° 35.92' W	1.4948	1.27099
XBT3	22° 20.89' S, 176° 33.96' W	1.4938	1.27192
XBT4	22° 26.45' S, 176° 47.57' W	1.4938	1.27192
XBT6	22° 22.51' S, 176° 40.75' W	1.4936	1.27209
XBT7	22° 28.58' S, 176° 35.81' W	1.4937	1.27201
XBT8	22° 22.36' S, 176° 40.04' W	1.4938	1.27192
XBT10	22° 31.05' S, 176° 42.18' W	1.4936	1.27209
XBT11	22° 31.67' S, 176° 42.38' W	1.4936	1.27209
XBT12	22° 31.45' S, 176° 41.92' W	1.4937	1.27201

**Table 2.3:** Mean water column velocities and travel times to 1.9 km depth derived from the SV dip meter and XBTs. Locations from Peirce *et al.* (1996).



A related issue is the uncertainty in the position of the seafloor. The swath bathymetry data has a nominal accuracy of 10 m (or 0.01 km), and the associated travel time uncertainty is equal to the difference between the travel time over a distance of 0.01 km at mean water velocity ( $1.49 \text{ km s}^{-1}$ ) and the velocity at the top of the crust ( $1.91 \text{ km s}^{-1}$ ). This calculation gives an uncertainty of  $\sim 1.5 \text{ ms}$ .

A more intractable problem is the uncertainty in seafloor ray entry point. This uncertainty arises because the forward modelling step endeavours to find the shortest travel times assuming an infinitely thin ray sensitive to every small-scale irregularity in the seafloor. In reality, the interaction of the wavefront with the seafloor will be considerably more complicated, with seismic energy observed at OBSs comprising a complex average of energy which constructively interferes as it propagates across the seafloor interface. Hence, the ray path identified by the forward modelling step may not be representative of the average path which would be taken by energy arriving at the OBS. This effect has the consequence that the calculated water column travel time may be in error, which in turn leads to an error in the travel time residual to be resolved by anomalies distributed along the crustal part of the ray path. When considering a tomographic dataset from the Juan de Fuca Ridge, Sohn *et al.* (1997) described a method for determining the average seafloor ray entry point by considering the shape of the effective Fresnel zone for rough seafloor, and demonstrated that there is significant associated uncertainty. However, this process is not employed by the *FAST* code. The uncertainty associated with rough seafloor was dealt with in part by smoothing the bathymetry data at an appropriate scale, as discussed in full in section 2.8, though this treatment is not rigorous. The difficulty in quantifying this uncertainty means it cannot be formally accounted for in the travel time residual uncertainties, and must be born in mind when interpreting the inversion results. In this light, the spatial distribution of travel time residuals with respect to the roughness of the seafloor near the ray entry point will be considered in section 3.6.

The final source of uncertainty considered is that associated with errors in the forward modelling step. These errors were assessed by considering synthetic models for which the first arrival travel time for a given shot-receiver pair is known. Resolution of these errors is discussed in full in section 2.7. The maximum RMS error for the chosen forward grid node spacing was 2 ms, and this was used as the predicted arrival time uncertainty due to ray tracing errors.

## 2.6 Travel time residual uncertainties

The travel time residual for a given shot–receiver pair is the difference between the observed first arrival travel time and the first arrival time predicted by the forward modelling step. Therefore the uncertainty associated with each travel time residual comprises elements arising from uncertainty in the observed first arrival travel time (discussed in section 2.4) and uncertainty in the predicted first arrival time (discussed in section 2.5). The overall uncertainty associated with each travel time residual is obtained by calculating the square root of the sum of the squares of the uncertainties arising from each element. All contributions to travel time residual uncertainty considered in the preceding sections are summarised in Table 2.4.

<b>Contributor</b>	<b>Contribution to total travel time pick uncertainty (ms)</b>
Travel time pick position uncertainty	0–50
Instrument location uncertainty	7–11
Shot location uncertainty	11
Finite difference travel time calculator inaccuracy	2
Bathymetry uncertainty	1.5
Water column velocity uncertainty	0.5
Total uncertainty	13–52

**Table 2.4:** Summary of contributions to travel time residual uncertainty.

A number of preliminary inversions were performed in order to determine suitable values for the inversion parameters described in section 2.2.3. It was found that the inversion did not converge towards a normalised  $\chi^2$  value of 1.0. However, when the uncertainties associated with each travel time residual were doubled, the inversion did converge. By doubling the travel time residual uncertainties the relative weighting of each travel time equation according to its associated uncertainty (section 2.2.3) is maintained whilst the misfit criteria by which the model is deemed to have converged on a solution are relaxed. A multiplier of two was chosen as the smallest integer multiplier for which the inversion reliably converged. Therefore final models resulting from the inversion do not satisfy the travel time data within their uncertainties, but they

are better representations of the velocity structure than initial models with higher values of  $\chi^2$ . All inversions described in this chapter and in chapter 3 were performed using the two standard deviation travel time residual uncertainties in the range 26–104 ms, i.e. double the values shown in Table 2.4, and all values of  $\chi^2$  were calculated using a revised version of equation 2.13

$$\chi^2 = \frac{1}{n} \sum_{i=1}^n \frac{\delta t_i^2}{(2\sigma_i)^2} = \frac{1}{4n} \sum_{i=1}^n \frac{\delta t_i^2}{\sigma_i^2}, \quad (2.18)$$

where the  $\sigma_i$  are the one standard deviation travel time residual uncertainties determined using the method outlined in this section and summarised in Table 2.4. The observation that the inversion method cannot resolve the velocity structure within their uncertainties suggests that there are lateral velocity heterogeneities which are beyond the resolving power of the inversion method, and that the velocity models produced by the inversion are averages of the true structure. The statistical significance of the inversion results will be discussed further in section 3.8.1.

## 2.7 Forward modelling grid

As described in section 2.2.2, the forward grid is parameterised using a regular grid of nodes. The node spacing affects the accuracy of the finite difference travel time calculator, and should be sufficiently small to allow first arrival travel times to be calculated to an appropriate degree of accuracy given that the travel time residual uncertainties used in the inversion lie in the range 26–104 ms as described in the previous section. A series of synthetic tests were performed to determine the appropriate node spacing specific to the VFR dataset.

A number of 1-D models of dimensions  $50 \times 50 \times 12$  km were constructed with a 1-D velocity structure of the form

$$v = v_0 + kz, \quad (2.19)$$

where  $v$  is the velocity at depth  $z$  below the datum level,  $v_0$  is the velocity at datum level and  $k$  is the vertical velocity gradient. For such a model the shortest travel time  $t$  between a shot and receiver at datum level, separated by a distance  $x$ , may be expressed analytically (Sheriff & Geldart 1995) as

$$t = \left( \frac{2}{k} \right) \sinh^{-1} \left( \frac{kx}{2v_0} \right). \quad (2.20)$$

Rays were traced through these models from a single shot, offset from the centre of the model by  $\frac{3}{4}$  of a node spacing in both the  $x$  and  $y$  directions, to a regular grid of receivers separated by one node spacing, but offset from model nodes by  $\frac{1}{4}$  of a node spacing in both the  $x$  and  $y$  directions. The source and receivers were placed  $\frac{1}{2}$  a node spacing below the top of the model. The travel times calculated by the finite difference travel time calculator were then compared with the theoretical first arrival travel times, defined by equation 2.20, for all receivers within 24 km of the source. The asymmetry in source and receiver geometry was introduced to avoid placing the source and receivers exactly on model nodes, which is unlikely to occur for any real dataset and could potentially introduce bias into the results of the synthetic tests.

For the Faeroe Basin experiment described by Zelt & Barton (1998), for which model velocities are similar to those found at the VFR, a node spacing of 0.4 km was used for the forward modelling step. Hence, a 0.4 km node spacing was similarly used for the synthetic tests initially. A number of values of  $v_0$  and  $k$  were considered, representative of those encountered in the initial model. The results are shown in Fig. 2.21 as plots of travel time calculation error against shot–receiver offset.

Fig. 2.21 shows that  $v_0$  is the most important parameter affecting the accuracy of the travel time calculator. Higher values of  $v_0$  give more accurate results. High values of the velocity gradient,  $k$ , give less accurate results than low values for a constant  $v_0$ . Therefore, to determine a suitable node spacing for the forward grid, synthetic models with  $v_0 = 2.0 \text{ km s}^{-1}$  and  $k = 2.0 \text{ s}^{-1}$  were used. These values are representative of those encountered in layer 2A in the models of Turner (1998) (shown in Fig. 1.10), the layer where the lowest velocities and largest velocity gradients are encountered. The resulting travel time errors are shown in Fig. 2.22 for node spacings of 0.4, 0.2 and 0.1 km plotted against both shot–receiver offset and azimuth. The latter is defined as  $000^\circ$  along the positive  $x$ -axis and  $090^\circ$  along the positive  $y$ -axis. All three plots show azimuthal dependence. The travel time calculator is most accurate when the shot–receiver azimuth parallels one of the co-ordinate axes, and least accurate at  $45^\circ$  to these directions. For the real 3-D dataset, all shot–receiver offsets lie in the range 2.8–36.1 km. Within this range, the 0.4 km grid gives errors of up to 20 ms, similar in magnitude to the uncertainty in the best travel time picks. This node spacing was, therefore, felt to be too inaccurate. The 0.2 km grid gives errors of up to 10 ms, and the

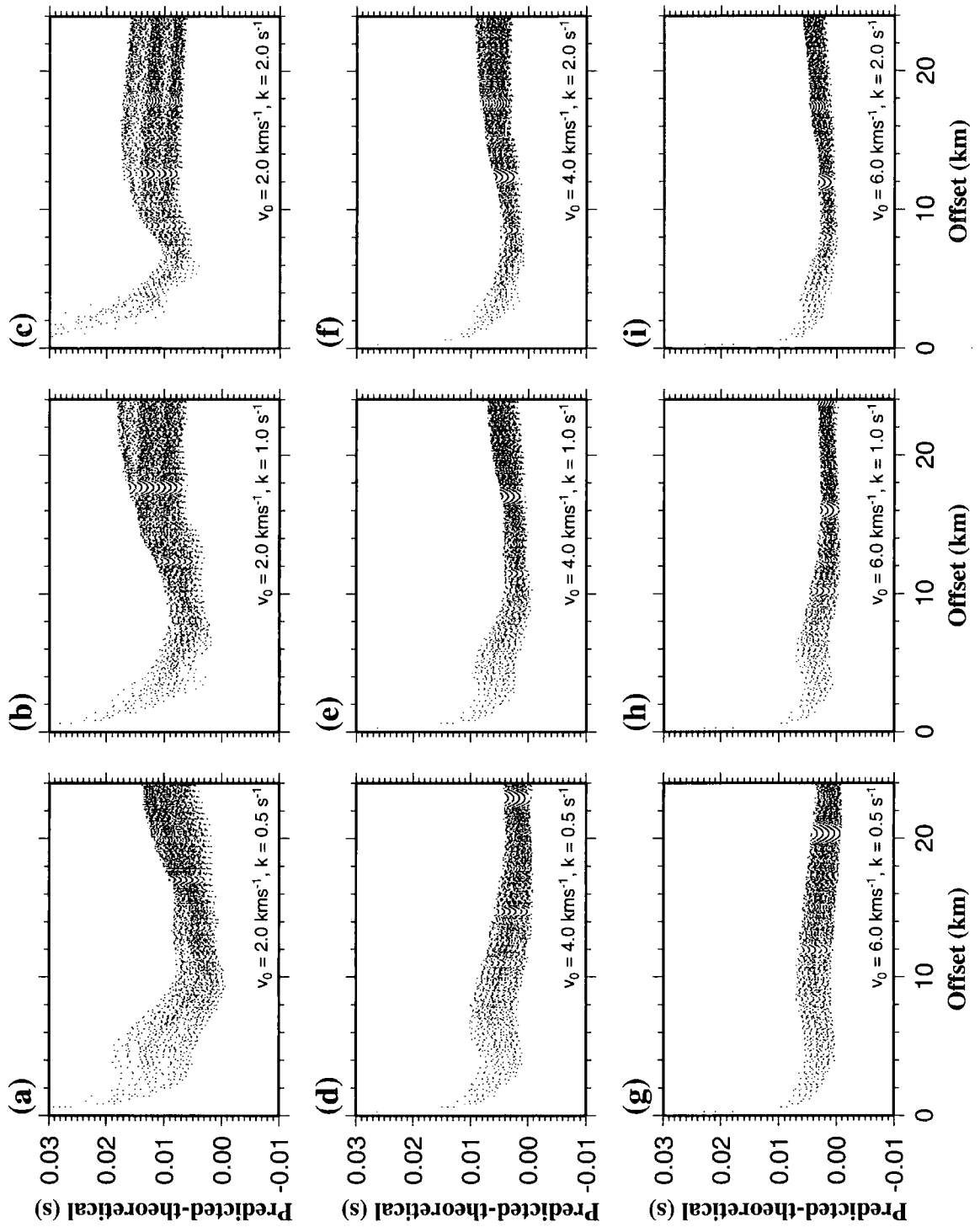


**Figure 2.21:** Graphs showing the difference between the first arrival travel time predicted by the 3-D finite difference method and the theoretical first arrival time defined by equation 2.20 for a number of 1-D velocity models of the form  $v = v_0 + kz$ , plotted against shot-receiver offset. The forward grid spacing was 0.4 km in all cases. A single synthetic shot was used offset from the centre of the model by 0.3 km in both x and y, and a regular array of synthetic receivers separated by 0.4 km and offset from model nodes by 0.1 km in x and y. The synthetic shot and receivers were placed at 0.2 km depth. Note that the range of errors is greatest for the smallest value of  $v_0$  and the largest value of  $k$ .

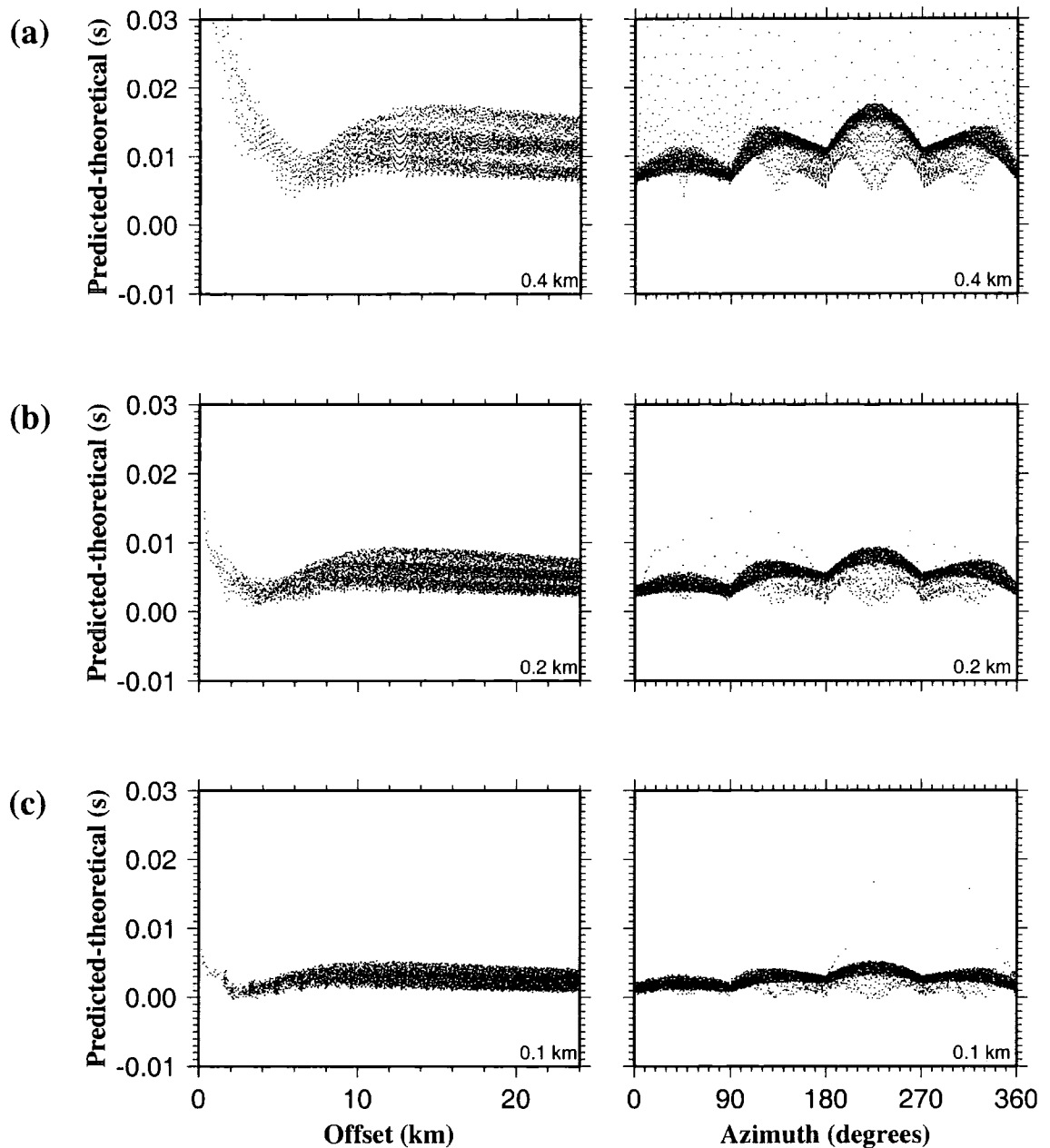


**Figure 2.22:** Graphs showing the difference between the first arrival travel time predicted by the 3-D finite difference method and the theoretical first arrival travel time calculated using equation 2.20 for a 1-D velocity model of the form  $v = v_0 + kz$  with  $v_0 = 2.0 \text{ km s}^{-1}$  and  $k = 2.0 \text{ s}^{-1}$ , plotted against both shot-receiver offset and shot-receiver azimuth. Shot-receiver azimuth is defined as  $000^\circ$  along the positive  $x$ -axis and  $090^\circ$  along the positive  $y$ -axis. The forward grid node spacings used are indicated in the bottom right-hand corner of each graph: a) 0.4 km, b) 0.2 km (only 1/4 of the modelled receivers are shown) and c) 0.1 km (only 1/16 of the modelled receivers are shown). Note the azimuthal dependence of the travel time calculation error, and the general improvement in accuracy of the 3-D finite difference travel time calculator as the node spacing is reduced. Although shot-receiver offsets for the real dataset lie in the range 2.8–36.1 km, the analysis shown was restricted to shot-receiver offsets  $< 24$  km for computational speed since the error distribution is observed to be approximately constant for each node spacing at offsets  $> \sim 15$  km.

0.1 km grid, with errors up to 6 ms, is the most accurate. However, the 0.1 km grid is computationally most expensive, since halving the node spacing produces an eight-fold increase in the number of model nodes over the 0.2 km grid. Run times increased by a much larger factor due to memory requirements (on the Sparc Ultra 10 used for performing inversions, calculating travel times for the 0.2 km grid took a few minutes, whilst the 0.1 km grid took several days). Given that errors of 10 ms, as produced by the 0.2 km grid, are much less than the smallest travel time residual uncertainties, this node spacing was used as it provides the best compromise between accuracy and computational efficiency for the shot-receiver offset range of interest.

## 2.8 Initial model

The inversion method described in section 2.2 can only determine relatively small perturbations to an initial model, otherwise the linearisation assumption on which it relies is not valid. Hence it is important that the initial model should be a reasonable representation of the known structure. For the VFR, 2-D subsets of the EW9512 dataset have been modelled by Turner (1998) and these were described in section 1.5.4 and examples shown in Fig. 1.10. A 1-D average velocity profile was obtained by averaging the velocity structure for the *Seismic South* and *Seismic North* profiles. These lines were used as they were modelled with the greatest in-line ray coverage and thus provide the most reliable estimate of velocity structure. Only those parts of the two lines which lie within the 3-D data volume were averaged. The resulting profiles for *Seismic South* and *Seismic North* plus the average of the two are shown in Fig. 2.23. The average profile was used to create the initial model. The water column velocity structure described in section 2.3.3 and shown in Fig. 2.6 was input as four horizontal constant velocity gradient layers.

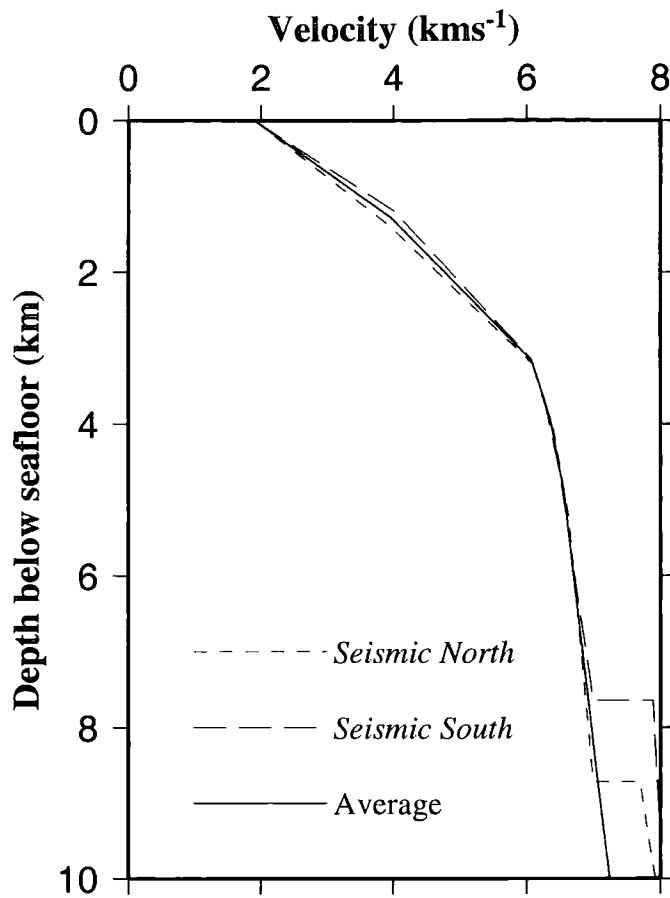


**Figure 2.23:** 1-D velocity profiles derived by averaging the relevant parts of the *Seismic South* and *Seismic North* 2-D models shown in Fig. 1.10. The average of these two profiles is also shown which was used to construct the initial model. The mantle layer has been removed from the average model and the layer 3 velocity gradient extrapolated to the base of the model. In this way all predicted ray paths were forced to turn in the crust which was necessary because the travel time dataset does not contain any arrivals which travelled in the mantle.

The 2-D models in Fig. 1.10 show that, whilst there is some lateral variation in layer thickness, the intracrustal layer boundaries approximately parallel the seafloor. The initial model was therefore constructed with approximately seafloor-parallel crustal layers. To incorporate irregular layer boundaries, the velocity at nodes adjacent to layer boundaries were set to an average of the "true" velocity over half the node spacing above and below the node (Zelt & Barton 1998). The "true" velocity at a given depth was obtained from the average profile shown in Fig. 2.23, and the velocity at each node ( $v_{\text{node}}$ ) was defined as

$$v_{\text{node}} = \frac{v_{a2} + 2v_{a4} + 2v_0 + 2v_{b4} + v_{b2}}{8}, \quad (2.21)$$



where  $v_0$  is the true velocity at node,  $v_{a2}$  and  $v_{a4}$  are the "true" velocities  $\frac{1}{2}$  and  $\frac{1}{4}$  node spacing above the node respectively, and  $v_{b2}$  and  $v_{b4}$  are the "true" velocities  $\frac{1}{2}$  and  $\frac{1}{4}$  node spacing below the node respectively. For nodes more than  $\frac{1}{2}$  node spacing away from a layer boundary,  $v_{\text{node}}$  as defined by equation 2.21 is equal to the "true" velocity at that depth. The seafloor position was determined from swath bathymetry data collected during cruise EW9512. The swath bathymetry data was gridded at 0.1' (approximately 0.185 km) intervals, and was transformed from latitude and longitude to a linear grid using the method described in section 2.3.2. The data were then gridded using a 0.2 km interval, the same scale as the velocity model. Fig. 2.4 shows that there are gaps in the swath bathymetry coverage centred on  $22^\circ 11' \text{ S}$ ,  $176^\circ 45' \text{ W}$  and  $22^\circ 24.5' \text{ S}$ ,  $176^\circ 53.5' \text{ W}$  within the 3-D data volume. These gaps were filled by finding and sampling a best-fitting surface to the surrounding data at the re-gridding stage.

However, the seismic data are insensitive to bathymetric features of 0.2 km scale because the *footprint* of the wavefront at the seafloor is larger than 0.2 km. *Footprint* is defined as the area of the wavefront within which energy constructively interferes. Seafloor irregularities on a scale smaller than the *footprint* of the wavefront may affect the positions of predicted seafloor ray entry points, and consequently the predicted travel times through the water column and the size of the travel time residuals to be resolved. This problem was described in greater detail in section 2.5, where it was demonstrated that the seafloor ray entry point and water column travel time should be represented as accurately as possible.

The lateral resolution of seismic reflection data is traditionally determined by considering the first Fresnel zone radius. This radius is defined as the area from which reflected energy will constructively interfere, i.e. the phase difference is  $\frac{1}{2}$  a period or less, and is given by the equation

$$R = \left( \frac{\lambda z}{2} \right)^{1/2} = \left( \frac{v z}{2 f} \right)^{1/2}, \quad (2.22)$$

where  $R$  is the first Fresnel zone radius,  $\lambda$  is the wavelength of seismic energy,  $v$  is the average velocity above the reflector,  $f$  is the source frequency and  $z$  is the depth to reflector (Sheriff & Geldart 1995). Equation 2.22 applies to reflected energy, for which incident energy with a phase separation of  $\frac{1}{4}$  of a period gives rise to reflected energy with a phase separation of  $\frac{1}{2}$  a period which will therefore destructively interfere.

However, for transmitted energy destructive interference will occur if the phase separation is  $\frac{1}{2}$  a period. Hence the appropriate equation for seismic refraction data is

$$R = \left( \frac{vz}{f} \right)^{1/2} . \quad (2.23)$$

For the VFR dataset, the dominant source frequency is 8 Hz, the average water column velocity is  $1.493 \text{ km s}^{-1}$  and water depths within the 3-D data volume range from 1.370 km to 2.842 km. Using equation 2.23, the radius of the footprint of the seismic wavefront at the seafloor therefore ranges from 0.506 km to 0.728 km. Hence, a 1.0 km square averaging filter was applied to the bathymetry data. This is a very approximate treatment of resolution at the seafloor, and will be discussed further in section 3.6. The resulting smoothed bathymetry with the gaps filled as described above, is shown in Fig. 2.24 together with the raw bathymetry data from which it is derived.

The smoothed bathymetry still contains a number of small-scale irregularities associated with seamounts and the ridge system itself which are unlikely to be present at depth below the surface. Hence, further smoothing was applied to model intracrustal interfaces in the initial model. A 1.5 km square averaging filter was applied at the layer 2A–2B/C boundary, and a 2.0 km filter applied at the layer 2B/C–3 boundary and all deeper interfaces. The choice of these filters is subjective, but they result in a smoother initial model, which is desirable to achieve stable inversions. The smoother initial model also better represents the scale of features which can be resolved at depth. Resolution at intracrustal interfaces was treated less rigorously than the seafloor because they are second-order interfaces and thus rays do not undergo refraction when incident upon them, so their positions are less critical to the accurate prediction of ray paths. Also, any gross errors in structure arising from these assumptions will be apparent in the inversion results.

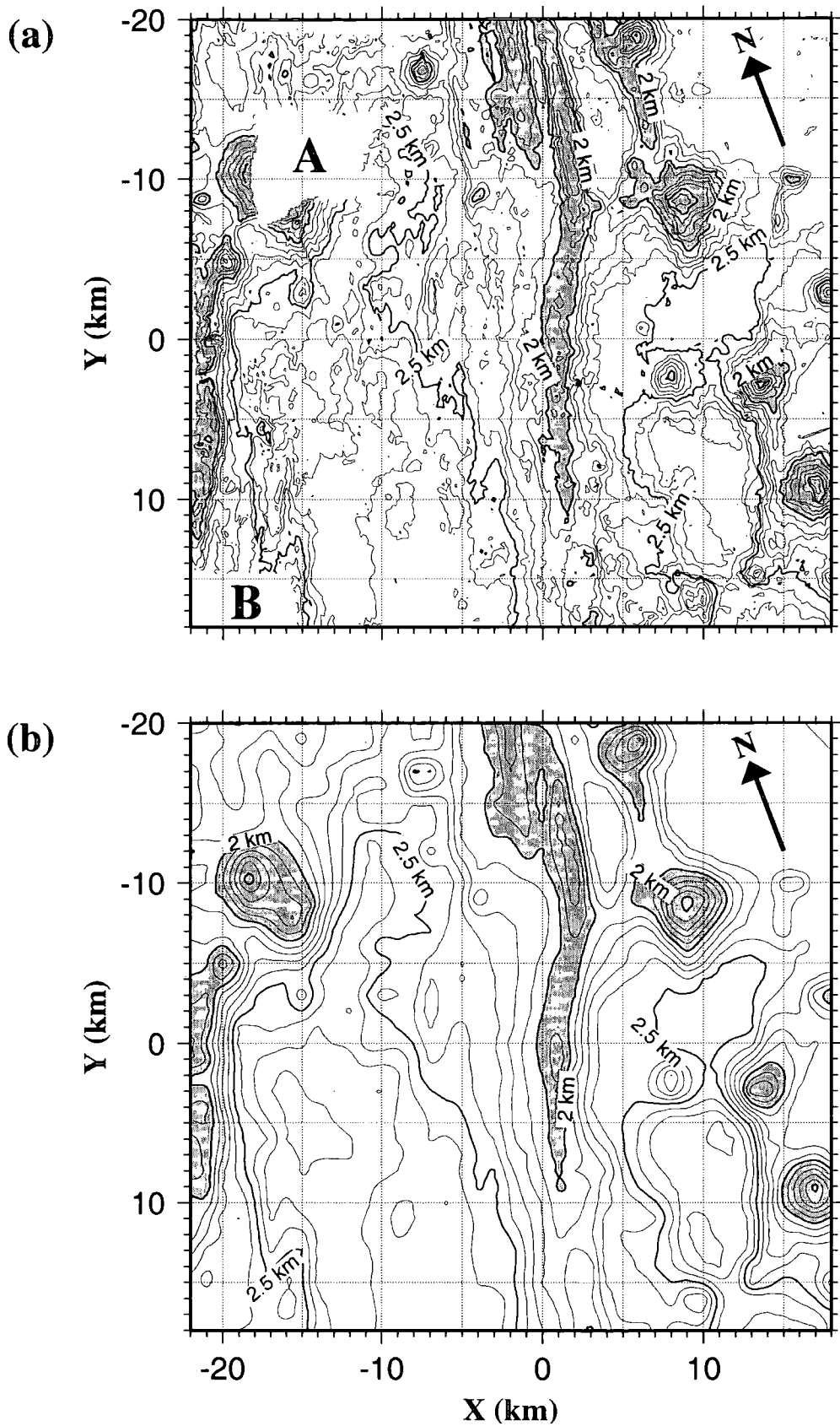


**Figure 2.24:** a) Raw and b) smoothed bathymetry within the 3-D study area. Bathymetric contours at 0.1 km intervals are plotted and regions shallower than 2 km grey shaded. Note that the gaps in the raw bathymetry coverage as shown by annotation A and B have been filled by a best-fitting surface in the smoothed version. The smoothed bathymetry was used to construct the initial model.

When rays were traced through the initial model described above, some were predicted to travel in the mantle layer. Interpretation of phases in the raw dataset indicates that none of the first arrivals used in the inversion are mantle diving rays since all the shot-receiver offsets are less than the offset observed for the triplication point between crustal diving rays, mantle diving rays and the Moho reflection. These predicted ray paths must, therefore, be in error. To resolve this problem the mantle layer was removed and the layer 3 velocity gradient extrapolated to the base of the 3-D model, which lies at 12 km below sea level. A cross-section through the resulting initial model is shown in Fig. 2.25.

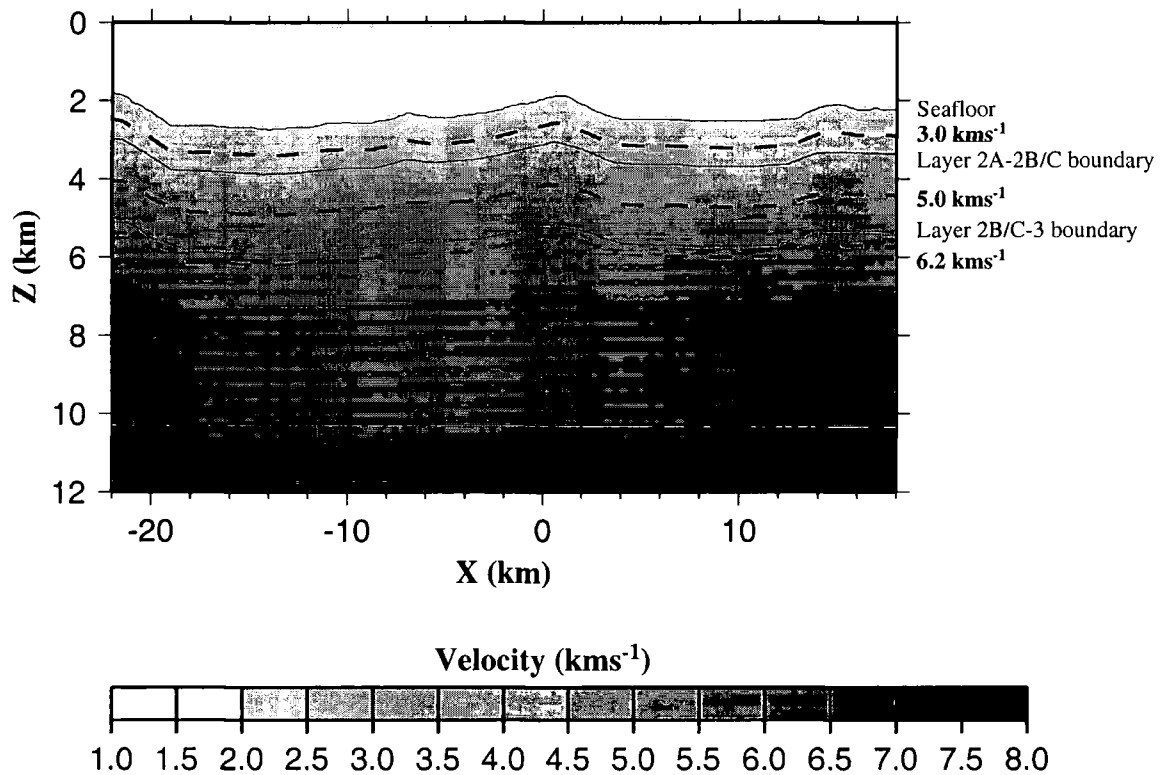


**Figure 2.25:** Cross-section through the initial model at  $y = 0$  km showing the principal layer boundaries (solid lines) and the positions of the  $3.0$ ,  $5.0$  and  $6.2$   $\text{kms}^{-1}$  constant velocity planes (dashed lines). Vertical exaggeration:  $\times 2$ . This model was constructed using the water column velocity structure in Fig. 2.6 and the average crustal velocity profile shown in Fig. 2.23 assuming seafloor-parallel layers. Layer boundaries were defined parallel to a smoothed approximation to the seafloor with a progressively greater degree of smoothing applied at greater depth reflecting the likelihood that small-scale irregularities associated with seamounts and the ridge system itself are unlikely to be present at depth below the seafloor. The grey area at depths shallower than  $0.5$  km represents that part of the water column for which the velocity exceeds  $1.5$   $\text{kms}^{-1}$  (see Fig. 2.6). The constant velocity planes indicated by dashed lines are used to display sections through 3-D velocity and resolution models in later figures in this chapter and chapter 3.

## 2.9 Inversion parameters

A number of preliminary inversions were performed using the initial model described in the previous section in order to determine suitable values for the inversion parameters described in section 2.2.3. Tests to determine the appropriate inversion cell size will be discussed in full in section 3.3. The remaining inversion parameters which must be provided by the user are an initial value for  $\lambda$  and  $s_z$  in equation 2.12 as discussed in section 2.2.3. This section describes how values were assigned for these parameters which remained invariant for all inversions described in chapter 3.

An initial value of 10 was used for the trade-off parameter  $\lambda$  (equation 2.12). Higher initial values of  $\lambda$  merely increased the number of iterations required for convergence with little effect on the final value of  $\lambda$  or the final model. For each iteration a maximum of five values of  $\lambda$  were tested as described in section 2.2.3, with the value of  $\lambda$  reduced in steps by dividing by  $\sqrt{2}$ . This value for the initial value of  $\lambda$  was chosen because the final value of  $\lambda$  was always less than 3, and the step by which  $\lambda$  was reduced was chosen to allow rapid convergence whilst also providing adequately fine control on the final value given these likely initial and final values of  $\lambda$ . The magnitude of perturbations near the edge of the model were minimised to prevent edge effects resulting from smoothing of anomalies in the interior of the model.

Inversions were also performed using a number of values of the  $s_z$  parameter which controls the relative importance of maintaining horizontal versus vertical smoothness of the final model (equation 2.12). The resulting final models were all found to be very similar. Hence  $s_z$  was set to 1.0 for simplicity so that the degree of vertical versus horizontal smoothing was controlled solely by the horizontal and vertical inversion cell dimensions, as fully described in section 2.2.3.

## 2.10 Resolution analysis

In this section, the method used to determine model resolution is described and the results specific to the VFR dataset presented. The method employed involves performing a number of inversions of synthetic datasets created by calculating the predicted first arrival travel times for synthetic shot-receiver pairs for known velocity structures. For all such tests, the initial model described in section 2.8 was used as the basis of the synthetic models and the initial model for the inversion, and was parameterised with a 0.2 km node spacing as described in section 2.7. The inversion

parameters were set to the values described in section 2.9. The shot and receiver positions were set to be the same as the real VFR dataset, and travel time uncertainties for the synthetic arrivals were set identical to their real data equivalents as described in section 2.6. An inversion cell size of  $1.0 \times 1.0 \times 0.4$  km was used, choice of which will be discussed in detail in section 3.3.

### 2.10.1 Method

A simple measure of model resolution commonly used in seismic tomography studies is hit count, in other words the number of rays sampling each inversion cell. A slightly more sophisticated measure is the cumulative length of rays sampling each cell. Fig. 2.26 shows the cumulative ray path length per inversion cell for rays traced through the initial model for planes of constant velocity in the initial model at 3.0, 5.0 and 6.2  $\text{kms}^{-1}$ . These planes lie at approximate depths of 0.7, 2.2 and 3.5 km below the seafloor as shown in Fig. 2.25, and correspond to the middle of layer 2A, the middle of layer 2B/C and near the top of layer 3 respectively. Fig. 2.26 shows that the ray coverage is most dense at layer 3 depths, with good coverage in parts of layer 2B/C also, and relatively sparse coverage in layer 2A. This pattern of ray coverage emphasises the fact that the seismic component of the VFR experiment was primarily targeted towards constraining the velocity structure at mid- and lower-crustal depths, and particularly targeted the structure of the axial magmatic system.

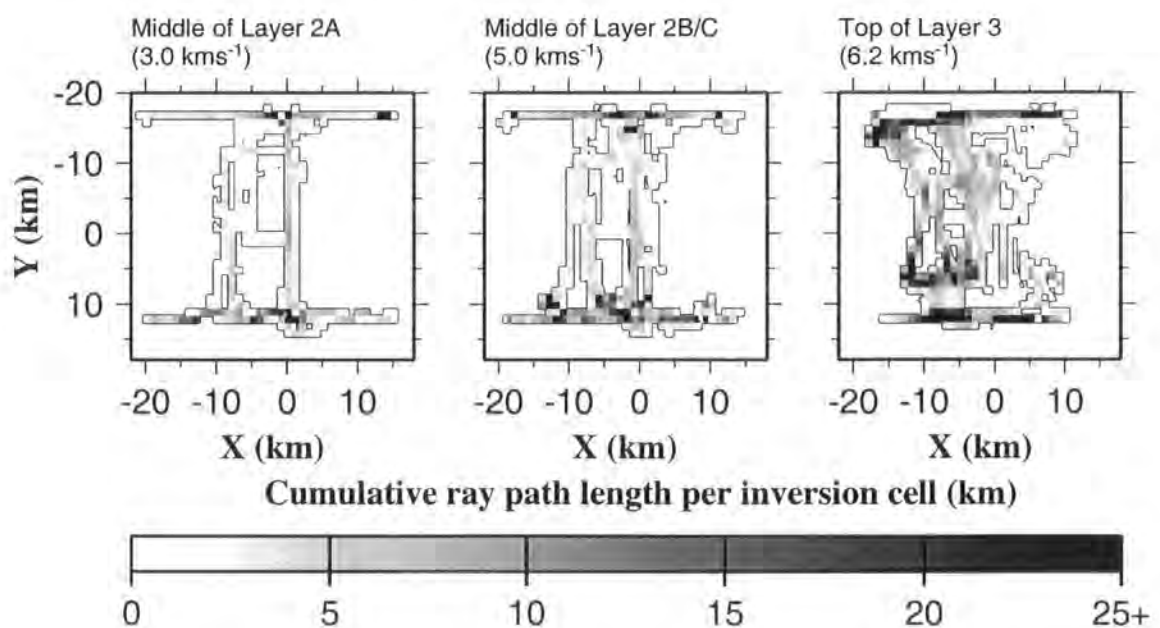


**Figure 2.26:** Total ray path length sampling each inversion cell in the initial model for the 3.0, 5.0 and 6.2  $\text{kms}^{-1}$  constant velocity planes. Note that ray coverage is generally most dense in layer 3.

However, considering ray path length alone takes no account of variable travel time residual uncertainties or azimuthal coverage within each inversion cell, which, intuitively, would be expected to affect the scale of features which can be resolved. Thus a better method of determining resolution which takes account of these factors is required. Checkerboard tests (e.g. Hearn & Ni 1994) are another common means of assessing resolution. A known regular alternating pattern of positive and negative anomalies are added to an initial model and synthetic first arrival travel times are calculated by ray tracing through that model. An inversion is then performed using the calculated synthetic first arrival travel time picks, and the recovered anomaly pattern compared with the known synthetic anomaly pattern to assess model resolution. The approach employed in this study is an extension of the checkerboard method, and was described in full by Zelt (1998). An overview is given here.

A synthetic checkerboard anomaly pattern was created which varies sinusoidally in  $x$  and  $y$  with an amplitude of 5% of the velocity of the initial model at that point (an example is shown in Fig. 2.27a). This pattern was added to the initial model. Ray tracing was then performed for the shot–receiver geometry of the real experiment to create a set of synthetic first arrival travel times. As the velocity field is smoothly varying, the ray tracer behaves reliably and the relatively small anomaly amplitude implies that ray paths for the synthetic model will be similar to those for the initial model. Thus the resolution derived from the synthetic tests is useful for assessing the resolution of the real data. The validity of this approach was discussed at length by Zelt (1998). Gaussian noise was then added to each first arrival travel time, with a variance determined by the travel time residual uncertainty for the equivalent arrival in the real dataset. An inversion was then performed. An example of the difference between the recovered model produced by the inversion and the initial model is shown in Fig. 2.27b. Comparison with Fig. 2.27a shows that areas where the recovered anomaly closely resembles the synthetic anomaly approximately correspond to those areas with the most dense ray coverage (*cf.* Fig. 2.26). In order to quantitatively assess the level of agreement between the synthetic and recovered models, the semblance ( $S$ ) between them was calculated for each node using the formula

$$S = \frac{\sum_{j=1}^M (\Delta v_{tj} + \Delta v_{rj})^2}{2 \sum_{j=1}^M (\Delta v_{tj}^2 + \Delta v_{rj}^2)} \quad (\text{after Zelt 1998}), \quad (2.24)$$

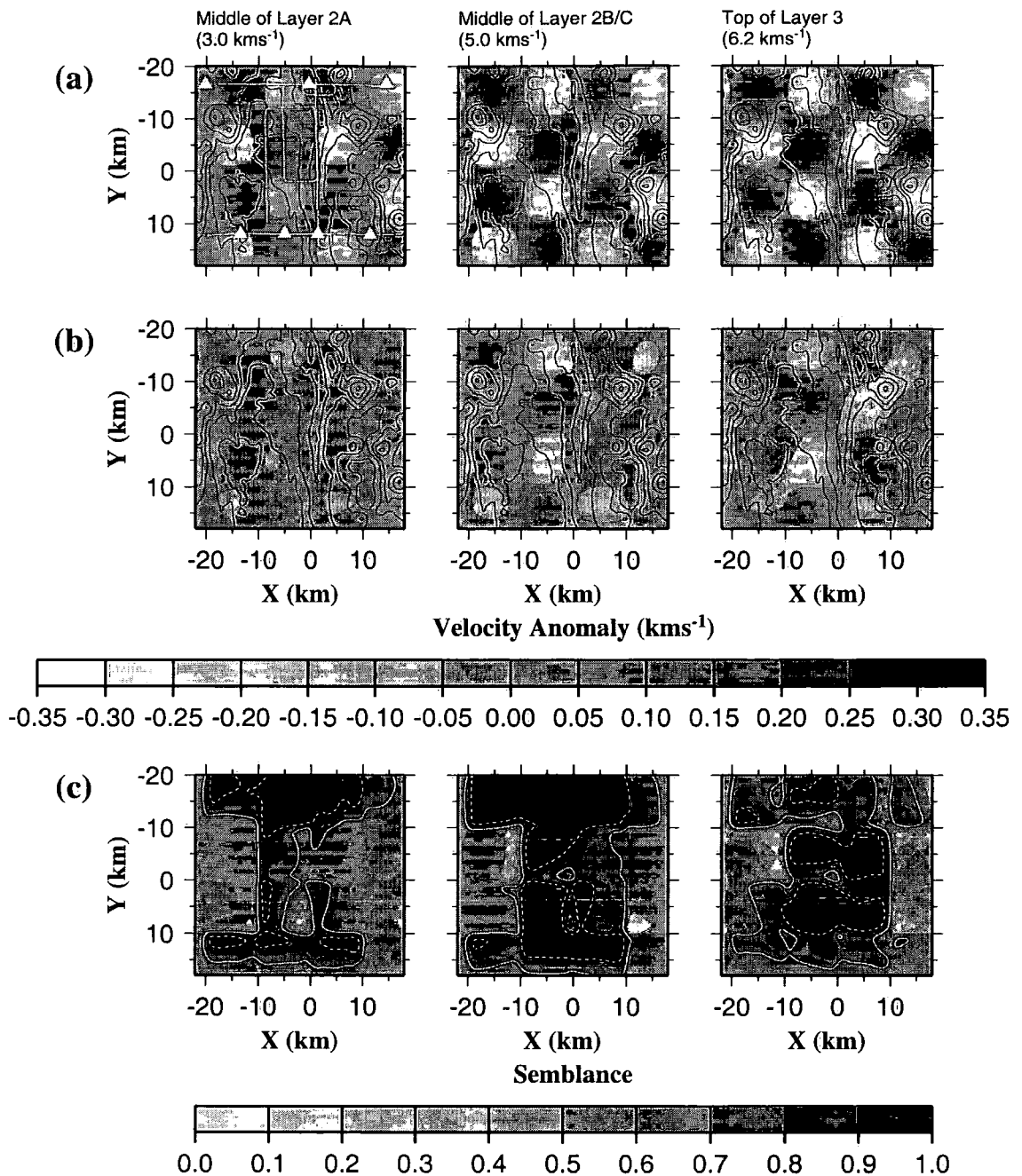


**Figure 2.27:** Checkerboard models used to assess lateral resolution. a) Example of a checkerboard model with 10 km checkerboard size. The anomaly relative to the background model is plotted for the 3.0, 5.0 and 6.2 km/s planes. The OBS locations (white triangles) and ship tracks (white lines) are shown on the 3.0 km/s plane plot. Bathymetric contours at 0.25 km intervals are plotted in black. b) Velocity anomaly recovered by the inversion from synthetic data traced through the model in a). c) Semblance between the synthetic and recovered models shown in a) and b) respectively. Semblance was calculated for every model node using equation 2.24. The solid and dashed contours are at semblance values of 0.7 and 0.9 respectively. Note that the areas of highest semblance in c) correspond to the areas where the recovered model in b) most closely resembles the test model in a).



where  $\Delta v_{ij}$  and  $\Delta v_{rj}$  are the true and recovered velocity anomalies at the  $j$ th node respectively. Summations were performed over the  $M$  nodes within a horizontal planar area of radius 2.5 km centred on the model node under consideration. The radius should be small enough to allow local semblance to be assessed but large enough to be insensitive to noise (Zelt 1998). The semblance fields described here are directly comparable with those described by Zelt (1998) which were calculated using a 5 km radius operator, because the velocity model node spacing used in that study was twice that used in this study. Hence the summations were performed over the same number of nodes in each study. A horizontal planar operator only measures lateral resolution. However, as most of the vertical velocity structure is believed to be included in the initial model, the variation of most importance is in the horizontal plane. Fig. 2.27c shows the semblance between the two anomaly fields shown in Figs. 2.27a and 2.27b. The areas of highest semblance are indicated and correspond to the areas where the recovered model closely resembles the synthetic model.

However, there is also a strong correlation between the areas of highest semblance and the position of the synthetic anomaly. This phenomenon is likely to arise from the highly irregular ray coverage such that if the centre of a synthetic anomaly falls in an area of locally high ray coverage it will be well resolved, whereas anomalies slightly offset from the high ray coverage area will be much less well resolved. In order to overcome this problem, the method of Zelt (1998) employs a number of checkerboard tests whereby the basic anomaly pattern depicted in Fig. 2.27a is altered by reversing its polarity, offsetting it by  $\frac{1}{2}$  a node spacing in both  $x$  and  $y$  directions, rotating it through  $45^\circ$  and all possible combinations of these transformations, to create eight distinct checkerboard geometries. These eight checkerboard models are shown in Fig. 2.28.

For each of the eight checkerboards, inversions were performed and the semblance field calculated. The mean of the eight semblance fields was obtained for each model node. In order to determine the scale of features which may be resolved, the mean semblance field was derived for a number of different checkerboard sizes, where the checkerboard size is defined as half the wavelength of the applied sinusoid. For the example in Figs. 2.27 and 2.28, the checkerboard size is 10 km. The minimum

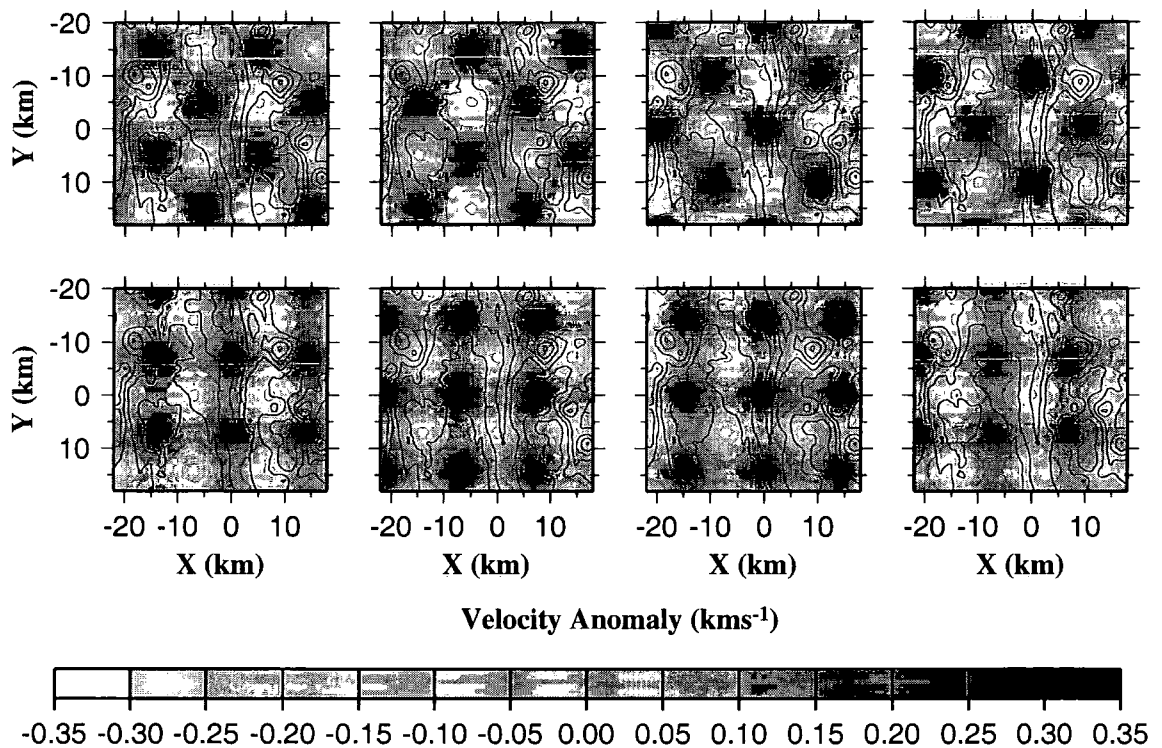


**Figure 2.28:** Example of the eight variations on the basic checkerboard model shown in Fig. 2.27a for a 10 km checkerboard size. The anomaly relative to the background model is shown for the  $6.2 \text{ km}^{-1}$  plane. Bathymetric contours at 0.25 km intervals are plotted in black.

checkerboard size for which the mean semblance exceeds a specified threshold defines the lateral resolution at each node in the model volume. For this study, checkerboard sizes of 4, 5, 6, 8, 10 and 15 km were considered. Thus lateral resolution may be determined to the nearest kilometre by interpolation between the mean semblance values for these checkerboard sizes.

### 2.10.2 Results

Fig. 2.29 shows synthetic models, recovered models and semblance plots for a number of checkerboard sizes at layer 3 depth. Zelt & Barton (1998) and Zelt (1998) use a semblance threshold of 0.7 to denote areas which are well resolved. Inspection of Fig. 2.29 shows that the positions of anomalies have generally been accurately recovered for semblance values exceeding 0.7. However the amplitude of the recovered anomaly is usually underestimated unless the semblance exceeds 0.9. Hence resolution plots were constructed using both semblance thresholds. The mean semblance for each

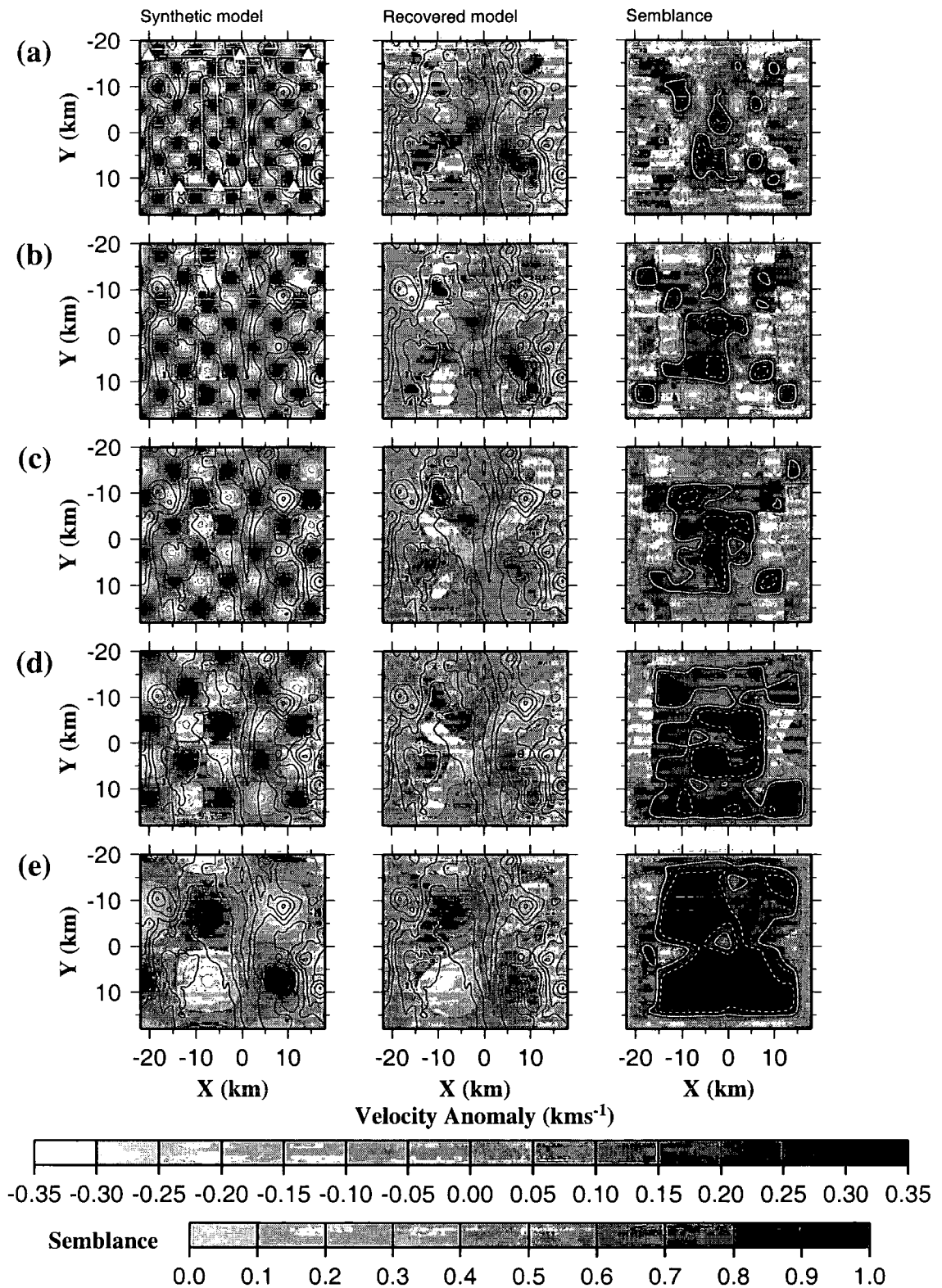


**Figure 2.29:** Example of a checkerboard model, the model recovered by inversion of synthetic data generated from that model, and the semblance between the synthetic and recovered models for checkerboard sizes of a) 4 km, b) 5 km, c) 6 km, d) 8 km and e) 15 km. All plots are for the 6.2 km<sup>-1</sup> plane. The solid and dashed contours for the semblance plots are at values of 0.7 and 0.9 respectively. Note that the positions of anomalies in the synthetic models are adequately reproduced in the recovered model in areas where the semblance exceeds 0.7, but anomaly amplitudes are generally underestimated unless the semblance exceeds 0.9.

checkerboard size is shown in Fig. 2.30 and the resulting resolution plots for the two semblance thresholds considered are shown in Fig. 2.31. The plot constructed using a threshold of 0.7 (Fig. 2.31a) indicates the size of velocity anomalies whose positions may be accurately determined, and that constructed using a threshold of 0.9 (Fig. 2.31b) indicates the size of features whose amplitudes may also be determined reliably.

Comparison of Figs. 2.26 and 2.31 shows that although the ray coverage is greatest at layer 3 depths, both semblance criteria indicate superior resolution in layer 2B/C. It is believed that this observation reflects the generally larger travel time residual uncertainties associated with arrivals sampling layer 3 compared to those sampling layer 2B/C. The layer 2B/C–3 transition marks a sharp decrease in vertical velocity gradient, and hence a sharp drop in amplitude occurs for rays which pass below this transition compared to those which do not due to divergence of the wavefield. In addition, rays which sample layer 3 have longer travel paths on average than those which sample layer 2B/C, and are thus subject to a higher degree of anelastic attenuation which will further reduce the amplitude. The lower amplitude implies lower SNR and hence larger pick position uncertainty adopting the criteria outlined in section 2.4. This example illustrates the pitfalls of using the ray coverage plot in Fig. 2.26 as a measure of model resolution.

Since the seismic experiment was designed to investigate the structure at mid-crustal depths, the resolution in layer 2B/C and layer 3 is of most interest. Inspection of Fig. 2.31a shows that the resolution is typically 6 km or better, and Fig. 2.31b indicates that the amplitude of anomalies on a scale of 10 km can generally be accurately determined. Within the layers, the variations in resolution largely reflect the irregular ray coverage shown in Fig. 2.26. The greatest discrepancy between Figs. 2.31a and 2.31b occurs in layer 2A. Poor resolution should be expected in layer 2A as there is poor azimuthal coverage and there are very few crossing ray paths away from the two across-axis lines containing the OBS deployment sites. Fig. 2.31a implies reasonable resolution over large areas of the model at this depth. By contrast, Fig. 2.31b implies resolution generally worse than 15 km except in a few isolated areas, mostly in the vicinity of OBS deployment sites. These results suggest that the positions of relatively small-scale velocity anomalies may be determined, but their amplitudes are likely to be greatly underestimated except in the few areas indicated in Fig. 2.31b.

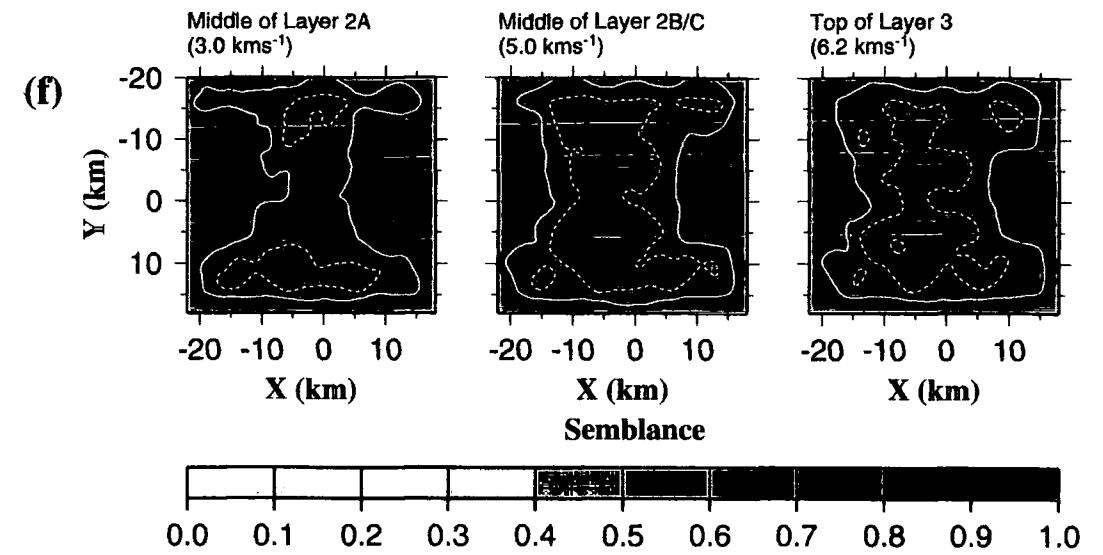
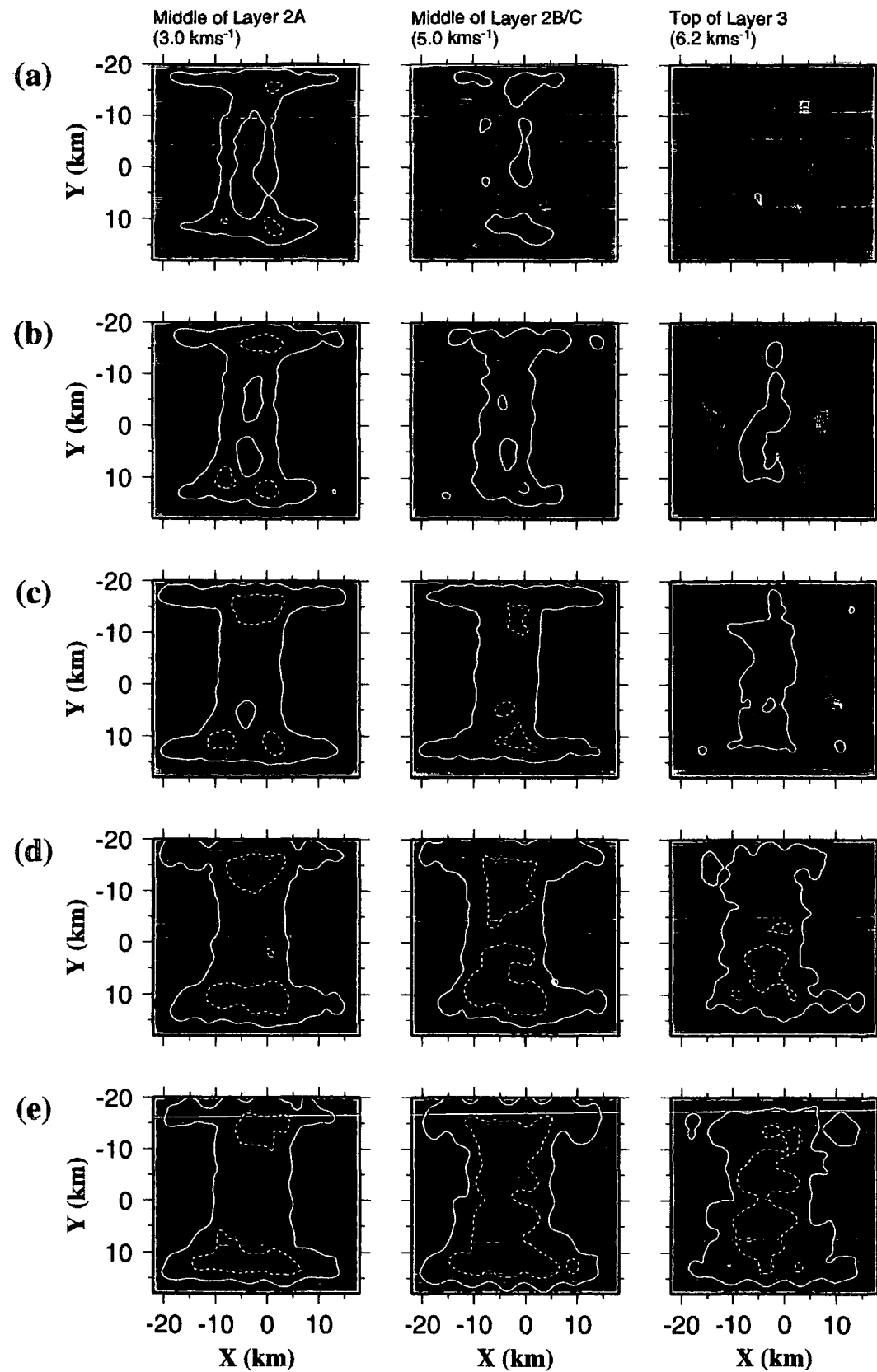


**Figure 2.30:** Mean of the semblance derived from the eight checkerboard patterns shown in Fig. 2.28 for the 3.0, 5.0 and 6.2 km/s planes and checkerboard sizes of a) 4 km, b) 5 km, c) 6 km, d) 8 km, e) 10 km and f) 15 km. The solid and dashed contours are at semblance values of 0.7 and 0.9 respectively. Note that the area of high semblance (>0.7) generally increases with increasing checkerboard size, and is generally greatest in layer 2B/C for a given checkerboard size.

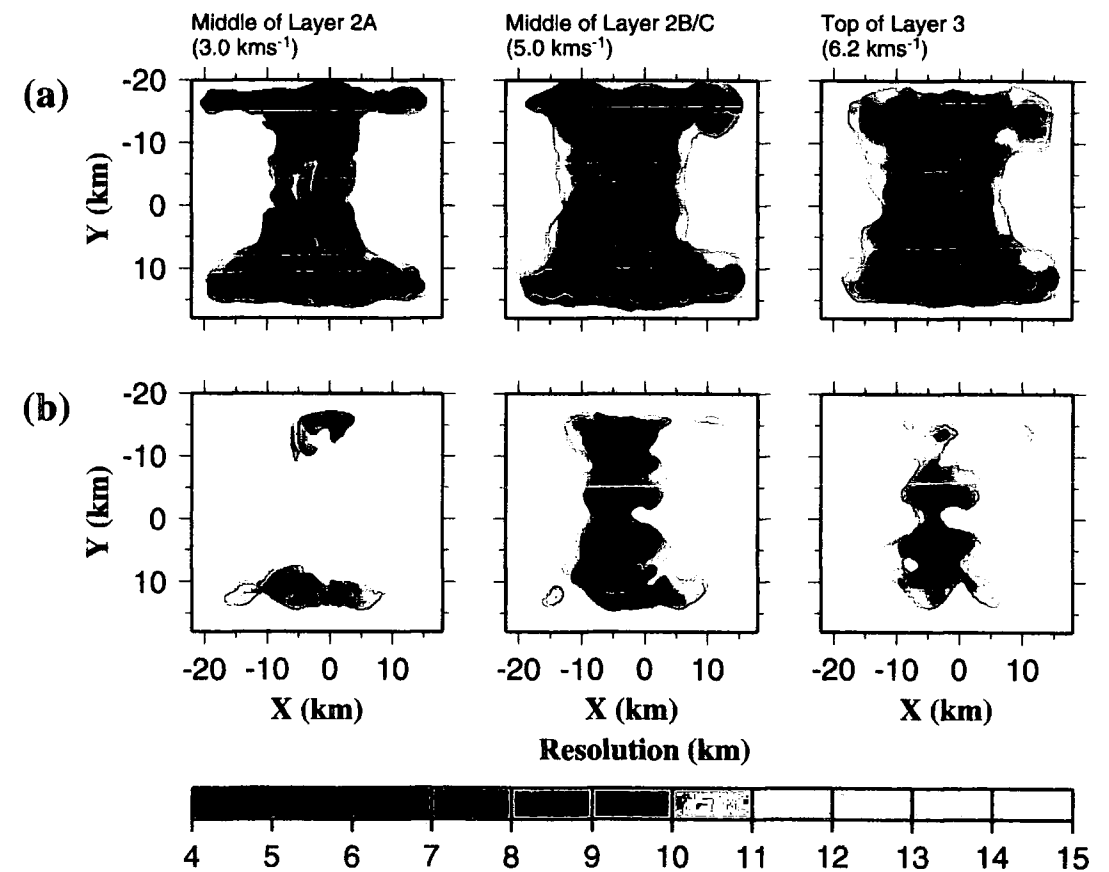


**Figure 2.31:** Model resolution at each node in the velocity model obtained by determining the minimum checkerboard size for which the semblance exceeds a) 0.7 and b) 0.9. The semblance fields in Fig. 2.30 were used. Part a) shows the size of anomalies whose position may be recovered, and b) shows the size of anomalies whose amplitudes may also be accurately recovered.

## 2.11 Summary

The basic information required by the tomographic inversion method, described in section 2.2, are first arrival travel times and the locations of shots and receivers. The means of determining these data specifically for the VFR dataset were described in section 2.3. In addition, it has been emphasised that reliable estimates of the travel time residual uncertainties are required in order to use the inversion routines to their fullest potential. The most variable contribution to travel time residual uncertainty arises from uncertainty in the precise position of the travel time pick for noisy data, and a method for determining this uncertainty based on SNR was described in section 2.4. All other possible sources of travel time residual uncertainty considered were evaluated in section 2.5 and the final results of this analysis summarised in section 2.6 and Table 2.4. The inversion did not converge to a model which satisfied the travel time data within these uncertainties, and therefore the convergence criteria were relaxed by doubling the travel time residual uncertainty associated with each arrival. Specific values of the other parameters required by the inversion method were then considered in sections 2.7, 2.8 and 2.9. In particular, it was shown that a node spacing of 0.2 km was most appropriate for the forward modelling step. The method of constructing a 1-D initial model with approximately seafloor-parallel layers, the most appropriate assumption based on 2-D interpretations of subsets of the seismic dataset by Turner (1998), was described. Finally, in section 2.10 the method used to determine model resolution was discussed and applied to the VFR dataset. Resolution at the depths targeted by the VFR experiment was found to be adequate.

The inversion method described in this chapter was applied to the VFR dataset. The results will be described in the next chapter.

# Chapter 3

## Seismic tomographic inversion at the Valu Fa Ridge

### 3.1 Introduction

In this chapter the results of application of the *FAST* regularised inversion algorithm, described in section 2.2, to the VFR seismic dataset are described. Included in this chapter are discussions of the determination of the most suitable cell size for the inverse step for the VFR dataset specifically, and refinements applied to the initial model in order to better represent true crustal structure at this ridge system. The effects on the inversion results of the axial melt lens, rough bathymetry and variable ray coverage resulting from acquisition geometry are considered in the context of interpretation of final anomalies as real geological features or artefacts of the inversion process. Synthetic tests, designed to establish which features of the models are required by the data and which are model artefacts, are described. A full geological interpretation of the inversion results, and the implications for the VFR and mid-ocean ridges in general, will be discussed in chapter 5.

### 3.2 Inversion travel time dataset

First arrival travel time picks were made and travel time residual uncertainties assigned using the methods described in chapter 2 for the subset of shots and receivers shown in Fig. 2.4. The model bounds were chosen to encompass the region of most dense 3-D ray coverage, with an additional margin of 2 km on each edge of the model within which no shots were considered. This margin was introduced to allow predicted ray paths to bend out of the shot-receiver vertical plane in the presence of 3-D velocity variations without reaching the edge of the model volume and terminating (Zelt & Barton 1998). The SNR was found to be highly variable and for some shot-receiver combinations it was not possible to identify the first arriving crustal phase due to very low SNR. Additional first arrival travel time picks were discarded on SNR grounds when assigning travel time observation uncertainties as described in section 2.4.3.

The crustal part of the predicted ray paths through the initial model described in section 2.8 are shown in Fig. 3.1 for the shot-receiver combinations used in the inversion. For all the inversions described in this chapter, the parameter values



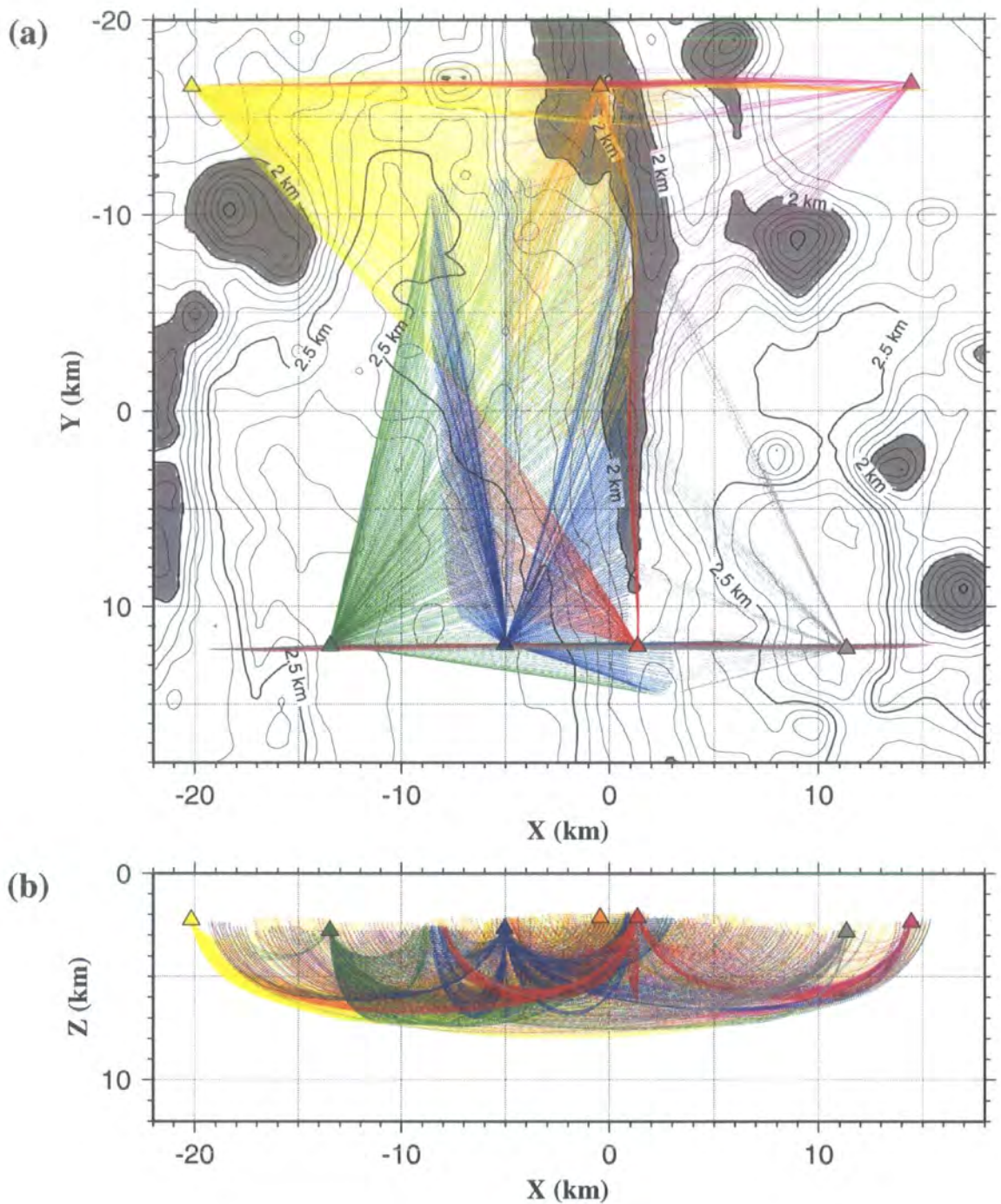


**Figure 3.1:** Crustal part of the predicted ray paths traced through the *basic 1-D initial model*, described in section 2.8, for all the shot-receiver pairs used in the inversions in a) plan view and b) cross-section parallel to the x-axis. Bathymetric contours at 0.1 km intervals are shown in a), and bathymetry shallower than 2 km has been shaded. Coloured triangles denote OBS locations, with ray paths colour coded according to the OBS at which they were recorded. Note that there is no ray coverage deeper than ~8 km.

described in section 2.9 were used. In each case, two iterations were required to achieve a model with a normalised  $\chi^2$ , defined by equation 2.18, of less than 1.01 unless otherwise stated. In most cases very many more iterations were required to achieve a model with a normalised  $\chi^2$  of 1.00 or less, which indicates that the model perturbations



satisfy the travel time residuals within their assigned uncertainties. The extra computational expense and introduction of additional structure for such a marginal improvement in misfit was not felt to be justified, so a normalised  $\chi^2$  threshold of 1.01 was chosen to indicate satisfactory convergence. As described in section 2.6, the uncertainties assigned to each travel time residual represent two standard deviation uncertainties since the inversion did not converge when the uncertainties were set to one standard deviation. Therefore the final models described in this chapter do not satisfy the data within their uncertainties which indicates that there is significant additional structure which is unresolvable with this dataset. This issue will be discussed further in section 3.8.1.

### 3.3 Inversion cell size

The dimensions of the inversion cells are usually chosen to be larger than the node spacing of the forward grid since the wavelength of anomalies which can be resolved by the inversion algorithm is generally very much larger than the node spacing required for accurate ray tracing. Larger inversion cells result in fewer model parameters, which is desirable for computational efficiency and increases the relative importance of the travel time data over the smoothing operator in the inversion process. However, the inversion cells should be sufficiently small to allow resolution of features without significant lateral smoothing. The dimensions of the inversion cells are permitted to be different in each of the co-ordinate directions. As the general vertical velocity structure and layering of the oceanic crust is relatively well known, and is globally consistent regardless of ridge setting, the generalities of the vertical velocity structure may be incorporated into the initial model. The inversion is thus targeted towards resolving lateral velocity variations relative to that structure. Therefore inversion cells of larger dimension in the horizontal plane than the vertical were used.

A number of inversions were performed using different trial combinations of horizontal and vertical inversion cell sizes in order to establish the most appropriate cell size for this particular study. Trial inversions were performed using all combinations of horizontal cell sizes of 1.0 and 2.0 km, with equal x and y cell dimensions, and vertical cell sizes of 0.4 and 0.8 km. The initial model described in section 2.8 was used for this process and is hereafter referred to as the *basic 1-D initial model*. The final models produced by the inversion routines are shown in Fig. 3.2 for each cell size as plots of the velocity anomaly relative to the *basic 1-D initial model*. The plots are of constant

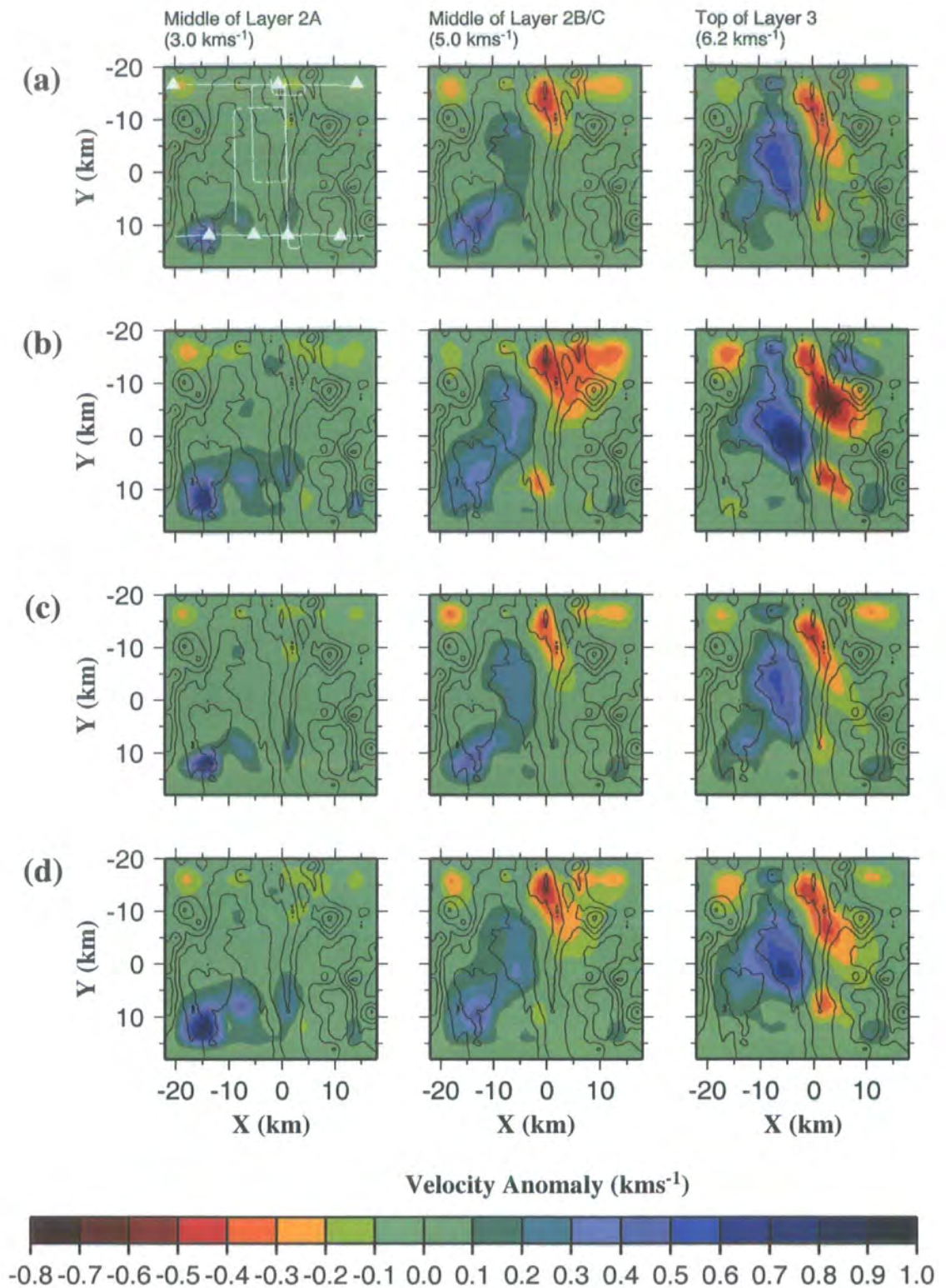
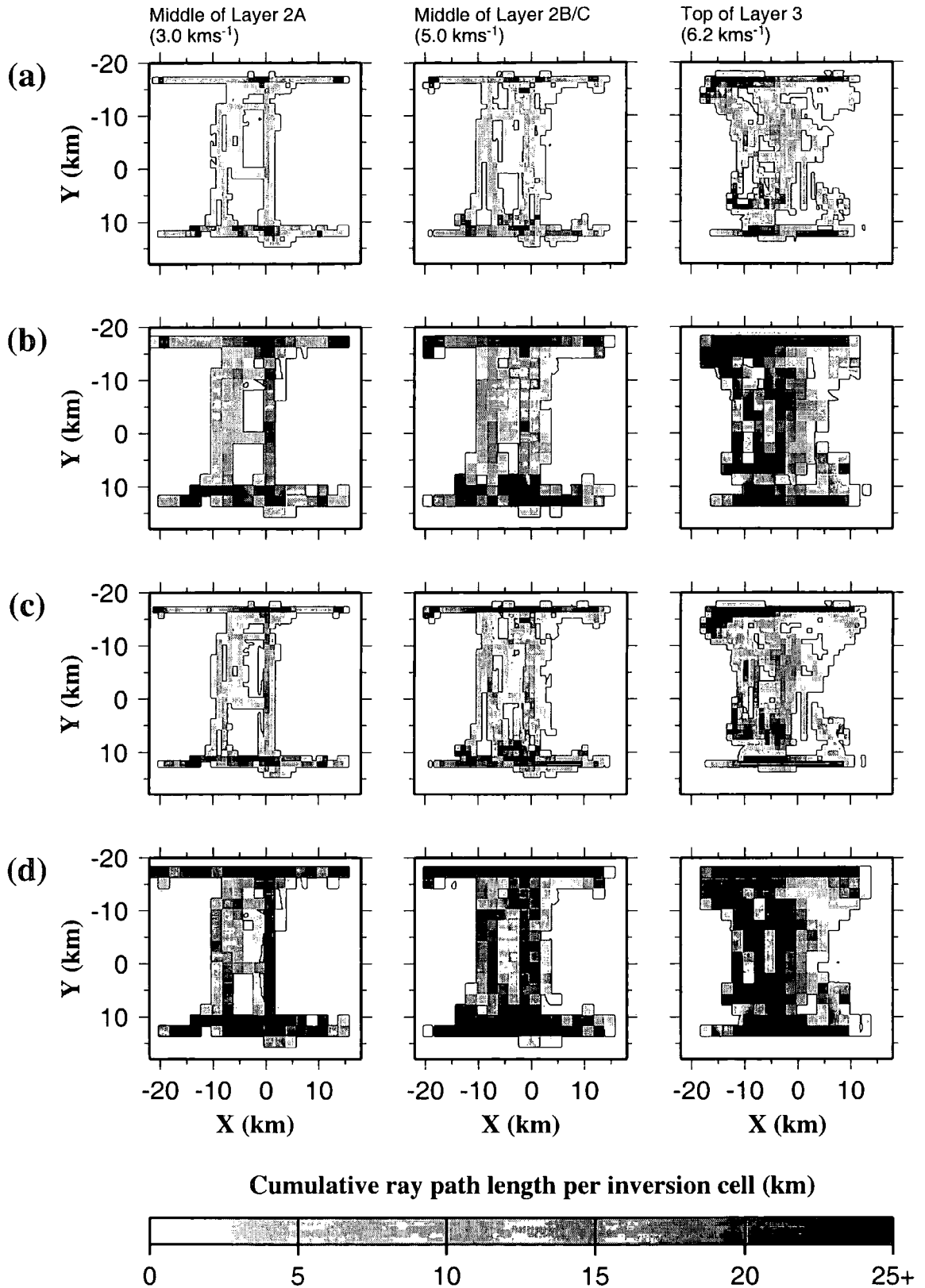


**Figure 3.2:** Velocity anomalies recovered by inversion using the *basic 1-D initial model* and inversion cell sizes of a)  $1.0 \times 1.0 \times 0.4$  km, b)  $2.0 \times 2.0 \times 0.4$  km, c)  $1.0 \times 1.0 \times 0.8$  km, and d)  $2.0 \times 2.0 \times 0.8$  km. The resulting velocity anomaly relative to the initial model is plotted for the 3.0, 5.0 and 6.2  $\text{kms}^{-1}$  planes of the initial model. OBS locations (white triangles) and ship tracks (white lines) are shown on the 3.0  $\text{kms}^{-1}$  plane plot in a) and apply to all plots. Bathymetric contours at 0.25 km intervals are plotted in black. All models show similar anomaly fields, but the magnitude of the recovered anomalies is generally larger for inversions performed using a 2.0 km horizontal cell size than for a 1.0 km horizontal cell size.



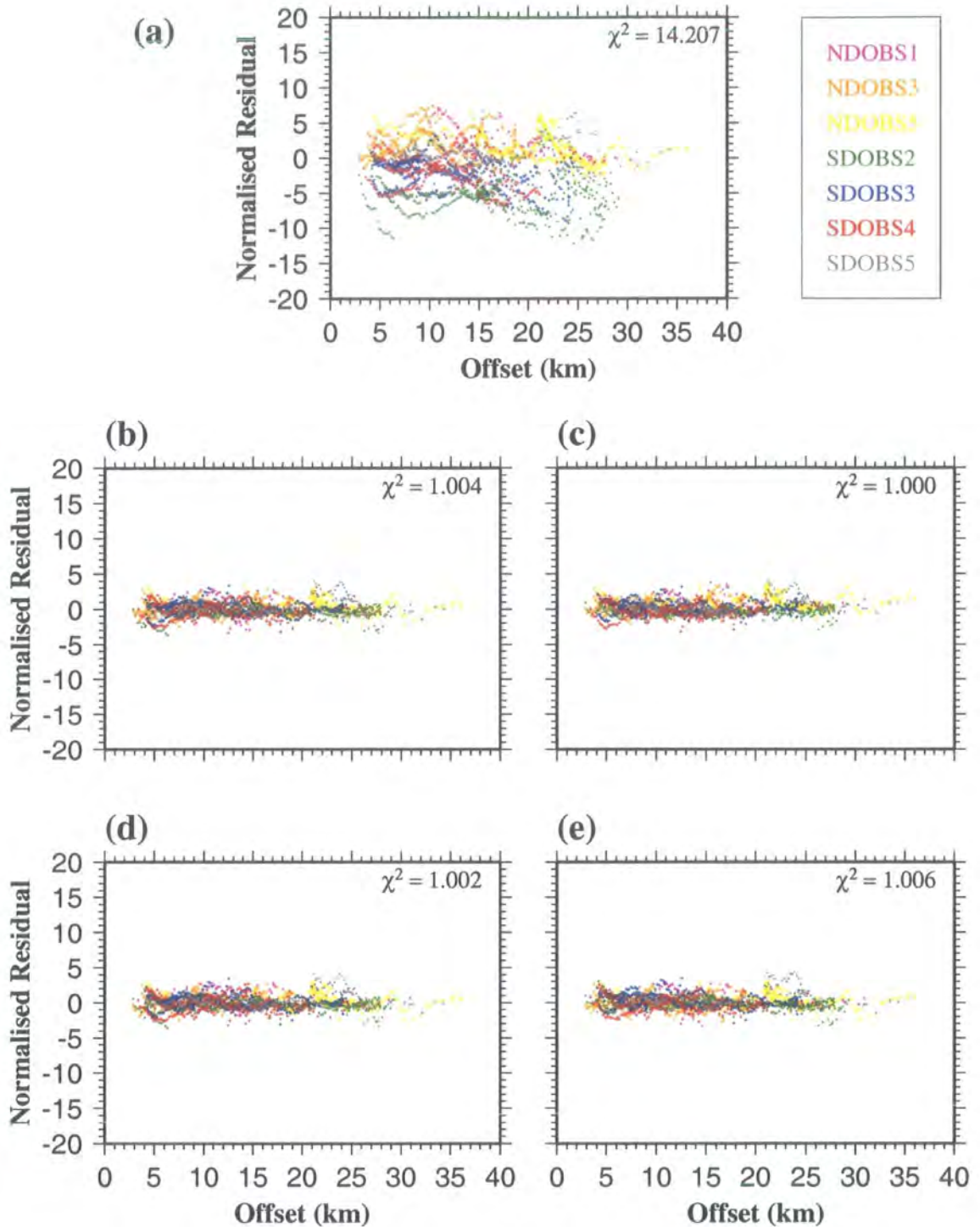
velocity planes at 3.0, 5.0 and 6.2  $\text{kms}^{-1}$ , which correspond to approximate depths of 0.7 km (the middle of crustal layer 2A), 2.2 km (the middle of layer 2B/C) and 3.5 km (near the top of layer 3) below the seafloor respectively (see Fig. 2.25). Bathymetric contours at 0.25 km intervals have been overlain on each plot to illustrate how each anomaly relates to features on the seafloor. Two iterations of the inversion were required to obtain the models shown in Figs. 3.2a and 3.2c, and five iterations were required to obtain the models shown in Figs. 3.2b and 3.2d. Ray coverage for each horizontal cell size is shown in Fig. 3.3 for the same planes as in Fig. 3.2. Fig. 3.3 shows that ray coverage is discontinuous and there are many isolated unsampled inversion cells when the smaller inversion cell sizes are used which correlate with anomalies in Fig. 3.2. However, the anomaly plots in Fig. 3.2 show positive and negative anomalies in similar places. Comparison with Fig. 2.31, which shows lateral anomaly resolution, indicates that none of the anomaly plots contain features which are beyond the resolution of the inversion method. The resolution plots shown in Fig. 2.31 were derived using a  $1.0 \times 1.0 \times 0.4$  km inversion cell size, for which the potential problem of cells remaining unsampled due to the discontinuous ray coverage is most acute. The relatively smooth appearance of this resolution plot, plus the similarity in size and position of anomalies resolved using all inversion cell sizes, suggests that model resolution is dominantly a function of ray coverage and data uncertainty rather than the cell size used to perform the inversion. Inspection of Figs. 3.2 and 3.3 suggests that groups of unsampled inversion cells which are much smaller than the lateral model resolution do not significantly affect the final anomaly distribution.

Fig. 3.4 shows plots of the normalised residual versus shot–receiver offset for each first arrival time observation used in the inversion, for the *basic 1-D initial model* and each of the final models in Fig. 3.2. Normalised residual is defined as the travel time residual divided by its associated uncertainty, which in the case of the inversions considered in this chapter is the two standard deviation uncertainty as discussed in section 2.6. The normalised  $\chi^2$  value indicated in each part of Fig. 3.4 is the mean square normalised residual (see equation 2.18). Fig. 3.4 shows that normalised residuals are generally much smaller at all shot–receiver offsets for the final models (Figs. 3.4b–e) relative to the initial model (Fig. 3.4a). This observation demonstrates



**Figure 3.3:** Cumulative ray path length per inversion cell in the initial model for the 3.0, 5.0 and 6.2 km s<sup>-1</sup> constant velocity planes for the *basic 1-D initial model* and inversion cell sizes of a)  $1.0 \times 1.0 \times 0.4$  km, b)  $2.0 \times 2.0 \times 0.4$  km, c)  $1.0 \times 1.0 \times 0.8$  km, and d)  $2.0 \times 2.0 \times 0.8$  km. The solid contour denotes the edge of the sampled volume. Note that when a horizontal cell size of 1.0 km is used (parts a) and c)) there are many more isolated unsampled cells than when a horizontal cell size of 2.0 km is used (parts b) and d)).





**Figure 3.4:** Plots of normalised residual against shot–receiver offset for each shot–receiver pair used in the VFR inversions, colour coded according to OBS location. Normalised residual is defined as the travel time residual divided by its associated uncertainty, and the  $\chi^2$  value indicated on each plot is the mean square normalised residual. Plots are shown for a) the *basic 1-D initial model*, described in section 2.8, and final models recovered by the inversion using inversion cell sizes of b)  $1.0 \times 1.0 \times 0.4$  km, c)  $2.0 \times 2.0 \times 0.4$  km, d)  $1.0 \times 1.0 \times 0.8$  km, and e)  $2.0 \times 2.0 \times 0.8$  km. Note that the normalised residuals are generally very much smaller for all the final models compared with the initial model, which implies that they are each a better representation of the velocity structure than the initial model. Also note that all the inversion cell sizes give similar normalised residual distributions.

that the final models produced by the inversion are all better representations of the velocity structure than the initial model. Furthermore the normalised residual distribution is similar for all of the final models, which indicates that none of the inversions have introduced bias with offset or instrument position when resolving travel time residuals.

Since all the models shown in Fig. 3.2 satisfy the data equally well, and the regularisation is targeted towards generating the smoothest model which satisfies the data within its errors, the horizontal cell size which results in the smoothest models was sought. Zelt & Barton (1998) quantified model structure by calculating the  $L_2$  norm of lateral model roughness,  $R$ , defined as

$$R = \sqrt{\frac{1}{M} \sum_{j=1}^M \left[ \frac{4v_j - v_j^{x-1} - v_j^{y-1} - v_j^{x+1} - v_j^{y+1}}{v_j} \right]^2}, \quad (3.1)$$

where  $M$  is the number of model nodes,  $v_j$  is the velocity at the  $j$ th node and  $v_j^{x-1}$ ,  $v_j^{y-1}$ ,  $v_j^{x+1}$  and  $v_j^{y+1}$  are the velocities at immediately adjacent model nodes in the  $x$  and  $y$  directions. Lateral model roughness was calculated for each of the models shown in Fig. 3.2. The results are summarised in Table 3.1.

Inversion Cell Size	Lateral Model Roughness ( $\times 10^{-2}$ )
$1.0 \times 1.0 \times 0.4$ km	1.106
$2.0 \times 2.0 \times 0.4$ km	1.185
$1.0 \times 1.0 \times 0.8$ km	1.044
$2.0 \times 2.0 \times 0.8$ km	1.321

**Table 3.1:** Lateral roughness, as defined by equation 3.1, for models generated by inversion using a variety of inversion cell sizes.

Comparing Fig. 3.2a with Fig. 3.2b and Fig. 3.2c with Fig. 3.2d shows that increasing the horizontal cell size results in larger magnitude anomalies in approximately the same positions as those obtained using the smaller horizontal cell size. This observation is substantiated by the lateral model roughness calculations shown in Table 3.1, which show greater roughness for the two models obtained using a

horizontal cell size of 2.0 km. Furthermore, inversions performed using a horizontal cell size of 2.0 km required five iterations to achieve convergence whilst only two iterations were required when the smaller horizontal cell size of 1.0 km was used. Therefore a horizontal cell size of 1.0 km was preferred for all subsequent inversions.

Comparing Fig. 3.2a with Fig. 3.2c and Fig. 3.2b with Fig. 3.2d suggests that changing the vertical inversion cell size has little effect on the final model produced by the inversion. Crustal layers 2A and 2B have average thicknesses of 1.2 km and 1.9 km respectively based on the 2-D modelling of Turner (1998). Since the inversion is primarily targeted towards resolving lateral velocity variations, a vertical cell size of 0.4 km was preferred as a larger vertical cell size might cause smoothing of the vertical structure which is known to exist. Hence, a cell size of  $1.0 \times 1.0 \times 0.4$  km was used for all subsequent inversions since, for this size, the inversion stabilises rapidly and results in a laterally smooth anomaly distribution whilst retaining the vertical structural complexities which are known to be present.

### 3.4 Preferred initial model

The inversion method calculates a velocity perturbation field relative to an initial model which best resolves the travel time residuals based on ray paths calculated for that initial model. This approach is based on a linearisation assumption which requires that the perturbed model is sufficiently similar to the initial model that the predicted first arrival ray paths through the perturbed and initial models are almost identical. Therefore only relatively small perturbations to the initial model may be determined. However, the non-uniqueness of the solution to the fundamental problem of first arrival seismic tomography, that of determining the velocity field from first arrival travel time data (expressed mathematically in equation 2.1), means that the inversion may converge to a mathematically acceptable solution even if there are gross errors in the initial model. Therefore it is essential that the initial model is a good representation of the true velocity structure in order to achieve inversion results which may be confidently interpreted in terms of the true geological structure. The refinements which were made to the *basic 1-D initial model* described in section 2.8 are investigated in this section.

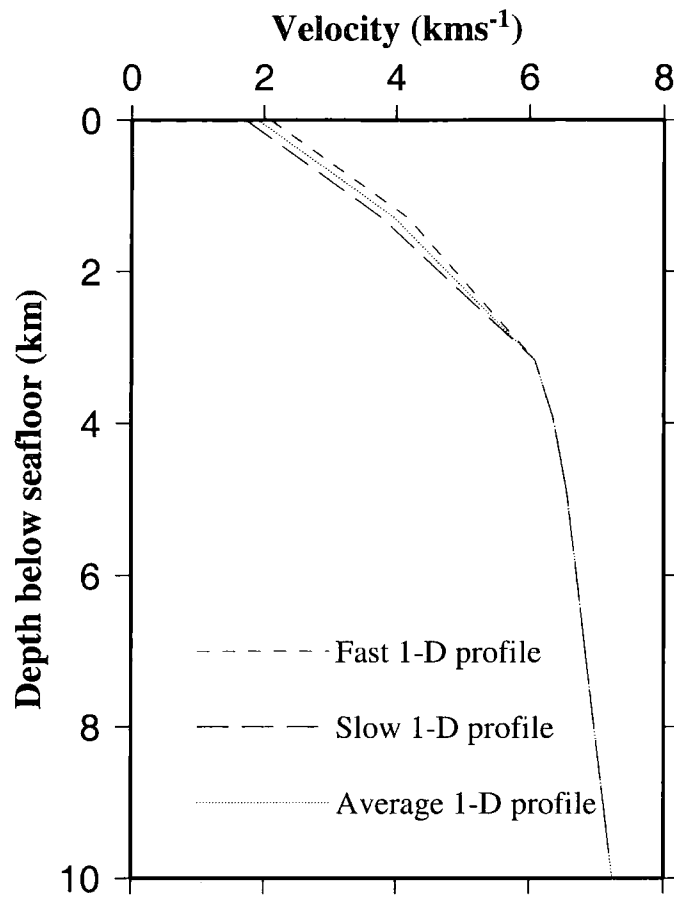
### 3.4.1 1-D initial models

Fig. 2.26 shows that ray coverage in the 3-D data volume is highly uneven and Fig. 2.31 illustrates the great variability in model resolution, particularly within layer 2. The primary aim of the experiment was to constrain the velocity structure at mid-crustal levels (layer 2B/C and the upper part of layer 3). The acquisition geometry was thus optimised for these target depths, and consequently anomaly resolution was expected to be poor at shallower depths. However, all rays which sample layer 2B/C and layer 3 also travel through shallow parts of the model. Therefore it is important that the velocity structure in areas of poor resolution is represented as accurately as possible so that anomalies resolved in areas of better resolution may be interpreted.

In order to investigate the sensitivity of the inversion results to layer 2 structure, the *basic 1-D initial model* described in section 2.8 was modified by increasing the velocity by 10% at the seafloor and 5% at the layer 2A–2B/C boundary. A further 1-D initial model was created with velocities decreased by the same proportions at these boundaries. The models were identical to the *basic 1-D initial model* at the layer 2B/C–3 boundary and greater depths. These models, hereafter referred to as the *fast* and *slow 1-D initial models*, were created using the method outlined in section 2.8 and the velocity–depth profiles described above and shown in Fig. 3.5.

The final models produced by the inversion routines using these initial models are shown in Fig. 3.6. Plots are shown as velocity anomalies relative to the relevant initial model for the same planes as in Fig. 3.2. It should be noted that due to the changes made to the 1-D velocity–depth profiles outlined above, these planes now represent different initial model velocities to those indicated in Fig. 3.2. As expected, the *fast 1-D initial model* requires dominantly negative velocity perturbations, and the *slow 1-D initial model* requires dominantly positive velocity perturbations to resolve the travel time residuals. The normalised residuals for the initial and final models, shown in Fig. 3.7, are consistent with the anomaly distributions produced by the inversion: the *fast 1-D initial model* shows predominantly positive residuals and the *slow 1-D initial model* shows predominantly negative residuals. Inspection of the normalised residual plots for the corresponding final models shows that this bias has largely been removed by the inversion.





**Figure 3.5:** 1-D velocity–depth profiles used to create the *fast* and *slow* 1-D initial models. The average 1-D profile, which was used to create the *basic* 1-D initial model, is shown for comparison.

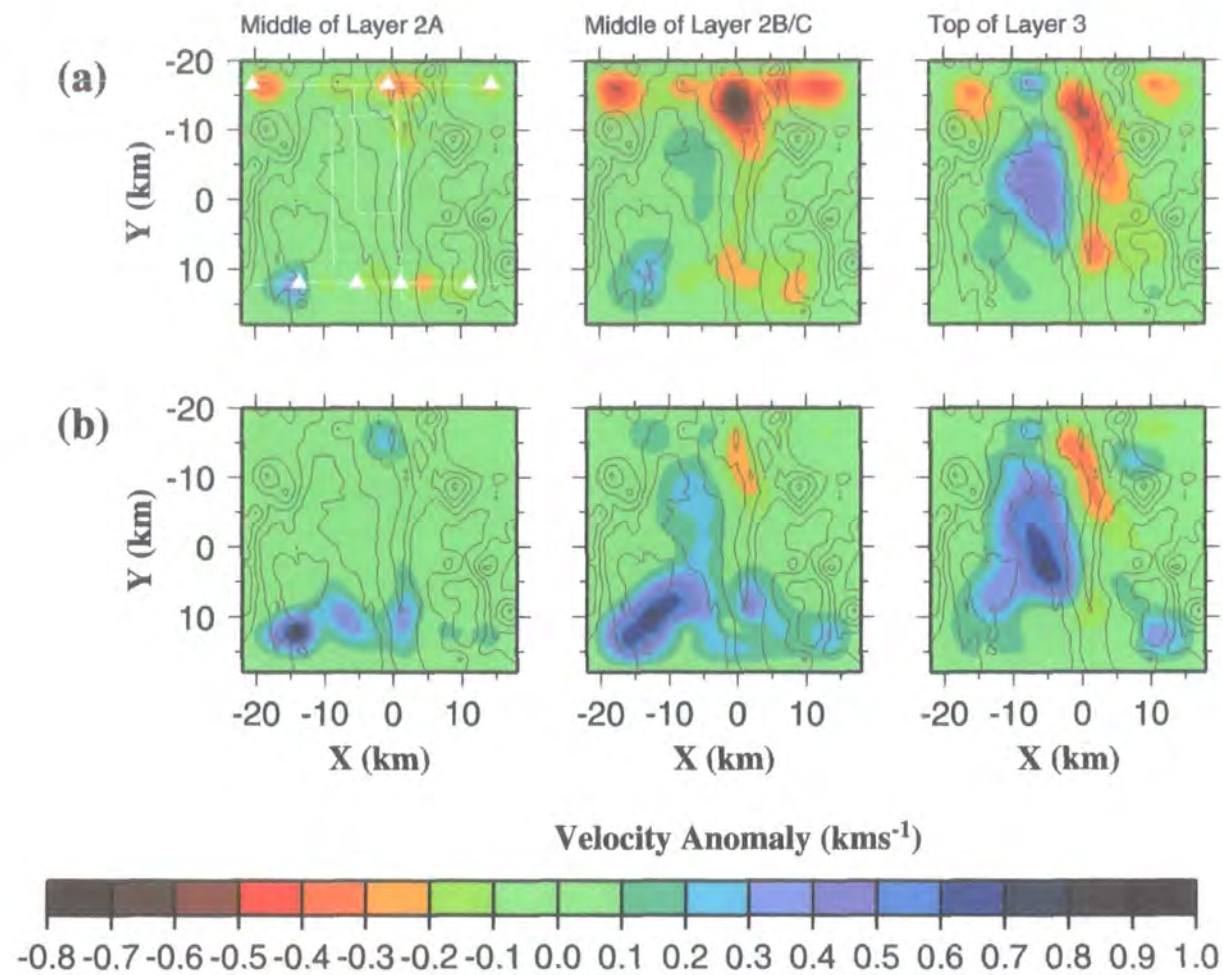


**Figure 3.6:** Velocity anomalies relative to the initial model recovered by inversion using a) the *fast 1-D initial model* and b) the *slow 1-D initial model*. Plots are shown for the same planes as in Fig. 3.2 and are similarly annotated. The *fast 1-D initial model* requires dominantly negative anomalies and the *slow 1-D initial model* requires dominantly positive anomalies to resolve the travel time residuals. However, note that the anomaly fields are different in layer 3 despite the fact that the *fast* and *slow 1-D initial models* are identical at this depth.

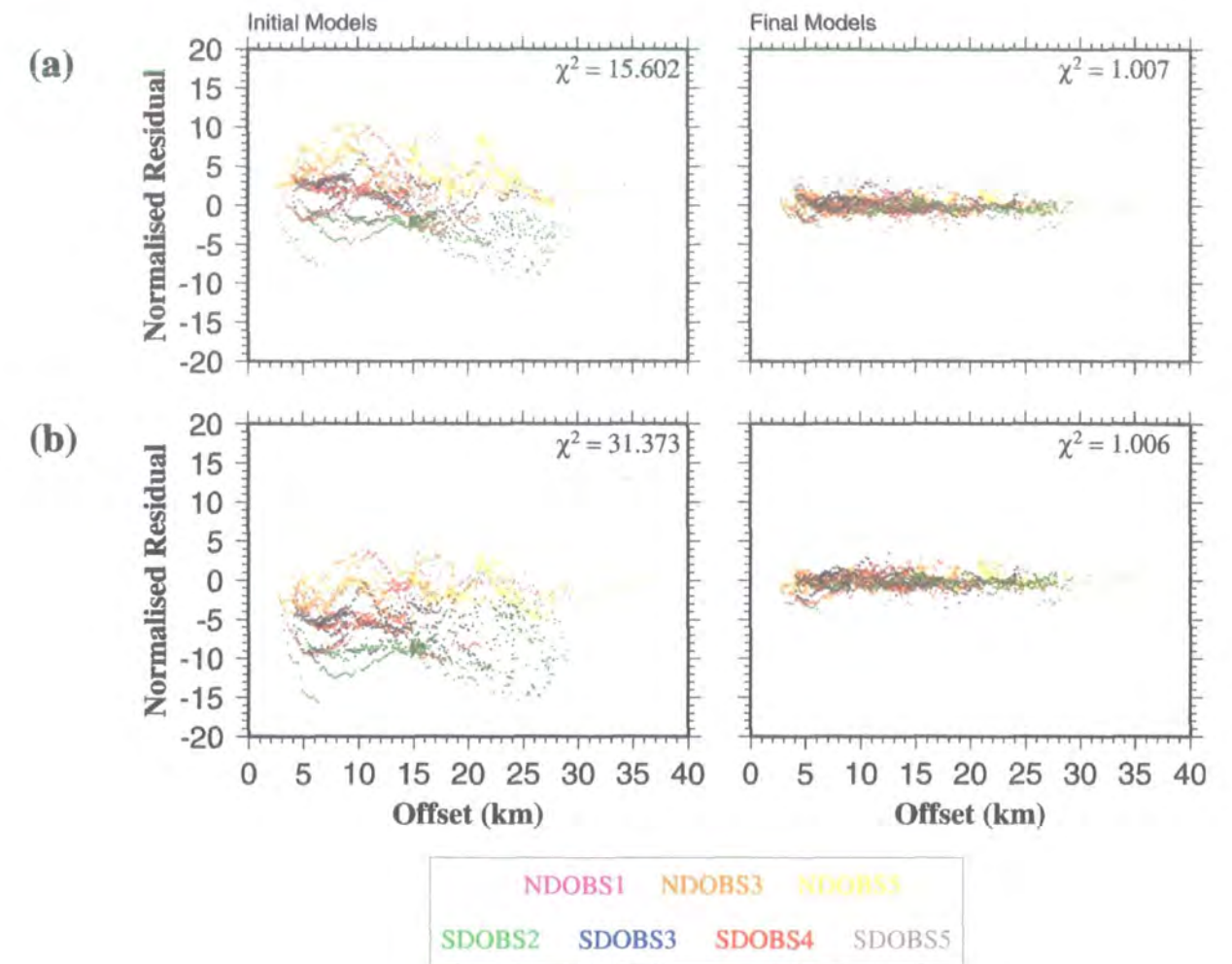


**Figure 3.7:** Plots of normalised residual against shot-receiver offset for each shot-receiver pair used in the inversion, colour coded according to OBS location, for a) the *fast 1-D initial model* and b) the *slow 1-D initial model*, and the models recovered by inversion using each of these initial models. The *fast 1-D initial model* shows dominantly positive normalised residuals, whilst the *slow 1-D initial model* shows dominantly negative normalised residuals. However, the normalised residual distributions for both final models indicate that the inversion has removed this bias.

The most noteworthy feature of the anomaly distributions shown in Fig. 3.6 is that they are markedly different from each other in layer 3, despite the fact that, at this depth, the initial models are identical. It is believed that this phenomenon arises primarily from the poor resolution at shallow–crustal levels, particularly in layer 2A as illustrated in Fig. 2.31. Fig. 3.1 shows that large numbers of rays are predicted to enter the crust in regions where no anomalies have been resolved, yet the velocities at the top of layer 2A differ by  $\sim 0.4 \text{ kms}^{-1}$  between the *fast* and *slow 1-D initial models*. Although this figure shows predicted rays for the *basic 1-D initial model*, the changes to this model are sufficiently small that the predicted seafloor ray entry points are likely to be almost identical for both the *fast* and *slow 1-D initial models*. Furthermore, comparing Fig. 3.6 with Fig. 2.31b shows that, in layer 2A, anomalies have only been resolved in the isolated areas of high lateral anomaly resolution. Hence, the component of travel time residuals arising from errors in the poorly sampled parts of layer 2 appears to be fit by anomalies incorporated into the better sampled parts of the model volume at greater depth. The layer 2 velocity structures represented by the *fast* and *slow 1-D initial model* are both reasonable given the extrusive nature of this layer. Analysis of lavas dredged from the VFR have shown that there are large variations in composition (Jenner *et al.* 1987; Frenzel *et al.* 1990; Vallier *et al.* 1991) and it is likely that there are significant variations in porosity arising from vesicularity of lavas and from faulting. Such variations would give rise to variations in layer 2A velocity, and it is likely that the layer 2A velocity structure is much more complex than it is possible to model using this dataset. These examples illustrate the importance of representing the velocity structure of the poorly resolved shallow parts of the model volume as accurately as possible in order to allow anomalies resolved at deeper levels arising from geological features to be distinguished from model artefacts arising from inadequate representation of shallow structure.

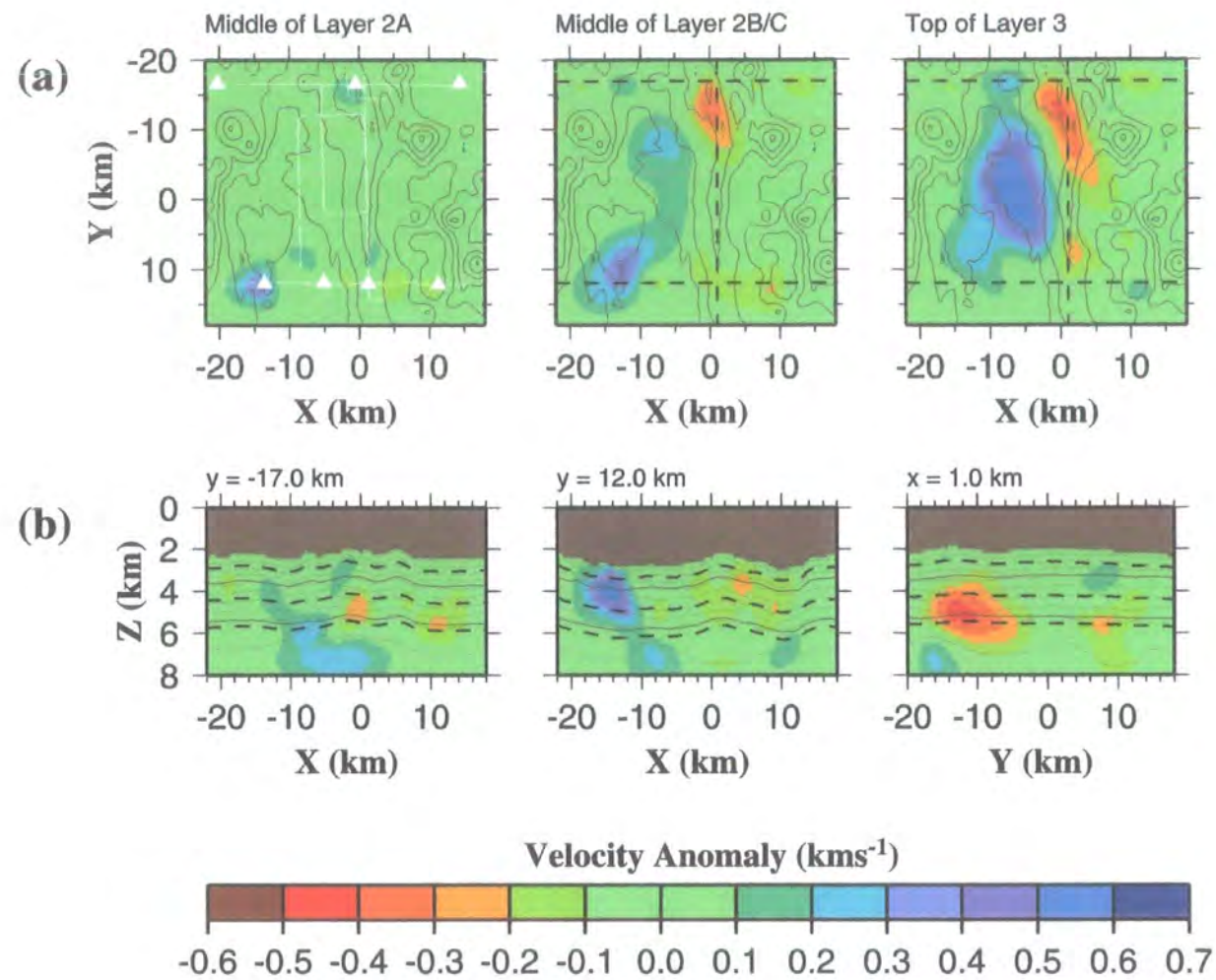
A second possible contributor to the difference in layer 3 anomaly distributions produced by inversions using the *fast* and *slow 1-D initial models*, is the difference in resolution in layer 2B/C and layer 3. Fig. 2.31 indicates that, in general, resolution is better in layer 2B/C than in layer 3. Therefore, the anomalies seen in layer 3 may, in part, arise from downward smoothing of anomalies in layer 2B/C above. This possibility will be investigated in section 3.8.

### 3.4.2 2-D initial model

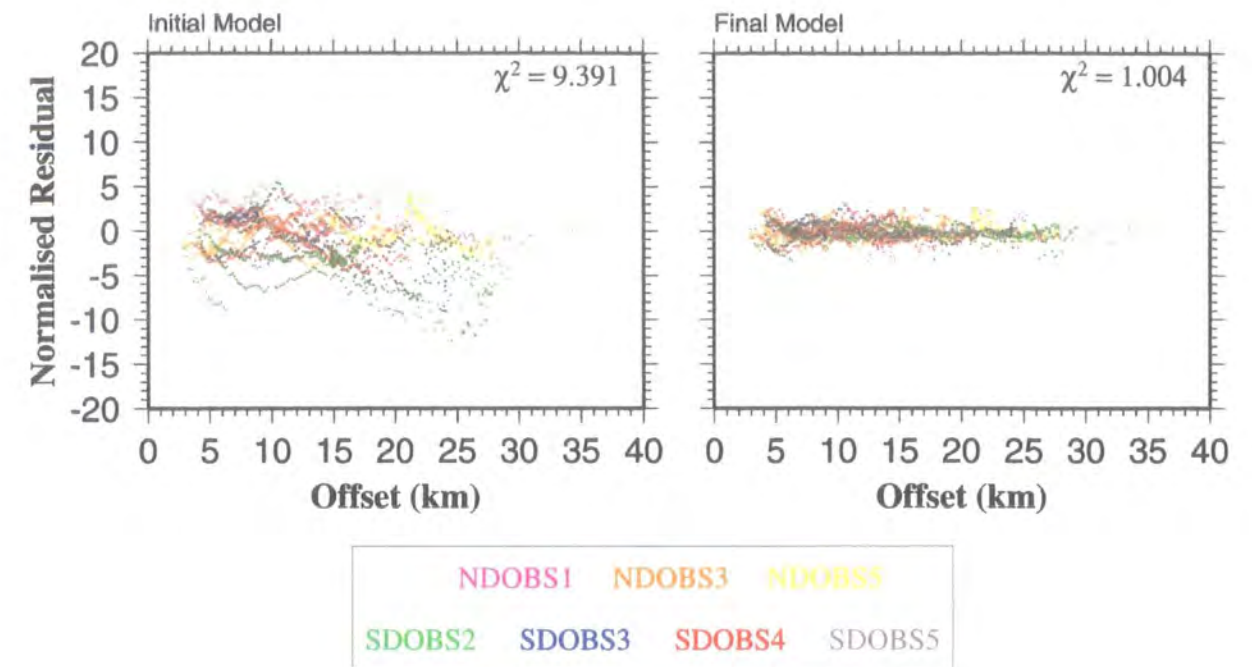
The anomaly fields shown in Figs. 3.2 and 3.6 exhibit more negative anomalies in the north of the study area than in the south, particularly so in layer 2. Furthermore, Fig. 2.23 shows that, at a given depth below the seafloor, the velocity in layer 2 is generally lower for the 1-D average of the *Seismic North* across-axis profile, which approximately corresponds to  $y = -17$  km in the 3-D study area, than for the 1-D average of the *Seismic South* across-axis profile, which approximately corresponds to  $y = 12$  km. This observation mirrors the anomaly patterns resolved by the inversion for the 1-D initial models, and suggests that a 2-D north-south varying initial model may better represent the velocity structure than a simple 1-D initial model. Therefore the *2-D initial model* was constructed using the basic method outlined in section 2.8. The vertical velocity structure was identical to the 1-D average of the *Seismic North* profile at  $y = -17$  km, and identical to the 1-D average of the *Seismic South* profile at  $y = 12$  km. The vertical velocity structure at all other  $y$ -positions was obtained by linear interpolation between these two end members.

Fig. 3.8a shows the final model resolved by inversion using the *2-D initial model*. Plots of the velocity anomalies relative to the *2-D initial model* for the same planes as in Fig. 3.2 are shown. Due to the north-south velocity variations described above, these are not planes of constant velocity in the *2-D initial model*. Three cross-sections through the model are shown in Fig. 3.8b, the planes of which are indicated in Fig. 3.8a. The north-south variation in the anomaly field is much less pronounced when the *2-D initial model* is used. Fig. 3.9 shows the normalised residuals for the *2-D initial model* and the final model produced by inversion using this initial model. Comparison of Figs. 3.9 and 3.4 shows generally smaller normalised residuals for the *2-D initial model* relative to the *basic 1-D initial model*, particularly at shot-receiver offsets of less than  $\sim 15$  km. Also, the normalised  $\chi^2$  for the *2-D initial model* is 9.391 compared with 14.207 for the *basic 1-D initial model*. These observations imply that the *2-D initial model* is a better representation of the velocity structure than any of the 1-D initial models. Moreover, the reduction in normalised residuals at small shot-receiver offsets suggests a particular improvement in shallow-crustal structure. Hence, even a crude attempt to model 2-D velocity variations in layer 2A produces better results than a 1-D approximation.





**Figure 3.8:** Velocity anomalies recovered by inversion using the 2-*D* initial model. a) Velocity anomalies relative to the 2-*D* initial model. Plots are shown for the same planes as in Fig. 3.2 and are similarly annotated. Dashed lines represent the locations of cross-sections shown in b). Note that the bias towards more negative anomalies in the north than the south of the study area, which was apparent for anomalies recovered using all the 1-*D* initial models, is less apparent in this figure. b) Cross-sections through the velocity anomaly field at the locations shown in a). Solid lines denote the seafloor and the layer 2A-2B/C and layer 2B/C-3 boundaries in the initial models. Dashed lines denote the planes of the plots shown in a).



**Figure 3.9:** Plots of normalised residual against shot-receiver offset for each shot-receiver pair used in the inversion, colour coded according to OBS location, for the 2-*D* initial model and the model recovered by inversion using this initial model. Note that the normalised residuals are generally smaller for the 2-*D* initial model at offsets  $< \sim 15$  km than for the basic 1-*D* initial model shown in Fig. 3.4a).

It is possible that the reduction in misfit occurs primarily because all the receivers and a significant proportion of shots lie close to  $y = -17$  km and  $y = 12$  km (i.e. along the *Seismic North* and *Seismic South* across-axis profiles). The mode of construction of the *2-D initial model* implies that it should represent the structure along these two lines better than the *basic 1-D initial model*. Hence, it is possible that the observed improvements in normalised misfit arise from reducing the misfit associated with shots near these lines rather than a general reduction in misfit for the whole model. In order to investigate this possibility, a subset of shot-receiver pairs with all those shots lying within 2.5 km of  $y = -17$  km and  $y = 12$  km removed was considered. Rays were traced through the *basic 1-D* and *2-D initial models* for this subset of shots, and the predicted ray paths are shown in Fig. 3.10 for the *basic 1-D initial model*. The normalised  $\chi^2$  for this subset of shot-receiver pairs is 19.858 for the *basic 1-D initial model* and 15.001 for the *2-D initial model*. Part of this reduction must result from better representation of the crustal velocity structure near each receiver position. However, it is unlikely that this could account for all of the improvement, especially since comparison of the initial model parts of Figs. 3.4 and 3.9 indicates a particular reduction in residuals for near-offset shots with a more modest reduction at longer offsets. Fig. 3.11 shows the normalised residual distribution for the subset of shot-receiver pairs in Fig. 3.10 traced through the *basic 1-D* and *2-D initial models*. This subset of shot-receiver pairs also shows a more marked reduction in normalised residuals for near-offset shots. Since this subset of shot-receiver pairs does not include any shots within 2.5 km of  $y = -17$  km and  $y = 12$  km, it appears that the *2-D initial model* is generally a better representation of the upper-crustal velocity structure across the whole model than the *basic 1-D initial model*. It should be emphasised, however, that the modelled velocity structure is probably an average of a much more complicated structure as pointed out in section 3.4.1 and by Turner (1998). There are likely to be lateral velocity variations present due to the extrusive nature of layer 2A which are unresolvable with this dataset.



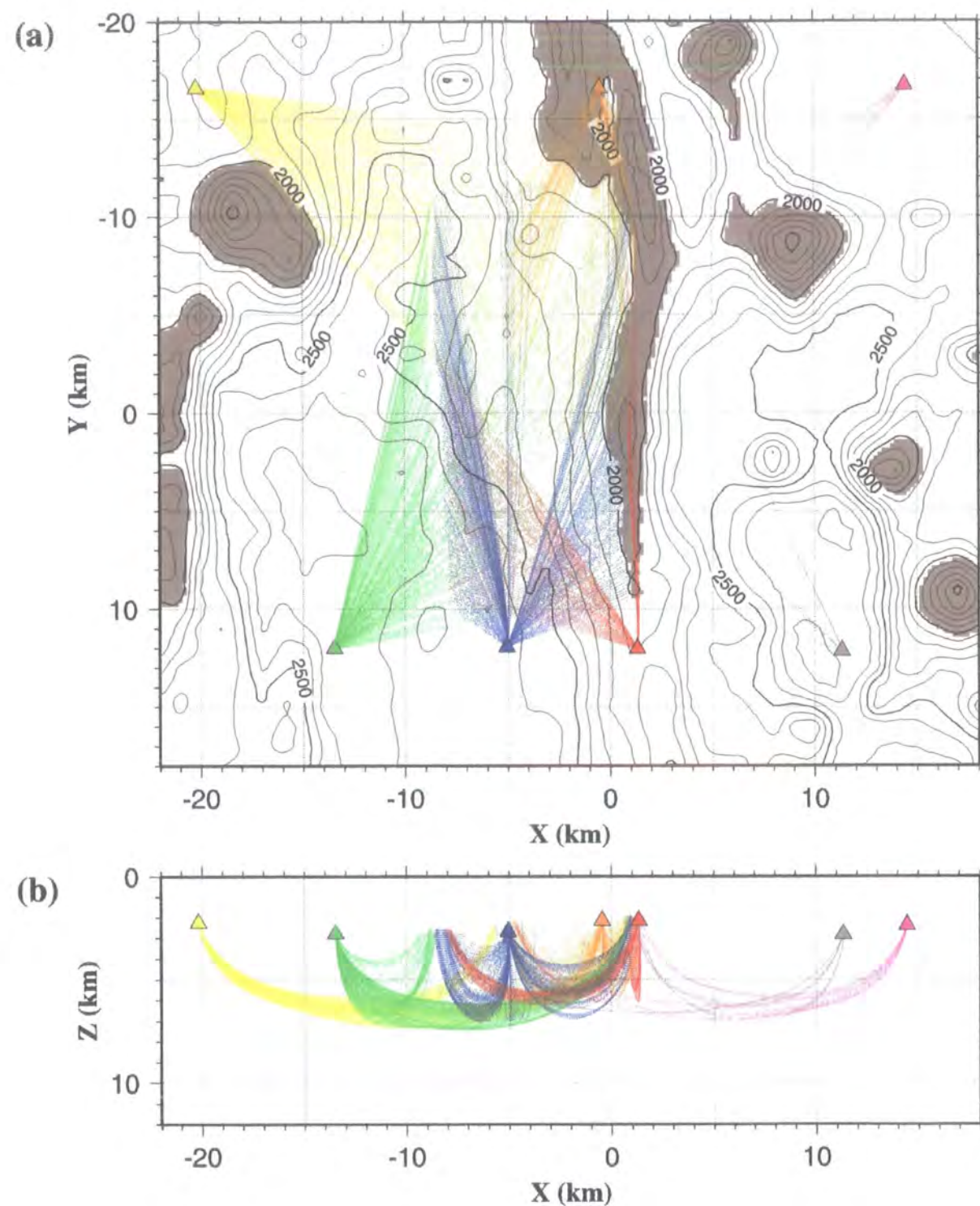


**Figure 3.10:** Crustal part of the predicted ray paths traced through the *basic 1-D initial model* for the subset of shot-receiver pairs used to determine whether the *2-D initial model* is generally a better representation of the upper-crustal structure than the *basic 1-D initial model* in a) plan view and b) cross-section parallel to the x-axis. All shots within 2.5 km of  $y = 12$  km and  $y = -17$  km have been removed. Bathymetric contours at 0.1 km intervals are shown in a), and bathymetry shallower than 2 km has been shaded. Coloured triangles denote OBS locations, with ray paths colour coded according to the OBS at which they were recorded.

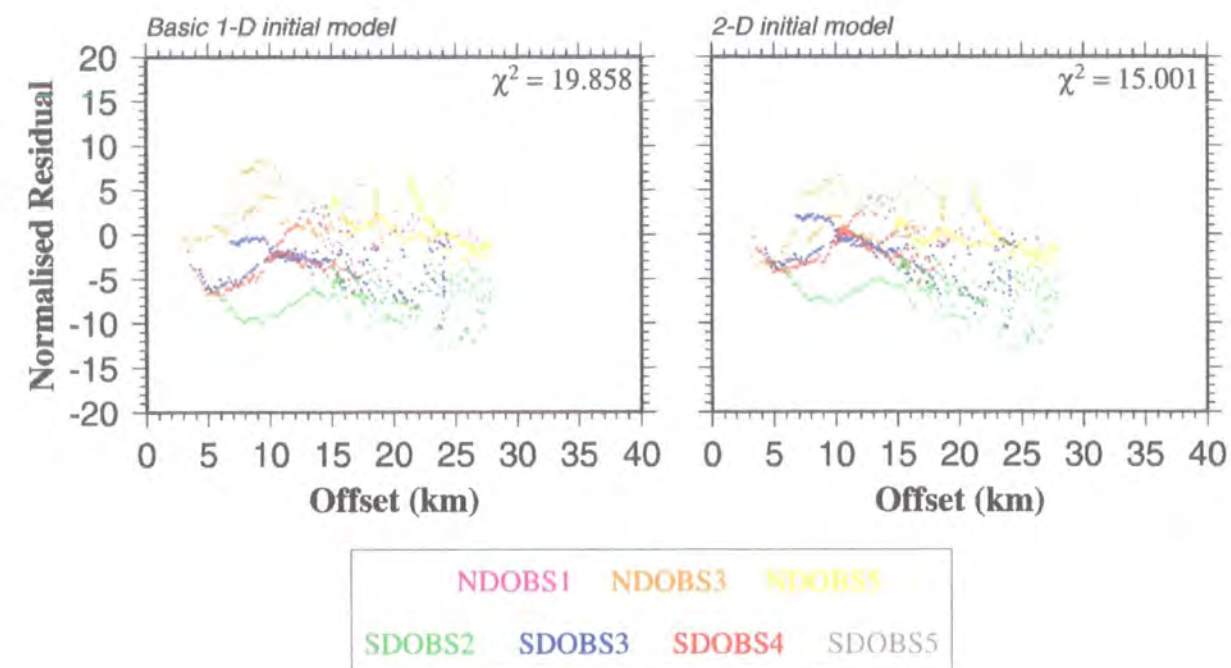


**Figure 3.11:** Plots of normalised residual against shot-receiver offset for the subset of shot-receiver pairs shown in Fig. 3.10, colour coded according to OBS location, for the *basic 1-D* and *2-D initial models*. Note that the normalised residuals are generally smaller for the *2-D initial model* at offsets  $< \sim 15$  km than for the *basic 1-D initial model*, a pattern similar to that observed for the full set of shot-receiver pairs. This observation suggests that the improvement in representation of the upper-crustal structure obtained by introducing 2-D north-south variation is not confined to the regions near the instrument deployment sites.

### 3.4.3 Unbiased 2-D initial model

As previously stated, the inversion algorithm can only resolve small perturbations relative to the initial model otherwise the linearisation assumption upon which it relies is not valid. Therefore an initial model which does not show any bias towards positive or negative anomalies at any depth is preferable in order to best satisfy this requirement. The averages of the anomaly fields resulting from inversions performed using the *basic 1-D* and *2-D initial models* are  $0.050 \text{ kms}^{-1}$  and  $0.058 \text{ kms}^{-1}$  respectively. These averages were calculated using only those parts of the anomaly field which lie within inversion cells which were sampled by rays for the relevant initial model. Inspection of Figs. 3.2a and 3.8 shows that, in layer 3, the anomalies are dominantly positive. In order to remove this bias, an initial model was created by adding an average of the anomaly distribution shown in Fig. 3.8 to the 2-D initial model using the method outlined below.

Since the preferred initial model incorporates 2-D north-south variation, an anomaly field was sought which also incorporated 2-D north-south variation. The anomaly distribution shown in Fig. 3.8 was divided into northern and southern halves at the  $y = -1 \text{ km}$  position. Each half of the anomaly distribution was averaged along planes separated by  $0.2 \text{ km}$  vertically, parallel to the smoothed bathymetry. Only inversion cells which were sampled by rays were considered, and where the average path length within inversion cells for a given plane was found to be less than  $1 \text{ km}$ , the average anomaly for that plane was set to zero. The  $1 \text{ km}$  threshold was arbitrarily chosen as an indication that a layer was poorly sampled in which case the average anomaly may be unrepresentative of the true structure. The resulting 1-D average velocity anomaly-depth profiles for both the northern and southern halves of the model are shown in Fig. 3.12. A 2-D average anomaly field was created with vertical structure identical to the northern average profile at  $y = -10.5 \text{ km}$  and the southern average profile at  $y = 8.5 \text{ km}$ . The vertical structure at all other  $y$ -positions was obtained by linear interpolation between these end members. The resulting average anomaly field was added to the *2-D initial model* to create the *unbiased 2-D initial model*.



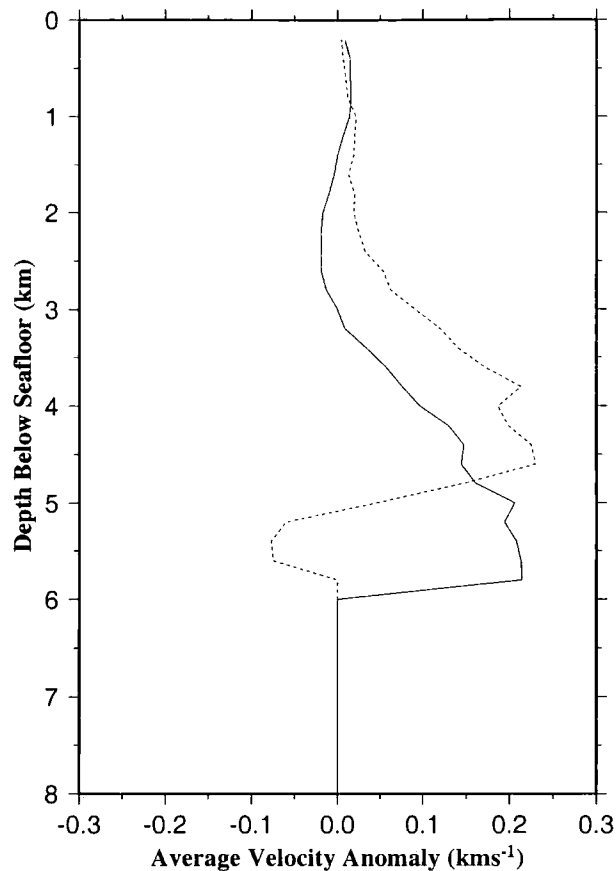


**Figure 3.12:** Average of the anomaly distribution shown in Fig. 3.8 plotted against depth beneath the seafloor for those parts of the study area north (solid line) and south (dashed line) of  $y = -1$  km. Averaging was performed only for those parts of the model which were sampled by rays. The generally positive anomalies in layer 3 are reflected in these average profiles at  $\sim 3.5$ – $4.5$  km depth, especially for the southern average profile. The negative average anomaly deeper than 5 km below the seafloor arises from averaging poorly sampled cells located much deeper than the region of interest.

The final model resolved by the inversion using the *unbiased 2-D initial model* is shown in Fig. 3.13 as plots of the velocity anomaly relative to the *unbiased 2-D initial model* for the same planes as shown in Fig. 3.8. The apparent positive bias in the anomaly field at layer 3 depths is no longer present, and the anomaly field average has been reduced to  $-0.007$   $\text{kms}^{-1}$ . The normalised residuals for the *unbiased 2-D initial model* shown in Fig. 3.14 are similar to those shown in Fig. 3.9 for the *2-D initial model*. However, there has been a slight positive shift in the values of normalised residuals for the initial model at offsets greater than  $\sim 15$  km. The normalised  $\chi^2$  for the *unbiased 2-D initial model* is 9.351, which is less than that for the *2-D initial model*. These observations, together with the appearance of the anomaly distribution itself, suggest that the *unbiased 2-D initial model* is a better representation of the actual velocity structure than the *2-D initial model*. Therefore the *unbiased 2-D initial model* was used for all subsequent inversions described in this chapter.

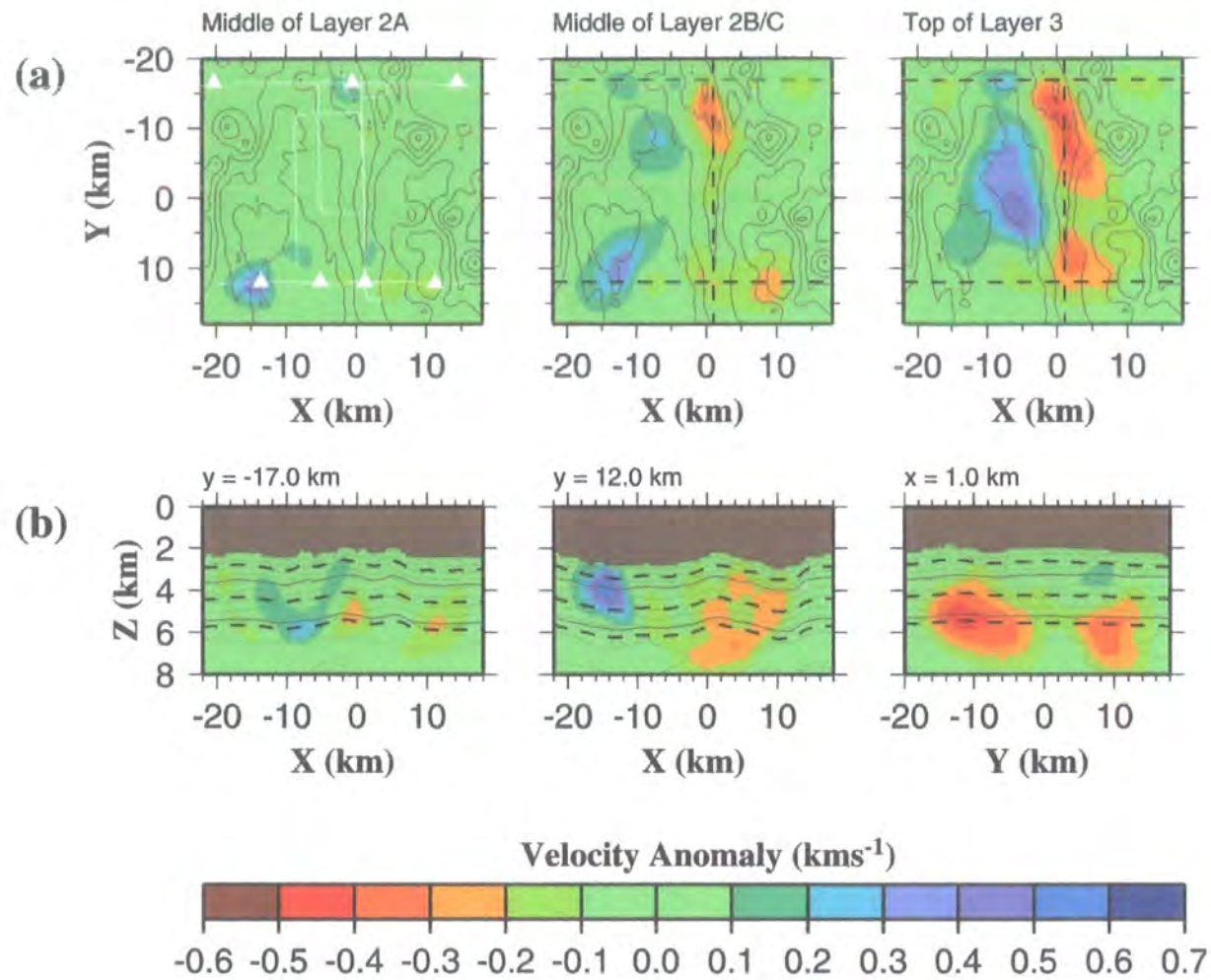


**Figure 3.13:** Velocity anomalies recovered by inversion using the *unbiased 2-D initial model*. a) Velocity anomalies relative to the *unbiased 2-D initial model* are shown for the same planes as in Fig. 3.8a and are similarly annotated. Note that the bias towards dominantly positive anomalies in layer 3, which was apparent in earlier inversion results, is no longer present. b) Cross-sections through the velocity anomaly field at the same locations and similarly annotated to those in Fig. 3.8b. The removal of positive bias at layer 3 depths has led to an increase in the magnitude of the axial negative anomaly shown on the  $x = 1.0$  km cross-section.

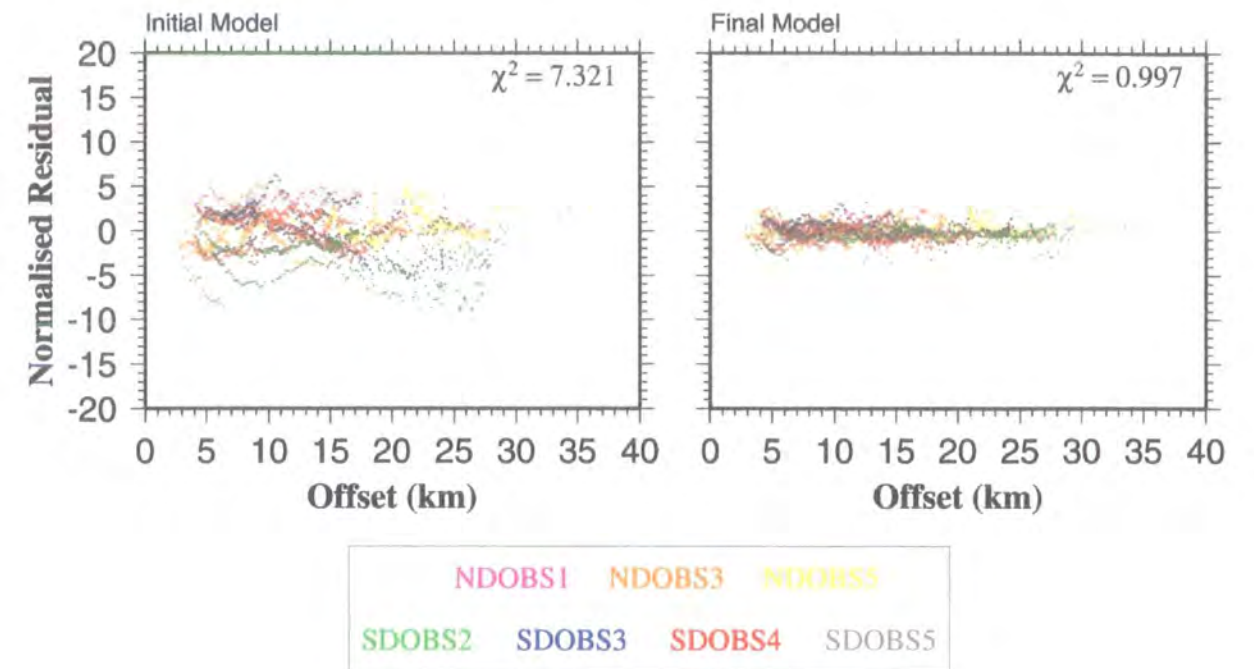


**Figure 3.14:** Plots of normalised residual against shot-receiver offset for each shot-receiver pair used in the inversion, colour coded according to OBS location, for the *unbiased 2-D initial model* and the model recovered by inversion using this initial model. Note the slight positive shift in normalised residuals at offsets  $> \sim 15$  km for the *unbiased 2-D initial model* compared to the equivalent distribution for the *2-D initial model* shown in Fig. 3.9, which results from the slightly higher velocities in layer 3 for the *unbiased 2-D initial model* relative to the *2-D initial model*.

### 3.5 Effect of the melt lens

The interaction of the wavefield with the axial magmatic system can be potentially problematic for seismic tomographic studies in a mid-ocean ridge environment. Wilcock *et al.* (1993) showed that in the presence of a sharp lateral velocity contrast associated with an axial melt lens at the EPR, diffracted arrivals which have travelled above and below the melt lens are observed. Wilcock *et al.* (1993) also showed that the first arrival changes abruptly from a diffraction above the melt lens to a diffraction below the melt lens which have very different ray paths. Therefore if these arrivals are misidentified the assumption that the predicted ray paths are close approximations to the true ray paths, upon which the inversion relies, may be violated.

A MCR has been mapped beneath the entire length of the CVFR (Collier 1990; Collier & Sinha 1992a) using seismic reflection data acquired during *RRS Charles Darwin* cruise CD34/88. This reflector was modelled by Collier (1990) with a width varying from 0.6 to 4.0 km (see Fig. 1.7) and at an approximately constant depth of 4.8 km below sea level, with prominent diffractions at the ends of the reflector signifying abrupt lateral termination. Collier (1990) interpreted this reflector as originating from a melt lens comprising a high percentage of partial melt located at the top of an axial magma chamber. This melt lens was modelled with a seismic velocity of  $3.0 \text{ km s}^{-1}$  to be consistent with laboratory measurements of the velocity of andesite melt (Murase & McBirney 1973). The vertical extent of the melt lens is believed to be very limited; modelling of coincident wide-angle seismic data by Turner (1998) indicated that the velocity must rise to at least  $\sim 5.5 \text{ km s}^{-1}$  0.25 km below the reflector. This structure is very similar to the EPR melt lens which was shown by Wilcock *et al.* (1993) to give rise to prominent diffracted arrivals in the wide-angle dataset they considered.

Fig. 3.15 shows detail of traces recorded by NDOBS5. The amplitude reduction between traces 245 and 249 is believed to be associated with rays which have travelled through the axial magma chamber based on the modelling of Turner (1998). There is no evidence of strong diffracted arrivals in this region which would be predicted by the model of Wilcock *et al.* (1993). Moreover, although an amplitude reduction is observed, the waveform appears to be approximately consistent with offset, which further suggests that the arrivals picked are refracted arrivals. These traces are typical of rays which have travelled through the axial magma chamber for all OBS locations, from which it may be concluded that there is no evidence of strong diffracted arrivals in the tomographic dataset considered in this study. The absence of diffracted



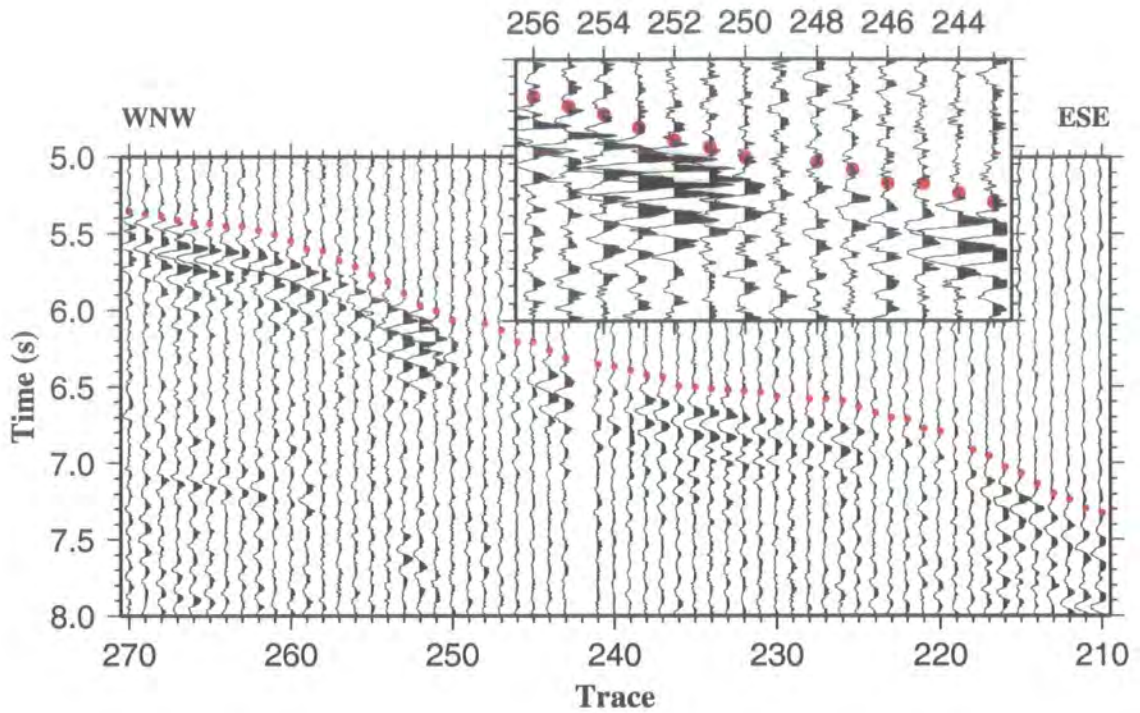


**Figure 3.15:** Example traces recorded by the vertical geophone of NDOBS5 showing first arrival travel time picks (centres of the red dots.) The traces correspond to shots at offsets of approximately 15 to 28 km along Line 6 (*Seismic North* – see Fig. 1.8). The inset shows detail of low amplitude arrivals associated with rays which have passed through the axial magmatic system. However there is no evidence of diffracted arrivals associated with rays passing close to the edge of the melt lens as predicted by Wilcock *et al.* (1993).

arrivals may reflect a more gradual velocity change at the edge of the melt lens rather than a sharp discontinuity as modelled by Wilcock *et al.* (1993). Alternatively diffracted arrivals may be present but are of such a low amplitude that they are not visible above the background noise.

Nevertheless, the large velocity contrast associated with the melt lens may influence refracted ray paths and travel times. Since the inversion method used in this study is unable to resolve such small features and abrupt changes in velocity, the melt lens must be incorporated into the initial model. This was achieved by establishing the  $x$  and  $y$  position of both lateral terminations of this reflector for each of the across-axis seismic lines modelled by Collier (1990) and shown in Fig. 1.7. The  $x$  position of both edges was determined at 0.2 km intervals in  $y$  (the node spacing of the forward grid) by linear interpolation. For each  $y$  position, the velocity of nodes lying between the melt lens limits at 4.8 km depth below sea level were set to  $3.0 \text{ km s}^{-1}$ , and the remaining nodes were left unaltered from the *unbiased 2-D initial model*. Collier (1990) and Collier & Sinha (1992a) modelled a complicated melt lens structure beneath the

northern OSC. Three separate melt lenses were modelled, one beneath each of the CVFR, NVFR and the overlap basin, although their spatial separation was close to the resolution limit of their seismic reflection data. However, Turner (1998) found that the EW9512 melt lens reflection data near the overlap basin could be modelled satisfactorily as a single body. Remodelling by Day (1997) of the Collier (1990) and Collier & Sinha (1992a) seismic reflection dataset suggests that the direct evidence cited for melt beneath the overlap basin is tenuous, and that it is impossible to distinguish between single and multiple melt lens models. Hence, for simplicity, the melt lens was modelled as a single body everywhere, and its extent is shown in Fig. 3.16.

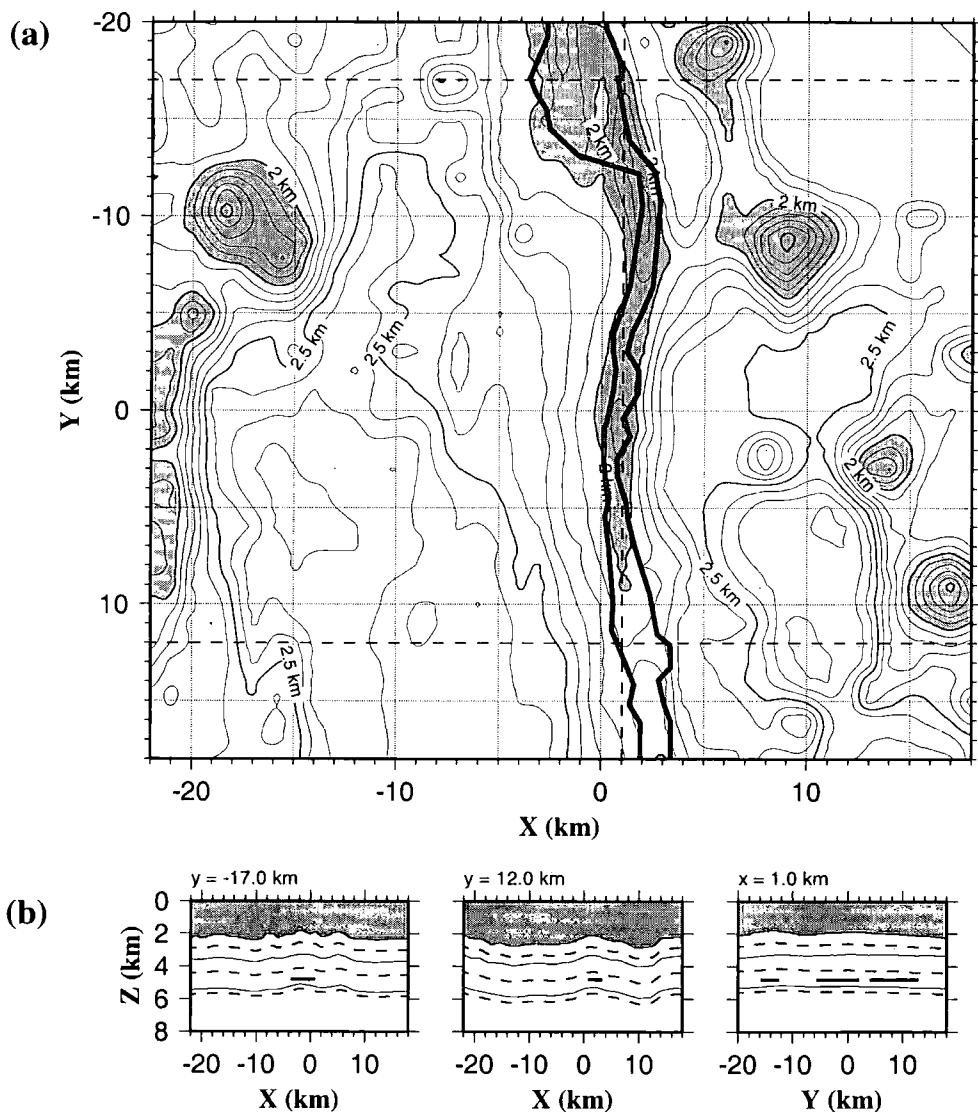


**Figure 3.16:** Melt lens extent within the 3-D study area in a) plan view overlain on the smoothed bathymetry and b) cross-section parallel to the dashed lines in a), which are the same cross-sections displayed for velocity anomaly fields in previous figures. Thick black lines denote the western and eastern edges of the melt lens as determined by Collier & Sinha (1992a) from modelling seismic reflection data acquired during cruise CD34/88. Bathymetric contours at 0.1 km intervals are shown in a) and regions shallower than 2 km have been shaded. The cross-sections in b) are annotated as in Fig. 3.8b.

When inversions were performed using this initial model, the resulting final model exhibits velocity anomalies centred on the location of the melt lens as shown in Fig. 3.17. Since the regularisation acts to create a smoothly varying velocity field, it is difficult to determine whether these anomalies result from geological features or are artefacts introduced by the regularisation to remove the sharp velocity contrast associated with the melt lens. In order to avoid this potential problem, the nodes corresponding to the melt lens were only set to  $3.0 \text{ km s}^{-1}$  during the forward modelling step so that predicted first arrival travel times and ray paths were calculated based on the assumption that a melt lens was present. These nodes were subsequently reset to their original values in the background model so that the inverse step was performed on a smoothly varying model and regularisation artefacts avoided. This approach is valid because the melt lens is very much smaller than the scale of features which may be resolved by the inversion.

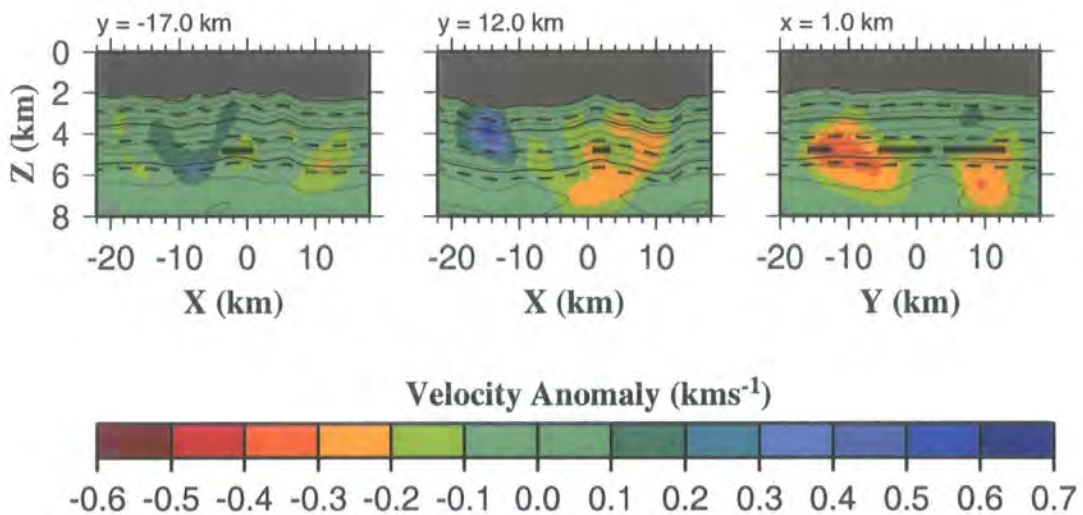


**Figure 3.17:** Cross-sections through the anomaly field recovered by the inversion using the *unbiased 2-D initial model* with the melt lens explicitly included, annotated as in Fig. 3.8b. The thick black lines denote the extent of the melt lens. Note that the axial negative anomaly in the north of the study area is centred on the melt lens, and therefore may be a regularisation artefact.

The final model obtained from inversion using the *unbiased 2-D initial model*, with the melt lens explicitly included as outlined above, is shown in Fig. 3.18 as plots of the velocity anomaly relative to the *unbiased 2-D initial model* for the same planes as shown in Fig. 3.8. Comparing Fig. 3.18b with Fig. 3.17 shows that the two models are almost identical, which suggests that the regularisation does not introduce any artefacts near the melt lens. The normalised error distribution, shown in Fig. 3.19, is almost identical to that of the *no melt lens unbiased 2-D initial model* shown in Fig. 3.14, and



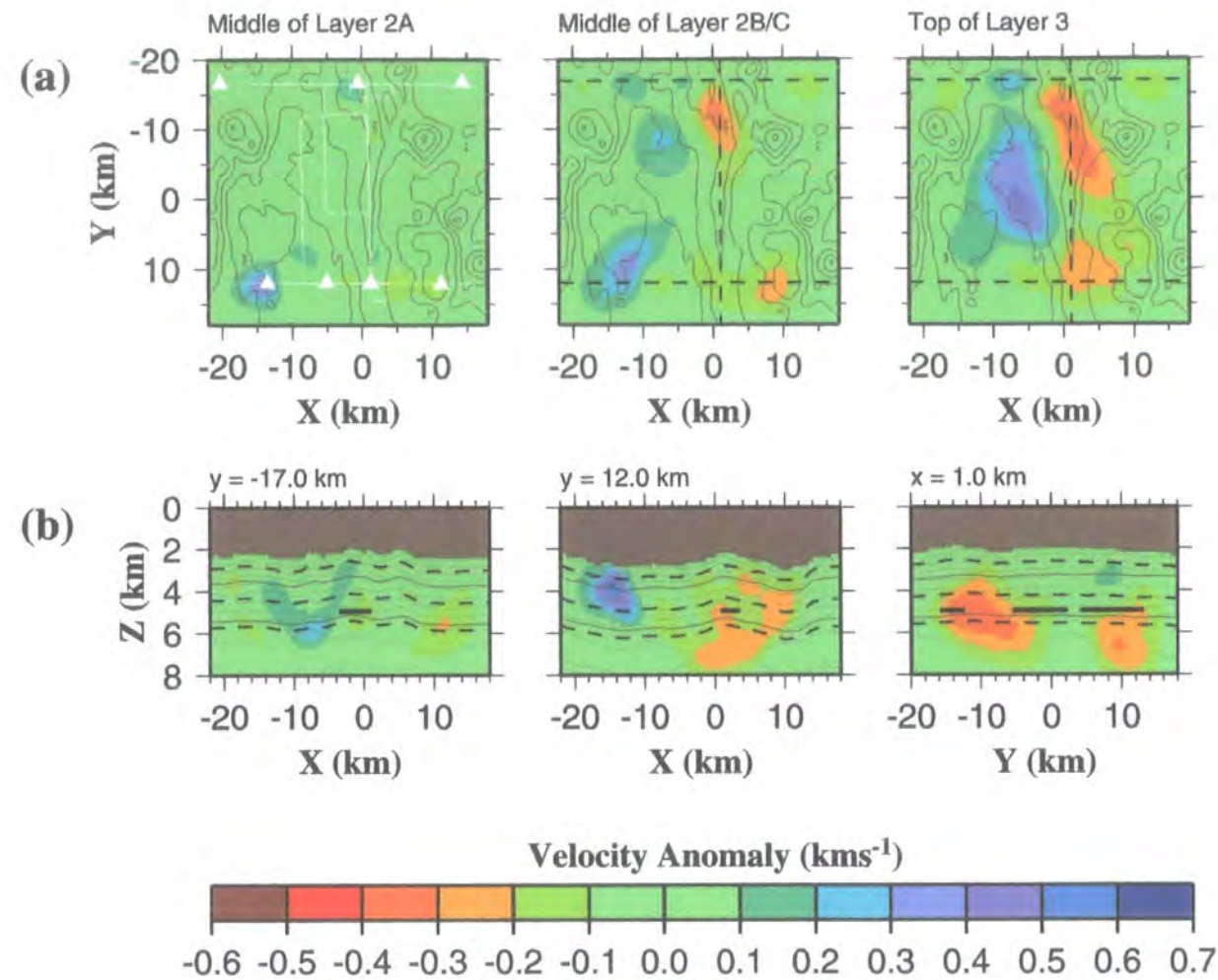


**Figure 3.18:** Velocity anomalies recovered by inversion using the *unbiased 2-D initial model* with the melt lens explicitly included for the forward modelling step only. a) Velocity anomalies relative to the *unbiased 2-D initial model* are shown for the same planes as in Fig. 3.8a and are similarly annotated. Note that the magnitude of the axial negative anomaly in layer 3 is smaller than in Fig. 3.13a where the melt lens was not explicitly included. b) Cross-sections through the velocity anomaly field at the same locations as in Fig. 3.8b and similarly annotated. The thick black lines denote the extent of the melt lens. Note that the model is almost identical to Fig. 3.17 which suggests that the axial negative anomaly in layer 3 is not a regularisation artefact.

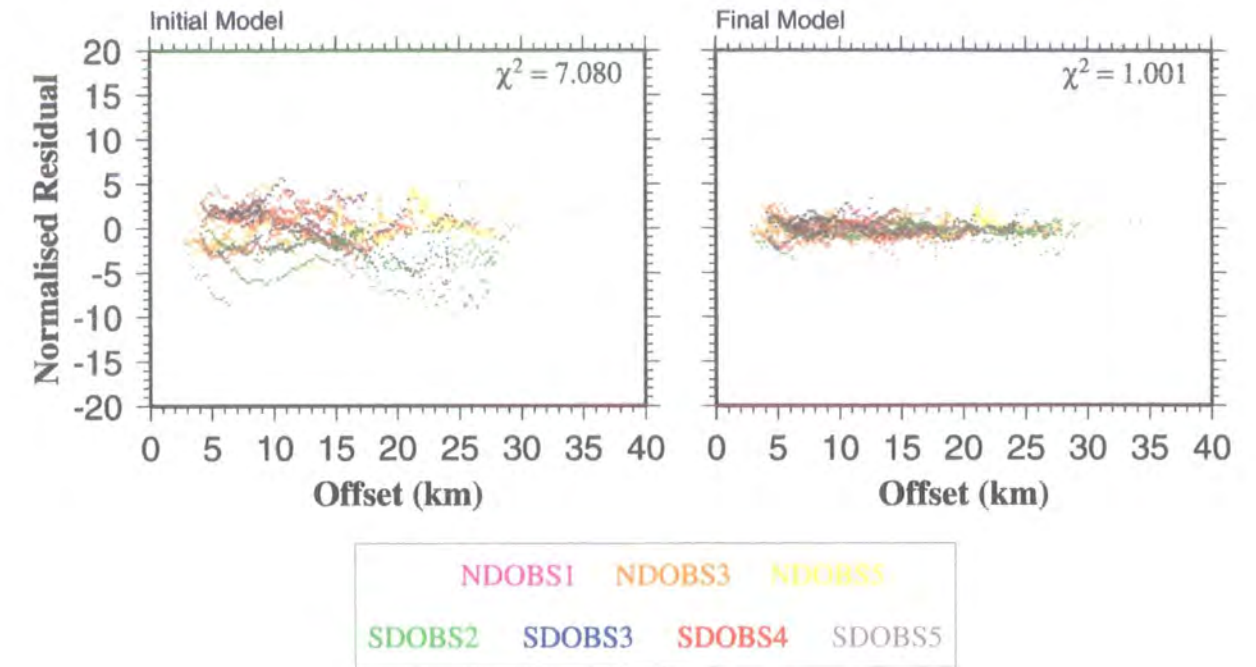


**Figure 3.19:** Plots of normalised residual against shot-receiver offset for each shot-receiver pair used in the inversion, colour coded according to OBS location, for the *unbiased 2-D initial model* with the melt lens explicitly included, and the model recovered by inversion using this initial model with the melt lens explicitly included at the forward modelling stage only. This figure is almost identical to Fig. 3.14 (melt lens not included), which shows that the melt lens has only a very small effect on the overall normalised residual distribution.

comparison of Fig. 3.18 with Fig. 3.13 further shows that inclusion of the melt lens has only a small effect on the appearance of the final model. Inclusion of the melt lens has resulted in a very slight reduction in normalised  $\chi^2$  from 7.321 to 7.080 for the *unbiased 2-D initial model*. The most noticeable change in the anomaly distribution is the slightly smaller magnitude of the on-axis negative anomaly in layer 3. This reduction probably results from deviation of ray paths which are predicted to sample the area beneath the melt lens to greater depths by its velocity field thus leading to an increase in the predicted travel times for these rays. The inversion results described previously imply the presence of an axial low velocity region in layer 3. An increase in the predicted first arrival travel times for rays sampling this region will lead to a reduction in the magnitudes of the positive travel time residuals associated with these rays. Hence the magnitude of the negative anomaly required to fit these residuals will also be reduced.

### 3.6 Effect of a rough seafloor

The rough bathymetry at mid-ocean ridges is potentially problematic for seismic experiments since the interaction of the wavefield with the seafloor is very complex. Significant scattering can occur with consequent loss of amplitude of the transmitted energy and arrivals with complex propagation paths which are not easily modelled may be present in the data. The particular problem for seismic tomography is the possibility that the predicted seafloor ray entry point, calculated on the assumption of an infinitely thin ray, may not be representative of the path taken by energy in the Earth due to this complex interaction. The inverse method assumes that the predicted ray paths are a close approximation to the true ray paths. If there are significant errors in the seafloor ray entry point, this assumption will be violated. In a tomographic study at the JDFR, Sohn *et al.* (1997) showed that, in the presence of rough bathymetry, the effective seafloor ray entry point may be significantly deviated and can make a substantial contribution to data uncertainty. In this study the problem of rough bathymetry was partially accounted for by applying a 1.0 km square smoothing filter to the swath bathymetry data when constructing the initial model as described in section 2.8. This smoothing filter represents the approximate size of the footprint of the wavefront at the seafloor. In this section, the distribution of travel time residuals is investigated to establish whether or not there is a relationship between large travel time residuals and rough seafloor.



The raw, unsmoothed bathymetry data were transformed onto a linear grid with 0.2 km spacing in both x and y corresponding to the node spacing of the forward grid, and hence the accuracy to which the seafloor ray entry point may be determined, and the gaps in coverage filled by finding a best fitting surface to the available data. The seafloor roughness at each grid point,  $R_{ij}$ , was defined using the finite difference 2-D Laplacian operator

$$R_{ij} = \frac{\partial^2 z_{ij}}{\partial x^2} + \frac{\partial^2 z_{ij}}{\partial y^2} = \frac{z_{i+1,j} + z_{i-1,j} + z_{i,j+1} + z_{i,j-1} - 4z_{ij}}{\Delta h}, \quad (3.2)$$

where  $z_{ij}$  is the depth at point  $x = i$ ,  $y = j$ , and  $\Delta h$  is the grid spacing (0.2 km in this case). This formula provides a crude measure of seafloor roughness on a 0.2 km scale, and smaller irregularities will not be detected. Given that the footprint of the seismic wavefront at the seafloor is of radius 0.506–0.728 km (see section 2.8) and the node spacing of the raw bathymetry grid is  $\sim 0.185$  km (0.1'), 0.2 km was felt to be an appropriate grid spacing for considering possible errors in seafloor ray entry point. A grid spacing smaller than the footprint of the seismic wavefront was required since the aim of this analysis was to detect possible errors in predicted seafloor ray entry point due to the approximation of an infinitely thin ray path and a grid size smaller than 0.2 km would be beyond the resolution of the raw bathymetry data. The seafloor roughness calculated using this formula is shown in Fig. 3.20 with bathymetric contours overlain to correlate the pattern with the actual seafloor. This figure shows that the roughest areas are associated with the ridge system and seamounts as would be expected, with large positive roughness associated with the ridge crest and top of seamounts and large negative roughness associated with basins.

In order to determine whether rough seafloor affects the travel time residual, rays were traced through the final velocity model determined by inversion using the *melt lens unbiased 2-D initial model* as shown in Fig. 3.18. This model was used as it is considered to be the best representation of the true velocity structure. The seafloor ray entry point was determined for each ray by finding the first point on the ray path traced from shot to receiver which lies beneath the seafloor, and the seafloor roughness at this point was extracted from the grid shown in Fig. 3.20. The seafloor roughness at the ray entry point was then compared with the normalised residual for each ray. Following Bazin *et al.* (2001) each normalised residual was adjusted by subtracting the mean normalised residual for all arrivals at the OBS location at which the arrival was

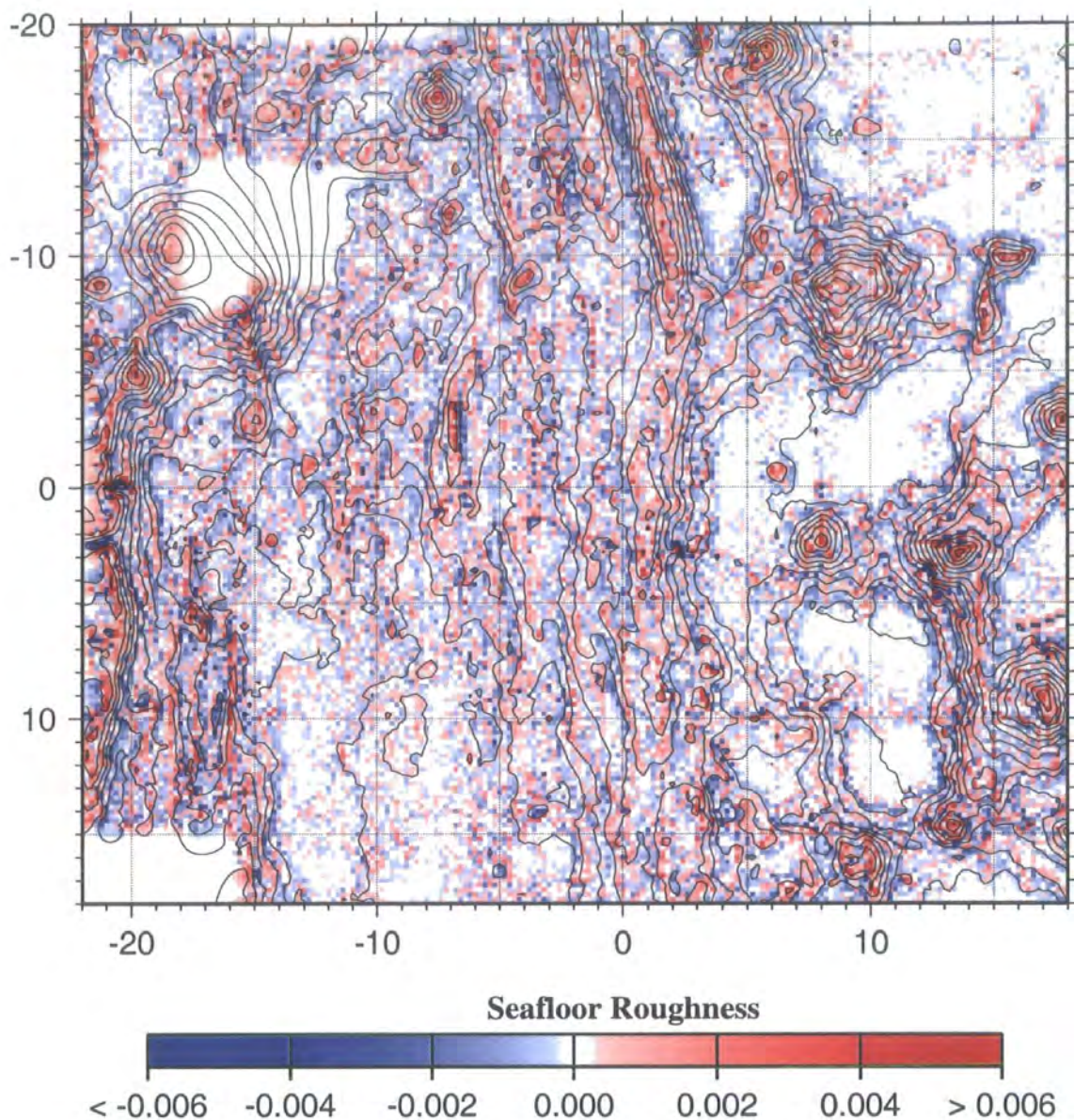


**Figure 3.20:** Seafloor roughness as defined by equation 3.2, with bathymetric contours at 0.1 km intervals overlain. This measure of roughness detects features on the scale of the gridding interval (0.2 km). Note that the tops of seamounts and the ridge crest have large positive roughnesses and basins (e.g. the overlap basin) have large negative roughnesses.

recorded in order to remove any bias which might be introduced due to inadequate representation of crustal structure near OBS locations. The resulting unbiased normalised residuals are shown in Fig. 3.21 plotted against seafloor roughness at the ray entry point determined using equation 3.2, and colour coded according to instrument position.



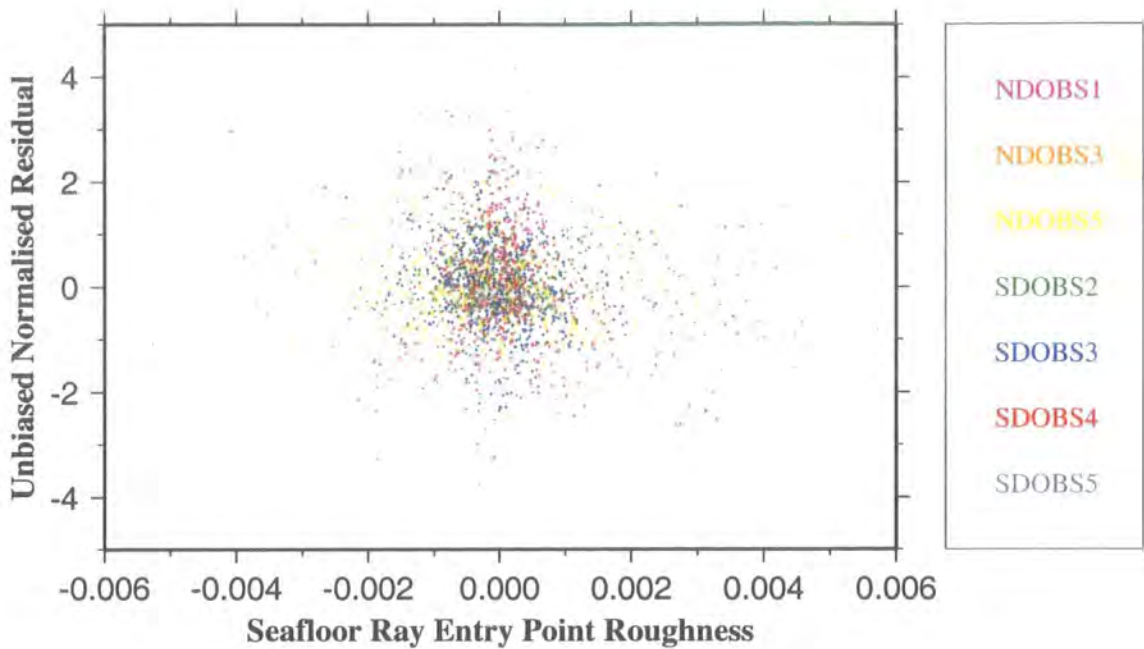


**Figure 3.21:** Plot of unbiased normalised residual for the model obtained by inversion using the *melt lens unbiased 2-D initial model* against seafloor roughness at the ray entry point as defined by equation 3.2 and shown in Fig. 3.20. Residuals are colour coded by OBS location as shown in the panel on the right of the figure. The random scatter of data points for each OBS location indicates that seafloor roughness on a 0.2 km scale does not introduce any bias into the normalised residuals.

If the mean seafloor ray entry points predicted by the forward modelling method were grossly in error due to the rough bathymetry as described above, it might be expected that large travel time residuals would be associated with those arrivals whose seafloor ray entry points were correlated with regions of rough seafloor. Fig. 3.21 shows that there is no systematic relationship between travel time residual and roughness of the seafloor at the ray entry point. Although this observation does not prove that the seafloor ray entry points have been correctly identified in all cases, it indicates that any errors due to misidentification of seafloor ray entry points are small relative to the other data uncertainties and that no bias has been introduced into the final model through any such misidentification. For more detailed experiments targeted towards resolving upper-crustal structure, or experiments conducted in areas with more extreme bathymetry (e.g. slow-spreading ridges such as the MAR), it may be necessary to perform a more rigorous analysis of seafloor ray entry points. A simple method of refining the forward modelling method to deal with refraction at rough interfaces will be described in section 5.5.3. However, for this study the existing forward modelling method appears adequate.

### 3.7 Effect of reduced ray coverage

Fig. 2.31 illustrates that there is great lateral variation in model resolution, primarily related to the uneven ray coverage shown in Fig. 2.26. The final models resulting from inversions performed using the *fast* and *slow 1-D initial models*, described in section 3.4.1, indicate that this variability has implications for the appearance of the anomaly distribution. It was suggested that the component of travel time residuals arising from inadequacies in the parts of the initial model where lateral anomaly resolution is poor are probably resolved by anomalies in the better resolved parts of the model.

In order to investigate the effect of variable ray coverage, an inversion was performed using a subset of the data created to reflect a more even ray coverage, and to include only the best data. Travel time residual uncertainties are discretised because the component due to travel time pick position uncertainty is discretised at 5 ms intervals (the sample interval). The reduced dataset was created for each OBS by considering each first arrival travel time observation with the smallest associated travel time residual uncertainty in turn. Shots were added to the reduced dataset only if they were located more than 1 km away from all the shots currently included in the reduced dataset. Next, first arrival travel time observations with the second smallest associated uncertainty were considered and similarly added to the dataset if they were located more than 1 km away from all the currently included shots. The travel time residual uncertainty threshold was gradually increased to the maximum value. The resulting dataset has an approximate shot spacing of 1 km for each instrument and comprises the most reliable (lowest uncertainty) data with that spacing.

Ray paths traced through the *unbiased 2-D initial model*, which was used for inversion of the reduced dataset, for this subset of shot-receiver pairs are shown in Fig. 3.22. This figure shows that ray coverage is much more evenly distributed throughout the data volume than for the full dataset. This observation is reinforced by the distribution of cumulative ray path lengths in each inversion cell shown in Fig. 3.23a. This ray path length distribution plot was created using the *basic 1-D initial model* even though this initial model was not used for the inversion to enable direct comparability with Fig. 2.26, which was created using the full dataset. This comparison reveals that whilst the cumulative ray path lengths are, as expected, generally lower for the reduced dataset, the distribution is much more even. Resolution tests were performed for the reduced dataset using the method described in section 2.10, and the

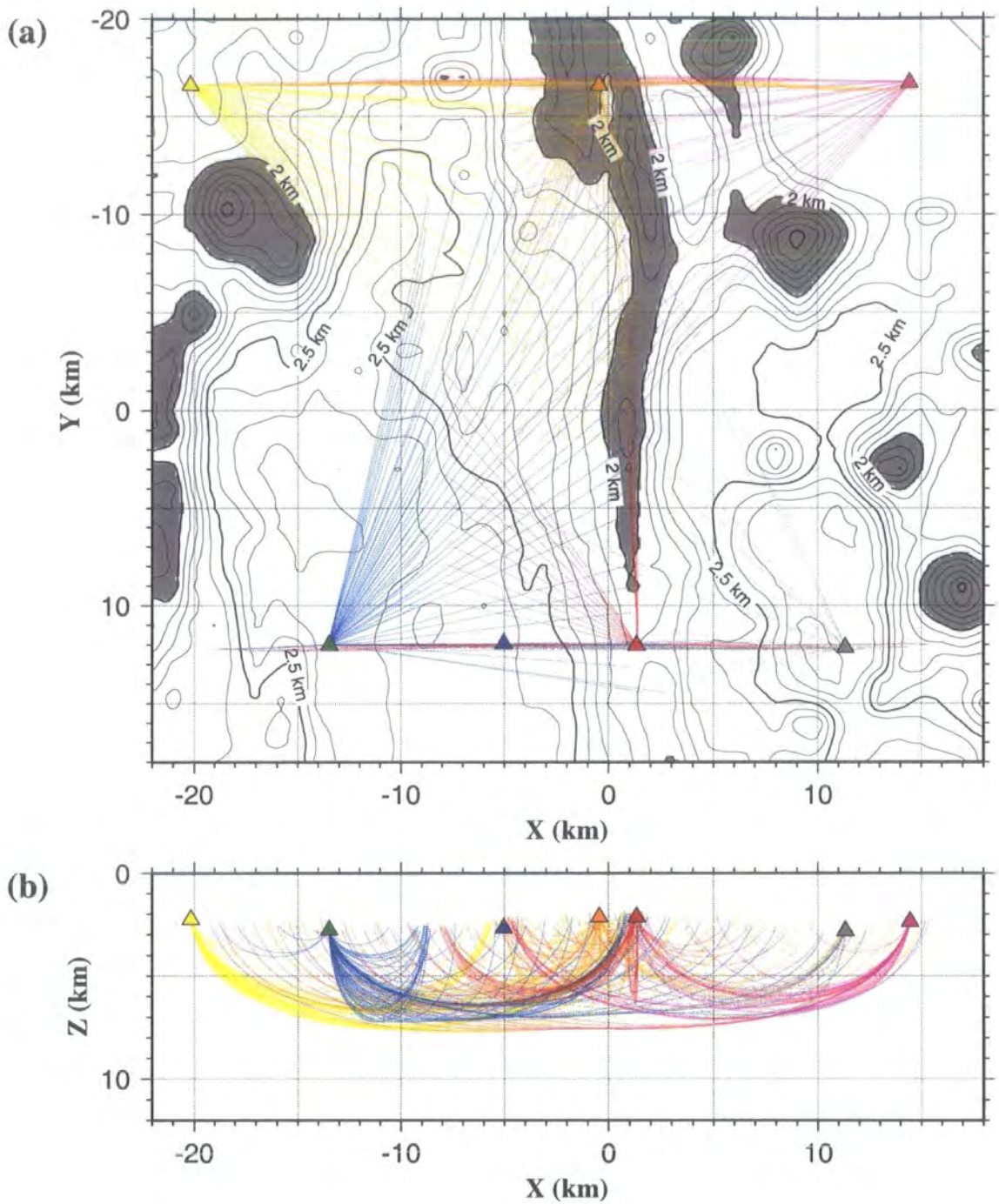


**Figure 3.22:** Crustal part of the predicted ray paths traced through the *unbiased 2-D initial model* in a) plan view and b) cross-section parallel to the  $x$ -axis for all the shot-receiver pairs in the reduced dataset created by preferentially selecting the best (smallest uncertainty) data with a minimum shot spacing of 1.0 km. Bathymetric contours at 0.1 km intervals are shown in a), and bathymetry shallower than 2 km has been shaded. Coloured triangles denote OBS locations, and the ray paths are colour coded according to the OBS at which they were recorded. Comparison with Fig. 3.1 shows that the ray coverage is now more uniform throughout the model volume in plan.

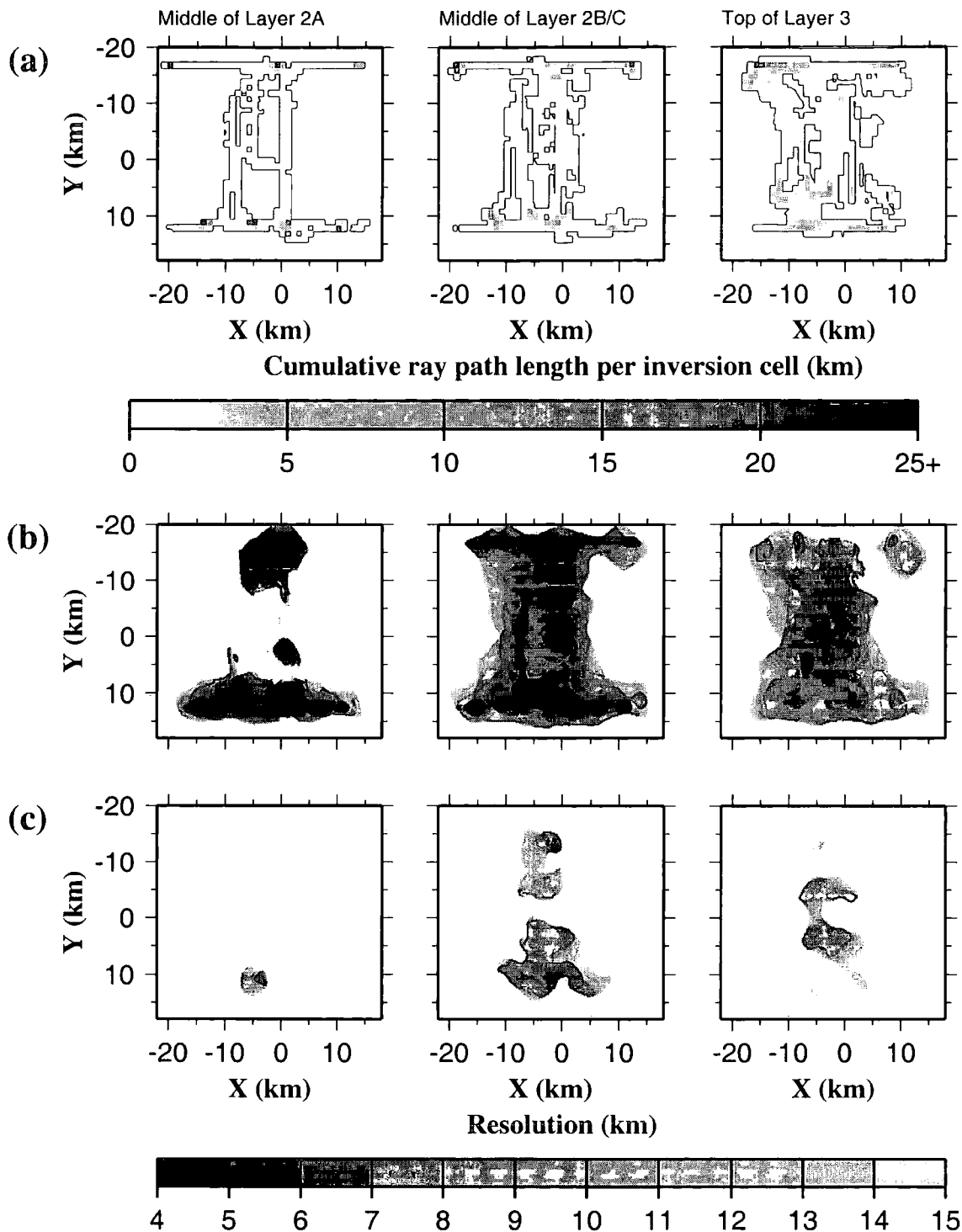


**Figure 3.23:** Ray coverage and lateral anomaly resolution for the reduced set of shot-receiver pairs shown in Fig. 3.22. a) The total ray path length sampling each inversion cell in the initial model for the 3.0, 5.0 and 6.2  $\text{kms}^{-1}$  constant velocity planes in the *basic 1-D initial model*. Note that ray coverage is generally more even than for the full set of shot-receiver pairs shown in Fig. 2.26. b) and c) Lateral anomaly resolution for the reduced set of shot-receiver pairs derived using the method described in section 2.10 for semblance thresholds of 0.7 and 0.9 respectively. Part b) shows the size of anomalies which may be accurately located and c) shows the size of anomalies whose amplitudes may also be reliably determined. Lateral resolution is similar to that for the full dataset (shown in Fig. 2.31) although the size of anomalies whose amplitudes may be reliably determined is generally slightly smaller for the reduced dataset than for the full dataset in layer 3.



results are shown in Figs. 3.23b and 3.23c for semblance thresholds of 0.7 and 0.9 respectively. These resolution tests were also conducted using the *basic 1-D initial model* and are therefore directly comparable with those performed using the full dataset, the results of which are shown in Fig. 2.31. This comparison shows that model resolution is similar for both datasets, though generally a little worse for the reduced dataset as expected.

An inversion was performed using this subset of first arrival time picks and the *no melt lens unbiased 2-D initial model*. The melt lens was not explicitly included for simplicity because it has been shown to have only a small effect on the appearance of final models. Three iterations of the inversion were required to achieve convergence. The resulting final model velocity anomaly distribution is shown in Fig. 3.24, and the corresponding normalised error distributions are shown in Fig. 3.25. Comparison of Figs. 3.13 (the *no melt lens unbiased 2-D initial model*) and 3.24 shows that the positions of the principal anomalies are very similar for both datasets, though their amplitudes are generally larger for the reduced dataset, especially so in layer 3. This observation suggests that lateral variations in ray coverage do not influence the appearance of the final model to any large degree. Furthermore, the less reliable data, which was excluded from the reduced dataset used to produce the model shown in Fig. 3.24, does not appear to introduce any significant model artefacts when it is included.



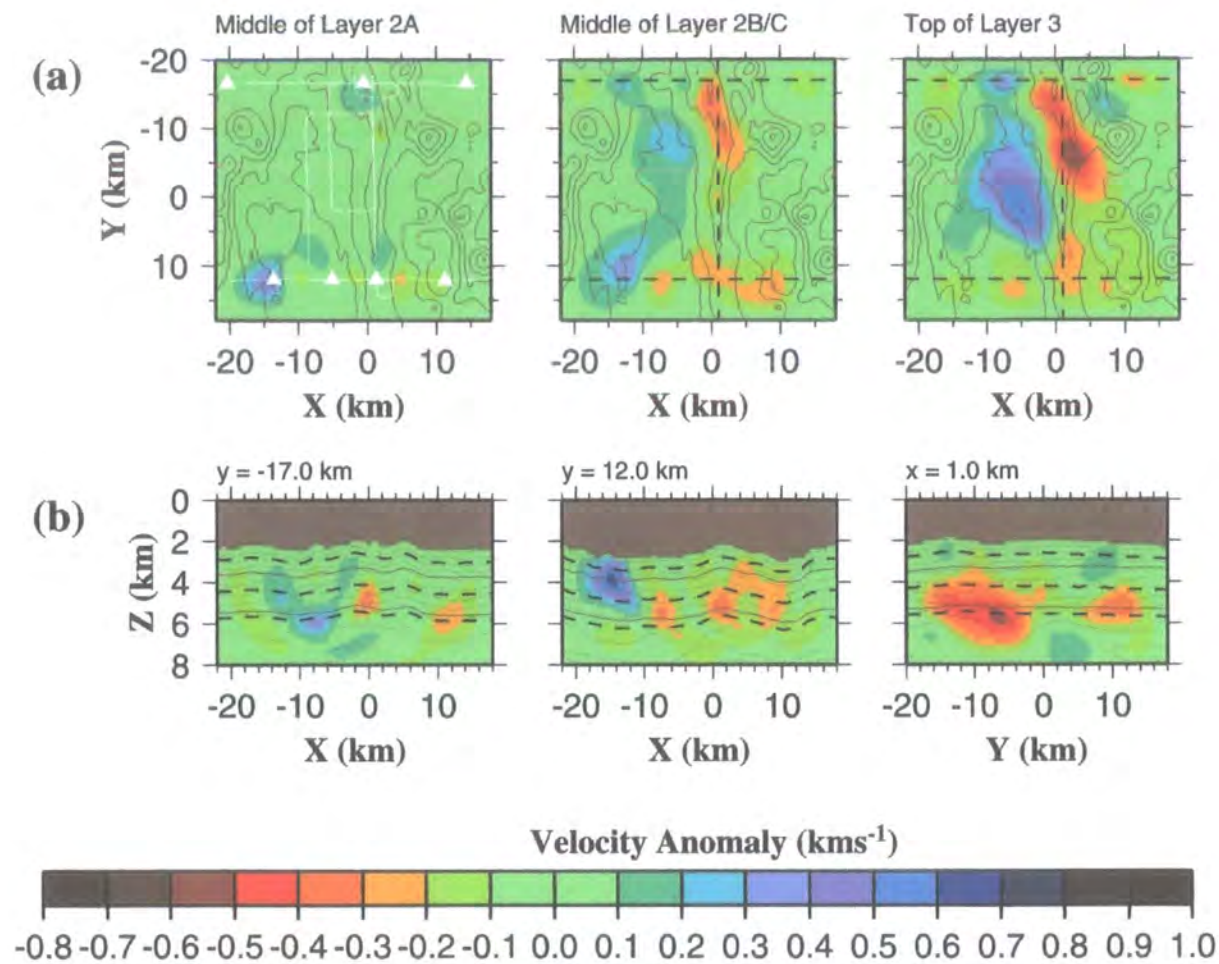


**Figure 3.24:** Velocity anomalies recovered by inversion using the *no melt lens unbiased 2-D initial model* and the reduced set of shot-receiver pairs. a) Velocity anomalies relative to the *no melt lens unbiased 2-D initial model* for the same planes as in Fig. 3.8a and similarly annotated. b) Cross-sections through the velocity anomaly field at the same locations as in Fig. 3.8b and similarly annotated. Note that anomalies are recovered in similar positions to those recovered using the full dataset (shown in Fig. 3.13), but their amplitudes are generally larger when the reduced dataset is used. This similarity suggests that the least reliable data does not introduce significant model artefacts.

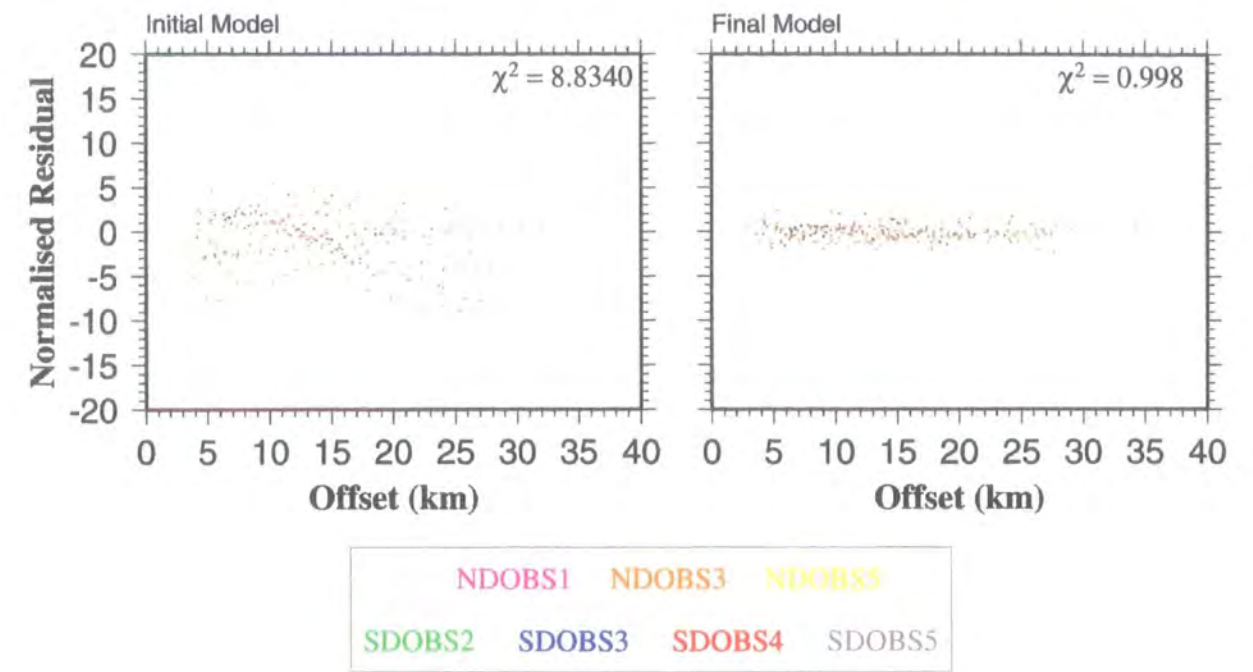


**Figure 3.25:** Plots of normalised residual against shot-receiver offset for each shot-receiver pair in the reduced dataset, colour coded according to OBS location, for the *no melt lens unbiased 2-D initial model* and the model recovered by inversion using this initial model and the reduced dataset.

### 3.8 Discussion

The initial conditions for the inversion which produced the model shown in Fig. 3.18 (the *melt lens unbiased 2-D initial model*) are believed to be the best representation of the known velocity structure of all the initial models considered. Hence the anomalies shown are most likely to be derived from geological features rather than artefacts arising from inadequacies in the initial model. Furthermore, the principal anomalies seen in Fig. 3.18 are also consistently present in models produced from inversions with different initial conditions incorporating a variety of possible laterally and vertically varying geological scenarios as described in sections 3.3–3.7, which further suggests that they are real and required to fit the data. In this section, the possible causes of these anomalies are discussed, with further testing undertaken to determine which anomalies arise from geological features and which are model artefacts. All inversions described in this section were performed using the *no melt lens unbiased 2-D initial model* described in section 3.4.3. The melt lens was not explicitly included for simplicity since it has only a small effect on the final model and is anyway beyond the resolving power of the inversion.

The statistical significance of the inversion results will firstly be discussed. Anomalies will then be considered for each layer in turn, starting with layer 3 and working upwards. A full discussion of the geological implications of interpretation of the real anomalies will be given in chapter 5.

#### 3.8.1 Statistical significance of the inversion results

Preliminary inversions using travel time residual uncertainties assigned using the methods outlined in sections 2.4 to 2.6 did not converge to a  $\chi^2$  value of 1.0 as defined by equation 2.13. For all the resolution tests described in section 2.10 and the inversions performed in this chapter, these travel time residual uncertainties were doubled. Normalised residuals displayed in this chapter were calculated on the basis of these doubled errors, and  $\chi^2$  values were calculated using equation 2.18. Comparison of equations 2.13 and 2.18 reveals that the  $\chi^2$  value calculated using equation 2.18 is a quarter of that calculated using equation 2.13. Hence the final models in this chapter all have a normalised  $\chi^2$  of less than 4.04 according to equation 2.13. Since the inversion algorithm is designed to iterate towards a normalised  $\chi^2$  of 1.00, increasing the travel time residual uncertainties was the easiest way to relax the convergence criterion in

practice. Hereafter in this subsection, "travel time residual uncertainty" refers to the one standard deviation uncertainty assigned using the methods outlined in sections 2.4 to 2.6, "normalised residual" is the travel time residual divided by its associated one standard deviation uncertainty, and "normalised  $\chi^2$ " was calculated using equation 2.13.

If the normalised residuals are assumed to be normally distributed with a mean of zero, normalised  $\chi^2$  is the variance of this distribution. A normalised  $\chi^2$  of 1.00 indicates that the travel time data have been satisfied within their uncertainties. This point may be illustrated by considering the case in which all travel time residual uncertainties are equal. Under these conditions, a normalised  $\chi^2$  of 1.00 would indicate that the standard deviation of the travel time residual distribution was identical to this constant travel time residual uncertainty. Similarly, a normalised  $\chi^2$  of 4.00 would indicate that the standard deviation of the travel time residual distribution was twice the travel time residual uncertainty. Therefore, the models described in this chapter do not satisfy the travel time data within their uncertainties, and the true normalised  $\chi^2$  value calculated using equation 2.13 provides a measure of this misfit.

It is possible that by applying a smaller, non-integer multiplier to the travel time residual uncertainties, models with smaller misfits might be obtained. However, extensive testing would be required in order to find the smallest multiplier for which all the inversions performed in this chapter, and as part of the resolution tests described in section 2.10, reliably converge. In the initial stages of this study, inversions were performed using a variety of travel time residual uncertainty distributions. The anomalies resolved by these inversions, whilst different in detail, were generally similar to those presented in this chapter. Additionally, the resolution tests described in section 2.10 were performed using the same travel time uncertainties as the real inversions, and therefore provide a measure of the scale of features which may be resolved within these uncertainties. In view of these observations, the interpretation of the anomalies resolved by the inversion in the remainder of this section and chapter 5 is believed to be valid.

### 3.8.2 Layer 3

The most prominent anomalies in layer 3 (Fig. 3.18) are a negative anomaly beneath the ridge axis and a positive anomaly to the west of the axis. The negative along-axis anomaly corresponds in position and depth to the axial low-velocity zone identified by Turner (1998) and Turner *et al.* (1999) from modelling the 2-D across-axis profiles (see Fig. 1.10), which they interpreted as representing a mush zone comprising a small percentage (<1%) of partial melt. The positive anomaly west of the ridge axis probably represents normal off-axis crust. The positive anomaly arises because the initial model for the inversion was derived from 1-D averages of Turner (1998) and Turner *et al.* (1999)'s across-axis 2-D models shown in Fig. 1.10 which include the axial LVZ. As this anomaly is interpreted to be related to the axial magma chamber, and therefore non-existent off-axis, the velocity off-axis is likely to be greater than these averages and a positive anomaly is required.

The inversion results shown in Fig. 3.18 indicate considerable along-axis variability in amplitude of the negative anomaly, and there is a gap between  $y = 0$  km and  $y = 5$  km. This variation and gap may reflect real variation in the properties of the axial magmatic system. Alternatively, the characteristics may simply be artefacts of the irregular ray coverage and resolution at this depth, which are illustrated in Figs. 2.26 and 2.31 respectively.

In order to investigate further, a synthetic model was created based on the average 2-D across-axis structure. An across-axis average of the anomaly field shown in Fig. 3.18 was determined by considering planes parallel to the smoothed bathymetry derived using a 2.0 km square averaging filter and separated vertically by 0.2 km. For each plane, the average anomaly at each  $x$ -position was determined for those inversion cells sampled by rays. By this method, a 2-D anomaly field as a function of  $x$  and depth below the seafloor was obtained. The anomalies corresponding to layers 2A and 2B/C were set to zero, and the amplitudes of anomalies in layer 3 were adjusted so that they were representative of those recovered by the inversion. The layer boundaries referred to above were those for the *unbiased 2-D initial model*. Fig. 3.18 shows that the melt lens, which is believed to lie at the layer 2B/C-3 boundary, is shallower than the average position of the layer 2B/C boundary used in the construction of the *unbiased 2-D initial model*. This discrepancy occurs because layer 2 thickens slightly away from the axial region (see the models of Turner (1998), Fig. 1.10) and hence the true position of the layer 2B/C boundary on-axis is shallower than the average position. The

resulting anomaly field, shown in Figs. 3.26a and 3.26b, was added to the *unbiased 2-D initial model*. A synthetic dataset was created by calculating the predicted first arrival times for the set of shot–receiver pairs used when inverting the real data and adding noise according to their associated uncertainties by the method described in section 2.10.1 related to the resolution tests. This dataset was then inverted using the *no melt lens unbiased 2-D initial model*, and the final recovered anomaly field is shown in Figs. 3.26c and 3.26d.

Comparison of Figs. 3.26c and 3.26d with Figs. 3.26a and 3.26b respectively shows that the true position and amplitude of the positive anomaly west of the axis have generally been recovered quite well near the top of layer 3. Some lateral smoothing has occurred near  $y = 12$  km and  $y = -17$  km, corresponding to instrument deployment positions, and the anomaly amplitude has generally been underestimated near its extremities. However, the axial negative anomaly recovered by the inversion is fragmented and of very much lower amplitude than the synthetic. Also, the recovered position of the axial negative anomaly is offset slightly to the east of its true position. This offset may be a regularisation artefact arising from smoothing of real anomalies in well resolved regions of the model into the region east of the ridge axis where resolution is generally very poor (see Fig. 2.31). Comparison of Figs. 3.26c and 3.26d with Figs. 3.18a and 3.18b respectively shows that regions where a negative anomaly has been recovered during the synthetic test approximately correspond to regions where the negative anomaly recovered when inverting the real data has maximum amplitude. Moreover, the position of the discontinuity in the negative anomaly recovered when inverting the real data corresponds to an area where the negative anomaly is not recovered during synthetic testing. These observations suggest that the along–axis variations in amplitude of the axial negative anomaly and the gap between  $y = 0$  km and  $y = 5$  km, which are recovered by inverting the real data, are at least partly artefacts of irregular model resolution.

These findings are consistent with the resolution tests described in full in section 2.10, where the amplitude of checkerboard anomalies recovered by the inversion was generally underestimated except in areas of highest resolution. Fig. 2.31a shows the size of anomalies whose positions may be determined and Fig. 2.31b shows the size of anomalies whose amplitudes may also be resolved. Both figures indicate that model resolution west of the ridge axis is generally better than on–axis and to the east of the axis in layer 3. The accurate recovery of the positive anomaly west of the axis by the



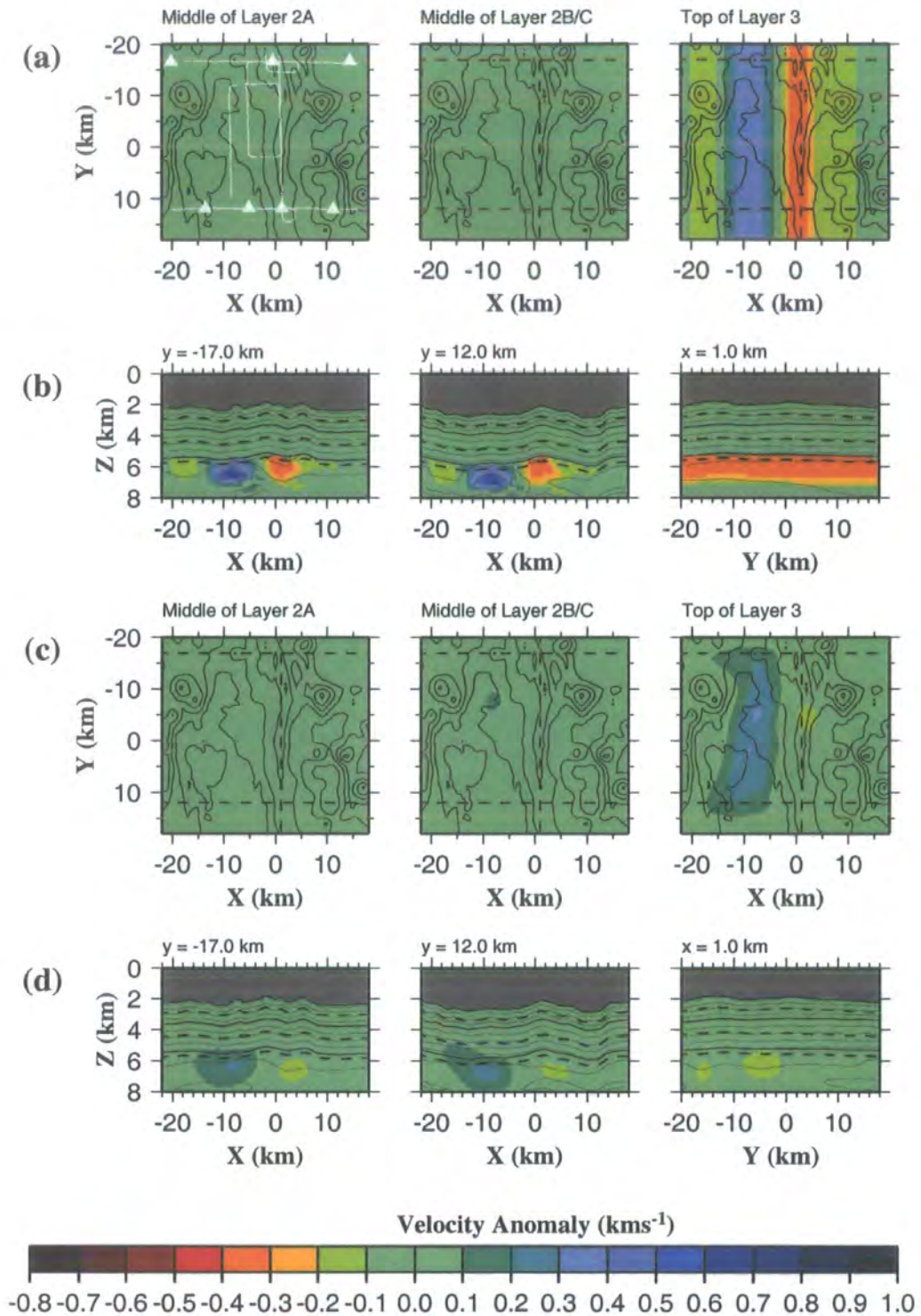


**Figure 3.26:** Synthetic inversion to establish the degree of continuity in the axial negative anomaly in layer 3. a) Velocity anomaly relative to the *no melt lens unbiased 2-D initial model*, shown for the same planes as in Fig. 3.8a and similarly annotated, for a synthetic model based on a 2-D average of the layer 3 structure obtained by inversion using the *no melt lens unbiased 2-D initial model*. b) Cross-sections through the anomaly field at the same locations as in Fig. 3.8b and similarly annotated. c) and d) are equivalent plots to a) and b) derived by inverting synthetic data created by tracing rays through the synthetic model shown in a) and b) using the shot-receiver geometry and uncertainties used in the real inversion. Note that the positive anomaly in layer 3 west of the axis has been recovered, though its amplitude is underestimated at the northern and southern model extremities, but the axial negative anomaly is fragmented and its amplitude greatly underestimated. This result suggests that the observed along-axis amplitude variations and gap in the negative anomaly obtained by inversion using the real dataset are probably model artefacts, and its amplitude may also be underestimated.

synthetic inversion depicted in Fig. 3.26 is consistent with this observation. Furthermore, Fig. 2.31b shows that anomaly amplitudes west of the axis are least well resolved at the northern and southern extremities of the model. The recovered anomaly field shown in Figs. 3.26c and 3.26d reflects this variation in that the amplitude of the positive anomaly recovered by the inversion is underestimated at the northern and southern extremities of the model. Fig. 2.31b also shows that the size of anomaly whose amplitudes may be determined is generally in excess of 15 km on-axis, and the underestimation of the amplitude of the axial negative anomaly by the synthetic inversion is consistent with this finding. Moreover the positions where the negative anomaly has maximum amplitude for the real data (Fig. 3.18) and synthetic test (Fig. 3.26), approximately correlate with areas of best resolution indicated in Fig. 2.31. These observations lend further credence to the hypothesis that the along-axis variations in the amplitude of the axial negative anomaly in layer 3 are artefacts of the variable model resolution due to irregular ray coverage, and the anomaly resolved by the inversion may, in reality, arise from a continuous along-axis feature. The geological implications of these findings will be discussed in section 5.2.1.

Negative anomalies are also present in layer 3 (Fig. 3.18) east of the axis at  $y = -17$  km and between  $y = 5$  km and  $y = 10$  km. These anomalies may represent thickening of layer 2, which would lead to the velocity at a given depth being overestimated by the initial model, as the transition towards island arc generated crust is approached. A similar thickening was modelled by Turner (1998) (see Fig. 1.10). Ray coverage east of the ridge axis is generally very poor, and consequently so is the model resolution shown in Fig. 2.31. Therefore any general eastward crustal thickening would only be resolvable in a few places. However, the very poor model resolution suggests that anomalies in this area most likely result in part from lateral smoothing of anomalies resolved elsewhere in the model by the regularisation.

### 3.8.3 Layer 2B/C

The most prominent features of the anomaly field in layer 2B/C (Fig. 3.18) are: an axial negative anomaly which has largest magnitude towards the north; a positive anomaly west of the axis; a broad negative anomaly across most of the west-east extent of the model between  $y = 10$  km and  $y = 15$  km; and a prominent positive anomaly in the southwest of the model. The latter two anomalies correlate with similar anomalies in layer 2A, and will be discussed in section 3.8.4. The former two anomalies correlate with similar anomalies in layer 3, and it is therefore possible that they result from



vertical smoothing of anomalies related to the mush zone in layer 3. However the synthetic test shown in Fig. 3.26 suggests that this is probably not the case. The synthetic anomaly pattern (see Figs. 3.26a and 3.26b) comprises anomalies in layer 3 only, and the recovered models (Figs. 3.26c and 3.26d) exhibit only a very small degree of upward vertical smoothing into layer 2B/C. This synthetic inversion suggests that if the axial negative anomaly were confined to layer 3 only, there would be no axial negative anomaly recovered in layer 2B/C for the shot–receiver configuration and uncertainties of the real dataset. Similarly, the positive anomaly west of the axis does not appear to have been vertically smoothed.

A further test was conducted to verify this finding using the real data. Rays were traced through the model recovered by inversion using the *no melt lens unbiased 2-D initial model*, and arrivals removed which resulted from rays travelling in layer 3. An inversion was then performed using the *no melt lens unbiased 2-D initial model* and the remaining data, i.e. travel time residuals for those rays which travel only in the water column and layer 2. The subset of rays considered is shown in Fig. 3.27. The layer boundaries refer to the average layer boundary positions used in construction of the *no melt lens unbiased 2-D initial model*. Therefore this subset will include some rays which sample the uppermost part of layer 3 in the axial region where layers 2A and 2B/C are slightly thinner than average. The final inversion results are shown in Fig. 3.28. Comparison with Fig. 3.13 shows that the principal features of the anomaly field in layer 2B/C, including the axial negative anomaly in the north, are also present when inverting the reduced dataset. The anomaly magnitudes are also similar in each case. Moreover, axial negative anomalies are recovered in parts of layer 3 where there is no ray coverage. Hence, these anomalies must be artefacts arising from downward smoothing of shallower anomalies. These observations suggest that the negative anomalies in layer 2B/C are required by data which does not travel to deeper levels, and that vertical smoothing of these anomalies may contribute to the axial negative anomaly recovered in layer 3.

The axial negative anomaly in layer 2B/C exhibits along–axis variation in its amplitude, with larger amplitude in the north than the south. This variation mirrors the amplitude variation observed for the axial negative anomaly in layer 3, which has been shown to be partly an artefact of variable model resolution. The same explanation might apply to the apparent variations in the axial negative anomaly in layer 2B/C. However, inspection of Fig. 2.31 shows that model resolution is generally better in layer 2B/C

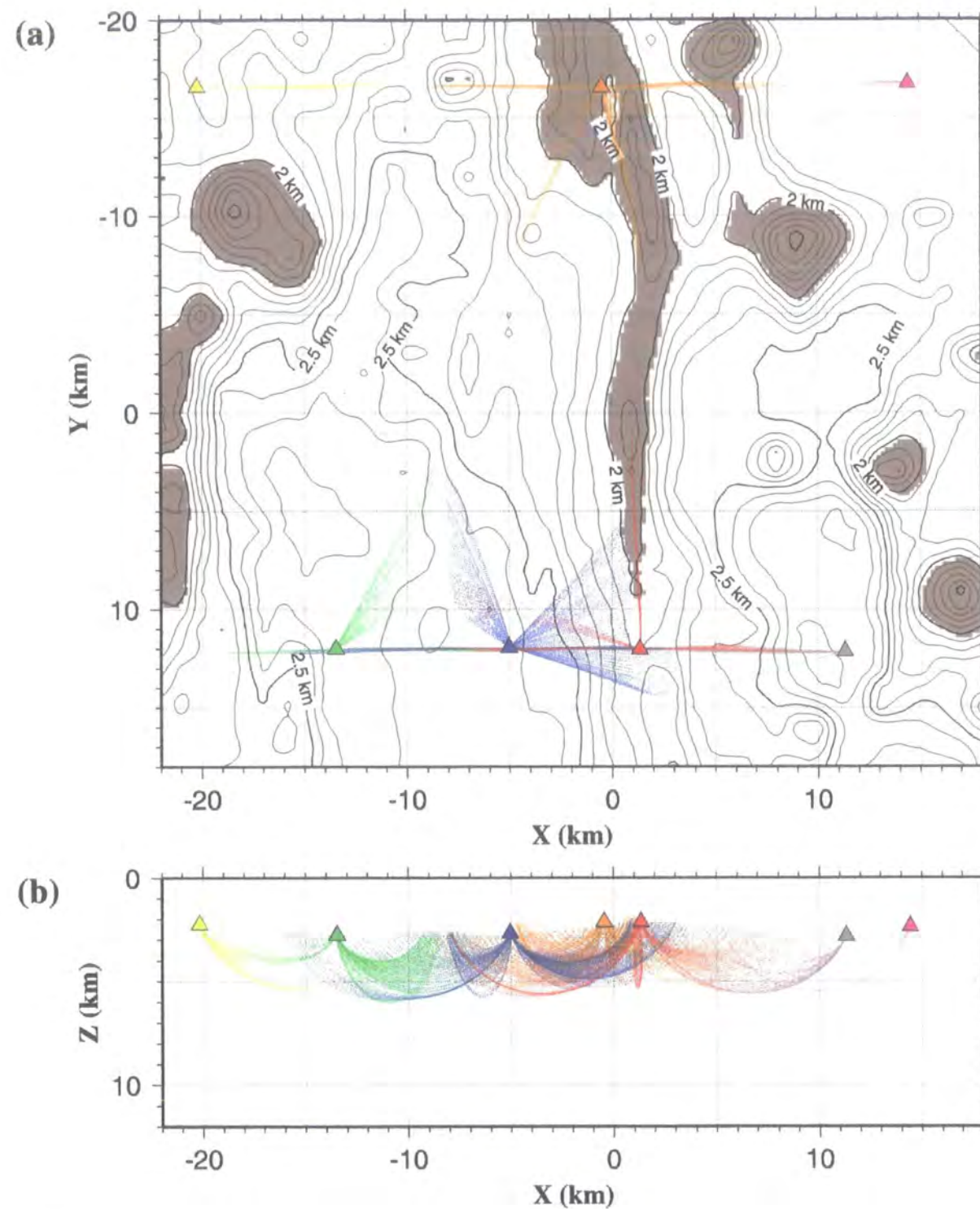


**Figure 3.27:** Crustal part of the predicted ray paths traced through the *no melt lens unbiased 2-D initial model* in a) plan view and b) cross-section parallel to the x-axis for a subset of the shot-receiver pairs used in the inversion to test which anomalies in layer 2 are required by rays which travel in that layer and the water column only. In order to obtain this subset of shot-receiver pairs, rays were traced through the final model recovered by the inversion using the *unbiased 2-D initial model*, and those rays which were predicted to travel in layer 3 were removed. Coloured triangles denote OBS locations, and ray paths are colour coded according to the OBS at which they were recorded.

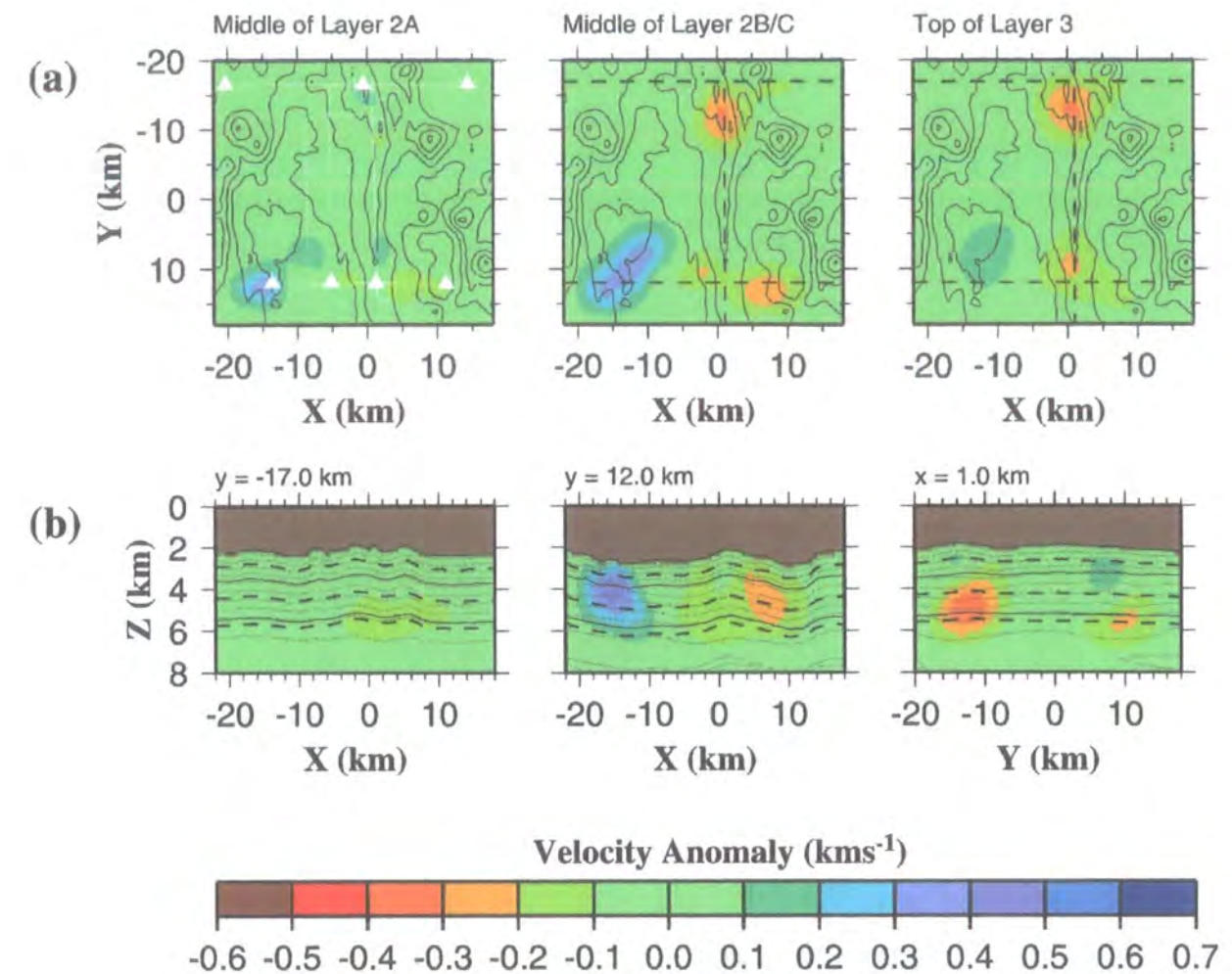


**Figure 3.28:** Velocity anomalies recovered by inversion using the *no melt lens unbiased 2-D initial model* and the set of shot-receiver pairs shown in Fig. 3.27. a) Velocity anomalies relative to the *unbiased 2-D initial model* are shown for the same planes as in Fig. 3.8a and are similarly annotated. b) Cross-sections through the anomaly field at the same locations as in Fig. 3.8b and similarly annotated. Note that the anomalies recovered in layer 2B/C are similar to those shown in Fig. 3.13 for the full dataset. Also note that anomalies are recovered in layer 3 despite there being no ray coverage predicted at these depths, so these anomalies must be regularisation artefacts.

than in layer 3 near the axis. The two best resolved areas in layer 2B/C correspond approximately to  $y = -12$  km and  $y = 10$  km. Comparing these two areas, the anomaly is seen to be larger in the north than in the south. Moreover, the negative anomaly in the south is a much wider feature, and the velocity contrast between the axial region and the surrounding crust is far greater in the north than the south. Therefore, the along-axis variation in the axial negative anomaly in layer 2B/C is believed to be real. This observation is consistent with the 2-D velocity models of Turner (1998) shown in Fig. 1.10. These profiles show depressed velocities in the axial region in layer 2B/C relative to off-axis crust for the *Seismic North* across-axis profile, i.e. at the OSC, whilst a similar feature is not modelled on the *Seismic South* across-axis profile. Possible geological causes of a negative anomaly in layer 2B/C centred on the overlap basin in the north include: local thickening of layer 2A leading to overestimation of the velocity at any given depth in the initial model; higher porosity associated with increased fracturing; or a subsolidus temperature anomaly associated with the underlying magmatic system. These possibilities will be discussed further in section 5.2.3.

The positive anomaly west of the axis is not present in the anomaly field shown in Fig. 3.28, which was recovered by inversion using the subset of rays which do not travel in layer 3. Fig. 3.27 shows that none of the rays used in the reduced dataset pass through this part of the model, therefore the anomaly cannot be resolved by inverting the reduced dataset. However, Fig. 2.31 shows that model resolution in this area is adequate to resolve an anomaly of that size, so it is most likely real. This positive anomaly probably represents the velocity of average off-axis crust since the average initial model incorporates lower than average velocities modelled in layer 2B/C in the axial region by Turner (1998) (see Fig. 1.10).

### 3.8.4 Layer 2A

Model resolution is generally poor in layer 2A, mostly as a result of a lack of crossing ray paths at this depth since the acquisition geometry was designed primarily to image the structure of layer 2B/C and layer 3. This low resolution is reflected in the inversion results shown in Fig. 3.18 for which few anomalies were resolved in layer 2A. However, the modifications which it was necessary to make to the initial model in order to best represent the upper-crustal structure (see section 3.4) in themselves yield information about the gross structure. In particular, the introduction of along-axis variation such that the layer 2A thickness increases from south to north, markedly

reduced the travel time misfit with respect to any 1-D initial models considered. This observation indicates that the layer 2A thickness varies in a similar manner to the thickness of the whole crust, which has also been seen to exhibit northward thickening based on modelling of the gravity field (Sinha 1995; Turner 1998; Turner *et al.* 1999; Peirce *et al.* 2001). A second contributory factor may be compositional variations. Samples dredged from the ridge crest suggest that progressively more silicic magmas are found when traversing the ridge crest from south to north (*cf.* Fig. 1.7) (Collier 1990; Frenzel *et al.* 1990; Vallier *et al.* 1991; Hilton *et al.* 1993), which would also cause lower velocities in the north.

Those anomalies which are resolved in layer 2A generally correlate with isolated regions of high resolution associated with instrument deployment positions, as shown in Fig. 2.31b. The most prominent anomaly is a large positive anomaly in the southwest of the model, which also extends into layer 2B/C. This feature arises because the travel time residuals shown in Fig. 3.19 for the *melt lens unbiased 2-D initial model* are almost all negative for all shot-receiver offsets at SDOBS2, which is located in the southwest corner of the model. This observation implies a velocity anomaly in the upper crust near this OBS. Negative travel time residuals indicate that the initial model velocity is too slow, and a positive velocity perturbation is required to resolve these residuals. A similar feature was observed by Turner (1998) when modelling the across-axis *Seismic South* profile, and was interpreted as representing thinner layer 2. If the initial model comprises layers which are too thick, the velocity at a given depth will be underestimated and a positive anomaly required to resolve this. Turner (1998) interpreted the thinner layer 2 as representing the onset of rifting, analogous to the thinner layer 2 widely observed at passive continental margins near the boundary between oceanic and continental crust. At the VFR thinner layer 2 is believed to result from thinning of pre-existing crust prior to rifting and thinner layer 2 generated immediately after the onset of rifting due to reduced melt supply before the magmatic system is fully established and more rapid cooling of dykes and lava following accretion onto cold crust. This explanation is favoured due to the proximity of a pseudofault in the southwest of the study area, which Wiedicke & Collier (1993) interpreted as representing the boundary between pre- and post-rift crust. This study provides further evidence for the existence and location of this feature.



To the east of the large positive anomaly discussed above, smaller magnitude negative anomalies are observed in layer 2A, which extend down into layer 2B/C. These anomalies most probably arise from the fact that the initial model at  $y = 12$  km is derived from a 1-D average of the 2-D model shown in Fig. 1.10b for the across-axis *Seismic South* profile, which incorporates the thinner layer 2 modelled in the west. Therefore layer 2 thicknesses are slightly underestimated in the initial model in areas of normal thickness post-rift crust, and small negative velocity perturbations are required to counteract this inadequacy.

### 3.8.5 Evidence for anisotropy

The anomaly distribution shown in Fig. 3.18 exhibits negative anomalies in layer 2A near the *Seismic South* instrument deployment sites ( $y = \sim 12$  km, Line 1 in Fig. 1.8) whilst immediately north of this line, positive anomalies have been recovered. A similar pattern is observed in layer 2B/C, though the effect is less marked. This structure requires an abrupt increase in velocity, which may reflect a decrease in layer thickness, immediately north of the *Seismic South* instrument deployment sites. Whilst such a velocity structure is viable and satisfies the first arrival travel time data, it contradicts the overall trend of increasing layer 2 and crustal thickness towards the north. A second possible explanation is the presence of a small degree of azimuthal anisotropy (ray azimuth dependent velocity structure). The velocity structure of the upper oceanic crust is widely observed to exhibit azimuthal anisotropy, which is usually attributed to the presence of preferentially aligned near-vertical water-filled cracks, often perpendicular to the spreading direction (i.e. parallel to the ridge crest in general) (e.g. White & Whitmarsh 1984; Shearer & Orcutt 1985; Caress *et al.* 1992; McDonald *et al.* 1994; Sohn *et al.* 1997; Barclay *et al.* 1998). For such a structure, rays travelling parallel to the cracks would be expected to encounter a velocity similar to the background medium whilst rays travelling perpendicular to the cracks would be more influenced by the properties of the infilling medium (water in this case) and would therefore be expected to encounter a lower velocity. At the VFR the velocity structure near  $y = 12$  km is dominantly constrained by rays whose paths travel perpendicular to the ridge axis. Therefore in the presence of anisotropy arising from ridge-parallel cracks, these rays would dominantly travel at the slower velocity which could give rise to the observed anomalies.

Azimuthal anisotropy can often be identified in 3-D datasets from an azimuthal dependence in the magnitude of travel time residuals before and after inversion for an isotropic velocity structure. A  $\cos 2\theta$  azimuthal dependence identified in travel time residuals, where  $\theta$  denotes the shot–receiver azimuth relative to the slow direction, may be used as an indicator of azimuthal anisotropy (e.g. Caress *et al.* 1992; Sohn *et al.* 1997). If the simple scenario of azimuthal anisotropy arising from ubiquitous ridge–parallel cracks applies at the VFR, an isotropic velocity model which perfectly represented the lateral velocity heterogeneities would be expected to give rise to an azimuthal distribution of travel time residuals similar to that shown in Fig. 3.29a for the shot–receiver geometry of this study, where shot–receiver azimuth is defined as  $000^\circ$  parallel to the positive x direction and  $090^\circ$  parallel to the positive y direction. The maximum magnitude of the residual is arbitrary as the azimuthal dependence of the sign of residuals is the feature of interest. Fig. 3.29b shows similar plots for both the *melt lens unbiased 2-D initial model* and the preferred final model created by inversion using this initial model with the melt lens explicitly included (Fig. 3.18). There is a slight indication that the normalised residuals for the initial model may show some azimuthal dependence similar to that shown in Fig. 3.29a for the southern instruments. This dependence is not apparent in the normalised residuals for the final model, which suggests that the travel time residuals can be resolved within their errors by an isotropic velocity model alone. However, the azimuthal coverage for this experiment is not ideal for evaluating whether azimuthal anisotropy is present or otherwise, and the resulting isotropic velocity model exhibits unusual features in the south of the model which are inconsistent with the regional trends as outlined above. Therefore the possibility that there is a small degree of anisotropy present cannot be definitely ruled out.

Other authors have employed alternative methods for identifying *P*-wave anisotropy. Shearer & Orcutt (1985) demonstrated that the direction of particle motion is deviated away from the direction of travel of a ray in the presence of azimuthal anisotropy. However, such deviations are very small and, for the VFR experiment, would be impossible to distinguish from deviations from the expected direction of particle motion due to the large lateral velocity gradients and rough seafloor topography which are known to exist. White & Whitmarsh (1984) demonstrated the presence of azimuthal anisotropy in the upper crust of the MAR by comparing 1-D average velocity models determined using shot–receiver pairs with a restricted range of azimuths. This

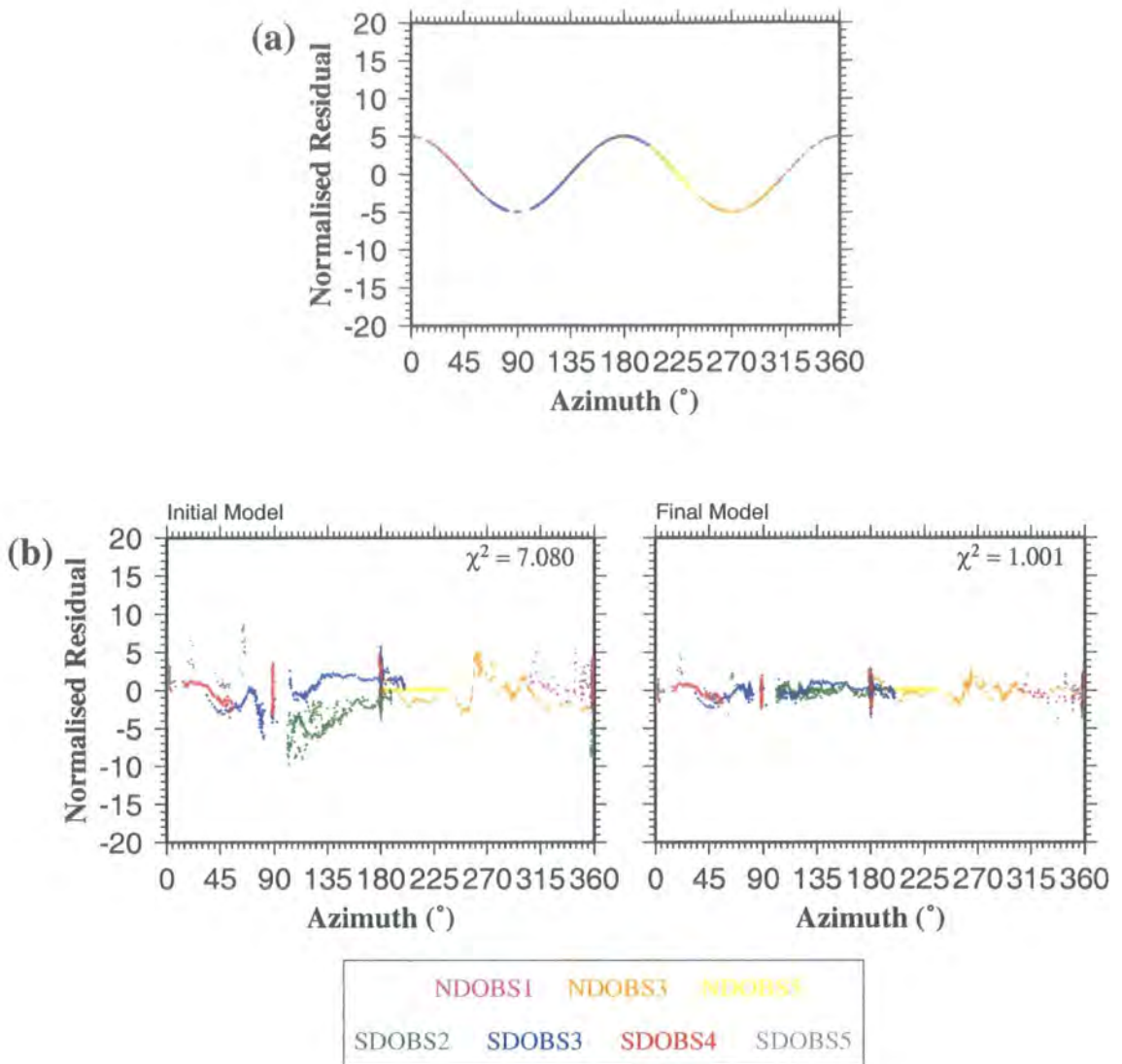


**Figure 3.29:** Plots of normalised residual against shot–receiver azimuth for each shot–receiver pair used in the inversion, colour coded according to OBS location. Shot–receiver azimuth is defined as  $000^\circ$  parallel to the positive x–axis and  $090^\circ$  parallel to the positive y–axis. a) The distribution which would be observed for an idealised scenario with an isotropic velocity model which perfectly represents the lateral velocity heterogeneities, but does not account for azimuthal anisotropy arising from vertical cracks aligned parallel to  $090^\circ$ . The maximum normalised residual value is arbitrary since the variation in sign of residuals with azimuth is the only feature of interest. Note the  $\cos 2\theta$  dependence. Predicted arrivals for SDOBS2 are obscured by those for SDOBS3 (see legend for colour code). b) The distributions observed for the *melt lens unbiased 2–D initial model* and the model recovered by the inversion using this initial model. Note that the distribution for the southern instruments displays some similarities with the ideal model in a) for the initial model, but not for the final model. This suggests that the degree of anisotropy is very small if it exists at all, and that the inversion can resolve the travel time residuals for this dataset within their uncertainties using an isotropic model alone.

approach is unlikely to work well at the VFR due to the known large lateral velocity variations which are likely to mask any velocity variations considering that the degree of anisotropy and consequent velocity variations are likely to be small by comparison.



A possible solution is to consider  $S$ -wave arrivals.  $S$ -wave velocity is much more sensitive to the presence of cracks, which are widely thought to be the dominant cause of azimuthal anisotropy observed in upper oceanic crust. Any  $S$ -wave velocity anisotropy arising from such features would be much easier to detect, and would indicate the likely presence of similar anisotropy in the  $P$ -wave velocity structure also. The OBSs used in the VFR experiment were equipped with two orthogonal, horizontal geophones allowing the identification of horizontally polarised phases. A number of horizontally polarised arrivals were recorded which were interpreted as  $P$ - $S$  mode converted arrivals. These will be fully discussed and interpreted in the next chapter and the possibility that the velocity structure is anisotropic investigated.

### 3.9 Summary

The tomographic inversion method described in chapter 2 was applied to the VFR dataset, and the results were presented in this chapter. A number of inversion cell sizes were investigated. The smallest cell size of  $1.0 \times 1.0 \times 0.4$  km was found to be most appropriate for this experiment and was therefore used for all subsequent inversions. Small vertical dimensions relative to the scale of vertical structure incorporated into the initial model are desirable to avoid vertical smoothing of that structure by the inversion, and it was demonstrated that small horizontal cell dimensions yield smoother inversion results without introducing artefacts beyond the resolution of the inversion method.

The *basic 1-D initial model* was refined in order to better represent the known structure, particularly in layer 2A. It has been shown that a 1-D model is inadequate for representing the upper-crustal structure in particular, and that inadequacies in the initial model representation of the upper crust, where anomaly resolution is generally very poor, could influence the magnitudes of anomalies recovered in better resolved parts of the model. Therefore 2-D initial models were used for all subsequent inversions. These models incorporated along-axis variation determined by interpolation between 1-D averages of two across-axis velocity models derived by Turner (1998) near the northern and southern extremities of the study area. A further refinement aimed to remove bias in the initial model by modifying it to reflect an average of the vertical structure of the anomaly field derived from inversion using the *2-D initial model*. The inversion results obtained using this approach showed no significant bias towards positive or negative anomalies at any depth, which is desirable for achieving reliable inversion results. The final refinement aimed to explicitly incorporate an axial melt lens in the initial model. A

melt lens is known to exist from previous reflection studies and might influence predicted first arrival ray paths due to the associated large lateral and vertical velocity gradients surrounding it. Inclusion of the melt lens resulted in slightly smaller anomaly magnitudes in layer 3, but otherwise the inversion results were very similar to those obtained without the melt lens included.

Analysis of the travel time residual distribution for the preferred final model showed no correlation with the seafloor roughness at the ray entry point suggesting that any errors due to misidentification of these entry points in regions of rough bathymetry are small when considered in context of the overall data uncertainties. An inversion performed using a reduced dataset with more even ray coverage and data with the largest uncertainties removed, produced similar results to the full dataset, suggesting that lateral variations in ray coverage and the least reliable data did not introduce significant model artefacts.

The principal features of the anomaly field resolved by the inversion are: an axial negative anomaly in layer 3; a positive anomaly in layer 3 to the west of the axis; an axial negative anomaly in layer 2B/C with largest magnitude in the north of the study area; and a large magnitude circular positive anomaly in layers 2A and 2B/C in the southwest of the study area. Possible causes of these anomalies were considered, particularly to identify which anomalies result from geological features and which are artefacts of the inversion. The negative anomaly in layer 3 probably represents an axial mush zone comprising a small percentage of partial melt identified from wide-angle across-axis seismic profile modelled previously (Turner 1998). The tomographic results suggest that this feature is probably continuous along-axis since any discontinuities may be artefacts of variable model resolution. The positive anomaly in layer 3 probably represents normal, off-axis, post-rift crust. The positive anomaly in the southwest of the study area probably represents thinner layer 2 associated with the onset of rifting, reinforcing the findings of Turner (1998) who modelled a similar feature in two dimensions using the across-axis, wide-angle data. The negative anomaly in layer 2B/C was shown to be required by the data, and does not result from upward, vertical smoothing of deeper anomalies. Possible geological causes of this feature, and a full discussion of the geological implications of all the features outlined here, will be presented in chapter 5.

Finally, examination of the resulting velocity anomaly plots has suggested that there may be some evidence for  $P$ -wave anisotropy due to preferentially aligned cracks in the upper crust. Such anisotropy is easier to identify using  $S$ -wave arrivals, and this will be considered in the next chapter.

# Chapter 4

## Behaviour of $P$ - $S$ mode converted arrivals

### 4.1 Introduction

The 3-D tomographic inversion results for the VFR presented in chapter 3 show some evidence of  $P$ -wave anisotropy. Such anisotropy has been commonly observed in the upper oceanic crust and has been attributed to the presence of near-vertical cracks preferentially aligned perpendicular to the spreading direction (e.g. Caress *et al.* 1992; McDonald *et al.* 1994; Sohn *et al.* 1997; Barclay *et al.* 1998).  $S$ -wave velocity is more sensitive to crack geometry and alignment than  $P$ -wave velocity, and knowledge of both  $P$ - and  $S$ -wave velocity structure allows the porosity and geometry of porosity to be assessed. Preferentially aligned cracks would be expected to give rise to  $S$ -wave anisotropy, and  $S$ -wave splitting<sup>2</sup> might be observed. Therefore  $S$ -wave anisotropy should be easier to identify than  $P$ -wave anisotropy. The OBSs deployed at the VFR were equipped with two mutually orthogonal horizontal geophones as well as a vertical geophone so that  $S$ -wave arrivals could be observed and their mode of propagation identified. A number of  $S$ -wave arrivals were observed which were interpreted to be the result of  $P$ - $S$  mode conversion at an interface beneath each OBS. In this chapter, the methods used to model these arrivals are described and the results of this modelling presented.

In section 4.2 a simple preliminary interpretation of the  $P$ - $S$  mode converted arrivals is presented. In order to allow more sophisticated analysis of these arrivals, it is necessary to first determine the actual orientation of the horizontal geophones, and the method employed to achieve this is described in section 4.3. Travel times of the  $P$ - $S$  mode converted arrivals are interpreted in section 4.4, and particle motion azimuths, potentially an indicator of anisotropy, are analysed in section 4.5. A detailed description of the methods used to perform this analysis is provided in appendix D. Finally, a tentative geological model, based on the results of the preceding analysis, is presented in section 4.6.

---

<sup>2</sup>  $S$ -wave splitting is the phenomenon whereby an incident  $S$ -wave undergoes splitting on transmission at an interface with an anisotropic medium into two  $S$ -waves parallel and perpendicular to the fast and slow directions. This will be illustrated further in section 4.5.

## 4.2 Phase identification

The arrivals investigated in this chapter have an approximately constant time delay (typically  $\sim 0.8$  s) behind the crustal first arrivals (hereafter referred to as  $P$ -wave first arrivals). Fig. 4.1 comprises example vertical and horizontal geophone traces recorded by SDOBS2, which show how these mode converted arrivals were identified and illustrates that they are most prominent on the horizontal geophone sections. This observation indicates that particle motion is dominantly in the horizontal plane and, therefore, that these arrivals are  $S$ -waves when they reach the OBS. Since the source was in a fluid (the water column) which has no shear strength, these arrivals must have undergone  $P$ - $S$  mode conversion at some point on their propagation path. The approximately constant time delay behind the  $P$ -wave first arrivals indicates that the propagation paths for both arrivals are similar for most of their length, which implies that the  $S$ -wave arrivals arise from  $P$ - $S$  mode conversion in the vicinity of the OBS at a mid-crustal interface (Turner 1998). Similar arrivals have been observed by Christeson *et al.* (1997) at the EPR. The most plausible converting interface, based on modelling of the  $P$ -wave velocity structure, is the layer 2A-2B/C boundary since there is a change in vertical velocity gradient at this interface, and the relatively small time delay behind the  $P$ -wave first arrival suggests that the conversion cannot occur at any significantly deeper interface (e.g. the layer 2B/C-3 boundary). The feasibility of this interpretation is investigated in this section.

A simple analysis of the relative travel times of the  $P$ -wave first arrivals and  $P$ - $S$  mode converted arrivals was first undertaken in order to establish whether the observed travel times can be satisfactorily modelled by  $P$ - $S$  mode conversion at the layer 2A-2B/C boundary. Poisson's ratio ( $\sigma$ ), which is related to  $P$ - and  $S$ -wave velocity ( $V_p$  and  $V_s$  respectively) by the equation

$$\sigma = \frac{2 - (V_p/V_s)^2}{2(1 - (V_p/V_s)^2)}, \quad (4.1)$$

was calculated for layer 2A based on the assumption that the  $P$ - $S$  mode conversion occurs at the layer 2A-2B/C boundary. The calculated apparent layer 2A Poisson's ratio was compared with values observed elsewhere in young oceanic crust in order to assess whether the layer 2A-2B/C boundary is a viable candidate for the converting interface.

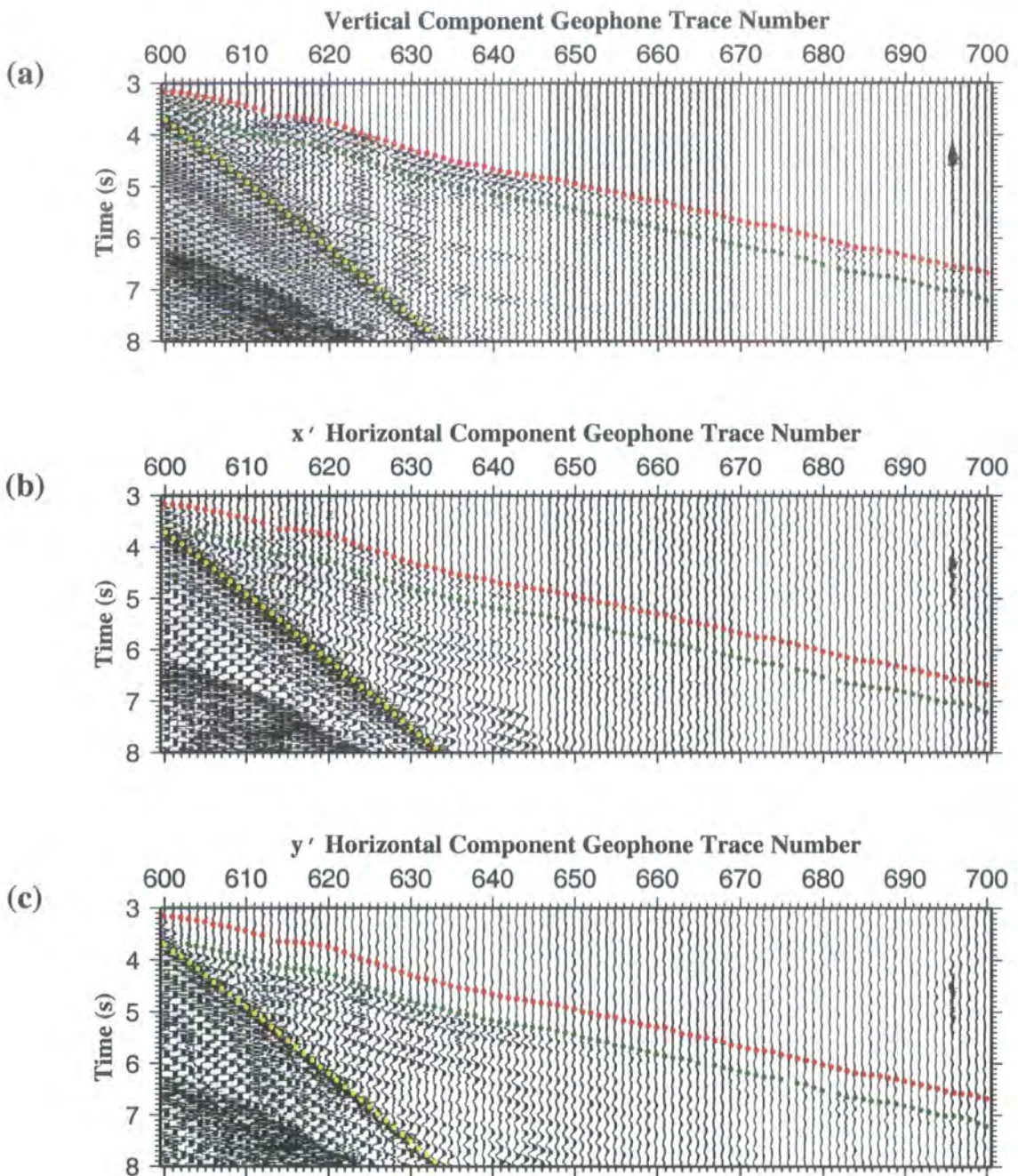


**Figure 4.1:** Detail of traces recorded by SDOBS2 with a) a vertical geophone and b) and c) two orthogonal horizontal geophones (denoted  $x'$  and  $y'$ ) whose orientations are unknown relative to model co-ordinates. Dot centres mark travel time picks of direct water-wave arrivals (yellow),  $P$ -wave first arrivals (red) and  $P$ - $S$  mode converted arrivals (green). All traces are plotted at true amplitude and the same relative scale, and the direct water-wave arrivals have been clipped for clarity. Note that the  $P$ - $S$  mode converted arrival amplitude recorded using the horizontal geophones is larger than the  $P$ -wave first arrival amplitude (especially so in part c) and vice-versa for the vertical geophone traces. This observation indicates that the  $P$ - $S$  mode converted arrival is an  $S$ -wave when it arrives at the OBS.

In order to perform this analysis, a number of further simplifying assumptions were made.

1. Both  $P$ - and  $S$ -wave arrivals travel vertically from the layer 2A-2B/C boundary to the OBS.
2. The ray paths, and hence travel times, for the  $P$ -wave first arrivals and  $P$ - $S$  mode converted arrivals from shot to converting interface are identical.
3. There is a constant vertical  $P$ - and  $S$ -wave velocity gradient in layer 2A in the vicinity of the OBS.
4. Poisson's ratio is constant in layer 2A in the vicinity of the OBS.

Given that there is no  $P$ -wave velocity discontinuity at the layer 2A-2B/C boundary based on the modelling of Turner (1998), assumption 1 implies that the  $P$ -wave first arrivals were travelling vertically when they approached the layer 2A-2B/C boundary since they would not undergo any refraction in the absence of a velocity discontinuity. In this case no  $P$ - $S$  mode conversion will occur. Therefore this assumption cannot be strictly valid. However, Fig. 4.1 shows that the horizontal component of particle motion for the  $P$ -wave first arrivals is very much smaller than the vertical component and vice-versa for the  $P$ - $S$  mode converted arrivals, which indicates that both arrivals were travelling almost vertically when they arrived at the OBS. Hence assumption 1 is thought to be a reasonable approximation. It is likely that assumption 2 is not strictly valid also, but that the difference in shot-converting interface travel time for the two arrivals is very small relative to the overall travel time difference between them. Therefore the difference in travel time between the crustal first arrivals and  $P$ - $S$  mode converted arrivals is assumed to arise solely from the difference in travel time for  $P$ - and  $S$ -waves through layer 2A.

Based on assumption 3, the  $P$ -wave velocity at depth  $z$  below the seafloor in layer 2A may be expressed as

$$V_p = V_{p0} + k_p z, \quad (4.2)$$

where  $V_{p0}$  is the  $P$ -wave velocity at the top of layer 2A (i.e. zero depth below the seafloor) and  $k_p$  is the vertical velocity gradient. The travel time,  $t_p$ , for a vertically travelling  $P$ -wave from the layer 2A-2B/C boundary at depth  $Z$  to the top of layer 2A is defined as



$$t_p = \int_0^Z \frac{dz}{V_p(z)} = \int_0^Z \frac{dz}{V_{p0} + k_p z} = \left( \frac{1}{k_p} \right) \ln \left( 1 + \frac{k_p Z}{V_{p0}} \right). \quad (4.3)$$

Equation 4.1 may be rearranged to express  $V_p$  in terms of  $\sigma$  and  $V_s$ ,

$$V_p = V_s \sqrt{\frac{2(1-\sigma)}{1-2\sigma}}. \quad (4.4)$$

Since Poisson's ratio ( $\sigma$ ) is assumed to be constant in layer 2A (assumption 4) this expression for  $V_p$  may be substituted into equation 4.2. Rearranging the resulting equation gives the following expression for  $V_s$

$$V_s = \sqrt{\frac{1-2\sigma}{2(1-\sigma)}} (V_{p0} + k_p z). \quad (4.5)$$

Equations 4.2 and 4.5 are of the same form. Therefore an expression for the travel time,  $t_s$ , for a vertically travelling  $S$ -wave from the layer 2A-2B/C boundary at depth  $Z$  to the top of layer 2A may be written by inspection of the form of equation 4.3 as

$$t_s = \left( \frac{1}{k_p} \sqrt{\frac{2(1-\sigma)}{1-2\sigma}} \right) \ln \left( 1 + \frac{k_p Z}{V_{p0}} \right). \quad (4.6)$$

Therefore the difference in travel time between the  $P$ - $S$  mode converted arrivals and  $P$ -wave first arrivals,  $\Delta t$ , may be expressed as

$$\Delta t = t_s - t_p = \left( \frac{1}{k_p} \right) \ln \left( 1 + \frac{k_p Z}{V_{p0}} \right) \left[ \sqrt{\frac{2(1-\sigma)}{1-2\sigma}} - 1 \right]. \quad (4.7)$$

Writing  $\frac{1}{\kappa} = \left( \frac{1}{k_p} \right) \ln \left( 1 + \frac{k_p Z}{V_{p0}} \right)$  and rearranging equation 4.7 in terms of  $\sigma$  gives

$$\sigma = \frac{(\kappa \Delta t + 1)^2 - 2}{2(\kappa \Delta t + 1)^2 - 2}. \quad (4.8)$$

The *basic 1-D initial model* (described in section 2.8) was used to determine suitable values for the parameters in equation 4.8 since this is the simplest initial model and is therefore the most appropriate to use given the simplifying assumptions upon which this analysis is based. In this model the average thickness of layer 2A ( $Z$ ) is  $\sim 1.3$  km, the average  $P$ -wave velocity at the top of layer 2A ( $V_{p0}$ ) is  $1.91 \text{ km s}^{-1}$ , and the average vertical  $P$ -wave velocity gradient ( $k_p$ ) is  $1.58 \text{ s}^{-1}$ . The typical travel time difference between  $P$ - $S$  mode converted arrivals and  $P$ -wave first arrivals ( $\Delta t$ ) is  $0.8 \text{ s}$ . Using these values, equation 4.8 gives an apparent Poisson's ratio ( $\sigma$ ) of  $0.42$ . This value is considerably higher than those obtained from laboratory samples of young oceanic crustal material, which typically lie in the range  $0.28$ – $0.31$  (Hyndman 1979). However, higher Poisson's ratios are widely modelled in layer 2A based on seismic experiments (e.g. Spudich & Orcutt 1980b; Bratt & Solomon 1984; Vera *et al.* 1990; Christeson *et al.* 1997; Collier & Singh 1998). These high values of Poisson's ratio are commonly attributed to the presence of low aspect ratio cracks (Shearer 1988), and a Poisson's ratio of  $0.42$  lies within the range of observed values. The geological implications of high Poisson's ratios will be discussed more fully in section 4.6.

In order to check the validity of the assumption that the layer 2A–2B/C boundary is the interface at which  $P$ - $S$  mode conversion occurs, the transmission coefficients for  $P$ - and  $S$ -waves for a  $P$ -wave incident on the layer 2A–2B/C boundary from below, as depicted in Fig. 4.2, were calculated by solving Zoeppritz's equations for the range of angles of incidence between  $0^\circ$  and  $90^\circ$ . These calculations were performed in order to establish whether  $P$ - $S$  mode converted arrivals of sufficient amplitude to allow detection could be generated at this interface. Three such plots are shown in Fig. 4.3, in which different assumptions have been made about the nature of the layer 2A–2B/C boundary. Based on the models of Turner (1998), a  $P$ -wave velocity of  $4.0 \text{ km s}^{-1}$  was assumed in both layers 2A and 2B/C since the modelled  $P$ -wave velocity structure was continuous at the boundary between these layers. When modelling the gravity field, Turner (1998) assumed densities of  $2250 \text{ kg m}^{-3}$  in layer 2A and  $2620 \text{ kg m}^{-3}$  in layer 2B/C. Therefore an average value of  $2435 \text{ kg m}^{-3}$  was used for the density at the layer 2A–2B/C boundary assuming a generally smooth increase in density with depth. The Poisson's ratio was assumed to be  $0.42$  in layer 2A as

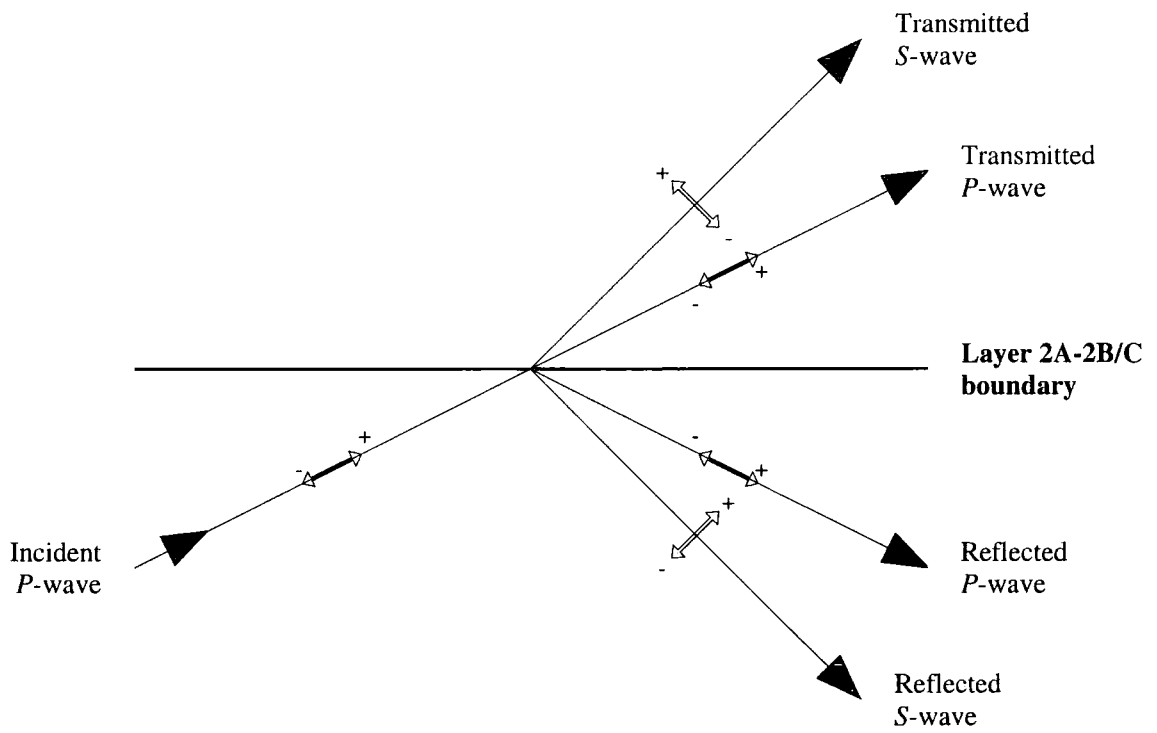


**Figure 4.2:** Transmitted and reflected  $P$ - and  $S$ -waves generated by a  $P$ -wave incident on the layer 2A-2B/C boundary from below. The solid arrows show propagation directions and the double headed arrows particle displacements for each wave. Displacement polarities, as defined in Zoeppritz's equations, are also indicated (after Sheriff & Geldart 1995).

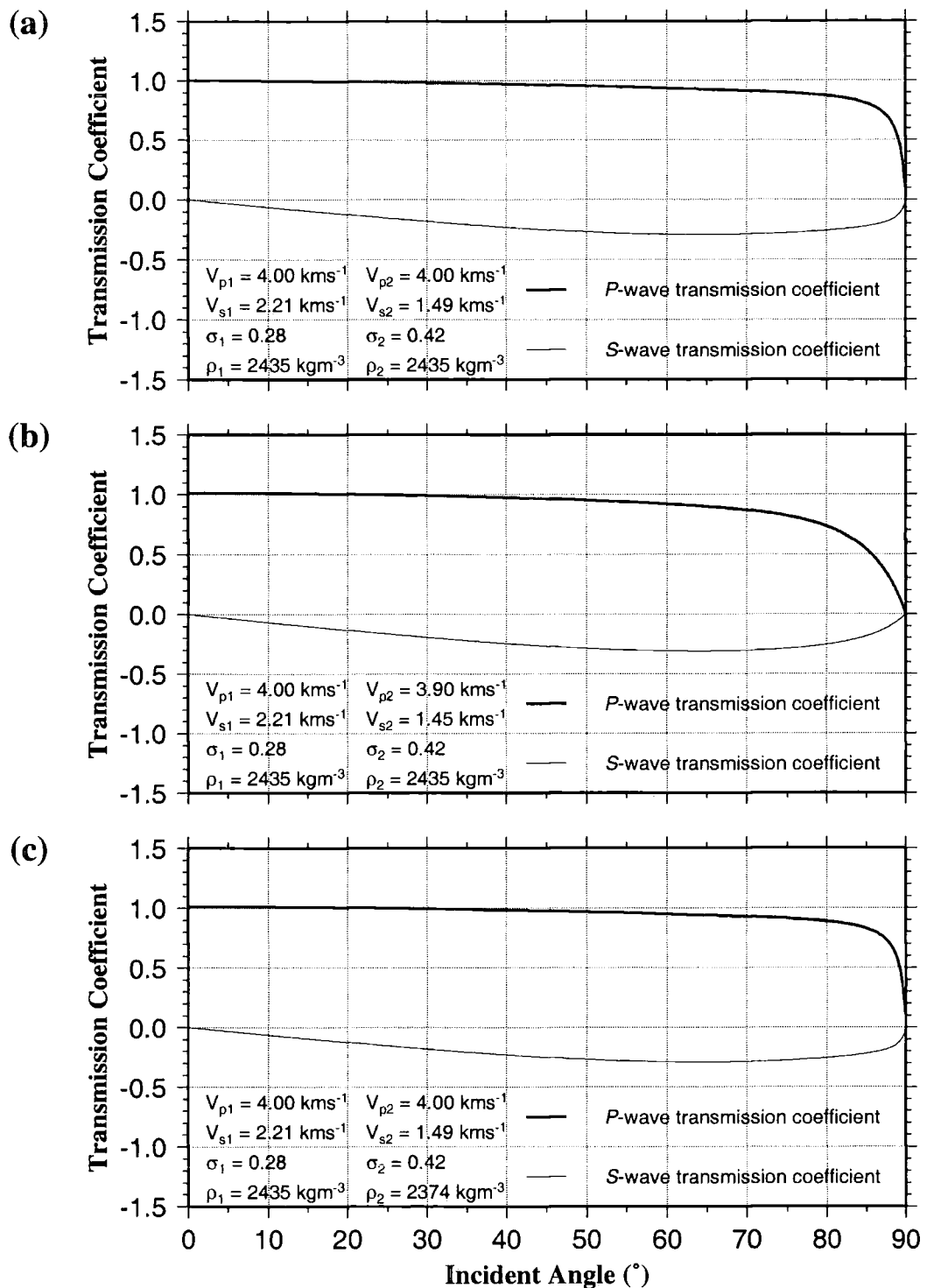


**Figure 4.3:**  $P$ - and  $S$ -wave transmission coefficients calculated for a  $P$ -wave incident on the layer 2A-2B/C boundary from below. The curves shown in each figure were calculated using different  $P$ - and  $S$ -wave velocity ( $V_p$  and  $V_s$  respectively), and density ( $\rho$ ) conditions in each layer, which are indicated in the bottom left-hand corner of each figure. Poisson's ratios ( $\sigma$ ) in each layer, which may be calculated from  $V_p$  and  $V_s$ , are also shown. Suffix 1 refers to layer 2B/C and suffix 2 to layer 2A. In a) the  $P$ -wave velocity and density is continuous at the boundary, and  $P$ - $S$  mode conversion arises due to a change in  $S$ -wave velocity alone, whereas in b) a small change in  $P$ -wave velocity and in c) a small change in density are modelled. In each case, the  $S$ -wave transmission coefficient is  $\sim -0.3$  for incident angles  $> 50^\circ$ , which implies that detectable  $P$ - $S$  mode converted arrivals would be generated under these conditions. Note that a small change in  $P$ -wave velocity at the boundary slightly increases the magnitude of the  $S$ -wave transmission coefficient (compare parts a and b) but a small change in density at the boundary has little effect (compare parts a and c).

calculated above and 0.28 in layer 2B/C, a value typical of those modelled for the mid-lower oceanic crust in seismic experiments, which generally lie in the range 0.25–0.32 (e.g. Spudich & Orcutt 1980b; Au & Clowes 1984; Bratt & Solomon 1984; Christeson *et al.* 1997; Collier & Singh 1998). This Poisson's ratio is also representative of values obtained from laboratory measurements of fresh sheeted dykes, which are presumed to be the dominant component of crustal layer 2B (Hyndman 1979). Given that a continuous  $P$ -wave velocity at the layer 2A–2B/C boundary was assumed this change in Poisson's ratio implies a discontinuity in the  $S$ -wave velocity structure.

The transmission coefficients for the conditions described above are shown in Fig. 4.3a. Fig. 4.3b shows transmission coefficients for the case where there is a small (2.5%) reduction in  $P$ -wave velocity (from 4.0  $\text{kms}^{-1}$  to 3.9  $\text{kms}^{-1}$ ) between layer 2B/C and layer 2A, and Fig. 4.3c shows transmission coefficients for the case where there is a 2.5% reduction in density (from 2435  $\text{kgm}^{-3}$  to 2374  $\text{kgm}^{-3}$ ) between layer 2B/C and layer 2A. In each case, the transmission coefficient for  $S$ -waves is typically  $\sim -0.3$ , which suggests that any  $P$ - $S$  mode converted arrivals generated at such an interface should be detectable. Comparing Figs. 4.3b and 4.3c with Fig. 4.3a shows that a small density change at the interface has a negligible effect on the transmission coefficients, but a small change in  $P$ -wave velocity leads to a small increase in the magnitude of the  $S$ -wave transmission coefficient. When modelling the along-axis Line 4 (see Fig. 1.8), Turner (1998) found that a small velocity discontinuity at the layer 2A–2B/C boundary improved the travel time fit of this model. No such velocity discontinuity was modelled by Turner (1998) for the across-axis lines, though predicted travel times for a model incorporating a small  $P$ -wave velocity discontinuity at the layer 2A–2B/C boundary would probably fit the observed across-axis travel time data as well as the preferred continuous velocity structure. Therefore such a velocity discontinuity is feasible, though not necessary, for obtaining detectable mode conversions.

A number of other possible origins of the mode converted arrival were considered, and these are illustrated in Fig. 4.4. One possibility is that the arrival arises from a peg-leg reflection at the layer 2A–2B/C boundary. However, since the one-way  $P$ -wave vertical travel time through layer 2A is  $\sim 0.45$  s using equation 4.3, the delay of the mode converted arrival behind the  $P$ -wave first arrival would greatly exceed the typical observed delay of 0.8 s if energy propagated as an  $S$ -wave for one or both parts of the peg-leg path. Another possibility is that the converting interface does not coincide with the layer 2A–2B/C boundary. Navin (1996) observed  $P$ - $S$  mode

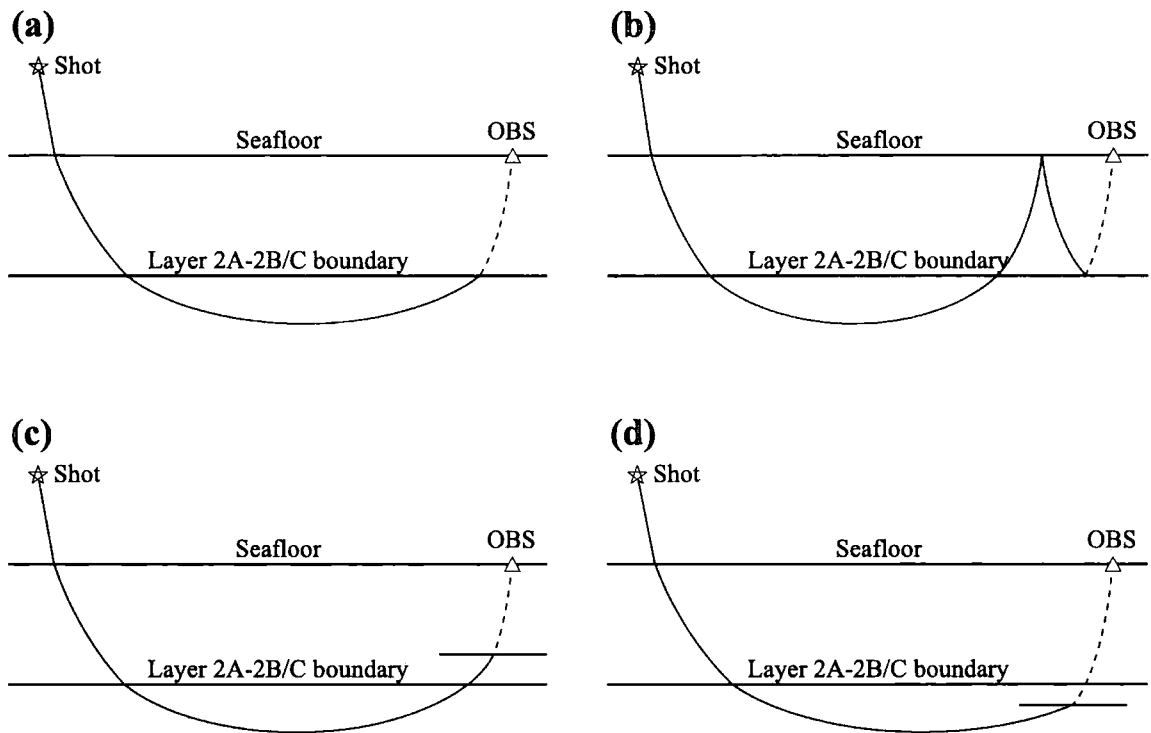


**Figure 4.4:** Possible ray paths for generation of  $P$ - $S$  mode converted arrivals. Solid lines represent the  $P$ -wave part of the ray path, and dashed lines the  $S$ -wave part. a)  $P$ - $S$  mode conversion at the layer 2A-2B/C boundary. b) Peg-leg multiple comprising reflection as a  $P$ -wave at the seafloor followed by reflection as an  $S$ -wave at the layer 2A-2B/C boundary. c)  $P$ - $S$  mode conversion at an interface between the seafloor and the layer 2A-2B/C boundary. d)  $P$ - $S$  mode conversion at an interface deeper than the layer 2A-2B/C boundary.

converted arrivals at the Reykjanes Ridge for which the converting interface was modelled at the layer 2B-3 boundary<sup>3</sup>. A significant change in vertical  $P$ -wave velocity gradient was modelled by Turner (1998) at the layer 2B/C-3 boundary<sup>3</sup> at the VFR, but there is no  $P$ -wave velocity discontinuity. If the travel time difference between  $P$ -wave first arrivals and  $P$ - $S$  mode converted arrivals arises from the difference in travel time for  $P$ - and  $S$ -waves travelling from the layer 2B/C-3 boundary to the seafloor, the implied Poisson's ratio for layer 2 must be much smaller than the value of 0.42 calculated above. Consequently the magnitude of the  $S$ -wave transmission coefficient implied for the layer 2B/C-3 boundary in this scenario would be smaller than the value of 0.3 calculated for the layer 2A-2B/C boundary above. Therefore the interpretation of  $P$ - $S$  mode conversion at the layer 2A-2B/C boundary is preferred as this model predicts  $P$ - $S$  mode converted arrivals which are more likely to be detectable. A further possibility is that  $P$ - $S$  mode conversion occurs at an interface which does not

<sup>3</sup> The terms "layer 2B-3" and "layer 2B/C-3" boundary are used to be consistent with the nomenclature of Navin (1996) and Turner (1998) respectively. In both cases, the boundary referred to corresponds to the structural level at which the melt lens was modelled.

correspond to one of the layer boundaries identified by Turner (1998) from  $P$ -wave travel time modelling. A shallower converting interface would imply a higher Poisson's ratio in the upper part of layer 2A, and similarly a deeper converting interface would imply a lower Poisson's ratio. Higher values of Poisson's ratio have been modelled in layer 2A at the EPR (Christeson *et al.* 1997; Collier & Singh 1998) where the modelled thickness of layer 2A was 0.1–0.6 km, which is significantly less than the layer 2A thickness modelled in this study (typically 1.3 km). However, for the EPR experiments, the layer 2A/2B boundary has been characterised with a high velocity gradient transition zone between two layers with lower velocity gradients. No such transition zone has been modelled at the VFR at depths of less than 1.3 km below the seafloor. A change in vertical  $P$ -wave velocity gradient suggests a change in the properties within the crust, possibly a lithological transition from dominantly extrusive material to dominantly intrusive dykes, or a porosity change within the extrusive layer. There is no evidence of such a  $P$ -wave velocity discontinuity or change in  $P$ -wave velocity gradient anywhere else in the upper crust apart from at the position of the layer 2A–2B/C boundary based on the modelling of Turner (1998), and on this basis the layer 2A–2B/C boundary is believed to be the most likely position for the converting interface. The remaining analysis in this chapter will proceed on this basis. However, Fig. 4.3 shows that an interface at which there is a change in  $S$ -wave velocity but no change in  $P$ -wave velocity is viable for generating detectable  $P$ - $S$  mode converted arrivals. Therefore the possibility that mode conversion occurs at such an interface which does not coincide with the layer 2A–2B/C boundary cannot be ruled out since it would not be detectable in the  $P$ -wave velocity structure.

A final point to note is that the  $S$ -wave transmission coefficients in Fig. 4.3 are negative. Inspection of Fig. 4.2 shows that, in this case, the polarity of first motion of the  $P$ - $S$  mode converted arrival recorded by a horizontal geophone at the seafloor should be the same as the polarity of first motion of the  $P$ -wave first arrival. This characteristic is useful for accurate picking of  $P$ - $S$  mode converted arrival times. In order to use this characteristic to its best advantage, it is desirable that the orientation of the horizontal geophones be known. This problem is addressed in the next section.



### 4.3 Horizontal geophone orientation

Each OBS was equipped with a gimballed three-component geophone package. The two horizontal geophones were orthogonal to each other, but their orientation with respect to model co-ordinates was unknown since the OBSs spin during their descent through the water column. Knowledge of the geophone orientation allows the horizontal geophone traces to be resolved into the vertical shot-receiver plane, for which the signal strength is expected to be maximum, and hence  $P$ - $S$  mode converted arrivals easiest to identify on the assumption that their polarities are the same as those of the equivalent  $P$ -wave first arrivals as outlined in the previous section. The horizontal geophone orientation was determined using direct water-wave arrivals as illustrated in Fig. 4.5. The  $x'$ - and  $y'$ -axes in Fig. 4.5 are defined as the direction of positive motion recorded by the two horizontal geophones and the  $x$ - and  $y$ -axes define the model co-ordinate system. The relative amplitude and polarity of a direct water-wave arrival recorded by the two horizontal geophones allows the azimuth of the direct water-wave arrival relative to the  $x'$ -axis ( $\phi$  in Fig. 4.5) to be determined. If the shot and receiver positions, and hence shot-receiver azimuth ( $\theta$ ), are known, the orientation of the  $x'$ - and  $y'$ -axes relative to the geographic co-ordinate system ( $\alpha$ ) may be calculated. Direct water-wave arrivals are most suitable for this purpose because they have very high SNR and their ray paths are unaffected by rough bathymetry, intracrustal interfaces and lateral velocity variations which might deviate crustal ray paths such that the azimuth of particle motion recorded by the OBS is not the same as the shot-receiver azimuth. This basic method was implemented for each OBS location as outlined below.

Shot positions were GPS navigated and OBS locations were determined using the direct water-wave travel times as described in section 2.3.3. Therefore the shot-receiver azimuth may be calculated for each shot-receiver pair ( $\theta$  in Fig. 4.5) The co-ordinate system described in section 2.3.2 was used, whereby the positive  $x$ -axis is approximately perpendicular to the ridge axis along a bearing of  $111^\circ$ . Azimuths quoted hereafter in this chapter are defined as  $000^\circ$  along the positive  $x$ -axis and  $090^\circ$  along the positive  $y$ -axis. The angle  $\phi$  in Fig. 4.5 was calculated automatically for each shot for which a direct water-wave arrival was identified by determining the maximum and minimum amplitude value of both horizontal geophone traces within a 30 ms time window after the position of the direct water-wave arrival travel time pick. For both traces, the polarity of first motion was determined by identifying whether the maximum value preceded the minimum value or vice-versa (see Fig. 4.6). Hence the amplitude

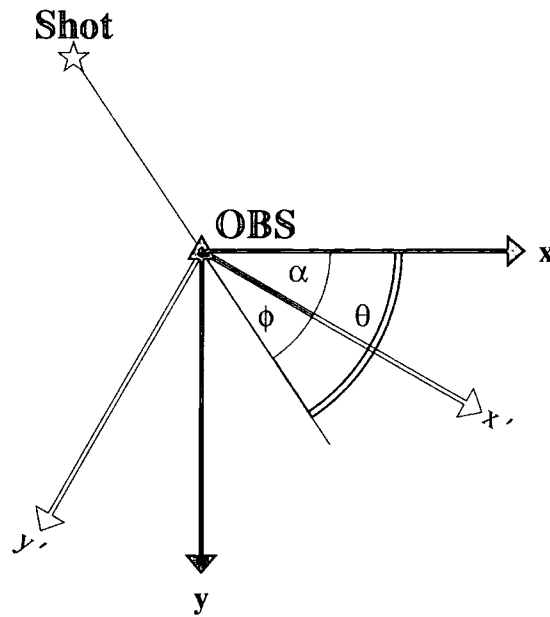


**Figure 4.5:** Determination of horizontal geophone orientation using direct water-wave arrivals. The  $x$ - and  $y$ -axes define model co-ordinates, and the  $x'$ - and  $y'$ -axes define the horizontal geophone orientations. If the shot and receiver positions are known, the shot-receiver azimuth ( $\theta$ ) may be determined. The shot-receiver azimuth relative to the  $x'$ -axis ( $\phi$ ) may be calculated using the relative amplitude and polarity of first motion of the direct water-wave arrival, and hence the azimuth of the  $x'$ -axis relative to the  $x$ -axis ( $\alpha$ ) may also be determined.

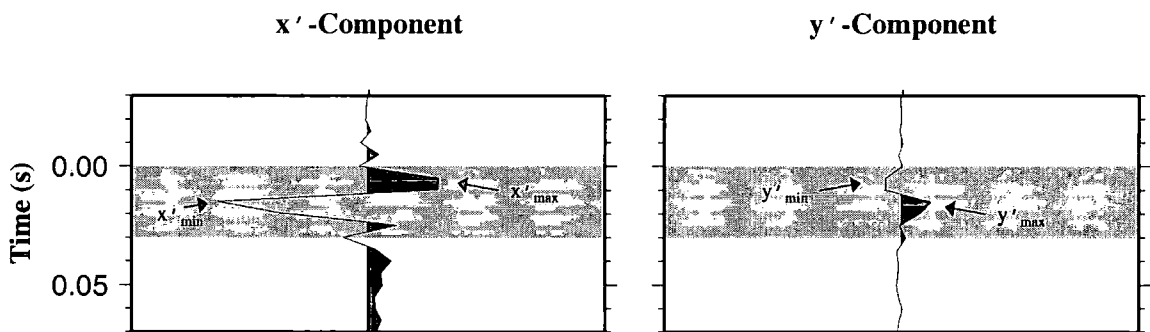


**Figure 4.6:** Direct water-wave arrivals recorded by the  $x'$ - and  $y'$ -component geophones. The trace has been shifted such that the direct water-wave travel time pick position is time zero, and the shaded area marks a 30 ms time window after this pick position. The algorithm for determining the angle  $\phi$  in Fig. 4.5 works by determining the maximum and minimum value of both traces within the time window indicated by the shaded area ( $x'_{max}$ ,  $x'_{min}$ ,  $y'_{max}$  and  $y'_{min}$ ), and the whether the maximum value precedes the minimum or vice-versa. In the example shown in this figure,  $\phi$  may be determined using equations 4.9 and 4.10 and calculating the mean where the two values agree to within  $5^\circ$ .

and polarity of both first and second motion for both horizontal geophones were identified. The 30 ms time window was selected to be as short as possible to minimise the possibility of interference from later arrivals while still encompassing a full wavelength.  $\phi$  was calculated using the amplitude and polarity of both first and second motion. In the example shown in Fig. 4.6, the polarity of first motion is positive for the  $x'$ -component geophone and negative for the  $y'$ -component geophone. Therefore, using the first motion amplitudes

$$\phi = \tan^{-1} \frac{y'_{\min}}{x'_{\max}}, \quad (4.9)$$

and using the second motion amplitudes

$$\phi = \tan^{-1} \frac{y'_{\max}}{x'_{\min}}, \quad (4.10)$$

where  $x'_{\max}$ ,  $x'_{\min}$ ,  $y'_{\max}$  and  $y'_{\min}$  represent the maximum and minimum values of the  $x'$  and  $y'$  traces within the 30 ms time window as shown in Fig. 4.6. The positive polarity of the  $x'$ -component first motion means  $\phi$  must lie in the range  $-90^\circ < \phi < 90^\circ$  in this case. Where the two values of  $\phi$  differed by more than  $5^\circ$  the result was discarded as unreliable. Such unreliable results occurred where there was interference from later arrivals or where the signal recorded by one of the geophones was particularly weak, in which case the automated approach may give spurious results. Where the two values of  $\phi$  were in good agreement the mean was calculated and subtracted from the known value of  $\theta$  to give the orientation of the  $x'$  geophone relative to the  $x$ -axis,  $\alpha$ .

Values obtained for the orientation of the  $x'$  geophone with respect to the  $x$ -axis ( $\alpha$  in Fig. 4.5) by this method are shown in Fig. 4.7 for each OBS location. For each instrument, most shots give fairly consistent results with a few outliers. These outliers were removed by calculating the mean and standard deviation of  $\alpha$ , rejecting any values which were more than two standard deviations from the mean, and recalculating the mean and standard deviation. This process was repeated until the value of the mean converged to an approximately constant value. The mean values of  $\alpha$  and standard deviation of the remaining results for each OBS location are shown in Fig. 4.7 and summarised in Table 4.1.

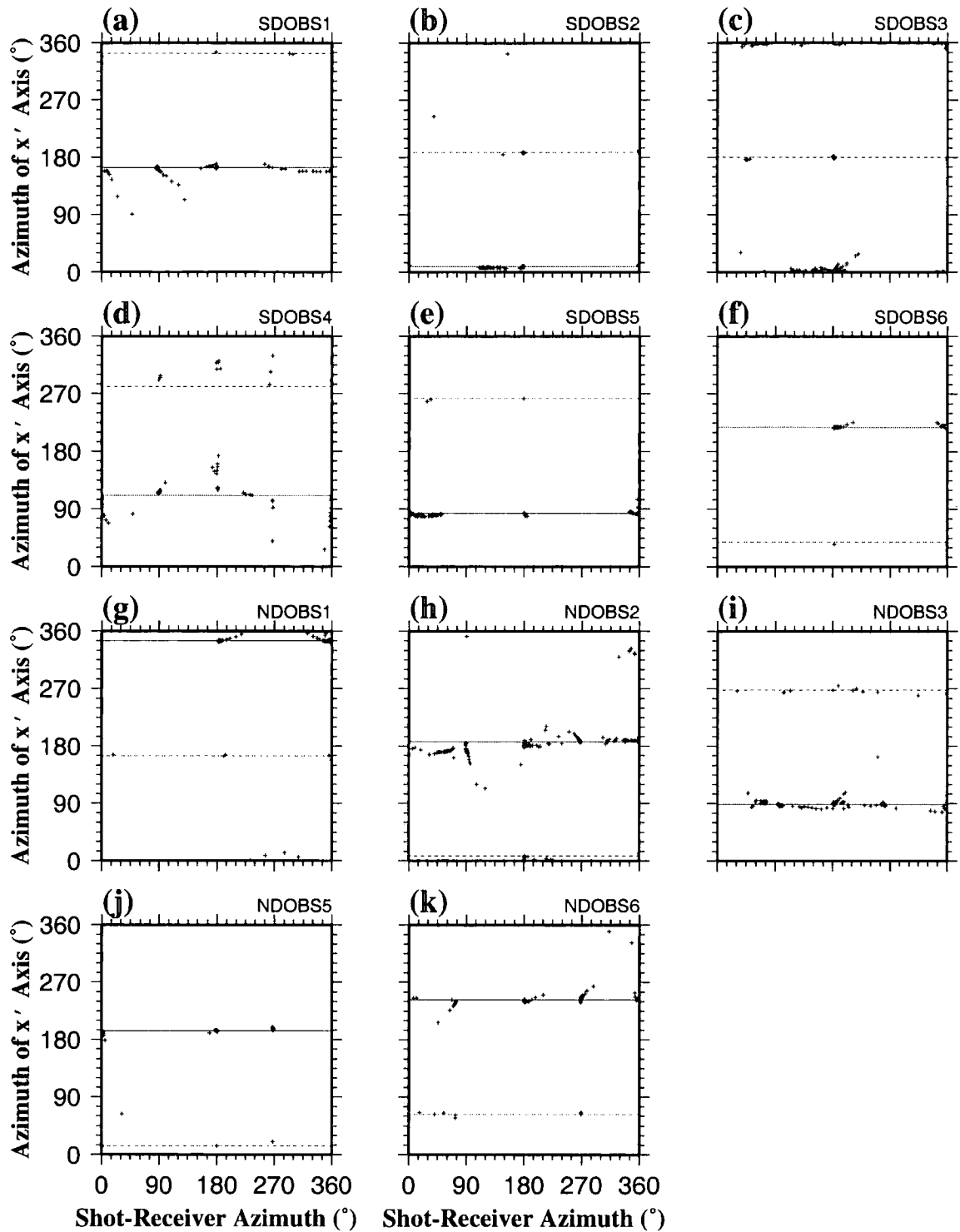


**Figure 4.7:** Horizontal geophone orientations for each OBS location, derived using the relative motion observed for each horizontal geophone based on analysis of direct water-wave arrivals. Each cross represents one direct water-wave arrival. For each OBS location, most direct water-wave arrivals gave similar azimuths for the  $x'$ -axis (defined in Fig. 4.5) which suggests that the method employed is reliable. The outliers probably arise from direct water-wave arrivals which have low amplitude on one or both horizontal geophones. Some outliers have azimuths  $\sim 180^\circ$  from the modal value, which suggests that the polarity of the water-wave arrivals has been misidentified for these shots. These mean azimuths for the  $x'$ -axis with these outliers discarded are shown as solid lines in each plot, and the dashed lines represent the azimuth  $180^\circ$  different from these mean values.

OBS Location	Mean Azimuth of $x'$ -axis ( $^{\circ}$ )	Standard Deviation of $x'$ -axis Azimuth ( $^{\circ}$ )	Number of points averaged	Number of Outliers Discarded
SDOBS1	163.6	2.8	145	10
SDOBS2	8.5	2.1	179	16
SDOBS3	0.1	2.5	229	36
SDOBS4	110.8	5.8	86	36
SDOBS5	83.1	2.4	193	4
SDOBS6	218.4	1.9	70	1
NDOBS1	344.6	2.1	93	12
NDOBS2	187.2	4.4	187	71
NDOBS3	88.5	3.5	161	21
NDOBS5	193.8	2.1	152	10
NDOBS6	242.8	3.6	121	12

**Table 4.1:** Summary of each OBS's horizontal geophone orientation determined using the relative phase amplitude recorded by the orthogonal horizontal geophones for direct water-wave arrivals. The mean and standard deviation of  $x'$ -axis azimuths were calculated for the shots plotted in Fig. 4.7. Any values more than two standard deviations away from the mean were discarded and the process repeated until the value of the mean converged to an approximately constant value. The number of outliers discarded before this convergence occurred and the number of points remaining are shown in the right-most columns of the table.

Once the orientation of the horizontal geophones has been established, horizontal geophone traces may be resolved into any direction. For example, traces that would have been recorded by geophones oriented parallel to the positive  $x$ - and  $y$ -axes may be calculated from the raw horizontal geophone traces using the formulae

$$\begin{aligned} x &= x' \cos \alpha - y' \sin \alpha \\ y &= x' \sin \alpha + y' \cos \alpha, \end{aligned} \quad (4.11)$$

where  $x'$  and  $y'$  are samples recorded by the horizontal geophones oriented parallel to the  $x'$ - and  $y'$ -axes respectively,  $x$  and  $y$  are equivalent samples parallel to the  $x$ - and  $y$ -axes, and  $\alpha$  is the angle between the  $x'$ - and  $x$ -axes as shown in Fig. 4.5. Hereafter,

these resolved traces will be referred to as  $x$ - and  $y$ -component traces. The  $x$ - and  $y$ -component sections are particularly useful for picking in-line arrivals for which the shot-receiver azimuth approximately parallels either the  $x$ - or  $y$ -axis. For the case of a 1-D isotropic structure the first motion azimuth of the  $P$ -wave first arrival and  $P$ - $S$  mode converted arrival are expected to also parallel the  $x$ - or  $y$ -axis. Therefore the  $P$ - $S$  mode converted arrivals for in-line shots should be strongest, and easiest to pick, on the  $x$ - and  $y$ -component sections. Picking and modelling of in-line  $P$ - $S$  mode converted arrival travel times is described fully in the next section. However, it will be shown that the assumption of a 1-D isotropic structure is an oversimplification, although it is a useful initial approximation. The method for resolving the horizontal geophone traces into different directions described above was used to investigate the first motion azimuth of  $P$ -wave first arrivals and  $P$ - $S$  mode converted arrivals by seeking the direction which gave a maximum in signal strength. This technique will be fully discussed in section 4.5.

#### 4.4 Travel time modelling

The simple travel time analysis described in section 4.2 suggests a typical Poisson's ratio of 0.42 for layer 2A. In this section, a more sophisticated travel time analysis is presented based on 2-D modelling of  $P$ - $S$  mode converted arrivals identified for in-line shots.  $P$ - $S$  mode converted arrivals were picked manually wherever they were observed on the  $x$ - or  $y$ -component sections according to whether the shot-receiver azimuth most closely paralleled the  $x$ - or  $y$ -axis. The automatic picking tool described in section 2.3.1 was occasionally used to aid picking, but was not employed extensively because there is significant coherent interference from earlier arriving phases which limits the effectiveness of the cross-correlation-based picking tool. The polarity of first motion of the  $P$ - $S$  mode converted arrival was expected to be the same as the  $P$ -wave first arrival as shown in Fig. 4.2. This characteristic was used as a picking aid, particularly for weaker arrivals. For each receiver, in-line shots were grouped according to shot-receiver azimuth.  $P$ - $S$  mode converted arrivals were identified for every instrument position except SDOBS5, although for some OBS locations they were not observed for every shot-receiver azimuth.

Turner (1998) modelled the 2-D  $P$ -wave velocity structure for a number of across-axis and axis-parallel profiles. The principal profiles are labelled in Fig. 1.8. These models were used as the basis for modelling the  $P$ - $S$  mode converted arrival travel times. The shot-receiver offset was calculated for each shot-receiver pair for which a  $P$ - $S$  mode converted arrival was identified, and a shot depth of 8 m (the nominal depth of the airgun array) assumed. *RAYINVR*, a 2-D ray tracing and travel time inversion package, was then used to trace rays for these shot-receiver pairs. A full description of the ray tracing method employed by *RAYINVR* is given by Zelt & Smith (1992). Rays were traced from receiver to shot for computational efficiency since there were many more shots than receivers. In order to model the  $P$ - $S$  mode converted arrivals, rays were traced as  $S$ -waves from the receiver to the layer 2A-2B/C boundary and as  $P$ -waves from there to the receiver. A locally constant Poisson's ratio in layer 2A in the vicinity of each receiver was assumed. The layer 2A Poisson's ratios in the vicinity of each receiver were then adjusted in order to best fit the predicted and observed travel times for the  $P$ - $S$  mode converted arrivals. No modifications were made to the  $P$ -wave velocity structure.

The predicted ray paths and best fitting travel times for  $P$ - $S$  mode converted arrivals, plus the observed travel times, are shown in Fig. 4.8 for each of the 2-D profiles. Given the assumptions upon which this analysis is based, a precise fit between predicted and observed travel time is an unrealistic aim. It is unlikely that the Poisson's ratio is locally constant within layer 2A at each OBS location, and the interface at which  $P$ - $S$  mode conversion occurs may not precisely coincide with the layer 2A-2B/C boundary modelled by Turner (1998). The observed travel times are plotted as bars in Fig. 4.8 indicating a nominal uncertainty of  $\pm 100$  ms, approximately corresponding to one period. Fig. 4.8 shows that the predicted travel times generally match the observed travel times within this uncertainty. For some OBS locations, the apparent Poisson's ratio modelled using groups of shots with azimuths differing by  $180^\circ$  was different. In such cases, the predicted travel times in Fig. 4.8 were calculated assuming the Poisson's ratio determined for the more reliable group of shots, and a large misfit is observed for the less reliable subset. The Poisson's ratio modelled in layer 2A lies in the range 0.39-0.45, which is similar to values observed in layer 2A elsewhere in young oceanic crust (Christeson *et al.* 1997; Collier & Singh 1998). These observations suggest that



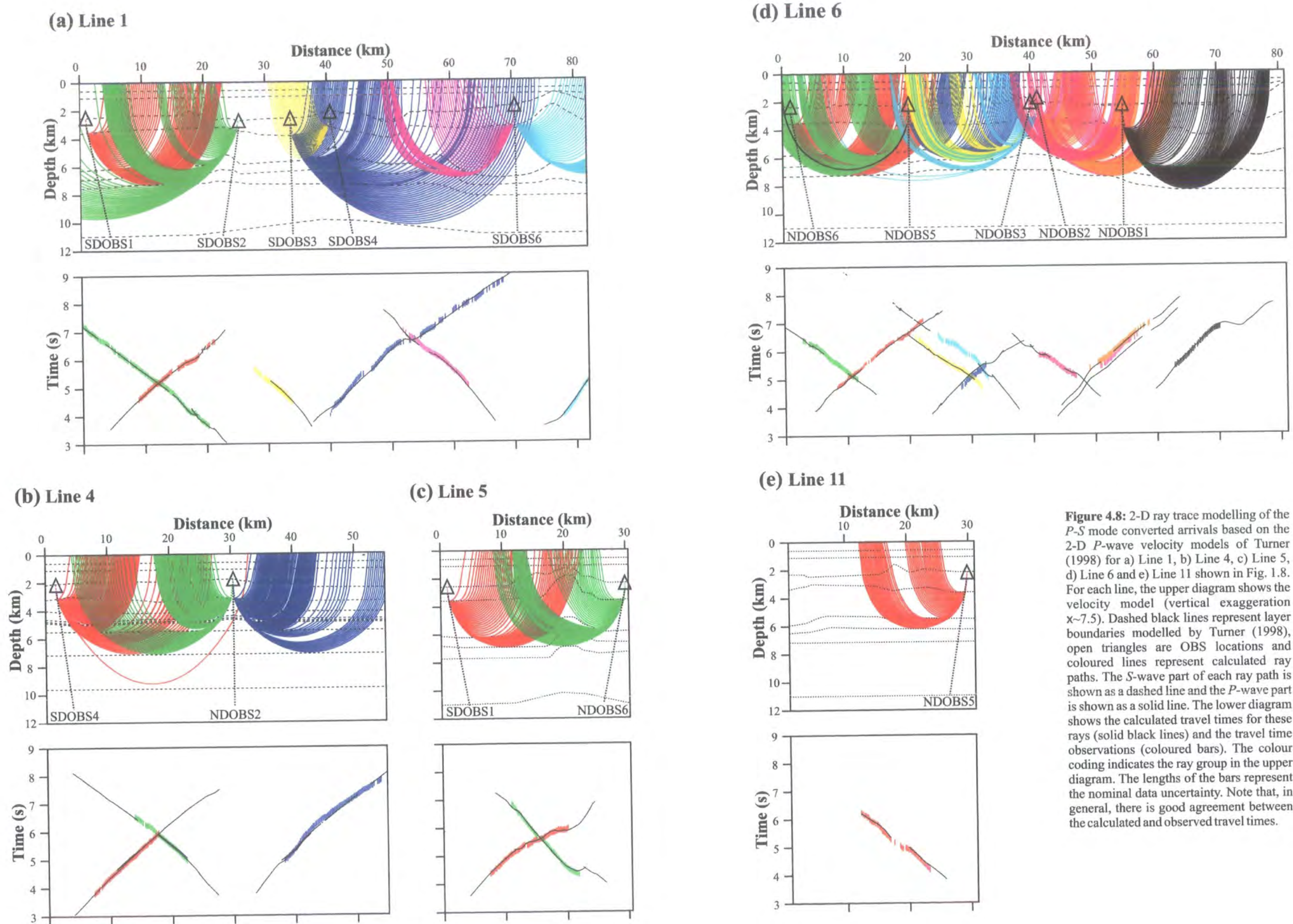


**Figure 4.8:** 2-D ray trace modelling of the *P-S* mode converted arrivals based on the 2-D *P*-wave velocity models of Turner (1998) for a) Line 1, b) Line 4, c) Line 5, d) Line 6 and e) Line 11 shown in Fig. 1.8. For each line, the upper diagram shows the velocity model (vertical exaggeration  $\times \sim 7.5$ ). Dashed black lines represent layer boundaries modelled by Turner (1998), open triangles are OBS locations and coloured lines represent calculated ray paths. The *S*-wave part of each ray path is shown as a dashed line and the *P*-wave part is shown as a solid line. The lower diagram shows the calculated travel times for these rays (solid black lines) and the travel time observations (coloured bars). The colour coding indicates the ray group in the upper diagram. The lengths of the bars represent the nominal data uncertainty. Note that, in general, there is good agreement between the calculated and observed travel times.

the assumptions upon which the modelling presented in this section is based are reasonable. Poisson's ratios modelled at each instrument position for each 2-D profile are summarised in Table 4.2, and their geological implications are considered in section 4.6.

OBS Position	Shot-Receiver Azimuth	Apparent Poisson's Ratio	OBS Position	Shot-Receiver Azimuth	Apparent Poisson's Ratio
SDOBS1	090°	0.44	NDOBS1	000°	0.41
SDOBS1	180°	0.44	NDOBS1	180°	0.41
SDOBS2	000°	0.42	NDOBS2	000°	0.43
SDOBS3	180°	0.43	NDOBS2	090°	0.44
SDOBS4	000°	0.41	NDOBS2	180°	0.44
SDOBS4	090°	0.43	NDOBS2	270°	0.44
SDOBS6	000°	0.42	NDOBS3	000°	0.43
SDOBS6	180°	0.42	NDOBS3	180°	0.45
			NDOBS5	000°	0.41
			NDOBS5	180°	0.39
			NDOBS5	270°	0.39
			NDOBS6	180°	0.45
			NDOBS6	270°	0.45

**Table 4.2:** Summary of apparent Poisson's ratio in layer 2A at each OBS location, derived using groups of in-line shots with approximately constant shot-receiver azimuth and the 2-D *P*-wave velocity models of Turner (1998).

The strongest *P-S* mode converted arrivals were recorded by instrument SDOBS4 from shots east of the OBS. Fig. 4.9 shows detail of *x*-component traces for this instrument. This figure shows that the polarity of first motion of the *P-S* mode converted arrival is positive, yet the shot-receiver azimuths for the traces shown is ~180°, i.e. parallel to the negative *x*-axis. The first motion direction of *P-S* mode converted arrivals arising from mode conversion at the layer 2A-2B/C boundary is

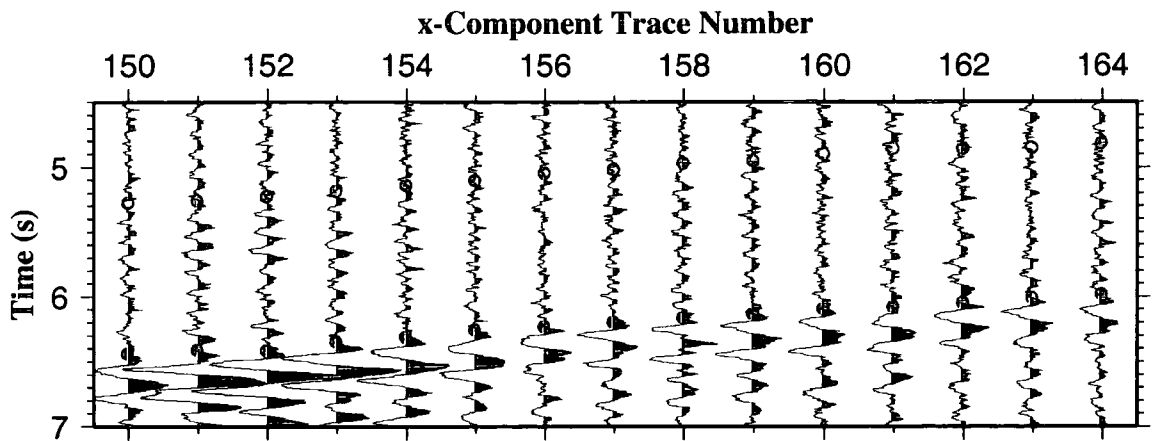


**Figure 4.9:** Detail of  $x$ -component traces for shots recorded by SDOBS4 with an approximate shot-receiver azimuth of  $180^\circ$  (i.e. parallel to the negative  $x$ -axis). Dot centres mark travel time picks of  $P$ -wave first arrivals (red) and  $P$ - $S$  mode converted arrivals (green). The  $P$ - $S$  mode converted arrivals are particularly strong, clearly show positive first motion, and are delayed behind the  $P$ -wave first arrivals by  $\sim 1.2$  s. These arrivals are interpreted as arising from  $P$ - $S$  mode conversion at the roof of an axial melt lens.

expected to be the same as the shot-receiver azimuth (see Fig. 4.2.) In addition, the mode converted arrivals are delayed behind the  $P$ -wave first arrivals by  $\sim 1.2$  s, which is considerably more than the typical delay of  $\sim 0.8$  s. These observations suggest that that these arrivals do not arise from  $P$ - $S$  mode conversion at the layer 2A-2B/C boundary.

It is hypothesised that the arrivals described above arise from  $P$ - $S$  mode conversion at the top of the axial melt lens identified by Collier & Sinha (1992a) and Turner (1998), which is situated directly beneath SDOBS4 (see Fig. 1.10b). In order to test this hypothesis, the transmission coefficient for  $S$ -waves generated by mode conversion at this interface was calculated by again solving Zoeppritz's equations. The melt lens is believed to comprise a high percentage of partial melt. Therefore the  $S$ -wave velocity is likely to be very small and the Poisson's ratio close to the maximum possible value of 0.5. Poisson's ratio in layer 2B/C was assumed to be 0.28 as in previous calculations. Turner (1998) modelled a  $P$ -wave velocity of  $\sim 5.5 \text{ km s}^{-1}$  at the layer 2B/C-3 boundary in the axial region, and densities of  $2620 \text{ kg m}^{-3}$  and  $2500 \text{ kg m}^{-3}$  in layer 2B/C and the melt lens respectively. A melt lens  $P$ -wave velocity of  $3.0 \text{ km s}^{-1}$  was assumed in order to be consistent with laboratory measurements of the  $P$ -wave velocity of andesitic melt (Murase & McBirney 1973). These assumptions of the melt lens properties will be discussed further in section 5.2.2. Fig. 4.10 shows the transmission coefficient for  $S$ -waves generated by mode conversions at an interface

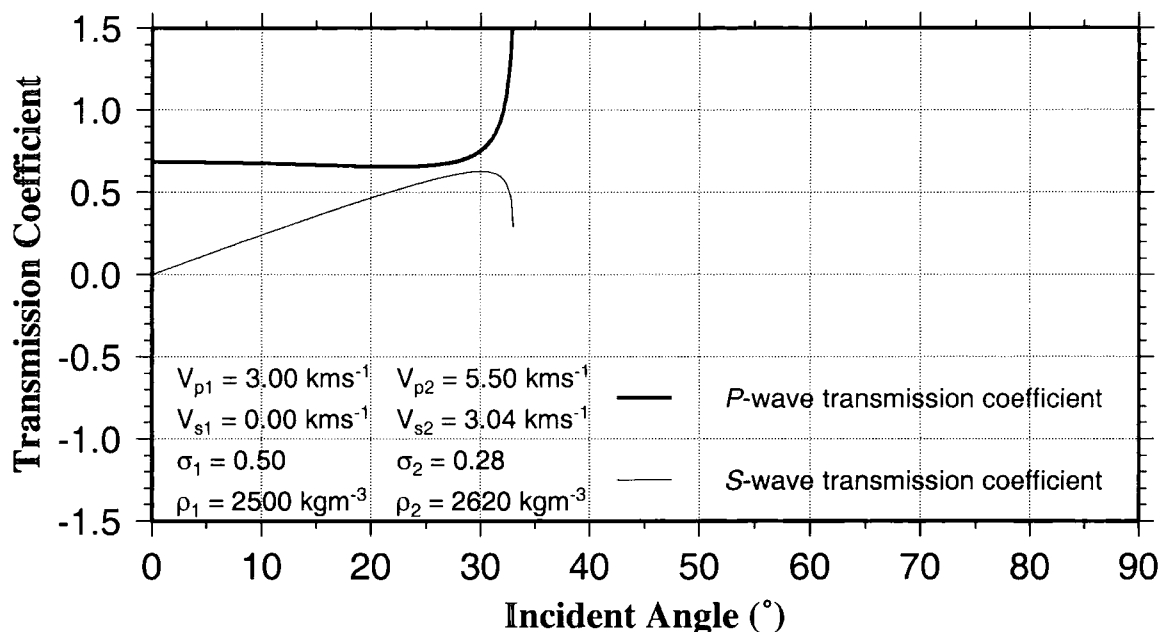


**Figure 4.10:**  $P$ - and  $S$ -wave transmission coefficients calculated for a  $P$ -wave incident on the roof of the melt lens from below. The  $P$ - and  $S$ -wave velocity ( $V_p$  and  $V_s$  respectively), and density ( $\rho$ ) conditions in each layer, are indicated in the bottom left-hand corner. Poisson's ratios ( $\sigma$ ) in each layer, which may be calculated from  $V_p$  and  $V_s$ , are also shown. Suffix 1 refers to the melt lens and suffix 2 to layer 2B/C. The  $S$ -wave transmission coefficient is of greater magnitude and opposite sign to that at the layer 2A-2B/C boundary. For angles of incidence  $>33^\circ$  the solutions to Zoeppritz's equations are complex and thus not shown.

with these properties. This figure shows that the transmission coefficient is positive and of greater magnitude than those in Fig. 4.3 for the layer 2A-2B/C boundary, which would account for the greater magnitude and opposite polarity of the anomalous  $P$ - $S$  mode converted arrivals recorded by SDOBS4. The greater depth to the melt lens would account for the increased travel time.

Rays were traced from SDOBS4 through the velocity structure modelled by Turner (1998) for Line 1, starting as  $S$ -waves, then undergoing mode conversion at the top of the melt lens and travelling as  $P$ -waves to shot positions east of the axis. A Poisson's ratio of 0.43 was assumed for layer 2A based on modelling of arrivals generated by  $P$ - $S$  mode conversion at the layer 2A-2B/C boundary for shot-receiver azimuths of  $090^\circ$  (see Table 4.2), which are stronger and more numerous than arrivals for shot-receiver azimuths of  $000^\circ$  and are therefore believed to give a more reliable measure of layer 2A Poisson's ratio. Fig. 4.11 shows the results of travel time modelling for the melt lens  $P$ - $S$  mode converted arrivals. This fit was obtained with a Poisson's ratio of 0.32 in layer 2B/C, which is at the upper end of the range 0.25-0.32



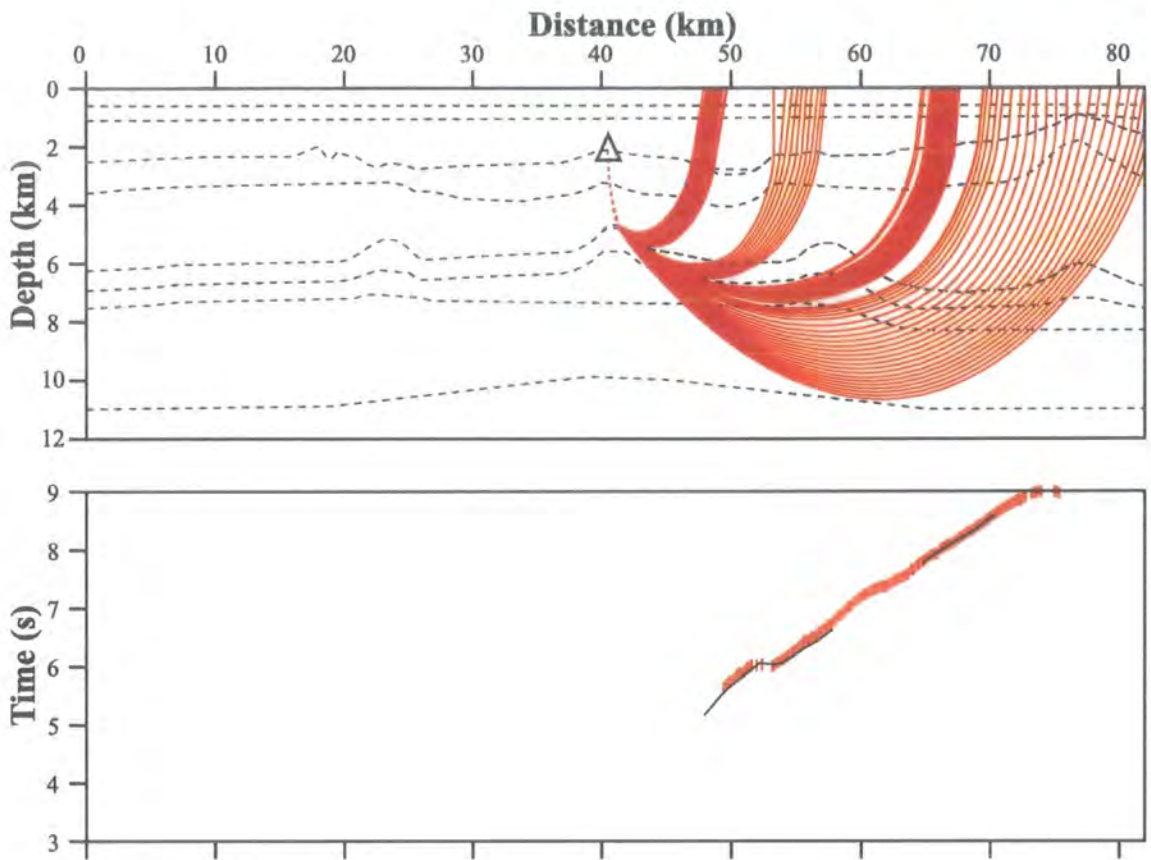


**Figure 4.11:** 2-D ray trace modelling of the melt lens  $P$ - $S$  mode converted arrivals, based on the 2-D  $P$ -wave velocity model of Turner (1998) for Line 1 (Fig. 1.10). The upper diagram shows the velocity model (vertical exaggeration  $\times \sim 7.5$ ). Dashed black lines represent layer boundaries modelled by Turner (1998), red lines represent calculated ray paths. The  $S$ -wave part of each ray path is shown as a dashed line and the  $P$ -wave part is shown as a solid line. The lower diagram shows the calculated travel times for these rays (solid black lines) and the travel time observations (red bars). The lengths of the bars represent the nominal data uncertainty. Note that, in general, there is good agreement between the predicted and observed travel times.

typically observed for mid-lower oceanic crust (Spudich & Orcutt 1980b; Au & Clowes 1984; Bratt & Solomon 1984; Christeson *et al.* 1997; Collier & Singh 1998). Therefore the top of the melt lens is believed to be a viable interface at which  $P$ - $S$  mode conversion might occur for these anomalous arrivals. SDOBS4 is situated above the western edge of the melt lens modelled by Turner (1998) whilst the predicted ray paths in Fig. 4.11 show that mode conversion is predicted to occur east of the OBS location. This observation may explain why arrivals arising from mode conversions at the top of the melt lens are not identified for shots west of the axis. Arrivals resulting from  $P$ - $S$  mode conversion at the top of the melt lens were not observed at any of the axial instruments in the *Seismic North* deployment despite the presence of a melt lens modelled by Collier & Sinha (1992a) and Turner (1998). A geological interpretation of the modelling described above is presented in section 4.6.2.

The analysis described in this section further suggests that the majority of the  $P$ - $S$  mode converted arrivals may be adequately modelled as arising from conversion at the layer 2A-2B/C boundary, with the exception of some anomalous arrivals recorded by an axial instrument which are believed to arise from conversion at the top of the axial melt lens. A Poisson's ratio of 0.39-0.45 is modelled in layer 2A, which is in good agreement with the value of 0.42 calculated in section 4.2. For some OBS locations (e.g. NDOBS5), different values of Poisson's ratio were modelled for different shot-receiver azimuths. This observation suggests the possibility that the  $P$ - and  $S$ -wave velocity structure of layer 2A may be anisotropic, a possibility which is investigated in the following section.

#### 4.5 Determination of first motion azimuth

For a 2-D isotropic velocity structure, the azimuth of first motion for both  $P$ -wave first arrivals and  $P$ - $S$  mode converted arrivals parallels the shot-receiver azimuth, as shown in Fig. 4.2. However, inspection of the  $x$ - and  $y$ -component sections suggests that this is not always the case. Fig. 4.12 shows detail of  $x$ - and  $y$ -component traces created for SDOBS2. The shot-receiver azimuths for these traces approximately parallel the  $x$ -axis. Therefore the amplitude of first motion would be expected to be greatest on the  $x$ -component section for both  $P$ -wave first arrivals and  $P$ - $S$  mode converted arrivals. Inspection of Fig. 4.12 shows that the  $P$ -wave first arrivals conform to this expectation, but the  $S$ -wave motion appears to have a significant  $y$ -component. This observation may be indicative of anisotropic structure. Azimuthal anisotropy has been commonly observed in the  $P$ -wave velocity structure of the upper oceanic crust and interpreted as arising from preferentially aligned vertical cracks (e.g. White & Whitmarsh 1984; Caress *et al.* 1992; McDonald *et al.* 1994; Sohn *et al.* 1997; Barclay *et al.* 1998). Such a structure would also give rise to  $S$ -wave velocity anisotropy, which may result in observable  $S$ -wave splitting. This phenomenon is illustrated in Fig. 4.13 for a  $P$ -wave travelling in an isotropic medium incident on an interface with a medium incorporating preferentially aligned vertical cracks which give rise to azimuthal anisotropy. However, the 3-D nature of the seafloor and intracrustal interfaces at the VFR may also cause significant deviation of the ray paths, and hence first motion azimuth of the  $P$ -wave first arrivals and  $P$ - $S$  mode converted arrivals. This effect must be accounted for before any anisotropy can be identified. Therefore a more thorough investigation of the first motion azimuths was undertaken.

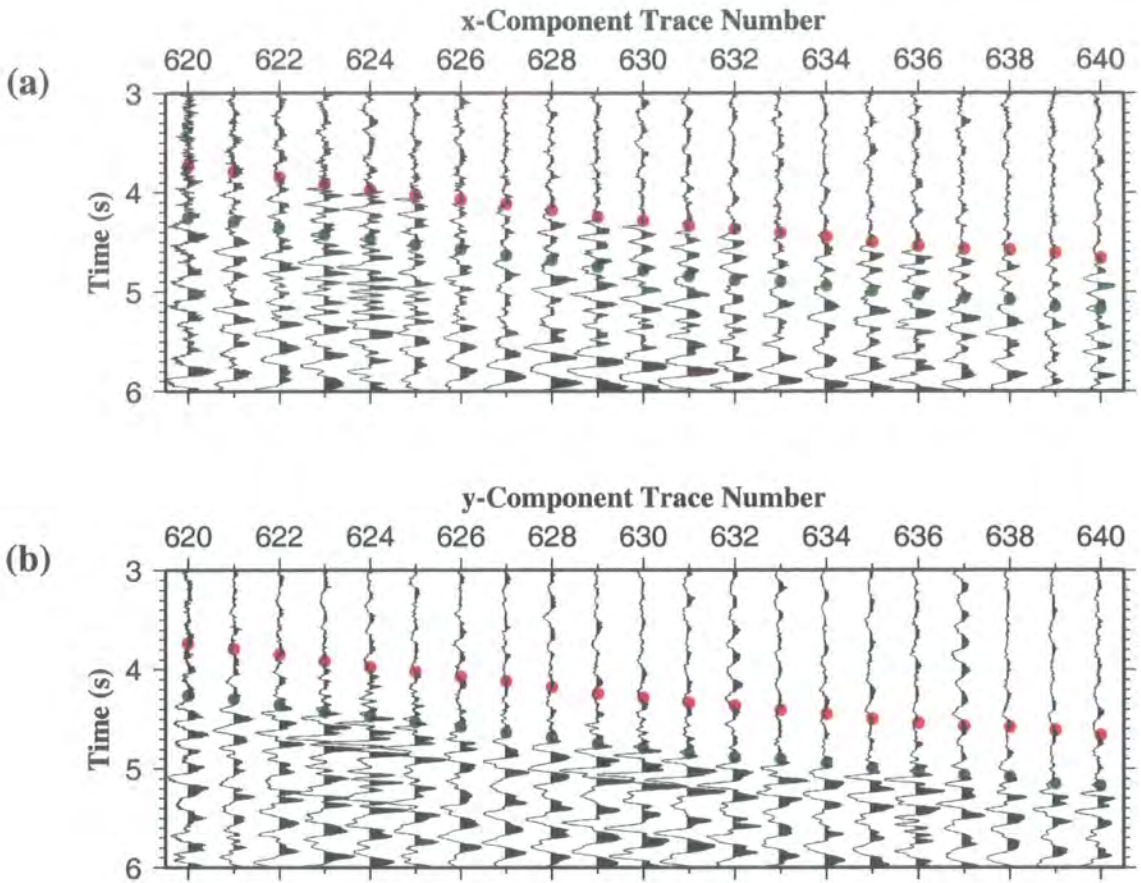


**Figure 4.12:** Detail of  $x$ - and  $y$ -component traces for shots recorded by SDOBS2 with an approximate shot-receiver azimuth of  $000^\circ$  (i.e. parallel to the  $x$ -axis). Dot centres mark travel time picks of  $P$ -wave first arrivals (red) and  $P$ - $S$  mode converted arrivals (green). For the  $P$ -wave first arrivals, the horizontal motion is strongest on the  $x$ -component section, whereas the  $P$ - $S$  mode converted arrival shows a strong component of motion on the  $y$ -component trace, indicating a strong transverse component of particle motion, contrary to expectation.



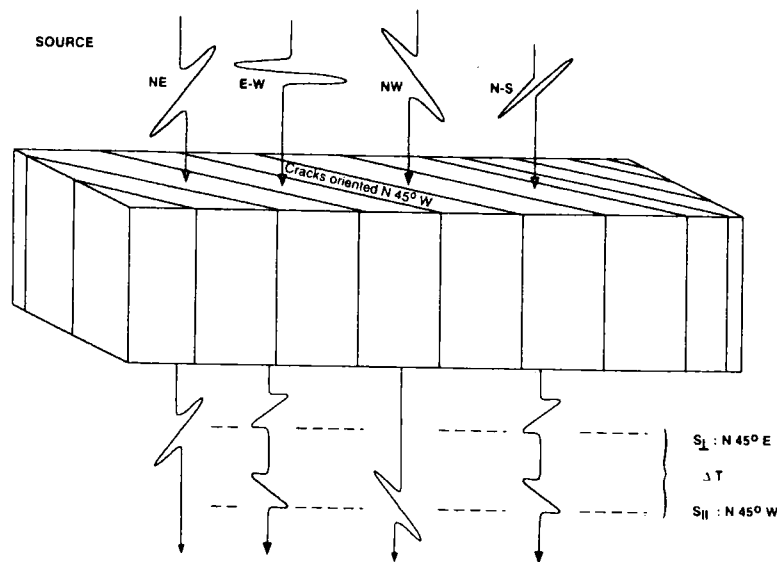


**Figure 4.13:** Illustration of the phenomenon of  $S$ -wave splitting. Particle motion directions for a number of  $S$ -waves incident on a boundary with a cracked, anisotropic medium are shown at the top of the diagram, and the  $S$ -waves after passing through the anisotropic medium are shown at the bottom. When particle motion azimuth is parallel or perpendicular to the cracks, only one  $S$ -wave is transmitted. The velocity when particle motion is parallel to the cracks is greater than when particle motion is perpendicular to the cracks. For all other incident particle motion azimuths, two  $S$ -waves are observed corresponding to the crack-parallel and perpendicular particle motion directions. (After Sheriff & Geldart 1995).

#### 4.5.1 Method

In theory, the method for determining horizontal geophone orientation using direct water-wave arrivals, described in section 4.3, could be applied to determine the first motion azimuth of the  $P$ -wave first arrivals and  $P$ - $S$  mode converted arrivals. However, these arrivals are of very much lower amplitude than direct water-wave arrivals and the waveform less pure, so the amplitude of first motion will be less reliably determined. Particle motion diagrams, whereby the signal recorded by the  $y$ -component geophone is plotted against that recorded by the  $x$ -component geophone have been commonly used to assess the direction of particle motion (e.g. Au & Clowes 1984; Bratt & Solomon 1984; Shearer & Orcutt 1986). In the case of  $P$ - $S$  mode converted arrivals considered in this section, this method is also likely to prove unreliable due to the low signal strength and interference from earlier phases. Therefore, an alternative method based on the mean square signal strength over a given time window was devised. This method is less susceptible to low signal strength and interference than the alternative methods outlined above because it relies on a measure of the average signal strength rather than correlation between individual samples recorded by the two horizontal geophones.

Resolved horizontal geophone traces were created using the method outlined in section 4.3 for each shot–receiver pair for which a  $P$ - $S$  mode converted arrival was identified. The traces were resolved along azimuths between  $000^\circ$  and  $180^\circ$  at  $1^\circ$  intervals. A Butterworth band–pass filter with a 3 dB attenuation point at 40 Hz was applied to each trace to eliminate the effects of the disk spin noise described in section 2.3.1. For each orientation, the mean square signal strength of the first arriving  $P$ -wave and the  $P$ - $S$  mode converted arrival were calculated in a 200 ms window after the pick position. The orientation which gave the maximum signal strength was assumed to represent the first motion azimuth for the arrival under consideration. The 200 ms time window was selected to sample the strongest part of the signal whilst avoiding interference from later arriving phases, and was found to give more consistent results than shorter or longer time windows. SNR was also calculated for each orientation by dividing the RMS value of the trace in a 200 ms time window after the pick position with the RMS value of the trace in a 200 ms time window prior to the  $P$ -wave first arrival pick position. This noise window was chosen to provide a measure of background noise which is unaffected by phases arriving prior to the  $P$ - $S$  mode converted arrival. Arrivals for which the maximum SNR was less than 1.0 were discarded as unreliable. The method described above does not allow the polarity of the  $P$ - $S$  mode converted arrivals to be determined. Inspection of the resolved traces would, in theory, allow the polarity to be identified. However, for many arrivals, adopting this approach did not allow the polarity to be conclusively identified due to low signal strength and interference from earlier phases. In the analysis which follows, the polarity of first motion for both  $P$ - and  $S$ -wave arrivals was assumed have a positive component parallel to the shot–receiver azimuth as shown in Fig. 4.2. This assumption implies that rays encounter a reduction in  $S$ -wave velocity at the converting interface, which is suggested by the high layer 2A Poisson's ratio modelled in the previous section.

The method described in this section was applied to all shot–receiver pairs for which a  $P$ - $S$  mode converted arrival was identified. The results will now be analysed for in–line shots (section 4.5.2) and off–line shots (section 4.5.3).

### 4.5.2 In-line shots

The first motion azimuth of the  $P$ - $S$  mode converted arrivals was first investigated for the in-line shots, for which travel time modelling was conducted as described in section 4.4. In order to account for the effects of the 3-D geometry of the seafloor, the  $P$ -wave first arrival first motion azimuth was also investigated. For each OBS location, shots were grouped according to shot-receiver azimuth. For a 2-D, isotropic velocity structure, the first motion azimuths of the  $P$ -wave first arrival and  $P$ - $S$  mode converted arrivals should be the same as the shot-receiver azimuth. However, rough bathymetry might result in the deviation of first arrival ray paths out of the vertical shot-receiver plane, in which case the  $P$ -wave first motion azimuth observed at the OBS would also be deviated away from the shot-receiver plane since, for  $P$ -waves in an isotropic medium, the particle motion azimuth parallels the ray path. For example, in the presence of a large off-line seamount near the shot position, the seafloor ray entry point for the  $P$ -wave first arrival may be deviated off-line towards the seamount due to smaller water column travel time relative to an in-line seafloor ray entry point. The resulting ray path and particle motion azimuth for the first arrival in this case is shown in Fig. 4.14. Rough intracrustal interfaces and lateral velocity variations would have a similar effect, but since the  $P$ -wave first arrivals considered in this section encounter no first-order velocity discontinuities at intracrustal interfaces, these effects are likely to be very small relative to the effect of rough bathymetry. In the example shown in Fig. 4.14, the  $P$ - $S$  mode converted arrival first motion azimuth would be expected to be the same as that for the  $P$ -wave in the presence of isotropic structure, because the ray paths for the two arrivals are approximately the same from the shot to the converting interface. For  $P$ - $S$  mode conversion, depicted in Fig. 4.2, particle motion for all  $P$ - and  $S$ -waves lies within the plane of the diagram, i.e. the particle motion azimuths for incident and transmitted  $P$ -waves, transmitted  $S$ -waves and the normal to the converting interface are coplanar. However, in the presence of anisotropy, particle motion may be excited perpendicular to this plane as shown in Fig. 4.13. Therefore any discrepancy between the  $P$ -wave first arrival and  $P$ - $S$  mode converted arrival first motion azimuths might indicate a component of transverse particle motion arising from anisotropy.

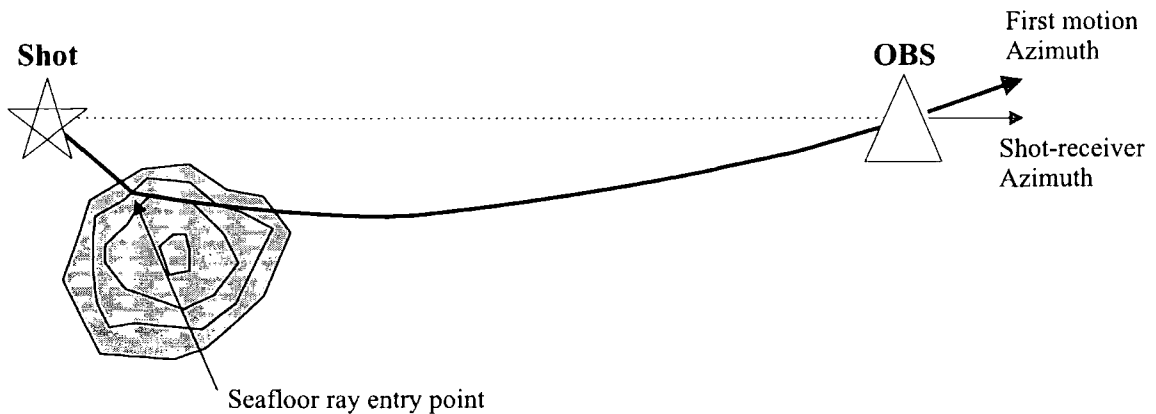


**Figure 4.14:** Schematic diagram showing a plan view of the  $P$ -wave first arrival ray path (solid line) to illustrate the effect of rough bathymetry on  $P$ -wave first motion azimuth. In the case illustrated above, the seafloor ray entry point does not lie in the vertical shot-receiver plane because of the large off-line seamount (shaded in grey). Therefore the first motion azimuth is not parallel to the shot-receiver azimuth.

The interpretation outlined above relies upon a number of assumptions about the velocity structure and geometry of the converting interface. These are:

1. the  $P$ - and  $S$ -wave arrivals follow similar paths up to the point at which conversion occurs;
2. lateral variations in the  $P$ - and  $S$ -wave velocity structure between the converting interface and the OBS are minimal; and
3. the converting interface has no component of dip out of the vertical plane containing the incident  $P$ -wave.

Assumption 1 need not be strictly valid provided the properties and geometry of the converting interface are approximately constant in the vicinity of the region in which  $P$ - $S$  mode conversion occurs and the  $P$ -wave first arrival crosses the interface. If assumption 2 is invalid,  $P$ - and  $S$ -wave ray paths may be deviated by different amounts by lateral velocity variations between the converting interface and the OBS, which could give rise to a discrepancy between the first motion azimuths for  $P$ -wave and  $P$ - $S$  mode converted arrivals. However, such effects are likely to be very small unless a first-order interface is encountered as discussed above in the context of the effect of rough seafloor on ray paths.

Assumption 3 requires further attention.  $P$ - $S$  mode conversion is believed to occur at an interface where there is no change in  $P$ -wave velocity. Therefore the transmitted  $P$ -wave will not be refracted at this interface and the particle motion azimuth will be similarly unchanged. However, the transmitted  $S$ -wave will be refracted and, in the isotropic case, the ray path and particle motion must lie in the plane containing the incident  $P$ -wave ray path and the normal to the converting interface. In order for the transmitted  $P$ - and  $S$ -wave first motion azimuths to be the same, this plane must be vertical. The converting interface is assumed to be the layer 2A-2B/C boundary, and wide-angle modelling by Turner (1998) and the 3-D tomographic analysis described in chapter 3 of this study suggest that this interface approximately parallels the seafloor, i.e. it is not horizontal. Therefore, it is likely that, for some  $P$ - $S$  mode converted arrivals, the dip of the converting interface at the point at which mode conversion occurs has a component perpendicular to the vertical plane containing the incident  $P$ -wave (i.e. assumption 3 is invalid). In this case, the normal to the converting interface does not lie in the vertical plane containing the incident  $P$ -wave particle motion direction. Therefore, the first motion azimuth of the transmitted  $S$ -wave may be different from that of the transmitted  $P$ -wave without the need for anisotropy simply because of the 3-D geometry of the converting interface. This possibility should be borne in mind when interpreting the results described below.

For each group of shot-receiver pairs, histograms were plotted for both  $P$ - and  $S$ -wave arrivals, with a class interval of  $10^\circ$ , showing the number of shots for which the first motion azimuth of the arrival in question was in each class. These histograms are shown in Fig. 4.15 for the *Seismic South* deployment and Fig. 4.16 for the *Seismic North* deployment. The mean first motion azimuths are summarised in Tables 4.3 and 4.4 for the *Seismic South* and *Seismic North* deployments respectively. These tables also highlight features of the arrivals and first motion azimuth histograms which should be considered when interpreting these results.

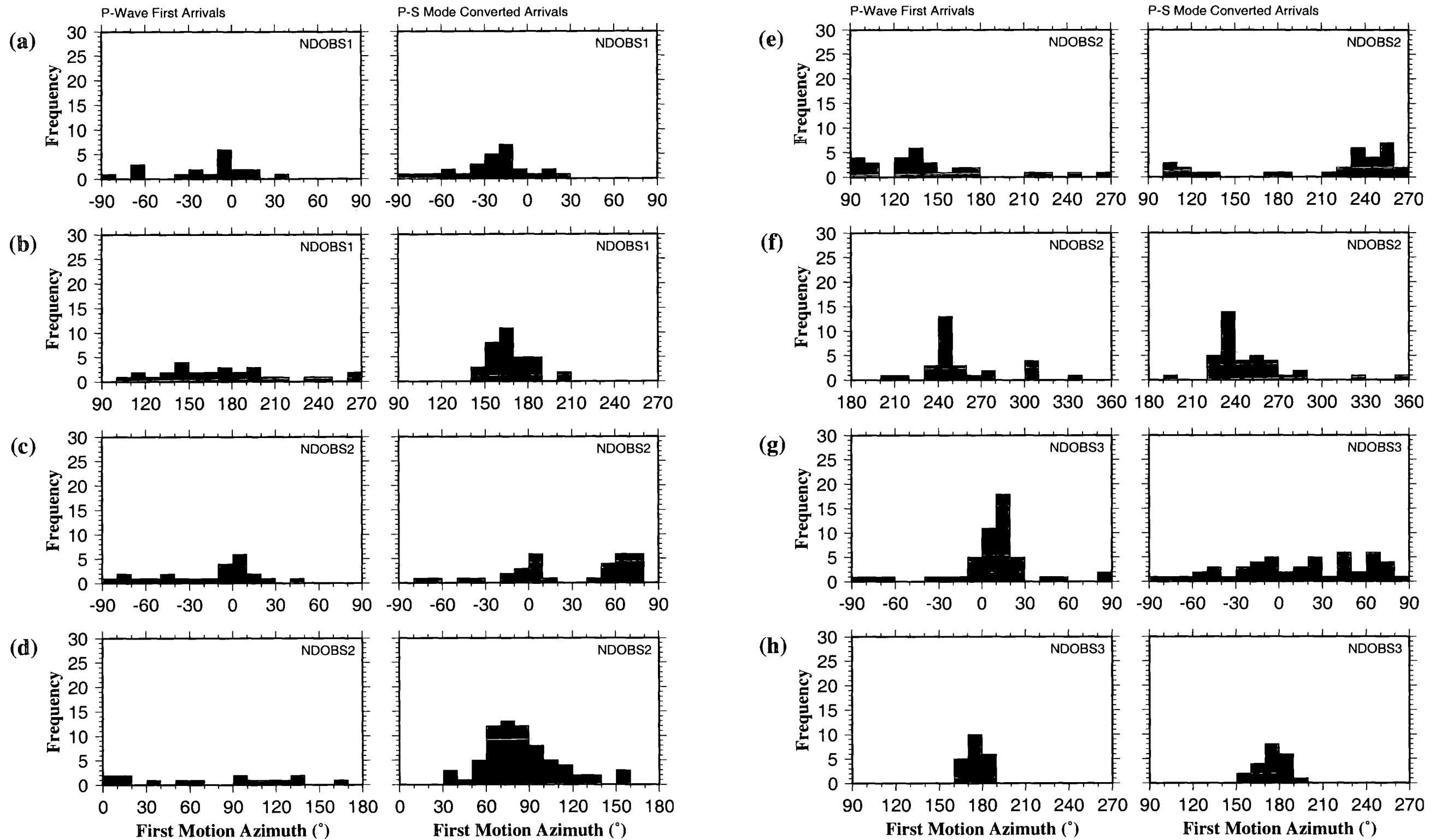
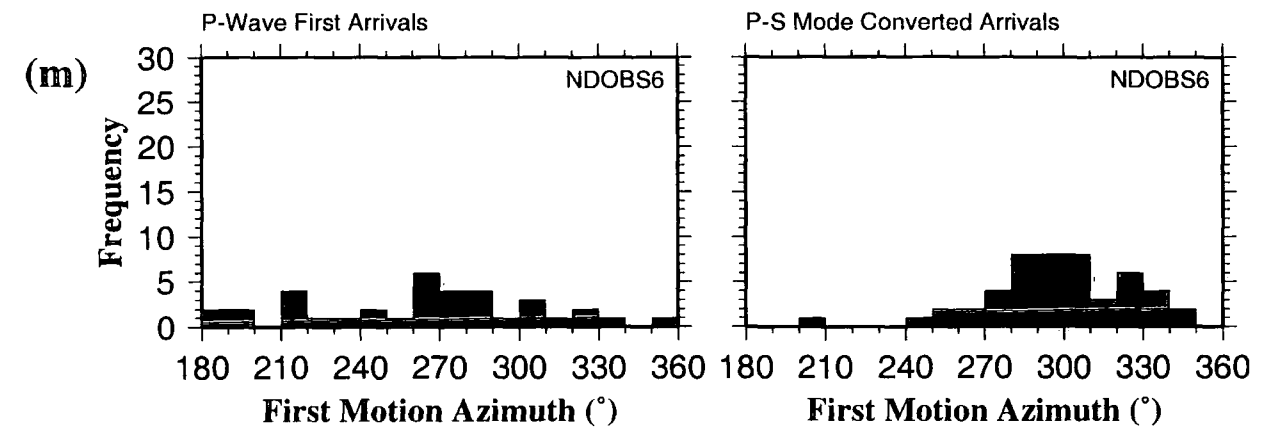
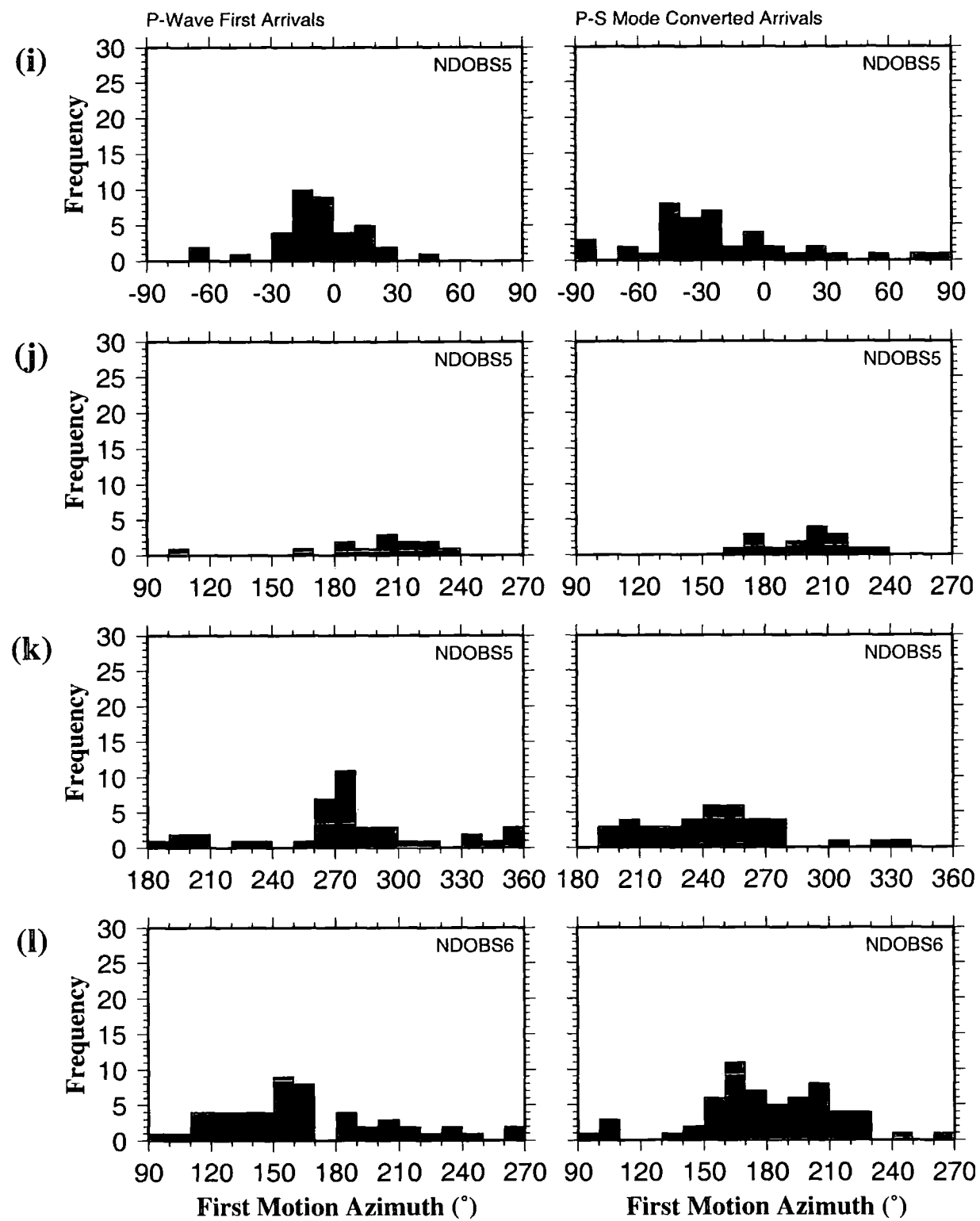
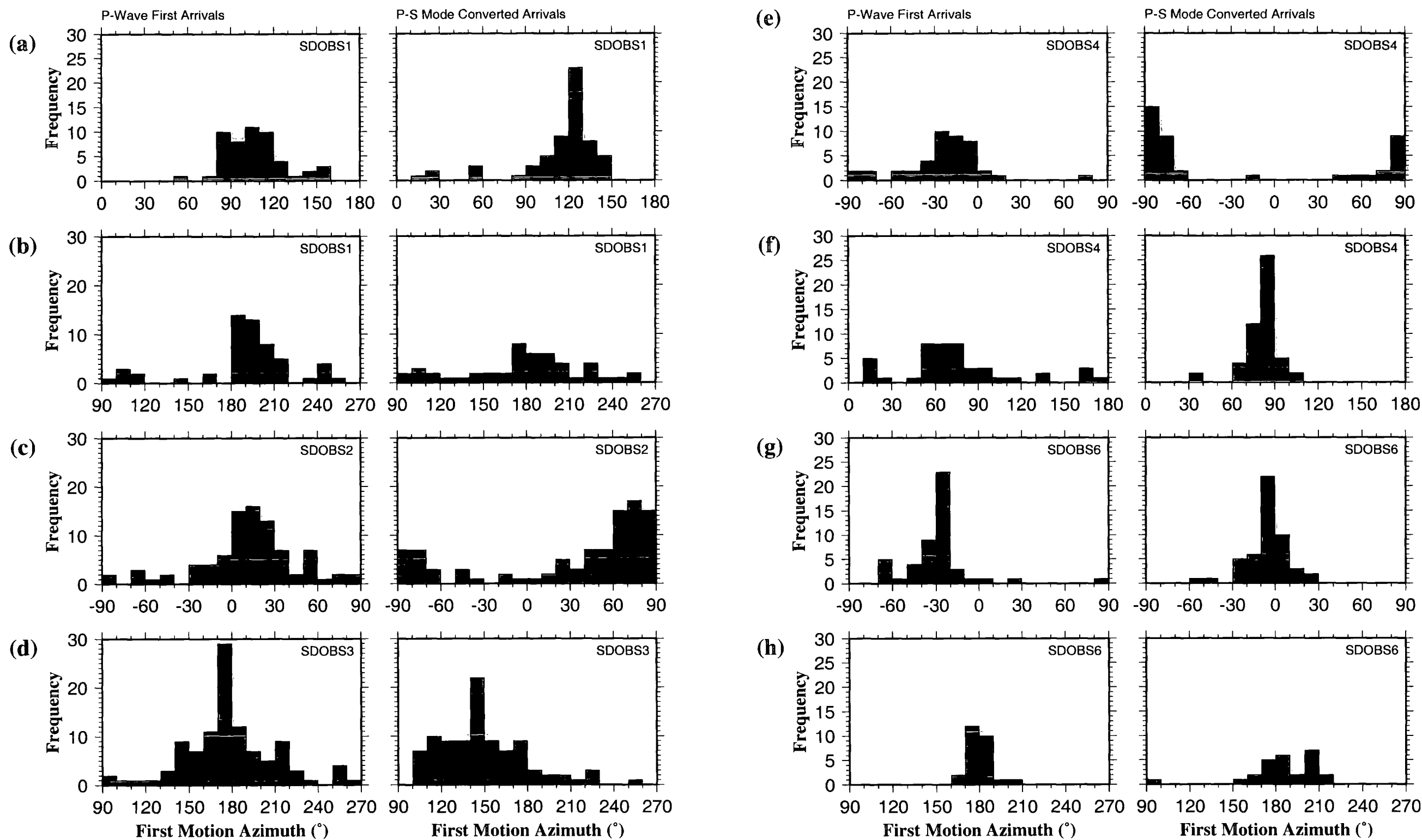


Figure 4.16: Caption on following page



**Figure 4.16:** Histograms of first motion azimuth for *P*-wave first arrivals and *P-S* mode converted arrivals for groups of shots with approximately constant shot-receiver azimuth for the *Seismic North* deployment. Each histogram is centred on the shot-receiver azimuth. Therefore, the greatest frequency of first motion azimuths for both *P*-wave and *P-S* mode converted arrivals would be expected to occur at the centre of each histogram, and any deviation from this behaviour might represent the effect of rough bathymetry or anisotropy. The following combinations of receiver position and shot-receiver azimuth are shown: a) NDOBS1, 000°, b) NDOBS1, 180°, c) NDOBS2, 000°, d) NDOBS2, 090°, e) NDOBS2, 180°, f) NDOBS2, 270°, g) NDOBS3, 000°, h) NDOBS3, 180°, i) NDOBS5, 000°, j) NDOBS5, 180°, k) NDOBS5, 270°, l) NDOBS6, 180° and m) NDOBS6, 270°.





**Figure 4.15:** Histograms of first motion azimuth for  $P$ -wave first arrivals and  $P$ - $S$  mode converted arrivals for groups of shots with approximately constant shot-receiver azimuth for the *Seismic South* deployment. Each histogram is centred on the shot-receiver azimuth. Therefore, the greatest frequency of first motion azimuths for both  $P$ -wave and  $P$ - $S$  mode converted arrivals would be expected to occur at the centre of each histogram, and any deviation from this behaviour might represent the effect of rough bathymetry or anisotropy. The following combinations of receiver position and shot-receiver azimuth are shown: a) SDOBS1, 090°, b) SDOBS1, 180°, c) SDOBS2, 000°, d) SDOBS3, 180°, e) SDOBS4, 000°, f) SDOBS4, 090°, g) SDOBS6, 000° and h) SDOBS6, 180°.

OBS Position	Shot- receiver azimuth	First motion azimuth		Comments
		<i>P</i> -wave	<i>S</i> -wave	
SDOBS1	090°	107°	123°	
SDOBS1	180°	209°	178°	<i>P</i> - <i>S</i> mode converted arrivals are very weak, and the first motion azimuth histogram does not show a clear peak.
SDOBS2	000°	017°	074°	Arrivals are particularly clear and the histograms show very clear peaks.
SDOBS3	180°	179°	147°	
SDOBS4	000°	333° (-027°)	274° (-086°)	
SDOBS4	090°	052°	081°	
SDOBS6	000°	328° (-032°)	356° (-004°)	The deviation of the <i>P</i> -wave first motion azimuth is probably due to the large seamount southwest of the OBS location.
SDOBS6	180°	180°	192°	

**Table 4.3:** Mean first motion azimuths for *P*-wave first arrivals and *P*-*S* mode converted arrivals for the *Seismic South* deployment in the range 0 to 360°. Numbers in brackets are equivalent values on a scale from -180° to 180° which were plotted on the histograms in Fig. 4.15 for convenience for shot-receiver azimuths of 000°.

OBS Position	Shot- receiver azimuth	First motion azimuth		Comments
		<i>P</i> -wave	<i>S</i> -wave	
NDOBS1	000°	339° (-021°)	335° (-025°)	Very few shots, <i>P</i> -wave histogram shows no preferred orientation.
NDOBS1	180°	161°	168°	Very few shots, <i>P</i> -wave histogram shows no preferred orientation.
NDOBS2	000°	343° (-017°)	034°	
NDOBS2	090°	162°	066°	
NDOBS2	180°	121°	251°	
NDOBS2	270°	257°	244°	
NDOBS3	000°	012°	017°	<i>P</i> - <i>S</i> mode converted arrival histogram shows no clear preferred orientation.
NDOBS3	180°	175°	175°	
NDOBS5	000°	352° (-008°)	330° (-030°)	
NDOBS5	180°	211°	199°	Very small no. of shots, weak signal.
NDOBS5	270°	280°	240°	
NDOBS6	180°	159°	180°	The double peak in the <i>P</i> - <i>S</i> mode converted arrival histogram is probably due to seamounts.
NDOBS6	270°	259°	302°	The deviation of the <i>P</i> - <i>S</i> mode converted arrival azimuth is probably due to the seamount southwest of the OBS. The <i>P</i> -wave histogram shows no clear preferred orientation.

**Table 4.4:** Mean first motion azimuths for *P*-wave first arrivals and *P*-*S* mode converted arrivals for the *Seismic North* deployment in the range 0 to 360°. Numbers in brackets are equivalent values on a scale from -180° to 180° plotted on the histograms in Fig. 4.16 for convenience for shot-receiver azimuths of 000°.

The first motion azimuths summarised in Tables 4.3 and 4.4 are represented in Fig. 4.17, which shows the bathymetry, OBS locations and first motion azimuths for  $P$ -wave first arrivals and  $P$ - $S$  mode converted arrivals at each OBS location determined by the method described above.  $P$ -wave first motion azimuths generally parallel the shot-receiver azimuth. For those groups of shots for which this is not the case, off-line seamounts can usually be identified to explain the discrepancy as indicated in Tables 4.3 and 4.4. The  $P$ - $S$  mode converted arrival first motion azimuths are much more variable. At SDOBS6, NDOBS1, NDOBS3 and NDOBS6, the first motion azimuths of  $P$ -wave first arrivals and  $P$ - $S$  mode converted arrivals are similar, which suggests an isotropic structure. At SDOBS1, SDOBS3 and NDOBS5, the  $P$ - $S$  mode converted arrival first motion azimuth is significantly different from that observed for  $P$ -wave first arrivals. This observation suggests the possibility of anisotropic structure at these OBS locations, i.e. the discrepancy between the behaviour of  $P$ - $S$  mode converted arrivals and  $P$ -wave first arrivals is too large to be explained by a rough converting interface. It should be noted that at NDOBS5, shots with shot-receiver azimuths of  $000^\circ$  do not conform to the behaviour shown by shots with shot-receiver azimuths of  $180^\circ$  and  $270^\circ$ . However, as noted in Table 4.4, these shots have very low signal strength and hence this result may be unreliable. At NDOBS2, SDOBS2 and SDOBS4, the  $P$ - $S$  mode converted arrival first motion azimuths behave in an entirely unexpected manner. At NDOBS2, the first motion azimuths for both  $P$ -wave first arrivals and  $P$ - $S$  mode converted arrivals are inconsistent with shot-receiver azimuth. It is believed that the rough ridge crest topography at this OBS location is responsible for this anomalous behaviour, and that no meaningful conclusions about first motion azimuths may be drawn. At SDOBS2 and SDOBS4, the  $P$ - $S$  mode converted arrival first motion azimuths for shots with shot-receiver azimuth of  $000^\circ$  are  $074^\circ$  and  $086^\circ$  respectively. In the case of SDOBS2, the  $P$ -wave first motion azimuth shows a smaller deviation ( $017^\circ$ ) but this cannot account for all the apparent rotation. In addition, the  $P$ - $S$  mode converted arrivals recorded at SDOBS2 are particularly strong. If the velocity structure is assumed to be isotropic,  $P$ - $S$  mode converted arrivals with first motion azimuths which deviate so greatly from those of the first arriving  $P$ -waves imply a converting interface with extremely unusual geometry. Therefore, these results strongly suggest anisotropic  $S$ -wave velocity structure at these OBS locations. The nature of this anisotropy and its geological implications will be discussed in section 4.6.

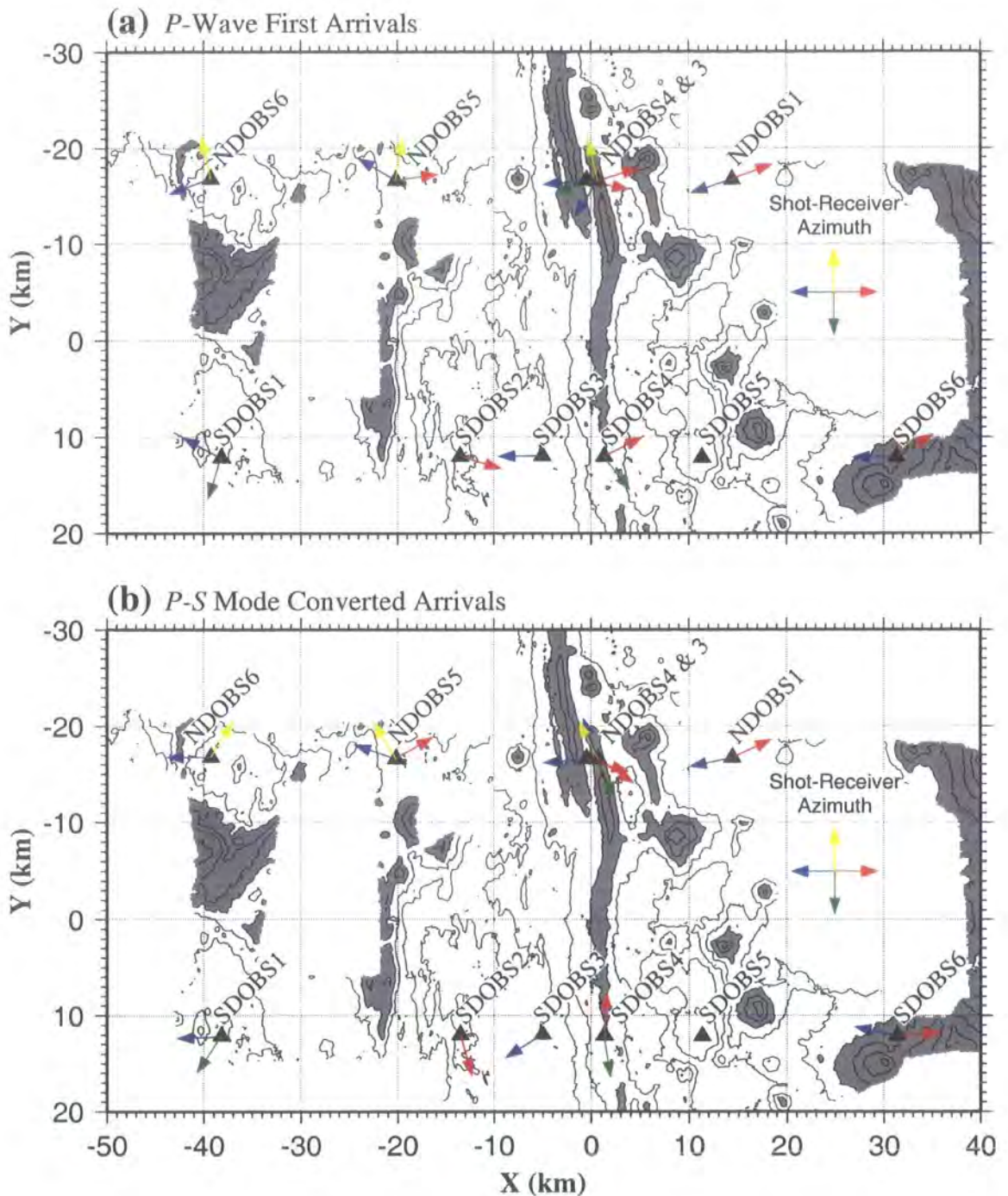


**Figure 4.17:** Mean first motion azimuths at each OBS location for a)  $P$ -wave first arrivals and b)  $P$ - $S$  mode converted arrivals, colour coded by shot-receiver azimuth as shown: red =  $000^\circ$ , green =  $090^\circ$ , blue =  $180^\circ$  and yellow =  $270^\circ$ . Solid black triangles denote OBS locations. Bathymetric contours at 0.25 km intervals are shown and regions shallower than 2 km have been shaded. For an isotropic structure with flat layers, the first motion azimuths should parallel the shot-receiver azimuths.  $P$ -wave first arrivals mostly conform to this behaviour, except in regions of rough bathymetry. The  $P$ - $S$  mode converted arrivals show more varied behaviour, and for some groups of shots, the first motion azimuth is deviated much more than the equivalent group of  $P$ -wave first arrivals away from the shot-receiver azimuth. This behaviour indicates possible anisotropy.

### 4.5.3 Off-line shots

The analysis described in the previous section involves averaging the first motion azimuths observed for large numbers of shots with approximately constant shot-receiver azimuth in order to obtain a more reliable estimate than can be obtained from a single arrival considered in isolation. This method cannot be applied to  $P$ - $S$  mode converted arrivals from off-line shots since the shot-receiver azimuth is not constant for a large number of these shots. An alternative method of analysis is to plot the first motion azimuth against shot-receiver azimuth. For a perfectly isotropic structure, the first motion azimuth for both  $P$ -wave first arrivals and  $P$ - $S$  mode converted arrivals would be the same as the shot-receiver azimuth, and any deviation from this behaviour might indicate anisotropy subject to the same assumptions as described in the previous section. Since this method considers individual arrivals rather than averaging the behaviour of many arrivals, it requires higher quality data in order to yield interpretable results.

The method described above was used to investigate off-line arrivals identified at SDOBS3 which appear to behave unusually. Figs. 4.18b and 4.18c show x- and y-component sections respectively for the off-line shots indicated in Fig. 4.18a. The  $P$ -wave first arrivals and direct water-wave arrivals show a maximum in x-component amplitude and minimum in y-component amplitude close to a shot-receiver azimuth of  $180^\circ$  as expected. This behaviour suggests that the method for determining horizontal geophone orientation and creating the resolved geophone sections works correctly. A strong horizontally polarised arrival is observed with an approximately constant delay of 0.6 s behind the first arriving  $P$ -wave, and is therefore interpreted as a  $P$ - $S$  mode converted arrival similar to those modelled in sections 4.4 and 4.5.2. However, the amplitudes of the x- and y-components appear to show the opposite relationship to shot-receiver azimuth when compared to the  $P$ -wave and direct water-wave arrivals.

In order to investigate further, apparent first motion azimuth was plotted against shot-receiver azimuth for all three arrivals identified in Fig. 4.18. The resulting plot, shown in Fig. 4.19, confirms the impression gained from inspection of the resolved traces, that there appears to be a very strong transverse component to the first motion of the  $P$ - $S$  mode converted arrival. This behaviour cannot be modelled by simple  $P$ - $S$  mode conversion as shown in Fig. 4.2. The behaviour is consistent with that observed at SDOBS4 for shots with shot-receiver azimuth of  $000^\circ$ , which also exhibited dominantly transverse first motion azimuth. The geological implications will be discussed in the following section.



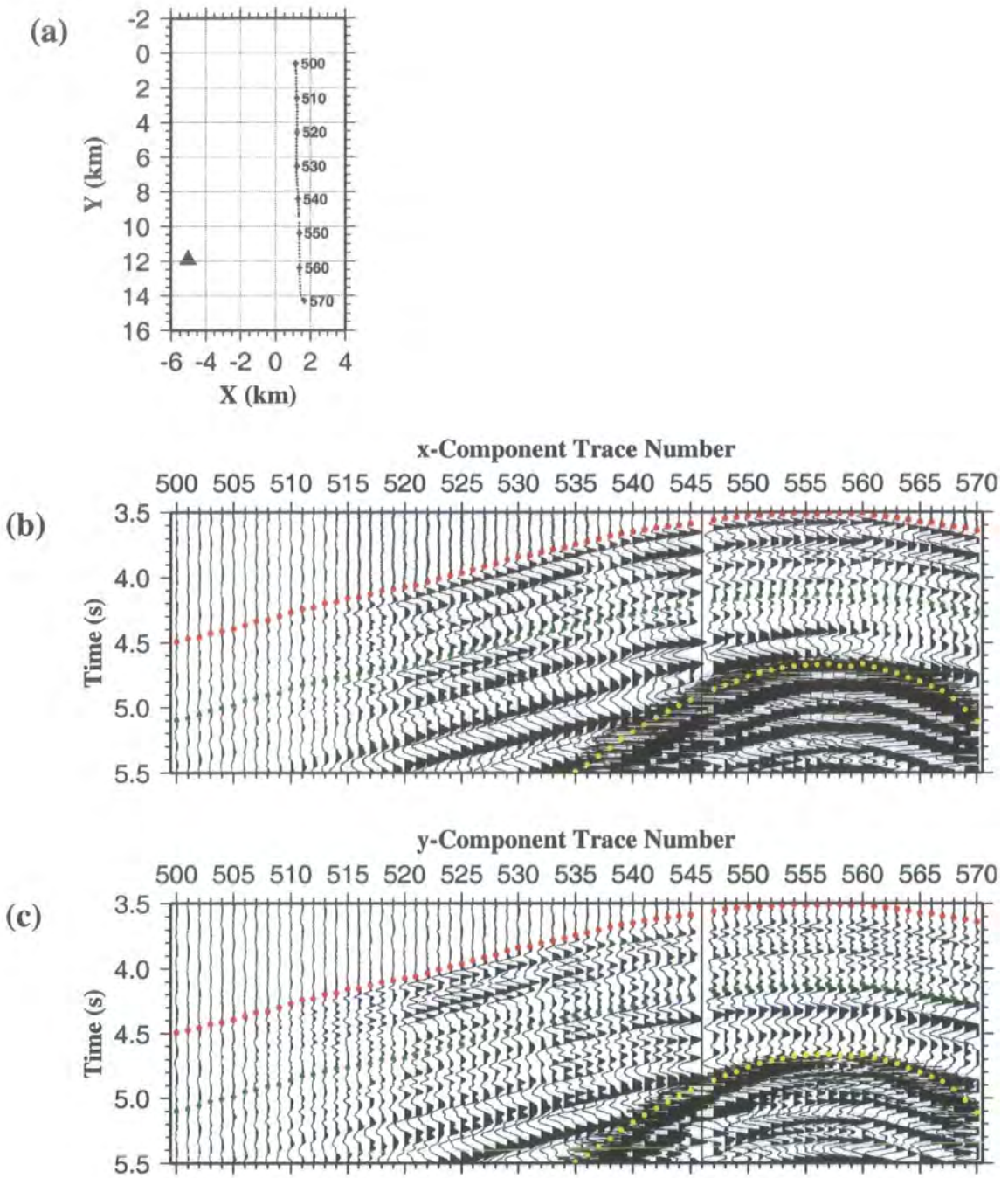


**Figure 4.18:**  $P$ - $S$  mode converted arrivals recorded from off-line shots. a) The relative positions of shots and receivers for the traces shown in b) and c). The solid triangle marks the position of SDOBS3, crosses mark shot positions. Every tenth shot is numbered. b) and c) Detail of  $x$ - and  $y$ -component traces respectively for SDOBS3 and the shots shown in a). Dot centres mark travel time picks of direct water-wave arrivals (yellow),  $P$ -wave first arrivals (red) and  $P$ - $S$  mode converted arrivals (green). All traces are plotted at the same scale, and the direct water-wave arrivals have been clipped for clarity. Note that the behaviour of the  $P$ - $S$  mode converted arrival amplitude is opposite to that of the  $P$ -wave first arrivals. The  $P$ - $S$  mode converted arrival amplitude is maximum on the  $y$ -component and minimum on the  $x$ -component close to shot 557. This arrival has a shot-receiver azimuth close to  $180^\circ$  and therefore the opposite behaviour would be expected.



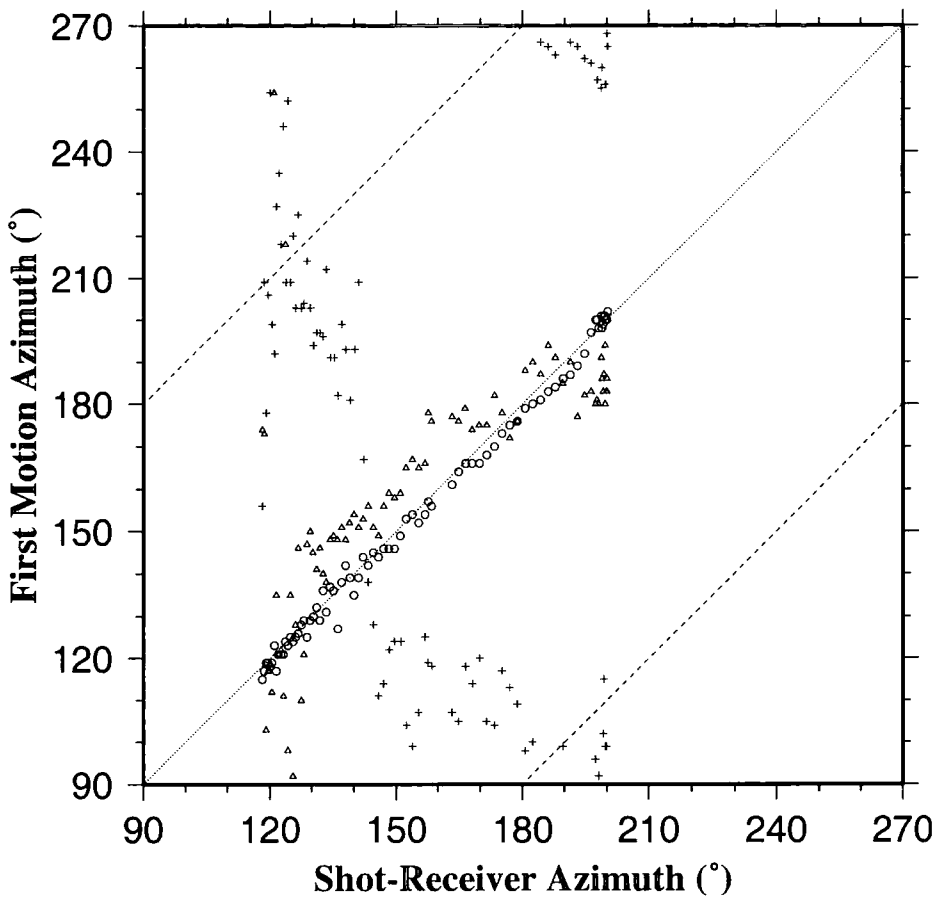


**Figure 4.19:** Plot of first motion azimuth versus shot-receiver azimuth for direct water-wave arrivals (circles),  $P$ -wave first arrivals (triangles) and  $P$ - $S$  mode converted arrivals (crosses) for off-line shots recorded at SDOBS3. Symbols represent individual shots. The  $P$ - $S$  mode converted arrival azimuths were calculated assuming that the component of first motion parallel to the  $x$ -axis was negative, i.e. the same polarity as the shot-receiver azimuth (see Fig. 4.18.) The dotted line represents the relationship that would be expected for  $P$ - $S$  mode conversion as depicted in Fig. 4.2, i.e. first motion direction identical to shot-receiver azimuth, whereas the dashed line represents particle motion at  $90^\circ$  to shot-receiver azimuth. Note that the first motion azimuths for direct water-wave arrivals and  $P$ -wave first arrivals are approximately the same as the shot-receiver azimuth, but this is not true of the  $P$ - $S$  mode converted arrivals, some of which appear to have transverse particle motions (i.e. particle motion at  $90^\circ$  to shot-receiver azimuth).

## 4.6 Discussion

### 4.6.1 Poisson's ratio structure of layer 2A

Typical Poisson's ratios observed for laboratory samples of young oceanic crust lie in the range 0.28–0.31 (Hyndman 1979). However, values greatly in excess of this range have been reported in young crustal layer 2A (e.g. Spudich & Orcutt 1980b; Bratt & Solomon 1984; Vera *et al.* 1990; Christeson *et al.* 1997; Collier & Singh 1998). It is widely believed that these high values of Poisson's ratio arise from the presence of thin cracks. Shearer (1988) demonstrated that cracks with an aspect ratio of  $<0.005$  give rise to an increase in Poisson's ratio, whilst cracks with an aspect ratio in the range 0.05–0.5 give rise to a decrease in Poisson's ratio, based on a variety of cracking theories (see Fig. 1.5). Travel time modelling of  $P$ - $S$  mode converted arrivals indicate a layer 2A Poisson's ratio of 0.39–0.45 at the VFR. These values lie within the range of values modelled elsewhere (e.g. Christeson *et al.* 1997; Collier & Singh 1998). It is therefore hypothesised that low aspect ratio cracks give rise to the elevated Poisson's ratios modelled in this chapter. These thin cracks may be formed due to stresses associated with seafloor spreading, which will be addressed in more detail below.

The layer 2A–2B/C boundary as modelled by Turner (1998) is interpreted as the most likely interface at which  $P$ - $S$  mode conversion might occur because a change in vertical  $P$ -wave velocity gradient is modelled at this boundary, which suggests a change in crustal properties. There is no evidence for a large  $P$ -wave velocity discontinuity at this interface. However, for significant  $P$ - $S$  mode conversion to occur, theoretical studies show that there must be a step change in  $S$ -wave velocity over a depth interval which is small relative to half the shear wavelength ( $\sim 0.1$  km) (White & Stephen 1980). Waveform inversion of similar arrivals recorded at the EPR also indicated that mode conversion is most efficient if the transition from low to high Poisson's ratio occurs over a narrow depth interval (Christeson *et al.* 1997).

The  $P$ -wave velocity at the VFR layer 2A–2B/C boundary is  $\sim 4.0$   $\text{kms}^{-1}$ , which implies significant porosity at this depth given that the velocity of laboratory samples of unfractured andesite and diorite typically lie in the range 5.5–6.5  $\text{kms}^{-1}$  (Christensen 1996), and assuming minimal alteration given that the post-rift crust is still very young. A step change in porosity is likely to result in a step change in  $P$ -wave velocity, which is not observed. However, a change in crack aspect ratio distribution with only a very small change in overall porosity might account for the observed behaviour. Porosity in the oceanic crust may occur on a variety of scales, and includes

vesicles, cooling cracks, voids between pillows and flows in addition to the low aspect ratio cracks used to explain the elevated Poisson's ratios in layer 2A. Wilkens *et al.* (1991) proposed a porosity model for the ocean crust in which thin cracks are preferentially closed and infilled with depth, ahead of other, higher aspect ratio forms of porosity. Thin cracks have a greater effect on  $P$ -wave velocity than other forms of porosity, so preferential closure of thin cracks may give rise to the large vertical  $P$ -wave velocity gradients widely observed in oceanic crust, including the VFR, without a large change in overall porosity. The closure of a population of thin cracks at the layer 2A-2B/C boundary could therefore account for the reduction in vertical  $P$ -wave velocity gradient at this boundary. Furthermore, Shearer (1988) showed that thin cracks have a proportionately greater effect on  $S$ -wave velocity than  $P$ -wave velocity. Therefore, closure of thin cracks could also give rise to the sharp reduction in Poisson's ratio required for  $P$ - $S$  mode conversion. The change in crack aspect ratio distribution is required to occur over a narrow depth interval in order to allow efficient  $P$ - $S$  mode conversion.

The models of Wilkens *et al.* (1991) and Shearer (1988) are based on cracking theories (e.g. Kuster & Toksöz 1974) which are not strictly valid at the high porosities widely found in young layer 2A volcanics including those dredged from the VFR which have typical porosities of ~25% (Vallier *et al.* 1991). However, Berge *et al.* (1992) developed theoretical velocity-porosity relationships, based on earlier cracking theories, which are applicable at higher porosities and demonstrate that the basic conclusions of Wilkens *et al.* (1991) and Shearer (1988) hold true at the high porosities found in layer 2A. Therefore the model described above is believed to be both plausible and consistent with the seismic data. The geological implications will be discussed in section 5.2.4.

#### 4.6.2 Melt lens mode converted arrivals

A number of  $P$ - $S$  mode converted arrivals recorded by SDOBS4 could not be satisfactorily modelled by mode conversion at the layer 2A-2B/C boundary. In particular, the  $P$ - $S$  mode converted arrivals lag the  $P$ -wave first arrivals by a larger amount, their amplitude is greater and their polarity opposite to that for  $P$ - $S$  mode conversion at the layer 2A-2B/C boundary. As outlined in section 4.4, the preferred explanation for this behaviour is that, for these arrivals,  $P$ - $S$  mode conversion occurs at the top of the axial melt lens identified by Collier & Sinha (1992a) and Turner (1998).

The polarity of the anomalous  $P$ - $S$  mode converted arrivals implies that they are generated at an interface at which up-going  $P$ -waves encounter an increase in  $P$ - or  $S$ -wave velocity, probably both, and the large amplitude of the anomalous arrivals suggests that this velocity increase is substantial. Therefore the occurrence of these  $P$ - $S$  mode converted arrivals provides further evidence for the existence of a melt lens comprising a high percentage of partial melt. The implications of these results for the properties of the melt lens will be discussed in section 5.2.2.

The travel times of the melt lens  $P$ - $S$  mode converted arrivals were best fit with a layer 2B/C Poisson's ratio of 0.32. This value lies near the upper end of the range 0.25–0.32 which is observed in the mid–lower oceanic crust (e.g. Spudich & Orcutt 1980b; Au & Clowes 1984; Bratt & Solomon 1984; Christeson *et al.* 1997; Collier & Singh 1998). Furthermore, the Poisson's ratio of unfractured andesite, which is the average composition of lava dredged from the VFR (Jenner *et al.* 1987; Vallier *et al.* 1991), is generally lower than the Poisson's ratio of unfractured basalt, of which normal oceanic crust is composed, owing to its higher silica content (Christensen 1996). If it is assumed that the dredge samples are representative of the composition of the upper crust, it might be expected that the Poisson's ratio in layer 2B/C would be lower than the typical value of 0.28 observed in the mid–lower oceanic crust and laboratory samples of unfractured dyke material (Hyndman 1979). Alteration is also generally thought to result in a decrease in Poisson's ratio (Shaw 1994), and is unlikely to be significant in the vicinity of SDOBS4 which is situated on the ridge crest (i.e. zero age crust). Therefore the value of 0.32 suggests that some thin cracks, which are inferred to be responsible for the widespread observation of high Poisson's ratio in layer 2A at the VFR, extend into layer 2B/C beneath SDOBS4. Since  $P$ - $S$  mode converted arrivals originating near the layer 2B/C–3 boundary are not observed at any other OBS location, and no  $P$ - $S$  mode converted arrivals generated on the down-going part of the ray path are observed, there are no other constraints on the Poisson's ratio in layer 2B/C. Therefore, the conclusion that there are thin cracks permeating layer 2B/C cannot be generalised to the whole study area, especially as the  $P$ -wave velocity structure in layer 2B/C in the axial region was shown to be anomalous as discussed in section 3.8.3.

### 4.6.3 $S$ -wave anisotropy

The Poisson's ratio interpretation described in section 4.6.1 does not require any preferential orientation of the thin cracks in layer 2A which are inferred to cause the high Poisson's ratio observations. However, if they are tectonic features resulting from seafloor spreading, they would be expected to be preferentially aligned perpendicular to the spreading direction, or parallel to the ridge crest in this case. Closely spaced ridge-parallel cracks on a scale of 0.5–3.0 m have been observed at the CVFR (Wiedicke & Kudrass 1990; Fouquet *et al.* 1993) and there is evidence of larger-scale normal faulting in the axial region aligned parallel to the ridge crest (Collier & Sinha 1992b). Azimuthal anisotropy is widely observed in the  $P$ -wave velocity structure of the upper oceanic crust (e.g. White & Whitmarsh 1984; Caress *et al.* 1992; McDonald *et al.* 1994; Sohn *et al.* 1997; Barclay *et al.* 1998), and is believed to arise from such preferentially aligned cracks. There is some evidence of possible  $P$ -wave anisotropy based on the results of tomographic inversions performed as part of this study, as outlined in section 3.8.5. Such cracks would also be expected to give rise to  $S$ -wave anisotropy, manifest as the  $S$ -wave splitting shown in Fig. 4.13. The percentage anisotropy in  $S$ -wave velocity would be expected to be greater than the percentage anisotropy in  $P$ -wave velocity since thin cracks have a proportionately greater effect on  $S$ -wave velocity than  $P$ -wave velocity (Shearer 1988). Therefore, in theory,  $S$ -wave anisotropy should be easier to identify and would imply probable  $P$ -wave anisotropy, which should be considered when interpreting the 3-D tomographic inversion results.

In practice, there is no clear evidence of  $S$ -wave splitting. This might occur because the shot-receiver azimuths for in-line shots approximately parallel one of the preferred orientations, in which case no  $S$ -wave splitting would occur as shown in Fig. 4.13. The approximate in-line shot-receiver azimuths are either parallel or perpendicular to the ridge crest, so, in the presence of anisotropy due to vertical ridge-parallel cracks this situation might occur. However, there is evidence that the first motion azimuths of some of the  $P$ - $S$  mode converted arrivals are significantly deviated relative to the  $P$ -wave first motion azimuth and shot-receiver azimuth. No  $S$ -wave splitting is observed in these cases. A possible explanation for this behaviour is that layer 2A is weakly anisotropic such that  $S$ -wave splitting occurs but the travel time difference between the two  $S$ -waves is so small that the two arrivals interfere and are not distinguishable as separate arrivals, as demonstrated by Crampin (1977). A second

possibility is that  $S$ -wave splitting occurs, but the amplitude of one of the transmitted  $S$ -waves is too small to be observed above the background noise. It would be expected that the transmitted  $S$ -wave for which the first motion azimuth was closest to that of the incident  $P$ -wave would have the larger amplitude (Keith & Crampin 1977a,b). Such behaviour could explain the observations for in-line shots recorded at SDOBS3 and NDOBS5, for which one  $P$ - $S$  mode converted arrival is observed with an apparent first motion azimuth which is deviated to a small degree relative to the  $P$ -wave first motion azimuth.

In-line shots recorded at SDOBS2 and SDOBS4 and off-line shots recorded by SDOBS3 show one  $P$ - $S$  mode converted arrival with apparent first motion azimuth deviated by very large amounts (close to  $90^\circ$  in the latter two cases). In the case of SDOBS2, the layer 2A-2B/C boundary is disrupted by thinning related to the nearby pseudofault marking the transition from pre- to post-rift crust (Wiedicke & Collier 1993), which may partly account for the anomalous behaviour. However, there are no such complications near SDOBS3 and SDOBS4. If  $S$ -wave splitting occurs and both arrivals are present within the 200 ms time window after the  $P$ - $S$  mode converted arrival pick position used to determine the apparent first motion azimuth, anomalous results might be obtained. However, given that the transmitted  $S$ -wave for which the first motion azimuth most closely parallels that of the incident  $P$ -wave would be expected to have the larger amplitude, this explanation cannot account for particle motion approximately transverse to the incident  $P$ -wave. Therefore, the behaviour of  $P$ - $S$  mode converted arrivals recorded at these OBS locations cannot be explained by a simple transversely isotropic structure as shown in Fig. 4.13. A full interpretation of these arrivals is beyond the scope of this study. However, it is suggested that the  $P$ - $S$  mode converted arrival first motion azimuths are indicative of structure in layer 2A. The following interpretation is based on this assumption.

If it is assumed that  $P$ - $S$  mode converted arrival first motion azimuths indicate preferred alignment of thin, near-vertical cracks, which are inferred to pervade layer 2A on the basis of Poisson's ratio considerations, this alignment is not consistent throughout the study area. Near the ridge axis, the first motion azimuth of  $P$ - $S$  mode converted arrivals recorded by SDOBS3 approximately parallels the ridge axis, which may indicate the presence of ridge-parallel cracks related to seafloor spreading. In the

north of the study area, results at NDOBS2 are inconclusive, probably due to the steep ridge crest topography. *P-S* mode converted arrivals recorded at NDOBS3 show ridge-perpendicular first motion azimuths for ridge-perpendicular shot-receiver azimuths, which would also be consistent with the presence of ridge-parallel cracks, though they are not required. The first motion azimuths of *P-S* mode converted arrivals recorded at SDOBS2 and NDOBS5 are consistent with cracks oriented at  $\sim 30^\circ$  to the ridge axis. Moreover, the apparent Poisson's ratio at NDOBS5 was modelled as 0.39 for shot-receiver azimuths of  $270^\circ$ , and 0.42 for shot-receiver azimuths of  $000^\circ$  (see Table 4.2). This observation suggests a slightly higher *S*-wave velocity parallel to the hypothetical cracks than perpendicular to them, which is consistent with theory. A Poisson's ratio of 0.39 in the "slow" direction suggests the presence of a population of randomly oriented thin cracks in addition to those which are inferred to be responsible for the first motion azimuth anomalies. SDOBS3 is an intermediate case in that *P-S* mode converted arrivals from in-line shots behave similarly to those recorded at NDOBS5, whilst the off-line shots behave similarly to arrivals recorded at SDOBS4.

The apparent *P-S* mode converted arrival first motion azimuths at SDOBS2 and NDOBS5 are strikingly similar to the azimuth of off-axis structures identified by Wiedicke & Collier (1993), particularly so the pseudofault which is close to SDOBS2 and is oriented at  $\sim 030^\circ$  to the ridge crest. This pseudofault is believed to represent the boundary between pre- and post-rift crust, and its oblique orientation arises from southward propagation of the ridge system. Therefore, the preferred crack orientations inferred above are consistent with the formation of thin, ridge-parallel cracks on-axis, whose orientation rotates as they move off-axis due to this southward propagation.

OBSs located on pre-rift and island arc crust (SDOBS1, NDOBS1 and SDOBS6) show little or no indication of anisotropy. However, the occurrence of strong *P-S* mode converted arrivals at similar delay behind the first arrivals indicates an abrupt change in *S*-wave velocity at similar depth to the converting interface modelled in post-rift crust. The high Poisson's ratios suggest that the uppermost pre-rift crust is pervaded by thin cracks, but the apparently isotropic behaviour suggests that these cracks have no preferred alignment.



The analysis of  $P$ - $S$  mode converted arrivals presented in this chapter relies on a number of assumptions, and the  $P$ - $S$  mode converted arrivals only sample the upper crust in the immediate vicinity of OBS locations. Therefore the geological model for the nature of layer 2A presented in this section must be regarded as speculative. Nevertheless, it is believed that the model is consistent with the  $S$ -wave data, the  $P$ -wave velocity structure presented in chapter 3 and by Turner (1998), the tectonic history of the VFR and structures modelled at other mid-ocean ridges. It is likely that the model presented is a greatly simplified version of the true structure, and there are a number of enigmatic  $P$ - $S$  mode converted arrivals whose behaviour implies greater complexity.

## 4.7 Summary

In this chapter, a number of techniques for modelling  $P$ - $S$  mode converted arrivals have been described and applied to the VFR seismic dataset. A number of  $S$ -wave arrivals were identified from horizontal geophone traces, and interpreted as arising from  $P$ - $S$  mode conversion on the up-going part of the ray path beneath each OBS. A method for determining horizontal geophone orientation using the direct water-wave arrivals has been described, and used to create resolved sections parallel to the dominant shot-receiver azimuths to aid picking  $P$ - $S$  mode converted arrivals. It has been shown from travel time modelling of in-line shots that the most plausible converting interface is the layer 2A-2B/C boundary. This travel time modelling requires high Poisson's ratios (0.39-0.45) in layer 2A, which is consistent with observations elsewhere in the ocean crust. The  $P$ -wave velocity structure is continuous at the layer 2A-2B/C boundary, but it has been shown that a sharp change in  $S$ -wave velocity alone, implied by the Poisson's ratio structure, is sufficient to generate detectable  $P$ - $S$  mode converted arrivals. Some arrivals recorded at SDOBS4 were interpreted as arising from  $P$ - $S$  mode conversion at the top of the axial melt lens. Travel time modelling of these arrivals suggests a layer 2B/C Poisson's ratio of 0.32. Finally, a method for determining the azimuth of first motion of arrivals was described, which was based on resolving the horizontal geophone traces onto a range of azimuths and identifying the azimuth for which the mean square signal strength in a 200 ms time window after the pick position was maximum. Application of this technique to the  $P$ - $S$  mode converted arrivals at the VFR suggests possible  $S$ -wave anisotropy.

A tentative geological model was presented to explain the behaviour of the  $P$ - $S$  mode converted arrivals in the context of the  $P$ -wave velocity structure described in chapter 3 and by Turner (1998). High Poisson's ratio in layer 2A is often attributed to the presence of porosity in the form of thin cracks. The particle motion azimuths are broadly consistent with the presence of cracks formed on-axis parallel to the ridge, which rotate as they move off-axis due to southward propagation of the ridge system. Sealing of a population of thin cracks at the layer 2A-2B/C boundary would account for the decrease in Poisson's ratio required for  $P$ - $S$  mode conversion to occur, and this sealing must occur over a small depth interval to allow efficient mode conversion. The layer 2B/C Poisson's ratio of 0.32 modelled beneath SDOBS4 suggests that, beneath this axial instrument, some thin cracks penetrate layer 2B/C, though this conclusion cannot be generalised owing to the absence of further measurements of layer 2B/C Poisson's ratio. The wider geological implications will be more fully discussed in conjunction with the  $P$ -wave velocity structure in the next chapter.

# Chapter 5

## Discussion and suggestions for further work

### 5.1 Introduction

This dissertation concerns modelling and interpretation of a seismic dataset acquired at the VFR. Modelling of a 3-D subset of the  $P$ -wave first arrivals, using a seismic tomographic method, and secondary  $P$ - $S$  mode converted arrivals has been described in chapters 3 and 4 respectively. The results of this modelling are interpreted in geological terms in section 5.2 in context of structures observed at other mid-ocean ridges, and the wider implications for global ridge segmentation considered in section 5.3. A summary of these results is provided in section 5.4. Several suggestions for further study are discussed in section 5.5, and include modelling of existing additional datasets to further improve the constraint on geological models for the crustal structure at the VFR obtained from this and other studies. In addition modifications which could be made to the acquisition geometry and inversion method to improve the resolution of future 3-D seismic experiments are also suggested. In the light of this discussion, a further 3-D seismic experiment at the VFR is proposed, which is designed to extend the existing studies southwards. This study would allow investigation of the nature of the crust and the development of the axial magmatic system related to the onset of rifting at the propagating rift tip through to a stable ridge system at the southernmost end of the CVFR.

### 5.2 Crustal structure at the Valu Fa Ridge

In this section, the geological implications of the  $P$ -wave seismic tomographic and  $P$ - $S$  mode converted arrival studies at the VFR, described in chapters 3 and 4 respectively, are discussed. The crustal structure resulting from accretion at this mid-ocean ridge and the spatial and temporal variations in accretionary processes are considered. Since the seismic component of the EW9512 experiment was targeted towards resolving the velocity structure of layers 2B/C and 3 following the identification of a MCR at the boundary between these layers (Morton & Sleep 1985; Collier 1990; Collier & Sinha 1992a), this section begins by discussing the structure of the axial magma chamber and works upwards through the crust to the seafloor.

### 5.2.1 Axial low velocity zone

The MCR imaged at the layer 2B/C boundary has been interpreted as representing a sill-like melt lens comprising a high percentage of partial melt (Collier 1990; Collier & Sinha 1992a; Turner 1998; Turner *et al.* 1999). Similar reflectors have been imaged at other mid-ocean ridges at a variety of spreading rates, including the fast-spreading EPR (e.g. Detrick *et al.* 1987 and 1993), the intermediate-spreading JDFR (Rohr *et al.* 1988) and the slow-spreading Reykjanes Ridge (Navin 1996; Navin *et al.* 1998). Wide-angle seismic experiments have also revealed the presence of LVZs in layer 3 underlying these melt lenses (e.g. Harding *et al.* 1989; Vera *et al.* 1990; Toomey *et al.* 1990; Caress *et al.* 1992; Navin *et al.* 1998). These LVZs are interpreted as representing mush zones which comprise a lower percentage of partial melt, and which constitute the main body of the axial magma chamber according to the model of Sinton & Detrick (1992). Turner (1998) modelled a similar LVZ in the axial region of the VFR on two across-axis 2-D wide-angle seismic profiles. The primary purpose of this study was to extend the work of Turner (1998) by adopting a three-dimensional approach in order to investigate the nature and along-axis continuity of this feature. In addition, the tomographic approach has the advantage that it provides a means of objectively assessing the shape and size of any velocity anomalies with a minimum of *a priori* geological constraints, and without any preconceived geological expectations of the likely outcome.

Turner (1998) and Turner *et al.* (1999) identified a negative velocity anomaly, with a maximum magnitude of  $0.4 \text{ kms}^{-1}$  in the axial region relative to the off-axis crustal structure, on each of the two across-axis 2-D profiles considered (see Fig. 1.10). This anomaly has a width of  $\sim 4 \text{ km}$  when defined by the  $-0.2 \text{ kms}^{-1}$  anomaly contour which was used by Vera *et al.* (1990) to denote the extent of the magma chamber and allows comparison of magma chambers imaged at different locations (see Fig. 1.3). The tomographic inversion results using the most realistic initial conditions (*melt lens unbiased 2-D initial model*) are shown in Fig. 3.18 as plots of the velocity anomaly relative to this initial model, and in Fig. 5.1 as a 3-D perspective view. A negative velocity anomaly has been recovered in the axial region, and a positive velocity anomaly recovered west of the axis which is believed to represent normal off-axis crust. Based on the anomalies shown in Fig. 3.18 for the top of layer 3, the negative velocity anomaly in the axial region has a typical velocity contrast of  $\sim -0.6 \text{ kms}^{-1}$  relative to off-axis crust, and up to a maximum difference of  $\sim -0.8 \text{ kms}^{-1}$ . These anomalies are of significantly larger magnitude than those modelled by Turner (1998). This discrepancy

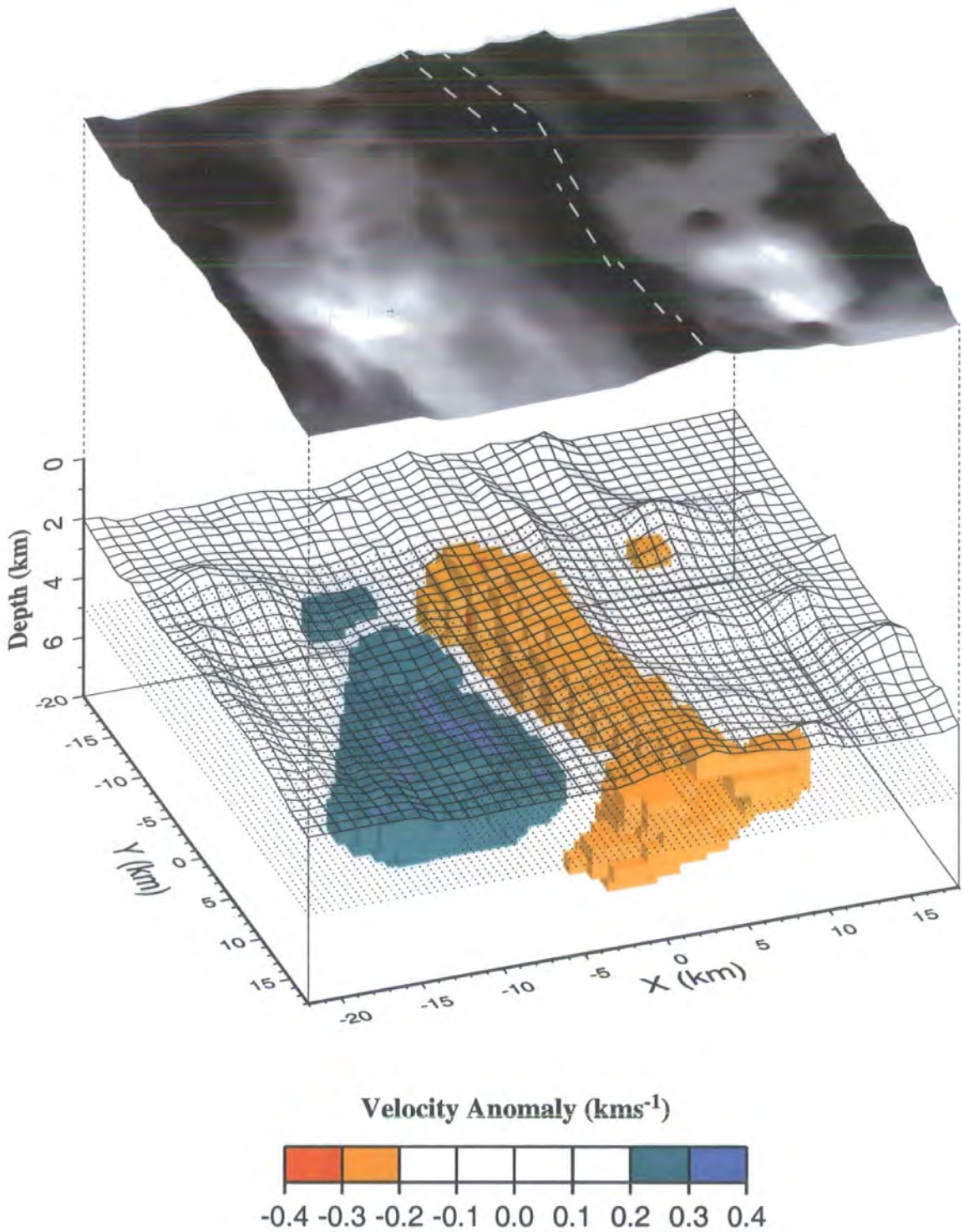


**Figure 5.1:** Summary 3-D perspective view of the velocity anomaly associated with the axial magma chamber beneath the CVFR. Velocity anomalies relative to the *melt lens unbiased 2-D initial model* are shown, together with the 5 km depth plane (dotted), showing anomaly outline shape. The seafloor bathymetry has been included for reference as an open mesh directly above the magma chamber anomaly, and as a grey-shaded surface to show more clearly the location of the OSC between the CVFR and NVFR segments. The dashed white lines denote the fourth-order segments shown in Fig. 1.7 and mark the ridge crest. Note that whilst this figure may indicate that velocity anomalies are confined to the middle crust, resolution is poor below about 7 km depth. Therefore these velocity anomalies shown may extend to greater depth but are unresolvable with this dataset.

may, in part, be due to downward vertical smoothing of anomalies in layer 2B/C, as illustrated by the testing shown in Fig. 3.28, which arises because of the superior model resolution in that layer. However, resolution tests (Fig. 2.31b) and synthetic model tests (Fig. 3.26) indicate that anomaly amplitudes in the axial region are generally underestimated. This effect would counteract that of downward vertical smoothing of shallower anomalies. Hence the amplitude of the negative axial anomaly cannot be reliably determined. However, all the estimates of anomaly magnitude lie in the range  $0.5\text{--}1.0\text{ km s}^{-1}$  observed for similar low velocity zones at the EPR and MAR (e.g. Toomey *et al.* 1990; Caress *et al.* 1992; Navin *et al.* 1998). Therefore, the magnitude of the axial negative anomaly, within the resolution of this tomographic dataset, is broadly consistent with the findings of Turner (1998) and similar results from experiments at other mid-ocean ridges. The width of the axial negative anomaly, defined by the  $-0.2\text{ km s}^{-1}$  anomaly contour, is typically  $\sim 7\text{ km}$ , which is significantly greater than the  $4\text{ km}$  width modelled by Turner (1998) based on the same criterion. This discrepancy may arise due to lateral smoothing of axial anomalies into regions of inferior resolution, particularly east of the axis (*cf.* Fig. 2.31). Overall, however, the extent of the low velocity zone is believed to be consistent with the models of Turner (1998) within the tolerance of the interpretation methods applied. The most important result of this analysis is that the 3-D tomographic inversions have confirmed the presence of an axial LVZ and provide an indication of its along-axis continuity.

As described in section 3.8.2, the tomographic inversion results suggest considerable along-axis variation in the amplitude of the negative velocity anomaly defining the LVZ. The along-axis compositional and geochemical variations in lavas dredged from the CVFR axis imply that it is supplied by a number of separate magmatic systems (Hilton *et al.* 1993). Collier & Sinha (1992b) showed that the CVFR may be subdivided into three fourth-order segments based on their bathymetric, morphological and magnetic characteristics (labelled V7 to V9 in Fig. 1.7), separated by SNOOs and devals. The differences in morphology between segments were interpreted by Collier & Sinha (1992b) as indicative of cyclic magma supply on the scale of the fourth-order segmentation such that volcanic constructs generated during a magmatically robust phase become disrupted during a subsequent period of amagmatic extension prior to the onset of the next magmatic phase. Hence the differences in ridge crest morphology arise because different segments are at different stages of this cycle.



Fig. 5.2 shows the relationship between the velocity anomaly recovered in layer 3 in this study, the extent of the MCR determined by Collier (1990) and Collier & Sinha (1992a) and the fourth-order ridge segmentation using the nomenclature of Wiedicke & Collier (1993). The largest amplitude anomaly is found beneath the V9

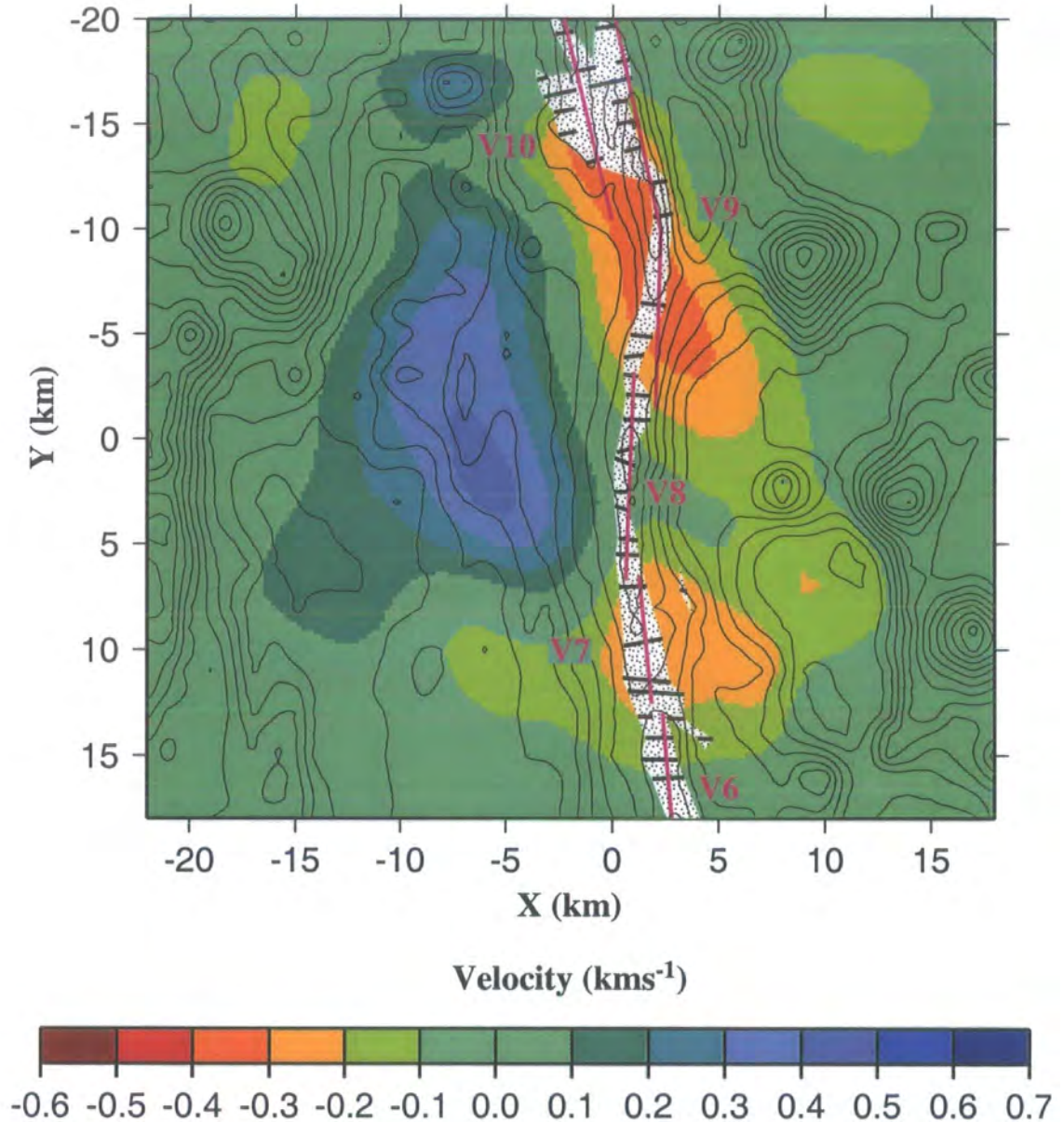


**Figure 5.2:** Velocity anomaly at the top of layer 3 recovered using the *melt lens unbiased 2-D initial model* overlain by the extent of the melt lens identified by Collier (1990) (black stippled region with the melt lens extent on individual across-axis profiles denoted by solid black lines) and fourth-order ridge segmentation identified by Wiedicke & Collier (1993) (pink lines labelled V6–V10). Bathymetric contours at 0.1 km intervals are shown to indicate how these features relate to the ridge crest. Note that the negative anomaly recovered by the inversion is generally very much wider than the inferred extent of the melt lens, and there is a gap in the negative anomaly corresponding to the V8 segment. This observation suggests that variations in negative anomaly amplitude may be correlated with morphological segmentation, though lateral resolution variations arising from variable ray coverage are probably also a significant contributor to these variations.



segment, which was interpreted by Collier & Sinha (1992b) as having experienced the highest magmatic budget in the recent past. The apparent gap in the LVZ between  $y = 0$  km and  $y = 5$  km coincides with the V8 segment, which would be expected to be relatively magma starved according to the model of Collier & Sinha (1992b). Note that the MCR width is also particularly narrow beneath the V8 segment (Wiedicke & Collier 1993). The increase in anomaly amplitude south of  $y = 5$  km coincides with the V7 segment where the melt lens reflector was observed to be particularly wide even though the ridge crest morphology implies that the segment is relatively magma starved and disrupted by post-magmatic tectonism. This wide reflector was interpreted by Collier & Sinha (1992b) as representing either a remnant of a particularly large magma chamber from an earlier period of high magmatic budget, or recharge from a recent magmatic influx. Therefore the along-axis variations in the axial negative velocity anomaly may represent real along-axis variations in the LVZ, and are broadly consistent with the along-axis variations in magma budget implied by earlier studies of the melt lens reflector and ridge crest morphology (Collier & Sinha 1992a,b; Wiedicke & Collier 1993).

However, the model resolution in the axial region of layer 3 is generally too poor to allow the along-axis variations in the anomaly amplitude to be assessed with confidence. In particular, the gap centred on  $y = 2.5$  km also coincides with a region of particularly poor resolution at layer 3 depths, and it has been shown in section 3.8.2 that the gap could simply be a model artefact. Also, the larger amplitude anomaly in the north may partly reflect downward vertical smoothing of large negative anomalies in layer 2B/C above at this location, although this cannot account for all the anomaly in layer 3 since the magnitude of the negative anomaly in layer 3 is greater than that in layer 2B/C. Despite these limitations, particularly the inability to accurately determine the amplitude of the velocity anomaly, it may be concluded that the along-axis variations in the amplitude of the negative axial velocity anomaly may partly reflect real variations in the properties of the LVZ which are related to along-axis variations in magma budget.

As discussed in section 1.3.1, there is considerable ambiguity about the melt fraction that a negative anomaly of this magnitude actually represents. An added complication at the CVFR is the more silicic magma compositions, which may affect the geometry of the solid-melt interface and hence the relationship between seismic velocity and melt fraction may be different to that for a basaltic melt. However, the

experimental results of Murase & McBirney (1973) suggest that the velocity of an andesitic melt responds to temperature changes in a similar manner to that of basaltic melts, so their elastic properties may be comparable. There are no constraints on the properties of the LVZ apart from the seismic models. The controlled-source electromagnetic experiment conducted at the CVFR during cruise EW9512 could not resolve the resistivity structure of the LVZ due to rapid attenuation of signals in the overlying high conductivity layer (MacGregor *et al.* 2001). Therefore, in view of the inconsistent melt fraction estimates derived from other ridges with LVZs of similar magnitude to that modelled at the CVFR, it is not possible to constrain the melt fraction present based on this seismic dataset alone.

### 5.2.2 Properties of the axial melt lens

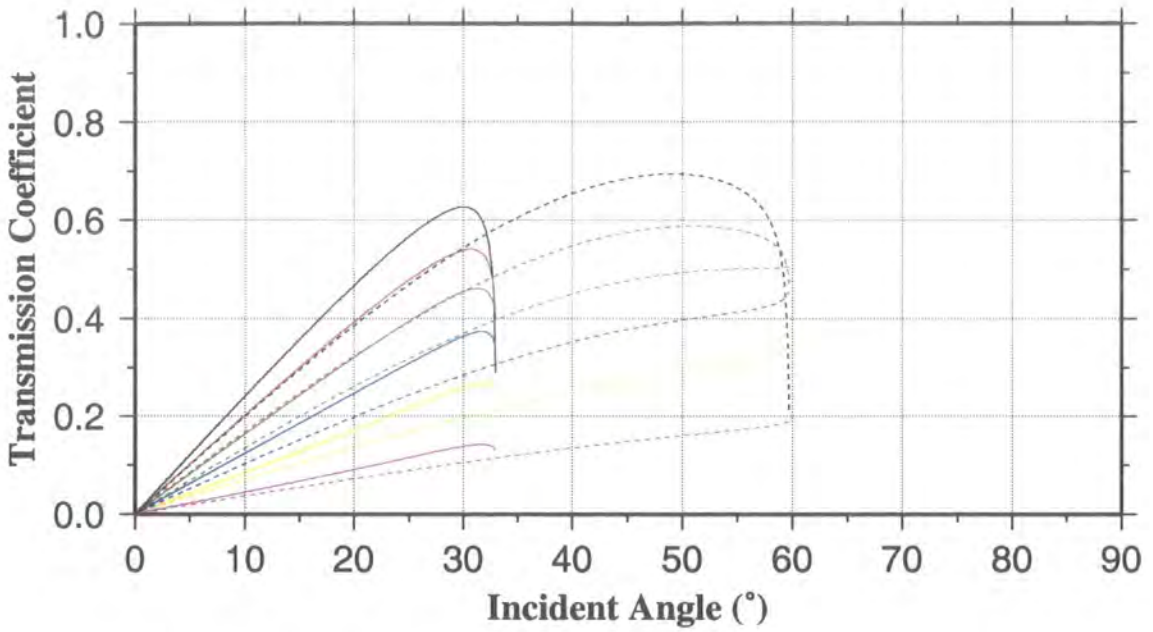
Previous normal-incidence seismic studies have identified the presence of a thin (no more than 0.25 km thick) low velocity region at the VFR which is believed to represent a sill-like melt lens comprising a high percentage of partial melt (Morton & Sleep 1985; Collier & Sinha 1992a; Turner 1998). *P*-*S* mode converted arrivals were recorded by one of the axial instruments which were successfully modelled as arising from mode conversion at the top of this melt lens (see section 4.4). These arrivals provide further evidence for the existence of this feature. Due to the ambiguities outlined in section 1.3.1, in context of discussion of the properties of the LVZ, it is not possible to constrain the precise percentage of melt present, however, the large amplitude reflection and *P*-*S* mode conversion suggests that it is relatively high. The experimental results of Murase & McBirney (1973) showed that, as temperature is increased, a rapid decrease in *P*-wave velocity is predicted when the melt phase becomes continuously connected. At the same time, the *S*-wave velocity is reduced to near zero since the melt phase has no shear strength.

A study of the along-axis properties of a melt lens reflector at the southern EPR near 14° S, showed that its variable amplitude could be attributed to variations in the melt lens properties (Singh *et al.* 1998). Waveform inversions of two common mid-point gathers, one with a strong melt lens reflector and one with a weaker melt lens reflector, showed that both *P*- and *S*-wave velocity were significantly lower for the stronger reflection relative to the weaker reflection. These differences were interpreted as representing differences in the percentage of partial melt present within the lens.

Lower  $P$ - and  $S$ -wave velocities in the melt lens would be expected to increase the magnitude of the transmission coefficient for  $P$ - $S$  mode converted arrivals. Singh *et al.* (1998) found that the difference in  $S$ -wave velocity between the two gathers was greater than the difference in  $P$ -wave velocity. Therefore in order to investigate the effect of  $S$ -wave velocity on the transmission coefficient for  $P$ - $S$  mode converted arrivals, Zoeppritz's equations were solved for several values of  $S$ -wave velocity in the melt lens.

Laboratory measurements of the properties of solid andesite indicate an  $S$ -wave velocity of approximately  $3.0 \text{ kms}^{-1}$  (Murase & McBirney 1973; Christensen 1996). Likewise the  $S$ -wave velocity of a pure andesite melt should be zero since a fluid has no shear strength. The  $P$ -wave velocity of a pure andesite melt is approximately  $3.0 \text{ kms}^{-1}$  (Murase & McBirney 1973) and this value was used by Turner (1998) to model the melt lens. In section 4.4, Zoeppritz's equations were solved using these values for the melt lens properties in order to demonstrate that the top of the melt lens is a viable interface at which to generate detectable  $P$ - $S$  mode converted arrivals. In this section, the analysis is extended by solving Zoeppritz's equations assuming a melt lens  $P$ -wave velocity of  $3.0 \text{ kms}^{-1}$  and a range of  $S$ -wave velocities between  $0.0$  and  $3.0 \text{ kms}^{-1}$  in order to obtain the transmission coefficients for  $P$ - $S$  mode conversion at the top of a melt lens with this range of properties. The results are shown as solid lines in Fig. 5.3. In practice, for low melt fractions the  $P$ -wave velocity would be expected to be greater than  $3.0 \text{ kms}^{-1}$ . Therefore Zoeppritz's equations were also solved assuming a melt lens  $P$ -wave velocity of  $4.75 \text{ kms}^{-1}$ , halfway between the velocity of a pure andesite melt and the velocity of  $5.5 \text{ kms}^{-1}$  modelled by Turner (1998) immediately above the melt lens. The  $S$ -wave transmission coefficients calculated based on this assumed melt lens  $P$ -wave velocity are shown as dashed lines in Fig. 5.3. These results show that the transmission coefficient for  $S$ -waves is greatly reduced for a small increase in  $S$ -wave velocity above zero.

No attempt has been made to model the melt lens  $P$ - $S$  mode converted arrival waveform, which could potentially constrain the  $P$ - and  $S$ -wave velocity in the melt lens. However, the melt lens  $P$ - $S$  mode converted arrivals are of greater amplitude than similar arrivals from the layer 2A-2B/C boundary, which implies a higher  $S$ -wave transmission coefficient at the top of the melt lens. Fig. 4.3 shows that  $P$ - $S$  mode



For solid curves:  $V_{p1} = 3.00 \text{ km s}^{-1}$

For dashed curves:  $V_{p1} = 4.75 \text{ km s}^{-1}$

For all curves:  $\rho_1 = 2500 \text{ kg m}^{-3}$ ,  $\rho_2 = 2620 \text{ kg m}^{-3}$ ,  $V_{p2} = 5.50 \text{ km s}^{-1}$ ,  $V_{s2} = 3.04 \text{ km s}^{-1}$ .

$V_{s1} = 0.00 \text{ km s}^{-1}$

$V_{s1} = 1.50 \text{ km s}^{-1}$

$V_{s1} = 0.50 \text{ km s}^{-1}$

$V_{s1} = 2.00 \text{ km s}^{-1}$

$V_{s1} = 1.00 \text{ km s}^{-1}$

$V_{s1} = 2.50 \text{ km s}^{-1}$

**Figure 5.3:** *S*-wave transmission coefficients calculated for a *P*-wave incident on the roof of the melt lens from below for a number of melt lenses with different properties (see legend). The *P*-wave velocity ( $V_p$ ), *S*-wave velocity ( $V_s$ ) and density ( $\rho$ ) conditions in each layer are shown. Suffix 1 refers to the melt lens and suffix 2 to layer 2B/C. The densities in both the melt lens and layer 2B/C and the *P*- and *S*-wave velocities in layer 2B/C are the same as in Fig. 4.10. Two *P*-wave and six *S*-wave velocities are assumed for the melt lens. For a constant melt lens *P*-wave velocity, an increase in melt lens *S*-wave velocity, which is diagnostic of the melt fraction, leads to a reduction in *S*-wave transmission coefficient. For large angles of incidence ( $>33^\circ$  for a melt lens *P*-wave velocity of  $3.0 \text{ km s}^{-1}$ ,  $>60^\circ$  for a melt lens *P*-wave velocity of  $4.75 \text{ km s}^{-1}$ ) the solutions to Zoeppritz's equations are complex and thus not shown.

conversion at the layer 2A–2B/C boundary can be satisfactorily modelled with a maximum *S*-wave transmission coefficient magnitude of  $\sim 0.3$ . Inspection of Fig. 5.3 shows that an *S*-wave transmission coefficient in excess of 0.3 implies a melt lens *S*-wave velocity of less than  $2.0 \text{ km s}^{-1}$  since, for larger *S*-wave velocities, the *S*-wave transmission coefficient is always less than 0.3 for all angles of incidence. Moreover, energy which has undergone *P*–*S* mode conversion at the top of the melt lens must have passed through the axial LVZ, which is inferred to be highly attenuating (Turner 1998).

Propagation through this highly attenuating region would reduce the amplitude of the  $P$ -wave energy incident on the top of the melt lens. If the melt lens has a sharp velocity discontinuity at its base, similar to that modelled by Singh *et al.* (1998), this interface would also lead to a reduction in amplitude of the incident  $P$ -wave through transmission losses. It is therefore likely that the  $S$ -wave transmission coefficient at the top of the melt lens is significantly greater than 0.3 in order to obtain  $P$ - $S$  mode converted arrivals of significantly greater amplitude than those generated at the layer 2A-2B/C boundary. This qualitative analysis suggests a very low  $S$ -wave velocity in the melt lens.

Singh *et al.* (1998) showed that melt lens properties varied along-axis at the southern EPR. For most of its length, the  $S$ -wave velocity was found to be significantly greater than zero, although three regions were identified where  $S$ -wave velocity was close to zero. Each of these three regions were ~2-4 km long and lay within a 60 km long ridge segment. These results were interpreted as representing a melt lens mostly comprising mush containing 40-60% melt with three pockets of 90-95% melt. Singh *et al.* (1998) suggested that melt bodies of these dimensions would cool and crystallise to form a mush within a few decades and that they, therefore, represent very recent localised melt injections. At the southern end of the CVFR, the presence of a melt lens inferred to have a low  $S$ -wave velocity suggests that there is a high percentage of melt beneath the ridge at this location.

It is not possible to conclusively identify along-axis variations in melt lens properties based on the seismic reflection imaging of Collier & Sinha (1992a), as the observed variations in reflection strength may in part result from variable seafloor scattering and upper-crustal structure. However, it is plausible that similar temporal and spatial variations in melt delivery could occur at the CVFR, especially as its spreading rate is very much lower than the southern EPR. If this model is valid, the implication of a high percentage of partial melt at the southern end of the CVFR is consistent with a very recent local injection of melt, which was one of the explanations offered by Wiedicke & Collier (1993) for the observation of a strong melt lens reflector despite morphological evidence that the southernmost segment has been relatively magma starved in the recent past. Singh *et al.* (1998) suggest that the existence of a high percentage of partial melt in the melt lens is likely to be a very short-lived feature and it is therefore unlikely to be a remnant of an earlier magmatic phase. The presence of an underlying LVZ, which is likely to be a much more stable feature than the melt lens,

suggests that this part of the ridge has recently entered a magmatically robust phase. The lack of melt lens  $P$ - $S$  mode converted arrivals at the *Seismic North* experiment may be due to a melt lens comprising a lower percentage of partial melt which would inhibit the generation of  $P$ - $S$  mode converted arrivals as shown in Fig. 5.3, but with a significant  $P$ -wave velocity contrast with the overlying material in order to generate a detectable melt lens reflection. However, other factors which might reduce the amplitude of melt lens  $P$ - $S$  mode converted arrivals, such as increased attenuation in the overlying crust, may also be significant. Therefore the absence of melt lens  $P$ - $S$  mode converted arrivals cannot be used as an indicator of melt lens properties.

### 5.2.3 Axial velocity anomalies in layer 2B/C

A negative velocity anomaly was recovered in the axial region in layer 2B/C with a maximum amplitude of  $-0.4 \text{ kms}^{-1}$  relative to normal off-axis crust. Figs. 3.18 and 5.1 show that the magnitude of this anomaly is maximum beneath the OSC and generally decreases in magnitude to the south. A smaller negative anomaly is centred on the southern end of the CVFR which is much broader than in the north and extends further off-axis. Therefore the axial negative anomaly relative to off-axis crust is greatest in the north. The resolution plot shown in Fig. 2.31 demonstrates that resolution is better in layer 2B/C than in layer 3, and therefore these along-axis variations in anomaly magnitude are likely to be real rather than artefacts of the inversion process. Possible geological causes of this anomaly were outlined in section 3.8.3, and include higher porosity caused by a local thickening of the extrusive layer or increased fracturing, or a subsolidus temperature anomaly associated with the underlying magmatic system. These possibilities will now be discussed in turn.

An increase in porosity leads to a decrease in  $P$ -wave velocity, and extruded lava is generally more porous than intrusive material due to its greater vesicularity. Lava samples dredged from the CVFR are highly vesicular and have typical porosities of 10–25% and up to 35% by volume (Vallier *et al.* 1991). Moreover, theoretical studies have shown that the geometry of the porosity also influences  $P$ -wave velocity and, particularly, that porosity in the form of thin cracks leads to a greater reduction in  $P$ -wave velocity relative to an uncracked rock than the same volumetric porosity in the form of spherical pores (Shearer 1988). The  $P$ - $S$  mode converted arrivals modelled in chapter 4 suggest high Poisson's ratios in layer 2A, which were interpreted as arising from the presence of thin cracks. The geological structure of layer 2 is discussed more fully in section 5.2.4. However, layer 2A is commonly interpreted as representing

dominantly extrusive material, and  $P$ - $S$  mode converted arrival studies indicate that it is pervaded by thin cracks, both of which may be associated with a reduction in  $P$ -wave velocity. If layer 2A were locally thicker than assumed in the initial model, the velocity at a given depth would be overestimated and hence a negative velocity anomaly would be required to resolve the travel time residuals. Thickening of layer 2A has been modelled off-axis at the EPR, associated with relict overlap basins near  $17^{\circ} 15' S$  (Bazin *et al.* 1998) and  $9^{\circ} 03' N$  (Bazin *et al.* 2001). The negative anomaly in layer 2B/C is of greatest magnitude near the OSC, so a similar thickening of layer 2A associated with the OSC could give rise to the observed anomaly distribution. Such thickening might occur if lava is supplied from both ridges simultaneously leading to a thicker extrusive layer between the two ridges than off-axis. Seismic reflection studies have shown that a melt lens is present beneath both ridges (Collier & Sinha 1992a; Turner 1998), and wide-angle studies (Turner 1998) and the tomographic results of this study suggest a broad mush zone underlying the melt lens providing evidence for a single robust magma chamber extending beneath both ridges. Therefore local thickening of layer 2A at the OSC is a viable mechanism for producing the negative velocity anomalies recovered in layer 2B/C.

Alternatively, along-axis variations in the porosity structure of layer 2B/C without any associated lithological variation could also account for the negative velocity anomaly. Travel time modelling of melt lens  $P$ - $S$  mode converted arrivals, described in section 4.4, suggests a Poisson's ratio of 0.32 in layer 2B/C, which is consistent with the presence of thin cracks. Since there are no other measurements of layer 2B/C Poisson's ratio, it is not possible to constrain the extent of such cracking elsewhere. However, this result demonstrates that an interpretation which relies on the presence of thin cracks in layer 2B/C is viable. Christeson *et al.* (1997) modelled a negative velocity anomaly of similar magnitude associated with a relict overlap basin at the EPR between  $9^{\circ}$  and  $10^{\circ} N$  as arising from the presence of such thin cracks. It is plausible that the overlap basin, with its complex ridge geometry, could be the site of particularly intense deformation, which would account for the largest magnitude negative anomaly being centred on the OSC at the VFR.



As described above, the porosity change which might give rise to these velocity anomalies depends on what the actual geometry of the porosity is. Christeson *et al.* (1997) modelled a negative velocity anomaly of 4–5% at the top of crustal layer 3 as a porosity increase of 0.5% in the form of thin cracks (aspect ratio of 0.015), based on the cracking model of Kuster & Toksöz (1974). This anomaly is similar in magnitude to the anomaly observed in layer 2B/C in this study. Wilkens *et al.* (1991) used the same theory to demonstrate that the large vertical *P*-wave velocity gradients commonly observed in the upper oceanic crust can be modelled by the preferential closure of a population of thin cracks. The theoretical model of Wilkens *et al.* (1991) comprises a basalt containing pores of eight different aspect ratios ranging from 0.001 to 0.5 and an initial porosity of 26%. By preferential closure of thin cracks, a velocity increase from 2.5 to 5.0  $\text{kms}^{-1}$  may be modelled by a porosity decrease of as little as 6%. A velocity reduction from 5.0  $\text{kms}^{-1}$  to 4.6  $\text{kms}^{-1}$  as modelled at the VFR was modelled as arising from a porosity increase from 20.0% to 21.5%. The crack theory of Kuster & Toksöz (1974), on which the models of Christeson *et al.* (1997) and Wilkens *et al.* (1991) are based, neglects crack–crack interactions and is therefore not strictly valid at these high porosities. However, subsequent theoretical work (Berge *et al.* 1992) has demonstrated that the general conclusion that porosity in the form of low aspect ratio cracks has a greater effect on seismic velocities than high aspect ratio cracks holds true at the high porosities often found in oceanic crust. Therefore the two studies quoted above are useful examples of the effect of porosity on seismic velocity as they demonstrate that negative velocity anomalies of similar magnitude to those modelled at the CVFR may arise from a relatively modest increase in porosity (<2%) although a larger increase cannot be ruled out.

Whilst an interpretation based on the assumption that the OSC is the site of most intense deformation is consistent with observations at the EPR, the ridge crest morphology indicates that the southern part of the CVFR, furthest away from the OSC, has undergone most tectonic disruption (Collier & Sinha 1992b). As described in section 5.2.1, the along-axis variations in ridge crest morphology are interpreted by Collier & Sinha (1992b) as representing along-axis variations in magma supply such that the OSC has been the site of most vigorous magmatism in the recent past, whilst segments further south have been relatively magma starved. The negative velocity anomaly in layer 2B/C also appears to correlate with morphological segmentation,

which suggests that it may be related to the underlying magmatic system. Toomey *et al.* (1994) observed a negative velocity anomaly of similar magnitude in layer 2B/C at the EPR at 9° 30' N, which they attributed to a subsolidus temperature anomaly. This interpretation was preferred because no *S*-wave velocity reduction was modelled, which would be expected if the velocity anomaly arose from a porosity increase (Vera *et al.* 1990). Based on the modelling of Christensen (1979), the observed *P*-wave velocity anomaly of 0.2–0.5  $\text{kms}^{-1}$  implies a temperature anomaly of 250–450 °C (Toomey *et al.* 1994). A similar explanation might apply at the VFR. A subsolidus temperature is required as the presence of even a very small percentage of partial melt would lead to significant attenuation of rays travelling in layer 2. This attenuation is not observed within the VFR wide-angle seismic dataset. High temperatures beneath the OSC would be consistent with vigorous magmatism, and might arise due to conductive heat transfer from a particularly active underlying magma chamber, or by advective heat transfer following a phase of dyke emplacement. A temperature anomaly is also consistent with the presence of a high temperature hydrothermal field (the Vai Lili field) near the OSC (Fouquet *et al.* 1991).

The correlation of the negative anomaly with ridge crest morphology suggests that it is related to the underlying magmatic system, which would imply that, of those possible origins discussed above, a subsolidus temperature anomaly is the most likely explanation. The electrical resistivity structure in layer 2B/C at the CVFR shows along-axis variations approximately corresponding to the observed fourth-order ridge segmentation, which suggests that these variations are also related to the underlying magmatic system (MacGregor *et al.* 2001). Although the electrical resistivity structure does not correlate well with the seismic velocity structure overall, which implies that the two methods are sensitive to different crustal properties, a very low resistivity has been modelled in layer 2B/C. This low resistivity may be explained by the presence of hot and/or saline fluid in layer 2B/C (MacGregor *et al.* 2001), which lends credence to the suggestion that a temperature anomaly might contribute to the along-axis variations in seismic velocity. Hence the observed velocity anomaly could arise from a thermal anomaly arising from a recent injection of melt into layer 2 on the scale of the fourth-order segmentation. However, enhanced magmatism at the OSC over a protracted period could also generate a greater thickness of extrusive material, which in turn would give rise to lower *P*-wave velocities without the need for a temperature anomaly.

An explanation based on greater deformation at the OSC is not related to the underlying magmatic system, but is consistent with the structure observed at a relict overlap basin near the EPR (Christeson *et al.* 1997). In the absence of widespread measurements of Poisson's ratio in layer 2B/C, which could potentially provide constraints on the porosity and geometry of porosity, it is not possible to distinguish between these possible origins for the axial negative velocity anomaly in layer 2B/C, and they are therefore all viable.

#### 5.2.4 Geological interpretation of layer 2

The *P*-wave crustal velocity structure at the VFR may be subdivided into layers which correspond to layers 2A, 2B/C and 3 according to the standard nomenclature for seismic layering of oceanic crust described by Houtz & Ewing (1976) and Bratt & Purdy (1984). By analogy with ophiolite sequences, which are believed to represent ancient oceanic crust, the seismic layers are often interpreted as corresponding to extrusive lava (layer 2A), intrusive dykes (layer 2B/C) and massive gabbro (layer 3). However, as discussed in section 1.3.4, this straightforward correlation between seismic layering and lithology is probably not strictly true everywhere.

The hypothesised correlation between seismic and lithological layering outlined above is largely based on studies of young ocean crust at the EPR. Here, seismic layer 2A has been modelled as a low velocity layer with low velocity gradient, that is a few hundred metres thick and underlain by a high velocity gradient zone marking the transition into layer 2B (e.g. Harding *et al.* 1989; Vera *et al.* 1990; Grevemeyer *et al.* 1998; Collier & Singh 1998). The low velocity in layer 2A is attributed to the high porosity of extrusive material, and the markedly higher velocity in layer 2B is thought to be associated with the presence of intrusive dykes with significantly lower porosity. Therefore the layer 2A–2B boundary is believed to represent a lithological transition from extrusive lava to dykes in young EPR crust (Harding *et al.* 1993). This hypothesis is supported by the observed correlation between areas of high magnetisation, which is attributed to magnetised minerals in extrusive lava, and seismic layer 2A thickness (Schouten *et al.* 1999; Bazin *et al.* 2001). The thickness of layer 2A has been found to rapidly increase within a few kilometres of the axis, which is attributed to the progressive burial of the dykes by successive lava flows (Harding *et al.* 1993; Hooft *et al.* 1996).

Whilst the seismic velocity structure of the VFR is broadly similar to that observed at the EPR, there are a number of important differences; layers 2A and 2B/C are modelled with approximately constant velocity gradients, and the layer 2A–2B/C boundary marks a reduction in the velocity gradient. Additionally there is no significant off-axis thickening of layer 2A. The lower spreading rate at the VFR relative to the EPR and more viscous andesitic and dacitic magmas are believed to be responsible for these structural discrepancies between the two ridges. By analogy with the velocity structure at the EPR, the following speculative model for the structure of layer 2 at the VFR is proposed:

- Layer 2 corresponds to a gradual transition from extrusive lava to intrusive dykes with increasing depth rather than comprising distinct lava and dyke layers. The lower spreading rate and more episodic magma supply relative to the EPR is likely to contribute to the development of this structure since lava extruded at the VFR remains within the neovolcanic zone for longer and is thus more likely to be intruded by later dyking events. Additionally the more viscous magmas may solidify rapidly and plug the fissures through which they erupt (Wiedicke & Collier 1993) thus contributing to the mixing of lithological types.
- The more viscous magma compositions may also be responsible for the absence of off-axis thickening of layer 2A since lava will not flow as far away from the ridge before solidifying. Therefore the entire extrusive layer is emplaced within the neovolcanic zone.
- The high Poisson's ratios modelled in layer 2A using  $P$ – $S$  mode converted arrivals imply the presence of thin cracks. The polarisation of  $P$ – $S$  mode converted arrivals is consistent with the presence of thin cracks formed in the axial region and preferentially aligned perpendicular to the spreading direction. The preferential crack alignment inferred off-axis is consistent with rotation of cracks formed on-axis due to southward propagation of the ridge system (see section 4.6.3 and Fig. 4.17). The relatively low spreading rate contributes to the development of strong preferential alignment since the crust is likely to be disrupted by tectonism whilst still close to the ridge axis.

- The  $P$ - $S$  mode converted arrivals described above are interpreted as arising from mode conversion at the layer 2A-2B/C boundary and imply a step change in  $S$ -wave velocity at this interface even though the  $P$ -wave velocity structure is apparently continuous. As outlined in section 4.6.1, this behaviour is interpreted as reflecting a boundary at which a population of thin cracks becomes closed over a narrow depth interval relative to half the seismic wavelength ( $\sim 0.1$  km). The interpretation that the layer 2A-2B/C boundary is porosity controlled, is broadly consistent with modelling the Vai Lili high temperature hydrothermal field which is located near the OSC. The reaction zone at this field is estimated to be  $\sim 1$  km deep from quartz barometry (Fouquet *et al.* 1993), which is similar to the seismic layer 2A thickness of  $\sim 1.3$  km.

$P$ - $S$  mode converted arrivals have also been observed in young oceanic crust at the EPR (Christeson *et al.* 1997; Collier & Singh 1998) which were modelled as arising from mode conversion at the top of the high gradient zone marking the layer 2A-2B transition. As described above, at the EPR this boundary is believed to mark a lithological transition from extrusive lava to intrusive dykes. By contrast, at the VFR the interface at which the majority of the observed  $P$ - $S$  mode conversion occurs (the layer 2A-2B/C boundary) is thought to be a porosity boundary within a layer of mixed lava and dykes. Therefore the converting interface is believed to occur at a deeper structural level and its nature is thought to be different at the VFR compared to the EPR. This suggestion implies that pervasive cracking extends to a greater structural depth at the VFR, which is consistent with the idea that young crust is subjected to more tectonism whilst close to the axis at intermediate- and slow-spreading ridges due to the more episodic magma supply.

Since the seismic experiment on which this study is based was designed primarily to model the crustal structure at mid-crustal levels, the resolution in the upper part of layer 2 is generally poor. Therefore it is likely that the model of layer 2 structure presented above is an average of a much more complex structure. It is possible that the uppermost crust comprises a thin extrusive layer of approximately constant velocity underlain by a high velocity gradient zone similar to the structure modelled at the EPR. This structure was identified at the EPR based on the observation of wide-angle reflections turning in the high velocity gradient zone (Harding *et al.* 1989; Vera *et al.* 1990). Such arrivals would be difficult to observe at the VFR if they occurred as they would probably be masked by the direct water-wave arrivals due to the nature of the

acquisition geometry. Therefore it is possible that  $P$ - $S$  mode conversion occurs at a boundary which has not been specifically identified owing to the limitations of the acquisition geometry, or that the velocity structure near the layer 2A-2B/C boundary is more complicated and allows for more efficient  $P$ - $S$  mode conversion than is implied by the model described above. In the absence of direct evidence of such structures, the interpretation presented above is preferred.

There is evidence of systematic along-axis variation in layer 2 properties. Turner (1998) modelled thicker layer 2 and lower layer 2 velocities on the *Seismic North* across-axis profile than on the *Seismic South* across-axis profile. When this along-axis variation in structure was incorporated into the initial model, the misfit of the travel time data was improved suggesting that it better represents the true structure. The northward thickening of layer 2 mirrors the general northward thickening of the whole crust as determined by gravity studies (Sinha 1995; Turner 1998; Peirce *et al.* 2001), which may reflect along-axis variation in magma supply as described in sections 3.8.4 and 5.2.1. The south-north reduction in layer 2 velocities may also reflect along-axis changes in magma composition. Dredge samples (Frenzel *et al.* 1990) and ridge crest morphology (Collier & Sinha 1992b) suggest that there is a transition in the composition of magma erupted at the CVFR from basaltic andesite in the south to rhyolite in the north. Increasing silica content leads to a reduction in  $P$ -wave velocity, so this petrological trend is consistent with the modelled south-north reduction in  $P$ -wave velocity in layer 2.

### 5.3 Segmentation of the Valu Fa Ridge

The VFR exhibits segmentation of a similar style to that observed at fast-spreading ridges such as the EPR. Adopting the terminology of Macdonald *et al.* (1991), the VFR is divided into three third-order segments separated by OSCs, which are themselves divided into fourth-order segments separated by SNOOs and devals (von Stackelberg *et al.* 1988; Wiedicke & Collier 1993). The classic model of ridge segmentation presented by Macdonald *et al.* (1988), which is based on studies at the EPR, predicts that ridge axis discontinuities are magmatically starved relative to segment centres. Therefore, on this basis the OSC at the northern end of the CVFR, which is the most pronounced axial discontinuity at the VFR, would also be expected to be relatively magmatically starved. However, the opposite appears to be the case on the basis of the following evidence.

- This and other studies (Turner 1998; Turner *et al.* 1999) have shown that layer 2A exhibits south–north thickening and is thickest at the OSC.
- Modelling of the gravity field implies that the whole crust beneath the OSC is also locally thicker than elsewhere along the VFR (Sinha 1995; Peirce *et al.* 2001), and the general south–north shallowing of the bathymetry also mirrors this trend.
- The widest and largest magnitude negative anomalies in layer 2B/C and layer 3 modelled in this study, and the widest melt lens modelled by Collier (1990) and Collier & Sinha (1992a), are found in the north near the OSC. These results suggest that magma supply has been most robust beneath the OSC in the recent past. Furthermore, this study and the modelling of Turner (1998) suggest that there is probably a single magma chamber beneath the OSC which supplies both ridges.
- An active hydrothermal field (the Vai Lili field) has been observed near the OSC at 22° 13' S which discharges fluids at temperatures of up to ~350 °C (Fouquet *et al.* 1991 and 1993).

Therefore all these enhanced magmatic budget indicators suggest that the OSC is currently the site of particularly vigorous magmatism at the CVFR in direct conflict with the segmentation model of Macdonald *et al.* (1988).

As described in section 1.2.2 in the context of the EPR, some of these indicators of melt supply may be affected by local factors, particularly the efficiency of lateral melt transport. However, the fact that all of the evidence described above indicates abnormally high magmatic budget beneath the OSC provides strong evidence that the conclusion that the OSC has recently been the site of most vigorous magmatism is valid. Furthermore, given the more viscous magma and lower overall magmatic budget at the VFR relative to the EPR, and the likelihood that lateral melt transport will be less efficient as a consequence, the observations described above are likely to be more reliable indicators of local variations in magmatic budget than at the EPR. Wiedicke & Collier (1993) suggested that melt supply beneath the current site of the OSC might be abnormally high on the basis of the broad bathymetric minimum and the high density of seamounts in that area. Since these features extend into pre–rift crust, which suggests that they pre–date the onset of rifting, Wiedicke & Collier (1993) speculate that this enhanced melt supply may be subduction related, and possibly related to the subduction of the Louisville Ridge (see Fig. 1.6).



It is possible that the current association of the OSC with a region of high magmatic budget is a transient feature, and that over time it will migrate away. At the EPR, several examples of OSCs migrating away from the magmatically most robust parts of ridge segments have been identified based on reconstruction of the changes in ridge geometry over time using bathymetry data (e.g. Macdonald *et al.* 1992; Cormier *et al.* 1996). Such behaviour is consistent with the segmentation model of Macdonald *et al.* (1988). However, a similar reconstruction of the history of the OSC at 22° 10' S at the VFR by Wiedicke & Collier (1993) shows that it exhibits entirely different behaviour. The VFR is propagating south following regional tectonic trends (Parson & Wright 1996). At a typical OSC on the EPR, one ridge would be expected to propagate at the expense of the other. In the case of the OSC at 22° 10' S, the NVFR would be expected to propagate south at the expense of the CVFR to be consistent with the regional tectonics. The reconstruction of Wiedicke & Collier (1993) shows that the OSC has a complex history, and at times the CVFR has propagated north at the expense of the NVFR. The net result is that the OSC has remained in a similar place over a long period of time. Therefore, far from migrating away from a source of enhanced melt supply as the Macdonald *et al.* (1988) model would predict, the OSC appears to have remained located at a site of vigorous magmatism even though regional tectonic trends suggest it would be expected to have migrated to the south.

The OSC at the VFR is much smaller than many of its counterparts at the EPR. However, it is the most pronounced ridge axis discontinuity at the VFR and is thus significant in local context. Although the back-arc setting may influence the large-scale distribution of melt, notably the slight local enhancement in melt supply beneath the current site of the OSC, such variations in magmatic budget are of no greater magnitude than those at the EPR. Furthermore regional geophysical studies indicate that the principal source of magma at the VFR is decompression melting in common with other mid-ocean ridges (Xu & Wiens 1997; Zhao *et al.* 1997). Therefore a meaningful comparison of the relationship between ridge segmentation and melt supply at the two ridges can be made. Although there is evidence of a robust melt supply beneath the 9° 03' N OSC at the EPR (Kent *et al.* 2000), gravity studies imply that large-scale melt supply from the mantle is focussed at the segment centre (Wang *et al.* 1996) and the OSC appears to have migrated south away from this melt source on average (Macdonald *et al.* 1992). The observation of melt input beneath this OSC is significant to the study of ridge segmentation insofar as it indicates that the anomalously thick crust at segment

ends need not arise solely from lateral melt transport away from an upwelling at the segment centre. Nevertheless, on the longest length and time scales, mantle upwelling appears to occur predominantly, if not solely, at the centre of the segment at this site. The behaviour of the VFR is fundamentally different in that every available indicator of melt supply suggests that the OSC has been situated at a site of enhanced melt supply from the mantle for a protracted period. This result suggests that, at the VFR, the relationship between morphological segmentation and melt supply is very different to the general model for mid-ocean ridges.

## 5.4 Summary of results

This section summarises the conclusions about the crustal structure at the CVFR which may be drawn from the 3-D tomographic and *P-S* mode converted arrival studies described in chapters 3 and 4 respectively. In subsequent sections, further work which could be performed on the EW9512 dataset to provide further constraints will be described, and further experimental work at the VFR suggested.

Previous geophysical studies have demonstrated that the VFR exhibits morphological segmentation in common with most other mid-ocean ridges (von Stackelberg *et al.* 1988; Wiedicke & Collier 1993) and have identified an axial magmatic system similar to those observed at other mid-ocean ridges. Collier (1990) and Collier & Sinha (1992a) identified a MCR interpreted as representing reflection from the top of a thin axial melt lens, and modelling of 2-D subsets of the EW9512 wide-angle seismic data by Turner (1998) and Turner *et al.* (1999) identified a broad axial LVZ at two widely spaced locations. These studies also suggest that the gross *P*-wave velocity structure of the crust is continuous and broadly similar to that of young oceanic crust at other mid-ocean ridges, and may be subdivided into layers of approximately constant velocity gradient. These crustal layers have been interpreted as corresponding to layers 2A, 2B/C and 3 based on the classification of Houtz & Ewing (1976) and Bratt & Purdy (1984). The aims of this study were to extend work of Turner (1998) into three dimensions to assess the along-axis variations in structure, which is not possible from isolated 2-D profiles, and investigate the geological nature of the crustal layering. The geological implications of this study have been discussed at length in sections 5.2 and 5.3 and the following conclusions drawn.

1. The 3-D tomographic inversion identified an axial LVZ in layer 3, which is interpreted as representing a crustal magma body, beneath most of the CVFR. The dimensions and melt fraction cannot be determined accurately, but the velocity anomaly is consistent with other similar magma chambers observed at other mid-ocean ridge systems which are interpreted as comprising a broad zone of crystal mush.
2. The LVZ is approximately continuous along-axis which is consistent with the along-axis continuity of the melt lens reflector observed by Collier & Sinha (1992a). A discontinuity in the LVZ between  $y = 0$  km and  $y = 5$  km has been modelled in this study which is believed to be predominantly a model artefact arising from irregular ray coverage. However, it is possible that the discontinuity in part reflects real thinning or discontinuity of the mush zone. The apparent discontinuity correlates with a fourth-order segment which has been interpreted as being relatively magma starved at present and in the recent past on the basis of ridge crest morphology and the melt lens reflector characteristics (Collier & Sinha 1992a,b; Wiedicke & Collier 1993). These variations in axial morphology are believed to arise from episodic magma injection due to the intermediate-spreading rate, in contrast to the more steady-state upwelling inferred at the fast-spreading EPR.
3. The morphology of the southernmost fourth-order segment at the CVFR (labelled V7 in Figs. 1.7 and 5.2) suggests that it has been relatively magma starved in the recent past (Collier & Sinha 1992b). However, this study has imaged a LVZ under this segment, which is consistent with the model of Turner (1998) and the observation of a strong MCR by Collier (1990). The presence of a magma chamber beneath this segment was interpreted by Collier & Sinha (1992b) as representing either the remnant of an earlier magmatic phase or a recent melt injection.
4. *P-S* mode converted arrivals were recorded by the axial instrument at the *Seismic South* deployment, which were modelled as arising from mode conversion at the top of the axial melt lens, thus providing further evidence for the existence of this feature. A qualitative analysis of the amplitude of these arrivals suggests that the melt lens comprises a high percentage of partial melt beneath this site. Comparison with the structure of a similar melt lens at the fast-spreading southern EPR suggests that such high melt fraction regions are likely to be small, short-lived features

and their presence thus implies a very recent local melt injection event (Singh *et al.* 1998). This conclusion suggests that the underlying LVZ (described above), which is likely to be a more long-lived feature, represents a recent melt injection rather than a remnant of an earlier magmatic phase and provides direct evidence for a cyclic pattern of magmatic and amagmatic extension at this intermediate-spreading ridge.

5. The gross seismic structure of layer 2 does not exhibit the clear layering found at the EPR which has been interpreted as representing segregation into lava and dyke layers separated by a transition zone (Harding *et al.* 1989; Vera *et al.* 1990). It is suggested that, at the VFR, layer 2 comprises a more gradual transition from extrusive lava to intrusive dykes. These differences in structure between the VFR and EPR are consistent with the lower relative spreading rate at the VFR which results in erupted material remaining in the neovolcanic zone for longer where it may be intruded by later dyking events.
6. The tomographic inversion suggests thinning of layer 2 in the southwest of the area which is associated with the pseudofault between pre- and post-rift crust identified by Wiedicke & Collier (1993) thus supporting the conclusion of Turner (1998).
7. A negative axial velocity anomaly is present in layer 2B/C, with maximum amplitude beneath the OSC. Possible causes include increased porosity associated with increased faulting or thickening of the extrusive layer at the OSC, or a high temperature anomaly associated with the underlying magmatic system. It is not possible to distinguish between these possibilities with this dataset.
8. *P-S* mode converted arrivals are observed which are believed to arise from mode conversion at the layer 2A-2B/C boundary. Since the vertical *P*-wave velocity structure is continuous, these arrivals imply a boundary at which there is a sharp discontinuity in *S*-wave velocity with no accompanying *P*-wave discontinuity. Theoretical studies and seismic experiments at other mid-ocean ridges indicate that, in the oceanic environment, such a structure is likely to arise from the presence of a population of thin cracks in layer 2A which become closed over a depth interval of ~0.1 km or less in the region of the layer 2A-2B/C boundary.
9. The polarisation of *P-S* mode converted arrivals suggests that the thin cracks in layer 2A are formed on-axis perpendicular to the spreading direction (i.e. parallel to the ridge axis) and rotate towards a pseudofault-parallel direction as they move off-axis due to the southward propagation of the rift system.

10. The modifications made to the initial model used for tomographic inversion suggest that layer 2A exhibits south–north thickening, which mirrors the south–north thickening of the whole crust determined by modelling the gravity field (Sinha 1995; Peirce *et al.* 2001). These results, in conjunction with the along–axis variations in the properties of the magmatic system and evidence from bathymetric and hydrothermal studies, strongly suggest that the OSC has been the site of enhanced magmatism over a long period. This finding directly conflicts with the standard model for the relationship between morphological segmentation and magmatic budget which predicts that ridge axis discontinuities should be relatively starved of magma (Macdonald *et al.* 1988). This result suggests that, on the scale of third–order segmentation, the relationship between magmatic budget and morphological segmentation at the VFR is very different to other mid–ocean ridges.

## 5.5 Suggestions for further work

In this section, suggestions for further analysis of existing datasets collected during cruise EW9512 are described including modifications to the acquisition geometry and inversion method which would be beneficial to future seismic experiments. Further surveys at the VFR incorporating these modifications are suggested which would significantly extend existing knowledge of the accretionary and tectonic processes at a back–arc spreading centre.

### 5.5.1 Existing datasets

The geological interpretation of crustal structure at the CVFR described in section 5.2 contains a number of ambiguities which cannot be constrained from the studies of the seismic, gravity and electromagnetic datasets performed to date. However, further analysis of existing datasets could potentially provide additional constraints on the ambiguities in crustal structure. Magnetic data were collected throughout EW9512 which have not yet been analysed in detail. At the EPR, high magnetisation has been associated with young extrusive lavas. This high magnetisation is believed to arise from the presence of highly magnetic titanomagnetite in young lava, which is rapidly weathered to less magnetic titanomaghemite on a time scale of less than 100 kA, and also the effect of recent doubling of the magnetic field intensity (Schouten *et al.* 1999). This observation has been used to study extrusive layer thickness variations at the EPR

and also provides evidence that the seismic layer 2A–2B boundary corresponds to a lithological transition from extrusive lava to dykes at this ridge (e.g. Schouten *et al.* 1999; Bazin *et al.* 2001). Collier & Sinha (1992b) presented the results of a study of magnetic data acquired during cruise CD34/88 and found a correlation between seafloor magnetisation and fourth-order segmentation which they tentatively ascribed to different degrees of seafloor weathering. By combining the CD34/88 and EW9512 magnetic datasets and interpreting them in conjunction with the improved constraints on structure available from seismic and electromagnetic experiments, a more comprehensive study of the magnetisation at the CVFR would be possible. Such a study could potentially provide insights into extrusive layer thickness and hence the nature of the seismically determined crustal layering. In particular, such a study might help determine whether the extrusive layer thickens at the OSC, which is one possible explanation for the occurrence of a negative velocity anomaly in layer 2B/C. However there are likely to be complications at the CVFR due to the large along-axis variations in lava chemistry inferred from dredge samples (Frenzel *et al.* 1990) and the likelihood that layer 2 is not divided into discrete extrusive and intrusive layers as at the EPR. A further target for magnetic interpretation would be the pseudofault which is believed to mark the transition from pre- to post-rift crust (Wiedicke & Collier 1993). Turner (1998) modelled significant thinning of layer 2 at this boundary on the *Seismic South* profile and a less dramatic thinning on the *Seismic North* profile. The tomographic analysis conducted as part of this study is consistent with this result. Mapping the magnetisation in this area might help identify the north–south variations of this feature.

Further analysis of the seismic data could also provide more information about the nature of the crust. Travel time tomography takes no account of arrival amplitudes which could potentially be used to determine the attenuation structure of the crust. Wilcock *et al.* (1995) described a spectral tomographic technique for determining this apparent attenuation structure which they applied to a 3-D tomographic dataset collected near 9° 30' N on the EPR. It is generally not possible to separate the effects of intrinsic attenuation from other mechanisms which might affect the amplitude of arrivals (e.g. scattering, short-path multiples, focusing and defocusing of energy at a rough interface such as the seafloor etc.) so the attenuation estimate obtained is an apparent attenuation which incorporates all these effects. Nevertheless, a measurement of apparent attenuation can provide useful information about the nature of the crust especially if the relative attenuation of groups of rays travelling in different crustal

layers are compared. Wilcock *et al.* (1995) imaged high attenuation in layer 2A which they interpret as arising from high levels of scattering plus frictional and fluid flow effects, and an axial high attenuation region in layer 3 coinciding with the seismic LVZ. The attenuation modelled in the LVZ is similar to that measured at temperatures near the basalt solidus in laboratory experiments, which indicates a very low melt fraction. A similar study of the attenuation structure at the CVFR could help to constrain the properties of the axial LVZ and the geological cause of the negative velocity anomalies in layer 2B/C.

The spectral technique of Wilcock *et al.* (1995) would not be appropriate for the VFR dataset. The EW9512 seismic experiment was conducted using an airgun source with a relatively narrow bandwidth whereas the data analysed by Wilcock *et al.* (1995) had an explosive source which consequently leads to higher SNR, clearer waveforms and, crucially, greater bandwidth with which to perform the spectral analysis. A simpler method, which might be more successful at determining the attenuation structure at the CVFR, is to consider the peak, or average, amplitudes within a given time window after the pick positions. Such a method was implemented by White & Clowes (1994) in a 2-D study of attenuation at the JDFR. Amplitude reduction due to divergence of the wavefield and transmission losses at any velocity discontinuities encountered along the ray path (e.g. the seafloor) must be accounted for. The forward modelling method used for the 3-D tomographic inversions performed in this study could be modified to explicitly include discrete interfaces which would allow transmission losses to be accounted for by using Zoeppritz's equations to calculate the transmission coefficient at each velocity discontinuity encountered by a ray. This modification is described in section 5.5.3. The problem of amplitude variations due to focusing or defocusing effects of rough seafloor topography could be partially accounted for by only considering arrivals for which the seafloor near the ray entry point is relatively smooth on the scale of the footprint of the wavefront, such that the plane wave approximation assumed by the forward modelling code and by Zoeppritz's equations is valid. The inverse method of White & Clowes (1994) could then be used to calculate the 3-D attenuation since the mathematical basis is essentially the same in 3-D as in the 2-D case. Therefore, relatively simple modifications to the forward modelling method for predicting first arrival travel times and ray paths could form the basis of a method for forward modelling the effects of attenuation, which itself could be used in a tomographic method for determining the 3-D attenuation structure.



### 5.5.2 Acquisition geometry

This study and others have shown that 3-D experiments can potentially provide very much better constraint on crustal structure which is inherently three-dimensional. In this section the theoretical resolution of a number of acquisition geometries is investigated in order to determine the requirements for obtaining adequate model resolution in the mid-ocean ridge environment using the VFR as the example. The EW9512 wide-angle seismic experiment was designed primarily with 2-D data acquisition in mind although a degree of 3-D coverage in the axial region resulted. Hence ray coverage within the 3-D model volume was not optimum. A further issue is that the EW9512 experiment was targeted towards resolving the structure at mid-crustal depths (layers 2B/C and 3) with the result that model resolution in layer 2A was generally very poor. This study has shown that inadequate representation of the velocity structure in regions of poor model resolution at levels shallower than the primary target depth may influence the anomalies recovered in regions of better resolution. Therefore, it is desirable that models should also have reasonable resolution at depths shallower than the primary target. This requirement should be born in mind when interpreting the resolution test results which follow.

Resolution tests were performed for a number of acquisition geometries using the method described in section 2.10. In order to allow direct comparison of the results of these resolution tests, the following initial conditions were applied to the model:

- Model dimensions were  $100 \times 70 \times 12$  km with x- and y-axes identical to the models in chapter 3. This area encompasses the CVFR and NVFR, extends east as far as the Tonga ridge and west into rifted island arc crust (*cf.* Fig. 1.6). This expanded area allows longer offset shot-receiver pairs to be included in the synthetic inversions to investigate the resolution at deeper levels. Within this area bathymetry data were obtained from Zellmer *et al.* (1998) which was also used to determine the synthetic instrument depths.
- The initial model was similar to the *basic 1-D initial model* with a velocity discontinuity at the Moho included to allow resolution in the uppermost mantle to be assessed, and was constructed using the bathymetry data indicated above and the method described in section 2.8.

- A 0.2 km shot spacing (equivalent to the EW9512 experiment) was modelled and 100% data recovery assumed for shots between 4 and 50 km offset from each receiver. An offset of 4 km is representative of the typical minimum shot–receiver offset at which crustal refracted arrivals are visible ahead of the direct water–wave arrivals at the VFR. The 50 km offset was arbitrarily chosen to reflect a likely maximum offset to which arrivals might be detectable when using an airgun source.
- An uncertainty of 40 ms was associated with each synthetic arrival in the inversion, and also used to determine the level of noise to add to the synthetic data as described in section 2.10. This uncertainty is typical of the mean uncertainty at each OBS location for the inversions described in chapter 3. Although data uncertainty might be expected to increase with shot–receiver offset, no such systematic relationship was observed for the real data at the VFR. However, given this likely relationship, the assumption of a constant uncertainty means model resolution may be overestimated at deep levels and similarly underestimated at shallow levels.
- A node spacing of 0.4 km was used for the forward grid for computational efficiency since the analysis described in section 2.7 and shown in Fig. 2.22 indicates that this grid size is adequate for calculating travel times given that the data uncertainty is 40 ms.
- All other initial conditions were identical to the resolution tests described in section 2.10. In most cases the inversion did not converge to a  $\chi^2$  value of less than 1.01 within five iterations indicating that the inversion was unable to resolve the travel time residuals within the 40 ms uncertainties. In these cases the model with the minimum associated  $\chi^2$  value was selected as the model which best satisfied the synthetic travel time data. However the semblance calculations indicate that the checkerboard anomalies have generally been adequately recovered even though the travel time residuals have not been resolved within their uncertainties.
- Checkerboard sizes of 5, 7, 10 and 15 km and a semblance operator radius of 5 km were used. This semblance operator radius is double that used for the resolution tests in section 2.10 and was chosen so that the summation in the semblance calculation (equation 2.24) was performed over the same number of points given that the forward grid spacing had been doubled. The results are also directly comparable with those of Zelt (1998) which were calculated using the same forward grid and semblance operator sizes.

- Resolution was calculated based on semblance thresholds of 0.7 and 0.9 as described in section 2.10. The resulting resolution plots represent the size of anomalies whose locations may be adequately resolved and those whose amplitudes may also be determined respectively.

Five experimental geometries were investigated, and these are shown in Fig. 5.4 overlain on the smoothed bathymetry. For real experiments, the geometry will be limited by the number of OBSs and days of ship time available. Therefore experimental geometries which employ different numbers of shots and OBSs have been tested, and each could be adapted according to the limitations of the available time and instrumentation, and the primary target depth of interest. The *EW9512* geometry (Fig. 5.4a) is identical to the EW9512 experimental geometry and was included to test the theoretical resolution of this experiment assuming 100% data recovery for those OBSs which recorded data (i.e. excluding NDOBS4). Two geometries were tested where the OBSs are arranged in a square grid and shots fired along the axis-parallel and perpendicular profiles which define the grid. The *Small grid* geometry (Fig. 5.4b) uses nine OBSs whilst the *Large grid* geometry (Fig. 5.4c) uses twenty OBSs and a closer grid spacing providing ray coverage in a slightly larger area, nine and twenty being the minimum and average number of OBSs typically available for such an experiment. The *Star* geometry (Fig. 5.4d) uses ten OBSs and ship tracks defining a five pointed star, and the *Combined star and grid* geometry (Fig. 5.4e) incorporates a modified version of the *Star* geometry with additional ship tracks and OBSs arranged in an irregular grid. The number of OBSs and shots required for each geometry are summarised in Table 5.1.

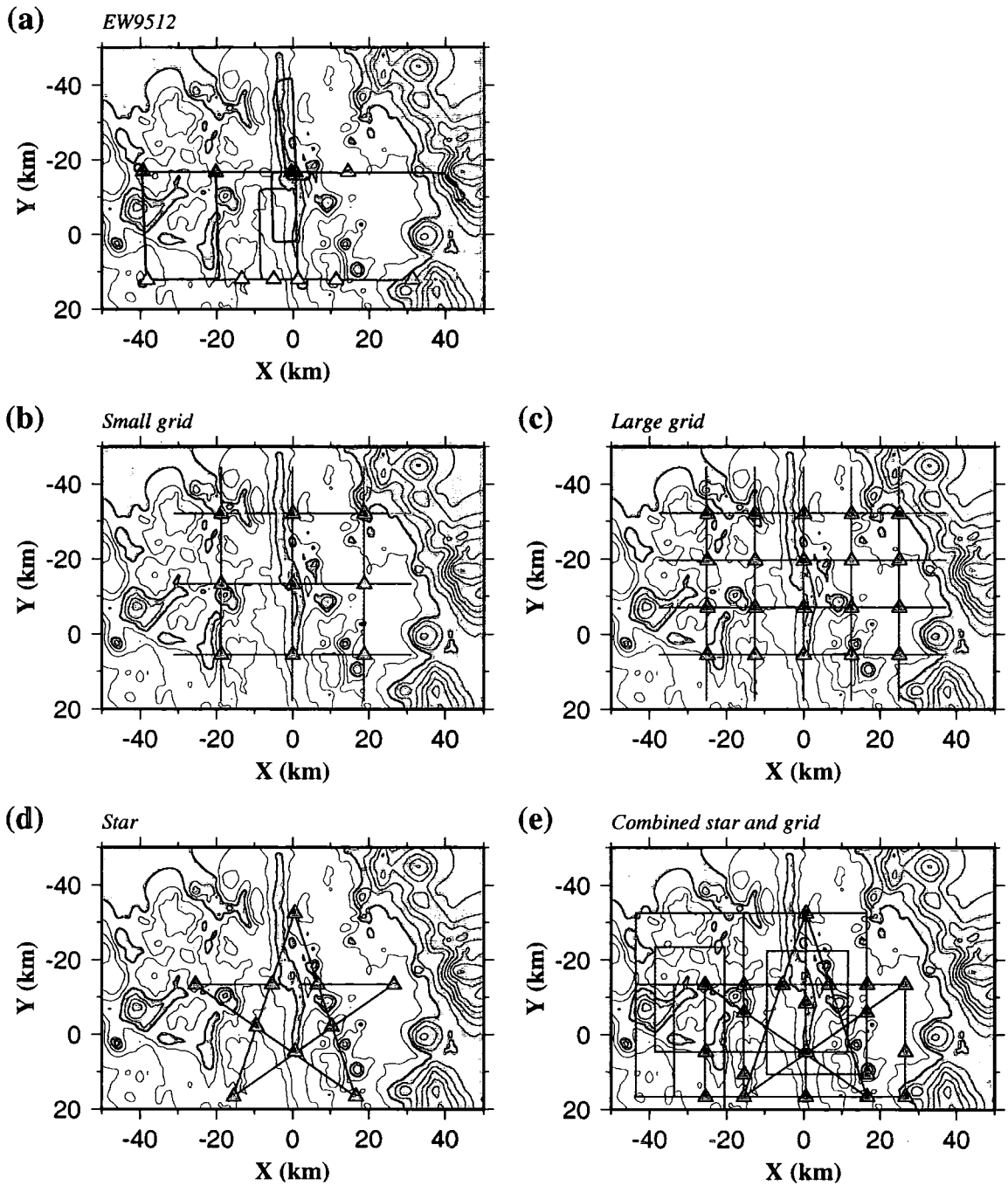


**Figure 5.4:** Tested acquisition geometries. a) *EW9512*, b) *Small grid*, c) *Large grid*, d) *Star* and e) *Combined star and grid* geometries are shown. Triangles represent OBS locations, coloured lines denote "ship tracks" along which synthetic shots are positioned at 0.2 km intervals. For the *EW9512* geometry two instrument deployments were used, and the OBS positions and associated ship tracks for these deployments colour coded in red and blue. For all other geometries, a single instrument deployment is proposed. Bathymetric contours at 0.25 km intervals have been plotted and bathymetry shallower than 2 km grey shaded.

Experimental Geometry	Number of OBSs	Number of Shots
<i>EW9512</i>	6	2441
<i>Small grid</i>	9	1878
<i>Large grid</i>	20	3069
<i>Star</i>	10	1295
<i>Combined star and grid</i>	20	5499

**Table 5.1:** Summary of the number of OBSs and shots necessary for each synthetic experimental geometry.

The resolution for each experimental geometry will now be considered in turn. Resolution is plotted for planes of constant velocity in the initial model at 3.00, 5.00, 6.20, 6.75 and 7.85  $\text{kms}^{-1}$ . These planes are shown on a cross-section through the initial model in Fig. 5.5 and correspond to the middle of layer 2A, middle of layer 2B, top of layer 3, middle of layer 3 and uppermost mantle respectively. The first three planes are equivalent to those used to display resolution in Fig. 2.31 and the inversion results presented in chapter 3.

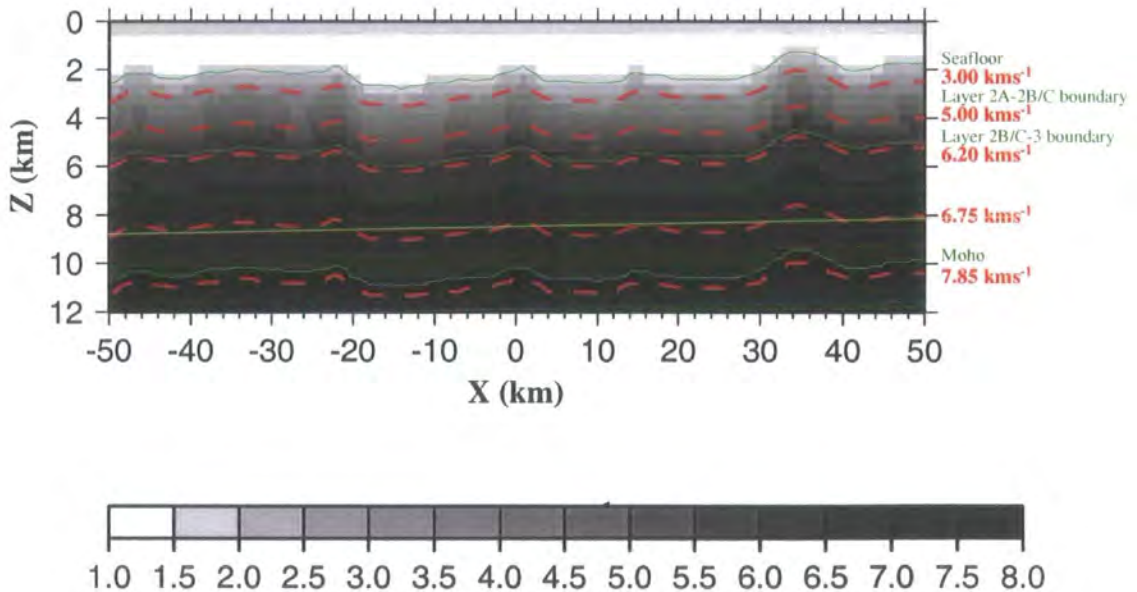


**Figure 5.5:** Cross-section through the initial model used in the synthetic resolution tests at  $y = 0$  km showing the principal layer boundaries (solid green lines) and the positions of the 3.00, 5.00, 6.20, 6.75 and 7.85  $\text{kms}^{-1}$  constant velocity planes (dashed red lines). Vertical exaggeration:  $\times 3$ . These constant velocity planes are used to display sections through 3-D synthetic resolution models in later figures in this chapter.

Resolution for the *EW9512* geometry (Fig. 5.4a) is shown in Fig. 5.6. Comparison of Fig. 5.6a–c with Fig. 2.31 shows that the theoretical resolution in the axial region is similar to that for the real inversions described in chapter 3. This observation implies that ray coverage geometry is the primary control on resolution rather than variations in data uncertainties. Resolution away from the axial region is generally poor and regions of high resolution tend to lie along 2–D profiles, which suggests that 2–D modelling such as that performed by Turner (1998) is most appropriate off–axis. Furthermore resolution in the lower crust and uppermost mantle is predicted to be poor. These findings arise from the predominantly 2–D acquisition geometry of the *EW9512* experiment and suggest there is little to be gained by extending the 3–D analysis of the *EW9512* dataset to greater depth or further off–axis. The remaining experimental geometries considered have been proposed with 3–D data acquisition in mind.

Grid geometries are commonly employed for 3–D data acquisition as their simplicity allows interpretation in 1–D, 2–D and 3–D as required. Prior modelling of subsets of the data in 1–D and 2–D provides good control on the initial model for a subsequent 3–D tomographic inversion thus increasing the confidence in the inversion results. Two grid geometries were investigated which provide coverage in a similar region using different numbers of OBSs and shots. The *Small grid* (Fig. 5.4b) employs nine OBSs with an 18.5 km spacing whilst the *Large grid* (Fig. 5.4c) employs twenty OBSs with a 12.5 km spacing.

The resolution for the *Small grid* geometry is shown in Fig. 5.7. Comparison with Fig. 5.6 for the *EW9512* geometry shows very much better resolution at lower–crustal and uppermost–mantle depths. Hence this geometry would be more appropriate than that employed during cruise *EW9512* for investigating the structure at these depths. At shallower levels, although the resolution is generally significantly better than for the *EW9512* geometry on average, the areas of highest resolution correspond with OBS locations and lines along which shots were fired. This observation suggests that this geometry is only able to accurately constrain the structure of the uppermost crust in 2–D and thus would provide no better coverage than that provided by the *EW9512* approach for shallow levels in the crust. However, this study has shown that poor resolution at shallow depths is potentially problematic for interpreting anomalies recovered at deeper levels where resolution is superior.

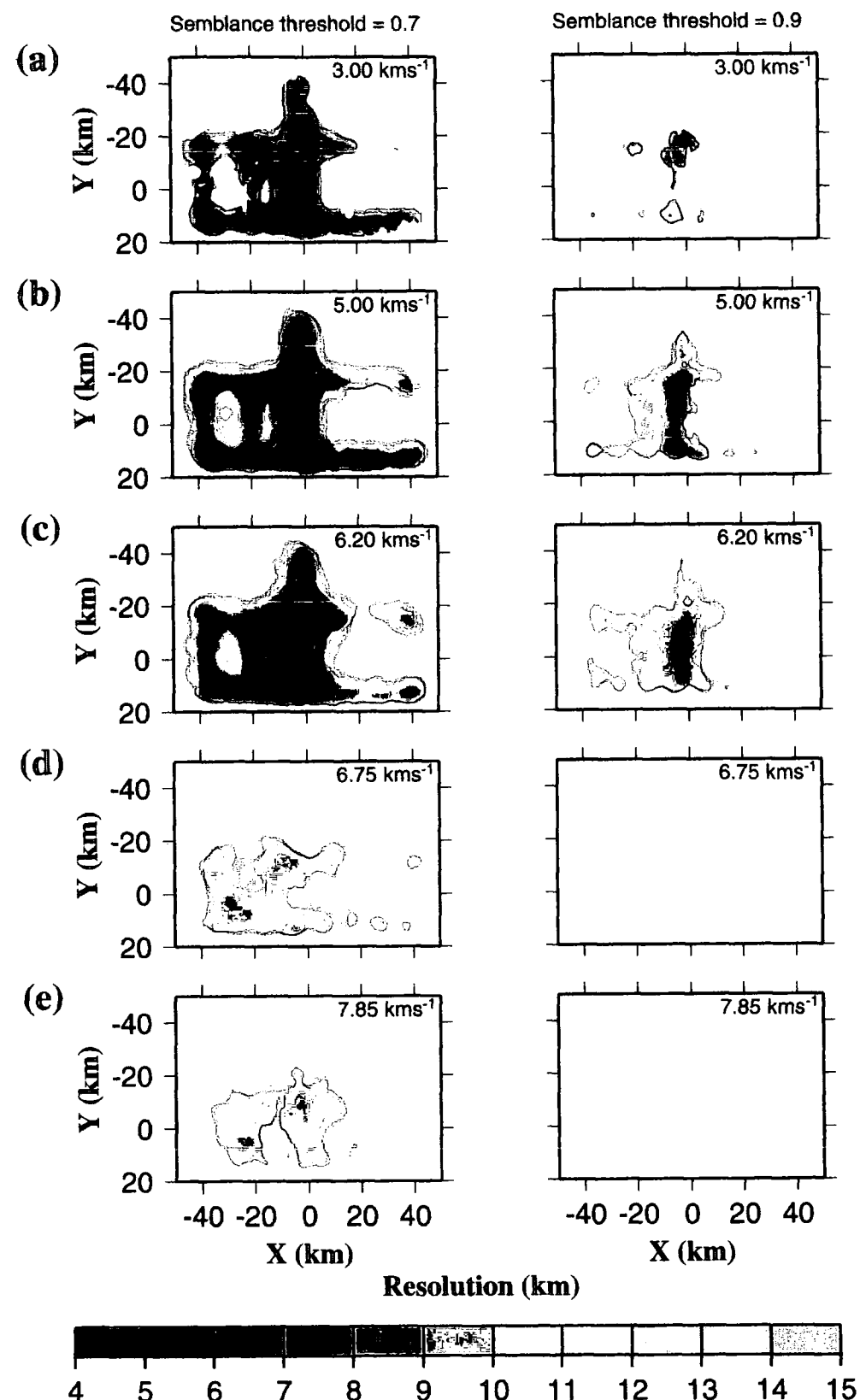


**Figure 5.6:** Resolution for the *EW9512* geometry in Fig. 5.4a plotted for the constant velocity planes shown in Fig. 5.5 (indicated in the top right-hand corner of each plot). Resolution has been calculated using semblance thresholds of 0.7, representing the scale of anomaly which can be accurately located, and 0.9, representing the scale of anomaly whose amplitude may also be accurately determined. Note that the resolution is generally similar to that for the real experiment shown in Fig. 2.31 in the axial region, and poor further off-axis, particularly at lower-crustal and uppermost-mantle depths where it is not possible to resolve anomaly amplitudes at the 15 km scale.

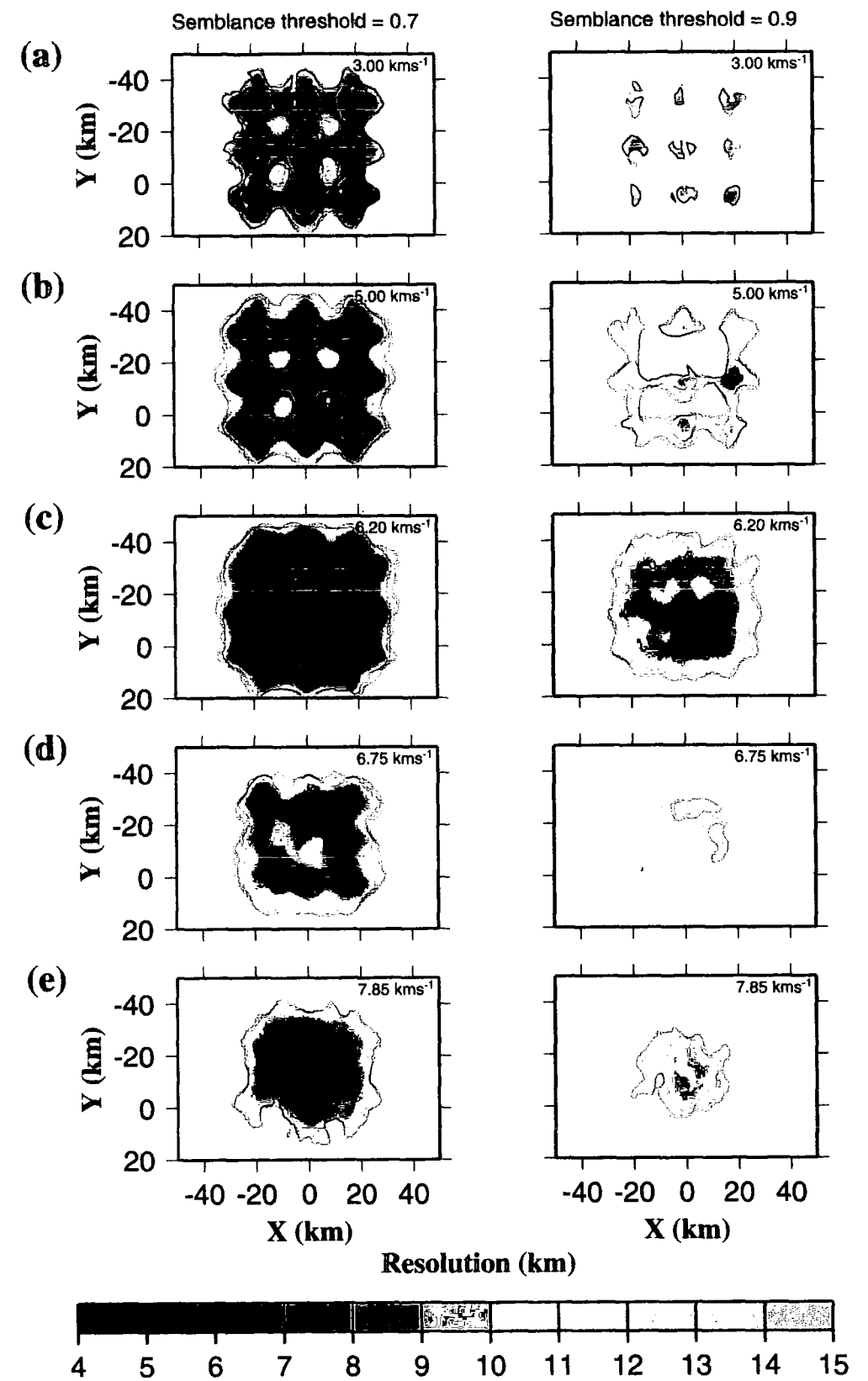


**Figure 5.7:** Resolution for the *Small grid* geometry shown in Fig. 5.4b. Note that resolution is generally better than for the *EW9512* geometry, especially off-axis and at lower crust and mantle levels, but regions of high resolution are disjointed at shallow-crustal levels correlate with OBS and shot positions.



The resolution for the *Large grid* geometry, shown in Fig. 5.8, is significantly better than for the *EW9512* and *Small grid* geometries at all depths. It should be noted that the lateral variations in resolution at a given depth must reflect the effect of rough seafloor bathymetry on ray coverage since the geometry is otherwise totally regular and would therefore give a regular resolution pattern if the seafloor were horizontal. The smaller OBS spacing means that although there is still some correlation between OBS and shot positions and regions of high resolution in the uppermost crust, this effect is much less pronounced than for the *Small grid* geometry. The denser ray coverage also leads to a significant improvement in resolution at lower-crustal and uppermost-mantle depths. However the *Large grid* geometry requires many more OBSs and shots than the *Small grid* geometry (Table 5.1). If instruments and ship time are limited, trade-off between resolution at shallow and deep levels will inevitably result. As poor shallow resolution appears to influence the anomalies recovered at deeper levels the grid spacing should therefore be the minimum which provides satisfactory resolution at the target depth of interest in order to also provide adequate resolution at shallower levels. A further point to note is that resolution is generally better in the uppermost mantle than in the lower crust. This feature arises because no arrivals turn in the lowermost crust so this region is sampled solely by rays which turn in the mantle; a problem discussed more fully in the next section.

The correlation between regions of high resolution at shallow levels and OBS location for the grid geometries described above is, in part, a function of the restricted range of ray azimuths in the uppermost crust arising from the regular geometry of shot positions. The *Star* geometry (Fig. 5.4d) was investigated as a possible way of providing improved azimuthal coverage in the uppermost crust. The resolution for this geometry is shown in Fig. 5.9. Although resolution in layers 2A and 2B is still fragmented and correlates with OBS and shot positions, this effect is much less pronounced than for either grid geometry despite comparable OBS spacing. Upper-crustal resolution is generally poor in the centre of the star, though this problem could be addressed by placing an extra OBS here or firing shots in this region into the existing array. Resolution in the lower crust and mantle is comparable to that for the *Small grid* geometry shown in Fig. 5.7 despite requiring only one extra instrument and the fewest shots of all the geometries considered, though the region of good resolution is more restricted in area. However, given the generally superior resolution at shallower depths, this geometry would be superior to a grid when OBS numbers and ship time are limited.

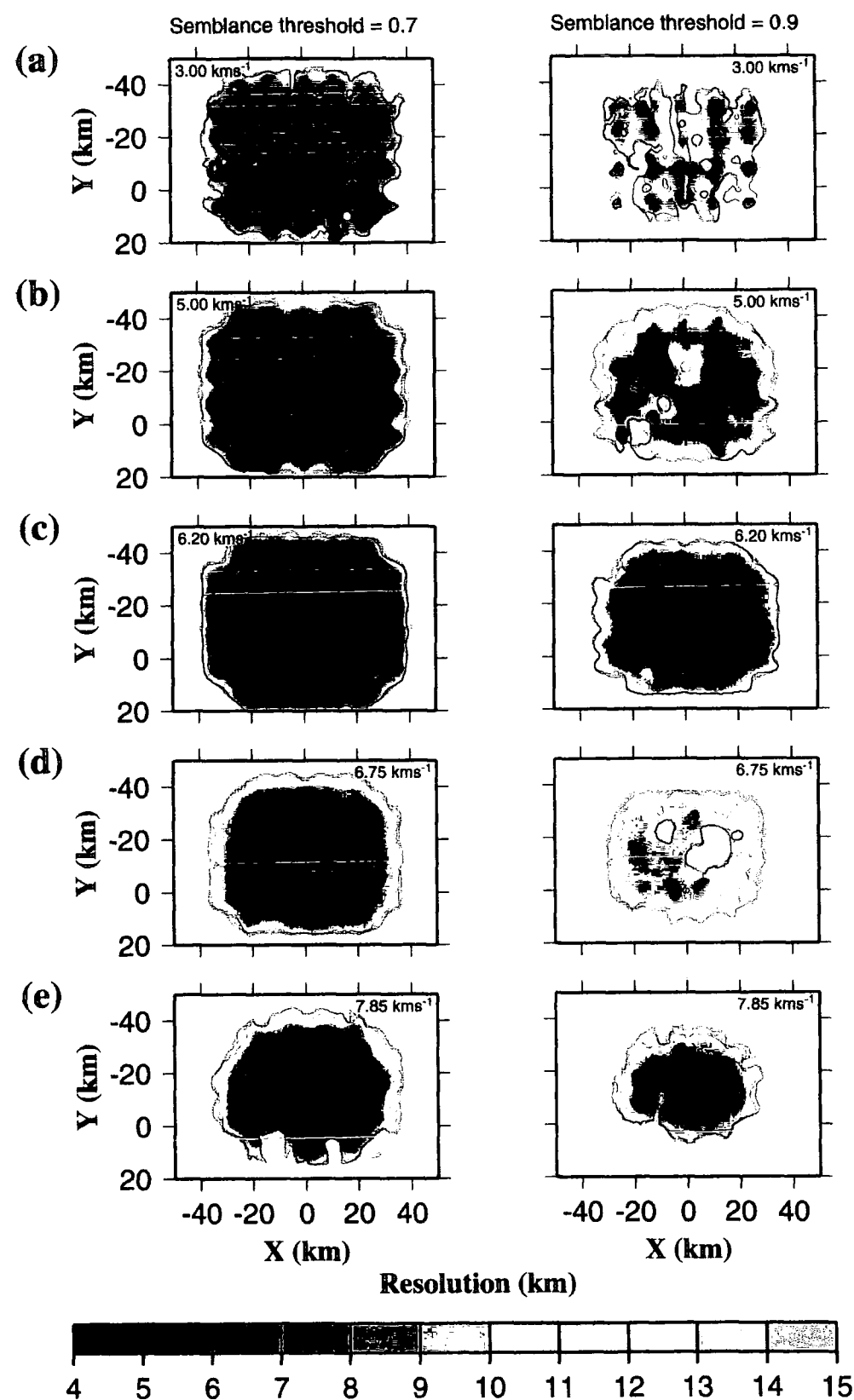


**Figure 5.8:** Resolution for the *Large grid* geometry shown in Fig. 5.4c. Resolution is very much better than for either the *EW9512* or *Small grid* geometries, though there is still a correlation between regions of high resolution and OBS and shot positions at shallow-crustal levels, albeit less pronounced than for the *Small grid* geometry.

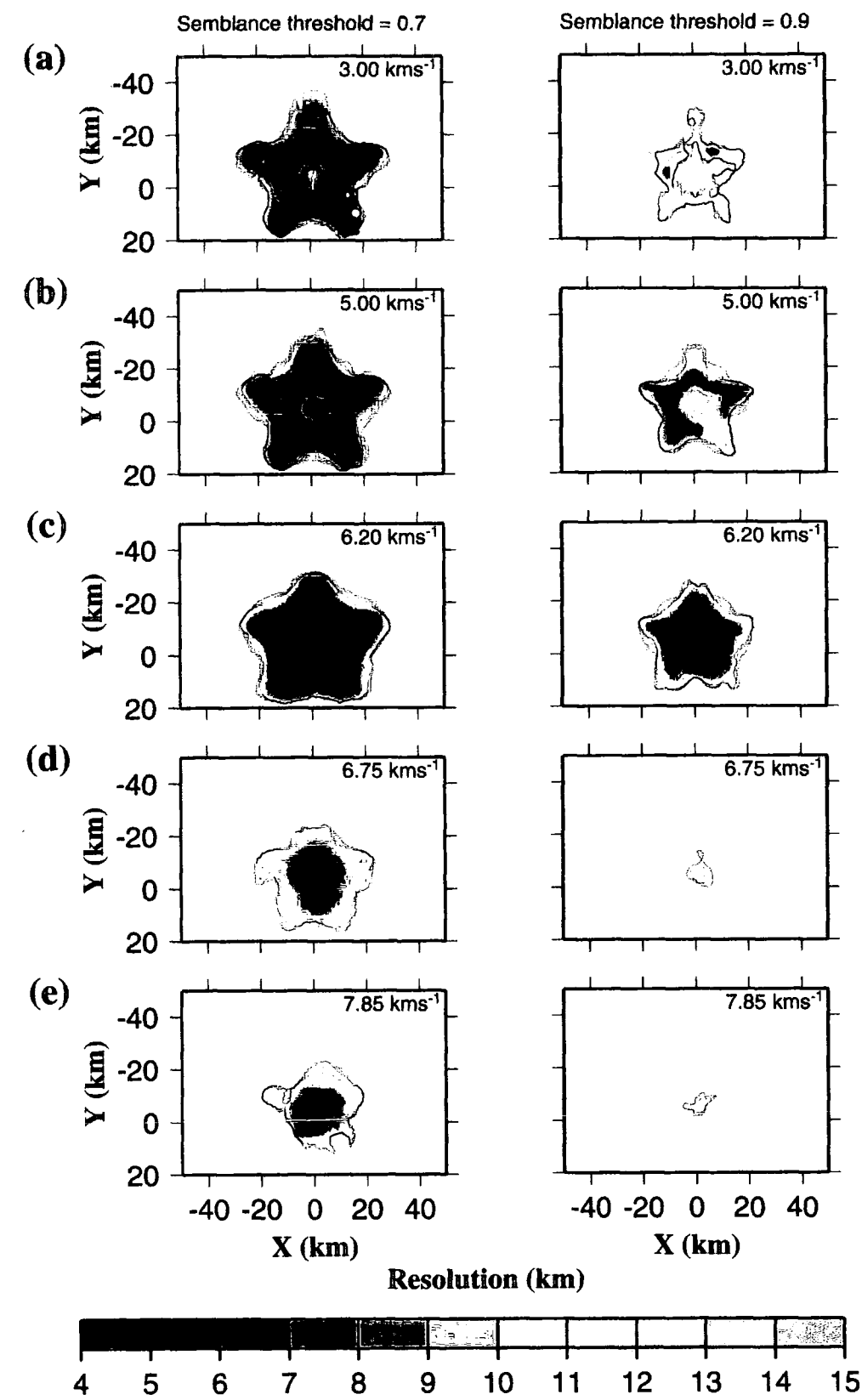


**Figure 5.9:** Resolution for the *Star* geometry shown in Fig. 5.4d. Comparison with Fig. 5.7 shows that the *Star* geometry provides more even resolution than the *Small grid* geometry at shallow-crustal levels even though the two geometries use similar numbers of OBSs and shots. The resolution at lower-crustal and uppermost-mantle depths is comparable for the two geometries, although the *Star* geometry ray coverage encompasses a smaller region.

The final geometry considered is a combination of the *Star* geometry with a number of axis-perpendicular and axis-parallel OBS deployments and shot lines. This *Combined star and grid* geometry and the resulting resolution are shown in Figs. 5.4e and 5.10 respectively. Comparison with the resolution for the *Large grid* geometry (Fig. 5.8), which requires the same number of OBSs but significantly fewer shots, reveals that the coverage and resolution for the two geometries is similar. However, resolution is much more consistent in layer 2A and 2B/C for the *Combined star and grid* geometry. Therefore, if sufficient resources are available, a geometry such as this, which provides good azimuthal coverage at all structural levels, is desirable. A further useful feature of the *Combined star and grid* geometry is that, as for the grid geometries, a number of axis-parallel and perpendicular 2-D profiles may be extracted from the whole dataset and interpreted to create a well constrained initial model for subsequent 3-D inversion.

Although this analysis has concentrated on 3-D data acquisition at mid-ocean ridges, using the VFR as an example, the general conclusions apply in many locations. In particular it is desirable to design experiments which allow adequate resolution at all structural levels down to the primary target depth since inadequate recovery of velocity heterogeneities at these shallower levels may influence the anomalies recovered at the target depth. To this end shot and receiver spacing and geometry should be designed to allow suitable azimuthal coverage at all levels. It is also desirable that subsets of the data can be interpreted in 1-D and 2-D in order to obtain a well constrained initial model for the 3-D inversion, and that any such 2-D profiles should ideally be appropriately oriented relative to any known structural features (parallel and perpendicular to the ridge crest in this example).

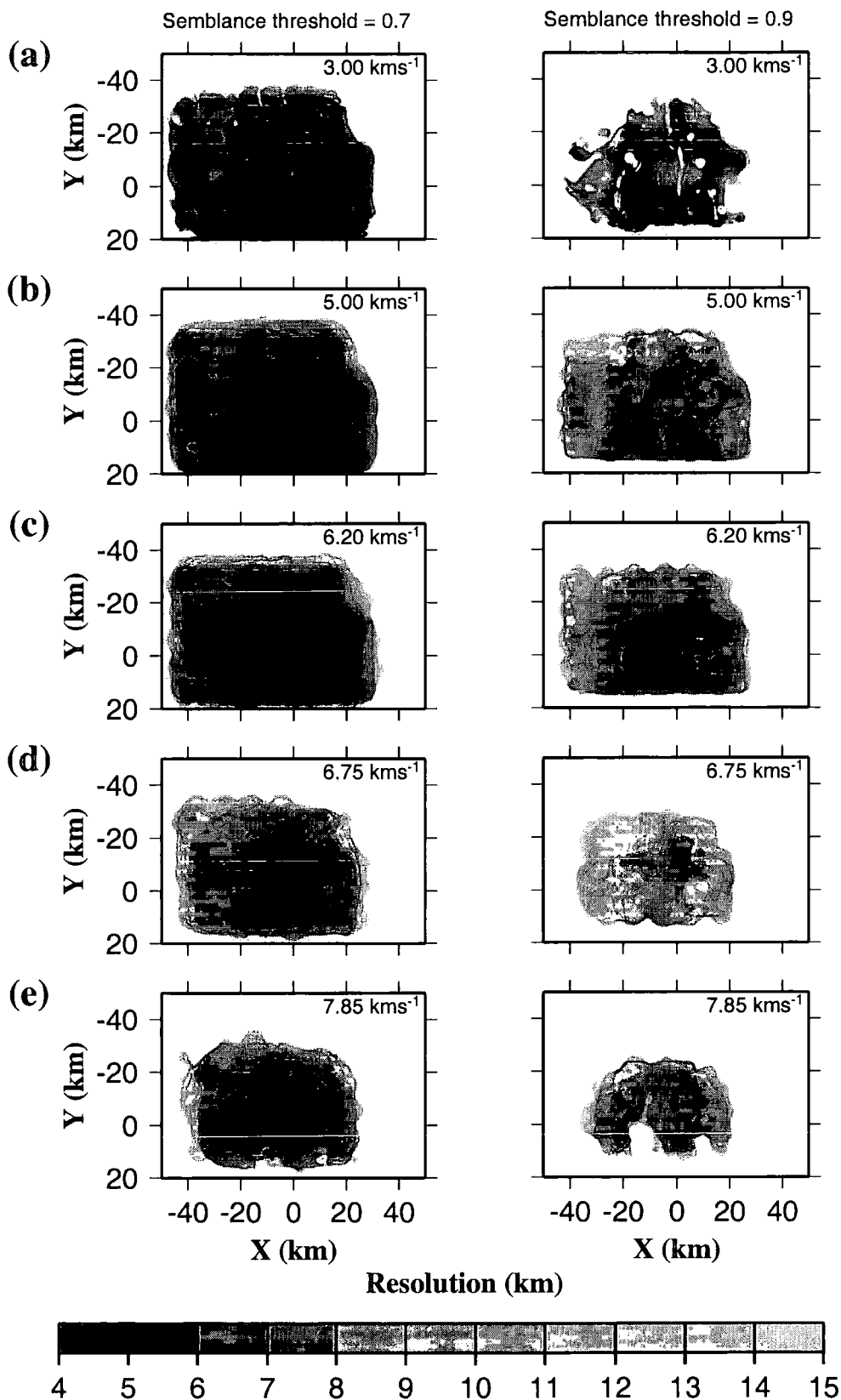


**Figure 5.10:** Resolution for the *Combined star and grid* geometry shown in Fig. 5.4e. The combination of star and grid components provides the best resolution of all the geometries tested at all depths.

### 5.5.3 Suggested modifications to the inversion method

The tomographic inversion method used in this study only deals with first arrivals because the forward modelling method employed only predicts first arrival travel times and ray paths. This method was adequate for this study, which was targeted towards resolving the structure at mid-crustal depths. However, for studies with a deeper target, problems may arise due to a lack of refracted first arrivals turning in the lower crust. This problem is illustrated in Fig. 5.11, which shows the predicted first arrival ray paths through the *basic 1-D initial model* with a velocity contrast at the Moho included. This figure shows that for shot-receiver offsets slightly less than those at which the refracted first arrival turns just beneath the Moho, the crustal first arrival turns at mid-crustal depths. Although mantle first arrivals sample the deep crust, the ray paths through the deep crust are steep and as such few will cross. This ray geometry leads to generally poor resolution in the lower crust compared to the shallow crust and uppermost mantle, as demonstrated by the synthetic resolution tests described in the previous section.

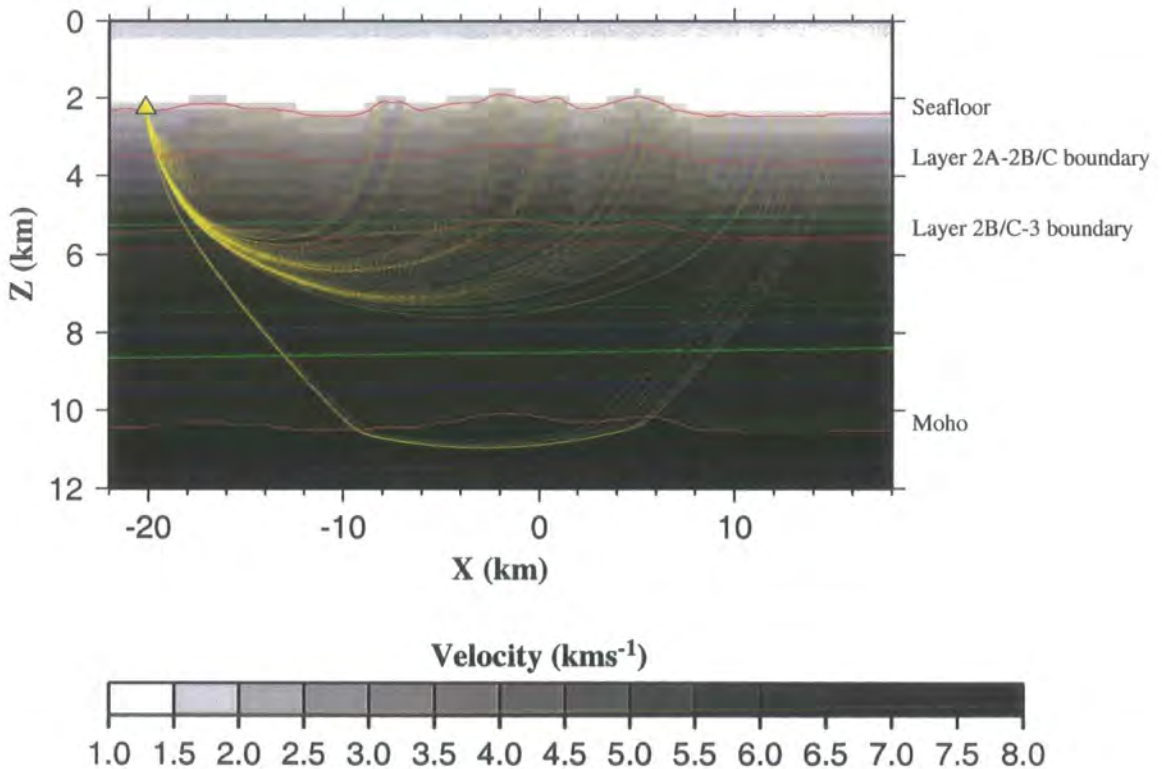


**Figure 5.11:** Cross-section at  $y = -17$  km through the *basic 1-D initial model* with a velocity discontinuity at the Moho included showing the principal layer boundaries in red. Vertical exaggeration  $\times 2$ . The crustal part of the predicted ray paths for shots recorded by NDOBS5 (yellow triangle) close to  $y = -17$  km have been projected onto this plane and plotted in yellow. These shots do not lie exactly at  $y = -17$  km, hence the seafloor ray entry points do not precisely coincide with the marked seafloor interface. Note that some rays are predicted to travel beneath the Moho and that the ray paths for these arrivals are very different from those crustal diving rays at slightly shorter shot-receiver offsets. Hence it is important that mantle diving rays are correctly identified and the Moho geometry accurately known in order to predict ray paths accurately.

In addition, the ambiguity between Moho depth and lower-crustal velocity structure will be difficult to resolve. Although the synthetic resolution tests described in the previous section show that good resolution is theoretically possible in the uppermost mantle if a suitable shot-receiver geometry is employed, these synthetic tests assume that the Moho geometry is known. Hence any ambiguity in Moho depth will limit this resolution in practice. Therefore, a tomographic method which can help to resolve this ambiguity is desirable to improve resolution in the lower crust and uppermost mantle for experiments targeted at these depths.

In the scenario described above, the model resolution in the lowermost crust would be significantly improved if Moho reflections were also included in the inversion. Such arrivals have been widely observed in marine wide-angle seismic datasets, and could provide better constraint on Moho position and also lower-crustal structure since the ray paths will be less steep. Therefore, there will be more crossing ray paths provided the shot-receiver geometry allows good azimuthal coverage. Hole & Zelt (1995) describe a method for determining travel times and ray paths for arrivals which have undergone reflection at an irregular 3-D interface. This method involves calculating first arrival times from the source to the reflecting interface using the process described in section 2.2.2, and replacing the travel times to nodes lying immediately above the reflector with reflected travel times based on Snell's law assuming a locally planar wavefront and reflecting interface. A reverse propagation, as described in section 2.2.2, is then performed from the base of the model using these travel times (see Hole & Zelt (1995) for a full discussion). This method would allow Moho reflections to be included in the inversion if the position of the Moho were defined by the user. Modelling 2-D subsets of the data which include Moho reflections could be used to provide an initial estimate of the 3-D Moho geometry for this purpose. Although this technique would not resolve the ambiguity between Moho position and overlying velocity structure, it would provide significantly better constraint than inversion using first arrivals alone.

Hole & Zelt (1995) also stated that a similar method could be employed to model refracted arrivals which pass below a sharp velocity discontinuity by determining travel times below the interface based on Snell's law. In general this process is unnecessary because the forward modelling method calculates refracted first arrival times and ray paths in the presence of velocity discontinuities with sufficient accuracy.

However, the ray paths in Fig. 5.11 show an abrupt change from crustal to mantle diving rays which follow significantly different ray paths. Since the tomographic inversion method assumes that the predicted ray path through the initial model is a close approximation to the true ray path, it is important that arrivals are correctly identified as crustal or mantle diving rays and predicted ray paths calculated accordingly otherwise this assumption will be violated. Therefore, if the nature of the arrival can be identified from the record section, the ability to constrain its ray path to pass above or below the Moho would improve the accuracy of the inversion. This aim could be achieved using a modified form of the method of Hole & Zelt (1995).

The ability to deal explicitly with refraction at rough 3-D interfaces could be applied to other interfaces apart from the Moho. The roughest and best defined interface in a marine geophysical experiment is likely to be the seafloor. The method outlined above would potentially provide a more rigorous treatment of the behaviour of ray paths at a rough seafloor by ensuring that ray paths obey Snell's law. This treatment would also allow amplitude losses due to transmission at the seafloor and any other first-order interfaces encountered by the ray path to be calculated using Zoeppritz's equations, which would assist in the development of the method for determining the 3-D attenuation structure of the crust outlined in section 5.5.1. Finally, the method could also be modified to predict the travel times and ray paths for  $P$ - $S$  mode converted arrivals by explicitly including the layer 2A-2B/C boundary as the converting interface. These modifications would allow a fully 3-D approach to forward modelling of  $P$ - $S$  mode converted arrival travel times which would allow lateral velocity heterogeneity and the 3-D nature of the seafloor and converting interface to be modelled more rigorously.

A further complication in the mid-ocean ridge environment is the possible presence of diffracted arrivals associated with the axial melt lens as described by Wilcock *et al.* (1993). If such diffracted arrivals, which have travelled above and below the melt lens, are present in a dataset, problems may arise if these arrivals are misidentified as refracted arrivals as this will lead to the possibility that the associated ray path will be misidentified in violation of one of the key assumptions on which the inversion relies. It has been shown in section 3.5 that there is no evidence of diffracted arrivals in the dataset considered in this study, and that the inversion method adopted



is therefore appropriate. However, Wilcock *et al.* (1993) clearly demonstrate that diffractions from the edge of a melt lens can occur in the mid-ocean ridge environment, and hence wherever such arrivals occur, a tomographic method which can accommodate their existence would be advantageous.

The forward modelling method of Vidale (1990), as modified by Hole & Zelt (1995), deals with sharp velocity contrasts and calculates the first arrival time and ray path whether it be a refracted or diffracted arrival. However, as in the case of mantle diving rays described above, a forward modelling method which explicitly deals with diffracted arrivals would be advantageous if these phases can be confidently identified. Diffracted arrivals arising from a discrete diffracting point could be included in the forward modelling method by appealing to Huygen's principle and treating the diffracting point as an extra source. The diffracted ray path for a given source-receiver pair would then comprise the predicted ray path from the source to the diffracting point followed by the predicted ray path from the diffracting point to the receiver. Diffracted arrivals from the edge of a melt lens could be treated by first calculating the travel times from the source to the edge of the melt lens. The diffracted arrival travel times and ray paths could then be determined using a similar method to that employed by Hole & Zelt (1995) for calculating reflected travel times and ray paths except using the travel times to the edge of the melt lens as a linear source rather than using a planar source as in the case of the reflected travel time calculation described above. Arrivals which have diffracted above and below the melt lens could be distinguished by constraining the take-off angle for rays travelling from the melt lens edge to the receiver to lie above or below the horizontal respectively. In this way, diffracted arrivals which have travelled above and below the melt lens, and which can be identified as such, could be included in the inversion.

#### 5.5.4 Future experiments

The VFR represents a good example of a relatively young mid-ocean ridge system. Similar multidisciplinary geophysical surveys to those undertaken during cruise EW9512 conducted further south would allow the structure associated with the propagating rift tip to be investigated. The proposed seismic survey geometry shown in Fig. 5.12, in conjunction with the data collected during cruises CD34/88 and EW9512, would allow detailed modelling of the crustal structure from beyond the propagating rift tip past the southernmost point of the SVFR to the OSC at the northern end of the CVFR, a distance of some 100 km. Such an experiment would allow a study of the

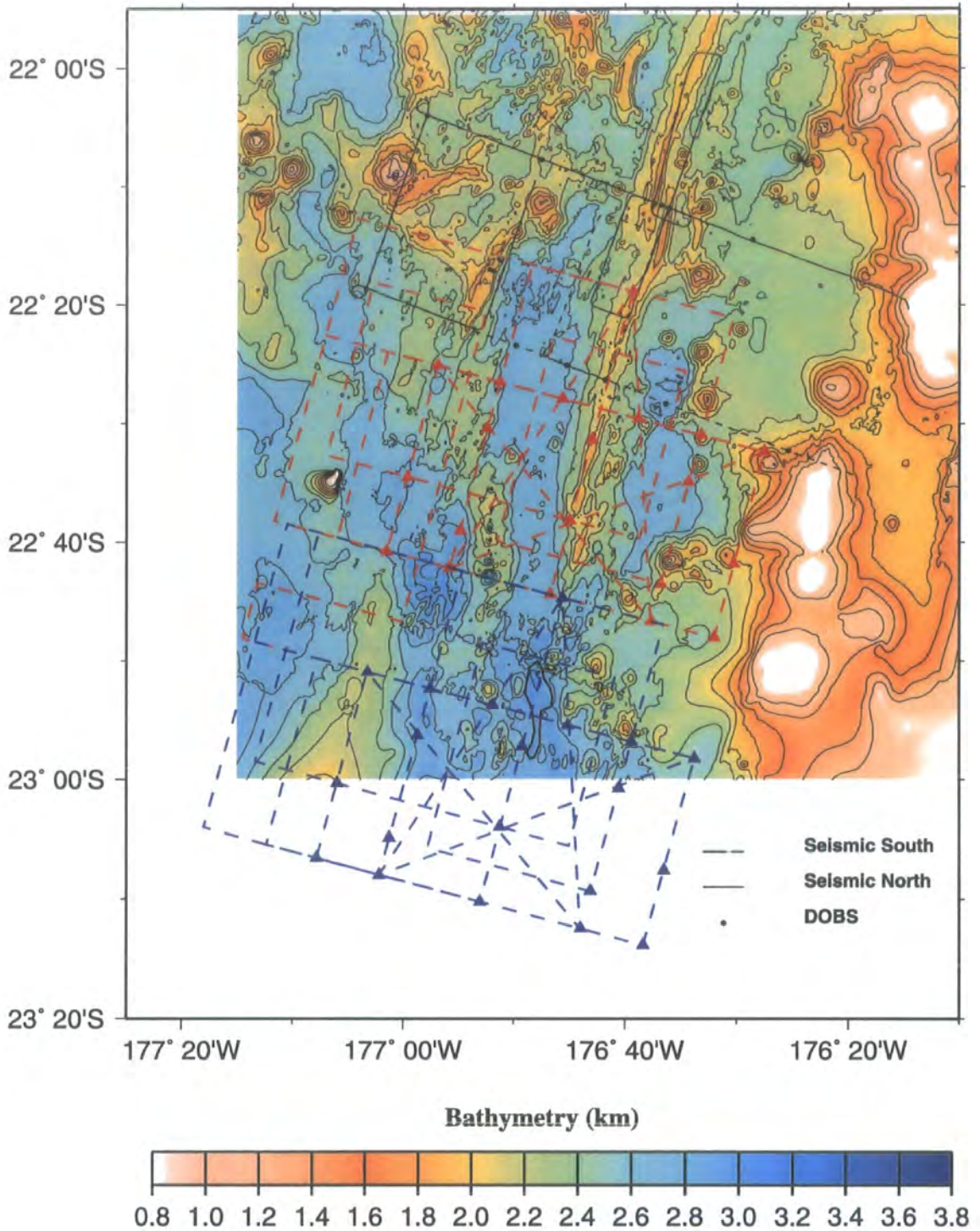


**Figure 5.12:** Bathymetry of the SVFR and CVFR overlain with the proposed experimental configuration for a 3-D seismic tomographic experiment targeted towards resolving the structure of the SVFR and the propagating rift tip (after Peirce, pers. comm.). The acquisition geometry of the seismic component of the EW9512 experiment is shown in black. Two experiments, colour coded in red and blue, are proposed. For each, OBS deployment positions are shown as triangles, and dashed lines represent ship tracks along which airgun and explosive shots would be fired. The *Combined star and grid* acquisition geometry shown for the proposed new experiments would provide superior 3-D coverage to the EW9512 acquisition geometry.

development of the VFR from a propagating rift to a stable system to be undertaken, and structures associated with rupture of pre-existing crust may also be investigated. The EW9512 cruise has demonstrated that by collecting a variety of geophysical datasets, much greater constraint can be placed on the crustal structure than is possible using a single dataset in isolation. Therefore gravity, magnetic and electromagnetic data should also be acquired and interpreted in conjunction with the seismic model, which provides a framework within which to model the inherently ambiguous potential field datasets. Gravity data can help identify crustal thickness and mantle density variations, magnetic data has been used to study extrusive layer thickness and electromagnetic studies can help to constrain the melt fraction present in the mantle and in any crustal magma chambers. The following discussion will focus on the proposed seismic experiment.

This study has shown that the crustal structure, and hence accretionary processes, at the VFR is three-dimensional, and studies at other locations suggest that this is a general feature of mid-ocean ridges no matter the spreading rate. Therefore future wide-angle seismic experiments should be designed with this in mind. The proposed experimental geometry shown in Fig. 5.12 is the *Combined star and grid* geometry from section 5.5.2. Synthetic resolution tests using this geometry (Fig. 5.10) show that good resolution is predicted at all depths down to the uppermost mantle, thus reducing the problem of inadequate representation of poorly resolved shallow structure influencing the anomalies recovered at the primary target depth which this study encountered. The lower-crustal resolution could be further improved by adapting the inversion method to include Moho reflections as described in section 5.5.3. However, the acquisition geometry also allows 2-D subsets to be extracted. By modelling the data in 1-D and 2-D before attempting to model the whole 3-D dataset, a well constrained initial model may be created which is desirable for achieving reliable and stable inversions. The good azimuthal coverage of this acquisition geometry would allow any upper-crustal and uppermost-mantle anisotropy to be identified. Upper-crustal anisotropy is suggested by the tomographic inversions performed in this study and by the behaviour of *P-S* mode converted arrivals. If significant anisotropy is observed, an alternative tomographic inversion scheme which explicitly accommodates anisotropy,

unlike that employed in this study, may be required. It would be advantageous to use a number of explosive shots in addition to an airgun source in order to generate larger amplitude arrivals particularly those which turn in the mantle. Explosive shots would also enhance the amplitude of any  $P$ - $S$  mode converted arrivals. This study has shown that these arrivals can provide useful information about the crustal structure when considered alongside the  $P$ -wave velocity structure. Therefore, as many of the receivers as possible should be fitted with three-component geophone packages in addition to a simple hydrophone in order to allow  $S$ -wave arrivals to be identified and modelled.

In order to use the wide-angle seismic data to its best advantage, it would be useful to conduct a seismic reflection experiment in the axial region. Although the VFR crust is generally unreflective, the seismic reflection technique is useful for identifying the presence of an axial melt lens and constraining its dimensions. Therefore a separate reflection experiment targeted solely on the ridge axis should ideally be performed, although if time and resources preclude such an experiment, contemporaneous acquisition of normal-incidence and wide-angle seismic data as undertaken during EW9512 would provide useful data. Reflection data would allow the position of the melt lens to be mapped which would in turn allow possible problems arising from diffraction at its edges to be identified and modelled should diffracted arrivals be observed in the wide-angle dataset. The along-axis characteristics of the melt lens would also provide a further, independent measure of the along-axis variation in magma supply at the present time.

## 5.6 Conclusions

The EW9512 seismic experiment was primarily designed to allow 2-D modelling of the crustal structure at the VFR whilst providing 3-D coverage in the axial region. Modelling of this 3-D subset of the data using a tomographic technique has been described in this dissertation and has built on earlier 2-D modelling by providing constraint on along-axis variations in structure which are not available from isolated 2-D models. This structure has been interpreted in terms of along-axis and temporal variations in magmatic budget which may be related to ridge crest morphology. By considering secondary  $P$ - $S$  mode converted arrivals, it has been possible to interpret layer 2 structure in geological terms, which is not possible using the  $P$ -wave velocity structure alone, and thus provides constraint on the mode of accretion of layer 2.

Therefore, this study has provided constraint on crustal accretionary processes at the VFR operating on a variety of length and time scales which contribute to the body of knowledge of similar processes at other mid-ocean ridges. These results have clearly shown that 3-D data interpretation provides very much more constraint on these processes than is possible from 2-D studies. It would be advantageous to design future seismic experiments at mid-ocean ridges with 3-D data acquisition in mind, and suggested improvements to the acquisition geometry and inversion method employed in this study have been outlined.

# References

- Au, D. & Clowes, R.M., 1984. Shear-wave velocity structure of the oceanic lithosphere from ocean bottom seismometer studies, *Geophys. J. R. astr. Soc.*, **77**, 105–123.
- Babcock, J.M., Harding, A.J., Kent, G.M. & Orcutt, J.A., 1998. An examination of along-axis variation of magma chamber width and crustal structure on the East Pacific Rise between 13° 30' N and 12° 20' N, *J. geophys. Res.*, **103**, 30 451–30 467.
- Barclay, A.H., Toomey, D.R. & Solomon, S.C., 1998. Seismic structure and crustal magmatism at the Mid-Atlantic Ridge, 35° N, *J. geophys. Res.*, **103**, 17 827–17 844.
- Barry, K.M., Cavers, D.A. & Kneale, C.W., 1975. Recommended standards for digital tape formats, *Geophysics*, **40**, 344–352.
- Barth, G.A. & Mutter, J.C., 1996. Variability in oceanic crustal thickness and structure: Multichannel seismic reflection results from the northern East Pacific Rise, *J. geophys. Res.*, **101**, 17 951–17 975.
- Bazin, S., Harding, A.J., Kent, G.M., Orcutt, J.A., Tong, C.H., Gee, J.S., Pye, J.W., Singh, S.C., Barton, P.J., Sinha, M.C., White, R.S., Hobbs, R.W. & Van Avendonk, H.J.A., 2001. 3-D shallow crustal emplacement at the 9° 03' N overlapping spreading center on the East Pacific Rise – I: correlations between magnetization and seismics, *J. geophys. Res.*, submitted.
- Bazin, S., Van Avendonk, H., Harding, A.J., Orcutt, J.A., Canales, J.P., Detrick, R.S. & MELT group, 1998. Crustal structure of the flanks of the East Pacific Rise: Implications for overlapping spreading centers, *Geophys. Res. Lett.*, **25**, 2213–2216.
- Begnaud, M.L., McClain, J.S., Barth, G.A., Orcutt, J.A. & Harding, A.J., 1997. Velocity structure from forward modeling of the eastern ridge-transform intersection area of the Clipperton Fracture Zone, East Pacific Rise, *J. geophys. Res.*, **102**, 7803–7820.
- Berge, P.A., Fryer, G.J. & Wilkens, R.H., 1992. Velocity–porosity relationships in the upper oceanic crust: Theoretical considerations, *J. geophys. Res.*, **97**, 15 239–15 254.
- Bevis, M., Taylor, F.W., Schutz, B.E., Recy, J., Isacks, B.L., Helu, S., Singh, R., Kendrick, E., Stowell, J., Taylor, B. & Calmant, S., 1995. Geodetic observations of very rapid convergence and back-arc extension at the Tonga arc, *Nature*, **374**, 249–251.
- Bratt, S.R. & Purdy, G.M., 1984. Structure and variability of oceanic crust on the flanks of the East Pacific Rise between 11° and 13° N, *J. geophys. Res.*, **89**, 6111–6125.
- Bratt, S.R. & Solomon, S.C., 1984. Compressional and shear wave structure of the East Pacific Rise at 11° 20' N: Constraints from three-component ocean bottom seismometer data, *J. geophys. Res.*, **89**, 6095–6110.
- Brown, G.C. & Musset, A.E., 1981. *The inaccessible earth*, George Allen and Unwin Ltd.

- Calvert, S.E.E., 1996. Southern Valu Fa Ridge, the Lau Basin: a gravity and bathymetric investigation, *MSc thesis*, University of Durham.
- Cann, J.R., 1974. A model for oceanic crustal structure developed, *Geophys. J. R. astr. Soc.*, **39**, 169–187.
- Carbotte, S., Mutter, C., Mutter, J. & Ponce-Correa, G., 1998. Influence of magma supply and spreading rate on crustal magma bodies and emplacement of the extrusive layer: Insights from the East Pacific Rise at 16° N, *Geology*, **26**, 455–458.
- Carbotte, S., Welch, S.M. & Macdonald, K.C., 1991. Spreading rates, rift propagation, and fracture-zone offset histories during the past 5 My on the Mid-Atlantic Ridge – 25°–27° 30' S and 31° –34° 30' S, *Mar. geophys. Res.*, **13**, 51–80.
- Caress, D.W., Burnett, M.S. & Orcutt, J.A., 1992. Tomographic image of the axial low-velocity zone at 12° 50' N on the East Pacific Rise, *J. geophys. Res.*, **97**, 9243–9263.
- Christensen, N.I., 1979. Compressional wave velocities in rocks at high temperatures and pressures, critical thermal gradients, and crustal low-velocity zones, *J. geophys. Res.*, **84**, 6849–6857.
- Christensen, N.I., 1996. Poisson's ratio and crustal seismology, *J. geophys. Res.*, **101**, 3139–3156.
- Christeson, G.L., Kent, G.M., Purdy, G.M. & Detrick, R.S., 1996. Extrusive thickness variability at the East Pacific Rise, 9° –10° N: constraints from seismic techniques, *J. geophys. Res.*, **101**, 2859–2873.
- Christeson, G.L., Purdy, G.M. & Fryer, G.J., 1992. Structure of young upper crust at the East Pacific Rise near 9° 30' N, *Geophys. Res. Lett.*, **19**, 1045–1048.
- Christeson, G.L., Purdy, G.M. & Rohr, K.M.M., 1993. Structure of the Northern Symmetrical Segment of the Juan de Fuca Ridge, *Mar. geophys. Res.*, **15**, 219–240.
- Christeson, G.L., Shaw, P.R. & Garmany, J.D., 1997. Shear and compressional wave structure of the East Pacific Rise, 9° – 10° N, *J. geophys. Res.*, **102**, 7821–7835.
- Collier, J.S., 1990. Seismic imaging of magma chambers and mud diapirs, *PhD thesis*, University of Cambridge.
- Collier, J.S. & Singh, S.C., 1997. Detailed structure of the top of the melt body beneath the East Pacific Rise at 9° 40' N from waveform inversion of seismic reflection data, *J. geophys. Res.*, **102**, 20 287–20 304.
- Collier, J.S. & Singh, S.C., 1998. Poisson's ratio structure of young oceanic crust, *J. geophys. Res.*, **103**, 20 981–20 996.
- Collier, J.S. & Sinha, M.C., 1990. Seismic images of a magma chamber beneath the Lau Basin back-arc spreading centre, *Nature*, **346**, 646–648.
- Collier, J.S. & Sinha, M.C., 1992a. Seismic mapping of a magma chamber beneath the Valu Fa Ridge, Lau Basin, *J. geophys. Res.*, **97**, 14 031–14 053.



- Collier, J.S. & Sinha, M.C., 1992b. The Valu Fa Ridge: The pattern of volcanic activity at a back-arc spreading centre, *Mar. Geol.*, **104**, 243–263.
- Cormier, M.-H., Macdonald, K.C. & Wilson, D.S., 1995. A three-dimensional gravity analysis of the East Pacific Rise from 18° to 21°30' S, *J. geophys. Res.*, **100**, 8063–8082.
- Cormier, M.-H., Scheirer, D.S. & Macdonald, K.C., 1996. Evolution of the East Pacific Rise at 16° – 19°S since 5 Ma: Bisection of overlapping spreading centers by new, rapidly propagating ridge segments, *Mar. geophys. Res.*, **18**, 53–84.
- Crampin, S., 1977. A review of the effects of anisotropic layering on the propagation of seismic waves, *Geophys. J. R. astr. Soc.*, **49**, 9–27.
- Crampin, S., 1984. Effective anisotropic elastic constants for wave propagation through cracked solids, *Geophys. J. R. astr. Soc.*, **76**, 135–145.
- Cudrak, C.F. & Clowes, R.M., 1993. Crustal structure of Endeavour Ridge Segment, Juan de Fuca Ridge, from a detailed seismic refraction survey, *J. geophys. Res.*, **98**, 6329–6349.
- Day, A.J., 1997. Seismic reflection imaging and modelling of the melt lens beneath the Valu Fa Ridge, *MSc thesis*, University of Durham.
- Detrick, R.S., Buhl, P., Vera, E.E., Mutter, J.A., Orcutt, J.A., Madsen, J. & Brocher, T., 1987. Multichannel seismic imaging of a crustal magma chamber along the East Pacific Rise, *Nature*, **326**, 35–41.
- Detrick, R., Collins, J., Stephen, R. & Swift, S., 1994. In situ evidence for the nature of the seismic layer 2/3 boundary in oceanic crust, *Nature*, **370**, 288–290.
- Detrick, R.S., Harding, A.J., Kent, G.M., Orcutt, J.A., Mutter, J.C. & Buhl, P., 1993. Seismic structure of the southern East Pacific Rise, *Science*, **259**, 499–503.
- Detrick, R.S., Needham, H.D. & Renard, V., 1995. Gravity-anomalies and crustal thickness variations along the Mid-Atlantic Ridge between 33° N and 40° N, *J. geophys. Res.*, **100**, 3767–3787.
- Detrick, R.S., Toomey, D.R. & Collins, J.A., 1998. Three-dimensional upper crustal heterogeneity and anisotropy around hole 504B from seismic tomography, *J. geophys. Res.*, **103**, 30 485–30 504.
- Dunn, R.A. & Toomey, D.R., 1997. Seismological evidence for 3-D melt migration beneath the East Pacific Rise, *Nature*, **388**, 259–262.
- Fouquet, Y., von Stackelberg, U., Charlou, J.L., Donval, J.P., Foucher, J.P., Erzinger, J., Herzig, P., Mühe, R., Wiedicke, M., Soakai, S. & Whitechurch, H., 1991. Hydrothermal activity in the Lau back-arc basin: Sulphides and water chemistry, *Geology*, **19**, 303–306.
- Fouquet, Y., von Stackelberg, U., Charlou, J.L., Erzinger, J., Mühe, R. & Wiedicke, M., 1993. Metallogenesis in back-arc environments: The Lau Basin example, *Ec. Geol.*, **88**, 2154–2181.
- Fox, P.J., Grindlay, N.R. & Macdonald, K.C., 1991. The Mid-Atlantic Ridge (31° S – 34° 30' S) – temporal and spatial variations of accretionary processes, *Mar. geophys. Res.*, **13**, 1–20.

- Frenzel, G., Mühe, R. & Stoffers, P., 1990. Petrology of the volcanic rocks from the Lau Basin, Southwest Pacific, *Geol. Jahrb., Reihe D*, **72**, 395–479.
- Garbin, H.D. & Knopoff, L., 1975. Elastic moduli of a medium with liquid-filled cracks, *Q. appl. Math.*, **33**, 301–303.
- Grevenmeyer, I., Weigel, W. & Jennrich, C., 1998. Structure and ageing of oceanic crust at 14° S on the East Pacific Rise, *Geophys. J. Int.*, **135**, 573–584.
- Harding, A.J., Kent, G.M. & Orcutt, J.A., 1993. A multichannel seismic investigation of upper crustal structure at 9° N on the East Pacific Rise: implications for crustal accretion, *J. geophys. Res.*, **98**, 13 925–13 944.
- Harding, A.J., Orcutt, J.A., Kappus, M.E., Vera, E.E., Mutter, J.C., Buhl, P., Detrick, R.S. & Brocher, T.M., 1989. Structure of young oceanic crust at 13° N on the East Pacific Rise from expanding spread profiles, *J. geophys. Res.*, **94**, 12 163–12 196.
- Hearn, T.M. & Ni, J.F., 1994.  $P_n$  velocities beneath continental collision zones: The Turkish–Iranian Plateau, *Geophys. J. Int.*, **117**, 273–283.
- Herron, T.J., Stoffa, P.L. & Buhl, P., 1980. Magma chamber and mantle reflections – East Pacific Rise, *Geophys. Res. Lett.*, **7**, 989–992.
- Hilton, D.R., Hammerschmidt, K., Loock, G. & Friedrichsen, H., 1993. Helium and argon isotope systematics of the central Lau Basin and Valu Fa Ridge: Evidence of crust / mantle interactions in a back-arc basin, *Geochim. cosmochim. Acta*, **57**, 2819–2841.
- Hole, J.A. & Zelt, B.C., 1995. Three-dimensional finite-difference reflection travel times, *Geophys. J. Int.*, **121**, 427–434.
- Hooft, E.E.E., Detrick, R.S. & Kent, G.M., 1997. Seismic structure and indicators of magma budget along the Southern East Pacific Rise, *J. geophys. Res.*, **102**, 27 319–27 340.
- Hooft, E.E.E., Detrick, R.S., Toomey, D.R., Collins, J.A. & Lin, J., 2000. Crustal thickness and structure along three contrasting spreading segments of the Mid-Atlantic Ridge, 33.5° – 35°, *J. geophys. Res.*, **105**, 8205–8226.
- Hooft, E.E.E., Schouten, H. & Detrick, R.S., 1996. Constraining crustal emplacement processes from the variation in seismic layer 2A thickness at the East Pacific Rise, *Earth Planet. Sci. Lett.*, **142**, 289–309.
- Houtz, R. & Ewing, J., 1976. Upper crustal structure as a function of plate age, *J. geophys. Res.*, **81**, 2490–2498.
- Hudson, J.A., 1980. Overall properties of a cracked solid, *Math. Proc. Camb. phil. Soc.*, **88**, 371–384.
- Hyndman, R.D., 1979. Poisson's ratio in the oceanic crust – a review, *Tectonophysics*, **59**, 321–333.
- Jenner, G.A., Cawood, P.A., Rautenschlein, M. & White, W.M., 1987. Composition of back-arc basin volcanics, Valu Fa Ridge, Lau Basin: Evidence for a slab-derived component in their mantle source, *J. Volc. Geotherm. Res.*, **32**, 209–222.

- Karson, J.A., Hurst, S.D. & Lonsdale, P., 1992. Tectonic rotations of dikes in fast-spread oceanic-crust exposed near Hess Deep, *Geology*, **20**, 685–688.
- Keith, C.M. & Crampin, S., 1977a. Seismic body waves in anisotropic media: reflection and refraction at a plane interface, *Geophys. J. R. astr. Soc.*, **49**, 181–208.
- Keith, C.M. & Crampin, S., 1977b. Seismic body waves in anisotropic media: synthetic seismograms, *Geophys. J. R. astr. Soc.*, **49**, 225–243.
- Kent, G.M., Harding, A.J. & Orcutt, J.A., 1990. Evidence for a smaller magma chamber beneath the East Pacific Rise at 9° 3' N, *Nature*, **344**, 650–653.
- Kent, G.M., Singh, S.C., Harding, A.J., Sinha, M.C., Orcutt, J.A., Barton, P.J., White, R.S., Bazin, S., Hobbs, R.W., Tong, C.H. & Pye, J.W., 2000. Evidence from three-dimensional seismic reflectivity images for enhanced melt supply beneath mid-ocean-ridge discontinuities, *Nature*, **406**, 614–618.
- Kuo, B.-Y. & Forsyth, D.W., 1988. Gravity anomalies of the ridge-transform system in the South Atlantic between 31° and 34.5°S upwelling centres and variations in crustal thickness, *Mar. geophys. Res.*, **10**, 205–232.
- Kuster, G.T. & Toksöz, M.N., 1974. Velocity and attenuation of seismic waves in two phase media, 1, Theoretical formulations, *Geophysics*, **39**, 587–606.
- Lin, J. & Phipps-Morgan, J., 1992. The spreading rate dependence of 3-dimensional midocean ridge gravity structure, *Geophys. Res. Lett.*, **19**, 13–16.
- Lin, J., Purdy, G.M., Schouten, H., Sempéré, J.C. & Zervas, C., 1990. Evidence from gravity data for focused magmatic accretion along the Mid-Atlantic Ridge, *Nature*, **344**, 627–632.
- Macdonald, K.C., 1982. Mid-ocean ridges: Fine scale tectonic, volcanic and hydrothermal processes within the plate boundary zone, *Ann. Rev. Earth planet. Sci.*, **10**, 155–190.
- Macdonald, K.C., Fox, P.J., Miller, S., Carbotte, S., Edwards, M.H., Eisen, M., Fornari, D.J., Perram, L., Pockalny, R., Scheirer, D., Lighe, S., Weiland, C. & Wilson, D., 1992. The East Pacific Rise and its flanks 8° – 18° N: History of segmentation, propagation and spreading direction based on SeaMark II and Sea Beam studies, *Mar. geophys. Res.*, **14**, 299–344.
- Macdonald, K.C., Fox, P.J., Perram, L.J., Eisen, M.F., Hayman, R.M., Miller, S.P., Carbotte, S.M., Cormier, M.-H. & Shor, A.N., 1988. A new view of the mid-ocean ridge from the behaviour of ridge-axis discontinuities, *Nature*, **335**, 217–225.
- Macdonald, K.C., Scheirer, D.S. & Carbotte, S.M., 1991. Mid-ocean ridges: Discontinuities, segments and giant cracks, *Science*, **253**, 986–994.
- MacGregor, L.M., Constable, S. & Sinha, M.C., 1998. The RAMESSES experiment – III. Controlled-source electromagnetic sounding of the Reykjanes Ridge at 57° 45' N, *Geophys. J. Int.*, **135**, 773–789.

- MacGregor, L., Sinha, M. & Constable, S., 2001. Electrical resistivity structure of the Valu Fa Ridge, Lau Basin, from marine controlled source electromagnetic sounding, *Geophys. J. Int.*, submitted.
- Maia, M. & Gente, P., 1998. Three-dimensional gravity and bathymetric analysis of the mid-Atlantic ridge between 20° N and 24° N: Flow geometry and temporal evolution of the segmentation, *J. geophys. Res.*, **103**, 951–974.
- Matthews, P.A., 1993. Crustal structure of the Baltic Shield beneath the Sea of Bothnia: BABEL line 6, *PhD thesis*, University of Durham.
- McDonald, M.A., Webb, S.C., Hildebrand, J.A., Cornuelle, B.D. & Fox, C.G., 1994. Seismic structure and anisotropy of the Juan de Fuca Ridge at 45° N, *J. geophys. Res.*, **99**, 4857–4873.
- Morton, J.L. & Sleep, N.H., 1985. Seismic reflections from a Lau Basin magma chamber, in *Geology and Offshore Resources of Pacific Island Arcs – Tonga Region*, pp. 441–453, eds. Scholl, D.W. & Vallier, T.L., Earth Sci. Ser. 2, Circum-Pacific Council for Energy and Mineral Resource, Houston, TX.
- Murase, T. & McBirney, A.R., 1973. Properties of some common igneous rocks and their melts at high temperatures, *Geol. Soc. Am. Bull.*, **84**, 3563–3592.
- Murton, B.J. & Parson, L.M., 1993. Segmentation, volcanism and deformation of oblique spreading centres: a qualitative study of the Reykjanes Ridge, *Tectonophysics*, **222**, 237–257.
- Mutter, J.C., Carbotte, S.M., Su, W., Xu, L., Buhl, P., Detrick, R.S., Kent, G.M., Orcutt, J.A. & Harding, A.J., 1995. Seismic images of active magma systems beneath the East Pacific Rise between 17° 05' S and 17° 35' S, *Science*, **268**, 391–395.
- Navin, D.A., 1996. Seismic investigation of crustal accretion at the slow-spreading Mid-Atlantic Ridge – The Reykjanes Ridge at 57° 45' N., *PhD thesis*, University of Durham, UK.
- Navin, D.A., Peirce, C. & Sinha, M.C., 1998. The RAMESSES experiment – II. Evidence for accumulated melt beneath a slow spreading ridge from wide-angle refraction and multichannel seismic profiles, *Geophys. J. Int.*, **135**, 746–772.
- Niu, Y.L. & Batiza, R., 1992. Magmatic processes at a slow-spreading ridge segment – 26° S Mid-Atlantic Ridge, *J. geophys. Res.*, **99**, 19 719–19 740.
- Nolet, G., 1987. Seismic wave propagation and seismic tomography, in *Seismic Tomography*, pp. 1–24, ed. Nolet, G., D. Reidel, Norwell, Mass.
- O'Connell, R.J. & Budiansky, B., 1974. Seismic velocities in in dry and saturated cracked solids, *J. geophys. Res.*, **79**, 5412–5426.
- Offer, A.R., 1996. Geophysical investigation of the off axis crustal structure of the Lau Basin (SW Pacific), *MSc thesis*, University of Durham.
- Orcutt, J.A., Kennett, B.L.N., Dorman, L. & Prothero, W., 1975. Evidence for a low velocity zone underlying a fast spreading ridge crest, *Nature*, **256**, 475–476.

- Paige, C.C. & Saunders, M.A., 1982. LSQR: An algorithm for sparse linear equations and sparse least squares, *Assoc. Comput. Mach. Trans. Math. Software*, **8**, 43–71.
- Parson, L.M., Murton, B.J., Searle, R.C., Booth, D., Evans, J., Field, P., Keeton, J., Laughton, A., McAllister, E., Millard, N., Redbourne, L., Rouse, I., Shor, A., Smith, D., Spencer, S., Sumerhayes, C. & Walker, C., 1993. En echelon axial volcanic ridges at the Reykjanes Ridge: a life cycle of volcanism and tectonics, *Earth Planet. Sci. Lett.*, **117**, 73–87.
- Parson, L.M., Pearce, J.A., Murton, B.J., Hodkinson, R.A. & R.R.S. Charles Darwin Scientific Party, 1990. Role of ridge jumps and ridge propagation in the tectonic evolution of the Lau back-arc basin, Southwest Pacific, *Geology*, **18**, 470–473.
- Parson, L.M. & Wright, I.C., 1996. The Lau–Havre–Taupo back-arc basin: a southward-propagating, multi-stage evolution from rifting to spreading, *Tectonophysics*, **263**, 1–22.
- Pearce, J.A., Lippard, S.J. & Roberts, S., 1984. Characteristics and tectonic significance of supra-subduction zone ophiolites, in *Marginal basin geology: Volcanic and associated sedimentary and tectonic processes in modern and ancient marginal basins*, pp. 77–94, eds. Kokelaar, B.P. & Howells, M.F., Spec. Publ. Geol. Soc. Lond. 16, Blackwell Scientific Publications, Oxford.
- Peirce, C., 1990. Crustal structure of the Africa–Eurasia plate boundary, *PhD thesis*, University of Cambridge.
- Peirce, C., Sinha, M.C. & Constable, S., 1996. Controlled source electromagnetic and seismic investigation of the Valu Fa Ridge, Lau Basin, SW Pacific, R/V Maurice Ewing 9512 Cruise Report.
- Peirce, C., Turner, I.M. & Sinha, M.C., 2001. Crustal structure, accretionary processes and rift propagation: a gravity study of the intermediate-spreading Valu Fa Ridge, Lau Basin, *Geophys. J. Int.*, accepted.
- Raitt, R.W., 1963. The crustal rocks, in *The Sea*, 3, pp. 85–102, ed. Hill, M.N., Wiley (Interscience), New York.
- Rohr, K.M.M., Milkereit, B. & Yorath, C.J., 1988. Asymmetric deep crustal structure across the Juan de Fuca Ridge, *Geology*, **16**, 533–537.
- Rushforth, I.M., 1996. A seismic investigation of crustal properties near the Central Valu Fa Ridge, Lau Basin, SW Pacific, *MSc thesis*, University of Durham.
- Sato, H., Sacks, I.S. & Murase, T., 1989. The use of laboratory velocity data for estimating temperature and partial melt fraction in the low-velocity zone: Comparison with heat flow and electrical conductivity studies, *J. geophys. Res.*, **94**, 5689–5704.
- Scheirer, D.S., Forsyth, D.W., Cormier, M.-H. & Macdonald, K.C., 1998. Shipboard geophysical indications of asymmetry and melt production beneath the East Pacific Rise near the MELT experiment, *Science*, **280**, 1221–1224.

- Schouten, H., Tivey, M.A., Fornari, D.J. & Cochran, J.R., 1999. Central anomaly magnetization high: constraints on the volcanic construction and architecture of seismic layer 2A at a fast-spreading mid-ocean ridge, EPR at 9° 30' – 50' N, *Earth Planet. Sci. Lett.*, **169**, 37–50.
- Sempéré, J., Lin, J., Brown, H.S., Schouten, H. & Purdy, G.M., 1993. Segmentation and morphotectonic variations along a slow-spreading centre: The Mid-Atlantic Ridge (24° 00' N – 30° 40' N), *Mar. geophys. Res.*, **15**, 153–200.
- Sempéré, J.C., Purdy, G.M. & Schouten, H., 1990. Segmentation of the Mid-Atlantic Ridge between 24° N and 30° 40' N, *Nature*, **344**, 427–431.
- Shaw, P.R., 1994. Age variations of oceanic crust Poisson's ratio: Inversion and a porosity evolution model, *J. geophys. Res.*, **99**, 3057–3066.
- Shearer, P.M., 1988. Cracked media, Poisson's ratio and the structure of the upper oceanic crust, *Geophysical Journal*, **92**, 357–362.
- Shearer, P. & Orcutt, J., 1985. Anisotropy in the oceanic lithosphere – theory and observations from the Ngendei seismic refraction experiment in the south-west Pacific, *Geophys. J. R. astr. Soc.*, **80**, 493–526.
- Shearer, P.M. & Orcutt, J.A., 1986. Compressional and shear wave anisotropy in the oceanic lithosphere – the Ngendei seismic refraction experiment, *Geophys. J. R. astr. Soc.*, **87**, 967–1003.
- Sheriff, R.E. & Geldart, L.P., 1995. *Exploration Seismology*, 2nd edn., Cambridge University Press.
- Shiobara, H., Nakanishi, A., Shimamura, H., Mjelde, R., Kanazawa, T. & Berg, E.W., 1997. Precise positioning of ocean bottom seismometer by using acoustic transponder and CTD, *Mar. geophys. Res.*, **19**, 199–209.
- Singh, S.C., Kent, G.M., Collier, J.S., Harding, A.J. & Orcutt, J.A., 1998. Melt to mush variations in crustal magma properties at the southern East Pacific Rise, *Nature*, **394**, 874–878.
- Sinha, M.C., 1995. Segmentation and rift propagation at the Valu Fa Ridge, Lau Basin: Evidence from gravity data, *J. geophys. Res.*, **100**, 15 025–15 043.
- Sinha, M.C., Constable, S.C., Peirce, C., White, A., Heinson, G., MacGregor, L.M. & Navin, D.A., 1998. Magmatic processes at slow spreading ridges: implications of the RAMESSES experiment at 57° 45' N on the Mid-Atlantic Ridge, *Geophys. J. Int.*, **135**, 731–745.
- Sinton, J.M. & Detrick, R.S., 1992. Mid-ocean ridge magma chambers, *J. geophys. Res.*, **97**, 197–216.
- Sohn, R.A., Webb, S.C., Hildebrand, J.A. & Cornuelle, B.D., 1997. Three-dimensional tomographic velocity structure of upper crust, CoAxial segment, Juan de Fuca Ridge: Implications for on-axis evolution and hydrothermal circulation, *J. geophys. Res.*, **102**, 17 679–17 695.
- Spetzler, H. & Anderson, D.L., 1968. The effect of temperature and partial melting on velocity and attenuation in a simple binary system, *J. geophys. Res.*, **73**, 6051–6060.

- Spudich, P. & Orcutt, J.A., 1980a. A new look at the seismic velocity structure of the oceanic crust, *Rev. Geophys. Space Phys.*, **18**, 627–645.
- Spudich, P. & Orcutt, J., 1980b. Petrology and porosity of an oceanic crustal site: Results from wave form modeling of seismic refraction data, *J. geophys. Res.*, **85**, 1409–1433.
- Stocker, R.L. & Gordon, R.B., 1975. Velocity and internal friction in partial melts, *J. geophys. Res.*, **80**, 4828–4836.
- Taylor, B., Zellmer, K., Martinez, F. & Goodliffe, A., 1996. Sea-floor spreading in the Lau back-arc basin, *Earth Planet. Sci. Lett.*, **144**, 35–40.
- Tolstoy, M., Harding, A.J. & Orcutt, J.A., 1993. Crustal thickness on the Mid-Atlantic Ridge: Bull's-eye gravity anomalies and focused accretion, *Science*, **263**, 726–729.
- Toomey, D.R., Purdy, G.M., Solomon, S.C. & Wilcock, W.S., 1990. The three-dimensional seismic velocity structure of the East Pacific Rise near latitude 9° 30' N, *Nature*, **347**, 639–645.
- Toomey, D.R., Solomon, S.C. & Purdy, G.M., 1994. Tomographic imaging of the shallow crustal structure of the East Pacific Rise at 9° 30' N, *J. geophys. Res.*, **99**, 24 135–24 157.
- Tucholke, B.E., Lin, J., Kleinrock, M.C., Tivey, M.A., Reed, T.B., Goff, J. & Jaroslow, G.E., 1997. Segmentation and crustal structure of the western Mid-Atlantic Ridge flank, 25° 25' – 27° 10' N and 0–29 m.y., *J. geophys. Res.*, **102**, 10 203–10 223.
- Turner, I.M., 1998. Crustal accretionary processes at mid-ocean ridges – Valu Fa Ridge, Lau Basin, *PhD thesis*, University of Durham, UK.
- Turner, I.M., Peirce, C. & Sinha, M.C., 1999. Seismic imaging of the axial region of the Valu Fa Ridge, Lau Basin – the accretionary processes of an intermediate back-arc spreading ridge, *Geophys. J. Int.*, **138**, 495–519.
- Vallier, T.L., Jenner, G.A., Frey, F.A., Gill, J.B., Davis, A.S., Volpe, A.M., Hawkins, J.W., Morris, J.D., Cawood, P.A., Morton, J.L., Scholl, D.W., Rautenschlein, M., White, W.M., Williams, R.W., Stevenson, A.J. & White, L.D., 1991. Subalkaline andesite from Valu Fa Ridge, a back-arc spreading center in southern Lau Basin: petrogenesis, comparative chemistry, and tectonic implications, *Chem. Geol.*, **91**, 227–256.
- Van Avendonk, H.J.A., Harding, A.J., Orcutt, J.A. & McClain, J.S., 1998. A two-dimensional tomographic study of the Clipperton transform fault, *J. geophys. Res.*, **103**, 17 885–17 899.
- Vera, E.E. & Diebold, J.B., 1994. Seismic imaging of oceanic layer 2A between 9° 30' N and 10° N on the East Pacific Rise from two-ship wide-aperture profiles, *J. geophys. Res.*, **99**, 3031–3041.
- Vera, E.E., Mutter, J.C., Buhl, P., Orcutt, J.A., Harding, A.J., Kappus, M.E., Detrick, R.S. & Brocher, T.M., 1990. The structure of 0– to 0.2-m.y.-old oceanic crust at 9° N on the East Pacific Rise from expanded spread profiles, *J. geophys. Res.*, **95**, 15 529–15 556.
- Vidale, J.E., 1988. Finite-difference calculation of travel times, *Bull. Seismol. Soc. Am.*, **78**, 2062–2076.



- Vidale, J.E., 1990. Finite-difference calculation of travel times in three dimensions, *Geophysics*, **55**, 521–526.
- Von Stackelberg, U. & the Shipboard Scientific Party, 1988. Active hydrothermalism in the Lau back-arc basin (SW Pacific): First results from the SONNE 48 Cruise, *Mar. Min.*, **7**, 431–442.
- Walsh, J.B., 1969. New analysis of attenuation in partially melted rock, *J. geophys. Res.*, **74**, 4333–4337.
- Wang, X. & Cochran, J.R., 1993. Gravity anomalies, isostasy, and mantle flow at the East Pacific Rise crest, *J. geophys. Res.*, **98**, 19 505–19 531.
- Wang, X., Cochran, J.R. & Barth, G.A., 1996. Gravity anomalies, crustal thickness, and the pattern of mantle flow at the fast spreading East Pacific Rise, 9°–10°N: Evidence for three-dimensional upwelling, *J. geophys. Res.*, **101**, 17 927–17 940.
- Watt, J.P., Davies, G.F. & O'Connell, R.J., 1976. The elastic properties of composite materials, *Rev. Geophys. Space Phys.*, **14**, 541–563.
- Weiland, C.M. & Macdonald, K.C., 1996. Geophysical study of the East Pacific Rise 15°–17°N: An unusually robust segment, *J. geophys. Res.*, **101**, 20 257–20 273.
- Wessel, P. & Smith, W.H.F., 1995. New version of the Generic Mapping Tools released, *EOS, Trans. Am. geophys. Un.*, **76**, 329.
- White, D.J. & Clowes, R.M., 1994. Seismic attenuation structure beneath the Juan de Fuca Ridge from tomographic inversion of amplitudes, *J. geophys. Res.*, **99**, 3043–3056.
- White, R.S. & Stephen, R.A., 1980. Compressional to shear wave conversion in oceanic crust, *Geophys. J. R. astr. Soc.*, **63**, 547–565.
- White, R.S. & Whitmarsh, R.B., 1984. An investigation of seismic anisotropy due to cracks in the upper oceanic crust at 45° N, Mid-Atlantic Ridge, *Geophys. J. R. astr. Soc.*, **79**, 439–467.
- White, R.S., McKenzie, D.P. & O'Nions, R.K., 1992. Oceanic crustal thickness from seismic measurements and rare earth element inversions, *J. geophys. Res.*, **97**, 19 683–19 715.
- Wiedicke, M. & Kudrass, H.R., 1990. Morphology and tectonic development of the Valu Fa Ridge, Lau basin (southwest Pacific): Results from a deep-towed side-scan sonar survey, *Mar. Min.*, **9**, 145–156.
- Wiedicke, M. & Collier, J., 1993. Morphology of the Valu Fa spreading ridge in the southern Lau Basin, *J. geophys. Res.*, **98**, 11 769–11 782.
- Wilcock, W.S.D., Dougherty, M.E., Solomon, S.C., Purdy, G.M. & Toomey, D.R., 1993. Seismic propagation across the East Pacific Rise: Finite difference experiments and implications for seismic tomography, *J. geophys. Res.*, **98**, 19 913–19 932.
- Wilcock, W.S.D., Solomon, S.C., Purdy, G.M. & Toomey, D.R., 1995. Seismic attenuation structure of the East Pacific Rise near 9° 30' N, *J. geophys. Res.*, **100**, 24 147–24 165.

- Wilkens, R.H., Fryer, G.J. & Karsten, J., 1991. Evolution of porosity and seismic structure of upper oceanic crust: Importance of aspect ratios, *J. geophys. Res.*, **96**, 17 981–17 995.
- Xu, Y. & Wiens, D.A., 1997. Upper mantle structure of the southwest Pacific from regional waveform inversion, *J. geophys. Res.*, **102**, 27 439–27 451.
- Zellmer, K.E., Taylor, B., Martinez, F. & Goodliffe, A., 1998. Complexities in the seafloor spreading history of the Lau Basin, *EOS, Trans. Am. geophys. Un.*, **79**, 908.
- Zelt, C.A., 1998. Lateral velocity resolution from three-dimensional seismic refraction data, *Geophys. J. Int.*, **135**, 1101–1112.
- Zelt, C.A. & Barton, P.J., 1998. Three-dimensional seismic refraction tomography: A comparison of two methods applied to data from the Faeroe Basin, *J. geophys. Res.*, **103**, 7187–7210.
- Zelt, C.A. & Forsyth, D.A., 1994. Modeling wide-angle seismic data for crustal structure: Southeastern Grenville province, *J. geophys. Res.*, **99**, 11 687–11 704.
- Zelt, C.A. & Smith, R.B., 1992. Seismic travel-time inversion for 2-D crustal velocity structure, *Geophys. J. Int.*, **108**, 16–34.
- Zhao, D., Xu, Y., Wiens, D.A., Dorman, L., Hildebrand, J. & Webb, S., 1997. Depth extent of the Lau back-arc spreading center and its relation to subduction processes, *Science*, **278**, 254–257.

# Appendix A

## *zplot* file format

As described in section 1.5.3, interpretation of record sections was performed using *zplot*, a seismic data plotting program written by Colin Zelt of Rice University, Houston, Texas. This program was used because it incorporates an automatic picking tool which was employed to speed up the picking of first arrival travel times. In this appendix, a full description of the *zplot* file format is provided and an indication of its mode of use presented for reference. This information is based on the *zplot* user documentation which has been modified to reflect the correct format for the file and trace headers.

The seismic data is stored in a data file which comprises a binary file header followed by each trace including its associated binary trace header. Traces may optionally be sorted into gathers, referred to as records, which are assumed to be common shot records. Hence if common receiver records are required, the shot and receiver number trace header words should be interchanged. A header file containing the binary trace headers only, and record file containing display parameters for each record in the data file, may optionally be specified. Other input parameters are specified in the file `zplot.in` (see *zplot* user documentation for details). *zplot* does not enforce specific naming conventions on the input data and trace header files. However, in this study, data files were given the extension `.dat` and header files the extension `.hdr`.

The binary file and trace headers comprise a series of four byte integer or floating point words and are detailed in the following tables.

File header:

Header word	Integer or Float	Description
1	integer	Number of traces in file.
2	integer	Number of points per trace.
3	integer	Sampling interval ( $\mu s$ ).
4	integer	Trace start time (ms).
5	integer	Trace end time in (ms).
6	integer	Number of records in file.
7	integer	Number of pick words [np].
8	float	Reduction velocity ( $kms^{-1}$ ).
9	integer	Trace data format flag; 0 = two byte integer, 1 = four byte floating point.
10–13	float	Not used.

Trace header:

Header word	Integer or Float	Description
1	integer	Shot station or number.
2	integer	Trace sequential number within record.
3	integer	Receiver station or number.
4	integer	Data type flag for trace selection. The user may specify that only traces with a given value of this word should be plotted.
5	integer	Dead trace flag, to omit unwanted traces.
6	float	Shot–receiver offset (m).
7	float	Receiver–shot azimuth (minutes of arc).
8	integer	Multiplicative gain factor.
9	float	Exact trace start time (s) adjusted for reduction velocity.
10	float	Shot latitude.
11	float	Shot longitude.
12	float	Shot elevation.
13	integer	Water depth at shot.
14	float	Receiver latitude.
15	float	Receiver longitude.
16	float	Receiver elevation.
17	integer	Shot x position (UTM).
18	integer	Shot y position (UTM).
19	integer	Shot z position.
20	integer	Receiver x position (UTM).
21	integer	Receiver y position (UTM).
22	integer	Receiver z position.
23– 22+np	float	Travel time picks (s) – np is determined from file header word 7.

The trace data file comprises the binary file header padded to the same length as all subsequent records, followed by each trace preceded by its header. The data considered in this dissertation were in floating point format and were not subdivided into records – hence the shot and receiver numbers were set to 1 in each trace header. The shot and receiver location fields in the trace headers were not populated, and hence no reduction velocity could be applied as no shot–receiver range information was present in the raw data. These default values were written to the file and trace headers by *sgyi2z*, a program written by Anthony Day to convert seismic data from SEG–Y<sub>1</sub> format to *zplot* format .

*zplot* allows interactive plotting, picking and band–pass filtering of data, and these tools were used to assist arrival time picking as described in section 2.3.1. When picks are made using *zplot*, modifications to the trace headers are logged in an output file (*zplot.out*). The program *headup* is then run, which requires that the user specify a header file (a binary file comprising trace headers only) and the number of pick words in each trace header. *headup* then applies the modifications logged in *zplot.out* to the specified header file. Hence the trace headers in the trace data file are not altered.

The default value of 10 was used for the number of pick words (word 7 in the file header). Pick words were assigned to arrivals as follows:

- 1 – Direct water–wave arrivals.
- 2 – Crustal first arrivals.
- 3 – *P–S* mode converted arrivals with an approximate shot–receiver azimuth of 090° or 270° as defined in section 4.3.
- 4 – *P–S* mode converted arrivals with an approximate shot–receiver azimuth of 000° or 180° as defined in section 4.3.
- 5 & 6 – Not used.
- 7 – First sea surface multiple of the direct water–wave arrival.
- 8, 9 & 10 – Not used.

# Appendix B

## Methods for constructing data files and performing inversions

The inversion method and data required were described in sections 2.2 and 2.3. In this appendix, the step-by-step procedure for constructing each data file and performing an inversion are described as a reference for others wishing to adopt a similar approach. The raw data file formats described here are specific to the acquisition system employed during cruise EW9512, and many of the scripts and programs described were written specifically to deal with this dataset. Hence modification will be required if similar techniques are to be adopted to process datasets dissimilar from that described in this dissertation. Data from instrument SDOBS3 is used as the example, and the raw seismic data is shown in Figs. B.1 and B.2. Each process will now be discussed in turn, and a diagrammatic summary is shown in Fig. B.3.

### 1. Picking direct water-wave and first arrival travel times

**Program used and author:** *zplot* (Colin Zelt)

**Description:** Direct water-wave arrivals were picked from hydrophone sections and first-arrival travel times were picked from vertical geophone sections using *zplot*. This package incorporates an automatic picking tool which was used to assist travel time picking as described in section 2.3.1. *zplot* also includes a Butterworth band-pass filter which was used to enhance traces affected by disk spin noise as described in section 2.3.1. Direct water-wave travel times were stored in the first pick word and first arrival travel times were stored in the second pick word in the *zplot* header file as described in appendix A. Band-pass filtered vertical geophone traces for SDOBS3 are shown in Fig. B.1 for all shots within the 3-D study area, with direct water-wave and first arrival travel time picks marked. Fig. B.2 shows detail of selected traces, which will be used to illustrate subsequent steps in the inversion procedure, with and without band-pass filtering applied. Operational details for *zplot* can be found in its accompanying on-line manual and hence will not be repeated here.



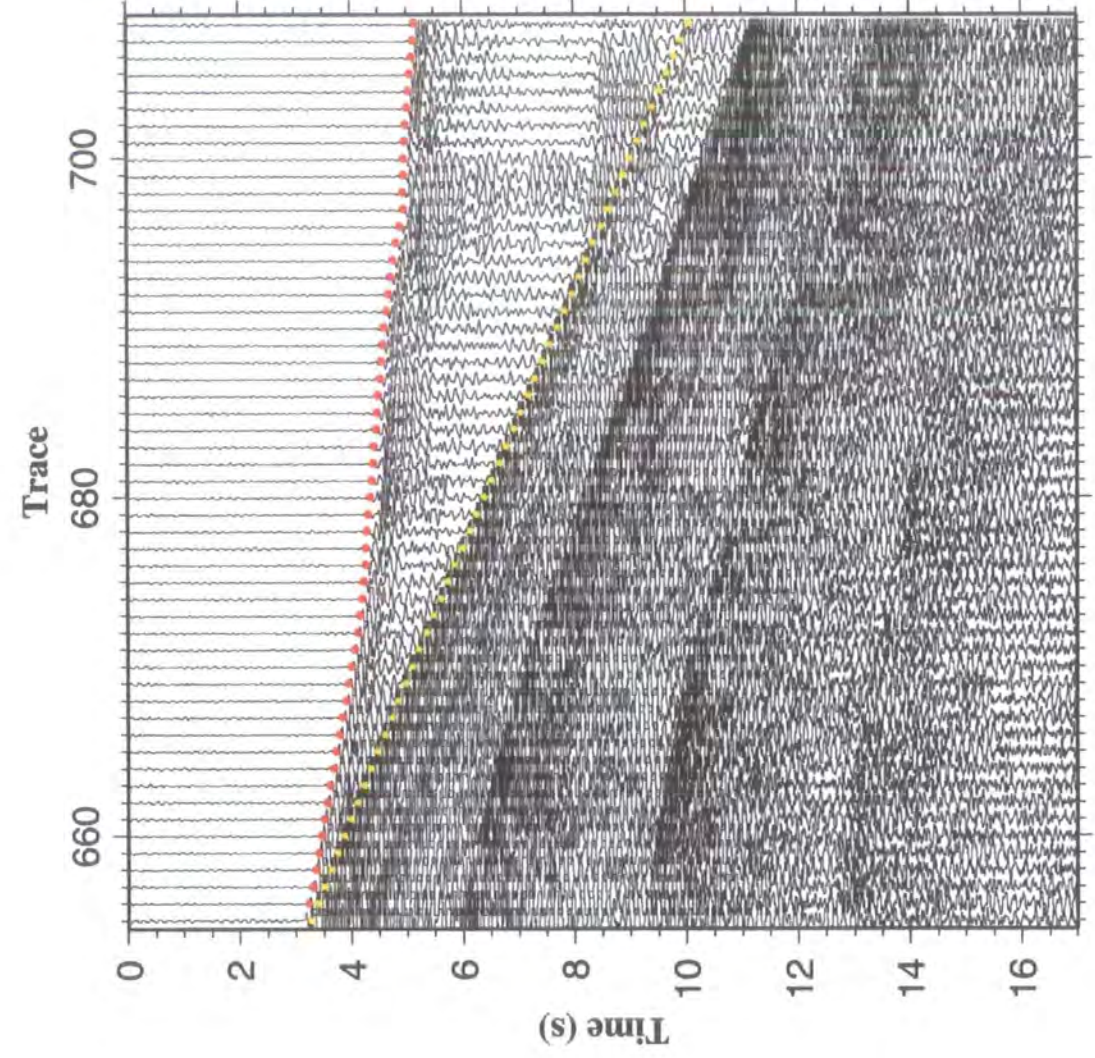
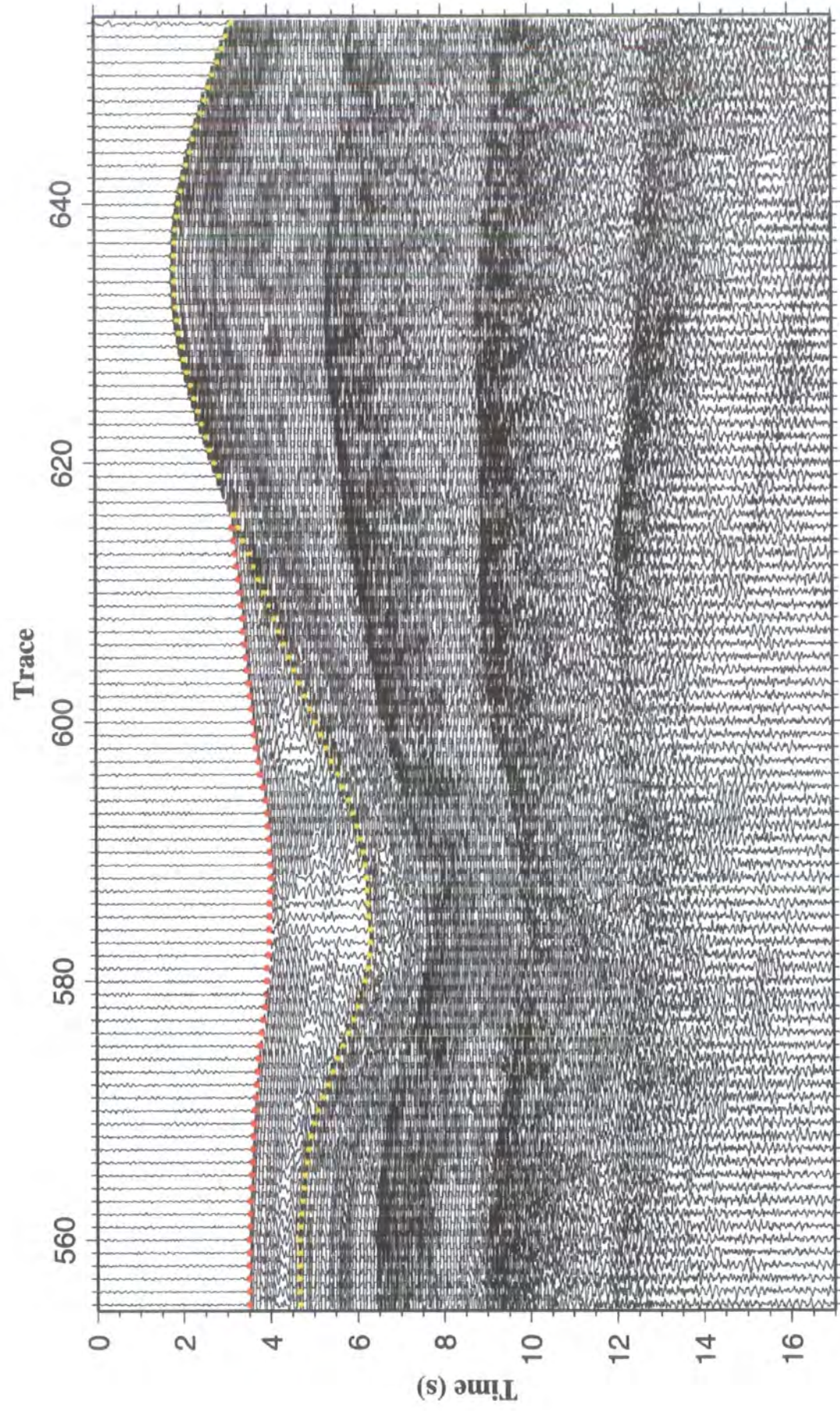


**Figure B.1.1:** Vertical geophone traces recorded at SDOBS3. All shots within the 3-D study area are shown. Blank traces arise from failed shots. A 40 Hz low-pass filter has been applied to remove high frequency disk spin noise, and all traces are plotted at true amplitude. Clipping has been applied for clarity. Dot centres mark travel time picks of direct water-wave arrivals (yellow) and crustal first arrivals (red). Note the large variation in arrival amplitude across the section.



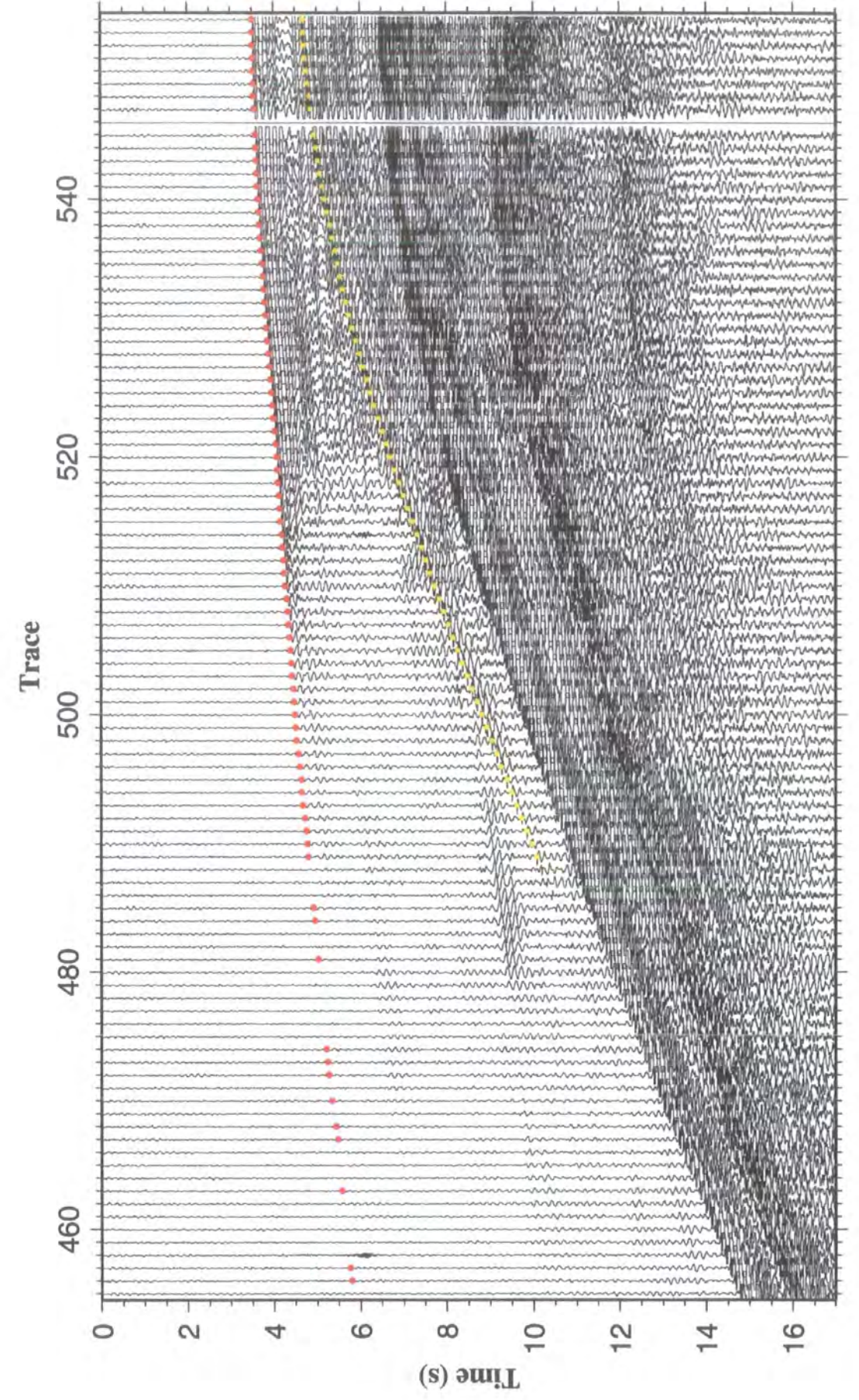
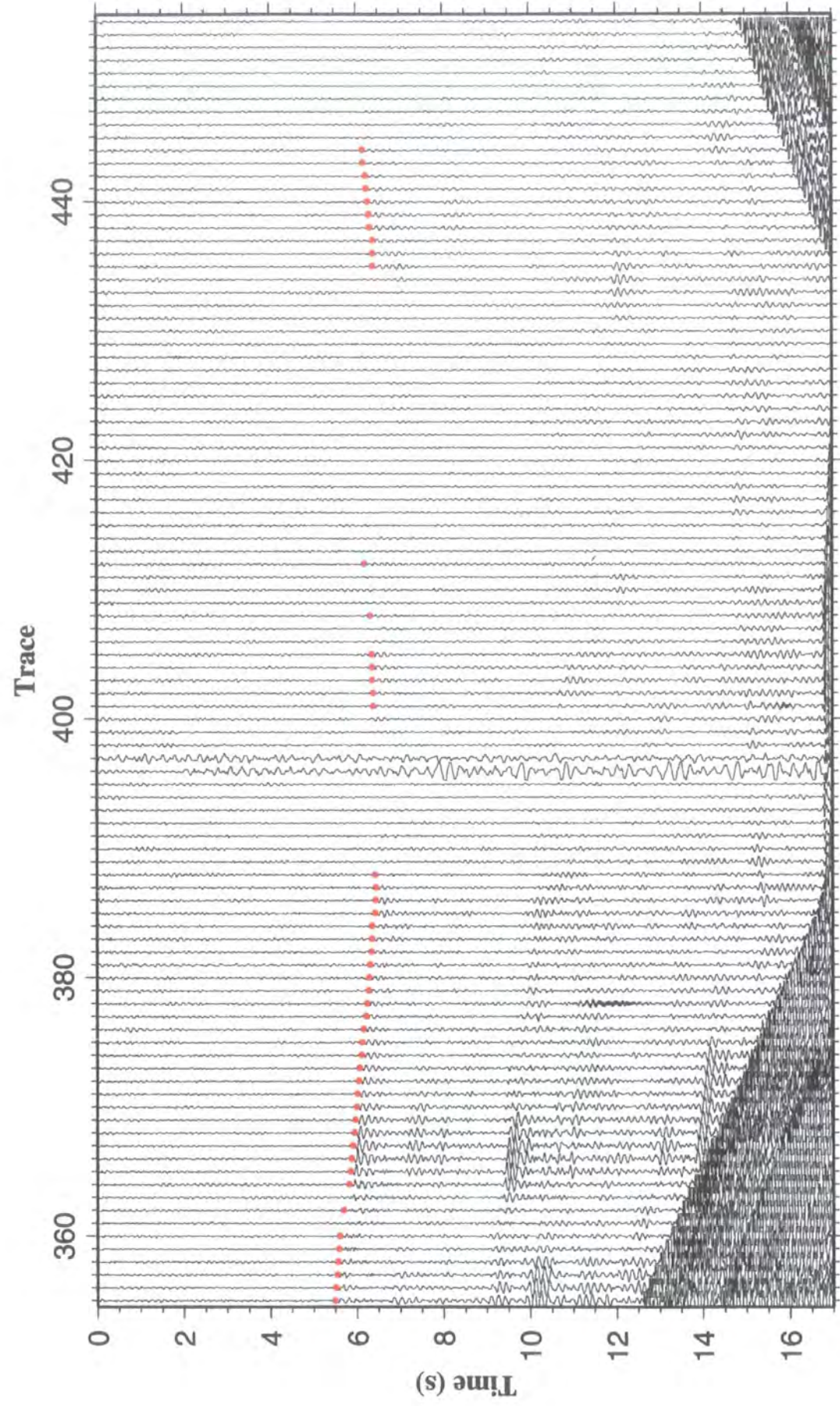


Figure B.1: Caption on page 259.



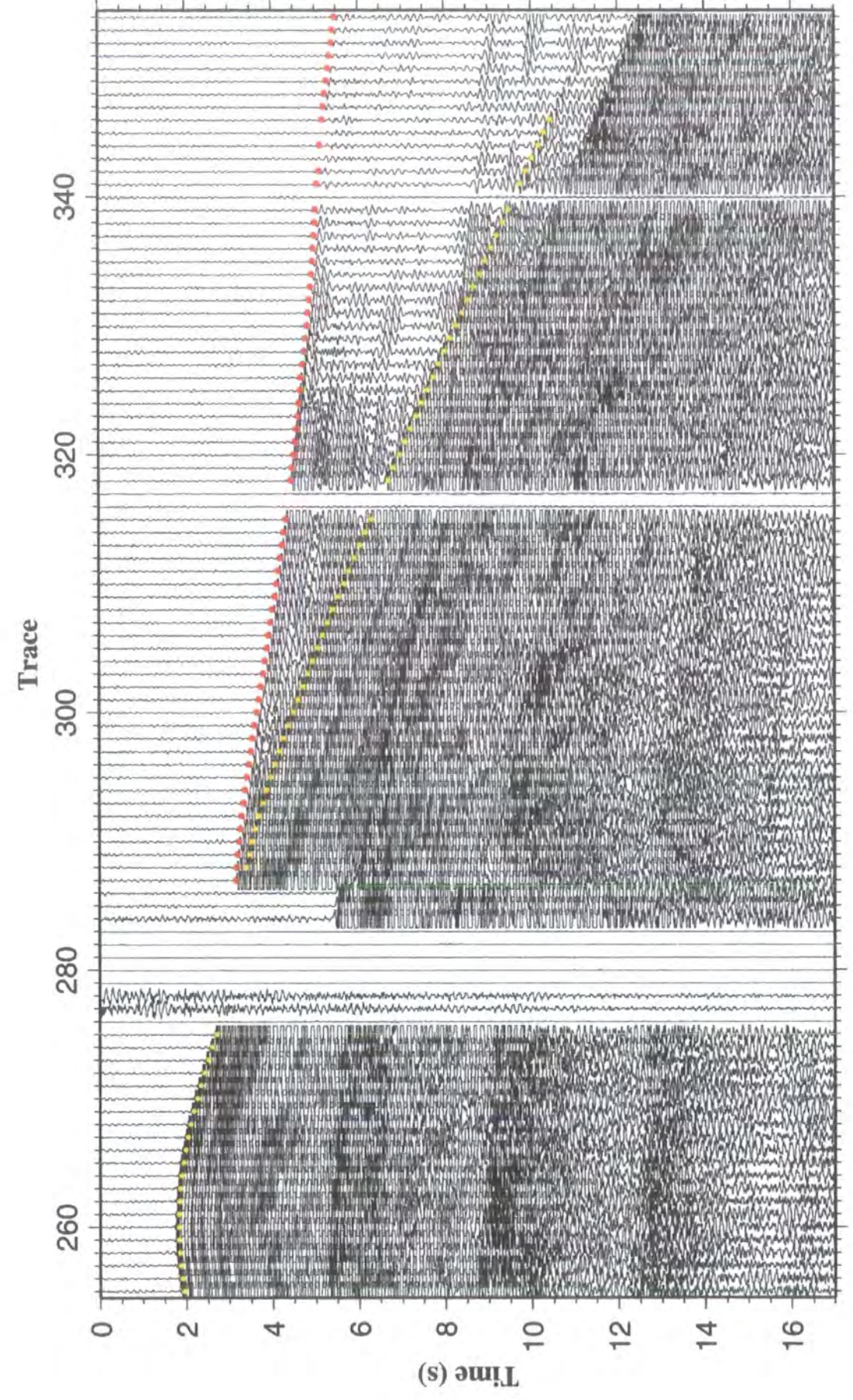
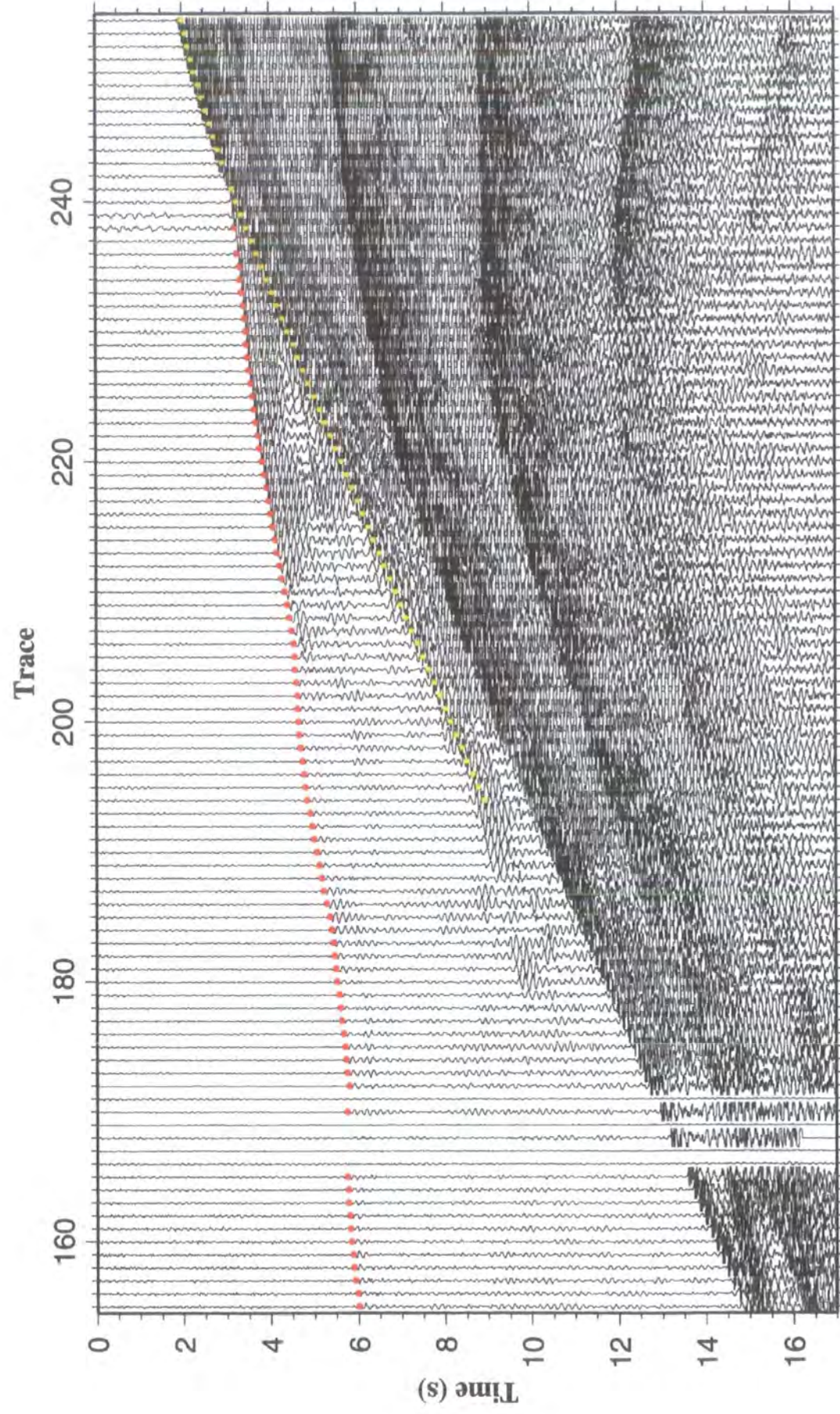
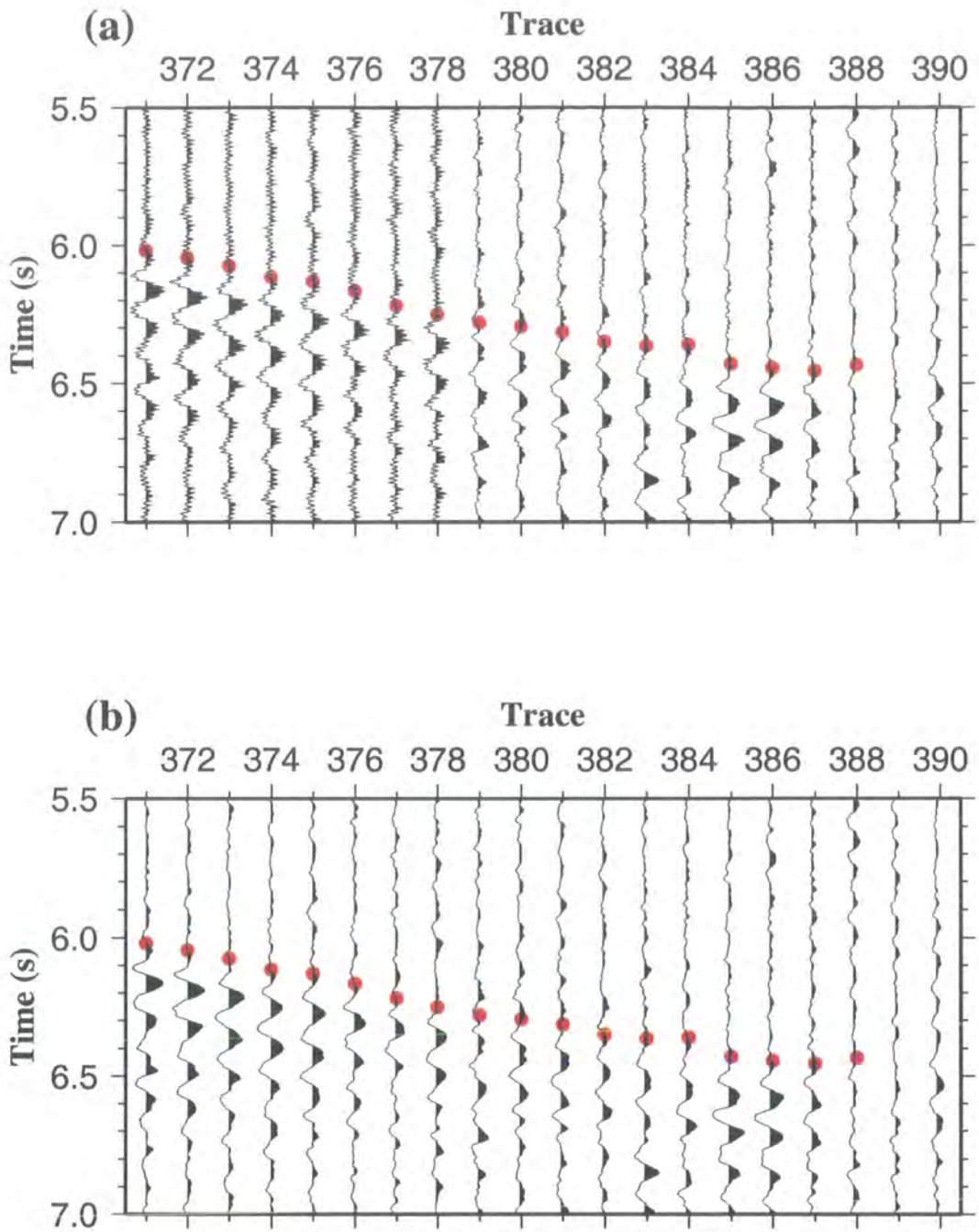


Figure B.1: Caption on page 259.





**Figure B.2:** Detail of some of the traces shown in Fig. B.1: a) unfiltered and b) with a 40 Hz low-pass Butterworth band-pass filter applied. Red dot centres denote first arrival travel time pick positions in both cases.

## 2. Determining shot positions

**Programs used and authors:** *writeshot*, *shiplatlon* and *calcshot* (Anthony Day); *mapproject* (GMT – Wessel & Smith)

**Description:** *writeshot* is a script which generates a file relating trace numbers as shown in Figs. B.1 and B.2 to individual shot latitudes and longitudes. This script is listed at the end of this section for reference purposes. The raw data, and hence the shot instant files, for both northern and southern deployments were split into two parts (numbered 1 and 2) for convenience in dealing with the large number of shots. The script first calls *shiplatlon* which reads the raw shot instant file (*scs<expt>\_#* where *<expt>* is south or north and *#* is 1 or 2) and navigation files (*ts.n<day>* where *<day>* is the Julian day), and determines the latitude and longitude of the GPS receiver at each shot instant by linearly interpolating between entries in the navigation file. The latitude and longitude of the previous and successive shots are also output. These positions are then projected onto a linear grid using *mapproject* as described in section 2.3.2 and passed to *calcshot* which determines the position of the centre of the airgun array which, in the case of cruise EW9512, was located 88.4 m behind the GPS receiver position as shown in Fig. 1.9. The algorithm for determining these shot positions is described in section 2.3.2. *mapproject* is then used again to convert the shot positions back to latitude and longitude. Parts of the relevant files relating to the traces shown in Fig. B.2 are reproduced below.

*writeshot* script.

```
shiplatlon << END | mapproject -Joa-176:40/-22:20/111/1:100000
-R-177:05/-176:15/-22:35/-21:55 -C | calcshot | mapproject
-Joa-176:40/-22:20/111/1:100000 -R-177:05/-175:15/-22:35/-20:55 -I
-C | awk '{if($1==279) {printf("%3d%12.5f%12.5f\n", $3, 9999, 9999) }
else {printf("%3d%12.5f%12.5f\n", $3, $1-360, $2) }}'
$1
END
```

The *\$1* parameter passed to *shiplatlon* is the shot instant file name. The resulting output is piped to a file called *shot<expt>\_#* according to the convention previously described. Hence, the script should be executed with a command of the form: `writeshot scssouth_1 > shotsouth_1`

Raw shot instant file: `scssouth_1`

Format: line number (1), shot time (hh:mm:ss.sss), shot ID number, six unused columns, shot depth (m), three unused columns, Julian day, trace length (s). Note that the shot ID number increment is 2 because each trace recorded by the OBS represents alternate shots as described in section 1.5.2

```
1124239951 742 0 0 0.00 0 0 0.00 8.0 0 0 .0 335 15
1124359955 744 0 0 0.00 0 0 0.00 8.0 0 0 .0 335 15
1124519989 746 0 0 0.00 0 0 0.00 8.0 0 0 .0 335 15
1124640012 748 0 0 0.00 0 0 0.00 8.0 0 0 .0 335 15
11248 0025 750 0 0 0.00 0 0 0.00 8.0 0 0 .0 335 15
```

Raw navigation file: `ts.n335`

Format: year, Julian day, hours, minutes, seconds, ID number, south/north, degrees latitude, minutes latitude, west/east, degrees longitude, minutes longitude, seismic line name

```
95+335:12:42:00.117 00406 S 22 13.9996 W 176 43.0051 SeislineS
95+335:12:42:40.136 00407 S 22 13.9456 W 176 42.9799 SeislineS
95+335:12:43:20.143 00408 S 22 13.8911 W 176 42.9558 SeislineS
95+335:12:44:00.140 00409 S 22 13.8362 W 176 42.9327 SeislineS
95+335:12:44:40.166 00410 S 22 13.7824 W 176 42.9099 SeislineS
```

Final shot position file: `shotsouth_1`

Format: trace number, longitude, latitude

```
371 -176.71666 -22.23316
372 -176.71585 -22.23134
373 -176.71511 -22.22956
374 -176.71432 -22.22779
375 -176.71356 -22.22603
```

### 3. Determining OBS locations and associated uncertainties

**Programs used and authors:** *mapproject* (GMT – Wessel & Smith), *readpicks*, *writellte*, *writetx*, *wtx* (Anthony Day) and *RAYINVR* (Colin Zelt)

**Description:** Whilst the OBS deployment positions are known, instruments may drift in the water column before reaching the seafloor due to water column currents, and hence direct water–wave arrivals are used to determine their true positions on the seafloor. For each OBS position, *readpicks* is used to read direct water–wave travel times from the *zplot* header files and output a file containing trace numbers, direct water–wave travel times and a nominal travel time uncertainty (which is not used). The output file name is of the form `water107s_1` where 107 is the PDAS number, s or n denotes the southern or northern deployment and 1 or 2 refers to the part of the divided raw data file (described in step 2 above). *writellte* is then used to

join the two data files together by reading the `water107s_#` files and the corresponding shot position files created in step 2 above (`shotsouth_#` in this case), and creating a file containing the latitude, longitude, travel time and travel time uncertainty for each shot, named `w_11te107s`. The `writetx` script is then run which reads this file and also the OBS deployment position and transforms them onto a linear grid using `mapproject` as described in section 2.3.2. The results are passed to `wtx` which writes `tx.in`, a file of travel time versus shot–receiver offset which can be read by `RAYINVR`, a 2–D ray tracing package (see `RAYINVR` user documentation for a full description of file formats and operational details). The water depth at the OBS deployment position is extracted from the gridded bathymetry data acquired during the cruise and input manually into `RAYINVR`, which is then run to trace rays from a single shot at this depth and zero offset to an array of receivers at offsets defined in `tx.in`. The latitude and longitude of each OBS is then manually adjusted and the process repeated until a best fit of the predicted and observed direct water–wave travel times is obtained. Minor adjustments are then made to each OBS depth if necessary to further improve the fit, and the RMS travel time misfit noted and used to determine the travel time uncertainty due to OBS locational uncertainty as described in section 2.5.

The `writetx` script is listed below:

```
#!/bin/csh

grep $1 /grp/poseidon/dgl3ajd/masters/data/instllz | awk
 '{printf("%f %f %f\n", $3, $4, $5)}' | mapproject -Joa-176:40/-22:20/
111/1:100000 -R-177:05/-176:15/-22:35/-21:55 -C >
/grp/poseidon/dgl3ajd/masters/data/instxy
awk '{printf("%f %f %f %f\n", $2, $3, $4, $5)}'
/grp/poseidon/dgl3ajd/masters/data/w_11te$1 | mapproject
-Joa-176:40/-22:20/ 111/1:100000 -R-177:05/-176:15/-22:35/-21:55 -C
> /grp/poseidon/dgl3ajd/masters/data/xyte
wtx $1
rm /grp/poseidon/dgl3ajd/masters/data/instxy
rm /grp/poseidon/dgl3ajd/masters/data/xyte
```

The parameter passed to the script on the command line (`$1`) is the PDAS number and deployment in the form `107s`, and the file `instllz` contains the latitude, longitude and depth of each OBS deployment position (listed in step 5). `wtx` reads the temporary files `instxy` and `xyte` written by this script.



#### 4. First arrival travel time uncertainties

**Program used and author:** *snrinfo* (Anthony Day)

**Description:** The contributions to first arrival travel time uncertainty are described in section 2.6 and summarised in Table 2.4. For each OBS position, the only variable contribution to first arrival time uncertainty is that associated with the pick position uncertainty. The method for determining pick position uncertainty is described in section 2.4 and details of the programs used will be presented in appendix C. *snrinfo* is used to create SNR information files with names of the form *snrinfo107s\_1* for each OBS position containing details of the parameters which should be input into the routines for determining first arrival travel time uncertainty. Each line in these files contains the following parameters: trace number, name of the file containing the pick position uncertainty versus SNR relationship to be used, a flag to indicate whether a 40 Hz, 20 Hz or no low-pass filter should be used when calculating SNR, the time window which should be used for calculating SNR, and the root-sum-square of all sources of uncertainty shown in Table 2.4 apart from that arising from pick position uncertainty (see section 2.4 for the significance of each of these parameters). *snrinfo* writes default values for each parameter, and the resulting file is then manually edited after inspection of the raw data using *zplot*. An extract from the resulting file for a number of the traces in Fig. B.2 is shown below.

SNR information file: *snrinfo107s\_1*

Format: trace ID, pick position uncertainty versus SNR relationship file, band-pass filter flag (0 = no band-pass filter, 1 = 40 Hz low-pass filter, 2 = 20 Hz low-pass filter), SNR calculation window (ms), root-sum-square uncertainty (s) for SDOBS3

371	<i>snr107s.noise</i>	1	300	0.014
372	<i>snr107s.noise</i>	1	300	0.014
373	<i>snr107s.noise</i>	1	300	0.014
374	<i>snr107s.noise</i>	1	300	0.014
.				
.				
379	<i>snr107s</i>	0	300	0.014
380	<i>snr107s</i>	0	300	0.014
381	<i>snr107s</i>	0	300	0.014
382	<i>snr107s</i>	0	300	0.014

## 5. Creating *FAST* raw data files

**Programs used and authors:** *readpicks2*, *writellte*, *writefd* (Anthony Day), *mapproject* (GMT – Wessel & Smith) and *rec\_binary* (Colin Zelt)

**Description:** The raw data files read by the *FAST* inversion routines are written in binary. These files are named *fd##.picks* where *##* is a two digit instrument ID number. The first record contains the *x,y,z* co-ordinates of an OBS, and each subsequent record contains the *x,y,z* co-ordinates of a shot, the first arrival travel time and associated uncertainty. The raw first arrival travel time data is read from the *zplot* header files by *readpicks2* which also reads the SNR information file described in step 4. The output file name is of the form *fbreak107s\_1* and contains the trace number, first arrival travel time and associated uncertainty determined using the selected band-pass filter, SNR calculation window and pick position uncertainty determined from the pick position uncertainty versus SNR relationship indicated for that trace in the SNR information file. The step-by-step method for determining these relationships will be described in appendix C. An extract from *fbreak107s\_1* for the traces shown in Fig. B.2 is reproduced below.

*readpicks2* output: *fbreak107s\_1*

Format: trace ID number, first arrival travel time (s), travel time uncertainty (s)

371	6.020	0.015
372	6.045	0.015
373	6.075	0.014
374	6.115	0.015
375	6.130	0.021
376	6.165	0.015
377	6.220	0.018
378	6.250	0.021
379	6.280	0.043
380	6.295	0.033
381	6.315	0.021
382	6.350	0.029
383	6.365	0.029
384	6.360	0.025
385	6.430	0.014
386	6.445	0.014
387	6.455	0.015
388	6.435	0.038

*writellte* is then used to join the two halves of the dataset for each instrument together and extract the shot latitude and longitude from the shot position files created in step 2. At this stage, first arrival travel times are corrected for clock drift as described in section 2.3.1 by reading the shot time from the shot instant file and a look-up table giving the total clock drift during both deployment periods for each OBS. The resulting file name is of the form *llte107s*, and an extract is shown below for a number of the traces shown in Fig. B.2.

*writellte* output: *llte107s*

Format: trace ID number, longitude (°), latitude (°), clock drift-corrected first arrival travel time (s), travel time uncertainty (s)

371	-176.71666	-22.23316	5.998	0.015
372	-176.71585	-22.23134	6.023	0.015
373	-176.71510	-22.22956	6.053	0.014
374	-176.71432	-22.22779	6.093	0.015
375	-176.71356	-22.22603	6.108	0.021

The *writefd* script is then run which reads the OBS position and the file created by *writellte*, uses *mapproject* to convert latitude and longitude to x,y co-ordinates and writes a text version of the *FAST* raw data file called *fd##.txt*. A shot depth of 8 m (0.008 km – the nominal towing depth of the airgun array) is assumed for the EW9512 dataset. First arrival travel time uncertainties were doubled at this stage as described in section 2.6. The *writefd* script is listed below:

```
#!/bin/csh
grep -w $1 /grp/poseidon/dgl3ajd/masters/data/instllz | awk
'{printf("%12.5f%12.5f%6d\n", $3, $4, $5)}' | mapproject -Joa-176:40/
-22:20/111/1:100000 -R-177:05/-176:15/-22:35/-21:55 -C | awk
'{printf("%10.3f%10.3f%10.3f%10.3f%3d\n", $1, -1.*$2, $3/1000.,
0,0,-1)}' > fd$1.txt
set ext = `grep -w $1
/grp/poseidon/dgl3ajd/masters/data/instllz | awk
'{printf("%4s\n", $1)}'`
awk '{printf("%12.5f%12.5f%10.3f%10.3f\n", $2, $3, $4, $5)}'
/grp/poseidon/dgl3ajd/masters/data/llte$ext | mapproject -Joa-176:40
/-22:20/111/1:100000 -R-177:05/-176:15/-22:35/-21:55 -C | awk
'{printf("%10.3f%10.3f%10.3f%10.3f%10.3f%3d\n", $1, -1.*$2, 0.008, $3,
2*$4, 1)}' >> fd$1.txt
```

The parameter passed to the script on the command line (*\$1*) is the instrument ID number used in the *FAST* routines, and the *\$ext* parameter is the PDAS number deployment in the form *107s* which is extracted from the *instllz* file which contains both ID numbers. *instllz* is listed below.

Format: instrument ID (PDAS number plus south or north deployment), *FAST* instrument ID, longitude (°), latitude (°), depth (m)

112n	01	-176.96404	-22.06558	2363.0
111n	02	-176.79166	-22.12891	2248.0
107n	03	-176.61296	-22.19267	2148.0
106n	04	-176.60269	-22.19648	1800.0
105n	05	-176.47742	-22.23956	2357.7
105s	06	-177.05579	-22.31183	2563.0
106s	07	-176.83098	-22.39050	2770.0
107s	08	-176.75388	-22.41723	2688.0
108s	09	-176.69653	-22.43856	2133.0
111s	10	-176.60600	-22.47195	2818.0
112s	11	-176.42369	-22.53582	1823.5

*rec\_binary* is then used to convert this text file into the binary input format of the *FAST* routines (*fd##.picks*). An extract from the text version of this file for a number of the traces in Fig. B.2 is shown below.

*FAST* raw data file: *fd08.txt*

Format: x position (km), y position (km), z position (km), first arrival travel time (s), travel time uncertainty (s), ray group ID (not used)

-8.795	-8.554	0.008	5.998	0.030	1
-8.790	-8.773	0.008	6.023	0.030	1
-8.789	-8.985	0.008	6.053	0.028	1
-8.785	-9.198	0.008	6.093	0.030	1
-8.782	-9.409	0.008	6.108	0.042	1

## 6. Creating the *basic 1-D initial model*

**Program used and authors:** *velint9* (Colin Zelt and modified by Anthony Day)

**Description:** *velint9* reads a 1-D velocity–depth profile from a text file (*velint.in*), a file containing the model dimensions (*for.header*), and three binary bathymetry files which are created by smoothing the raw bathymetry with 1.0, 1.5 and 2.0 km square averaging filters (*bathymetry.1000*, *bathymetry.1500* and *bathymetry.2000*). The choice of these averaging filters is discussed in section 2.8. The velocity–depth profile file takes the form of a series of velocity–depth pairs defining the top and bottom of constant velocity gradient layers. The *velint.in* file used to create the *basic 1-D initial model* is listed below:

0.00	1.53
0.34	1.52
0.34	1.52
0.60	1.49
0.60	1.49
1.15	1.48
1.15	1.48
3.20	1.51
3.20	1.91
3.62	3.96
3.62	3.96
5.51	6.08
5.51	6.08
6.26	6.35
6.26	6.35
7.26	6.56
7.26	6.56
10.54	7.00
10.54	7.00
12.01	7.20

The velocity model is created in a 3-D array with elements corresponding to nodes separated by the forward grid spacing of 0.2 km as described in section 2.7. Each x,y position is considered in turn and the raw velocity–depth profile adjusted by forcing the top of the uppermost crustal layer to lie at the seafloor as defined by the 1.0 km smoothed bathymetry file. The position of the base of this layer and top of the layer beneath it are adjusted by the difference between the mean position of the seafloor and the position at that x,y position defined in the 1.5 km smoothed bathymetry file. All deeper layer boundaries are similarly adjusted based on the 2.0 km bathymetry file. This smoothing scheme is specific to the EW9512 data, and the rationale behind it is discussed in section 2.8. Velocities are then assigned to all nodes at that x,y position according to the scheme outlined in section 2.8 and the process repeated for all x,y positions to create an initial model with approximately seafloor parallel layers as discussed in section 2.8. The array is then output to a binary file of two byte integers, called `vel.int`. When used in the *FAST* inversion, this file is renamed `ve10` according to the file naming convention employed by the calling script (see step 9). All velocity model files written by the inversion are in the same format.

## 7. Creating the 2-D initial model

**Program used and authors:** *velint2d* (Colin Zelt and modified by Anthony Day)

**Description:** *velint2d* was adapted from *velint9* to create 2-D initial models. This program reads two velocity–depth profile files which, in the case of the EW9512 dataset, correspond to the averages of the *Seismic North* and *Seismic South* profiles of Turner (1998) shown in Fig. 1.10. At each  $y$  position the raw velocity–depth profile is created by linear interpolation between these two profiles which are located at  $y = -17$  km and  $y = 12$  km respectively in this case. The mean position of the seafloor used to calculate adjustments to this profile is a distance weighted average of the mean seafloor position for the *Seismic North* and *Seismic South* profiles. The velocity–depth profile at each  $x,y$  position is then adjusted as described in step 6 above, velocities assigned to each element in the array as described in section 2.8 and the array output as a two byte integer binary file (*vel.int*).

## 8. Creating the unbiased 2-D initial model

**Programs used and authors:** *difference* (Colin Zelt), *avganom4* (Anthony Day) and *add* (Colin Zelt)

**Description:** The *unbiased 2-D initial model* was based on the *2-D initial model*. The anomaly relative to the *2-D initial model* recovered by the *FAST* inversion (described in the following step) is obtained using *difference* which calculates the difference between two velocity model files at each node and outputs the results as a binary file (*diff.out*). In this case, the *2-D initial model* is subtracted from the final model generated by inversion. The resulting anomaly file is then averaged using *avganom4*, which is designed to deal specifically with the velocity models produced in this study. This program reads *diff.out*, the 2.0 km smoothed bathymetry (*bathymetry.2000*) and a binary file containing the cumulative ray path length within the inversion cell surrounding each velocity node (*length.cell*). The method for creating this latter file is described in step 11. The velocity model is divided into northern and southern halves at the  $y = -1$  km position. For each half, the average velocity anomaly and cumulative ray path length is calculated along planes parallel to the smoothed bathymetry and separated vertically by 0.2 km (the velocity model node spacing). In this manner profiles of

average velocity anomaly versus depth beneath the seafloor are calculated for the northern and southern halves of the model. The anomalies for planes for which the mean cumulative ray path length is less than 1.0 km are set to zero. The resulting profiles are used to create a 2-D anomaly field by the method described in step 7 above. This anomaly field (*anom.out*) is added to the 2-D *initial model* using the *add* program, which outputs a velocity model file named *add.out*, to create the *unbiased 2-D initial model*.

## 9. FAST regularised inversion method

**Description:** Regularised inversion is performed using code written by Colin Zelt and called from the *inversion* script which is listed below. For all inversions described in this dissertation, the *numi* and *numl* parameters were both set to 5. Full descriptions of the various programs called by this script and details of the input file formats are given in the *FAST* user documentation. A brief overview of the most important files and each program is provided here.

```

echo " "
echo " *** EVERYTHING CORRECT: starting model, f.in, r.in, ...?
*** "
echo " "
echo "enter number of non-linear iterations:"
read numi
echo "enter number of lambda values to test:"
read numl

EXEDIR=../execs

rm log.file

$EXEDIR/init2
$EXEDIR/ireg
$EXEDIR/smodel < s0.rsp

numc=`expr $numi `

while [ $numc -gt 0 ]
do

    it0=`expr $numi - $numc `
    it1=`expr $numi - $numc + 1 `

    num=`expr $numl `
    $EXEDIR/init3

    while [ $num -gt 0 ]
    do

        cp vel$it0 vel.mod

        $EXEDIR/nfd
        $EXEDIR/zero < zero1.rsp
        $EXEDIR/nray

        $EXEDIR/smodel < s.rsp

        rm *.values
        grep chi    log.file > chi.values
        grep lambda log.file > lambda.values
    
```



```

$EXEDIR/lambda2
$EXEDIR/inverse
$EXEDIR/regrid < regrid.rsp
$EXEDIR/update
$EXEDIR/reset

$EXEDIR/copy
$EXEDIR/nfd

rm chi.values
grep chi    log.file > chi.values

$EXEDIR/istop

num=`expr $num - 1`

done

rm *.values
grep chi    log.file > chi.values
grep lambda log.file > lambda.values

$EXEDIR/select2

mv log.file log.$it1
cp vel.mod vel$it1

numc=`expr $numc - 1`

done

```

## Files:

vel0	Initial velocity model created by the method described in steps 6–8 above.
vel.mod	Current velocity model (archived and updated automatically).
fd##.picks	Pick file for shot ## created by the method described in step 5.
fd##.times	Calculated time file for shot ##. These are the first arrival times at each node of the forward grid.
bathymetry	Interface file used to fix the model above an interface, derived from the raw bathymetry by applying a 1.0 km square averaging filter.
vel#	Archived velocity model representing the best model from the # non-linear iteration.
vel.#	Models corresponding to each value of $\lambda$ tested for each non-linear iteration from which the best model (vel#) is selected.
log.file	The current log file which archives key parameters output by each of the programs called by the <i>inversion</i> script. Once archived for each non-linear iteration they are called log.#.

<code>for.header</code>	Text file containing the size of the forward grid. The values correspond to: <code>xmin</code> , <code>xmax</code> , <code>ymin</code> , <code>ymax</code> , <code>zmin</code> , <code>zmax</code> , <code>size</code> , <code>nx</code> , <code>ny</code> , <code>nz</code> . These are the model limits (km) and number of nodes in each direction and "size" is the node spacing (km).
<code>inv.header</code>	Text file containing the size of the inverse grid. The values correspond to <code>nxi</code> , <code>nyi</code> , <code>nzi</code> . These are the number of inversion cells in the x,y,z directions.
<code>stop.in</code>	Control file created and updated automatically by the inversion script and used to exit programs inside the inner loop over $\lambda$ under certain circumstances.
<code>nzero.kernel</code>	A file created by <code>nray</code> containing the number of non-zero elements of the data kernel and the total number of data.
<code>file.names</code>	The names of the velocity model files for each value of $\lambda$ tested for each non-linear iteration are listed in order in this file.
<code>chi.values</code>	List of $\chi^2$ values for each iteration of the inner loop extracted from <code>log.file</code> .
<code>lambda.values</code>	List of $\lambda$ values for each iteration of the inner loop extracted from <code>log.file</code> .

#### Programs:

<code>init2</code>	Initialises control files.
<code>ireg</code>	Resamples binary bathymetry file on the inverse grid to determine the top inversion cell at which regularisation should be applied during inversion.
<code>smodel</code>	Converts a velocity model to slowness parameterised on the inverse grid.
<code>init3</code>	Initialises control files for the inner loop.
<code>nfd</code>	Finite difference travel time calculator. Outputs <code>fd##.times</code> files.
<code>zero</code>	Initialises slowness tomography files with zero values.
<code>nray</code>	Trace rays through the <code>fd##.times</code> files and calculates the cumulative ray path length in each inversion cell.
<code>lambda2</code>	Calculate the current value of the trade-off parameter $\lambda$ .

<i>inverse</i>	Calculates the 3-D slowness perturbation using regularised inversion based on the cumulative ray path lengths calculated by <i>nray</i> .
<i>regrid</i>	Regrids a 3-D data volume from the inverse cell parameterisation to the forward node parameterisation.
<i>update</i>	Adds the calculated slowness perturbation to the initial model.
<i>reset</i>	Resets the velocities above the bathymetry to those in the background model.
<i>copy</i>	Archive and copy new velocity model to current model.
<i>select2</i>	Select the model with the lowest $\chi^2$ value to be carried forward to the next non-linear iteration by reading the <code>chi.values</code> file. Also reads <code>lambda.values</code> to determine the appropriate value of $\lambda$ to be carried forward.

## 10. Performing an inversion with the melt lens included

**Programs and authors:** As in step 9 above, plus *meltlens* (Anthony Day)

**Description:** The *inversion* script listed in step 9 above was adapted for inversions for which a melt lens is included for the forward modelling step only as described in section 3.5. The program *meltlens* is used to set velocity nodes in a specified velocity model file (`vel.mod` in the script below) corresponding to the melt lens to a user-specified value (3.0 kms<sup>-1</sup> in this case). The melt lens position is defined in a text file (`meltlens.xy` in this case) comprising the x,y positions of each edge of the melt lens, which are then resampled at y positions separated by the forward grid spacing by linear interpolation, and a user-specified depth (4.8 km at the VFR).

The revised *inversion* script is as follows:

```
echo " "
echo "**** EVERYTHING CORRECT: starting model, f.in, r.in, ...?"
echo " "
echo "enter number of non-linear iterations:"
read numi
echo "enter number of lambda values to test:"
read numl

EXEDIR=./execs

rm log.file

$EXEDIR/init2
$EXEDIR/ireg
$EXEDIR/smodel < s0.rsp
```

```

numc=`expr $numi `
while [ $numc -gt 0 ]
do
    it0=`expr $numi - $numc `
    it1=`expr $numi - $numc + 1 `

    num=`expr $numl `
    $EXEDIR/init3

    while [ $num -gt 0 ]
    do
        cp vel$it0 vel.mod

        cp vel.mod vel.save
        $EXEDIR/meltlens < meltlens.rsp
        $EXEDIR/nfd
        $EXEDIR/zero < zero1.rsp
        $EXEDIR/nray
        mv vel.save vel.mod

        $EXEDIR/smodel < s.rsp

        rm *.values
        grep chi    log.file > chi.values
        grep lambda log.file > lambda.values

        $EXEDIR/lambda2
        $EXEDIR/inverse
        $EXEDIR/regrid < regrid.rsp
        $EXEDIR/update
        $EXEDIR/reset

        $EXEDIR/copy

        cp vel.mod vel.save
        $EXEDIR/meltlens < meltlens.rsp
        $EXEDIR/nfd
        mv vel.save vel.mod

        rm chi.values
        grep chi    log.file > chi.values

        $EXEDIR/istop

        num=`expr $num - 1 `
    done

    rm *.values
    grep chi    log.file > chi.values
    grep lambda log.file > lambda.values

    $EXEDIR/select2

    mv log.file log.$it1
    cp vel.mod vel$it1

    numc=`expr $numc - 1 `
done

```

The processing steps described in this appendix so far are summarised in the block diagram in Fig. B.3.

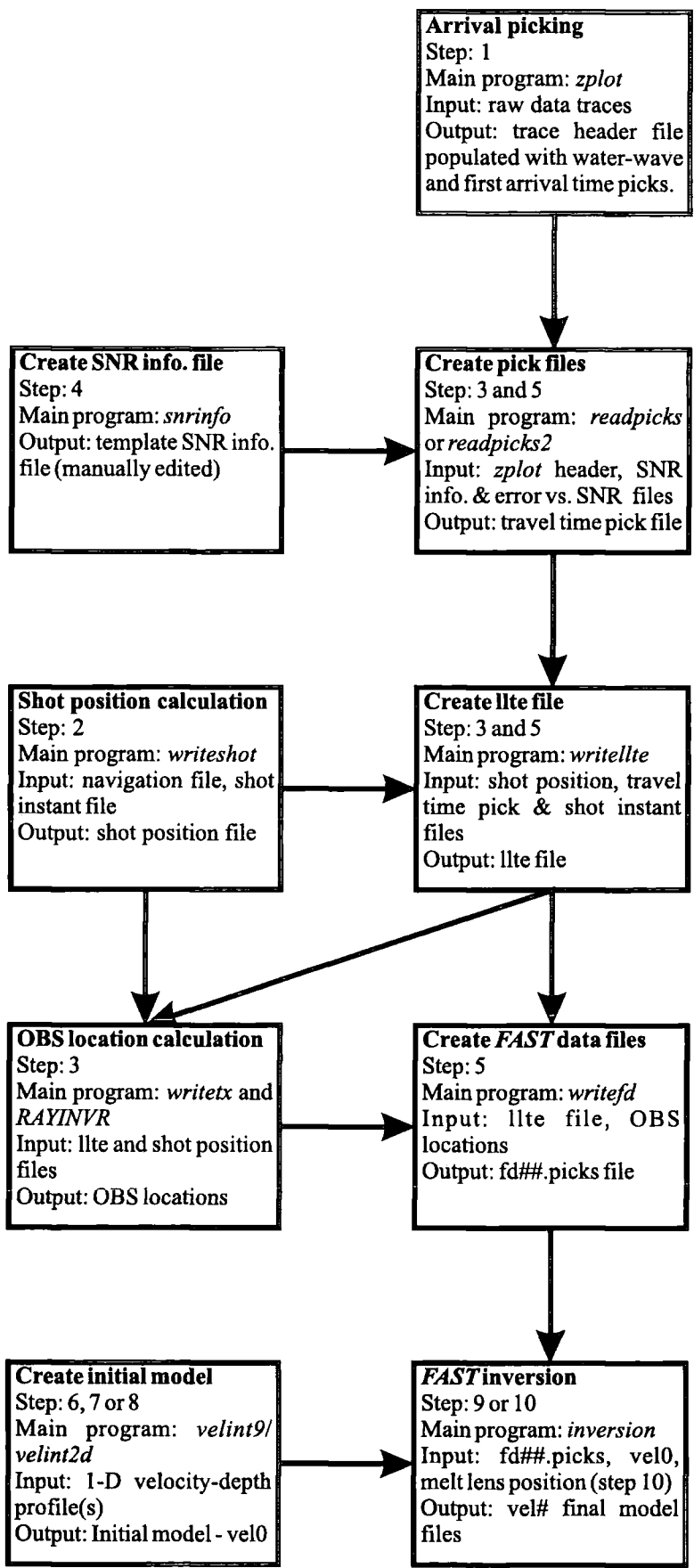


Figure B.3: Flow diagram summarising the principal processing steps described in this appendix so far.

## 11. Calculating the ray path length in each inversion cell

**Programs and authors:** *nray\_len* (Colin Zelt, and modified by Anthony Day)

**Description:** The `length.cell` file, which contains the cumulative ray path length in each inversion cell, is used in step 8 in the construction of the *unbiased 2-D initial model* and is also used as a measure of resolution (e.g. Figs. 2.26 and 3.3 display `length.cell` files). The method for creating this file is similar to the first part of the *inversion* script listed in step 9 above. *nfd* is run with the relevant velocity model to generate `fd##.times` files described above, and *nray\_len* is then run using these files. This program is a modified version of the ray tracing program *nray* which outputs the cumulative ray path length in each inversion cell as a binary file of four byte floating point numbers on the same grid as the velocity models.

## 12. Checkerboard tests

**Programs and authors:** *anomaly6*, *nfd*, *rec\_noise2*, and *inversion* (Colin Zelt)

**Description:** The checkerboard resolution tests described in section 2.10 are performed using a number of controlling scripts, an annotated example of which is listed below, which create synthetic first arrival travel time data and then perform inversions using it. The programs called by these scripts will now be described in turn. *anomaly6* adds a sinusoidally varying anomaly to an existing velocity model and writes the resulting velocity model to `vel.anomaly`. The magnitude and geometry of this anomaly may be defined by the user. This program also reads a binary bathymetry file and does not add any checkerboard anomaly at points shallower than this interface. In the example script below, a 6 km checkerboard is used offset from the model origin by 3 km in the *x* and *y* directions and rotated through 45°. *nfd* is then run in travel time calculation mode, which calculates the synthetic travel times through the perturbed model for shot–receiver pairs specified in binary files of the same form as the `fd##.picks` files and named `rec.##`. For these tests the `rec.##` files were identical to the equivalent `fd##.picks` files for the real dataset thus simulating the geometry of the real experiment. Noise is then added to the output files, named `fd##.calc`, using *rec\_noise2*. This program adds Gaussian noise to a pick file with variance determined by the associated travel time uncertainties, which were also determined from the `fd##.picks` files for the real dataset in this case to simulate the uncertainty distribution of the real experiment.

The output of *rec\_noise2* is stored as *fd##.picks* files which are then used to perform an inversion using the script listed in step 9. A typical controlling script for a checkerboard test is listed below.

```
#!/bin/csh

anomaly6 << END
vel0                                {initial velocity model file}
6 6                                {x,y size of checkerboard}
3 3                                {x,y offset of basic checkerboard pattern}
45.                                {angle through which basic checkerboard pattern is rotated}
1                                  {multiplier for checkerboard pattern (use -1 to invert)}
0. 12.                             {minimum and maximum depth in model to add checkerboard to initial file}
5.                                  {amplitude of sinusoid as percentage of background velocity}
END

cp vel.anomaly vel.mod              {vel.mod is the file read by nfd}
cp vel.anomaly testmod             {archive the test model with anomaly included}
cp f.in.calc f.in                  {f.in contains nfd input parameters; f.in.calc contains
                                     parameters for calculating travel times}
init2                               {initialise control files}
init3
nfd                                  {calculate synthetic travel times}
rec_noise2 << END
2                                  {seed for random number generator}
fd02.calc                            {input pick file - written by nfd}
fd02.picks                          {output pick file with noise added}
fd03.calc
fd03.picks
fd05.calc
fd05.picks
fd07.calc
fd07.picks
fd08.calc
fd08.picks
fd09.calc
fd09.picks
fd10.calc
fd10.picks

END
cp f.in.inv f.in                   {f.in.inv contains nfd input parameters for performing
                                     inversions}

setup                               {simple script to delete old files from previous inversions}
inversion << END                     {inversion script listed in step 9}
5                                  {number of non-linear iterations}
5                                  {number of  $\lambda$  values to test at each iteration}
END
```

### 13. Semblance analysis and resolution calculation

**Programs and authors:** *difference*, *ave*, *ave4* (Colin Zelt), *semblance3* (Colin Zelt and modified by Anthony Day) and *resolution* (Anthony Day)

**Description:** The output files from the checkerboard tests described above are inspected to determine which of the velocity models (*ve11-ve15*) best fits the synthetic data on the basis of the normalised  $\chi^2$  value archived in the *log.#* files. In the example script listed below, *ve12* is the best fitting model. The semblance between this model and the test model from which the synthetic data was derived is



calculated by subtracting the initial model (*vel0*) from each of the models using *difference* (described in step 8) and passing the resulting files to *semblance3*. This program calculates the semblance between the models at each node using a planar circular semblance operator of specified radius (see section 2.10.1 for a full description of the method) and outputs the results to a binary, two byte integer file, *semb.mod*. An annotated example script used to create this file is listed below.

```
#!/bin/csh

difference << END
testmod                {test model including checkerboard anomaly}
vel0                   {initial model for creating both the test model and performing the inversion}
                        {default response indicates two byte integer file}
END
mv diff.out diff.test  {archive difference output file}

difference << END
vel2                   {best fitting model recovered by inversion}
vel0                   {initial model for creating both the test model and performing the inversion}
                        {default response indicates two byte integer file}
END

semblance3 << END
diff.out               {first test file name}
diff.test              {second test file name}
0                      {flag indicating that semblance should be calculated for all points below seafloor}
2.5                   {semblance operator radius}
END
```

For each checkerboard size, eight checkerboard patterns are investigated as described in section 2.10.1. The resulting *semb.mod* files are archived as *semb.mod1.#km* to *semb.mod8.#km* where # represents the checkerboard size. The mean semblance for each checkerboard size is calculated using a combination of the *ave4* and *ave* programs which calculate the mean of four and two specified model files (*semb.mod?.#km* in this case) respectively. The resulting models are archived as *semb.ave.#km* files for checkerboard sizes of 4, 5, 6, 8, 10 and 15 km in the case of the resolution tests described in section 2.10.1. *resolution* is then used to calculate the resolution at each model node. The user specifies a semblance threshold and the program then reads the *semb.ave.#km* files for the checkerboard sizes listed above, calculates the checkerboard size for which the semblance exceeds the specified threshold at each point in the velocity model by linear interpolation between the semblance values in the *semb.ave.#km* files, and writes the resulting resolution to a binary file (*res.mod*). *resolution* is specifically written to deal with the resolution tests described in section 2.10, but may easily be modified to deal with other tests (e.g. those described in section 5.5.2).

## 14. Plotting routines

**Programs and authors:** *difference*, *gmtslice5* (Colin Zelt), *gmtslice6* (Colin Zelt and modified by Anthony Day) and various GMT programs (Wessel & Smith)

**Description:** The script used to create Fig. 3.8 is listed below. This script illustrates most of the features used to generate similar plots of velocity anomalies, cumulative ray path length, semblance and resolution, and is loosely based on similar scripts written by Colin Zelt to produce plots presented in Zelt & Barton (1998). *gmtslice5* and *gmtslice6* are used to extract data from 3-D models along specified planes. *gmtslice5* extracts planes perpendicular to one of the co-ordinate axes whilst *gmtslice6* extracts data along planes specified in binary files in the same format as the bathymetry files. The output files are text files containing relevant co-ordinate pairs and the value in the velocity file at that point. The functionality of the various GMT programs is described in the user documentation and is not reproduced in detail here.

```

#! /bin/csh

gmtset GRID_PEN 5

                                                                    {paths to various archived files}

set modpath = /grp/poseidon/dgl3ajd/zelt/final_models1_sq
set invpath = /grp/poseidon/dgl3ajd/zelt/inversion1
set datpath = /grp/poseidon/dgl3ajd/zelt/data
set scale = 0.1/-0.1                                                                    {x,y scale for plans}
set pal = small_anomaly.cpt                                                            {colour palette file for all plots}
'rm' ../ps/anomaly_2d.ps

difference << END
$modpath/vel.mod11                                                                    {archived final velocity model}
$datpath/velstart.2d.par2000                                                            {archived initial velocity model}
                                                                    {default response indicates two byte integer file}

END

# part a

set range = -22./18./-20./18.                                                            {xmin/xmax/ymin/ymax for plans}

gmtslice6 << END
diff.out                                                                                {output file from difference above}
mid2A                                                                                    {name of binary file containing plane along which to extract data}
201 191 61                                                                                {number of points in x, y and z directions in output file}
.001                                                                                    {multiplier to convert two byte integer to floating point}
0                                                                                          {flag to mask unsampled cells (not used)}
END

                                                                    {the output file from this call to gmtslice6 is called slice.mid2A}

gmtslice6 << END
diff.out
mid2B
201 191 61
.001
0
END

```

```

gmtslice6 << END
diff.out
top3
201 191 61
.001
0
END

                                     {convert gmtslice6 output to GMT grid files}
xyz2grd slice.mid2A -Gz01.grd -I0.2 -R$range -V
xyz2grd slice.mid2B -Gz02.grd -I0.2 -R$range -V
xyz2grd slice.top3 -Gz03.grd -I0.2 -R$range -V
#-----

                                     {draw velocity anomaly image}
grdimage z01.grd -C$pal \
          -Jx$scale -P -X5 -Y23 -V -K > ../ps/anomaly_2d.ps
psbasemap -B10.0f5.0:"X (km)"/10.0f5.0:"Y (km)":WenS \
          -Jx -R$range -V -O -K >> ../ps/anomaly_2d.ps

                                     {add bathymetric contours - bath1000.grd is a GMT grid representation of the 1.0 km
                                     smoothed bathymetry}
grdcontour bath1000.grd -C250 -Jx -K -O >> ../ps/anomaly_2d.ps

                                     {add instrument positions and ship tracks}
psxy $datapath/instpos.xy -Jx -R -St0.3 -G255 -K -O >>
../ps/anomaly_2d.ps
psxy $invpath/fd02.txt -Jx -R -Sp -L -W1/255/255/255 -H1 -K -O -V
>> ../ps/anomaly_2d.ps
psxy $invpath/fd03.txt -Jx -R -Sp -L -W1/255/255/255 -H1 -K -O -V
>> ../ps/anomaly_2d.ps
psxy $invpath/fd05.txt -Jx -R -Sp -L -W1/255/255/255 -H1 -K -O -V
>> ../ps/anomaly_2d.ps
psxy $invpath/fd07.txt -Jx -R -Sp -L -W1/255/255/255 -H1 -K -O -V
>> ../ps/anomaly_2d.ps
psxy $invpath/fd08.txt -Jx -R -Sp -L -W1/255/255/255 -H1 -K -O -V
>> ../ps/anomaly_2d.ps
psxy $invpath/fd09.txt -Jx -R -Sp -L -W1/255/255/255 -H1 -K -O -V
>> ../ps/anomaly_2d.ps
psxy $invpath/fd10.txt -Jx -R -Sp -L -W1/255/255/255 -H1 -K -O -V
>> ../ps/anomaly_2d.ps
pstext -Jx -R -W \
        -N -V -K -O << END >> ../ps/anomaly_2d.ps
-22.0 -24 10 0 0 1 Middle of Layer 2A
-45.0 -20 18 0 5 TC (a)
END

#-----

grdimage z02.grd -C$pal \
          -Jx -X5 -V -K -O >> ../ps/anomaly_2d.ps
psbasemap -B10.0f5.0:"X (km)"/10.0f5.0:"Y (km)":WenS \
          -Jx -R -V -O -K >> ../ps/anomaly_2d.ps
grdcontour bath1000.grd -C250 -Jx -K -O >> ../ps/anomaly_2d.ps

                                     {draw positions of planes of cross-sections shown in part b)}
psxy -Jx -R -W3ta -M -K -O -V << END >> ../ps/anomaly_2d.ps
>
1 -20
1 18
>
-22 12
18 12
>
-22 -17
18 -17
END

pstext -Jx -R -W \
        -N -V -K -O << END >> ../ps/anomaly_2d.ps
-22.0 -24 10 0 0 1 Middle of Layer 2B/C
END

#-----

```

```

grdimage z03.grd -C$pal \
    -Jx -X5 -V -K -O >> ../ps/anomaly_2d.ps
psbasemap -B10.0f5.0:"X (km)":/10.0f5.0:"":wenS \
    -Jx -R -V -O -K >> ../ps/anomaly_2d.ps
grdcontour bath1000.grd -C250 -Jx -K -O >> ../ps/anomaly_2d.ps
psxy -Jx -R -W3ta -M -K -O -V << END >> ../ps/anomaly_2d.ps
>
1 -20
1 18
>
-22 12
18 12
>
-22 -17
18 -17
END

pstext -Jx -R -W\
    -N -V -K -O << END >> ../ps/anomaly_2d.ps
-22.0 -24 10 0 0 1 Top of Layer 3
END

# part b

set range = -22./18./0./8.          {xmin/xmax/zmin/zmax for cross-sections}
set scale = 0.1/-0.3                {x,z or y,z scale for cross-sections}

gmtslice5 << END
diff.out
y
-17.0 12.0 29.0
201 191 61
.001
0
END

xyz2grd y01.slice -Gy01.grd -I0.2 -R$range -V
xyz2grd y02.slice -Gy02.grd -I0.2 -R$range -V

gmtslice5 << END
$modpath/vel.mod11                {output file from difference}
y                                  {output slices of constant y (i.e. perpendicular to the y-axis)}
-17.0 12.0 29.0                    {minimum and maximum values of y and increment}
201 191 61                          {number of points in x, y and z directions in output file}
.001                                 {multiplier to convert two byte integer to floating point}
0                                    {flag to mask unsampled cells (not used)}
END

    {the above call to gmtslice5 outputs two files: y01.slice and y02.slice, corresponding to
    the positions y = -17 km and y = 12 km respectively, which are converted to GMT grid files
    below}

xyz2grd y01.slice -Gvel_y01.grd -I0.2 -R$range -V
xyz2grd y02.slice -Gvel_y02.grd -I0.2 -R$range -V

#-----

grdimage y01.grd -C$pal -R$range \
    -Jx$scale -X-10 -Y-5 -V -O -K >> ../ps/anomaly_2d.ps
psbasemap -B10.0f2.0:"X (km)":/2.0f2.0:"Z (km)":WenS \
    -Jx -R -V -O -K >> ../ps/anomaly_2d.ps

grdcontour vel_y01.grd -Cvely.con -Jx -R -Wto -K -O >>
../ps/anomaly_2d.ps

```

{bathymetry, base2A etc are files in the same format as the binary bathymetry which contain the positions of these planes. *readbath* converts these files to text for plotting on the cross-section}

```

readbath << END |awk '{if($2==-17.0){printf("%f
%f\n", $1, $3/1000)}}' | psxy -Jx -R -M -K -O -V >>
../ps/anomaly_2d.ps
bathymetry
END
readbath << END |awk '{if($2==-17.0){printf("%f
%f\n", $1, $3/1000)}}' | psxy -Jx -R -M -K -O -V >>
../ps/anomaly_2d.ps
base2A
END
readbath << END |awk '{if($2==-17.0){printf("%f
%f\n", $1, $3/1000)}}' | psxy -Jx -R -M -K -O -V >>
../ps/anomaly_2d.ps
base2B
END

readbath << END |awk '{if($2==-17.0){printf("%f %f\n", $1, $3)}}' |
psxy -Jx -R -W3ta -M -K -O -V >> ../ps/anomaly_2d.ps
mid2A
END
readbath << END |awk '{if($2==-17.0){printf("%f %f\n", $1, $3)}}' |
psxy -Jx -R -W3ta -M -K -O -V >> ../ps/anomaly_2d.ps
mid2B
END
readbath << END |awk '{if($2==-17.0){printf("%f %f\n", $1, $3)}}' |
psxy -Jx -R -W3ta -M -K -O -V >> ../ps/anomaly_2d.ps
top3
END

pstext -Jx -R -W \
-N -V -K -O << END >> ../ps/anomaly_2d.ps
-22.0 -1.0 10 0 0 1 y = -17.0 km
-45.0 0 18 0 5 TC (b)
END
#-----

grdimage y02.grd -C$pal -R$range \
-Jx$scale -X5 -V -O -K >> ../ps/anomaly_2d.ps
psbasemap -B10.0f2.0:"X (km)":/2.0f2.0:"":wenS \
-Jx -R -V -O -K >> ../ps/anomaly_2d.ps

grdcontour vel_y02.grd -Cvely.con -Jx -R -Wto -K -O >>
../ps/anomaly_2d.ps

readbath << END |awk '{if($2==12.0){printf("%f %f\n", $1, $3/1000)}}'
| psxy -Jx -R -M -K -O -V >> ../ps/anomaly_2d.ps
bathymetry
END
readbath << END |awk '{if($2==12.0){printf("%f %f\n", $1, $3/1000)}}'
| psxy -Jx -R -M -K -O -V >> ../ps/anomaly_2d.ps
base2A
END
readbath << END |awk '{if($2==12.0){printf("%f %f\n", $1, $3/1000)}}'
| psxy -Jx -R -M -K -O -V >> ../ps/anomaly_2d.ps
base2B
END

readbath << END |awk '{if($2==12.0){printf("%f %f\n", $1, $3)}}' |
psxy -Jx -R -W3ta -M -K -O -V >> ../ps/anomaly_2d.ps
mid2A
END
readbath << END |awk '{if($2==12.0){printf("%f %f\n", $1, $3)}}' |
psxy -Jx -R -W3ta -M -K -O -V >> ../ps/anomaly_2d.ps
mid2B
END
readbath << END |awk '{if($2==12.0){printf("%f %f\n", $1, $3)}}' |
psxy -Jx -R -W3ta -M -K -O -V >> ../ps/anomaly_2d.ps
top3
END

```

```

pstext -Jx -R -W \
        -N -V -K -O << END >> ../ps/anomaly_2d.ps
-22.0 -1.0 10 0 0 1 y = 12.0 km
0 16 14 0 5 10 Velocity Anomaly (kms@+-1@+)
END
#-----

set range = -20./18./0./8.          {ymin/ymax/zmin/zmax for last cross-section}

gmtslice5 << END
diff.out
x
1.0 10.0 20.0
201 191 61
.001
0
END

xyz2grd x01.slice -Gx01.grd -I0.2 -R$range -V

gmtslice5 << END
$modpath/vel.mod11
x
1.0 10.0 20.0
201 191 61
.001
0
END

xyz2grd x01.slice -Gvel_x01.grd -I0.2 -R$range -V

grdimage x01.grd -C$pal -R$range \
        -Jx$scale -X5 -V -O -K >> ../ps/anomaly_2d.ps
psbasemap -B10.0f2.0:"Y (km)":/2.0f2.0:"":wenS \
        -Jx -R -V -O -K >> ../ps/anomaly_2d.ps

grdcontour vel_x01.grd -Cvely.con -Jx -R -Wto -K -O >>
../ps/anomaly_2d.ps

readbath << END |awk '{if($1==1.0){printf("%f %f\n", $2, $3/1000)}}'
| psxy -Jx -R -M -K -O -V >> ../ps/anomaly_2d.ps
bathymetry
END
readbath << END |awk '{if($1==1.0){printf("%f %f\n", $2, $3/1000)}}'
| psxy -Jx -R -M -K -O -V >> ../ps/anomaly_2d.ps
base2A
END
readbath << END |awk '{if($1==1.0){printf("%f %f\n", $2, $3/1000)}}'
| psxy -Jx -R -M -K -O -V >> ../ps/anomaly_2d.ps
base2B
END

readbath << END |awk '{if($1==1.0){printf("%f %f\n", $2, $3)}}' |
psxy -Jx -R -W3ta -M -K -O -V >> ../ps/anomaly_2d.ps
mid2A
END
readbath << END |awk '{if($1==1.0){printf("%f %f\n", $2, $3)}}' |
psxy -Jx -R -W3ta -M -K -O -V >> ../ps/anomaly_2d.ps
mid2B
END
readbath << END |awk '{if($1==1.0){printf("%f %f\n", $2, $3)}}' |
psxy -Jx -R -W3ta -M -K -O -V >> ../ps/anomaly_2d.ps
top3
END

pstext -Jx -R -W \
        -N -V -K -O << END >> ../ps/anomaly_2d.ps
-20.0 -1.0 10 0 0 1 x = 1.0 km
END
#-----

gmtset TICK_PEN 5
psscale -C$pal \
        -D-3/-3/14.0/0.5h -L \
        -V -O >> ../ps/anomaly_2d.ps
gmtset TICK_PEN 2 GRID_PEN 1to          {draws scale bar}

```

# Appendix C

## Method for determining travel time pick uncertainty versus SNR relationships

In this appendix, the series of programs which were developed to determine travel time pick uncertainty versus SNR relationships are described as they are novel to the work undertaken in this dissertation. The method is based on assessing the performance of the automated picking tool incorporated in the *zplot* package as described in section 2.4. The process was automated by using a script to call the various programs, which will now be described in turn. An example script is listed after the program descriptions which demonstrates the parameters required by each program. The scripts and programs used to create the median pick position uncertainty versus SNR relationships are also described.

### 1. Program and author: *stack* (Anthony Day)

**Description:** Creates a reference trace by stacking real traces, then outputs a synthetic section comprising a specified number of copies of this trace each of which is optionally offset in time by a random amount up to  $\pm 50$  ms. The user specifies the traces to be stacked, the length of the output trace, the pick which is to be aligned and whether or not any band-pass filter is to be applied to the traces prior to stacking. The specified *zplot* trace data and header files are then read, the traces to be stacked adjusted in time such that the values of the specified pick word are equal to that for the first trace, and the traces stacked. Additionally, for the tests described in section 2.4, all samples prior to the pick position were multiplied by 0.1 to enhance the SNR. The output files are *zplot* format data and header files, *stack.dat* and *stack.hdr* respectively, as described in appendix A. For the tests described in section 2.4, a synthetic section comprising 1000 randomised traces was produced. The header file contains the true position of all the travel time picks stored in the pick word which was aligned when stacking raw traces to form the reference trace, and a subset of these picks is stored in the subsequent pick word. The frequency of picks to be included in this subset is specified by the user, and for the tests described in section 2.4 every seventh pick was included.



## 2. Program and author: *addnoise* (Anthony Day)

**Description:** In order to test the performance of the automatic picking tool, variable levels of noise are added to the stacked traces created in step 1 above using the *addnoise* program. The frequency spectrum of the noise to be added is obtained from a trace with no arrivals. The user specifies the *zplot* file, trace number, start time and length of the time window to be used to obtain this frequency spectrum. A band-pass filter may optionally be applied. For the tests described in section 2.4, a 15 s section starting at 1 s was extracted from a 17 s trace to avoid possible blank samples at the beginning and end of the trace arising from the randomised shot instants. The section of the specified trace is extracted from the *zplot* file and an inverse Fourier transform performed using an implementation of the Fast Fourier Transform (FFT) algorithm. The program may then either write a synthetic noise section or add noise to an existing *zplot* file. The latter option is employed in these synthetic tests, and noise is added to the *stack.dat* file created in step 1. For each data trace, a random noise trace is created using the frequency spectrum obtained from the blank trace as described above and an antisymmetric random phase spectrum, which are passed to the forward FFT algorithm (the antisymmetric phase spectrum ensures that the output trace is real rather than complex). A multiplier is applied to the resulting noise trace defined by the user-specified percentage noise, which in this example is determined by the controlling script, and the noise trace is then added to the data trace. The process is then repeated for each trace and the resulting traces output in *zplot* format as *noise.dat* and *noise.hdr* which have identical trace headers to *stack.dat*.

## 3. Program and author: *alt\_zplot* (Colin Zelt, and modified by Anthony Day)

**Description:** *alt\_zplot* is a modified version of *zplot* which runs the automatic picking tool and then exits. These modifications were made solely so that the controlling script runs continuously without requiring any keyboard input. The cross-correlation automatic picking tool is used to determine the pick positions for the traces for which the incomplete pick set does not define the pick position, using those pick positions which have been defined as bracketing picks. The operation of the automatic picking tool is described in the *zplot* user documentation and hence will not be repeated here.

#### 4. Program and author: *headup* (Colin Zelt)

**Description:** As described in appendix A, in order to retain changes to the trace headers resulting from running the automatic picking tool, *headup* must be run. For the tests described in section 2.4 and the script reproduced in this appendix, after *headup* has been run, *noise.hdr* contains the true pick positions for all traces in pick word 2 whilst pick word 3 contains the true pick position for every seventh trace and the pick position determined by the automatic picking tool for every other trace.

#### 5. Program and author: *pickerror* (Anthony Day)

**Description:** This program compares the true pick positions with those obtained using the automatic picking tool, and also calculates SNR using three different time windows. The user specifies the pick word which contains the complete set of true pick positions and the frequency of bracketing picks in the following pick word (2 and 7 respectively in this example). For each trace for which a pick has been determined using the automatic picking tool, the time difference between the true and automatically determined pick position is calculated and also the SNR based on the ratio of the RMS value of the trace within 100, 200 and 300 ms time windows before and after the true pick position. These values are sent to standard output. The mean and standard deviation of the travel time pick errors and three SNR values are also determined and sent to standard output.

The controlling script redirects the output of *pickerror* to a file (*op.txt*) and uses the *grep* utility to extract the mean values of SNR calculated using all three time windows and the standard deviation of pick position error. These values are used to relate pick position uncertainty to SNR using the three SNR calculation windows. Steps 2 to 5 are then repeated using different noise levels. In this way, three pick position uncertainty versus SNR files are constructed for the three SNR calculation windows under consideration. An annotated example of a controlling script used to generate these relationships is listed below.

Appendix C: Method for determining travel time pick uncertainty versus SNR relationships

```

stack << END
/grp/poseidon/dgl3ajd/masters/zplot/hdr/           {header file path}
/grp/poseidon/dgl3ajd/masters/zplot/zgeop/        {data file path}
south111a                                         {data and header file name}
15                                                 {first trace to stack}
21                                                 {last trace to stack}
15.                                                {length of output stacked trace (s)}
2                                                  {pick word to align when stacking traces}
0.1                                                {multiplier for samples before pick}
0                                                  {band-pass filter flag: 0 = no band-pass filter, 1 = 40 Hz, 2 = 20 Hz low-pass filter}
1000                                               {number of traces to output}
1                                                  {1 = randomise output traces}
7                                                  {frequency of picks in cut down set}
END

rm snr???.txt                                     {remove old SNR files}
awk '{printf("%11s%11s\n", $1, $2)}' << END > snr100.txt
SNR Error                                         {initialise SNR files with column headings}
END
cp snr100.txt snr200.txt
cp snr100.txt snr300.txt
pcnoise='expr 400'                               {initialise value of pcnoise, percentage noise to add}
while [ $pcnoise -gt 0 ]                         {loop for several values of pcnoise}
do
    echo $pcnoise
    rm op.txt

    addnoise << END
/grp/poseidon/dgl3ajd/masters/zplot/zgeop/        {data file path}
north111b                                         {data file name}
380                                               {trace number}
1.                                                 {start time of noise trace}
15.                                                {length of noise trace}
0                                                  {band-pass filter flag}
1                                                  {1 = add noise to existing file}
./                                                 {input header file path}
./                                                 {input data file path}
stack                                             {input data file name}
$pcnoise                                         {percentage noise to add to input data file}
END

    alt_zplot                                     {run modified version of zplot}

    headup << END
noise.hdr                                         {header file name}
10                                                 {number of pick words}
END

    pickerror << END > op.txt
./                                                 {header data file path}
./                                                 {data file path}
noise                                             {data file name}
2                                                  {pick word containing true pick positions}
7                                                  {frequency of bracketing picks in following pick word}
END

    sd='grep Picking op.txt|awk '{printf("%f\n", $9)}'
    snr='grep 100ms op.txt|awk '{printf("%f\n", $6)}'
    awk '{printf("%11.6f%11.6f\n", $1, $2)}' << END >> snr100.txt
$snr $sd
END
    snr='grep '200ms window' op.txt|awk '{printf("%f\n", $6)}'
    awk '{printf("%11.6f%11.6f\n", $1, $2)}' << END >> snr200.txt
$snr $sd
END
    snr='grep '300ms window' op.txt|awk '{printf("%f\n", $6)}'
    awk '{printf("%11.6f%11.6f\n", $1, $2)}' << END >> snr300.txt
$snr $sd
END
    pcnoise='expr $pcnoise - 3'                 {reduce percentage noise to add}
done

```

The process outlined in this appendix was conducted using a number of reference traces and noise frequency spectra, with and without band-pass filtering applied as discussed in section 2.4, and the resulting pick position uncertainty versus SNR relationships archived. The files used to assign the pick position uncertainties used in the *FAST* inversion are created by finding the median pick position uncertainty versus SNR relationship for a particular OBS position, channel (vertical geophone or hydrophone) and band-pass filter. The appropriate SNR calculation window is determined for each set of stacked traces as described in section 2.4. Each pick position uncertainty versus SNR relationship which is to be included in the median calculation is then resampled at 0.5 ms (0.0005 s) intervals in pick position uncertainty using the GMT program *sample1d* called from scripts of the form:

```
cat snr1_300.txt - << END|awk '{printf("%f %f\n", $2, $1)}'|filtersnr|
sort|sample1d -H1 -I0.0005 > sorta
0.0 9999.0
END
```

*snr1\_300.txt* is an archived pick position uncertainty versus SNR relationship determined using a 300 ms SNR calculation window. *filtersnr* is a simple program to remove repeated values of pick position uncertainty which occasionally arise from the irregular shape of the pick position uncertainty versus SNR relationships and which disrupt the operation of *sample1d*. *sort* is then called to arrange the pick position uncertainty versus SNR relationship in increasing order of pick uncertainty which is required by *sample1d* to which the output of *sort* is piped in order to resample the relationship at 0.0005 s intervals. The extra line (0.0 9999.0) is added to *snr1\_300.txt* as a termination line which is recognised by *filtersnr*.

The output files are read by the program *median*. The user specifies the number of input files, which must be named *sorta*, *sortb* etc. and comprise the resampled pick position uncertainty versus SNR relationships in increasing order of pick position uncertainty. *median* determines the median pick position uncertainty versus SNR relationship and outputs it as a text file (*snr\_median.txt*) in the same format as the raw input file *snr1\_300.txt*. This file is then resampled at 5 ms intervals to create the median pick position uncertainty versus SNR files used to assign pick position uncertainties as described in appendix B.

# Appendix D

## Methods for modelling *P*–*S* mode converted arrivals

In this appendix, details of the scripts and programs employed in the *P*–*S* mode converted arrival modelling described in chapter 4 are presented as they were purpose written for this work.

### 1. Determination of horizontal geophone orientation

**Programs and authors:** *orient* and *oinst* (Anthony Day), *mapproject* and *psxy* (GMT – Wessel & Smith)

**Description:** The method for determining horizontal geophone orientation is presented in section 4.3. For each OBS location, the *orient* script (listed below) is run with the OBS ID in the format 107s passed as a parameter on the command line (see appendix B, step 3, for the significance of this ID format). The OBS latitude and longitude is extracted from the file *instllz* (listed in appendix B, step 5) and converted to *x,y* co-ordinates, which are output to the file *instxy*, using *mapproject*. The script also reads the file *w\_llte<OBS ID>* (described in appendix B, step 3) which contains the latitude, longitude, direct water-wave arrival time and a nominal travel time uncertainty for each direct water-wave arrival pick. *mapproject* is called to transform each latitude and longitude pair to *x,y* co-ordinates, and these co-ordinates plus the associated travel time are output to *waterxyt*. *oinst* is then called with the OBS ID passed as a parameter, which is used to construct the file names of the two *zplot* format horizontal geophone data files and the associated header file (formats are described in appendix A). The header file is read and traces for which a direct water-wave arrival has been picked identified from the values recorded in pick word 1. For these arrivals, the shot-receiver azimuth is calculated using the *x,y* co-ordinates of shot and receiver recorded in the files *waterxyt* and *instxy* respectively. The apparent horizontal geophone orientation is then calculated for each direct water-wave arrival by the method described in detail in section 4.3. The mean and standard deviation of these apparent orientations is then calculated.

Since the apparent orientations are in the range  $0^\circ$  to  $360^\circ$ , whenever the true average orientation is close to  $0^\circ$  or  $360^\circ$  the calculated mean may be close to  $180^\circ$  because some orientations are close to  $0^\circ$  and others are close to  $360^\circ$ . In these instances, the apparent orientations are rotated through  $180^\circ$  in order to calculate the mean and standard deviation of apparent orientation, and then rotated back. The user then has the option to repeatedly reject orientations which lie outside two standard deviations from this mean orientation. The shot-receiver azimuth and apparent orientations for the resulting dataset with outliers removed are then written to `rot.txt`. The final part of `oinst` calls the GMT routine `psxy` to create a plot of these apparent orientations versus shot-receiver azimuth similar to those shown in Fig. 4.7.

Listing of the `orient` script:

```
#!/bin/csh
'rm' instxy
'rm' waterxyt
grep $1 /grp/poseidon/dgl3ajd/masters/data/instllz | awk '{printf("%f
%f\n", $3, $4)}' | mapproject -Joa-176:40/-22:20/111/1:100000
-R177:05/-176:15/-22:35/-21:55 -C|awk '{printf("%f %f\n", $1, -1*$2)}'
> instxy
awk '{printf("%f %f %f\n", $2, $3, $4)}'
/grp/poseidon/dgl3ajd/masters/data/w_llte$1 | mapproject
-Joa-176:40/-22:20/111/1:100000 -R-177:05/-176:15/-22:35/-21:55 -C
|awk '{printf("%f %f %f\n", $1, -1*$2, $3)}' > waterxyt
oinst $1
psxy rot.txt -R0/360/0/360 -Ba30f10:"Shot-receiver azimuth":/
a30f10:"Rotation of xp axis":WSne -JX15 -Sx0.1 -X5.0 -Y-8.0 -V >
plotrot.ps
```

## 2. Determination of first motion azimuths

**Program and author:** `swmotion2` (Anthony Day)

**Description:** The analysis of first motion azimuths described in section 4.5.1 was performed using the program `swmotion2`. The user specifies the following parameters: the name of the `zplot` file containing the traces to be considered, the orientation of the horizontal geophones determined by the method described in step 1, the pick word in the `zplot` header file which contains the arrival times for the  $P$ - $S$  mode converted arrivals which are to be considered (see appendix A for the pick word assignment convention), the first and last trace to consider, the length of time window (ms) used to calculate signal strength and SNR, whether to use maximum SNR or maximum signal strength to determine first motion azimuth, and a flag to indicate whether or not a 40 Hz low-pass filter should be applied. For the

analysis described in section 4.5 a 200 ms window was used to calculate signal strength and SNR, maximum signal strength was used to identify first motion azimuth, and the low-pass filter was applied. The program reads the specified *zplot* header file and looks for  $P$ - $S$  mode converted arrival travel time picks within the specified range. For each pick, the trace data is read for the two horizontal geophones and the low-pass filter applied if the flag is set. These traces are then resolved onto a series of directions between the positive and negative  $x$ -directions at  $1^\circ$  intervals. The signal strength and SNR is calculated for the specified time window for each orientation. The orientation of the maximum signal strength, or SNR as appropriate, is selected as the first motion azimuth unless the maximum SNR is less than 1, in which case the trace is discarded. This method was used to generate the data plotted in Figs. 4.15 and 4.16 for in-line shots and Fig. 4.19 for off-line shots. The mean orientation is also calculated for all traces for which a valid first motion orientation has been determined. This data is summarised in Tables 4.3 and 4.4 for in-line shots.

